3D SEISMIC CHARACTERISATION OF IGNEOUS SILL COMPLEXES IN SEDIMENTARY BASINS: NORTH-EAST ATLANTIC MARGIN

DORTHE MØLLER HANSEN

Submitted in partial fulfilment of the requirements for the degree of Ph.D.

Cardiff University

June 2004

ProQuest LLC
789 East Eisenhower Parkway
P.O. Box 1346
Ann Arbor, MI 48106-1346

DECLARATION

This work has not previously been accepted in substance for any degree and is not being concurrently submitted in candidature for any degree.

Signed.....(candidate)

Date 29th June 2004

STATEMENT 1

This thesis is the result of my own investigations, except where otherwise stated.
Other sources are acknowledged by footnotes giving explicit references. A bibliography is appended.

Signed.....(candidate)

Date 29th June 2004

STATEMENT 2

I hereby give consent for my thesis, if accepted, to be available for photocopying and for inter-library loan, and for the title and summary to be made available to outside organisations.

Signed.....(candidate)

Date 29th June 2004

SUMMARY

This thesis compiles the results of a 3D seismic-based study of the emplacement mechanics of igneous sills and sill complexes intruded into sedimentary basins along the NE Atlantic Margin. Detailed interpretation of the geometry, structural and stratigraphic context, and effects of igneous sill intrusion in four case-study areas has been carried out in order to further our current understanding of sill emplacement and magma transport in the upper crust in general.

The 3D seismic mapping has allowed for igneous sill complexes to be imaged in three dimensions for the first time. These complexes are found to form highly interconnected networks that cover many kilometres of vertical section (~8 km). Based on the interpretation a new model for the construction of sill complexes is proposed. In this model a sill complex builds up from deeper to shallower levels with sills intruded at one stratigraphic level acting as feeders for sills intruded at shallower levels. This model for sill complex construction suggests that these complexes are emplaced within <10,000 years.

The interpretation has revealed that sills adopt a wide range of geometrical styles, ranging from near-concordant sheet-like forms to complex discordant forms. Sills intruded into homogeneous and undeformed basin fills often adopt a saucer-shaped geometry, whilst more complex geometries develop when magma intrudes heterogeneous and structurally deformed sediments. When intruded at shallow depth (<500 m) sills may behave partly as sills and partly as lava flows, developing lobate and flow ridge morphologies. This is suggested to relate to the low resistance to flow offered by the poorly consolidated host-rock at shallow depth.

Interpretation of hydrothermal mounds and jack-up structures formed during sill intrusion has allowed for the timing of sill emplacement to be constrained in the four case-study areas. This has revealed that several discrete phases of intrusion took place during the Paleocene and earliest Eocene.

ACKNOWLEDGEMENTS

First and foremost I would like to thank my supervisor at Cardiff University, Joe Cartwright, for giving me the opportunity to undertake this research and for providing me with constant encouragement and inspiration.

I am grateful to Shell Expro UK for sponsoring the project and providing me with data. In particular, Stephen Wright and Dave Thomas deserve thanks for getting the project off the ground and for their subsequent input. David Owen and Jo Bagguley are thanked for helping out with data. Data contribution from Norsk Hydro is also gratefully acknowledged.

I am indebted to the Danish Research Agency and Holger Lykke-Andersen (University of Aarhus, Denmark) for their support, which has made my time as a PhD student much more flexible, enjoyable, and rewarding than it would otherwise have been.

Neil Ferguson, Duncan Irving, and Gwen Pettigrew are thanked for helping out with countless computer problems. Sverre Planke (Volcanic Basin Petroleum Research, Norway), David Leaman (University of Tasmania, Australia), and Julian Marsh (Rhodes University, Grahamstown, South Africa) are thanked for sharing invaluable field guides and James Trude and Susanne Frederiksen are thanked for helping out in the field. Deirdre Commins and Mairi Nelson are thanked for sharing their fieldwork with me and introducing me to the splendours of the Canyonlands, Utah.

Finally, I would like to thank my friends and family for their support, encouragement, and patience throughout my PhD time in Cardiff. In particular, Jez, Mads, and Valente are thanked for their ability to distract me from work and for many superb hours spent mountain biking, hill walking, BBQing, and enjoying the hospitality of the Chapter - without them my sanity would most likely have been long gone.

CONTENTS

CHAPTER 3: THE IGNEOUS COMPLEX OF TRANCHE 67 (NORTH-EASTERN FAEROE-SHETLAND BASIN)

LIST OF FIGURES

Chapter 1: Introduction

Chapter 2: 3D seismic interpretation of igneous sills in sedimentary basins

Chapter 3: The igneous complex of Tranche 67

Chapter 4: The igneous complex of the Solsikke survey area

Chapter 5: The igneous complex of Tranche 38

Chapter 6: Extrusive mound structures

Chapter 7: Summary and discussion

LIST OF TABLES

CHAPTER 1: INTRODUCTION

1.1 Rationale

This PhD project uses 3D seismic data in a novel way to address the problem of igneous intrusion in sedimentary basins in order to improve our understanding of the fundamental processes involved during sill emplacement.

The mechanics of emplacement of igneous sills in sedimentary basins is of great importance for the general problem of magma transport in the upper crust and for the impact of magma systems on the diagenetic and hydrothermal regimes in sedimentary basins. They are also important to understand in relation to hydrocarbon exploration along volcanic rifted margins as they have the potential to influence migration pathways, compartmentalise reservoirs, and influence depositional topography and trap formation through hydraulic elevation of the overburden.

Igneous sills have been studied at outcrop for more than a century (e.g. du Toit, 1920; Tweto, 1951, Francis, 1982). However, many questions related to their geometry, mode of emplacement, and relationship to their host rocks are still unanswered. Many of these questions are unresolved because of the inadequacy of the two-dimensional sampling afforded by outcrop-based studies, and the limited scale of semi-continuous exposure even in classical field areas such as the Karoo of South Africa.

Igneous sills intruded into sedimentary basin fills are strikingly well imaged on seismic data because of a significant difference in the acoustic properties of the host rocks and the intrusions. 3D seismic surveys, therefore, offer an outstanding opportunity to re-evaluate previously proposed field-based models and further the current understanding of sill emplacement mechanics with the three-dimensional and scale advantages that 3D seismic data offer.

This chapter provides a list of aims and summarises the significance of this PhD research project. A background to the geological setting of the study area and a short summary of previous work on igneous sills and sill complexes are also provided. The methods used in this study are briefly described and, finally, the thesis layout is outlined.

1.2 Aims of study

The overall aim of this PhD project is to undertake a detailed 3D seismic characterisation of igneous intrusion and associated seismic-scale phenomena in basins along the NE Atlantic Margin in order to improve our current understanding of the fundamental processes involved during shallow-level sill emplacement in sedimentary basins and aid in our recognition and prediction of igneous intrusions and their associated effects in (hydrocarbon prone) sedimentary basins.

This overall aim is tackled by systematically addressing a number of key aims within four case-study areas. These key aims are:

- To account for the three-dimensional geometry of igneous sill complexes. Special emphasis will be put on investigating the importance of sill junction relationships and the kinematics behind vertical and lateral emplacement of sill complexes
- To define and account for the typical geometrical styles of sills observed on 3D seismic data and discuss the controls and kinematics behind their emplacement
- To evaluate previous models for saucer-shaped sill emplacement and to further our understanding of the emplacement of this unique geometrical style of sill
- To evaluate the structural and stratigraphic controls upon emplacement and geometry of igneous sills
- To determine how space is created for igneous sills during emplacement
- To develop methods for constraining timing of sill emplacement independent of radiometric dating and based on this evaluate the timing of intrusive magmatism along the NE Atlantic Margin
- To account for any seismically resolvable hydrothermal effects
- To assess the implications of igneous sill intrusion and associated effects in relation to hydrocarbon exploration in sedimentary basins along volcanic margins

In order to address these aims, four 3D seismic datasets, provided by industry sponsors (Shell UK and Norsk Hydro), from volcanic basins along the NE Atlantic Margin have been interpreted (Fig. 1.1). The datasets are from the Møre Basin (Solsikke survey), Faeroe-Shetland Basin (T67 and T4), and the NE Rockall Basin (T38) where igneous sills of Paleocene-Eocene age are intruded into Upper Cretaceous and Paleocene sediments.

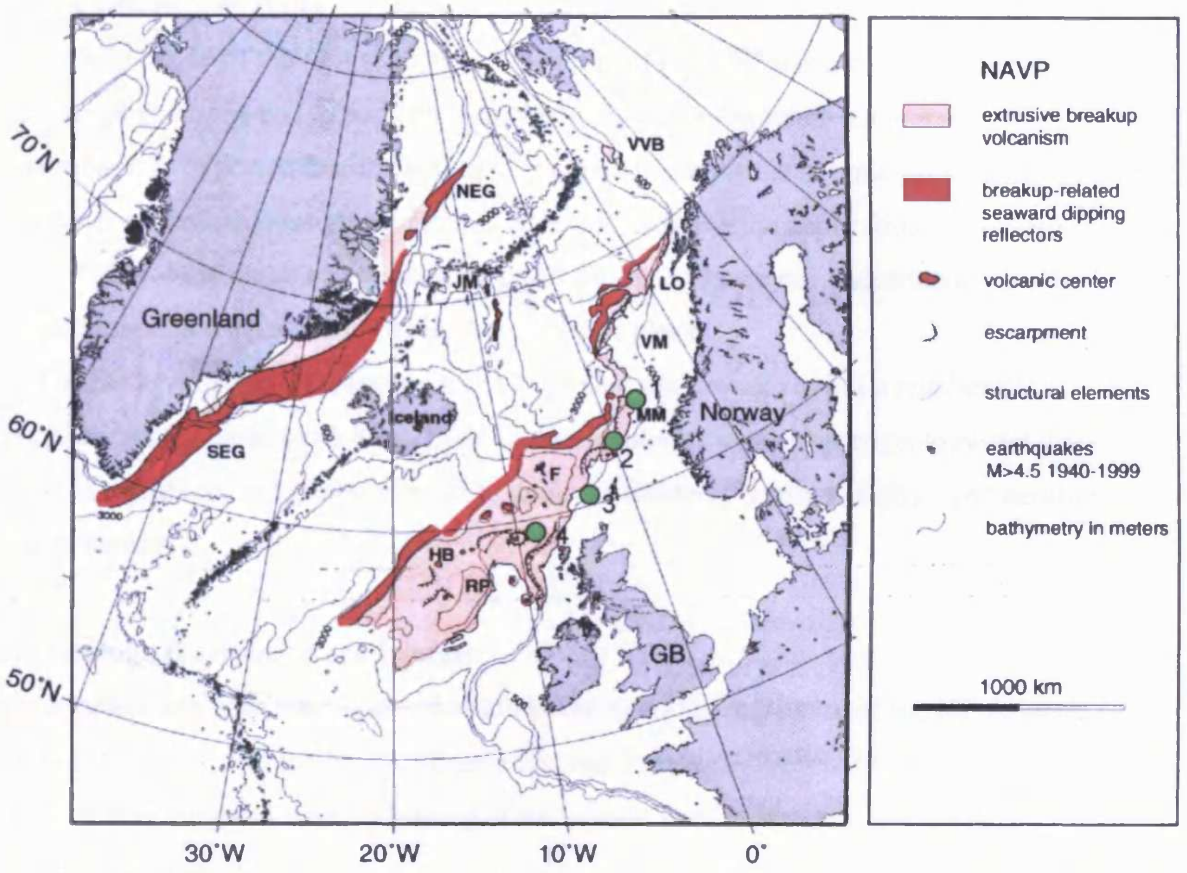

Fig. 1.1 Map of the North Atlantic Igneous Province showing the location of case-study areas (1: Solsikke; 2: T67; 3: T4; 4: T38) and distribution of break-up related volcanics. Modified from Berndt (2000).

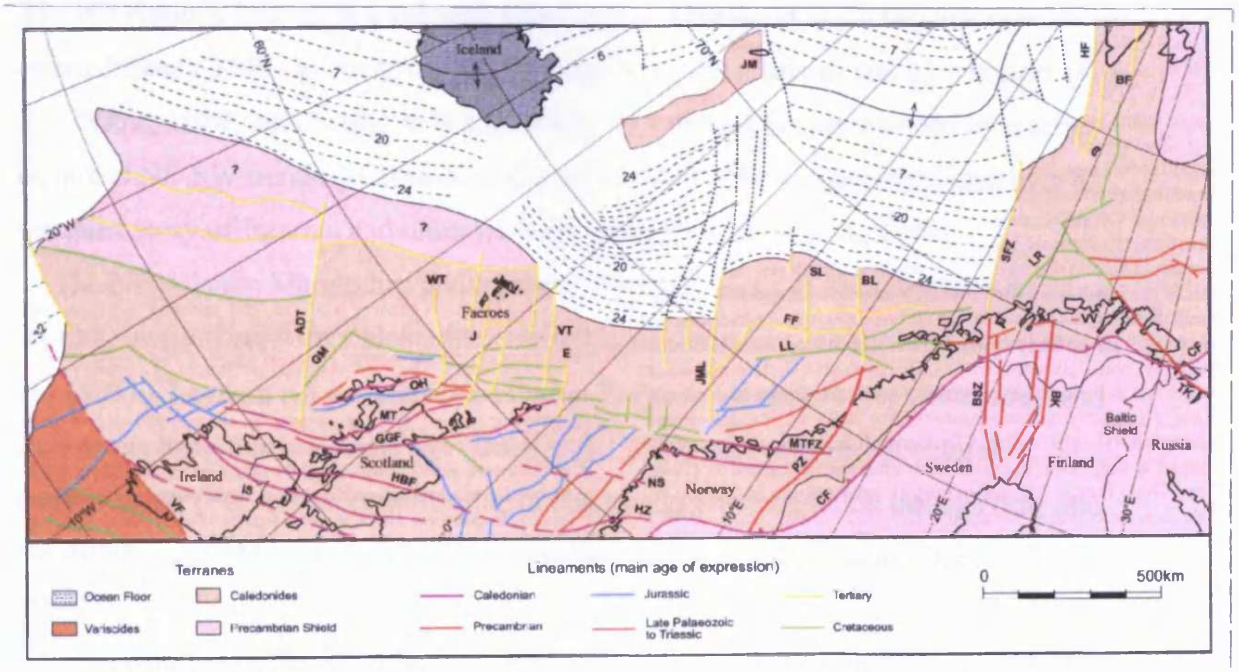

Fig. 1.2 Map showing the basement terranes and structural lineaments along the NE Atlantic Margin. From Dore et al. (1999).

1.3 Significance of study

This study is one of the first to explore the application of 3D seismic data to the study of igneous phenomena and as such has important value for further development in this direction. It is expected that the ability to image sill complexes in three-dimensions and at greater scale than possible at outcrop, available through the application of 3D seismic data, will provide much new insight that will further advance our understanding of the emplacement and significance of igneous sill complexes.

The furthering of our understanding of igneous sill complexes has a number of implications for basin modelling, hydrocarbon exploration, and hydrogeology and this study is, therefore, of general interest beyond the fields of igneous geology and seismic interpretation.

1.4 Geological setting of study area

This section provides a brief introduction to the structural evolution of the NE Atlantic Margin (Fig. 1.1) and the North Atlantic Igneous Province (NAIP). The more detailed geological setting and igneous history of each of the case-study areas will be presented within individual chapters.

1.4.1 Structural evolution of the NE Atlantic Margin

The NE Atlantic Margin is a volcanic rifted margin (Planke et al., 2000) that extends for approximately 2500 km covering the Norwegian, Faeroes, British and Irish sectors (Fig. 1.1; White, 1988; Smallwood & White, 2002). The margin is characterised by a series of linked NE-SW trending Cretaceous-Cenozoic Basins that are superimposed over a complex array of Jurassic and older rift basins (Fig. 1.2; Dore et al., 1999).

The NE Atlantic Margin has undergone multiple extensional episodes spanning a *ca.* 350 My interval between Caledonian consolidation and Early Eocene break-up (Dore et al., 1999). The main rift periods are of Permo-Triassic, Jurassic, Early Cretaceous, and Late-Cretaceous-Early Eocene age (Dore et al., 1999). The resultant structural configuration (Fig. 1.2) is complex due to changes in stress direction through time and the influence of older structures on the development of younger basins (Dore et al., 1999).

The evolution of the NE Atlantic is summarised in Fig. 1.3 (from Dore et al., 1999). Permo-Triassic extension immediately following the formation of Pangea exploited the Caledonian fold belt (Dore et al., 1999; Naylor et al., 1999). During the Jurassic an E-W

extensional stress field was established, possibly related to seafloor spreading in the northern Tethys and N-S trending Jurassic basins (Halten Terrace, Viking Graben and Porcupine Basin; Dore et al., 1999) were formed. These early rift systems were overprinted by Early Cretaceous rifting, which reflected a change in the stress field to NW-SE due to northward propagation of central Atlantic spreading (Dore et al., 1999). This NW-SE trending stress field was maintained until the time of seafloor spreading in the North Atlantic in the Late Paleocene and resulted in the development of a number of deep Cretaceous-Cenozoic basins (e.g. Møre Basin, Faeroe-Shetland Basin, and NE Rockall Basin; Dore et al., 1999). Paleocene extension was associated with major magmatism and thermal uplift and culminated with continental break-up and the onset of active seafloor spreading within the NE Atlantic Ocean in the latest Paleocene-Early Eocene (e.g. Andersen 1988; White 1988; White & McKenzie 1989; Ritchie & Hitchen 1996; Naylor et al. 1999; Ritchie et al. 1999). Continental break-up and the onset of seafloor spreading is believed to be associated with the impingement of the proto-Icelandic plume at the base of the lithosphere (Naylor et al., 1999; Smallwood & White, 2002).

Three main phases of Cenozoic compression have been recognised: (1) Late Paleocene-Early Eocene, (2) Oligocene, and (3) Middle to Late Miocene. These events have been linked to ocean spreading in the NE Atlantic and ridge-push associated with Alpine tectonics (Dore & Lundin, 1996; Boldrell & Andersen, 1999).

Following Palaeocene and Early Eocene break-up and magmatism, the NE Atlantic region underwent passive thermal subsidence during the Middle and Late Eocene. Subsequent regional Neogene uplift shaped the final basin configuration seen at present (Doré et al. 1999).

1.4.2 The North Atlantic Igneous Province

Continental break-up in the NE Atlantic during the Late Paleocene-Early Eocene was associated with extensive extrusive and intrusive volcanism, forming the North Atlantic

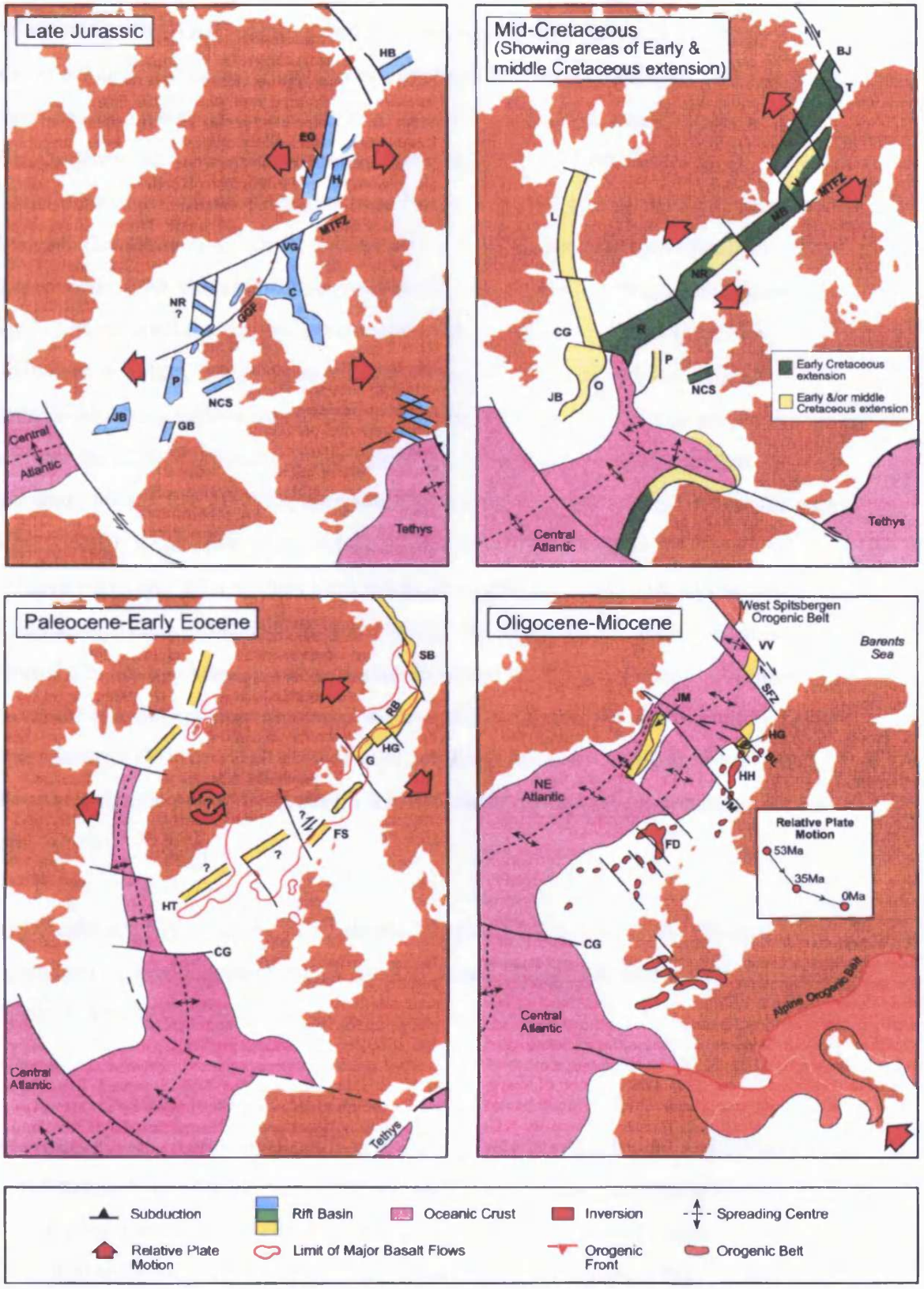

Fig. 1.3 Maps showing the evolution of the NE Atlantic. From Dore et al. (1999).

Igneous Province, NAIP (Fig. 1.1; White, 1988; Coffin & Eldholm, 1992; Smallwood & White, 2002). The NAIP is comprised of complex intrusive networks of largely concordant sills and near-vertical dykes intruded into Upper Cretaceous and Paleocene clay-dominated basin fills and lava flows extruded across vast areas (Ritchie et al., 1999; Naylor et al., 1999; Planke et al., 2000; Berndt et al., 2001).

The onset of volcanism throughout the North Atlantic region was at approximately 62-61 Ma (Smallwood & White, 2002) and volcanism continued sporadically until the Early Eocene, with the majority of emplacement taking place within a time period of only 2-3 My around the time of continental break-up at 56-53 Ma (White 1988; Smallwood & White, 2002). Seaward dipping reflectors (SDR) are seen almost continuously along both margins of the NE Atlantic Ocean. The pile of extrusive basalts that form the SDR is typically 3-6 km thick and the zone covered by the SDR commonly 50-100 km in width, comprising in excess of 1 million km^3 of basaltic rocks (White, 1988). It has been estimated that the NAIP comprises up to 2 million km^3 of extrusive rocks and 5-10 million km^3 of intrusive igneous rocks (sills, dykes, and underplating, White, 1988; White et al., 1992). The rapid and extensive volcanism within the NAIP has been linked to the development of an anomalously hot plume at the base of the lithosphere that is inferred to have influenced an area approximately 2000 km in diameter (White, 1988; Ritchie et al., 1999; Smallwood & White, 2002). At present this mantle plume lies beneath Iceland where it continues to generate volcanic rocks.

The igneous activity along the NE Atlantic Margin (Figs. 1.1 and 1.4) falls into three categories; (1) flood basalts, (2) sill complexes, and (3) igneous centres and these are described in the following sections.

1.4.2.1 The Faeroe Plateau Lava Group

The Faeroe Plateau Lava Group, FPLG (Ritchie et al., 1999) is found both onshore in the Faeroes and offshore in the Faeroe-Shetland Basin and is described in this section.

Onshore in the Faeroes wells have encountered a thick (> 5 km) continental flood basalts unit with minor intrusive and sedimentary units (Waagestein et al., 1984). The unit has been informally subdivided into a lower, a middle, and an upper series (Rasmussen & Noe-Nygaard, 1969). The age of the FPLG is poorly constrained with K-Ar ages ranging between 50-63 Ma, with 55-61 Ma probably more correctly indicating

the age (Ritchie et al., 1999). It is generally believed to have been extruded during C26r-C24r, with the Lower series extruding through C26r-C24r time followed by extrusion of the Middle and Upper series during C24r time (Naylor et al., 1999; Kiørboe, 1999; Waagestein et al., 2002).

The *Lower series* is up to 3 km thick and comprised of subaereial tholeiitic basalts that occur within flows exhibiting average thicknesses of around 20 m (Waagestein, 1988). The lower series basalts are thought to have been fed from kilometre long NW-SE trending fissures (Ritchie et al., 1999). The Lower series has recently been dated at 56.5±1.3 Ma to 58.9±1.3 Ma based on K/Ar whole rock analysis (Waagestein, et al., 2002), whilst recent dating based on palynoflora extracted from flow top soils and laterally continuous coals suggests dates of 57.5-60.5 Ma (Ellis et al., 2002; Jolley et al., 2002). The Lower series is separated from the overlying Middle series by an unconformity marked by the development of a terrestrial sequence (Waagestein, 1988; Naylor et al., 1999). The *Middle series* has an estimated thickness of around 1400 m and consists primarily of thin, subaerial, often vesicular tholeiitic basalts (Rasmussen & Noe-Nygaard, 1990). These basalts are thought to have been fed from shield volcanoes and vents (Rasmussen & Noe-Nygaard, 1990). The *Upper series* is more than 900 m thick and composed of subaerial, tholeiitic basalts with average flow thickness of approximately 10 m (Ritchie et al., 1999; Ellis et al., 2002). A hiatus has not been identified between the Middle and Upper series and it is considered unlikely that these would be identified as separate units on offshore data (Naylor et al., 1999).

Offshore, the Faeroe Plateau Lavas have been mapped into the Faeroe-Shetland Basin on seismic data. The lavas in the Faeroe-Shetland Basin appear to have been erupted from a number of extensive fissure systems into a largely subaerial environment (Naylor et al., 1999). The Faeroe-Shetland Escarpment (Figs. 1.4 and 1.5), which forms a prominent feature along the western margin of the Faeroe-Shetland Basin, has been interpreted as a lava delta that formed as a result of eruption of subaerial lavas into a marine basin, with the delta foresets indicating the water depths at the time of eruption (Kiørboe, 1999; Naylor et al., 1999). Correlation with the onshore FPLG suggests that the Faeroe-Shetland Escarpment is comprised of lavas of the Middle and Upper series (Naylor et al., 1999; Ritchie et al., 1999) and that the location of the escarpment is approximately coincident with the south-eastern extent of the underlying Lower series (Ritchie et al., 1999).

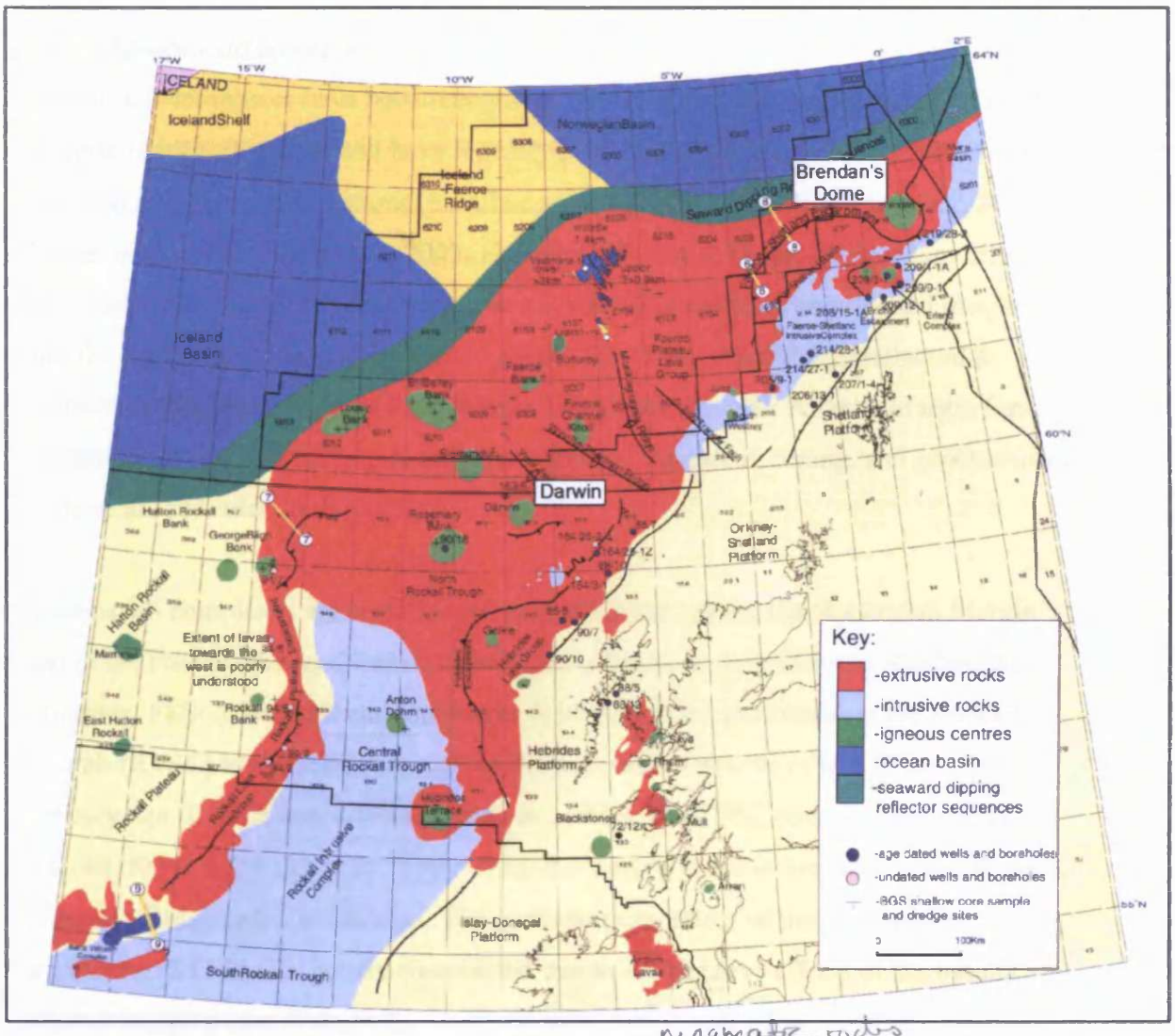

Fig. 1.4 Distribution of Late Cretaceous-Early Tertiary magmatism in the Rockall Trough, Faeroe-Shetland Basin, and surrounds. Disregard shown annotated line-sections. From Ritchie et al. (1999).

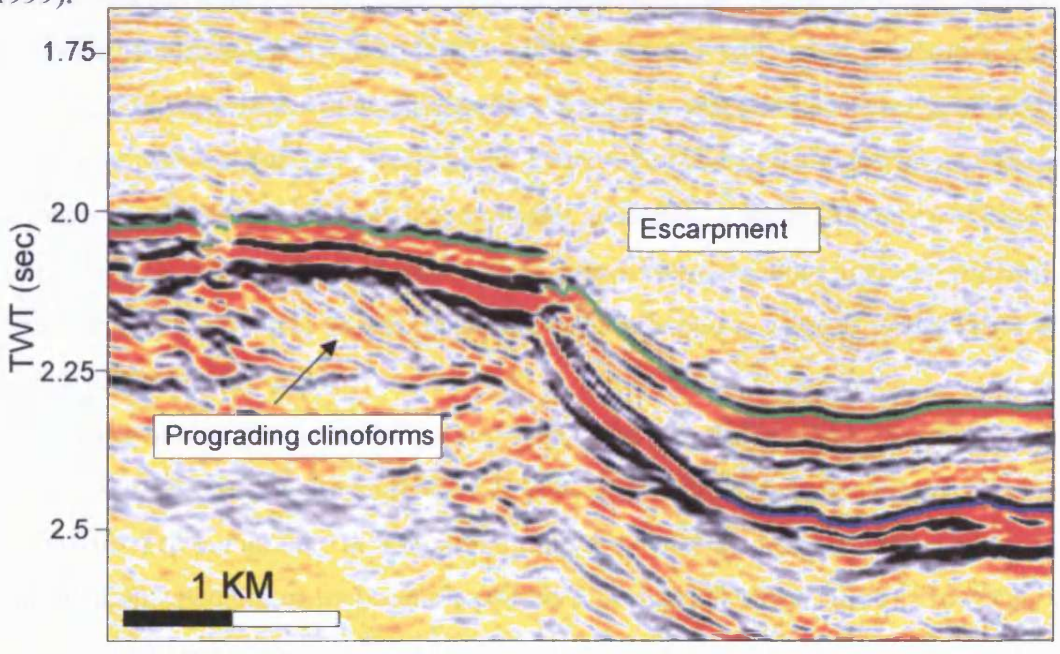

Fig. 1.5 Seismic section from the T67 3D seismic survey, showing the cross-sectional geometry of the Faeroe-Shetland Escarpment in the Brendan's Dome area.

1.4.2.2 Igneous sill complexes

Igneous sill complexes have been recognised on seismic data along the length of the NE Atlantic Margin (Fig. 1.4) and have recently been described in detail from 3D seismic in a limited number of publications (Smallwood & Maresh, 2002; Bell & Butcher, 2002; Davies et al., 2002; Trude et al, 2003; Hansen et al., 2004; Trude, 2004). Many sills have also been encountered during exploration drilling and this has provided insight into the composition, age, and physical properties of the intrusives (Smallwood & Maresh, 2002). The igneous sill complexes found along the NE Atlantic Margin form the main basis for this thesis and an introduction to the extent, timing, and geochemistry of these are provided in this section.

Igneous sill complexes are well imaged on seismic data along the Norwegian Margin and in the Faeroe-Shetland Basin (collectively referred to as the Faeroe-Shetland Sill Complex, FSSC), whilst their distribution is more poorly constrained in the Rockall Trough (RTSC) to the south-west due to the presence of extensive lava flows of early Tertiary age (Ritchie et al., 1999; Tate et al., 1999). The FSSC covers an area of more than 40,000 km^2 (Naylor et al., 1999) from the Vøring Basin to the north to the Wyville-Thomson Ridge to the south-west. The north-western extent of the sill complex underlying the FPLG is poorly constrained due to the negative effects of the basalts on seismic imaging (see Chapter 2).

The sills of the FSSC are primarily intruded into mud-dominated sediments of the Upper Cretaceous with some sills having been emplaced into Paleocene strata (Naylor et al., 1999; Smallwood & Maresh, 2002). The sills adopt a wide range of geometrical styles from fully concordant sheet-like bodies to highly complex discordant geometries (Hansen et al., 2004). The sills often exhibit upward concave cross-sectional geometries with relatively flat bases and limbs transgressing at angles of approximately 41° (see Chapter 7). When viewed in three dimensions, these concave shapes are often found to exhibit extraordinary saucer-shaped geometries (Smallwood & Maresh, 2002; Trude et al., 2003; Hansen et al., 2004).

The timing of intrusion is uncertain with published radiometric dates ranging between 50-80 Ma (see review in Ritchie & Hitchen, 1996). This is related to introduction of errors into the radiometric dating method due to alteration and poor sampling of sills penetrated by boreholes (Gibb & Kanaris-Sotiriou, 1988). However, most intrusive magmatism is believed to have been concentrated between 55-53 Ma,

approximately synchronous with the onset of spreading in the North Atlantic in the latest Paleocene and Early Eocene (Ritchie & Hitchen, 1996). The intrusion of sills is considered to have been synchronous with the extrusion of the Middle and Upper series basalts (Ritchie et al., 1999). Recently, 3D seismic-based studies have allowed for dating of subsurface igneous sills independent of radiometric dating (Davies et al., 2002; Trude, 2003). These studies suggest that sills were intruded at approximately 54.6-55 Ma in the T61/62 survey area of the central Faeroe-Shetland Basin overlying the Corona Ridge. The techniques used in these studies will be described in detail in chapters 5, 6, and 7.

Geochemical analysis of sills of the FSSC has established that they are dolerites to olivine-dolerites with modal mineralogy that indicate that the sills are tholeiites (Gibb & Kanaris-Sotiriou, 1988). Based on their content of light rare-earth elements they further classify as T-type Mid Ocean Ridge Basalts (MORB) that are transitional between N-type (normal) and E-type (enriched or plume-type) MORB (Gibb & Kanaris-Sotiriou, 1988) They vary in grain size from very fine, chilled dolerite to gabbroic or pegmatic dolerite (Gibb & Kanaris-Sotiriou, 1988). Major- and trace-element chemistry suggests that the sills resemble the Upper Basalt Series, but differ significantly from the Lower and Middle series lavas (Gibb & Kanaris-Sotiriou, 1988).

As mentioned above the sill complexes of the Rockall Trough region (RTSC) are poorly imaged on seismic data, but they appear to form a belt of igneous rocks from the Wyville-Thomson Ridge to the north to at least 54° N in the SW (Ritchie et al., 1999). The sills are intruded into Upper Cretaceous and Paleocene sediments (Corfield et al., 1999) and by analogy with the FSSC Ritchie et al. (1999) suggested that the RTSC are probably of earliest Eocene age. However, in the NE Rockall Basin and North Rockall Trough it has been suggested that extensive magmatic activity took place from at least the latest Cretaceous until the Early Eocene (Tate et al., 1999).

1.4.2.3 Igneous centres

A number of igneous centres are found along the NE Atlantic Margin (Fig. 1.4). These complexes are generally made up of large basic plutonic bodies that are linked to overlying lava fields (Ritchie et al., 1999). The centres vary in age from Late Cretaceous (Anton Dohrn and Rosemary Bank of the northern Rockall Trough) to Paleocene in age, with the vast majority of centres forming in the Paleocene (Ritchie et

al., 1999). The Paleocene igneous centres include Brendan's Dome (Smythe et al., 1983; Hodges et al., 1999) located in the north-eastern Faeroe-Shetland Basin and the Darwin Complex (Tate et al., 1999) located on the western margin of the NE Rockall Basin. These two igneous centres are relevant in relation to this particular study and further reference to these will be made in chapters 3 and 6, respectively.

1.4.2.4 Onshore igneous activity

Igneous activity has also been described and dated from a number of onshore areas along the NE Atlantic Ocean. The onshore lava series of the Faeroe Islands were described in section 1.4.2.1. This section provides a brief summary of the onshore igneous activity of the onshore British Tertiary Igneous Province and igneous activity in NE Greenland.

The British Tertiary Igneous Province (BTIP) is composed of continental lava sequences, intrusive centres, lava shields, dyke swarms, and sill complexes (Bell & Williamson, 2002). The igneous activity appears to have been intermittent and spanned a period from *ca.* 60.5 Ma to 55 Ma (Bell & Williamson, 2002) with the majority of igneous activity on the Isles of Skye and Mull taking place during Chron C26r (Chambers & Pringle, 2001). The lava fields of the Isles of Skye and Mull take the form of stratified sequences dominated by subaerial facies lavas of alkali olivine basalt to trachyte composition with less abundant tholeiitic basalts (Thompson, 1982).

Evidence from the East Greenland margin based on ^{40}Ar-^{39}Ar dating suggested that there were three main phases of igneous activity (Tegner et al., 1998). The first phase occurred pre break-up (62-59 Ma) and produced lavas and dykes. The second phase took place during break-up (57-54 Ma) and produced lavas, dykes, sills, and some gabbros. The third and final phase occurred post break-up (50-47 Ma) and produced gabbros, dykes, and rare lavas. Tegner et al. (1998) relate these three phases to plume impact under central Greenland (1), continental rifting and break-up (2), and plume passage of the plume beneath the East Greenland rifted margin.

Sills intruded into the Paleozoic-Mesozoic Jameson Land Basin in East Greenland are of basaltic composition (quartz tholeiitic dolerites) and appear to be most frequent within Lower and Upper Jurassic shales, but are also found within Triassic and Permian strata. They are generally thin (10-15 m) along the basin margin (Larsen & Marcussen, 1992), but in the deeper parts of the basin the sills are thicker, with sills up to 300 m thick intruding into the deep central part of the basin (Larsen & Marcussen, 1992). The

sills transgress stratigraphy from the deep part of the basin towards the basin margin where they intrude at younger stratigraphic levels (Larsen & Marcussen, 1992). Radiometric dating suggests that the sills were emplaced within magmatic Chron C24r (Larsen & Marcussen, 1992).

1.5 Igneous sills and sill complexes

Igneous sills have been studied at outcrop for more than a century and many field areas provide good insight into the geometry of sill complexes. Numerous models have been published to account for the geometry and emplacement of igneous intrusions at shallow level, (du Toit, 1920; Loewinson-Lessing, 1936; Tweto, 1951; Bradley, 1965; Leaman, 1975; Francis, 1982; Lister & Kerr, 1991; Kerr & Lister, 1995; Chevallier & Woodford, 1999) as well as the nature of associated hydrothermal systems (e.g. Einsele et al., 1980; Boulter, 1996). However, as pointed out in section 1.2 and 1.3 a number of issues remain poorly understood.

This section provides an introduction to previously published work on igneous sills and sill complexes in order to illustrate the general state of knowledge and the rationale behind the aims of the study. Much of the published literature will be described in relevant discussion sections throughout the thesis and this section is meant as a brief introduction to some key themes within the published literature rather than an in-depth review of the existing igneous sill literature.

1.5.1 Origin and occurrences of igneous complexes

Igneous complexes are commonly formed during the process of continental rifting and the development of volcanic rifted margins (e.g. Coffin & Eldholm, 1992; White, 1992; Planke et al., 2000). This relationship is due to the decompression and partial melting of the mantle as it rises beneath the stretched and thinned continental lithosphere (White, 1992). Typically, several million km^3 of igneous rocks are produced within a few millions years on volcanic continental margins during break-up, of which it is estimated that approximately a quarter is extruded, whilst the remainder underplates or intrudes the crust (White, 1992).

Igneous sill and dyke complexes of different ages are known from numerous field areas around the world (Fig. 1.6). They are primarily comprised of homogeneous tholeiitic basaltic extrusives and tholeiitic dolerite intrusives (Planke et al., 2000) that form well-preserved exposures due to their greater resistance to erosion than their

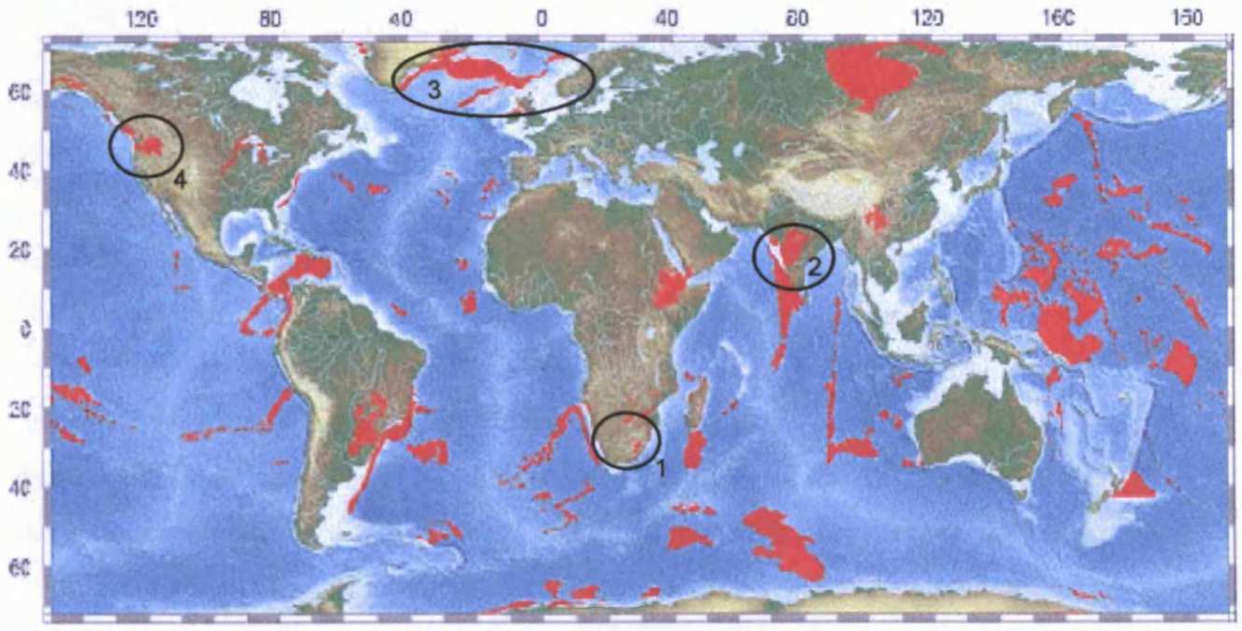

Fig. 1.6 Large Igneous Provinces of the world. 1: Karoo, South Africa; 2: Deccan Traps, India; 3: North Atlantic Igneous Province; 4: Columbia River Basalts, USA. From www.geolsoc.org

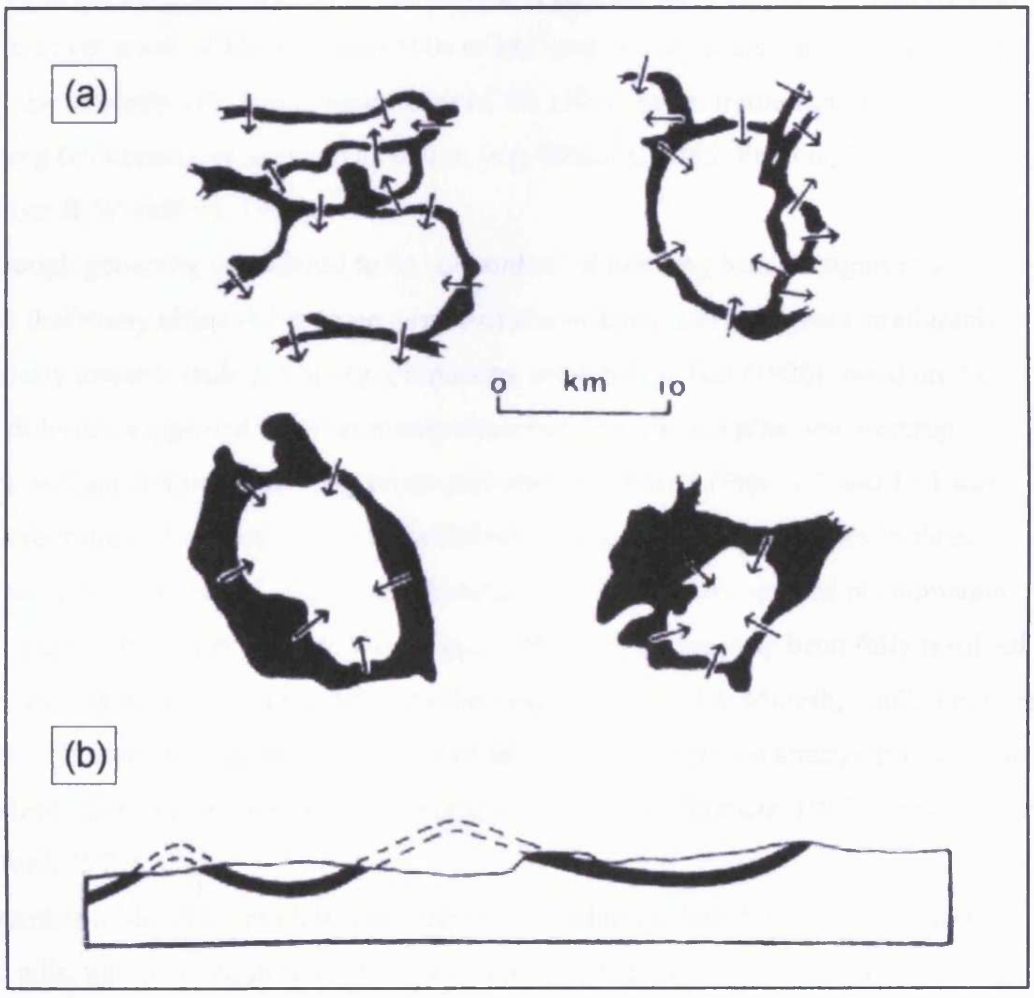

Fig. 1.7 Outcrop patterns of dolerite sills in the Karoo. (a) Map showing ring shaped outcrop pattern (du Toit, 1920). (b) Cross-section showing apparently undulating cross-sectional geometry (Bradley, 1965).

sedimentary host-rocks. Some of the world's most famous igneous provinces include the Karoo of South Africa, the Deccan Traps of India, The North Atlantic Igneous Province, and the Columbia River Basalts of North America (Coffin & Eldholm, 1992).

1.5.2 Characteristics of igneous sills

The geometry of igneous sills is a three-dimensional problem. The geometrical characteristics described in this section have all been extracted from two-dimensional outcrops where the full geometrical context of the sills cannot be resolved. The full three-dimensional geometry of sills can be obtained from 3D seismic data and one of the major contributions of this study is expected to be a better constraint on the variety of different geometrical styles of sills and factors that control their development.

Igneous sills constitute one type of intrusive igneous body that is traditionally distinguished from other types (e.g. dykes and laccoliths) by being sheet-like, concordant to bedding, and exhibiting a large length-to-thickness ratio (Pollard & Johnson, 1973; Press & Siever, 1994; Bell & Butcher, 2002). They have generally been found to cover areas of 10s and even 100s of km^2 and to vary in thickness from <1-350 m with the majority exhibiting thicknesses of 50-150 m and extreme examples exhibiting thicknesses of as much as 600 m (e.g. Bradley, 1965; Francis, 1982; Chevallier & Woodford, 1999).

Although generally considered to be concordant, it has long been recognised at outcrop that many sills exhibit some degree of discordance and transgress stratigraphy, particularly towards their periphery. Pioneering work by du Toit (1920) based on the Karoo dolerites suggested that commonly observed ring-shaped planview outcrop patterns and apparently undulating cross-sectional geometries (Figs. 1.7 and 1.8) was the outcropping expression of sills that exhibited saucer-shaped geometries in three dimensions. Saucer-shaped sills have subsequently become a recognised phenomenon (e.g. Francis, 1982; Chevallier & Woodford, 1998) and has recently been fully resolved in three-dimensions from 3D seismic studies (e.g. Smallwood & Maresh, 2002; Trude et al., 2003; Hansen et al., 2004). The limbs of such saucers cross-cut stratigraphy and the sills exhibit diameters between 2-15 km (e.g. du Toit, 1920; Francis, 1982; Chevallier & Woodford, 1999).

A number of different models have been proposed to explain the origin of saucer-shaped sills, but their origin remains unresolved. These previous models will be described and discussed in detail as part of one of the major points in the final

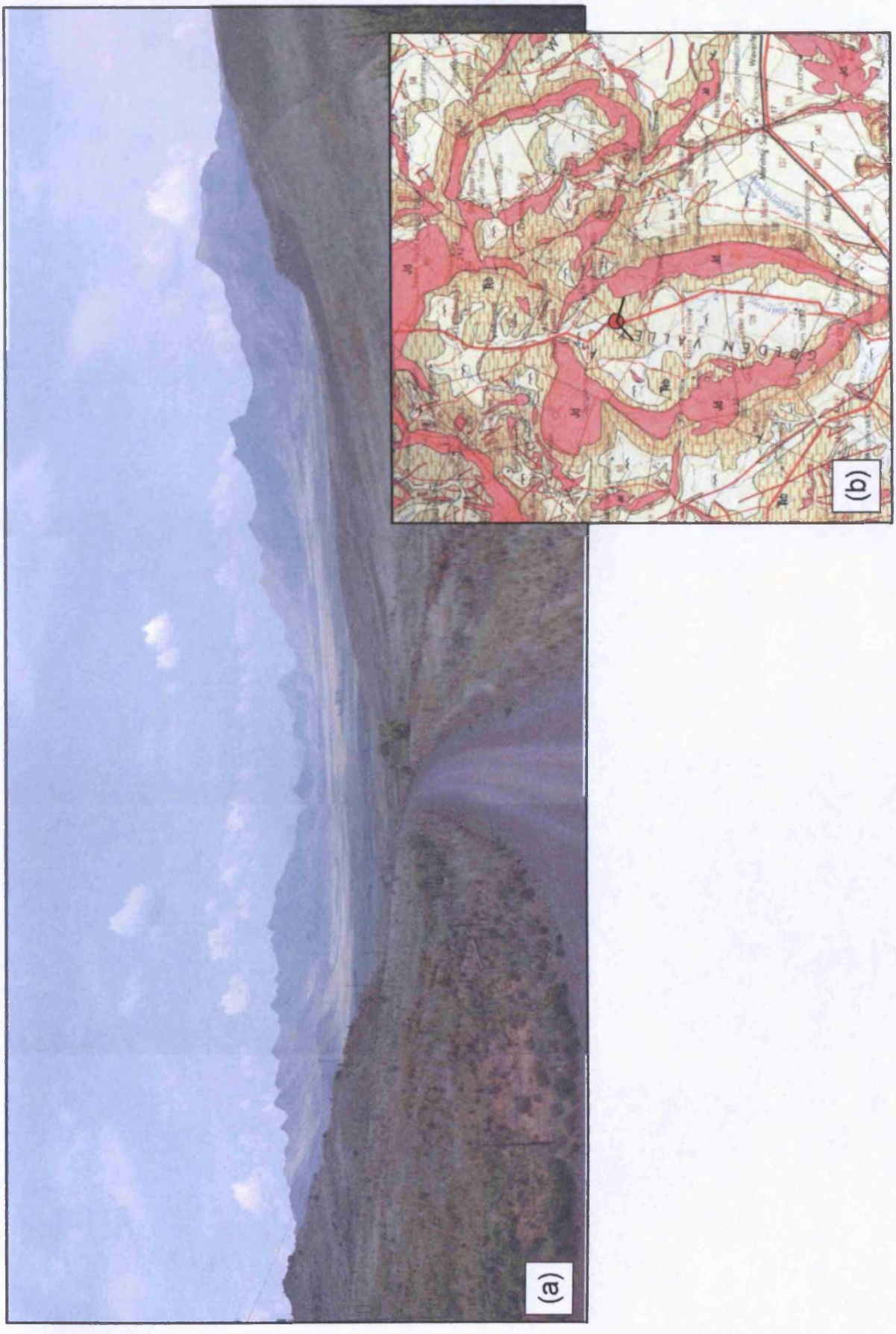

Fig. 1.8 (a) Photo mosaic showing the outcrop expression of the southern rim of the saucer-shaped Golden Valley sill, Karoo, from within the sill. (b) The planview expression of the Golden Valley sill on a geological map. Photo is taken facing south at location marked by red dot in Fig. 1.8b.

discussion of this thesis (Chapter 7) in the light of the analysis derived from seismic interpretation of the fully three-dimensional geometry of numerous saucer-shape sills within the case-study surveys.

1.5.3 Characteristics of igneous sill complexes

Igneous sill complexes are vertically and laterally extensive networks comprised of numerous interlinked sills. The detailed geometry of igneous sill complexes is poorly described due to lack of large field exposures. Compilation of field evidence in the Karoo was summarised in field sketches by du Toit (1920; Fig. 1.9a) and Lombard (1952; Fig. 1.9b). The sketches show sill complexes formed through several phases of intrusion in which dykes and transgressive sill segments connect layers of concordant and discordant sills. A similar geometry is illustrated by Press & Siever (1993; Fig. 1.9c). Igneous sill complexes may cover 1000s of km^2 (e.g. Karoo ~ > 500,000 km^2; Chevallier & Woodford, 1999), span vertical sections of more than 10 km (e.g. Jameson Land basin ~ 15 km; Larsen & Marcussen, 1992), and comprise magma volumes of the order of 10^4-10^5 of km^3 (e.g. crude estimate for the NAIP ~ 4.5-12.5*10^4 km^3; cf. Svensen et al., 2004).

The distribution of igneous sill complexes on a basin-scale has been addressed by several authors based on evidence from outcrop and seismic data. Igneous sills have been found to intrude at their deepest level in the central parts of basins and to step-up stratigraphy towards the basin margins (Gibb & Kanaris-Sotiriou, 1988; Larsen & Marcussen, 1992; Brekke 2000; Smallwood & Maresh, 2002). This was attributed to increased thickness of basement, and thus increased lithostatic pressure upon the magma chamber, towards the basin margin by Smallwood & Maresh (2002; see section 1.5.4.1). Francis (1982) and Larsen & Marcussen (1992) found that the intensity of intrusion is greatest in the deepest parts of the basin diminishing up-section. Bell & Butcher (2002) suggested that the lateral extent of sill complex is ultimately limited by the presence of up-faulted basement blocks, acting as a barrier to further lateral migration. A similar argument could be invoked to explain the decrease in intensity vertically, with the rise in basement towards the basin margins equating to a decrease in the thickness of the sedimentary package and thus the accommodation space for intrusion.

The size and thickness of individual sills within sill complexes appear to be related to the depth of intrusion. In the well-exposed Karoo igneous complex larger and more

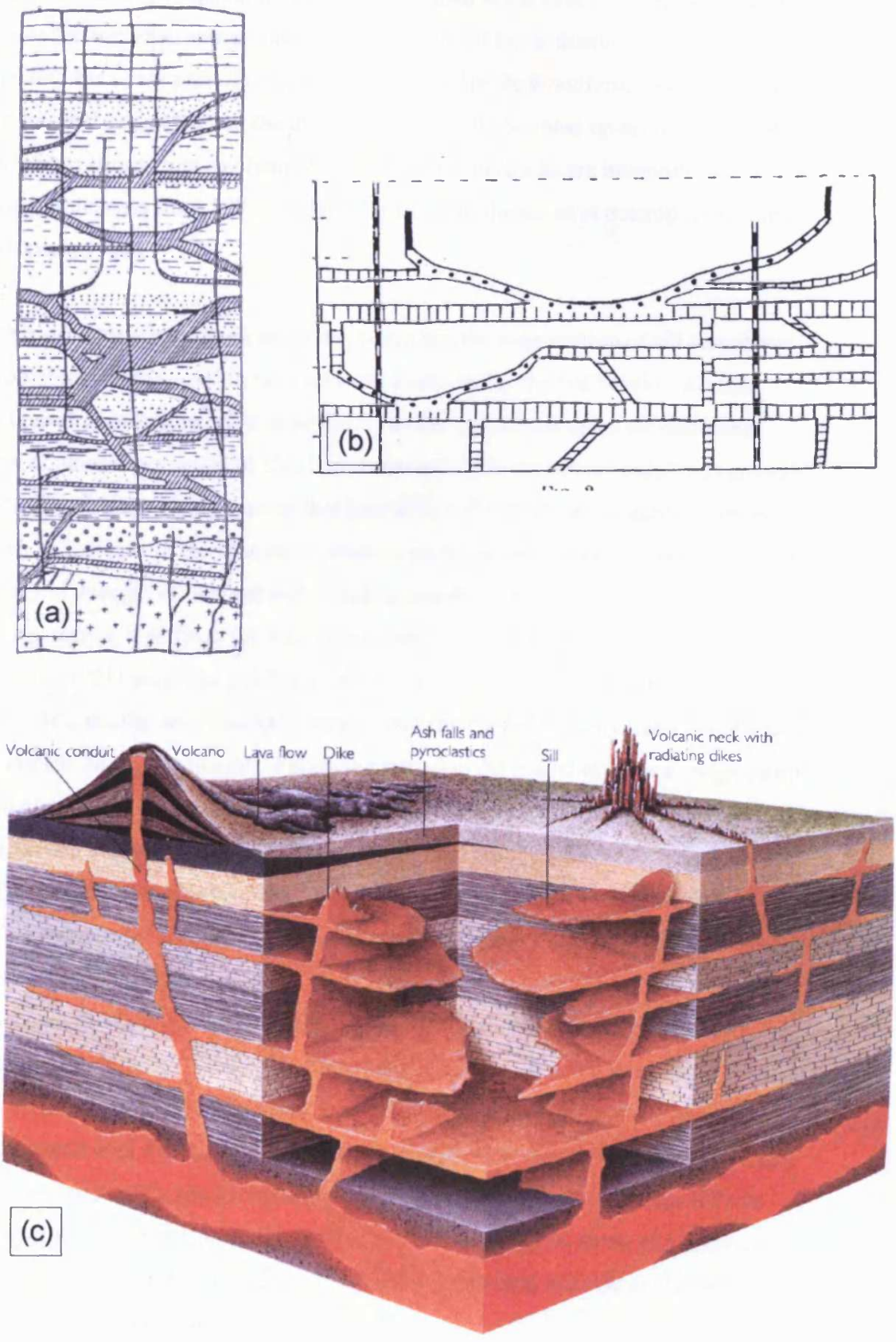

Fig. 1.9 Igneous sill complexes. (a) du Toit (1920), (b) Lombard (1952), and (3) Press & Siever (1993).

concordant dolerite sills appear to have been intruded at the base of the Karoo sequence, whilst smaller and often saucer-shaped intrusions (<10 km in diameter) have been intruded into the upper part of the sequence (Chevallier & Woodford, 1999). It has also been tentatively suggested that the thickness of the sills decrease up-section based on seismic observations from the Jameson Land basin where sills are interpreted to decrease in thickness from 300 m at depth to 10-20 m thickness at outcrop level (Larsen & Marcussen, 1992).

A number of models have been proposed to explain the construction of sill complexes. Based on observations made in the Guaymas Basin in the Gulf of Mexico, Einsele (1985) considers individual sills to be fed by dykes and argues that a sill-sediment complex of alternating layers of sheet intrusion and dyke-penetrated sediments grows upwards (Fig. 1.10a). The argument that later sills will intrude above earlier ones is related to an increase in the lithostatic pressure on the magma chamber and an increase of the tensile strength of the host sediments surrounding the earlier intrusions due to induration making it difficult for later sills to intrude below earlier ones (Einsele, 1985).

Sheridan (1981) proposed a different model (Fig. 1.10b). In this model an initial stage of uplift, rifting, and erosion of continental crust is followed by intrusion of a sill-dyke complex into rift sediments. Following intrusion the model invokes a 'ridge-jump' and initiation of active spreading. Gibb & Kanaris-Sotiriou (1988) suggested that aspects of both Einsele's (1985) and Sheridan's (1981) models have aspects applicable to the Faeroe-Shetland sill complex. They considered Sheridan's (1981) model most applicable overall, but suggested that Einsele's (1985) model is likely to be of importance to the NW of the basin.

Based on a detailed study of sill junction relationships, Hansen et al. (2004), in accordance with Einsele's (1985) findings, suggested that sill complexes intrude successively from deeper to shallower levels, but did not invoke that individual sills were associated with dykes. Rather, Hansen et al. (2004) suggested that sill complexes build-up to successively shallower levels, with deeper sills acting as feeders for sills emplaced at stratigraphically shallower levels. This fundamental mode of emplacement represents an entirely distinctive style of magmatic plumbing and will be further demonstrated throughout this thesis.

Contrary to the idea that sill complexes are emplaced from deeper to shallower levels, du Toit (1920) reached the conclusion that the relative order of intrusion within

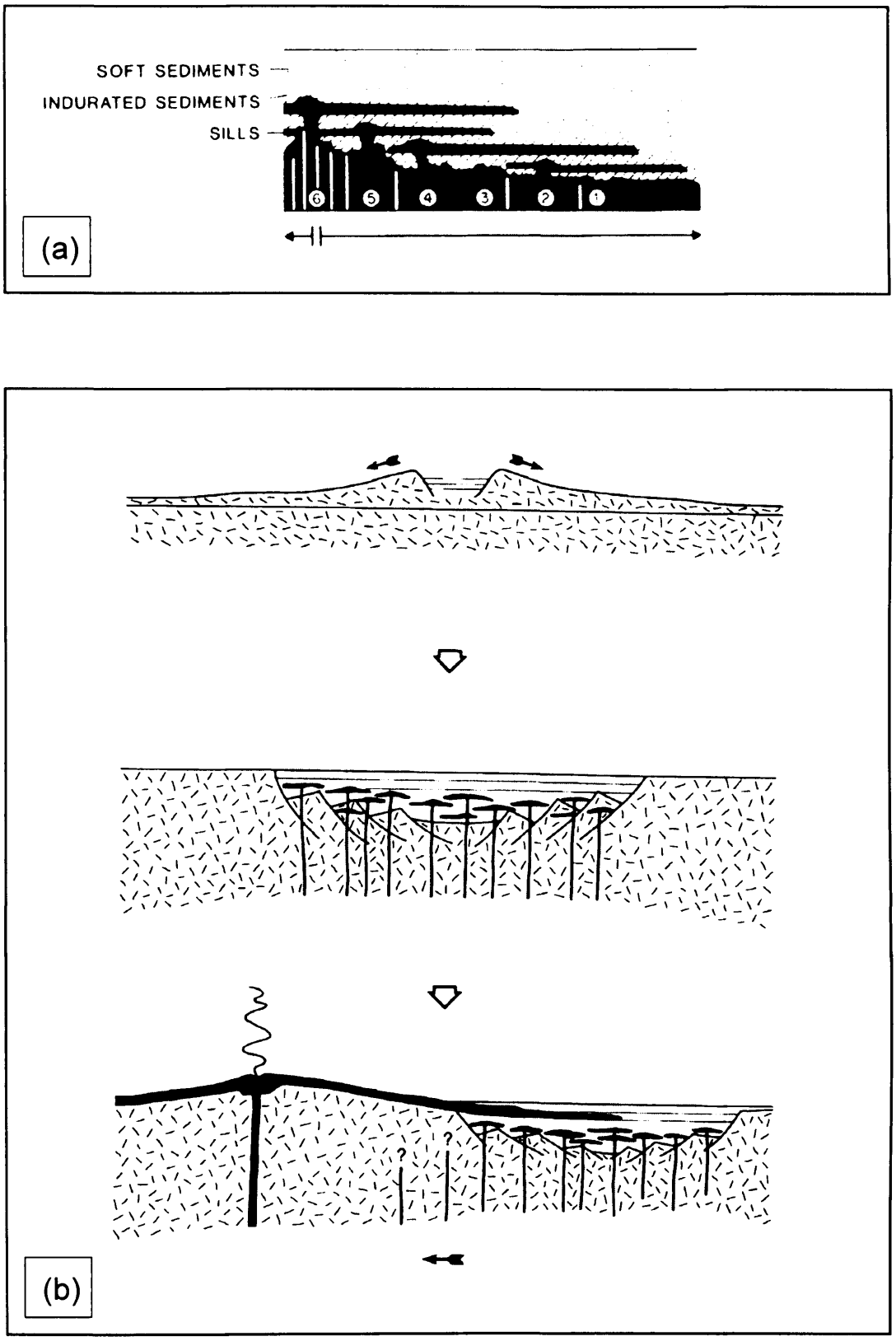

Fig. 1.10 Models for the development of igneous sill complexes. (a) Einsele (1985). (b) Sheridan (1981).

the Karoo complex was from the top downwards because later events were unable to penetrate earlier events. This view is according to Bradley (1965) not shared by most South African geologists and Bradley (1965) suggested that the Karoo complex evolved by upwards emplacement and that successively shallower horizons were invaded by magma as the magma pressure rose.

1.5.4 Magma transport and emplacement mechanics

Prior to intruding as sills and dykes in the crust, magma must migrate upwards from its source in the mantle. The mechanics behind the transport of magma from the mantle into the crust and the subsequent emplacement of sills and dykes are fundamental issues that have been addressed in numerous publications during the past century. However, many issues related to this transport are still unresolved. In this section the generally considered models for magma ascent and sill emplacement are described.

1.5.4.1 Magma ascent

The ascent of magma from the mantle to the crust is commonly suggested to be driven by buoyancy forces due to a density difference between the rising less dense magma and the more dense surrounding rock (Bradley, 1965; Johnson & Pollard, 1973; Walker, 1989; Lister & Kerr, 1991; Parsons et al., 1992; Kerr & Lister, 1995). The magma is often considered to rise vertically to, and subsequently intrude laterally along, a level, referred to as the level of neutral buoyancy (LNB), within the crust where the density of the magma and that of the surrounding host-rock are equal (Fig. 1.11; e.g. Bradley, 1965; Lister & Kerr, 1991).

However, sills are often found to be emplaced at levels where the density of the host-rock was less than that of the magma at the time of intrusion and it is thus unlikely that the sills were intruded at the LNB, but rather intruded above it (Pitcher, 1979; Parson et al., 1992; Smallwood & Maresh, 2002). The ability of the magma to intrude above the LNB suggests that the sills are supported by a pressure within the ascending magma (Loewinson-Lessing, 1936; McBirney, 1963; Parson et al., 1992; Smallwood & Maresh, 2002). The simplest way of creating such a pressure is by considering the lithostatic pressure upon the magma chamber supplying the melt (Bradley, 1965; Smallwood & Maresh, 2002). The magma pressure is further dependant upon the presence of gases, the expansion accompanying crystallisation, and dilation of the magma produced by fusion (Loewinson-Lessing, 1936; Pitcher, 1979). The resultant internal magma

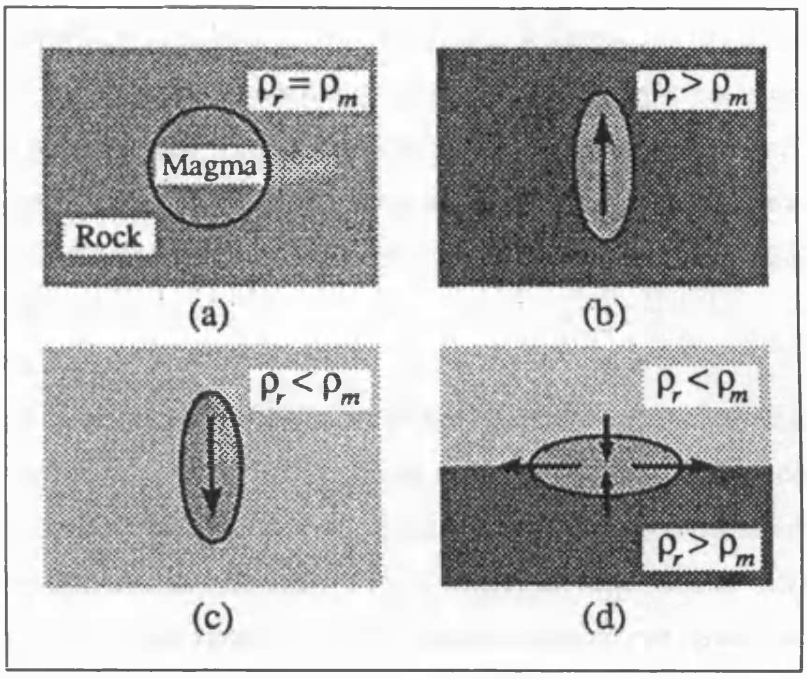

Fig. 1.11 Level of neutral buoyancy (LNB). Magma is often considered to rise vertically to, and subsequently intrude laterally along, a level (LNB) where the density of the magma and that of the surround host-rock are equal. From Lister & Kerr (1991).

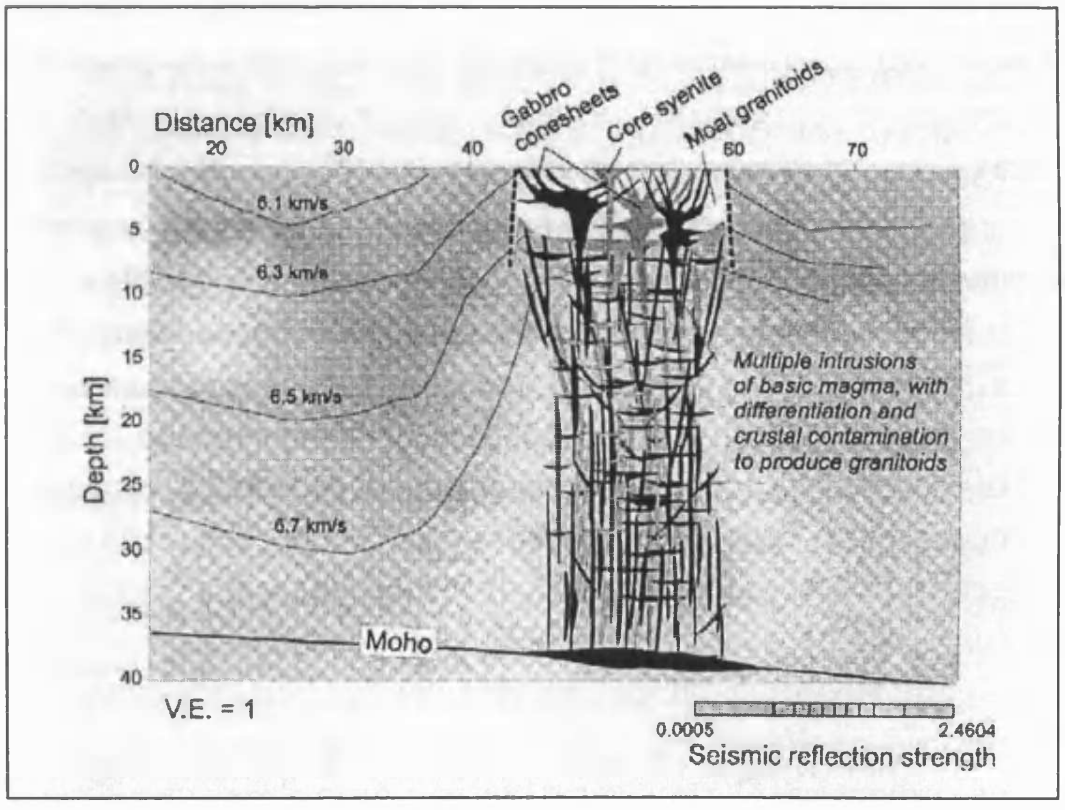

Fig. 1.12 Model for the Messum Ring Complex. In this model it is suggested that the complex is underlain by a heavily intruded root zone that may extend all the way to the Moho. From Bauer et al. (2003).

pressure combined with the buoyancy force will enable the magma to ascend beyond the LNB before the magma pressure has dropped to a level insufficient to overcome the strength of the host-rock and vertical ascent is replaced by lateral intrusion. If the magma pressure is sufficiently high, the magma will reach the free surface and erupt in the form of a volcano or lava flow (Bradley, 1965; Lister & Kerr, 1991 Smallwood & Maresh, 2002).

Smallwood and Maresh (2002) provide a number of simple equations to describe the pressure balance between the magma chamber and an intruding sill. They consider the effects of the lithostatic pressure upon the magma chamber, but do not account for the effects of the additional factors listed above. A simple pressure balance that considers the effect of the lithostatic pressure upon the magma chamber can be written:

$$P_{chamber} - \rho_{magma} gh + R = P_{sill} \qquad \text{(eq. 1.1)}$$

Where $P_{chamber}$ is the pressure in the magma chamber, ρ_{magma} is the density of the magma, g is the gravitational constant, h is the vertical distance between the level of sill intrusion and the magma chamber, R represents the strength of the host-rock that must be overcome by the ascending magma, and P_{sill} is the pressure in the sill (Smallwood & Maresh, 2002).

Smallwood & Maresh (2002) further simplify the above equation by assuming that; (1) the magma chamber is at the base of the crust, (2) the magma pressure in the chamber is lithostatic, (3) the pressure in the sill is equal to the lithostatic pressure at the depth of intrusion, and (4) the densities of the sedimentary section (ρ_{seds}) and the crystalline crust (ρ_{crust}) are constant.

The resultant pressure balance equation can be written:

$$h = \frac{c(\rho_{crust} - \rho_{seds}) - (R/g)}{(\rho_{magma} - \rho_{seds})} \qquad \text{(eq. 1.2)}$$

Where c is the thickness of the crystalline crust above the magma chamber.

Equation 1.2 suggests that where the basement is high (i.e. c is large) sills will be able to intrude at shallower levels than where the basement is deep and thus c is small. This suggestion is supported by seismic observations in the Faeroe-Shetland Basin where sills are seen to intrude at increasingly shallower levels towards the Corona Ridge (Smallwood & Maresh, 2002) and even extrude to form a lava flow immediately above the crest of the structure (Trude et al., 2004). A similar control may also explain the general emplacement of sills at deeper levels in the central parts of the Møre Basin than towards the north-western basin margin described by Brekke (2000). Similarly, sills in the Jameson Land basin show a comparable distribution with the deepest sills occurring near the basin axis and stepping up the stratigraphy towards the basin margin (Larsen & Marcussen, 1992), possibly further supporting the suggestion of equation 1.2.

The presence of gases, the expansion accompanying crystallisation, and dilation of the magma produced by fusion within the magma chamber (Loewinson-Lessing, 1936; Pitcher, 1979) have not been considered above, nor has the possibility that the magma chamber from which the magma ascends into the crust provides an irregular supply of magma through time (Anderson, 1938; Wadge et al., 1975) and is temporarily stored in shallow-level 'magma reservoirs' containing tens or even hundreds of km^3 of magma (Bardintzteff & McBirney, 2000; Gudmundsson, 2000; Gudmundsson, 1998). Whilst these factors do not directly influence the equations above they will influence the magma pressure through time and this will in turn influence the level to which the intruding magma will be able to rise.

The frequency and volume of magma pulsing is poorly constrained. According to Bardintzeff & McBirney (2000) the long-term activity of many volcanoes and the spacing of eruptions are governed by the volume of magma supplied from the mantle and the physical nature of the 'magma reservoirs'. Based on the volcanic rift zone in Iceland, Gudmundsson (1998) suggested that the frequency in eruption and intrusion events varies between a few hundred to several thousands of years and that closely spaced events involve smaller volumes (< 0.1 km^3) than more widely spaced events (> 1 km^3). Bardintzeff & McBirney (2000) and Wadge et al. (1975) described a similar relationship between eruption frequency and lava volumes and Wadge et al. (1975) further suggested that early activity is likely to be more voluminous than later activity.

Magma loss in the 'magma reservoir' following intrusive and eruptive pulses is replaced by influx of 'primitive' mafic magma from the mantle and the composition and

physical properties remain more or less constant (Bardintzeff & McBirney, 2000). However, during the later stages of activity, as the influx from the mantle starts to decline, cooling and crystallisation between relatively widely spaced intrusive and extrusive events (cf. Wadge et al., 1975), can lead to a more evolved magma composition (Bardintzeff & McBirney, 2000).

1.5.4.2 Dyke-to-sill transition

The transition from dyke (vertical)-to-sill (horizontal) emplacement is according to the arguments presented above governed by a relationship between magma pressure and buoyancy and the strength of the host-rock, with the transition occurring where the magma pressure is no longer sufficient to overcome the strength of the host-rock (e.g. Bradley, 1965; Lister & Kerr, 1991). In addition to this, it has long been suggested that the host-rock stress conditions at the time intrusion are of great importance and that dykes will form under conditions where the least principal stress is oriented in the horizontal plane and sills will form under stress conditions where the least principal stress is vertical (Anderson, 1951; Gretener, 1969; Howard, 1991; Parsons et al., 1992).

Several factors capable of locally changing the direction of least principal stress from horizontal to vertical and thus from conditions favouring dyke emplacement to those favouring sill emplacement have been proposed. Anderson (1951), Parsons et al. (1992), and Fialko (2001) propose that repeated dyke injection will increase the horizontal compressive stress and as a result the least principal stress may be re-oriented from horizontal to vertical. As a result, later magma pulses may form sills rather than dykes at a given depth.

Gretener (1969) argues that the local transition is controlled by the presence of stress barriers in the form of beds with relatively high effective Poisson's ratios. Gretener (1969) defines the three principal effective stresses according to Price (1966) as:

$$\sigma_z = (\rho_b - \rho_f)\, g\, z \qquad \text{(eq. 1.3)}$$

$$\sigma_x = \nu'/(1-\nu')\,\sigma_z + E\,\varepsilon_x \qquad \text{(eq. 1.4)}$$

$$\sigma_y = \nu'/(1-\nu')\,\sigma_z + \nu' E\,\varepsilon_x \qquad \text{(eq. 1.5)}$$

Where σ_z is the principal effective vertical stress, σ_x is the principal effective stress in the x-direction, σ_y is the principal effective stress in the y-direction, ρ_b is the bulk density for the overlying rocks, ρ_f is the fluid density of the pore fluid, v' is the effective Poisson's ratio, E is the Young's modulus of the rock, z is the depth, g is the acceleration of gravity, and ε_x is an arbitrary boundary condition.

According to Anderson (1951) sills will form when $\sigma_x > \sigma_y > \sigma_z$ a condition that may be fulfilled at several different levels within a sedimentary succession depending on the relationship between Young's modulus, the effective Poisson's ratio, and the overburden pressure within individual beds (Gretener, 1969).

Field evidence supports a local lithological control and hence influence of Poisson's ratio upon dyke-sill transition (Walker, 1958; Mudge, 1968; Leaman, 1975; Parson et al., 1992;). Vertical dolerite dykes in South Africa, for example, fail to penetrate, and spread out laterally upon encountering, a massive quartzite (Walker, 1958), whilst Mudge (1968) found that sills tended to be bound upwards by a mudstone sequence. However, many lithological boundaries in the subsurface are by-passed by intruding magma and a boundary that forms a 'stress barrier' at one level may not form a barrier at a higher level due to variations in stress state (Gretener, 1969).

A number of recent studies (Boudier et al., 1996; Bauer et al., 2003) have proposed that sills may form at much greater depth than previously considered. These studies, based on magma chambers in the Oman ophiolite (Boudier et al., 1996) and reflection seismic, gravity, and aeromagnetic studies of the Messum Ring Complex, Namibia (Bauer et al., 2003) suggest that these are underlain by heavily intruded root zones that may extend all the way to the Moho (Fig. 1.12, page 1-22). These studies suggest that there is an internal control on the nature of the intruded zone at all levels, possible related to high magma driving pressure and flux (Bauer et al., 2003) and deeper seated stress fields associated with mantle diapirism (Boudier et al., 1996). This research is still in the early stages, but further investigations of this phenomenon has the potential to dramatically further our understanding of magma transport in the crust and controls upon dyke-sill transition.

Later sills have commonly been found to intrude above earlier sills (Bradley, 1965; Leaman, 1975; Einsele, 1985; Hansen et al., 2004), suggesting that the level of dyke-sill transition becomes progressively shallower through time. This could be due to an

increase in lithostatic pressure acting on the magma chamber due to the emplacement of sills in the overburden (McBirney, 1963; Bradley, 1965). As the lithostatic pressure on the magma chamber increases through time, due to the added load provided by the intrusion of sills in the overburden (McBirney, 1963; Bradley, 1965), subsequent magma pulses of equal pressure (not including the lithostatic effect) should lead to the emplacement of sills at progressively shallower levels. If the magma supply is pulsed (e.g. due to magma being supplied from a chain of interlinked magma chambers rather than a single magma chamber; e.g. Gudmundsson, 2000) the level of dyke-sill transition is probably more likely to fluctuate between shallow and deep levels, depending upon the magma pressure at any given time.

1.5.4.3 Lateral magma emplacement and terminations

Once a level where conditions favouring sill rather than dyke intrusion is reached the intruding magma starts to spread laterally. It has long been recognised that sill tips are of particular interest because they form the locus of active sill propagation. Early work by Anderson (1938) argued that there would be a large stress concentration near the tip tending to 'wedge open' the host rock and enable the sheet intrusion to propagate. The only condition required being that the pressure of the intruding magma must be greater than the pressure normal to the fissure in the host rock (Anderson, 1938). Bradley (1965) also invoked a wedging mechanism to explain the propagation at the sill tip and suggested that the process of splitting relies on the build up of steam pressure in front of the sill tip formed as a result of interaction between the hot intrusive magma and the host rock pore water. He suggested that this mechanism formed a wedge-shaped cavity (propagation wedge) that could potentially extend up to a mile ahead of the sill (Fig. 1.13). Bradley (1963) suggested that the lateral propagation could be arrested when the steam filled wedge-shaped cavity in front of the sill tip encounters a vertical weakness, such as a fault plane or a permeable zone in the roof, and the steam escapes upwards.

Pollard & Johnson (1973) conducted a theoretical mechanical study building upon the findings of Anderson (1938) and illustrated the distribution of shear stresses and deformation around a sill. They found that there were concentrations of high stresses and deformation near the terminations of sills and that these dropped off rapidly away from the contact (Fig. 1.14). They agreed that a splitting mechanism related to the high concentration of tip stress was responsible for the propagation of the sill along its length. Pollard & Johnson (1973) also derive an equation for the propagation of sills

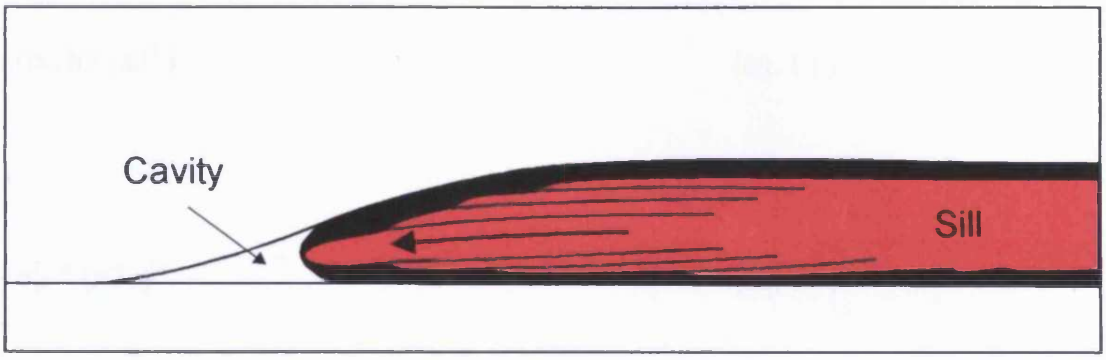

Fig. 1.13 Schematic showing splitting and wedging ahead of an intruding sill. The tip cavity may extend up to 1 mile ahead of the sill tip. The sill propagates by continuously splitting and infilling the tip cavity. From Bradley (1965).

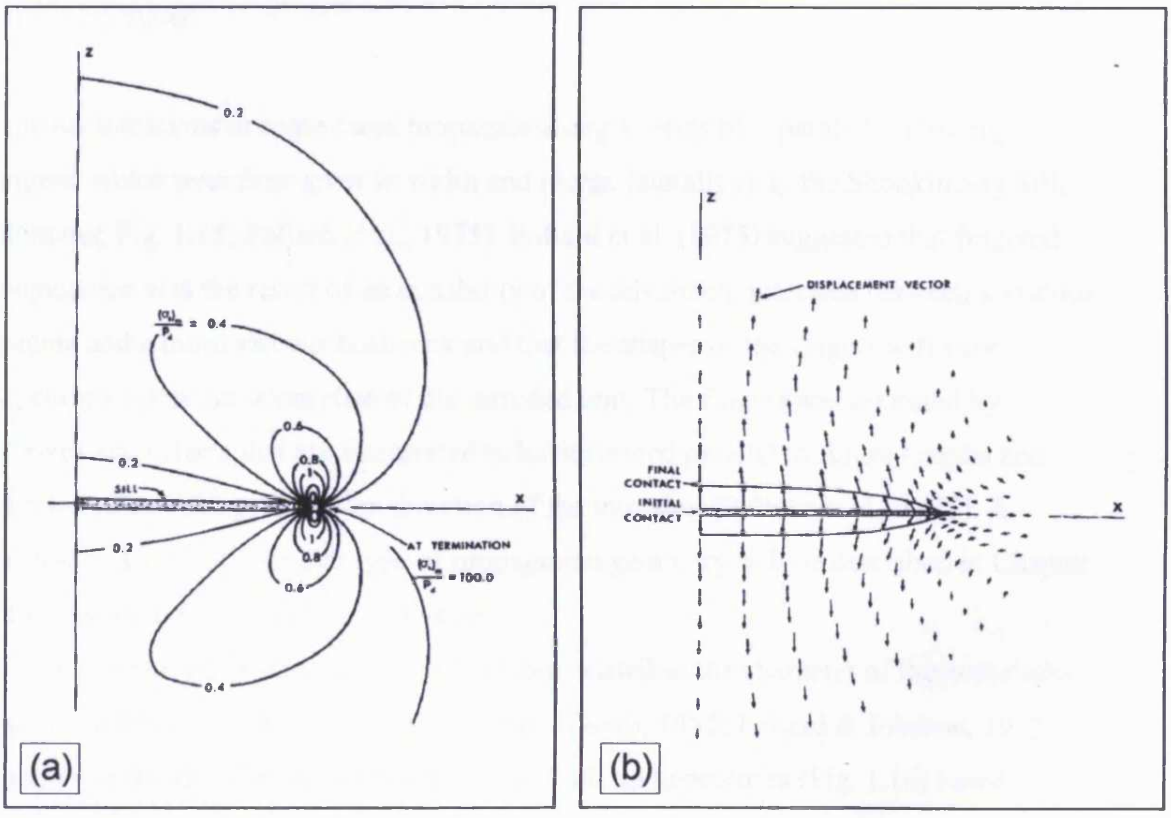

Fig. 1.14 The theoretical distribution of shear stress and displacement around a sill. (a) High shear stress is concentrated at the sill tip. Contours represent values of: max. shear stress at point/ driving pressure. (b) Lengths of arrows are proportional to displacements which are maximal around the center of the sill and die out away from the contact. From Pollard & Johnson (1973).

based on the driving pressure required to initiate yielding at the sill tips. The driving pressure required to initiate yielding is according to Pollard & Johnson (1973) given by:

$$P_d = (\sigma_{ys}\, b)/ (a3^{1/2}) \qquad \text{(eq. 1.6)}$$

or

$$P_d = \sigma_{ys} * (r/3a)^{1/2} \qquad \text{(eq. 1.7)}$$

Where P_d is the driving pressure (= total magma pressure – lithostatic pressure) that must be exceeded for the sill to propagate, σ_{ys} is the yield strength in tension, b is the half-thickness of the intrusion in the z-direction, a is the half-length of the intrusion in the x-direction, and r is the radius of curvature of sill termination.

Using equations 1.6 and 1.7 the driving pressure can be calculated if the length and thickness (eq. 1.6) or radius of curvature (eq. 1.7) of a sill can be measured and a value for σ_{ys} estimated.

Igneous intrusions in some cases propagate along a series of separated protruding fingers, which over time grow in width and merge laterally (e.g. the Shonkin Sag Sill, Montana; Fig. 1.15; Pollard et al., 1975). Pollard et al. (1975) suggested that fingered propagation was the result of an instability of the advancing interface between a viscous magma and a more viscous host-rock and that the shapes of the fingers will vary depending upon the stress state of the intruded unit. The fingers are separated by grooves and offsets that are interpreted to have formed parallel to finger lengths and thus to indicate the propagation direction of the intrusion (Pollard et al., 1975). A seismic example of a similar type of propagation geometry will be described in Chapter 4 in relation to the Solsikke lobe system.

The geometry of sill terminations has been related to the character of the host-rocks and the properties of the individual magmas (Tweto, 1951; Pollard & Johnson, 1973). Tweto (1951) identified six different types of sill tip geometries (Fig. 1.16) based on porphyry sills near Pando, Colorado, and suggested that the development of the different sill tip geometries was dependent on the host-rock lithology, but provided no further mechanical arguments. Pollard & Johnson (1973) found that small termination radii of curvature was indicative of intrusion into brittle rock, whilst large radii of

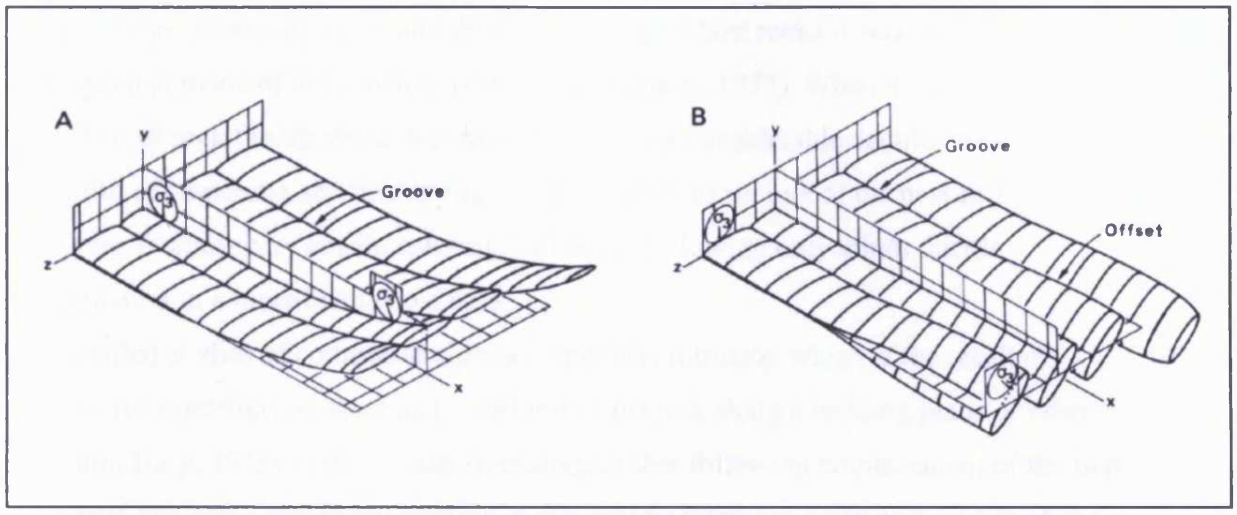

Fig. 1.15 Fingered sheet intrusions affected by changes in the direction of the least compressive stress (Sigma 3) along the intrusion path. (a) Sigma 3 changes orientation in the xy plane, resulting in a curved sheet. (b) Sigma 3 changes in the yz plane, resulting in en echelon fingers which coalesce to form offsets. From Pollard et al. (1975).

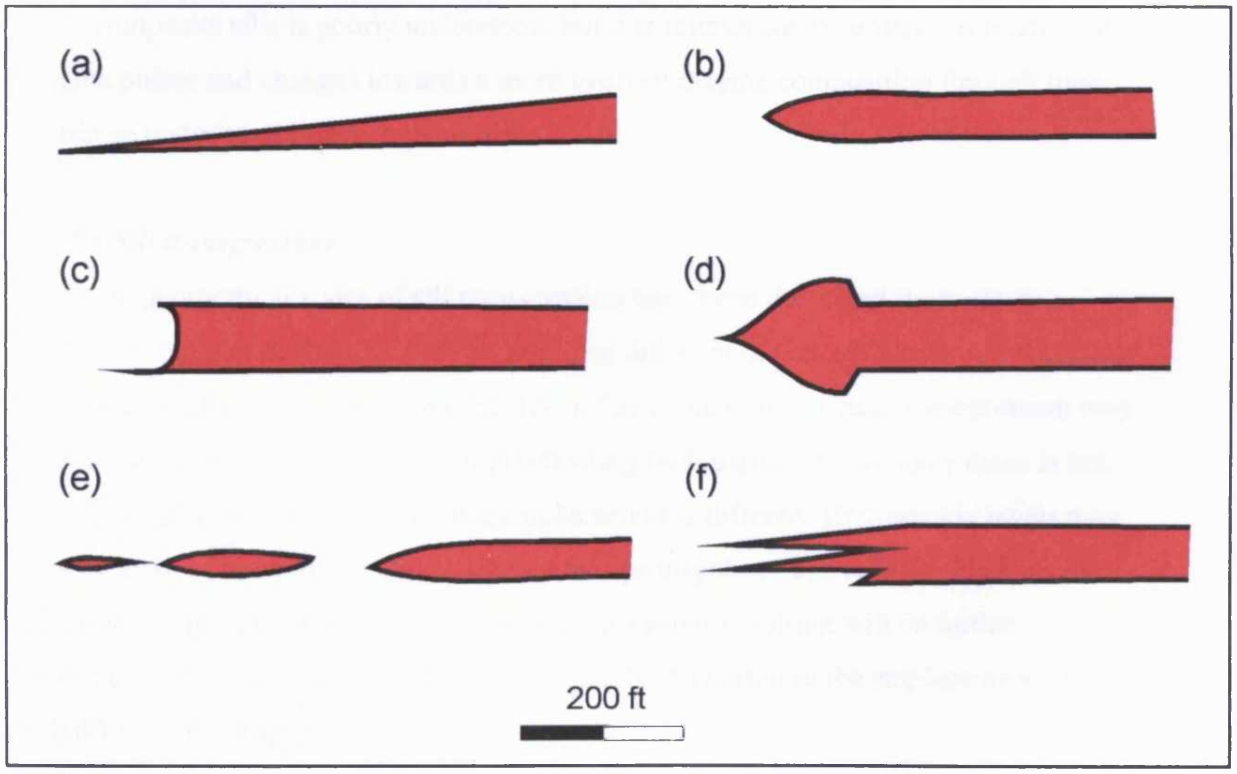

Fig. 1.16 Schematic illustration of sill tip geometries observed by Tweto (1951) who studied porphyry sills near Pando, Colorado.

curvature were indicative of intrusion into a more ductile host rock. The difference in tip geometry during intrusion into these two different host rocks is related to their strength and mode of deformation (Pollard & Johnson, 1973). When intruding into a ductile host rock the tip stress is considered to cause considerable ductile deformation in the form of stretching and thickening of the sill prior to rupture of the host rock. Whereas fracturing by tensile splitting will occur following only minor ductile deformation in a more brittle host rock.

Detailed studies of composite sills (a compound intrusion which is the result of successive injections of more than one kind of magma along a bedding plane or other fracture; Daly, 1933) in the British Isles suggest that following emplacement of the first intrusion and some peripheral cooling, a subsequent intrusive event will intrude along a 'plane of weakness' in the uncooled centre of the first intrusion (Buist, 1959; Buist, 1961; Rogers & Gibson, 1977; Bell & Pankhurst, 1993). Geochemical data suggest that the 'typical Scottish Tertiary composite sill' has basic (mafic) margins and an acidic (felsite) centre (Rogers & Gibson, 1977), as described from the composite sill of Rudh' a' Chromain, Carsaig, Mull by Buist (1961) and from the composite sill of Rubh'an Eireannaich, Skye by Buist (1959) and Bell & Pankhurst (1993). The development of these composite sills is poorly understood, but it is interesting to consider in relation to magma pulses and changes towards a more evolved magma composition through time within an underlying 'magma reservoir'.

1.5.4.4 Sill transgression

Different geometrical styles of sill transgression have been described from outcrop studies. Robertson & Haldane (1937) described different modes of angular transgression based on the Stirlingshire section (Fig. 1.17). They found that angular transgression may be accommodated by exploitation of pre-existing fault planes, but in many cases is not, and that angular sill segments linking emplacement at different stratigraphic levels may be indicative of upwards as well as downwards propagation. The relationship between sill emplacement and pre-existing and contemporaneous faulting will be further described and discussed in this thesis, particularly in relation to the emplacement of the Solsikke Sill in Chapter 4.

Transgression may also occur through a process of step-and-stair transgression where the intrusion repeatedly steps up to a shallower stratigraphic level and propagates laterally for some distance, giving rise to a stepped cross-sectional geometry (Fig. 1.18;

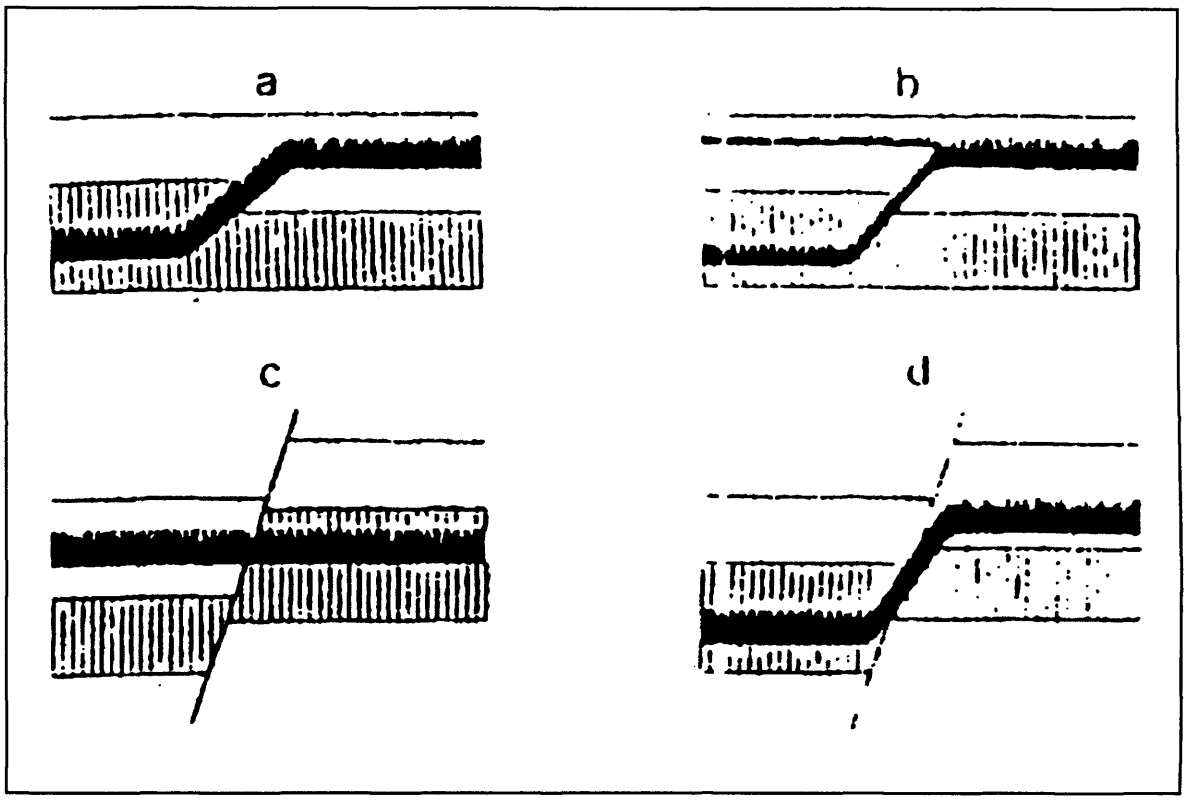

Fig. 1.17 Various modes of sill transgression. From Robertson & Haldane (1937).

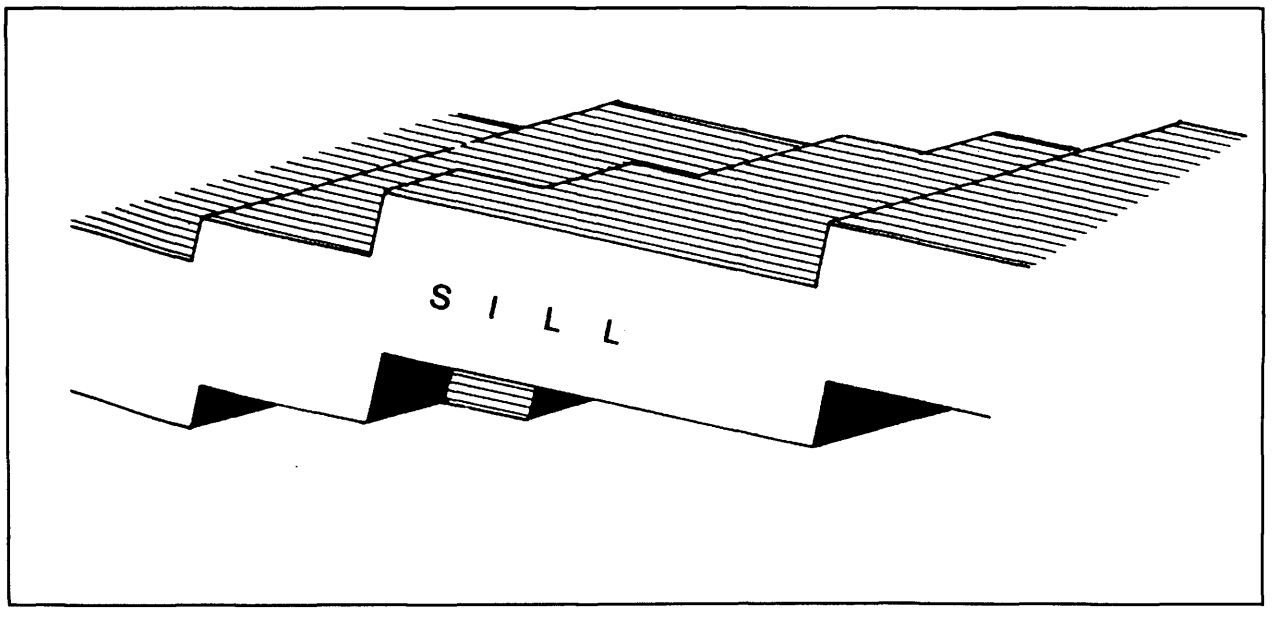

Fig. 1.18 Stepped sill transgression. From Francis (1982).

Knox, 1954; Bradley, 1965; Gretener, 1969; Francis, 1982). Bradley (1965) suggested that sill stepping was attributable to topographic irregularities, with the sill stepping up towards the centre of any topographic lows, often along fault planes. Gretener (1969), more convincingly, suggested that stepping is an indication of a local change of the state of stress in a 'stress barrier' (section 1.5.4.2), possibly caused by a slight flexure, differential compaction, or a change in the mechanical properties of the layer. A sill would then break through the stress barrier and rise to the next barrier, higher in the section. The implications of stepped sill geometries for determining the direction of sill propagation will be addressed in relation to the Solsikke lobe system in Chapter 4.

Based on illustrations by Robertson & Haldane (1937), Francis (1982) noted that all transgressive segments effectively become (reverse) faults with displacements equal to the thickness of the sill. This is an important observation in relation to seismic-based studies of igneous intrusions because thin, steeply dipping transgressive sill segments or sill tips and dykes may be poorly resolved by seismic data (see Chapter 2), but may be identifiable as vertical reverse offsets of stratal reflections across poorly defined discontinuities (i.e. poorly resolved igneous intrusion).

1.5.4.5 Synthesis

The above summary of previously published literature on magma ascent and emplacement mechanics has revealed that issues related to these fundamental aspects of igneous intrusive complexes are still not fully understood. For example, the relative importance of magma pressure, buoyancy forces, and stress conditions remain poorly constrained. It is very difficult to assess the mechanics and key controls upon magma ascent, sill-dyke transition, and lateral magma propagation based on seismic data because factors such as magma pressure and *in situ* stress conditions at the time of intrusion are poorly constrained. However, it is expected, and has already been demonstrated in Hansen et al. (2004), that this study will improve our understanding of magma transport and emplacement mechanics in the crust by providing a detailed and three-dimensional analysis of igneous sill complexes in the case-study areas.

1.6 Methods

This PhD project is primarily based on interpretation of high-resolution 3D seismic datasets from basins along the NE Atlantic Margin. The project has also benefited from three weeks of fieldwork in the Karoo, South Africa.

1.6.1 3D seismic interpretation

Four 3D seismic datasets from volcanic basins along the NE Atlantic Margin have been made available to this study from industry sponsors (Fig. 1.1); the Solsikke survey (Møre Basin), Tranche 67 (northern Faeroe-Shetland Basin), Tranche 4 (central Faeroe-Shetland Basin) and Tranche 38 (NE Rockall Basin). These datasets have provided a good coverage of the margin and have allowed for subsurface igneous complexes to be mapped in three-dimensions and at a much greater scale than possible in the field or from 2D seismic data.

Igneous sills have been mapped in each of four case-study areas in order to define their geometry, stratigraphic and structural context, and their impact on/ relationship with host sedimentary units. A number of key seismic horizons have also been mapped within each of the case-study areas. The mapping has provided an extensive database and has allowed for a number of fundamental general themes associated with sill emplacement in sedimentary basins to be addressed as well as allowing for detailed studies of locally recognised areas of interest.

The seismic data have been interpreted on a UNIX workstation running Schlumberger GeoFrame 3.7 software. An introduction to the phase, resolution and general quality of each of the datasets will be provided as the datasets are presented within subsequent chapters.

1.6.2 Fieldwork

Fieldwork was carried out over a three-week period in South Africa where a number of locations within the central Karoo were visited.

The aim of the fieldwork was to gather additional geometrical insights into the process of sill emplacement and allow for integration of geometrical features beneath the scale of seismic resolution. The fieldwork was particularly useful because the novelty of the seismic approach to the mechanics of sill emplacement taken in this study means that the limitations of this approach are poorly constrained.

1.7 Thesis layout

This thesis is based around four 3D seismic surveys. The igneous complexes within three of these case-study surveys (T67, Solsikke, and T38) have been interpreted in detail and each constitute a chapter of the thesis (chapters 3, 4, and 5, respectively). The

fourth 3D seismic survey (T4) has been used in combination with the other 3D seismic surveys to describe and discuss mound structures seen in association with sill complexes. These structures are described in a thematic chapter (Chapter 6). Many of the observations described in this thesis are discussed within individual chapters, whilst the discussion chapter of this thesis (Chapter 7) mainly deals with a number of more general themes that draw on a compilation of observations made in each of the case-study areas. The thesis comprises a total of eight chapters and the content of each chapter is briefly described below.

Chapter 2 provides a brief introduction into seismic interpretation of igneous sills including a summary of key interpretational challenges and artefacts.

Chapter 3 provides a detailed interpretation of the T67 igneous complex located in the north-eastern Faeroe-Shetland Basin. The case-study has two primary sections that focus on (1) classification of different sill geometries and (2) sill junction relationships and their implications for sill complex build-up, respectively.

Chapter 4 provides a detailed interpretation of the Solsikke igneous complex located in the Møre Basin. The case-study is sub-divided into three main parts that deal with three different levels of the Solsikke intrusive system: (1) the Solsikke sill complex, (2) the Solsikke Sill, and (3) the Solsikke lobe system.

Chapter 5 provides a detailed interpretation of the T38 igneous complex located in the north-eastern Rockall Basin. This chapter aims at discussing the geometrical and timing relationships between deep and shallow sills in order to establish the suquence of events that lead to the formation of the sills complex. This chapter also provides a detailed interpretation of overburden deformation associated with sill emplacement.

Chapter 6 is a thematic chapter concerned with the characterisation and origin of mound structures that are found associated with sill complexes. The chapter draws on observations made in all four case-study survey areas.

Chapter 7 forms the main discussion of this thesis and draws on observations made throughout the thesis. A number of general themes are discussed in this chapter: (1) Igneous sill geometries. (2) The development of saucer-shaped sills. (3) Soft-sediment deformation associated with sill emplacement and their implications for the timing of magmatic events in the case-study areas and along the NE Atlantic Margin. (4) Magma transport in the upper crust and the build-up of igneous sill complexes.

Chapter 8 is a short conclusion chapter that summarises the general conclusions of the study as well as the conclusions that have been drawn on a case-study level.

CHAPTER 2: 3D SEISMIC INTERPRETATION OF IGNEOUS SILLS IN SEDIMENTARY BASINS

2.1 Introduction

3D seismic data is the main type of data used in this study and in this chapter some key issues related to 3D seismic interpretation of igneous sills in sedimentary basins are briefly described. These issues include the acoustic properties of igneous sills (section 2.2), the resolution of seismic data (section 2.3), the seismic characteristics of igneous sills (section 2.4), and interpretational challenges and artefacts with special implications for interpretation of igneous intrusions on seismic data (section 2.5).

2.2 Acoustic properties of igneous sills

Igneous bodies intruded into sedimentary basin fills are strikingly well imaged by seismic data due to a significant acoustic impedance contrast between igneous material and siliciclastic sediments (Badley, 1985; Planke et al., 1999). As a seismic wavelet encounters an interface, such as an intrusive boundary, which separates media with different acoustic properties (a reflector) in the subsurface, part of the wave energy is reflected back to the surface, and is displayed as a reflection on a vertical seismic section. The acoustic properties of a rock (Badley, 1985) are characterised by its acoustic impedance (Z), which depends on formation density (ρ) and seismic wave velocity (v), with:

$$Z = \rho v \qquad \text{(eq. 2.1)}$$

The amplitude of a seismic reflection is an expression of the boundary reflection coefficient (RC). At normal incidence and assuming horizontal reflectors, the reflection coefficient is given by

$$RC = (\rho_2 v_2 - \rho_1 v_1)/ (\rho_2 v_2 + \rho_1 v_1) = (Z_2 - Z_1)/ (Z_2 + Z_1) \qquad \text{(eq. 2.2)}$$

where subscript 1 and 2 denote properties in the layer above and below the reflector, respectively (Badley, 1985).

The more extreme (positive or negative) the reflection coefficient is, the stronger is the amplitude of the reflection seen on the seismic section. According to the law of energy conservation, the seismic wave energy will decrease as the seismic wave travels downwards. As a result, a given reflection coefficient will give rise to a stronger reflection at shallow depth than deeper in the section. Controversy exists when it comes to displaying reflection coefficients using zero-phase wavelets. According to Badley (1985), a positive reflection coefficient ($Z_2 > Z_1$) should be imaged as a white trough on a seismic section at normal polarity, whilst Sheriff & Geldart (1995; SEG standards) suggests, that at normal polarity a positive reflection coefficient should be depicted as a black peak. In this thesis terminology according to Sheriff & Geldart (1995) will be used. The top of a sill represents a positive acoustic impedance interface whilst the base of a sill represents a negative acoustic impedance interface. According to SEG standards (Sheriff & Geldart, 1995) the top of a sill should be imaged as a peak with positive amplitude while the base of the sill should be imaged as a trough with negative amplitude on zero-phase migrated data displayed using normal SEG polarity.

In basins along the NE Atlantic Margin igneous sills were intruded into Upper Cretaceous and Paleogene clay-dominated sediments during the early Paleocene (section 1.4.2). Skogly (1998) extracted velocity and density data for 83 igneous sills from 16 exploration wells from the Faeroe-Shetland Basin and found that the sills had an average density (ρ_{sill}) of 2.84 ± 0.11 g/cm^3 and velocity (v_{sill}) of 5.55 ± 0.56 km/s and were emplaced into a host rock with a present-day average density (ρ_{sed}) of 2.60 ± 0.09 g/cm^3 and velocity (v_{sed}) of 3.55 ± 0.65 km/s (values most likely influenced by contact metamorphism). In the case-study areas v_{sed} and v_{sill} are both very poorly constrained due to lack of well ties, but throughout this thesis a sill velocity of v_{sill} = 5.55 km/s is used to calculate sill thickness and a sediment velocity of v_{sed} = 3.00 km/s (cf. Bell & Butcher, 2002) is used to calculate sediment thickness and vertical relief of sills. Where uncertainties on these values have been applied this is stated in the appropriate section. v_{sed} is highly likely to increase with depth and v_{sed} = 3.00 km/s is considered to be in the lower end of the true applicable velocity spectrum. In other words, the calculated emplacement depths and vertical relief on sills are minimum values. This as well as compaction effects will be considered in Chapter 7 where the entire collated sill dataset will be analysed to establish general relationships.

2.3 Seismic Resolution

The detail that can be extracted from seismic data depends upon the resolution of the seismic data. The datasest used in this study have all undergone 3D migration (cf. Yilmaz, 1987) that, in contrast to 2D migration, allows for out-of-plane disturbances to be eliminated due to the close line spacing within 3D seismic surveys (typically 12.5 or 25 m). Additional factors that influence the resolution of 3D migrated reflection seismic data include velocity field and signal-to-noise ratio (Brown, 1996).

2.3.1 Vertical Resolution

Vertical resolution is a measure of the bed thickness required for a unit of rock to be displayed on a seismic section. For a bed (or rock unit) to be seismically displayed without interference between the top and base acoustic-impedance contrasts (thickness of separability), the bed must be thicker than half the dominant wavelength ($\lambda/2$) of the seismic wavelet (Badley, 1985; Sheriff & Geldart, 1995). However, bed thickness can be resolved down to $\lambda/4$ (tuning thickness) for zero-phase migrated data, but the top and base reflections cannot be separated (Sheriff & Geldart, 1995). Below $\lambda/4$ the bed thickness cannot be resolved seismically (Sheriff & Geldart, 1995). The thickness of separability (i.e. $\lambda/2$) has been used as a measure of vertical seismic resolution in this thesis and has been calculated for each of the four case-study surveys. Beds with thicknesses down to approximately 1/30 of the dominant wavelength can be imaged on the seismic section, but the actual top and base cannot be picked out in such cases (Badley, 1985). Seismic wavelengths ($\lambda = v/f$) generally increase with depth due to frequency (f) attenuation and velocity (v) increase (Yilmaz, 1987), which means that deep features must be thicker than shallow features in order to be resolved and displayed.

At the depths where sills are intruded along the NE Atlantic Margin the dominant frequency of the used datasets is between 25-40 Hz and the thickness of separability ($\lambda/2$) thus approximately 70-110 m (assuming a sill velocity of 5.55 km/s). The thickness of sills thinner than this cannot be confidently estimated due to interference between the seismic response form the top and base of the sill. The approximate vertical resolution of the case-study surveys will be estimated in individual chapters.

2.3.2 Horizontal Resolution

Horizontal resolution refers to how close two reflecting points can be situated, and still be recognised as individual points (Yilmaz, 1987). It is difficult to determine the horizontal resolution of migrated 2D and 3D seismic data (Sheriff & Geldart, 1995). In the case of migrated seismic data Ebrom et al. (1995) argue that the horizontal resolution is approximately equivalent to the bin spacing and thus a few tens of meters.

2.4 Seismic character of igneous sills

The high amplitude seismic response is the primary characteristic of igneous bodies imaged by seismic data, but additional characteristics that can help confident interpretation of such reflections as igneous bodies include:

- Igneous sills often transgress and cross-cut stratal reflectors, which suggests an intrusive origin.
- Igneous sills are highly continuous often covering areas of 10s or even 100s km^2.
- The reflections from igneous intrusions generally terminate abruptly, although, a slight decrease in reflection amplitude may occur near the sill tip.
- Seismic chimneys are often seen rising above sill tips (Chapter 6).
- The added thickness provided by the forcible intrusion of igneous material is partly accommodated by jack-up of the overlying sedimentary sequence (Chapter 5).
- Sedimentary packages comprising one or more igneous sills are likely to show signs of differential compaction.

2.5 Seismic artefacts and interpretation pitfalls

A number of interpretational challenges and artefacts with special implications for interpretation of igneous intrusions on seismic data should be noted. There are only few examples of wells encountering sills within 3D seismic survey areas and well calibration of sills with 3D seismic datasets is therefore not often possible. This complicates the determination of the phase of the seismic wavelet, which again makes interpreting top and base of the sills difficult. Interpreting the top and base of a sill and estimating sill thickness is further complicated if the imaged sill is thinner than half the dominant wavelength of the seismic wavelet because in such a case the seismic responses from the two intrusive contacts cannot be separated. In addition the seismic

response from a series of thin sills separated by thin sedimentary sequences may be indistinguishable from the response from a single thick sill (Badley, 1985).

A seismic signal loses energy when it encounters a high impedance boundary, such as a sill-sediment contact (Smallwood & Maresh, 2002). As a result, the seismic response (amplitude) from geological features below sills is dimmed and they are poorly imaged (Fig. 2.1). This masks deeper sills and thus complicates the interpretation of highly interconnected and layered sill complexes.

Confident interpretation of sill terminations on seismic data is particularly challenging. If a sill gradually thins towards its tip interference between the reflections from the top and base sill boundaries could give rise to a tapering reflection amplitude and it would be difficult to locate the true termination (Fig. 2.2). Over-migration of the data also complicates detection of sill terminations (Fig. 2.3), as resultant upward curving diffractions at sill tips or from discontinuities in the main body of the sill could easily be interpreted as true continuations of the sill. Careful interpretation of a dense grid of lines can, however, greatly increase the chance of eliminating this artefact, as diffractions generally are lower in amplitude and much less consistent between neighbouring lines, than genuine reflections.

Lava flows have similar acoustic properties as igneous sills and it may in some cases be difficult to determine whether a high amplitude igneous body is intrusive or extrusive as shallow sills can be almost perfectly concordant with stratal reflections and morphologically very similar in appearance to lava flows (e.g. sill 44 of the T38 survey area, section 5.4.3; Trude, 2004). Through detailed interpretation of the morphology of the igneous body, its relationships with stratal reflections, and possible feeder relationship it should, in most cases, be possible to establish whether the igneous body is a surface lava flow or an igneous sill intrusion.

Finally, dykes, which play an important role in vertical magma transport, are difficult to recognise on seismic data, as the reflection seismic method is unsuited to image near-vertical features (Badley, 1985; Smallwood & Maresh, 2002).

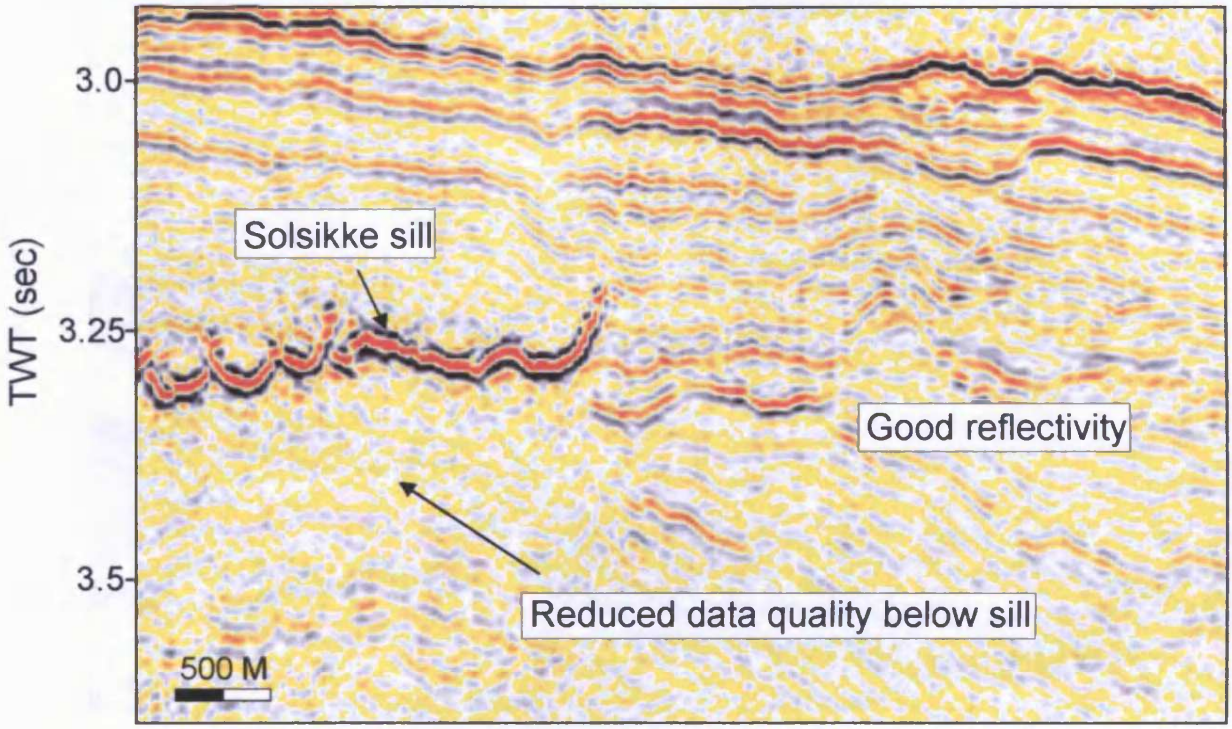

Fig. 2.1 Seismic section showing reduction of data quality underlying shallowly emplaced sill (Solsikke sill; Chapter 5).

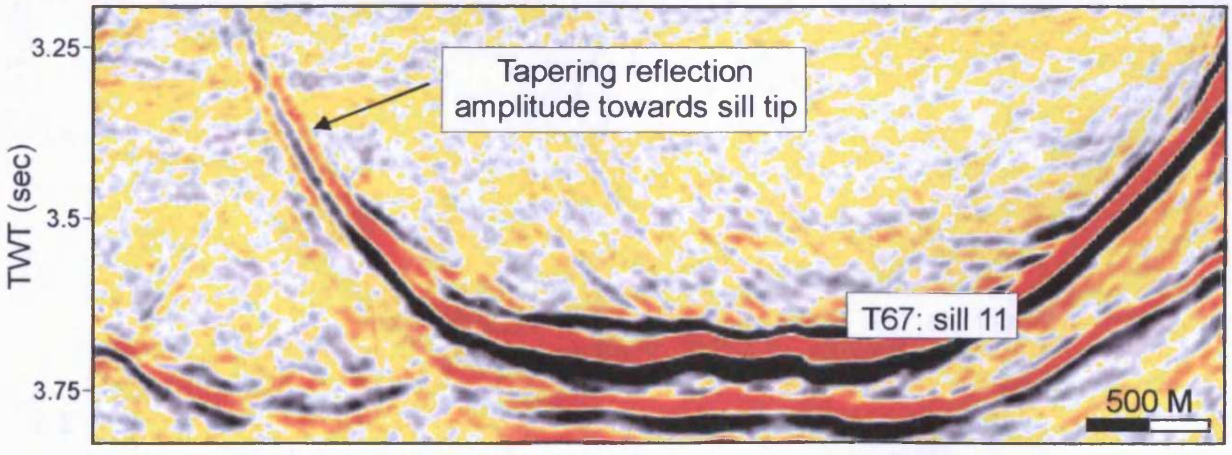

Fig. 2.2 Seismic section from the T67 survey area (Chapter 3) showing tapering reflection amplitude towards the transgressive tip of sill 11.

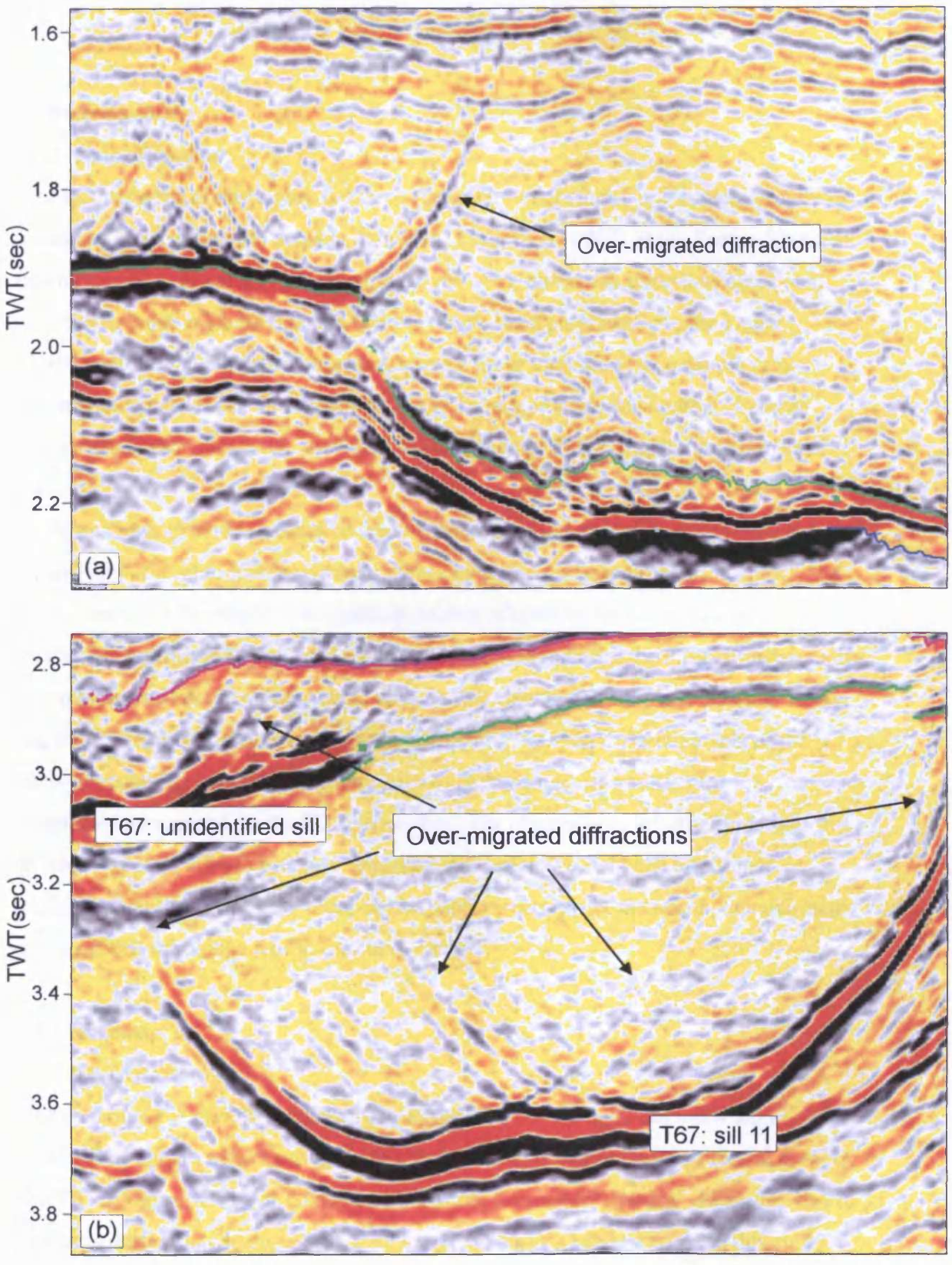

Fig. 2.3 Over-migrated diffractions. (a) Over-migrated diffraction at the edge of a lava escarpment (Section 3.2.4.1). (b) Over-migrated diffractions at sill tips and from the top surface of sill 11 and an unidentified sill in the T67 survey area.

CHAPTER 3: THE IGNEOUS COMPLEX OF TRANCHE 67 (NORTH-EASTERN FAEROE-SHETLAND BASIN)

3.1 Introduction

3.1.1 Aims of chapter

This chapter aims at describing the three-dimensional geometry and context of igneous intrusions observed on 3D seismic data from Tranche 67 (T67) of the Faeroe-Shetland Basin (Fig. 3.1). In the T67 3D seismic survey area, numerous intrusions associated with the Brendan's Dome igneous complex have been emplaced into the Upper Cretaceous and Paleocene sediments. Many of these intrusions have simple cross-sectional geometries and are relatively easily separated from one another. In three-dimensional space, however, the intrusions are seen to form a highly interconnected network.

This chapter provides a detailed three-dimensional interpretation of the geometries of, and junction relationships between, these intrusions. The interpretation shows that the terminology developed from outcrop studies of igneous intrusions and generally used in the published literature is inadequate when considering the three-dimensionality of intrusions revealed by 3D seismic data. In this chapter some simple informal terms are, therefore, introduced to assist in distinguishing between different levels of the three-dimensional geometrical complexity of igneous intrusions and intrusive complexes recognised on the 3D seismic data. The chapter also informally defines three different types of sill-sill junction relationships recognised between interlinked intrusions and illustrates how these can be used to reconstruct the spatial development of interlinked intrusions within the survey area.

3.1.2 Database

3.1.2.1 Seismic data

This case-study is almost exclusively based on 3D seismic data, but a few 2D seismic lines will be shown in order to place the study area within a regional structural context. The T67 3D seismic survey covers an area of approximately 600 km^2. However, due to problems during data loading only a subset of the survey has been used in this study (Fig. 3.2). The used subset covers an area of approximately 450 km^2 and spans the full inline range, but only approximately two thirds of the crossline range (XLN1080-3024). Within the available data area, two smaller data gaps occur (XLN 1515-1517 and XLN

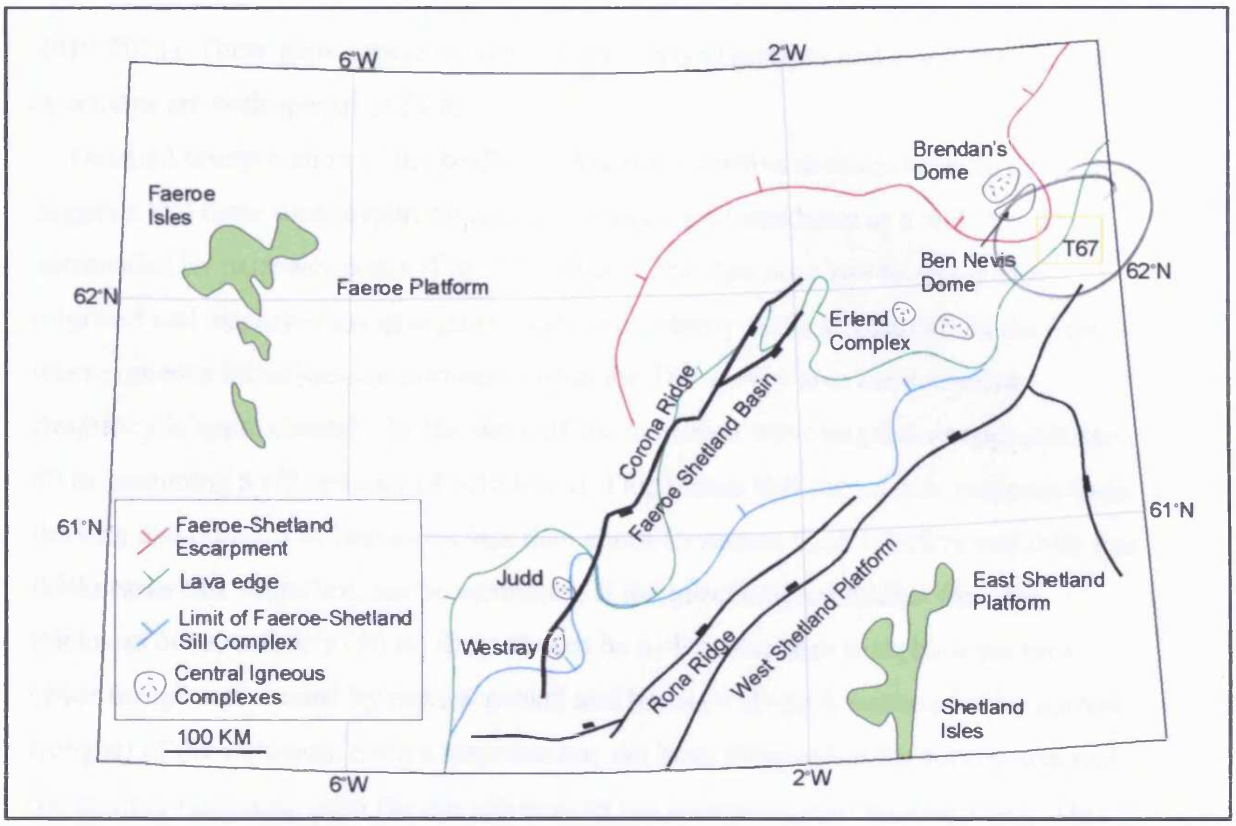

Fig. 3.1 Location map showing the location of the T67 3D seismic survey area, Brendan's Dome, and the Ben Nevis Dome. Note the location of the Faeroe-Shetland Escarpment, lava edge, and the limit of the Faeroe-Shetland sill complex. After Naylor et al., 1999.

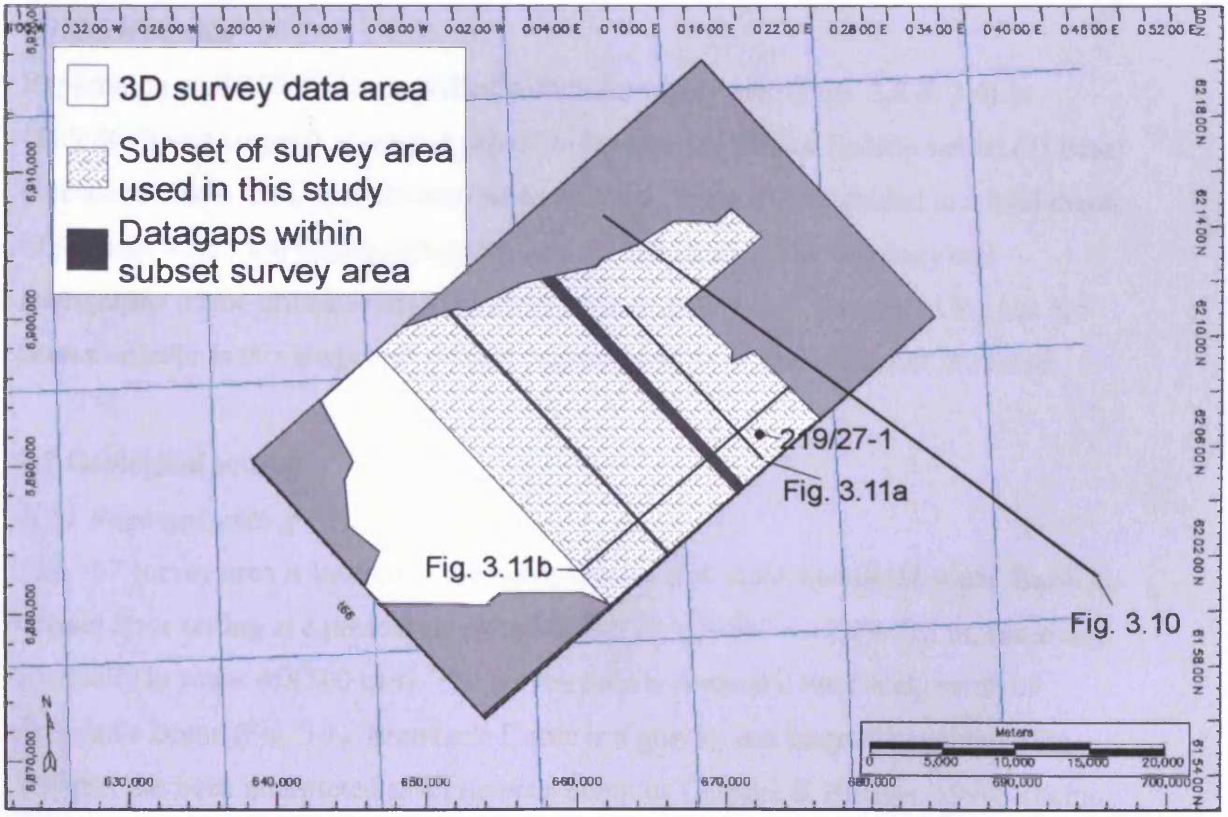

Fig. 3.2 Map showing the outline of the T67 3D seismic survey area. Note the locations of Figs. 3.11 and 3.10.

2019-2071). These gaps appear on some of the vertical sections and maps. Inlines and crosslines are both spaced at 25 m.

Detailed interpretation of the seafloor reflection (positive acoustic boundary) suggests that these data display an increase in acoustic impedance as a wide trough surrounded by narrower peaks (Fig. 3.3). That is, the data are close to zero-phase migrated and displayed using negative standard polarity (SEG standards). At the depth where igneous intrusions are intruded within the T67 survey area the dominant frequency is approximately 35 Hz and half the dominant wavelength thus approximately 80 m (assuming a sill velocity of 5.55 km/s). This means that the seismic response from the tops and bottoms of intrusions less than about 80 metres thick interfere and their true thicknesses can, therefore, not be estimated. If the intrusions are thicker than the thickness of separability (80 m) there should be a clear response from both the tops (wide trough surrounded by narrow peaks) and bases (wide peak surrounded by narrow troughs) of the intrusion. Such a response has not been observed in the survey area and the seismic responses from the top and base of the intrusions must be interfering. This suggests that the intrusions are generally less than 80 m thick, and that their true thicknesses can, therefore, not be estimated.

3.1.2.2 Well data

Exploration well 219/27-1 was drilled within the survey area (Figs. 3.2 & 3.4) in 1985/86. It was targeted at several objective horizons: (1) Basal Eocene sands; (2) Basal Paleocene sands; (3) Upper Cretaceous carbonates. The well was drilled to a total depth of just less than 3 km before being plugged and abandoned. The lithology and stratigraphy of the drilled section is described in section 3.2.3. The digital log has not been available to this study and a direct seismic well tie is, therefore, not provided.

3.2 Geological setting

3.2.1 Regional setting

The T67 survey area is located in the north-eastern part of the Faeroe-Shetland Basin in a basin floor setting at a present-day water depth of 378-962 ms (284-722 m, assuming a velocity in water of 1500 m/s). The survey area is situated immediately south of Brendan's Dome (Fig. 3.1). Brendan's Dome is a gravity and magnetic anomaly (Fig. 3.5) that has been interpreted as an igneous complex (Ritchie & Hitchen, 1996; Ritchie et al., 1999; Hodges et al., 1999). The Brendan's Dome igneous complex is believed to

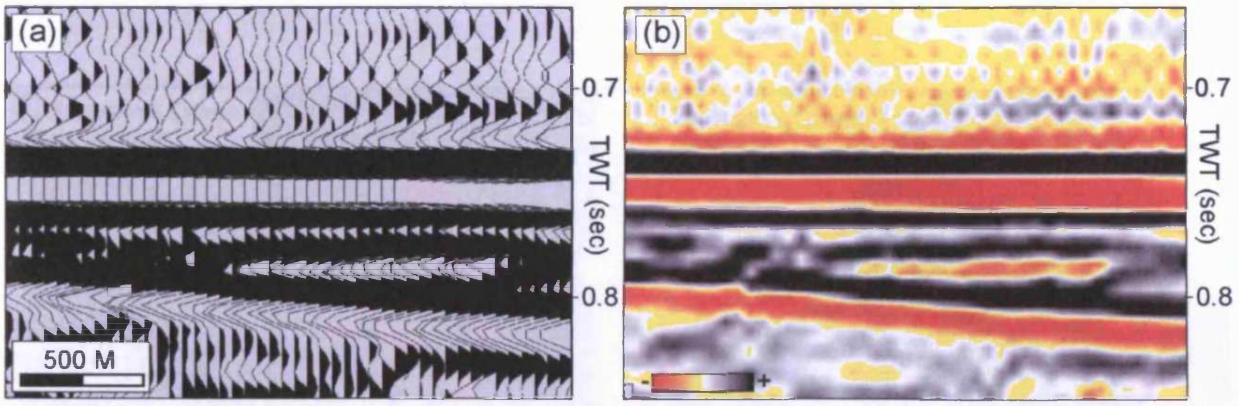

Fig. 3.3 Seismic character of the seabed reflection. (a) Variable area (VA) display. (b) Variable intensity (VI) display. The data are close to zero-phase migrated and displayed using negative standard polarity (SEG standards).

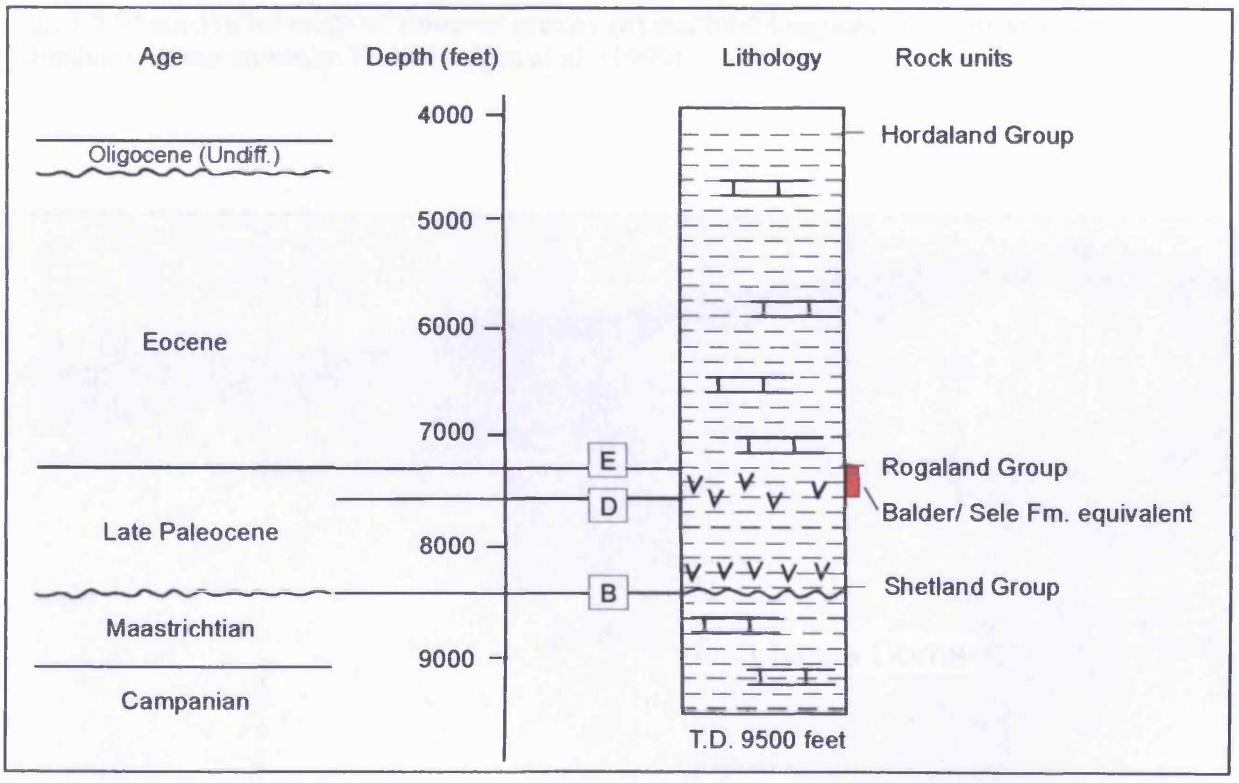

Fig. 3.4 Well summary for exploration well 219/27-1 drilled within the T67 3D seismic survey area. See Fig. 3.2 for well location.

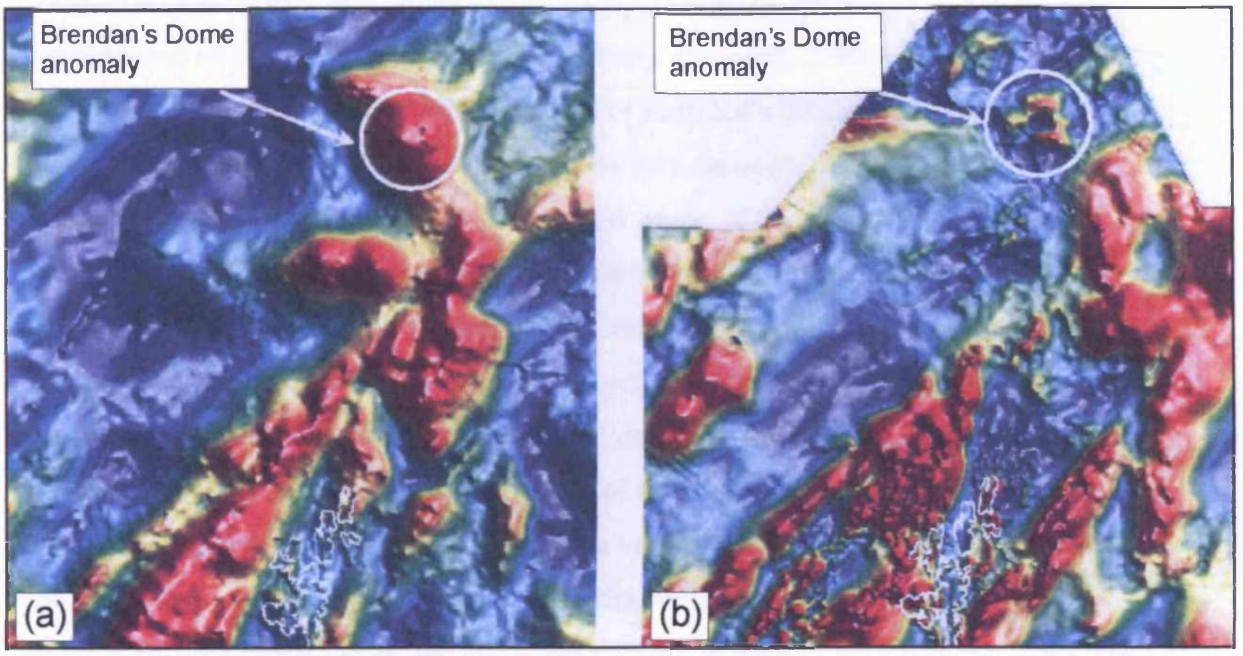

Fig. 3.5 Shaded relief maps of Bouguer gravity (a) and total magnetic field (b) across the Brendan's Dome anomaly. From Hodges et al. (1999).

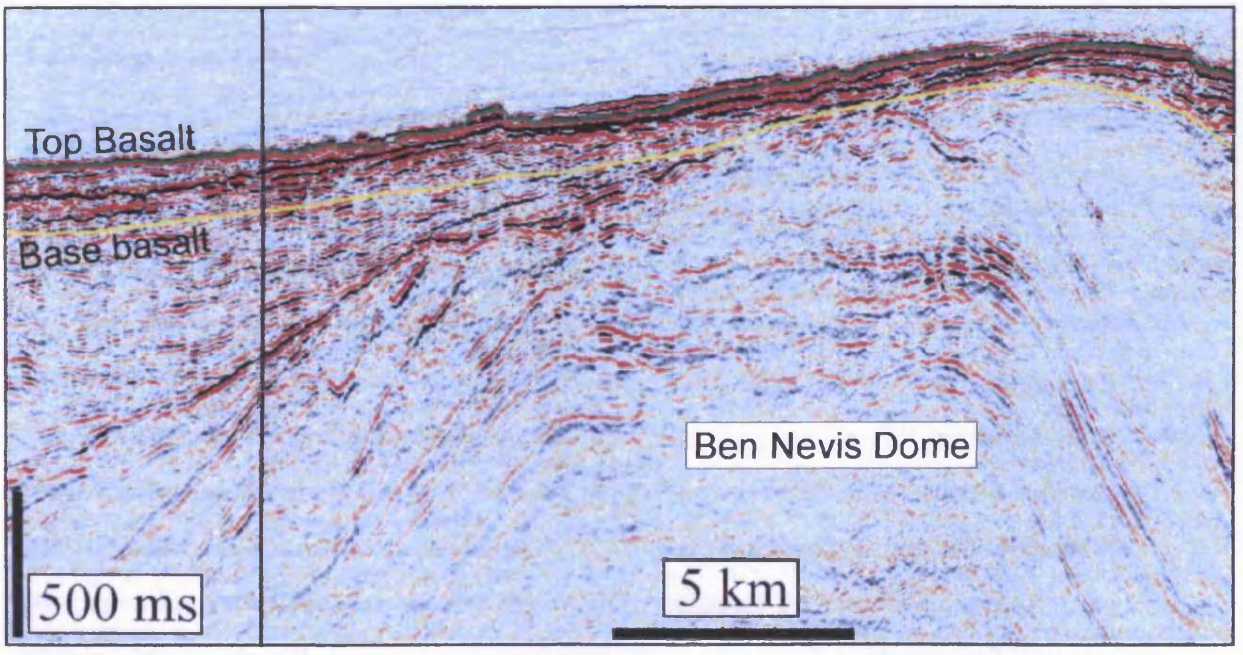

Fig. 3.6 Seismic cross-section through Ben Nevis Dome from T65/ T66 3D seismic survey north of the T67 3D seismic survey area. From Hodges et al. (1999).

have fed igneous sills intruded into Upper Cretaceous and Paleocene sediments and extrusion of lava flows at the seafloor in the area during the late Paleocene and early Eocene (Smythe et al. 1983; Hodges et al. 1999). A large (> 300 km^2) NE-SW trending dome-shaped structure with a vertical relief of approximately 2000 m, referred to as the Ben Nevis Dome, is located 20 km south-east of Brendan's Dome (Figs. 3.1 & 3.6; Hodges et al., 1999). The structure is draped by lava flows and its internal structure is, as a result, poorly resolved by seismic data. The origin of the Ben Nevis Dome is uncertain. Hodges et al. (1999) suggested that the structure formed as a result of uplift of a Jurassic fault block and inversion of the Cretaceous fill in the adjacent half-graben due to the intrusion of the Brendan's Dome igneous complex (Fig. 3.7). The Ben Nevis structure shows a striking resemblance to the Phoenix shield volcano imaged on regional 2D seismic lines in the northern part of the Walvis Basin offshore Namibia (Fig. 3.8). This buried seamount volcano has a vertical relief of approximately 5000 m and covers an area of 2000 km^2. Considering the similarities in seismic expression between the Ben Nevis Dome and the buried volcano as well as the closeness of the Ben Nevis Dome to the Brendan's Dome igneous complex it seems possible that the Ben Nevis Dome could be of igneous origin. A further investigation of the origin of the Ben Nevis Dome is beyond the scope of this study.

3.2.2 Structural context

The regional pre-Upper Cretaceous structural context of the T67 survey area is known from interpretation of regional 2D seismic lines. The schematic illustration presented in Fig. 3.9 shows that a series of NE-SW trending tilted fault blocks (some exhibiting footwall erosion) with throws of up to > 5 km dominate the pre-Upper Cretaceous in the area between the North Viking Graben to the south-east and Brendan's Dome to the north-west. Between the North Viking Graben and the Magnus Trough, the faults form a series of horsts and grabens, whilst north-west of the Magnus Trough the faults consistently downthrow to the NW. The faults formed as a result of rifting during the latest Jurassic-earliest Cretaceous (Dore et al., 1999). During rifting the half-grabens were essentially sediment starved but they were subsequently infilled with a flat-lying largely post-rift sequence of Lower Cretaceous sediments. During the post-rift stage the area subsided and the fault blocks were passively buried by Upper Cretaceous and later sediments. The Upper Cretaceous and Paleocene intruded sediments are largely

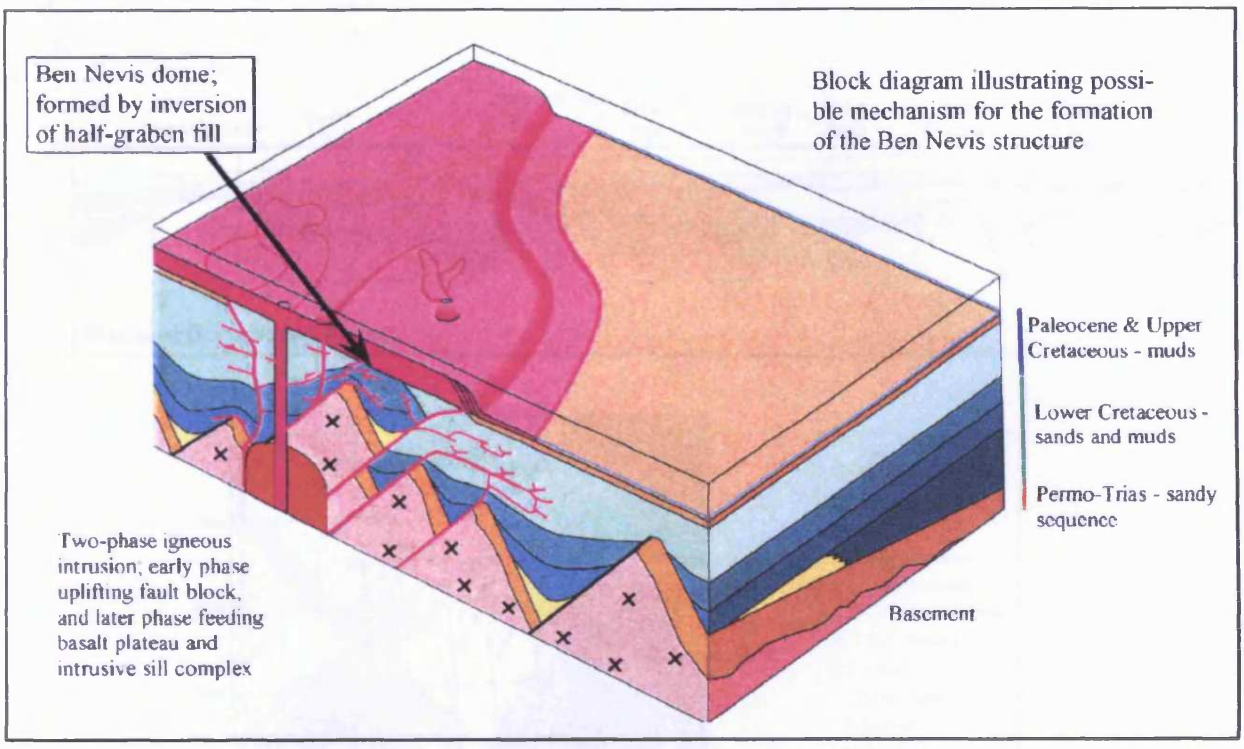

Fig. 3.7 Block diagram illustrating the development of Ben Nevis Dome as proposed by Hodges et al. (1999). The structure is interpreted to have formed as a result of uplift of a Jurassic fault block and inversion of the Cretaceous fill in the adjacent half-graben due to the intrusion of the Brendan's Dome igneous center.

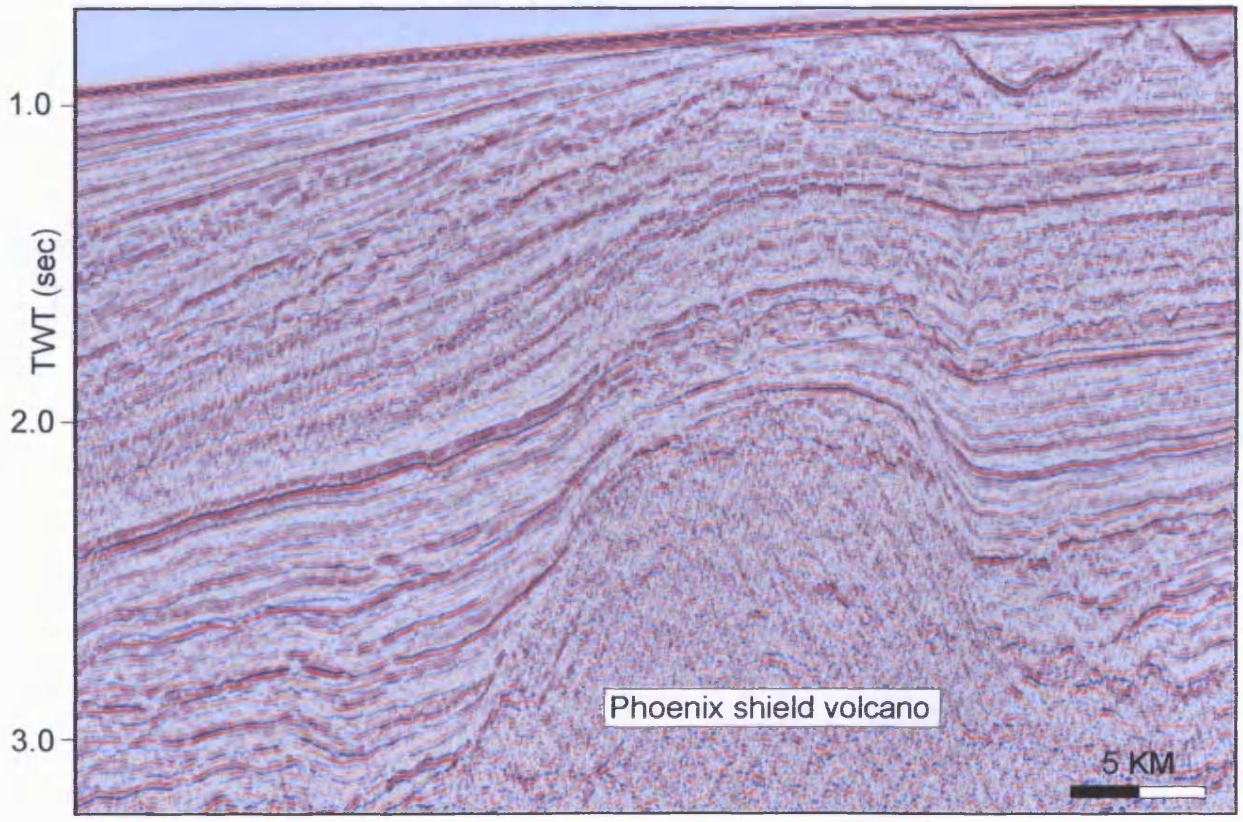

Fig. 3.8 2D seismic section showing the cross-sectional geometry of the Phoenix shield volcano in the Walvis Basin offshore Namibia. Data courtesy of R. Swart, Namcor.

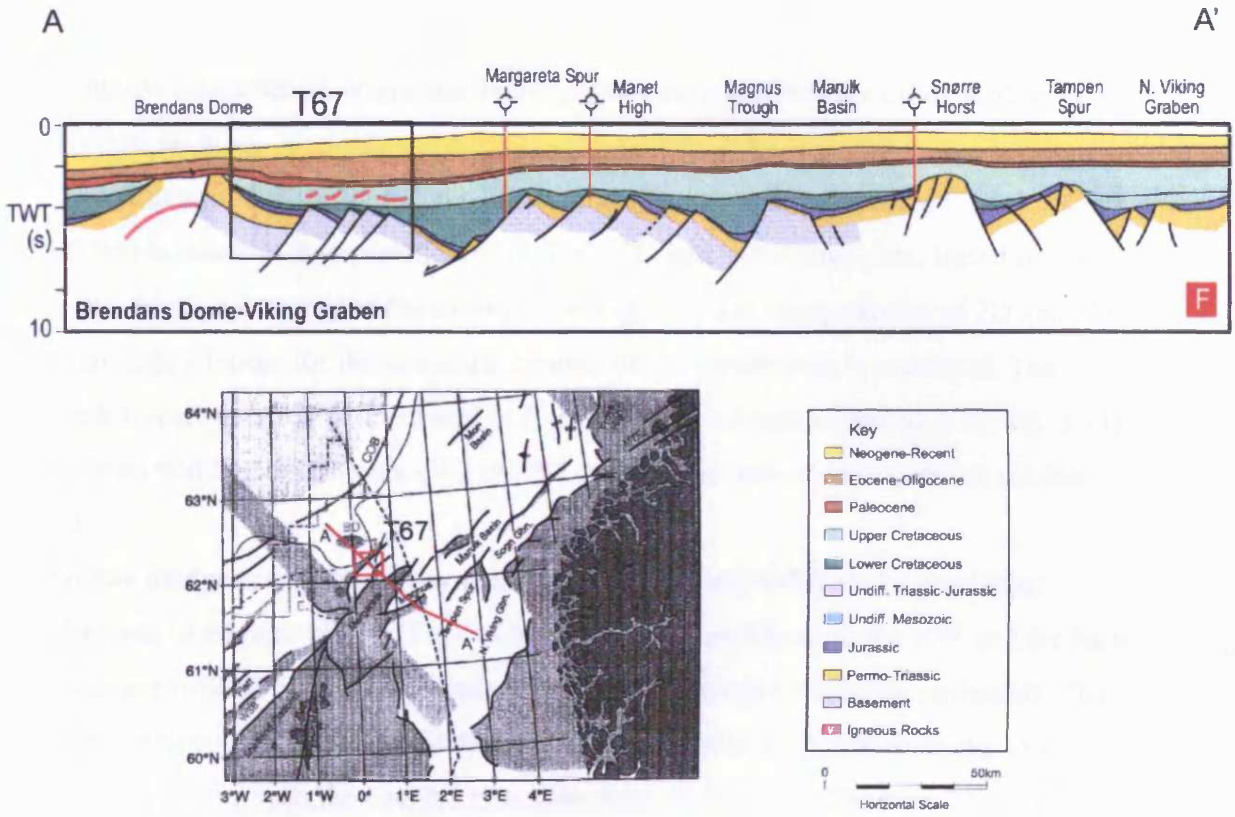

Fig. 3.9 Regional cross-section based on 2D seismic line NEST 90-123 showing the regional structural context of the T67 3D seismic survey area. After Dore et al. (1999).

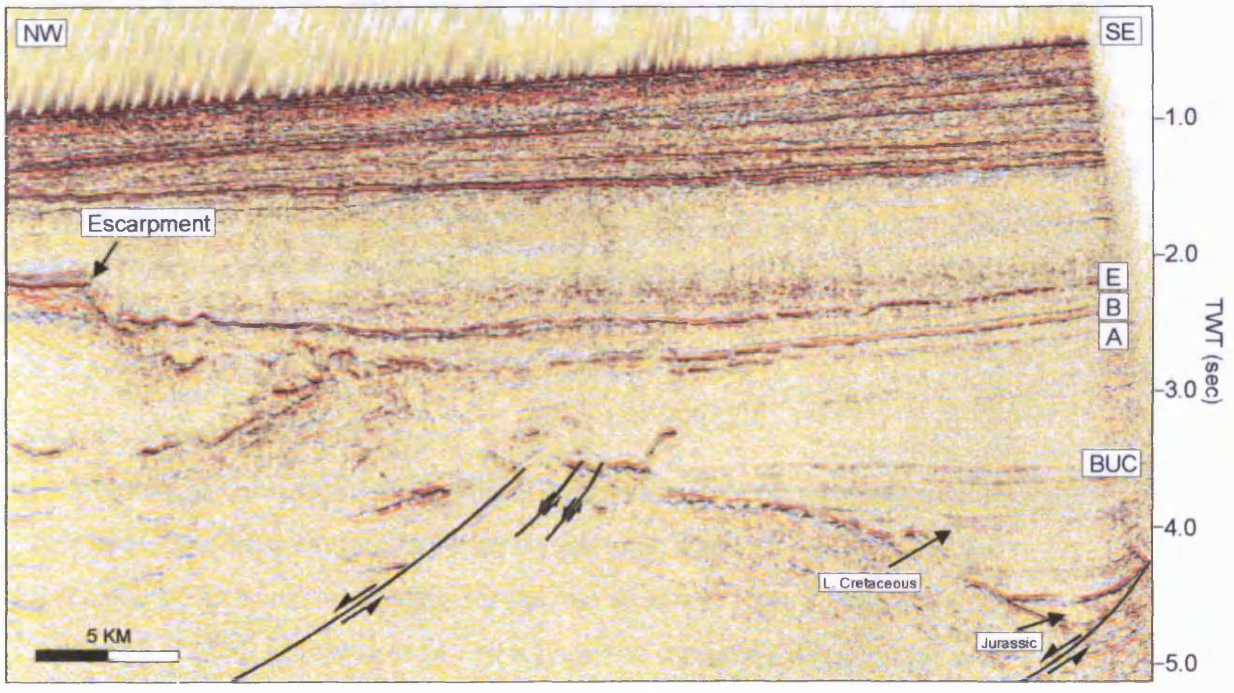

Fig. 3.10 2D seismic section (NEST 90-122) showing the structural context of the t67 3D seismic survey area. BUC = Base Upper Cretaceous. Horizons A-E are described in the text in section 3.2.2. See Fig. 3.2 for line location.

structurally undeformed, whilst the overlying Eocene sediments are influenced by polygonal faulting.

The structural and stratigraphic context of the survey area is shown in Figs. 3.10 and 3.11, and is based on interpretation of regional 2D and 3D seismic data. Based on the regional structural setting of the survey area (Fig. 3.9) and interpretation of 2D and 3D seismic data a model for the structural context of the survey area is presented. The structural interpretation is illustrated in Fig. 3.10. The horizons labelled A-E (Fig. 3.11) have been tied to exploration well 219/27-1 and will be described in detail in section 3.2.3.

In this interpretation the survey area is shown as being underlain by pre-Upper Cretaceous tilted fault blocks (Fig. 3.10). The faults downthrow to the NW and the half-grabens are infilled by a post-rift unit dominated by Lower Cretaceous sediments. The Lower Cretaceous graben-fill (sands and muds; Hodges et al., 1999) is shown to be sharply separated from the Upper Cretaceous mud-dominated sediments. The base of the Upper Cretaceous (BUC) is seismically imaged as a continuous positive reflection of moderate amplitude. Horizons A and B (Base Paleocene) have a curved geometry and dip towards the north-west (Fig. 3.11a). Horizon B is onlapped by a wedge-shaped unit that is bound upwards by horizon C. Horizons D and E (Paleocene-Eocene boundary) are concordant with horizon C. The dipping geometries of horizons A and B and the onlap wedge constrained by horizons B and C suggest that local deformation took place in the area around the time of horizon B. Withdrawal from below horizon A or loading onto horizon B to the north or some other mechanism must have led to the development of a local low area, which has been infilled by the B-C unit. The Eocene unit overlying horizon E is mud-dominated and intensely deformed by polygonal faults (Cartwright, 1994; Cartwright et al., 2003).

3.2.3 Stratigraphic context

A number of key horizons (horizons A-E) within the Upper Cretaceous and Paleogene succession have been interpreted in the survey area. They are illustrated in the representative sections through the 3D volume shown in Figs. 3.11a and 3.11b. Horizons B, D, and E have been tentatively tied to the near-by exploration well 219/27-1 (Fig. 3.4), based on a comparison of the seismic character of these horizons and identification of compatible seismic reflectors on the sonic log (logs were only made

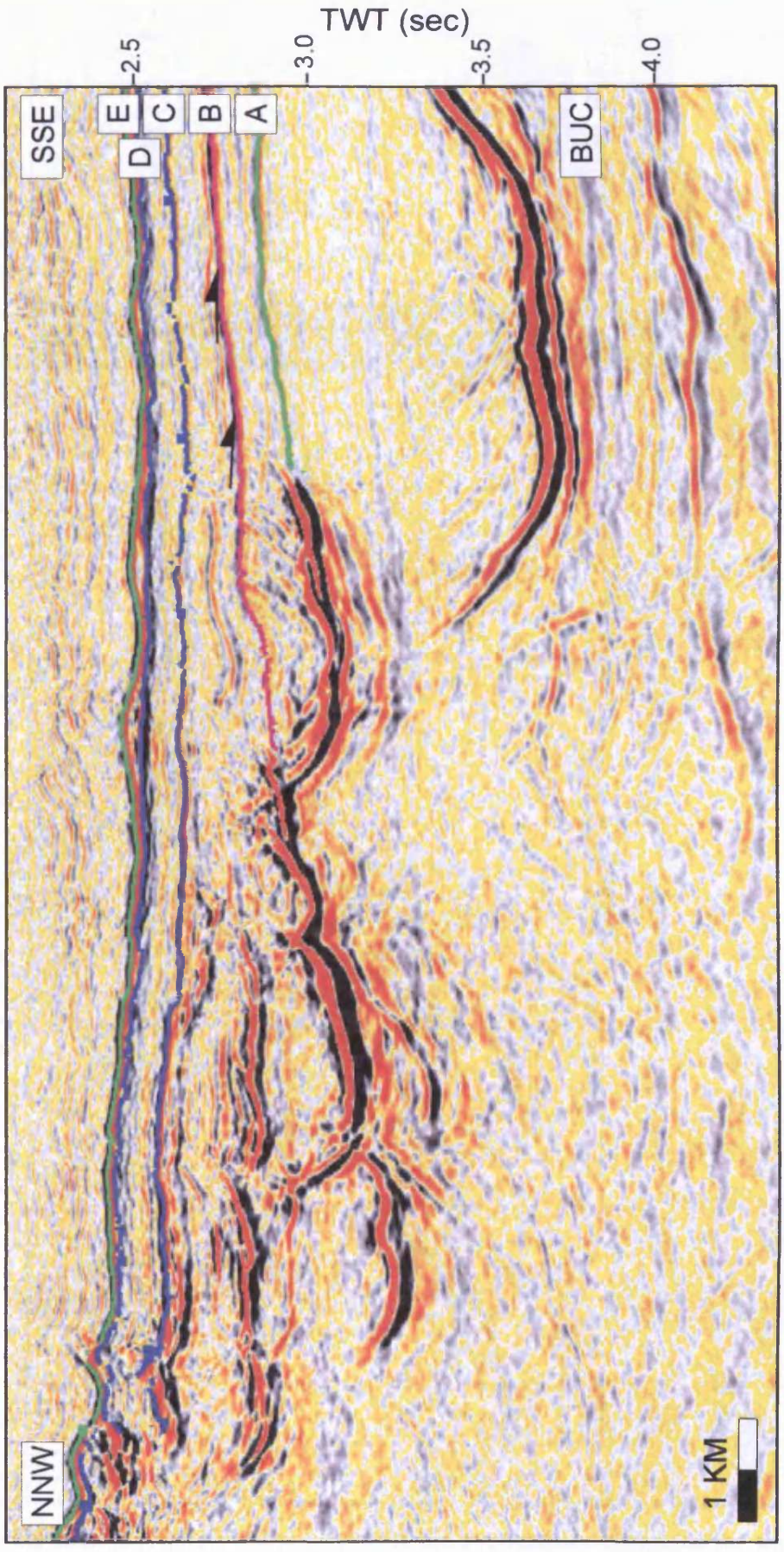

Fig. 3.11a 3D seismic section (cross-line) showing the stratigraphic context of the survey area and the seismic characters of horizons A-E. See Fig. 3.2 for line location.

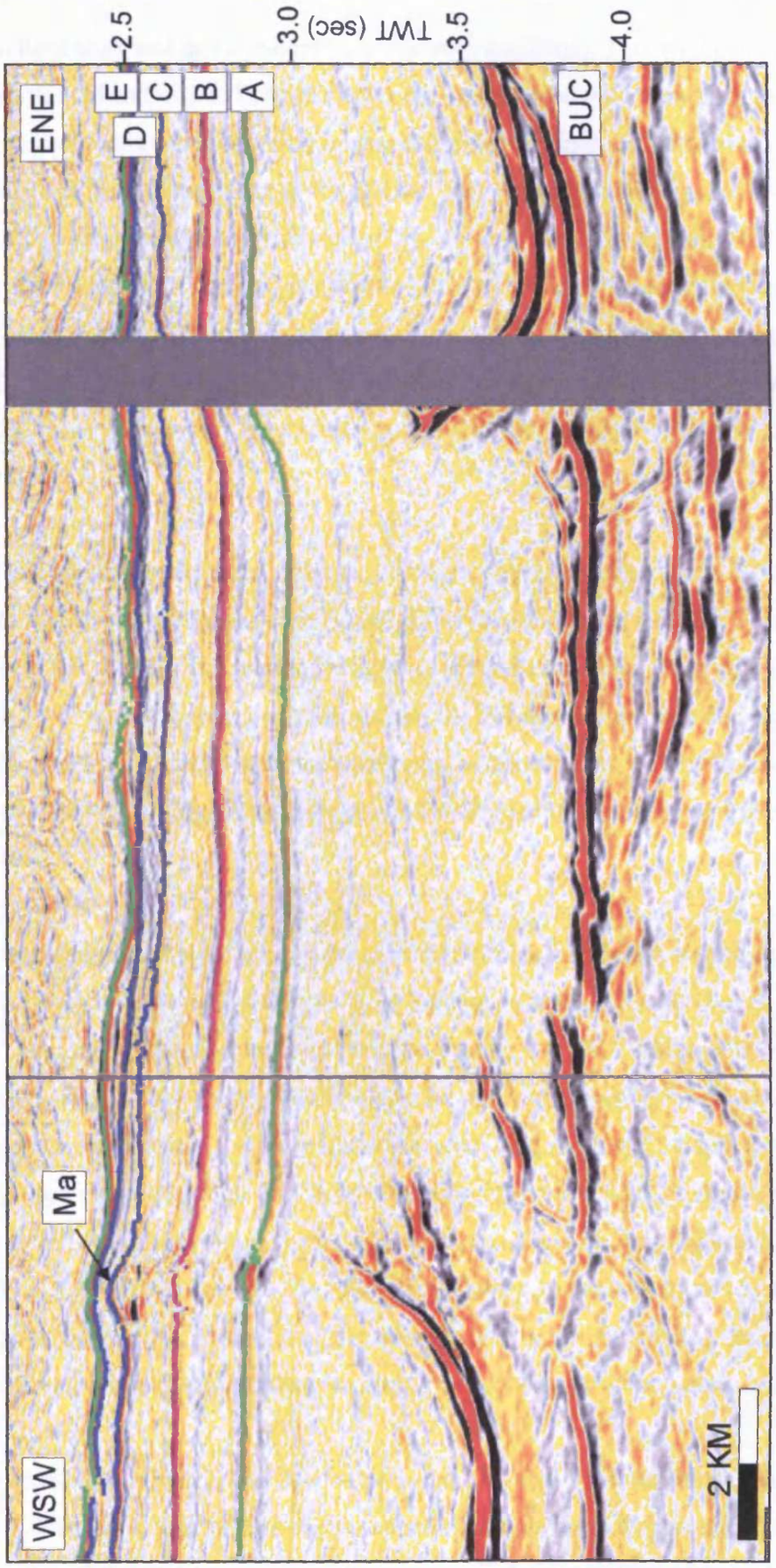

Fig. 3.11b 3D seismic section (in-line) showing the stratigraphic context of the survey area and the seismic characters of horizons A-E. A mound structure labelled Ma is also seen and this will be further described and discussed in chapter 6. Grey through-going zones indicate missing data. See Fig. 3.2 for line location.

available in hard copy and no time-depth curves were available). This well penetrated almost 1 km of Mid and Lower Eocene claystones interbedded with numerous thin (< 5 m) limestone beds before encountering an approximately 60 m thick tuffaceous unit. This volcanic tuff unit is equivalent to the Balder Tuff and approximately marks the Paleocene-Eocene boundary (Knox & Holloway, 1992; Smallwood & Gill, 2002). Underlying the Balder Tuff the well penetrates close to 300 m of Upper Paleocene claystone interbedded with thin limestone beds (< 5 m) before encountering a second 60 m thick tuff. The base of this Upper Paleocene tuffaceous unit unconformably overlies 400 m of claystone dominated Upper Cretaceous sediments before reaching its total depth (2,896 m).

Horizon A is a positive continuous reflector of Upper Cretaceous age. It can be mapped over an area of 110 km^2 along the eastern margin of the survey area at a TWT range of 2700-3100 ms (Fig. 3.12). The mapped reflection is low to moderate in amplitude, but towards the north it becomes less continuous and the reflection amplitude decreases, making it increasingly difficult and eventually impossible to interpret. The horizon, locally, forms the base to high amplitude positive reflections interpreted as igneous intrusions (Fig. 3.11a).

Horizon B was mapped at a continuous positive reflection of moderate amplitude. The reflection is interpreted to mark the base of the Paleogene and was mapped over an area of 160 km^2 along the eastern boundary of the survey area at a TWT range of 2550-3000 ms (Fig. 3.13). The horizon gently dips towards the north and forms the lower boundary to a wedge shaped onlap unit that expands in the northern direction. Towards the north-west reliable correlations became problematic in a region of low signal to noise ratio underlying a unit of high amplitude reflections interpreted as a package of stacked lava flows (Section 3.2.4.2) because of attenuation (Chapter 2). In the central and eastern parts of the survey area the horizon could not be interpreted where it forms the base to a series of high amplitude positive reflections interpreted as igneous intrusions.

Horizon C marks a moderately continuous, low amplitude positive reflection. The Horizon is Paleocene in age and has been mapped across an area of approximately 275 km^2 at a depth of 2200-2950 ms (Fig. 3.14). Horizon C defines the top of a number of small mound structures (Labelled Ma in Fig. 3.11b; further described in Chapter 6) as

Fig. 3.12 Time-structure map of horizon A.

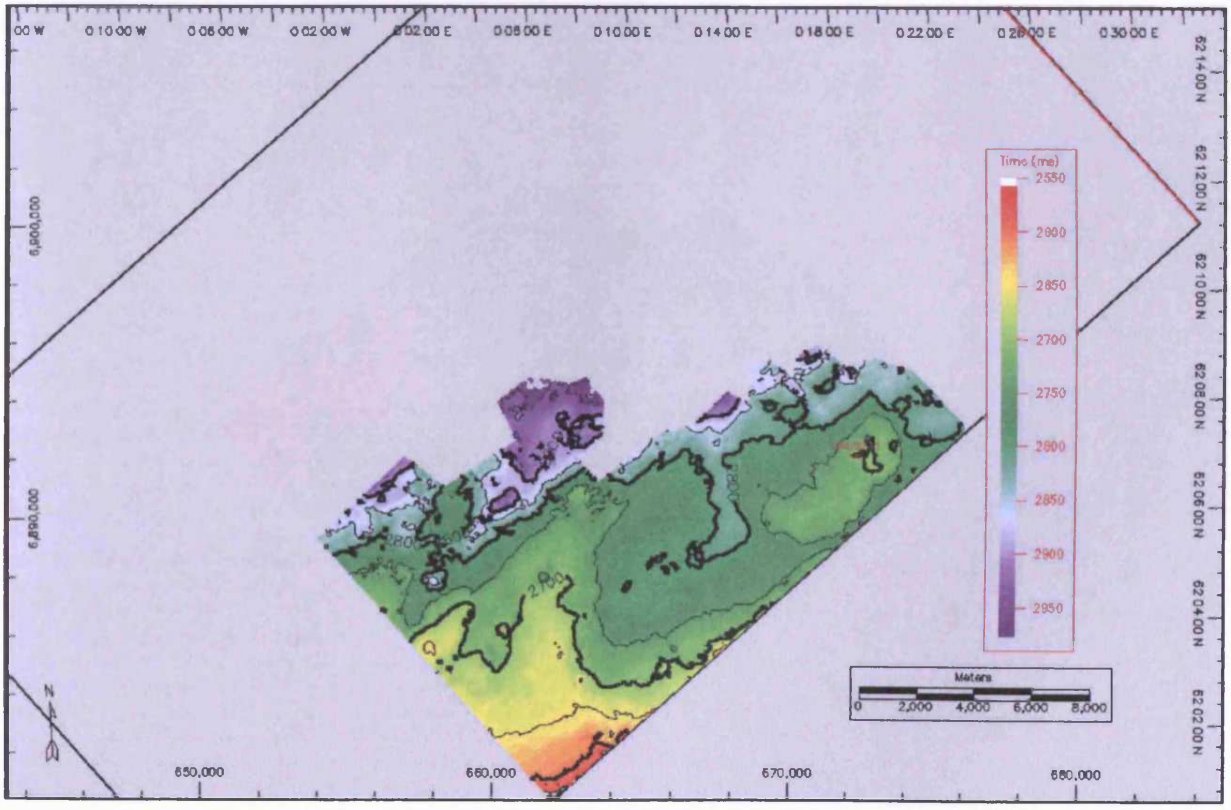

Fig. 3.13 Time-structure map of horizon B.

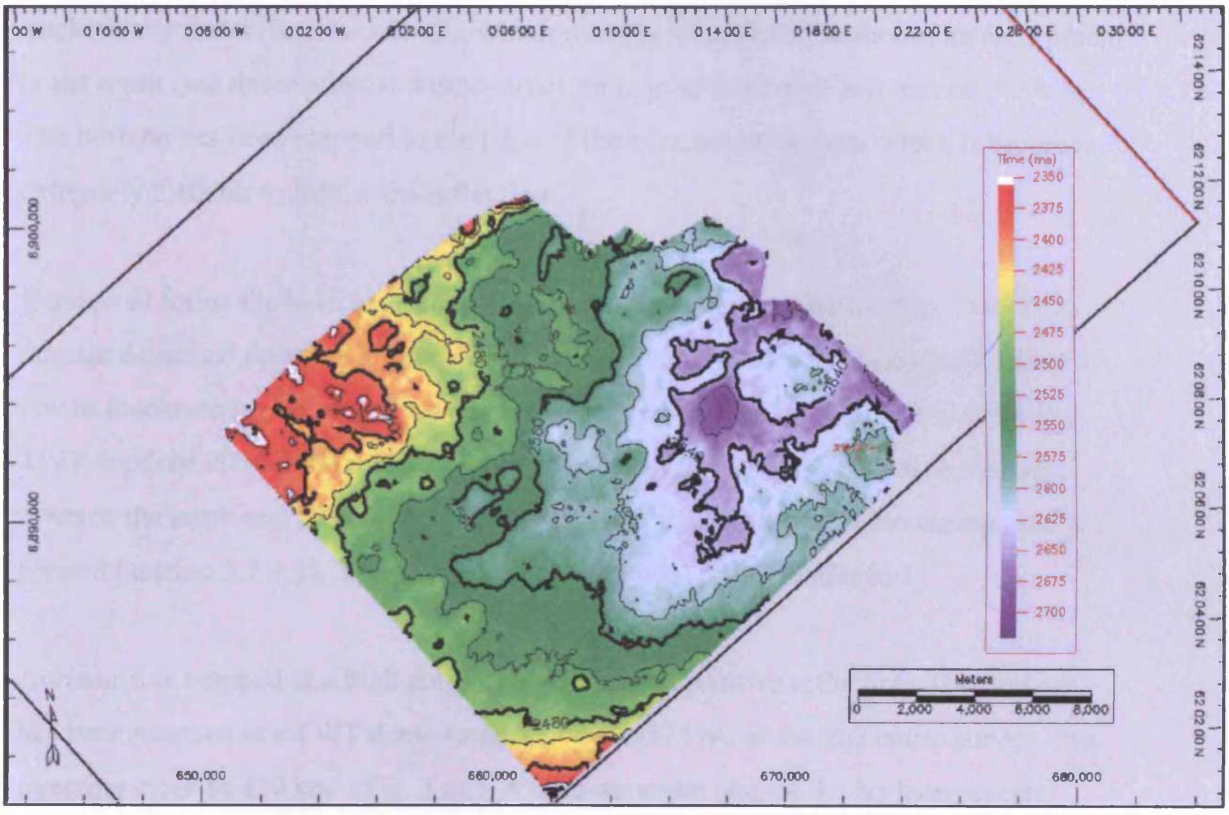

Fig. 3.14 Time-structure map of horizon C.

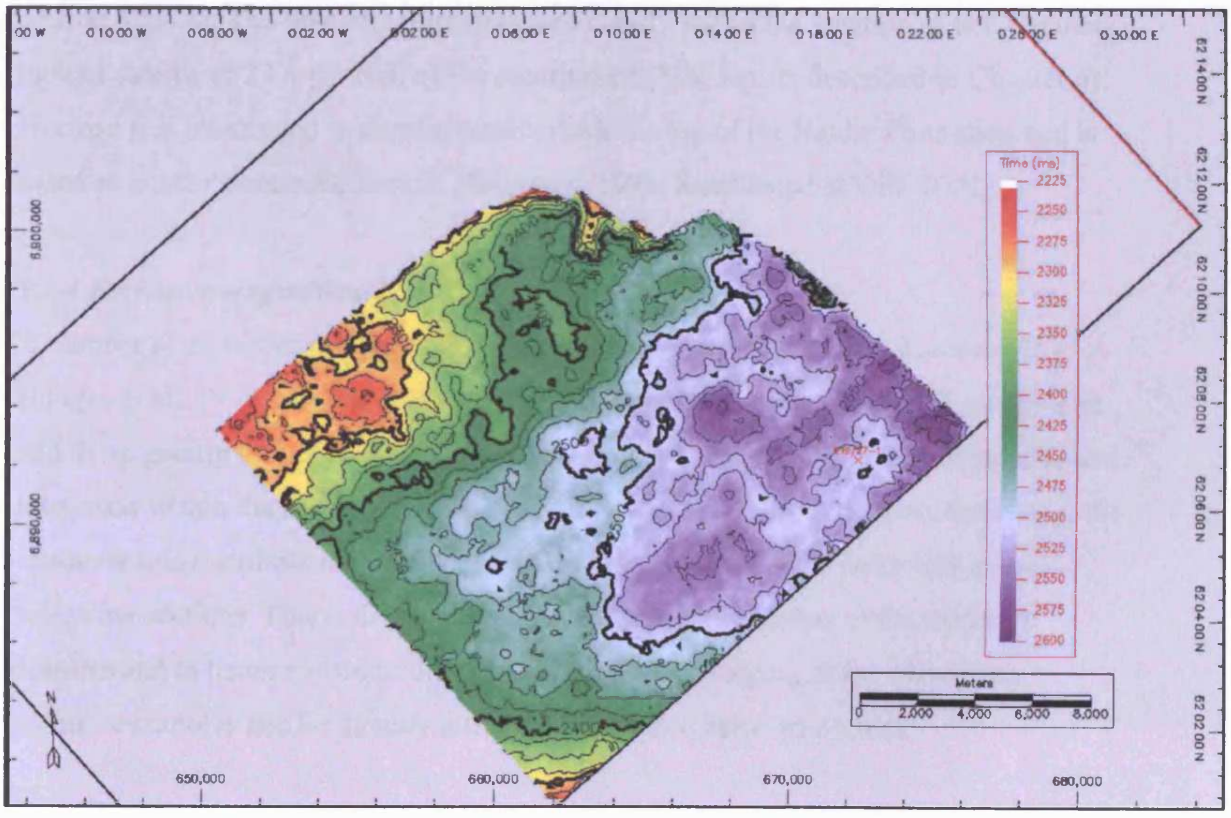

Fig. 3.15 Time-structure map of horizon D.

well as the top of a package of concordant high amplitude reflections, interpreted as stacked lava flows (section 3.2.4.2), which extends away from the foot of an escarpment to the north (see description and time-structure map of horizon E and section 3.2.4.1). The horizon has been mapped to the edge of the escarpment beyond which it becomes extremely difficult to follow the reflection.

Horizon D forms the base to a series of mounds (Mb; further described in Chapter 6) that are delimited upwards by horizon E. It has been mapped at a positive reflection of low to moderate amplitude across an area of approximately 300 km^2 at a present-day TWT depth of 2050-2600 ms (Fig. 3.15). The horizon becomes difficult to identify towards the north and mapping could not be done in the area where the escarpment is present (section 3.2.4.1). This horizon marks the base of the Balder tuff.

Horizon E is mapped at a high amplitude continuous positive reflection. The horizon has been mapped at a TWT depth range of 1800-2575 ms across the entire survey area covering close to 450 km^2 (Fig. 3.16). A time-structure map of the horizon reveals several interesting features. The horizon drapes an escarpment to the north, which accounts for the majority of the > 700 ms TWT vertical relief on the horizon (Fig. 3.16; section 3.2.4.1). The time-structure map also clearly shows the location of two circular mound structures 2 km in front of the escarpment (Mb; further described in Chapter 6). Horizon E is interpreted to approximately mark the top of the Balder Formation and is dated as latest Paleocene (Knox & Holloway, 1992; Smallwood & Gill, 2002).

3.2.4 Extrusive magmatism

A number of extrusive magmatic features, previously described in the literature (e.g. Hodges et al., 1999; Smythe et al., 1999), have been recognised in the T67 survey area and these greatly influence the ability of the seismic data to image deeper structures and intrusions within the survey area. Although this thesis focuses on igneous intrusions, the character and distribution of the extrusive features will be briefly described in the following sections. This is done to illustrate the seismic character of the extrusive features and to better constrain the area in which poor imaging of the underlying intrusive complex can be directly attributed to the extensive lava cover.

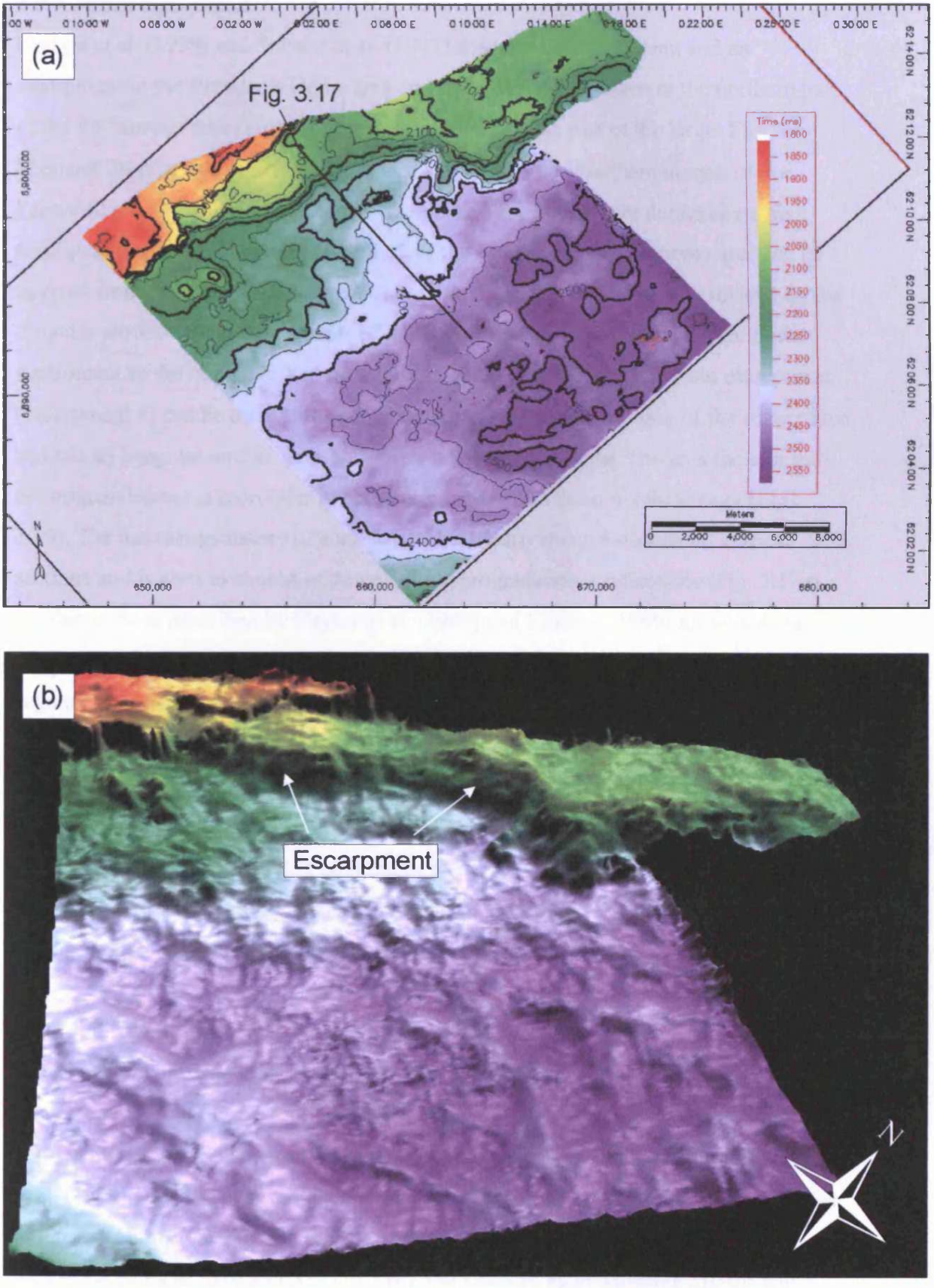

Fig. 3.16 Horizon E. (a) Time-structure map. Note line location for Fig. 3.17. (b) 3D display showing the presence of an escarpment to the north-west.

3.2.4.1 Lava escarpment

Hodges et al. (1999) and Smythe et al. (1983) described a lava plateau and an escarpment in the Brendan's Dome area and these features are seen in the northern part of the T67 survey area (Fig. 3.17). The escarpment forms part of the larger Faeroe-Shetland Escarpment, which can be traced along the entire northern margin of the Faeroe-Shetland Basin (Fig. 3.1). The plateau and escarpment are defined by a high amplitude positive reflection. The outline of the escarpment in the survey area can be inferred from the time-structure map of horizon E (Fig. 3.16), but is best imaged on the time-dip attribute map of horizon E (Fig. 3.18). This map also reveals an additional escarpment to the north, stacked on top of the main escarpment. The main escarpment (escarpment 1) can be traced along the entire north-western boundary of the survey area and has an irregular outline with an overall NE-SW orientation. Towards the east the escarpment becomes more poorly defined. Escarpment 1 is up to 600 m high (Fig. 3.19). The internal geometry of escarpment 1 is clearly imaged on several vertical sections and is seen to consist of downlapping progradational reflections (Fig. 3.19a), similar to those described by Naylor et al. (1999) and Kiørboe (1999) for lava delta propagation. Escarpment 2 has an irregular outline comprised of two NE-SW trending segments connected by a NW-SE trending segment (Fig. 3.18). The most western of these segments is coincident with the extent of escarpment 1. It has a slightly lower vertical relief than escarpment 1, generally measuring less than 300 m (Fig. 3.19). Where escarpment 2 is stacked on top of escarpment 1 the two escarpment blocks are clearly separated by a flat-lying continuous moderate to high amplitude reflection (Fig. 4.19b). Hodges et al. (1999) attributed the stacking of individual flows and formation of local scarps to changes in sea level during the construction of the plateau.

3.2.4.2 Lava flow unit

A package of concordant very high amplitude positive reflections is seen extending away from the foot of the escarpment (Figs. 3.17 & 3.19). The package is upwards defined by horizon C. The package was interpreted as a series of lava flows by Hodges et al. (1999) which seems reasonable considering the high amplitudes and concordance of the reflections (Chapter 2). The base of the package is poorly defined, but the package appears to have a maximum TWT thickness of approximately 210 ms and it gradually thins away from the escarpment. The time of extrusion is constrained by horizons C to the (Late) Paleocene.

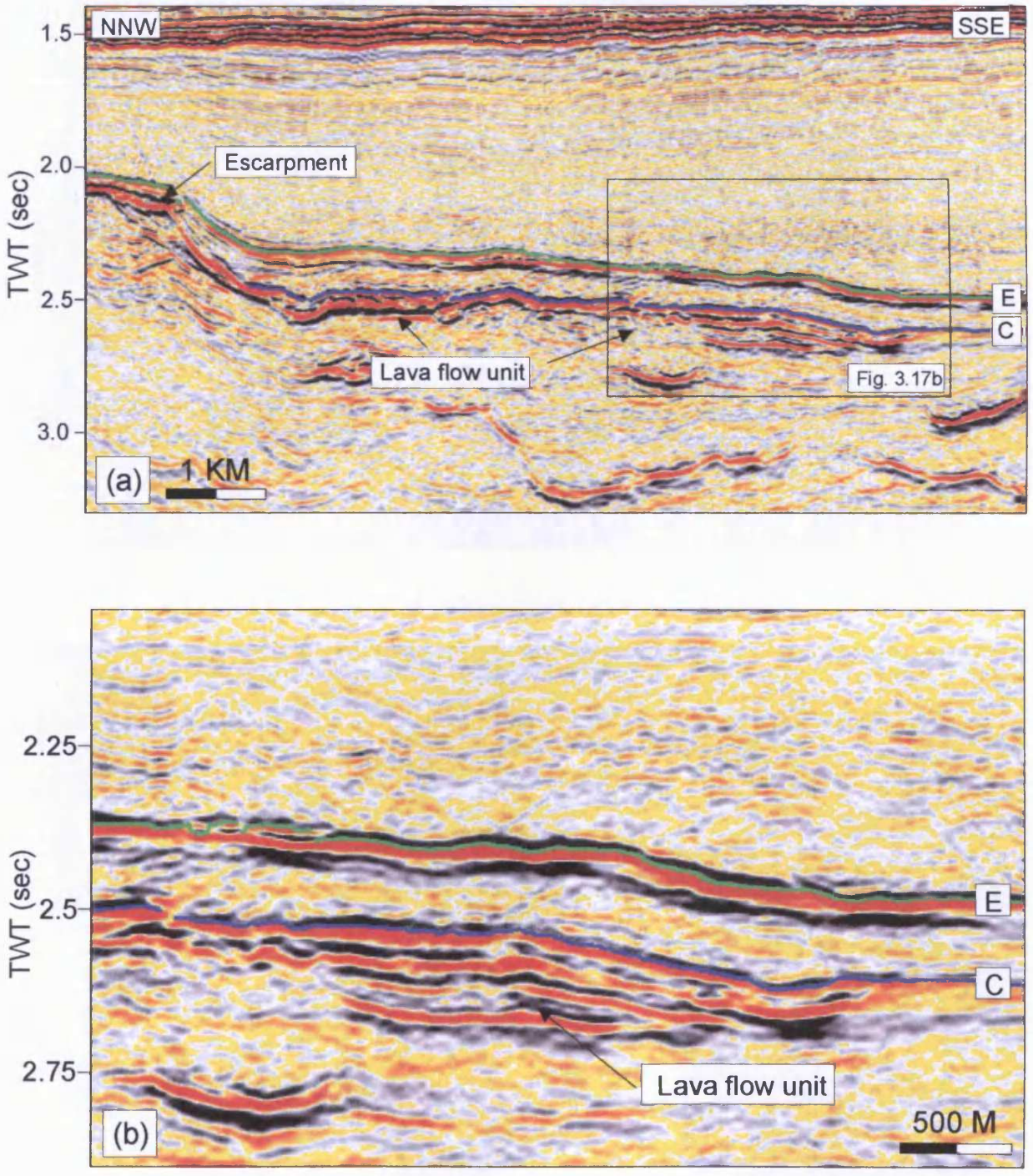

Fig. 3.17 Seismic sections showing a lava escarpment and lava flow unit in the northern part of the T67 survey area. (a) Escarpment and lava flow unit. (b) The tip of the tip of the lava flow unit. See Fig. 3.16 for line location.

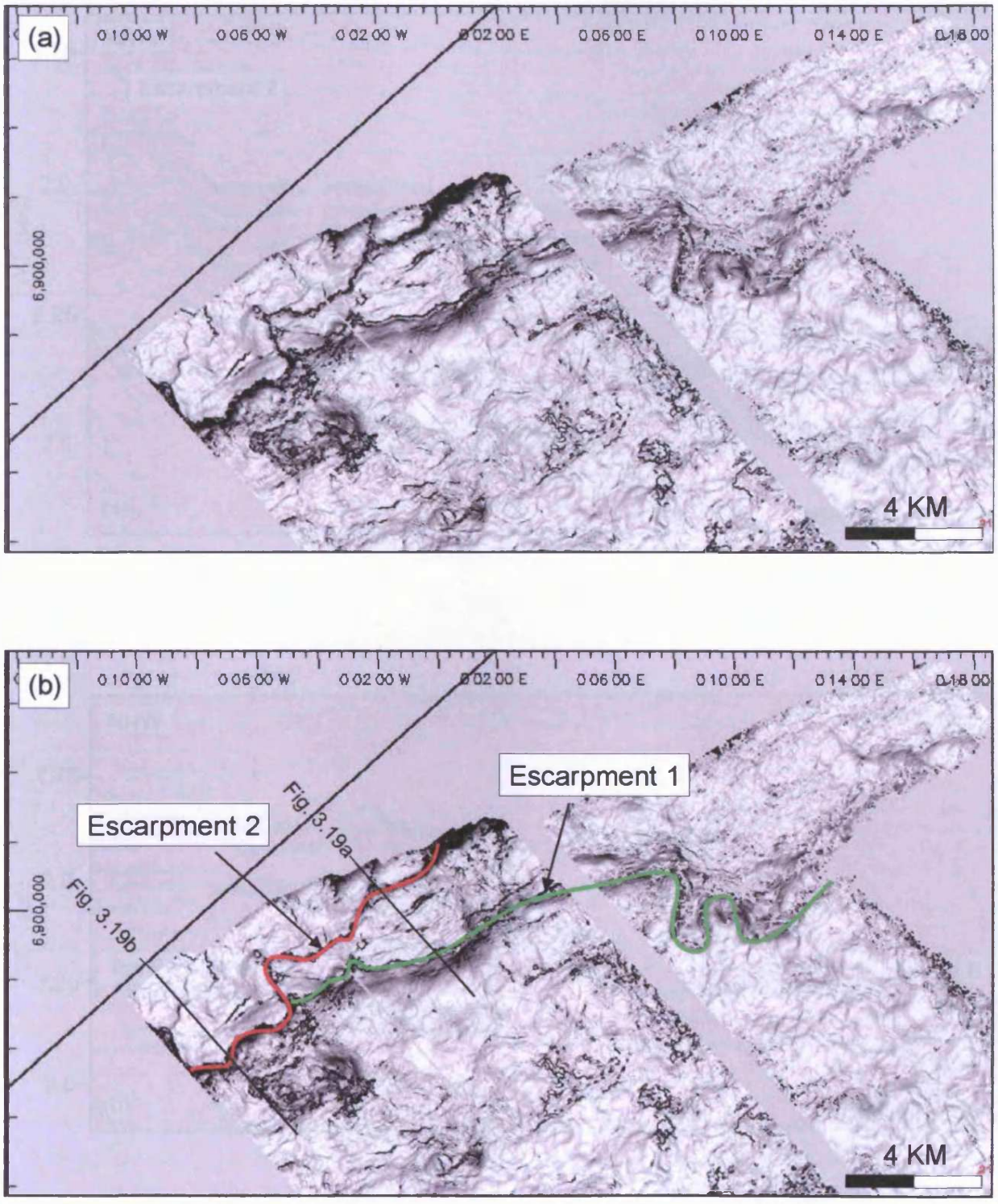

Fig. 3.18 (a) Time-dip map of horizon E. (b) Time-dip map of horizon E showing the outline of escarpments 1 and 2. Note line locations for Fig. 3.19.

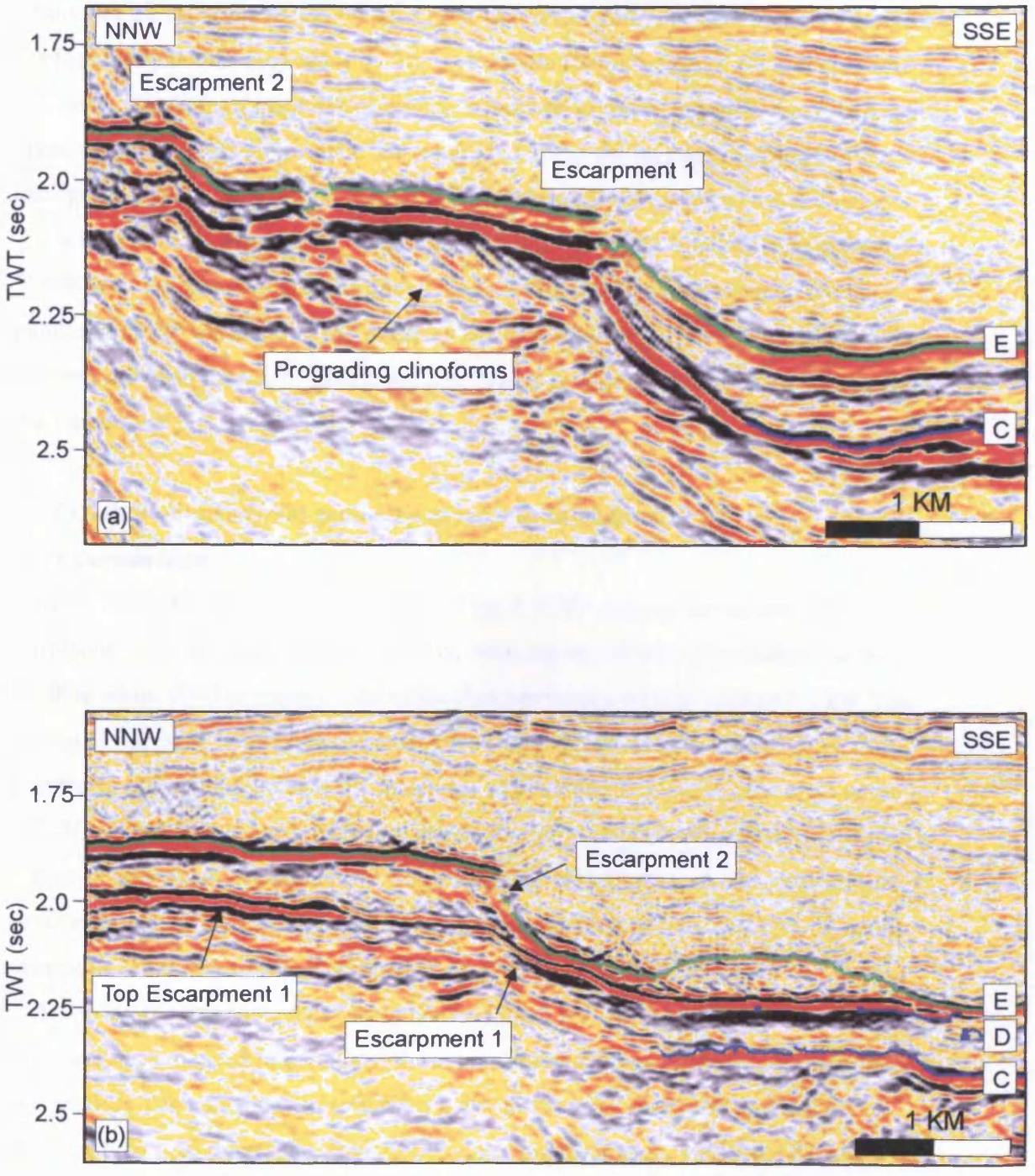

Fig. 3.19 Lava escarpments in the T67 survey area. (a) Seismic section showing stacking of escarpments and internal progradational reflection geometry of escarpment 1. (b) Seismic section showing clear vertical separation of escarpments 1 and 2. See Fig. 3.18 for line locations.

The extent of the lava flows was constrained by extracting the sum of negative amplitudes in a 2000-2700 ms window across the survey area. This 700 ms window comprises the escarpment and the lava flow unit where this is present in the survey area. On the resultant attribute map (Fig. 3.20) large numbers of negative value shows where there is a large sum of negative amplitude within the window and these areas represent areas where the lavas are present. The map shows that the lava plateau (north of the escarpment) and lava flow unit cover approximately half of the survey area. In Fig. 3.20a the outline of escarpment 1, as it was interpreted on the time-dip map of horizon E, has been superimposed on the map. The area in front of the escarpment, which exhibits a large value, shows the extent of the lava flow unit. The unit is limited to the western and central parts of the survey area where it extends almost 10 km in front of the escarpment.

3.3 The three-dimensional geometry of igneous intrusions

3.3.1 Introduction

Numerous intrusions have been mapped in the T67 3D seismic survey area. The intrusions stack up vertically and laterally, from approximately 6500 m depth to the south to about 3500 m depth to the north, thus covering a vertical section > 2 km. The timing of intrusion in this and the other case-study areas will be discussed in section 7.4. It is worth noting that the Upper Cretaceous and Paleocene intruded sediments in the T67 3D seismic survey area have undergone limited structural deformation. It will be shown in later chapter, particularly Chapter 4, that intrusion into structurally deformed sediments, e.g. heavily faulted sedimentary units, influences the geometry of igneous intrusions. This will also be discussed in detail in section 7.7.4.

Some simple statistical data have been compiled for 15 sills of the T67 sill complex that have been mapped in detail and these are summarised in Table 3.1 and described in this section. The sills range in area from a few km^2 to as much as 80 km^2 and a maximum vertical relief on a single intrusion of approximately 900 m has been measured. The majority of the intrusions have intermediate sizes and cover 10-30 km^2 and have a vertical relief of 300-600 m. Smaller intrusions have been interpreted at shallower depth (< 4500 m) further to the north underlying and immediately beyond the lava flow unit. The interpretation of these is related with greater uncertainty because of a noticeable decrease in the resolution of the data underlying the lavas. In the southern part of the survey area large intrusions are clearly imaged at a present-day depth of

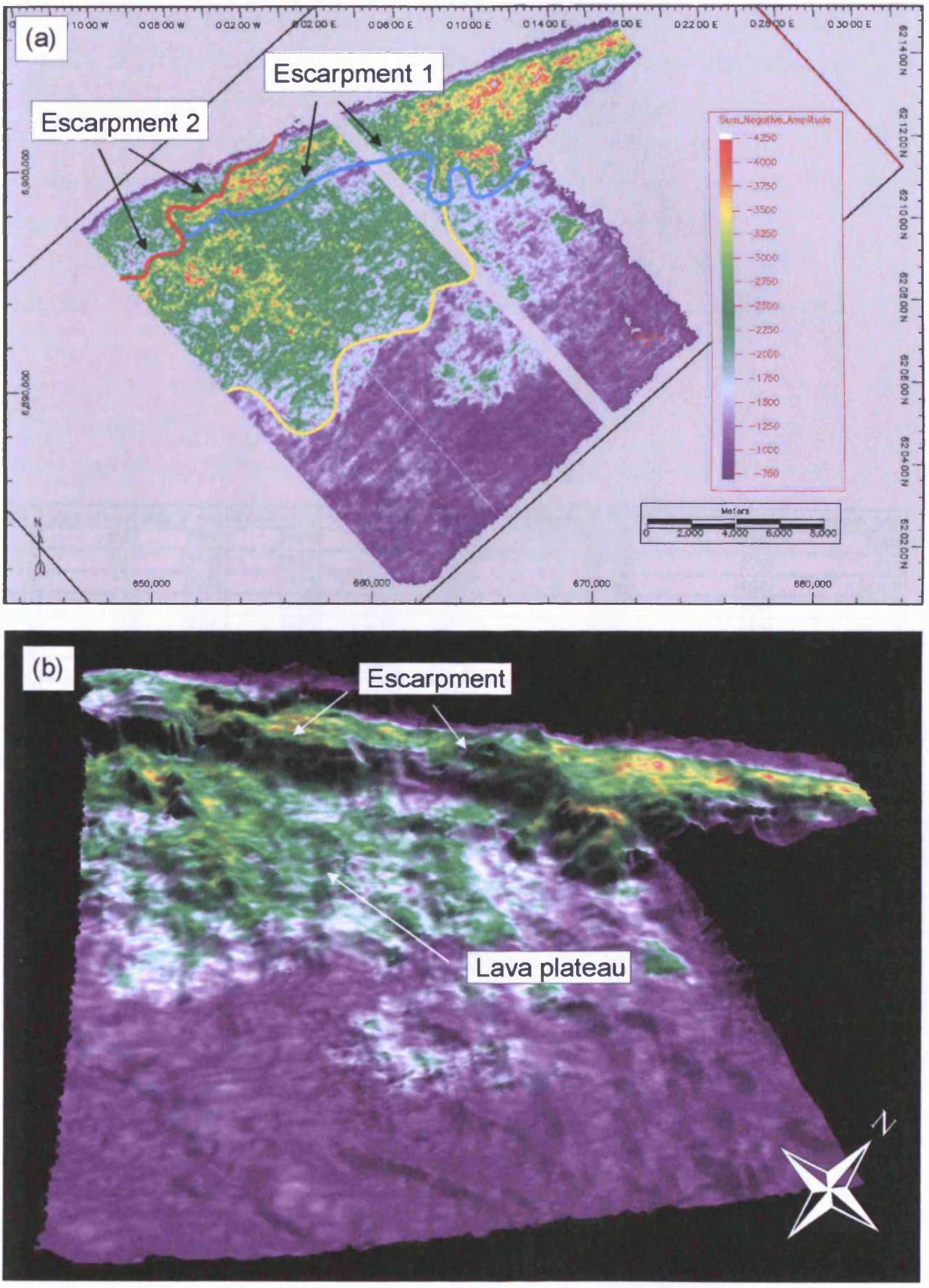

Fig. 3.20 (a) Interpretation of the extent of the lava flow unit (lava plateau) based on the sum of negative amplitude in 2000-2700 ms time (TWT)-window. The outlines of escarpments 1 and 2 as they were interpreted from the time-dip map of horizon E (Fig. 3.18) are superimposed on the map. (b) 3D display of the attribute map (sum of negative amplitude) draped over the time-structure map of horizon E (Fig. 3.16b).

sill	area (km2)	max Z (m)	min Z (ms)	v.r. (ms)	v.r. (m)	cont. seabed (ms)	empl. depth (ms)	empl. depth (m)
1	7.5	3300	3100	200	300	2574	726	1089
2	5.5	3125	2850	275	412.5	2576	274	411
3	11	3075	2775	300	450	2616	459	688.5
4	5.5	3000	2800	200	300	2650	350	525
5	13	3100	2675	425	637.5	2635	465	697.5
6	30	3800	3250	550	825	2554	1246	1869
7	15	3600	3125	475	712.5	2474	1126	1689
8	4	3500	3200	300	450	2515	985	1477.5
9	18	3300	3100	200	300	2634	666	999
10	80	3900	3400	500	750	2636	1264	1896
11	21	3700	3100	600	900	2624	1076	1614
12	7	3550	3050	500	750	2608	942	1413
13	6	3700	3325	375	562.5	2492	833	1249.5
14	5	3350	3000	350	525	2512	488	732
15	22	3500	3100	400	600	2548	552	828

Table 3.1 Summary of statistical data for 15 sills of the T67 sill complex. Depth conversion done using Vsed = 3.0 km/s, see Chapter 2. Max Z: maximum emplacement depth, min Z: shallowest emplacement depth, v.r.: vertical relief, cont. seabed: depth of seabed at time of intrusion, empl. depth: emplacement depth below contemporaneous seabed.

4500-6500 m. The graphs in Fig. 3.21 show that there is poor correlation between sill area and vertical relief (R^2 = 21 %; Fig. 3.21a) and between sill area and maximum emplacement depth (R^2 = 31 %; Fig. 3.21b), whilst there is moderate correlation between maximum emplacement depth and vertical relief (R^2 = 47 %; Fig. 3.21c).

The intrusions interpreted in the survey area have been sub-divided into three interconnected groups (Groups A, B, and C) based on their size, morphology, and stratigraphic level of emplacement. Bell & Butcher (2002) presented a similar sub-division of the sills in this survey area. These groups are described below and illustrated in Fig. 3.22.

3.3.1.1 Group A: Deep

The intrusions included in Group A (approximately equivalent to sill suite 1 of Bell & Butcher, 2002) are emplaced into what appears to be flat lying Upper Cretaceous sediments underlying Horizon A and are most clearly imaged in the southern-most part of the survey area. These intrusions are seen at a present-day depth of 4500-6500 m. They are large, covering 10s of km^2 and a vertical relief > 500 m. Some of the Group A intrusions have concave upwards cross-sectional geometries that are seen to form broad saucer-like shapes when mapped in three dimensions, whilst others adopt more sheet-like forms.

3.3.1.2 Group B: Intermediate

Group B (approximately equivalent to sill suite 2 of Bell & Butcher, 2002) intrusions are emplaced at a present-day depth of 4100-5250 m intruding both Upper Cretaceous and Paleocene sediments. They are smaller than the intrusions in Group A with areas of less than 10 km^2. They are emplaced into slightly NW dipping stratigraphy, partially along Horizons A and B. Most of the intrusions contain within Group B exhibit concave upward cross-sectional geometry with a vertical relief of around 300 m and are highly interconnected.

3.3.1.3 Group C: Shallow

The third group of intrusions (Group C; approximately equivalent to sill suite 3 of Bell & Butcher, 2002) is intruded at a present-day depth of 3500-4500 m into a wedge of apparently flat lying Paleocene sediments downwards bound by Horizon B. They underlie the lava flow unit and are, as a result, relatively poorly imaged by the seismic

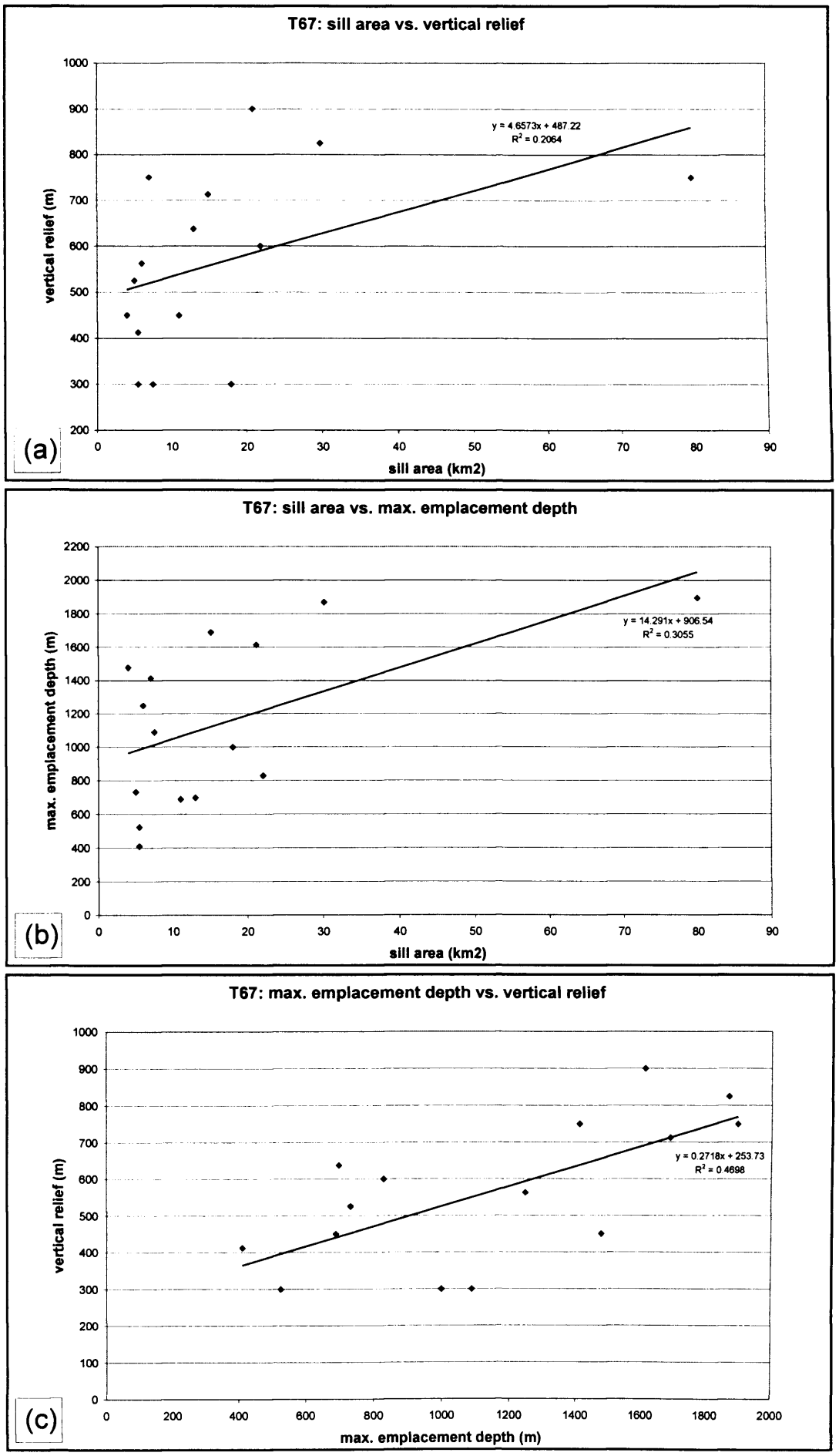

Fig. 3.21 Graphs illustrating statistical data for 15 sills of the T67 sill complex. (a) sill area vs. vertical relief, (b) sill area vs. maximum emplacement depth, and (c) maximum emplacement depth vs. vertical relief. Depth conversion done using Vsed = 3.0 km/s, see Chapter 2.

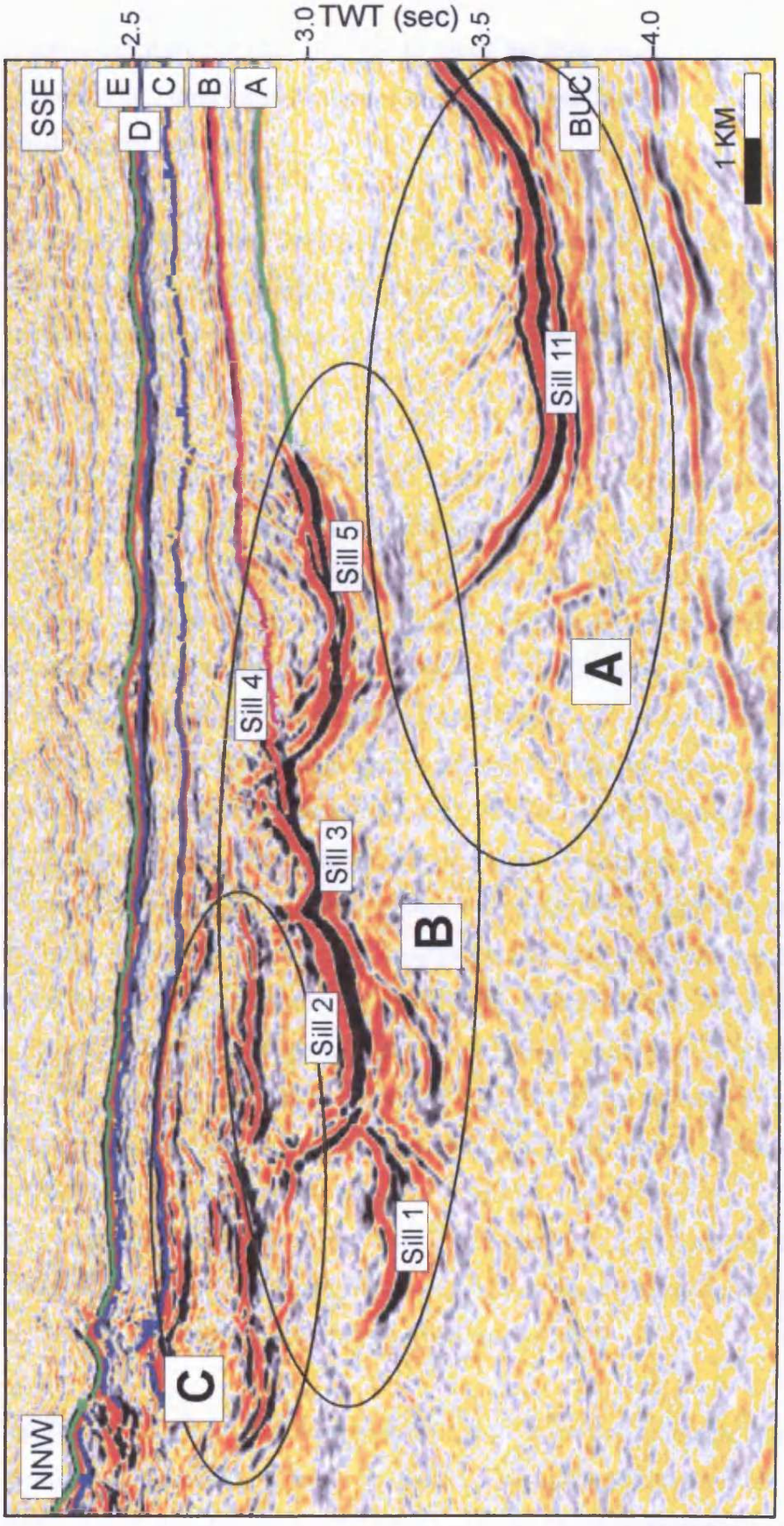

Fig. 3.22 Seismic section showing the cross-sectional geometries and relative depths of the three groups of sills interpreted in the T67 3D seismic survey area. Sills in Group A are large and form broad saucers-like sills and sheet-like intrusions. Group B comprises sills that display a concave cross-sectional geometry and are highly interconnected. Group C underlies the lava flow unit and the sills within it are poorly imaged. They for a complex stacked pattern. Line location is shown in Fig. 3.2 (labelled Fig. 3.11a).

data. These intrusions have not been mapped in detail, but they appear to be smaller (area and vertical relief) than those contained in Groups A and B and form a complex interconnected stacked pattern.

From the above description it appears that the sills get smaller upwards and there is evidence to suggest that the three different groups are interlinked vertically, with sills of Group A being linked to sills of Group B, and sills of Group B being linked to sills of Group C (Fig. 3.23).

3.3.2 Detailed description of a number of sills within the T67 survey area

A *sill* is traditionally defined as a tabular igneous intrusion with concordant surfaces of contact (Allaby & Allaby, 1999). However, it is evident from seismic mapping that sill-like igneous intrusions adopt a wide range of geometries from fully concordant sheet-like bodies to highly complex discordant geometries. This section provides a detailed description of a number of representative intrusions (from Groups A and B) interpreted in the survey area. Based on this a classification scheme for igneous intrusions is erected and a set of informal terms introduced to assist in distinguishing between different levels of three-dimensional complexity of igneous intrusions.

The 3D display shown in Fig. 3.24 shows some of the intrusions mapped in the T67 3D seismic survey area. From the display it is apparent that the intrusions have different geometries and sizes. The mapview and cross-sectional geometries of seven of these sills (sill 1, 3, 5, 6, 7, 9, and 12) are described in detail below in order to illustrate the range of three-dimensional geometrical styles recognised in the survey area. From the interpretation of geometrically similar intrusions in the other 3D seismic datasets used in this study (Chapters 4 and 5) and the published literature (e.g. Davies et al., 2002; Smallwood & Maresh, 2002; Trude et al., 2003; Trude, 2004), it is evident that the intrusions mapped in the T67 3D seismic survey area are representative of more general geometrical styles of intrusions observed in sedimentary basin.

Sill 1 (Group B; Fig. 3.25) has an almost perfect circular mapview geometry. The planview geometry of the intrusion measures 3 by 3.5 km and covers an area of approximately 7.5 km^2. The intrusion has a concave cross-sectional geometry with a vertical relief of approximately 300 m, and is located at a present-day depth of 4650-4950 m. The base of the intrusion (1.5 by 1.5 km) is relatively flat and concordant with

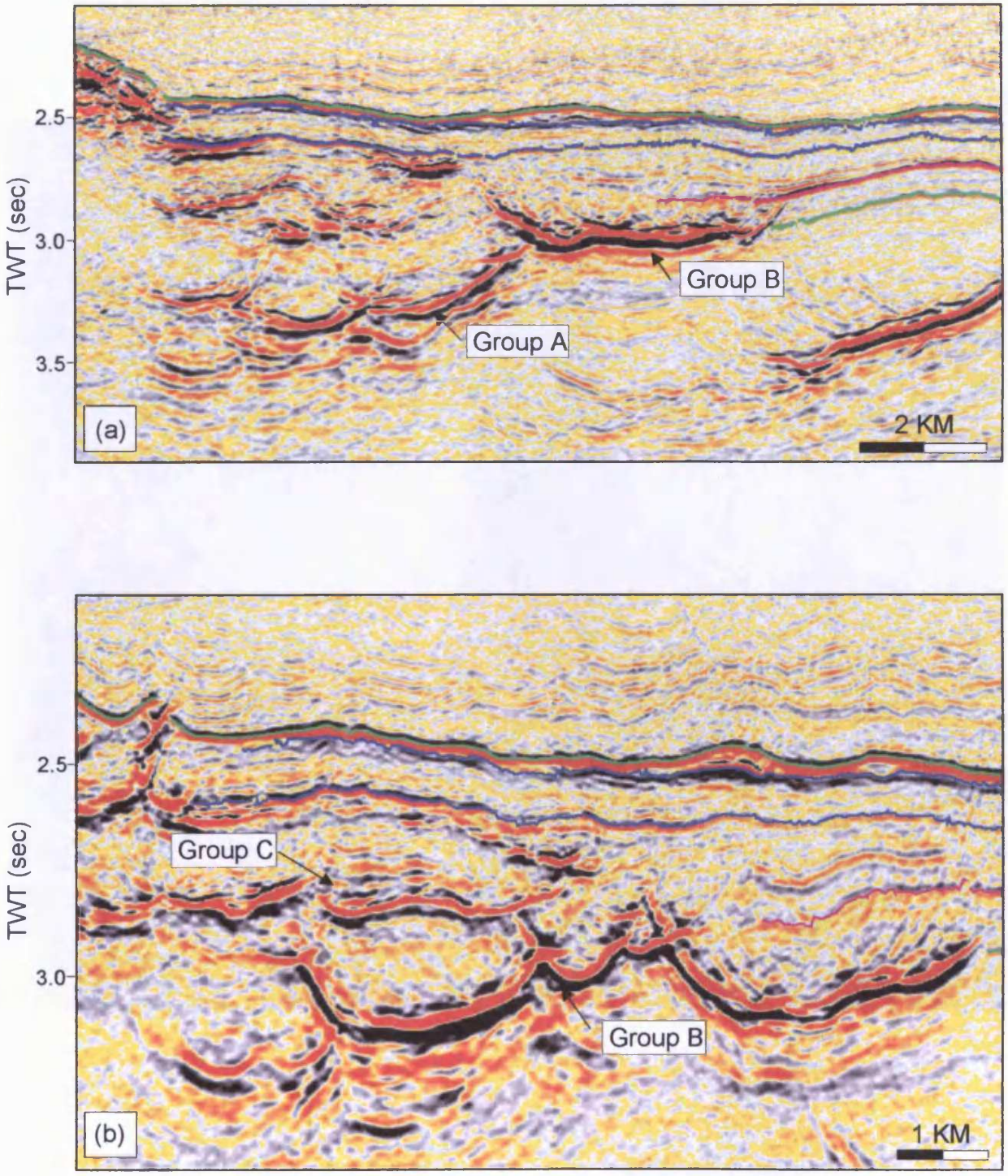

Fig. 3.23 Seismic sections showing linkage between sills of Group A and group B (a) and between Group B and Group C (b).

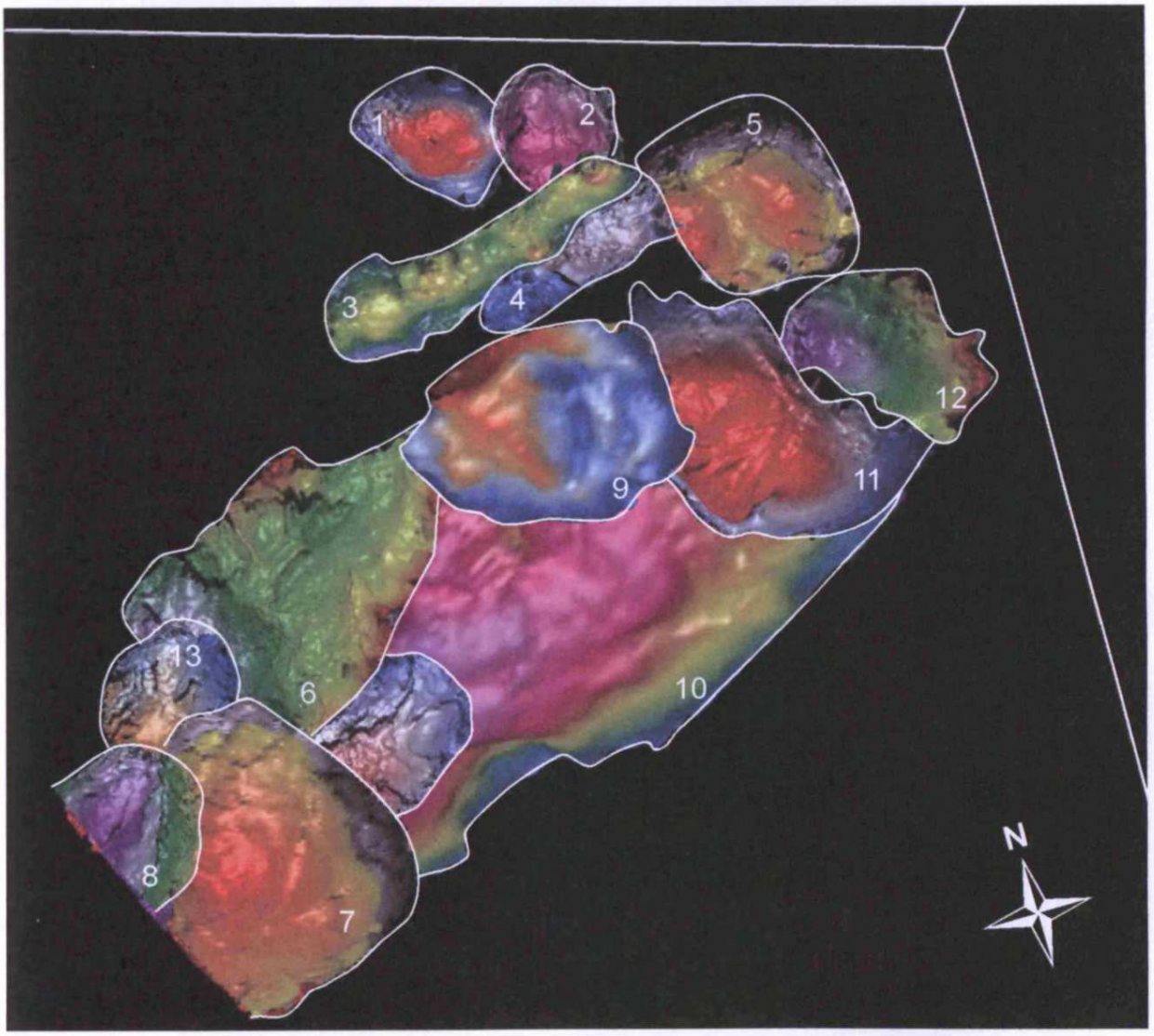

Fig. 3.24 3D display showing some of the sills that have been mapped in the T67 3D seismic survey area.

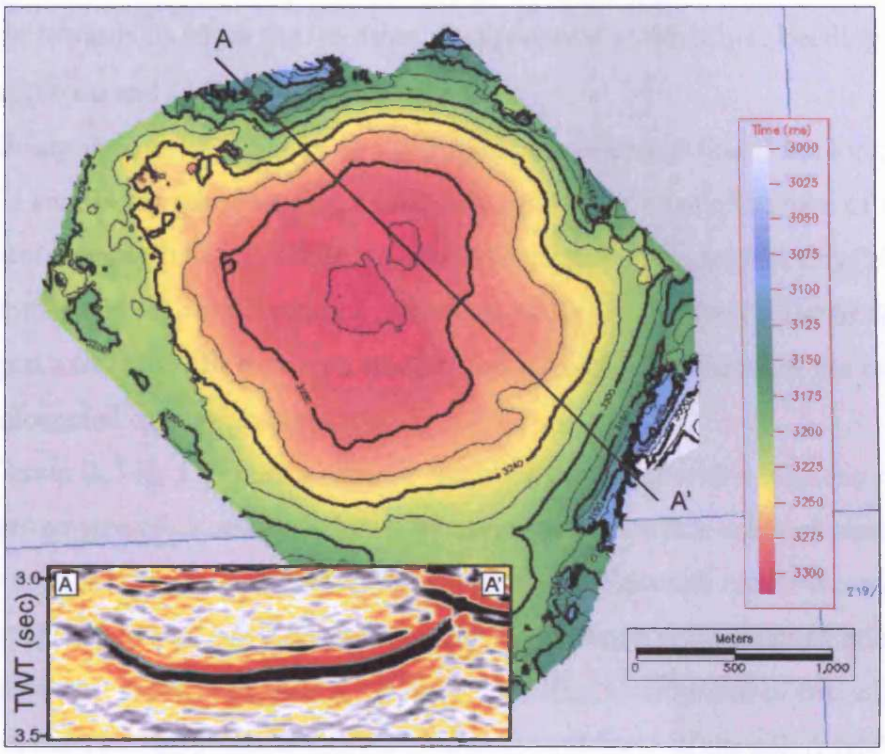

Fig. 3.25 Contoured time-structure map and vertical seismic section showing the planview and cross-sectional geometries of sill 1.

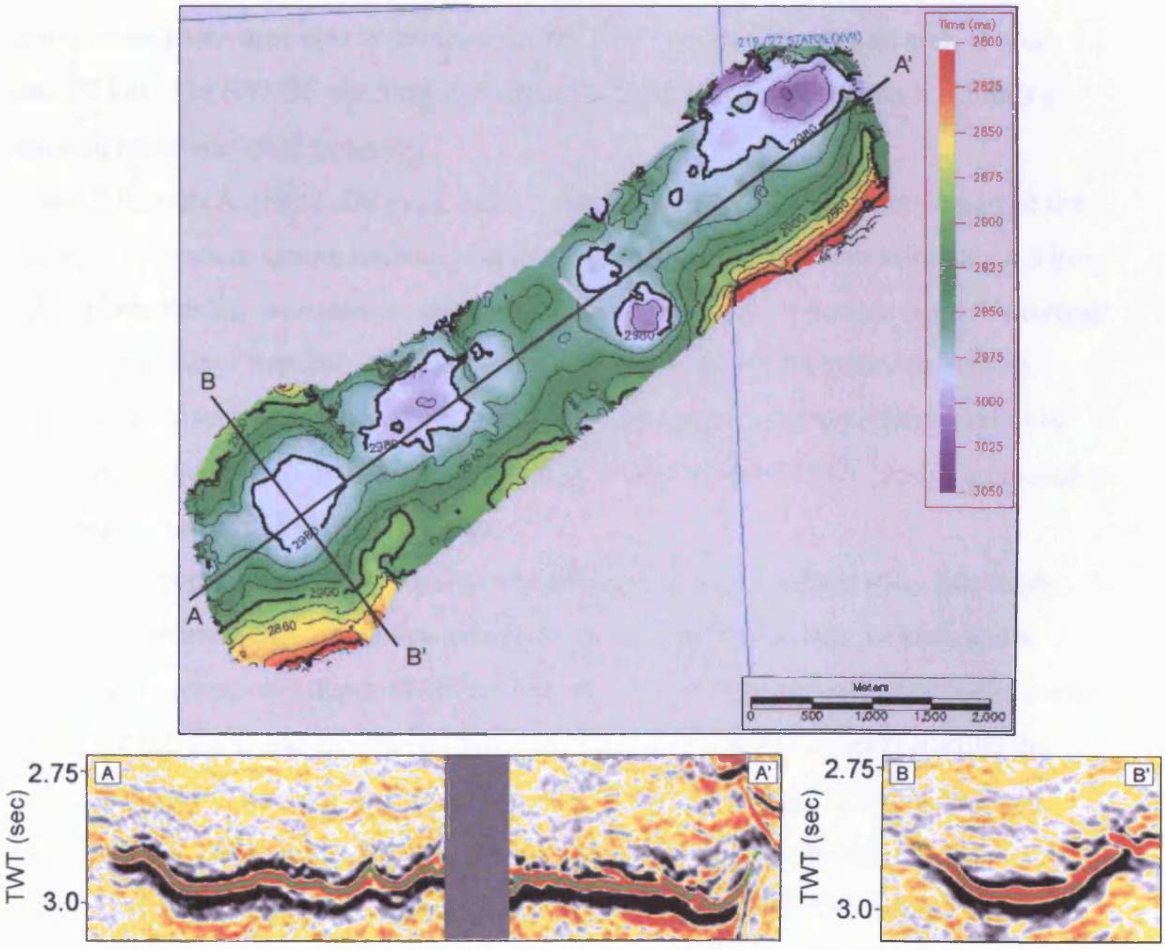

Fig. 3.26 Contoured time-structure map and vertical seismic sections showing the planview and cross-sectional geometries of sill 3.

bedding, but towards its edges the intrusion transgresses discordantly to bedding at angles of approximately 10° in all directions.

Sill 3 (Group B; Fig. 3.26) has an elongated shape and is more than 7 km long and between 1.3 and 2 km wide, covering a total area of almost 11 km^2. The base of the sill is at a present-day depth of 4350-4500 m. Sections parallel to the longest axis (NE-SW) show a complex, ridged cross-sectional geometry, while lines perpendicular to the strike of the longest axis (NW-SE) display a smooth concave shape. In mapview the sill adopts an elongated egg-box morphology.

Sill 5 (Group B; Fig. 3.27) has a circular mapview geometry with a diameter of 4 km and it covers an area of close to 13 km^2. It has a maximum vertical relief of more than 600 m. On sections oriented NNW-SSE the intrusion has a smooth concave cross-sectional geometry, whilst NE-SW striking sections display a more complex cross-sectional geometry in the form of an overall concave shape comprised of two adjacent depressions, each covering approximately half of the total area of the sill. A NNW-SSE trending ridge separates the two low areas.

Sill 6 (Group A; Fig. 3.28) has an irregular elongated planform (9.5 by 4 km) and transgresses more than 800 m towards the NE. The intrusion covers an area of more than 30 km^2. On NW-SE trending vertical section through the intrusion it exhibits a concave cross-sectional geometry.

Sill 7 (Group A; Fig. 3.29) has a complex mapview geometry. The main part of the intrusion appears to have a circular planform with a diameter of approximately 4.5 km, but towards the NE the contours and periphery of the intrusion deviate from this overall circular geometry. Vertical sections through the main part of the intrusion show a concave cross-sectional geometry and the intrusion has a maximum vertical relief of approximately 700 m. The intrusion covers an area of at least 15 km^2 and is emplaced at a present-day depth of 4800 to 5400 m.

Sill 9 (Group A; Fig. 3.30) is a near-circular intrusion characterised by two ridges. The intrusion measures 5 by 5 km, covers an area of approximately 18 km^2, and is located at a present-day depth of 4575-4950 m. The two ridges are located in the eastern part of the intrusion and are convex towards the east and approximately parallel the eastern sill edge. The most western and larger of the two ridges is 2700 m long and approximately 150 m high. The intrusion transgresses slightly towards the SE.

Sill 12 (Group A; Fig. 3.31) exhibits a concave shape on NE-SW striking sections and a southwards transgressing geometry on sections oriented NW-SE. The intrusion

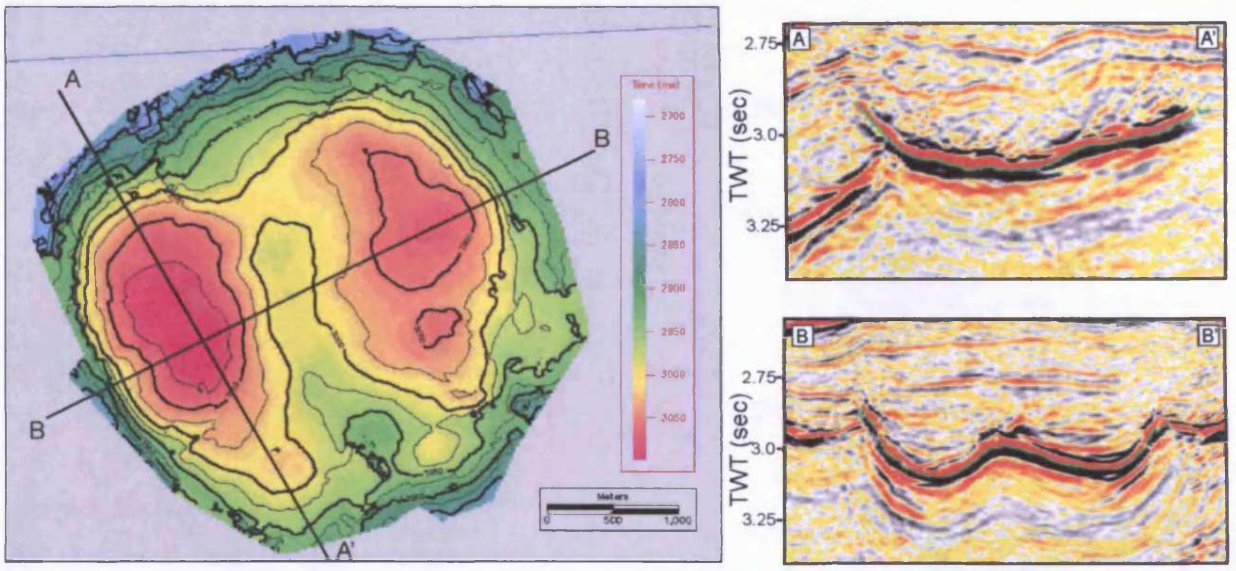

Fig. 3.27 Contoured time-structure map and vertical seismic sections showing the planview and cross-sectional geometry of sill 5.

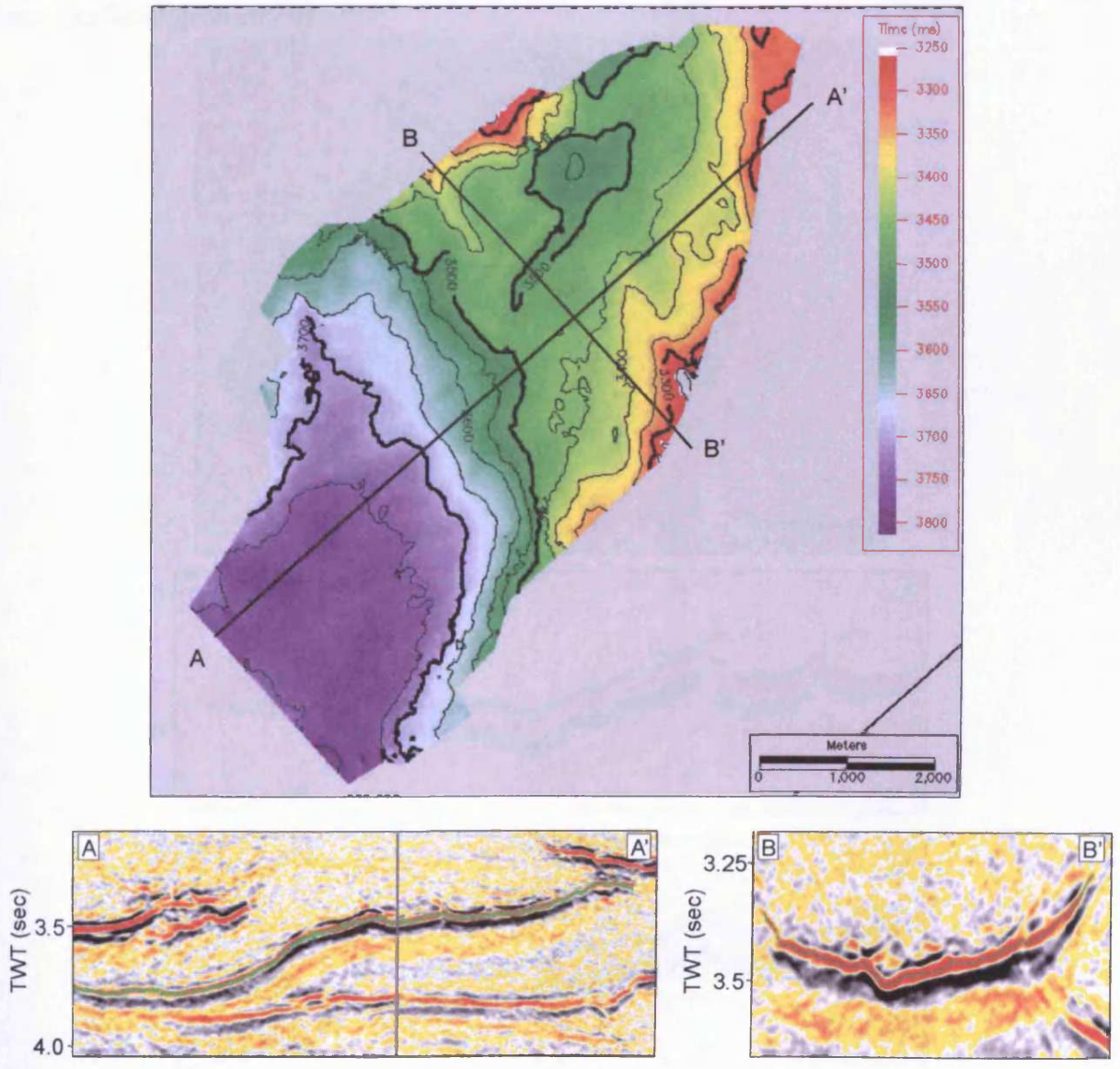

Fig. 3.28 Contoured time-structure map and vertical seismic sections showing the planview and cross-sectional geometry of sill 6.

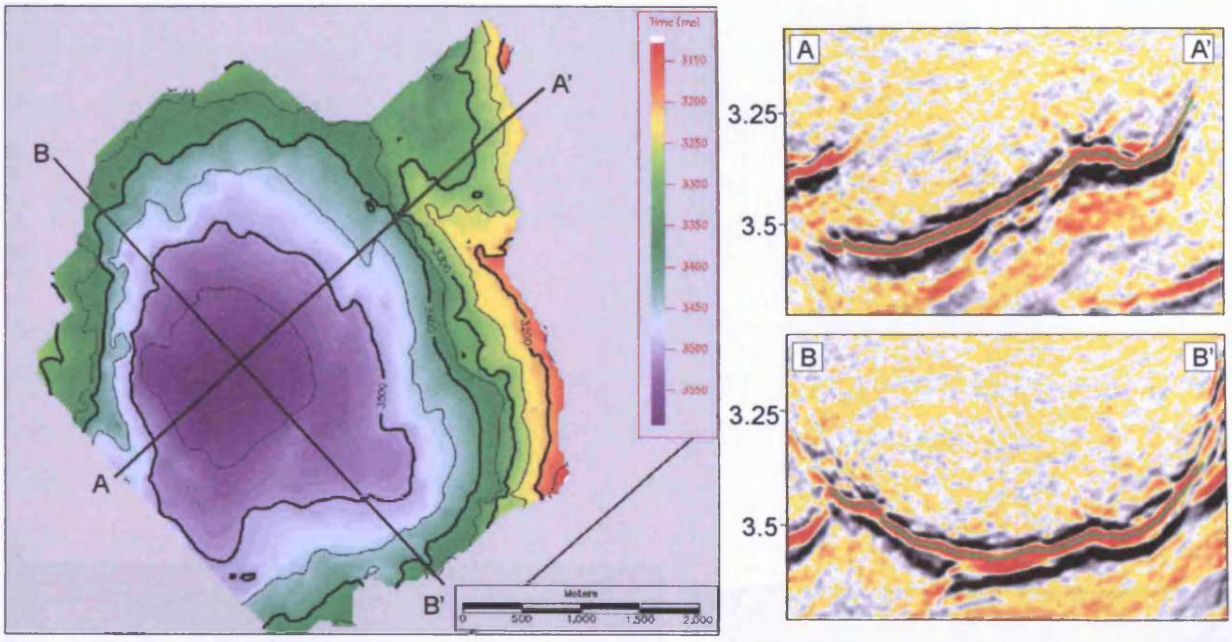

Fig. 3.29 Contoured time-structure map and vertical seismic sections showing the planview and cross-sectional geometry of sill 7.

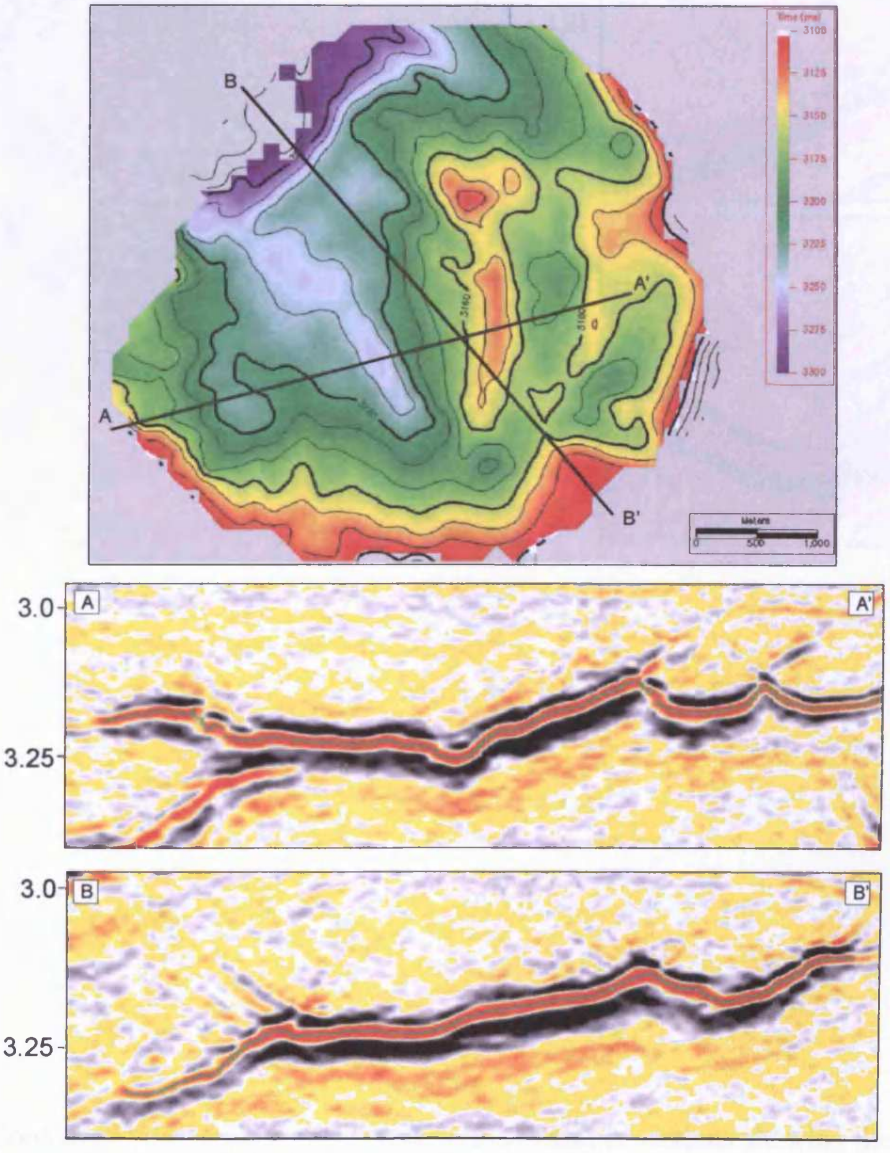

Fig. 3.30 Contoured time-structure map and vertical seismic sections showing the planview and cross-sectional geometry of sill 9.

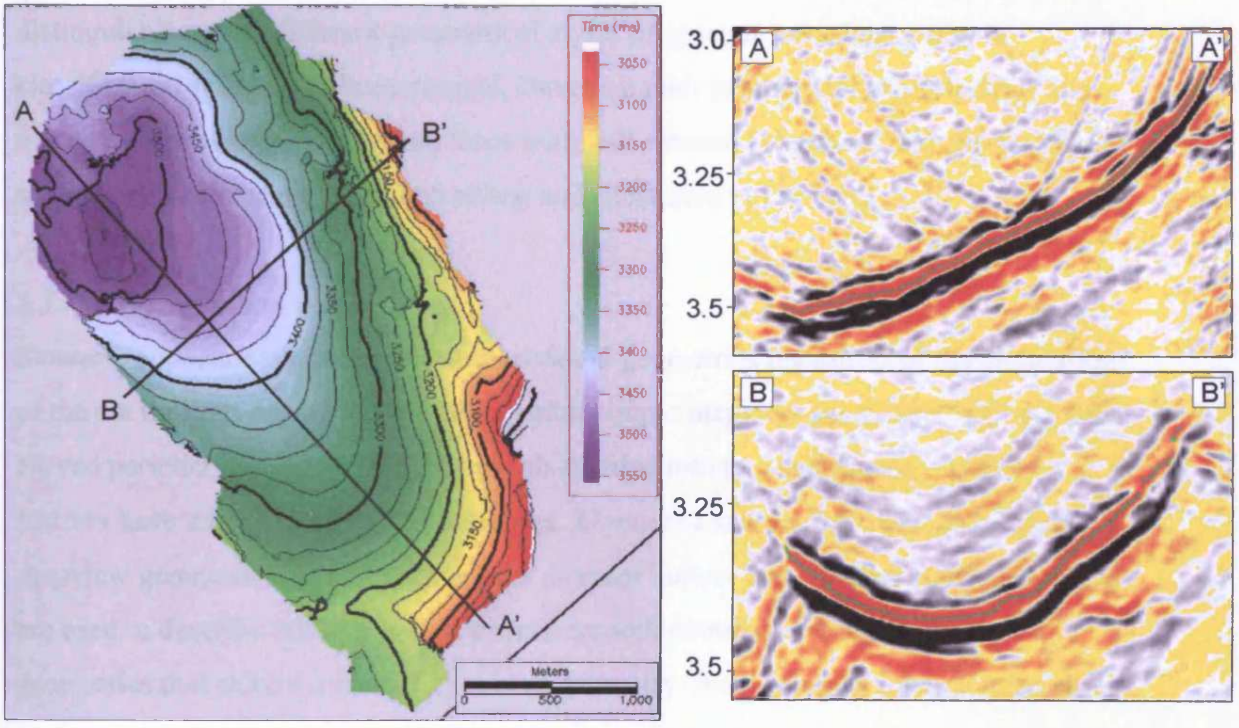

Fig. 3.31 Contoured time-structure map and vertical seismic sections showing the planview and cross-sectional geometry of sill 12.

measures 4 by 2 km and covers an area of just less that 7 km^2. It transgresses approximately 750 m from 5325 m to the north to 4575 m to the south.

3.3.3 Classification scheme for igneous intrusions

3.3.3.1 Introduction

From the above descriptions of some of the intrusions mapped in the 3D seismic survey area it is clear that intrusions adopt a wide range of geometrical styles. The majority of the intrusions mapped in the case-study areas show clear discordance with stratal reflections and thus do not fit the standard definition of a sill as an igneous body with concordant surfaces of contact (Allaby & Allaby, 1999). In order to help better distinguish between different geometrical styles of igneous intrusions a simple classification scheme has been erected. Based on their geometrical characteristics the intrusions have been grouped into three main ***sill classes***; (1) saucers, (2) sheets, and (3) sill segments. These are described below and illustrated in Fig. 3.32.

3.3.3.2 Classification

Saucers: *Saucers* have concave cross-sectional geometries regardless of the orientation of the cut through the intrusion. They exhibit simple mapview geometries with smooth curved peripheries. Saucers have been sub-divided into two sub-groups. C*ircular saucers* have circular mapview geometries. *Elongated saucers* have oval to elliptical mapview geometries. The terms *complex circular saucer* and *complex elongated saucer* are used to describe intrusions with overall smooth circular or elongated mapview geometries that exhibit a complex internal geometry. Such complex internal geometries include folds, multiple depressions, overhangs, and steps.

Sheets: *Sheets* have simple horizontal, curved, or transgressive cross-sectional geometries depending on the orientation of the cut through the intrusion. They can have simple or complex mapview geometries. Sheets have been subdivided into two sub-groups. C*oncordant sheets* are concordant with the intruded stratigraphy. T*ransgressive sheets* have an obvious transgressive cross-sectional geometry in one direction. The cross-sectional geometry of a transgressive sheet will depend on the orientation of the cut through the intrusion.

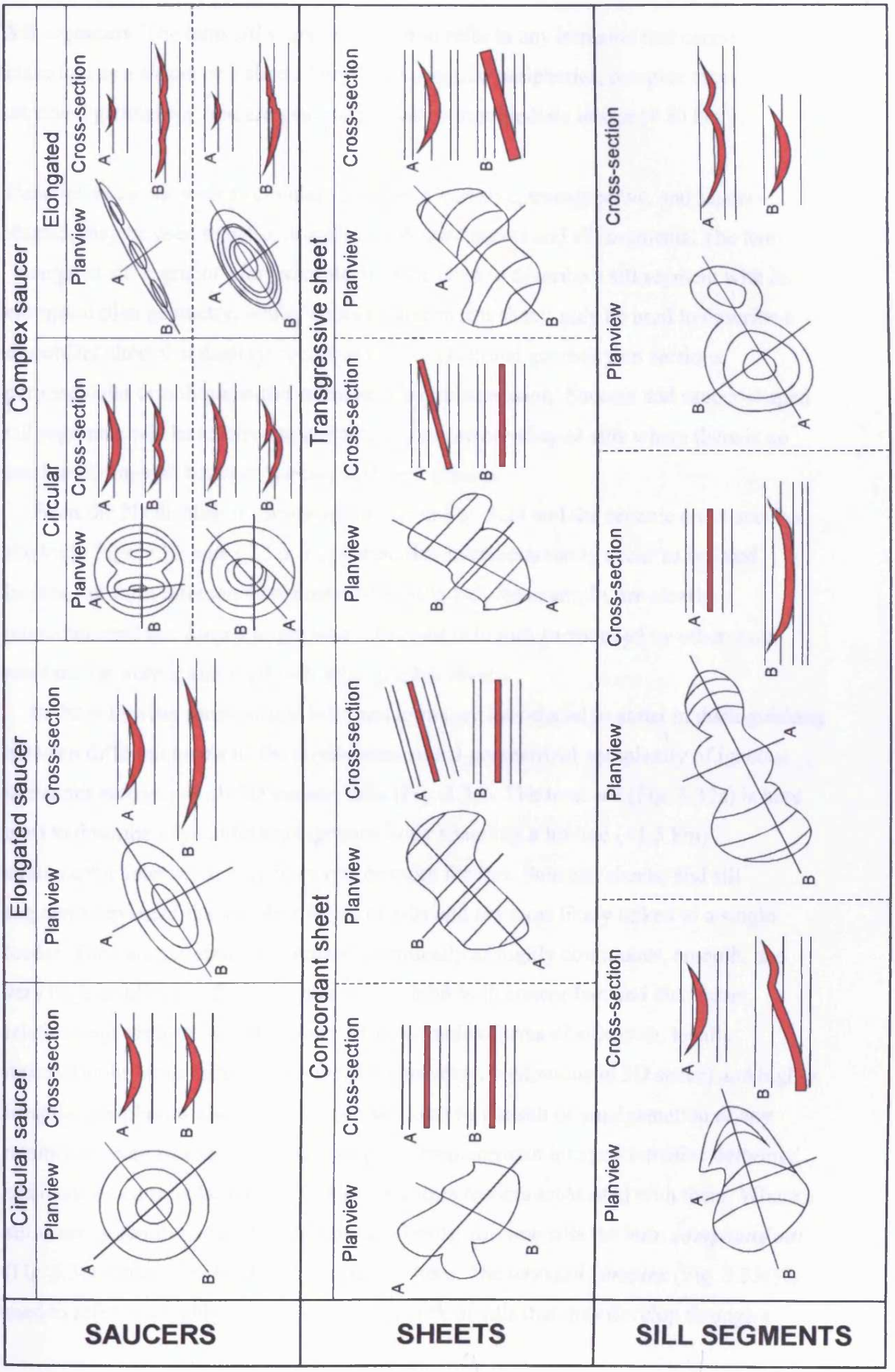

Fig. 3.32 Schematic illustration of sill classification scheme. Sills are subdivided into three main sill classes; saucers, sheets, and sill segments.

Sill segments: The term s*ill segment* is used to refer to any intrusion that cannot be classified as a saucer or a sheet. They have irregular peripheries, complex cross-sectional geometries, and are generally small to intermediate in size (< 30 km^2).

Descriptive terms, such as circular, elongated, concave, transgressive, and saucer-shaped, may be used to better describe individual sheets and sill segments. The term 'elongated sill segment', for example, may be used to describe a sill segment with an elongated plan geometry, while 'concave discordant sheet' may be used to describe a discordant sheet that displays a concave cross-sectional geometry on sections perpendicular or oblique to the orientation of transgression. Saucers and saucer-shaped sill segments will be referred to collectively as ***saucer-shaped sills*** where there is no need to distinguish between the two different classes.

From the 3D display of intrusions shown in Fig. 3.24 and the seismic cross-section shown in Figs. 3.22 and 3.23 it is apparent that intrusions rarely occur as isolated bodies, but form interconnected networks. Sills 1-5, for example, are clearly interconnected and form a larger unit. This unit is in turn surrounded by other units emplaced at deeper and shallower stratigraphic levels.

In the following some simple informal terms are introduced to assist in distinguishing between different levels of the three-dimensional geometrical complexity of igneous intrusions recognised on 3D seismic data (Fig. 3.33). The term ***sill*** (Fig. 3.33a) is here used to describe any continuous igneous body spanning a limited (<1.5 km) stratigraphic interval. It may have one or more feeders. Saucers, sheets, and sill segments represent the simplest forms of sills and are most likely linked to a single feeder. They are generally recognised seismically as highly continuous, smooth, and very high amplitude reflections that may exhibit both concordant and discordant relationships with stratal reflections. More complex forms of sills with, locally, discontinuous cross-sectional geometries (however, continuous in 3D space) and highly irregular peripheries also exist. These may form as a result of amalgamation of any number of more simple sills or as a result of emplacement into pre-intrusive deformed sedimentary units and are likely to have multiple feeders associated with them. Where a sill is easily sub-divided into a number of simpler discrete sills the term ***compound sill*** (Fig. 3.33b) may be used to further specify these. The term ***sill complex*** (Fig. 3.33c) is used to refer to a highly interconnected network of sills that may develop through a

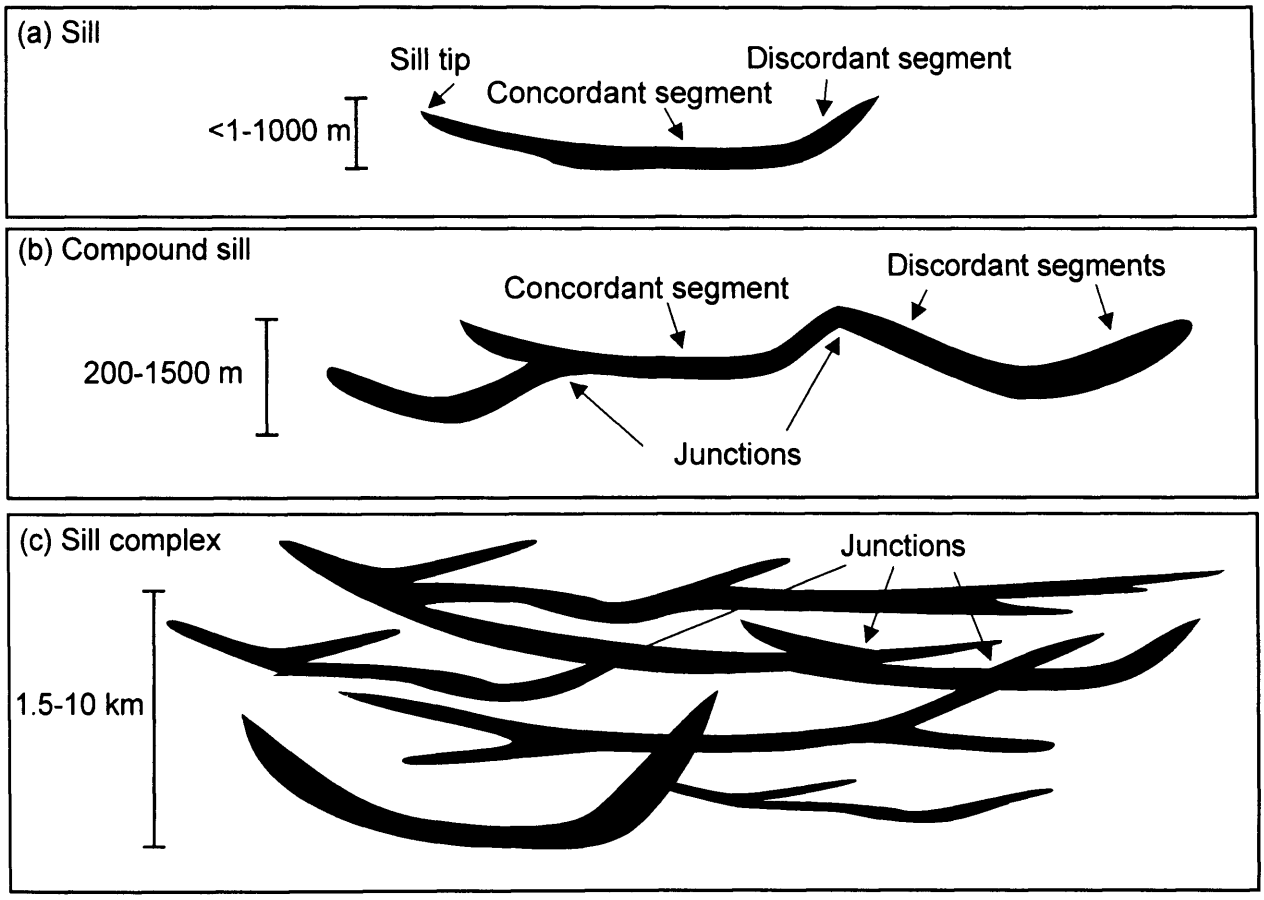

Fig. 3.33 Schematic cross-sections illustrating: (a) Sill. (b) Compound sill. (c) Sill complex.

succession of repeated intrusive events. Sill complexes usually span several kilometres of vertical section.

3.3.3.3 Interpreter's guide to classifying intrusions

The classification scheme introduced above is based on the three-dimensional geometries of the intrusions and it allows any igneous body with known mapview and cross-sectional geometries to be classified using the simple flow-chart shown in Fig. 3.34. The flow-chart allows the seismic interpreter to distinguish between sill complexes, compound sills, and sills and also provides a way of distinguishing between the three sill classes.

The first characteristic to be addressed in the flow-chart is the span of the stratigraphic interval within which the intrusion is seen. Sills and compound sills cover limited (< 1.5 km) stratigraphic intervals whilst a sill complex spans a wide (> 1.5 km) stratigraphic interval. The next step in the flow chart distinguishes between intrusions with smooth and irregular peripheries. If the intrusion has a smooth periphery it is a sill, which based on its plan and cross-sectional geometries can be assigned to one of the three sill classes. If the intrusion has an irregular periphery it may be either a sill segment or a sheet. If it has a simple horizontal, transgressive, or concave cross-sectional geometry it is assigned to the sheet sill class. If the cross-sectional geometry is best described as complex it is assigned to the sill segment sill class.

The classical definition of a sill as a tabular igneous intrusion with concordant surfaces of contact corresponds to that of a concordant sheet in the context of the classification scheme presented here. From the flow-chart it is obvious that this definition is too simplistic to cover the wide range of geometrical styles of igneous intrusions identified using 3D seismic data in this study. This thus clearly illustrates the need for the more extensive classification scheme presented herein.

3.3.3.4 Classification of case-studies

The use and usefulness of the sill intrusion classification flow-chart is demonstrated through a classification of the intrusions described in section 3.3.2. These intrusions all cover limited stratigraphic intervals and the first question to be addressed is thus, according to the flow-chart, the character of the periphery.

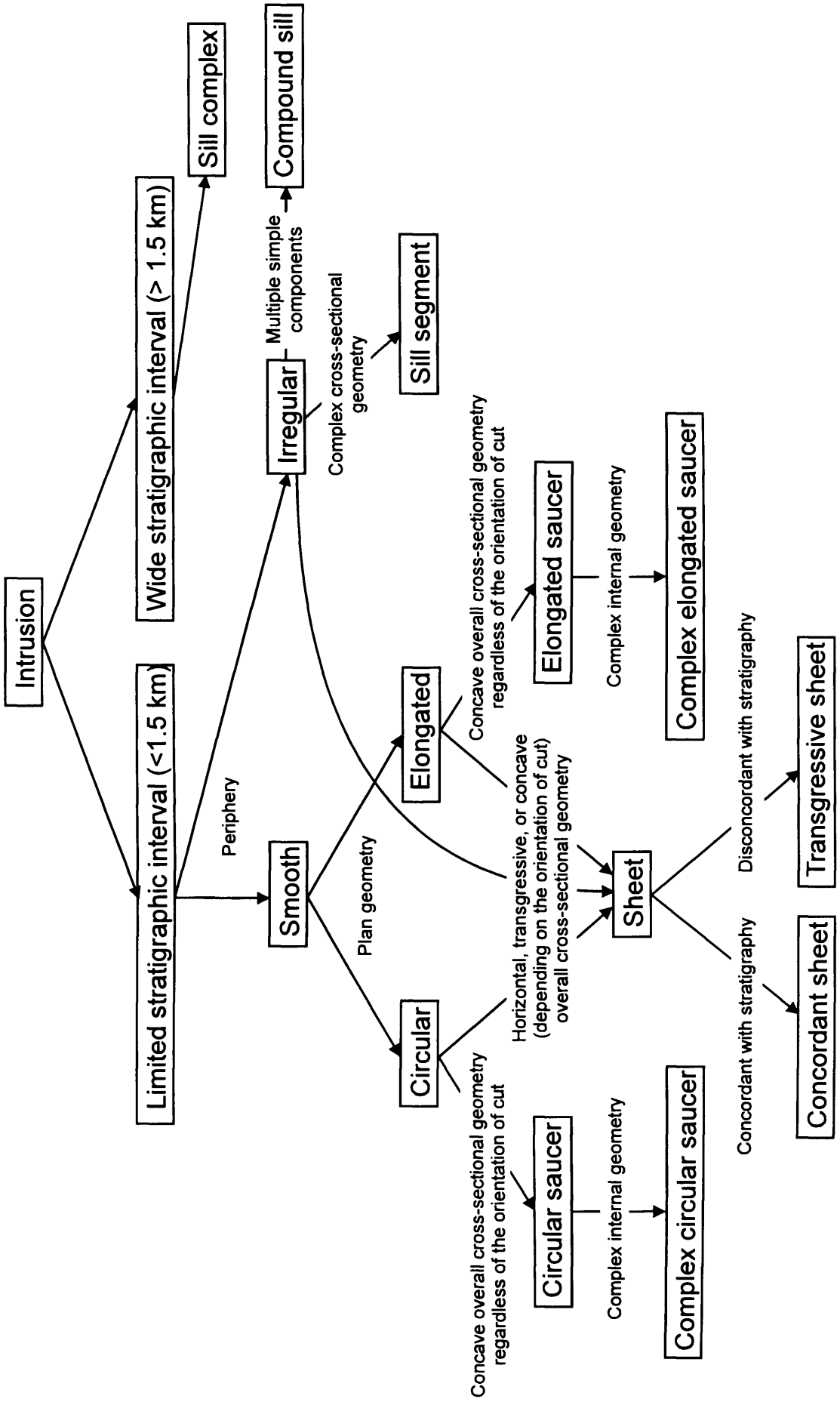

Fig. 3.34 Flow-chart for classification of igneous intrusions based on their planview and cross-sectional geometries.

Sill 1 (Fig. 3.25) has a smooth periphery, a circular plan geometry, and a concave cross-sectional geometry regardless of the orientation of the cut through it. Based on this sill 1 can be classified as a circular saucer. *Sill 3* (Fig. 3.26) has a smooth periphery, an elongated plan geometry, and an overall concave cross-sectional geometry. The subtle undulations seen on NE-SW trending sections through the intrusion gives rise to a complex internal geometry. Sill 3 is classified as a complex elongated saucer. *Sill 5* (Fig. 3.27) has a smooth periphery and a circular plan geometry. It has an overall concave cross-sectional geometry and exhibits a complex internal geometry in the form of two adjacent depressions. Sill 5 is classified as a complex circular saucer. *Sill 6* (Fig. 3.28) has an irregular periphery and an elongated plan geometry. It exhibits a simple transgressive cross-sectional geometry on NE-SW trending sections and a concave cross-sectional geometry on sections oriented NW-SE. The intrusion is discordant with stratigraphy and is classified as a discordant sheet. Sill 6 may be referred to as an elongated curved discordant sheet. *Sill 12* (Fig. 3.31) is also classified as a curved discordant sheet. *Sill 7* (Fig. 3.29) has an irregular periphery and exhibits a complex cross-sectional geometry on NE-SW trending sections. Sill 7 is classified as a sill segment. The main part of sill 7 has the characteristics of a circular saucer, but because of the irregularity along the northern periphery of the sill, described above, it does not fulfil the smooth periphery criteria required for it to be classified as a circular saucer. Sill 7 may be referred to as a saucer-shaped sill segment, but it belongs to the sill segment sill class and not to the saucer sill class. *Sill 9* (Fig. 3.30) has a smooth periphery and a circular plan geometry. The sill has a complex cross-sectional geometry and clearly transgresses on NW-SE trending lines. Based on this sill 9 is placed in the sheet class and it may be referred to as a circular discordant sheet.

In Fig. 3.22 sills 1-5 are interconnected and form a larger unit, which in 3D can be shown to be surrounded by similar units emplaced at deeper and shallower stratigraphic levels. All the intrusions imaged on the shown section taken together span a wide stratigraphic level and can, therefore, using the flow-chart, be classified as a sill complex. The smaller unit comprising sills 1-5 is restricted to a limited stratigraphic interval. The unit has an irregular periphery and a complex cross-sectional geometry. Sills 1-5 all classify as saucers and the unit can thus be referred to as a compound sill.

3.3.4 Summary

Detailed mapping of a number of sills in the T67 survey area (and other areas) has illustrated that the generally accepted definition of a sill as an igneous body with concordant surfaces of contact is inappropriate. Igneous sills often display some degree of discordance with stratal reflections and in the T67 survey area they often adopt saucer-shaped geometries with vertical relief of several 100 metres. A simple classifications scheme based on the three-dimensional geometry of sill has been erected to better constrain the geometrical differences as well as similarities between igneous sills. The classification scheme comprises three main sill classes: saucers, sheets, and sill segments and these have been informally defined and illustrated with seismic examples from the T67 dataset.

3.4 Sill junction relationships

3.4.1 Introduction

Compound sills and sill complexes are commonly developed in basins along the NE Atlantic Margin and within these many examples of sill-to-sill junctions are seen. This section provides a detailed description and classification of three-dimensional sill junction relationships observed in the T67 seismic survey area.

Some simple terms are introduced to assist in the description of sill junction relationships (Fig. 3.35). A *sill junction* can form either as a result of sill intersection or sill bifurcation. *Sill intersections* form between two sills that are propagating independently, while *sill bifurcations* form between two sills where one of the sills act as a feeder for the other sill. The junction between two sills defines an approximately linear trace on contour maps of the interconnected sills. This line is referred to as the *line of junction*, although it should be noted that strictly speaking it is not a line, but a narrow surface. On a given vertical section two interconnected sills will connect at a point with the two joining limbs defining an *angle of junction*. This point of junction is referred to as the *junction point* (or simply the junction), although it is more correctly a short line than a point. The *length of junction* will vary from junction to junction, but will in almost all cases be defined by a line of junction and only in exceptional cases be defined by a junction point.

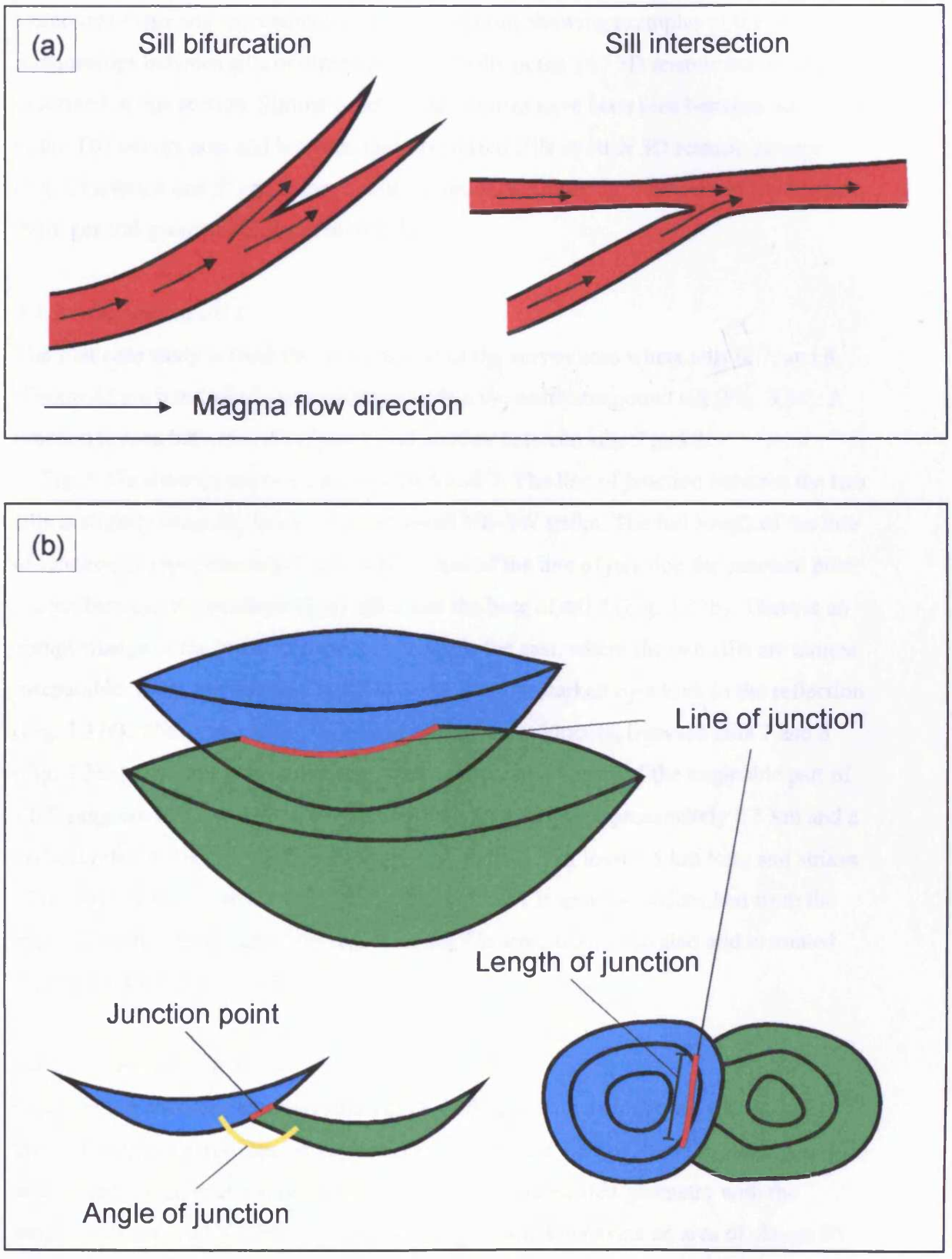

Fig. 3.35 Sill junction terminology. (a) Sill junctions can form either as a result of sill bifurcation or sill intersection. (b) Schematic illustration of the terms: line of junction, junction point (or junction), angle of junction, and length of junction.

3.4.2 Case studies

Contoured maps and representative seismic sections showing examples of the junction relationships between sills of three compound sills in the T67 3D seismic survey are described in this section. Similar junction geometries have been seen between other sills in the T67 survey area and between interconnected sills in other 3D seismic surveys (e.g. Chapters 4 and 5) and these junction relationships are, therefore, considered to be more general geometrical features of sills.

3.4.2.1 Compound sill 1

The first case study is from the western part of the survey area where sills 6, 7, and 8 (Group A) are interlinked and contained within the same compound sill (Fig. 3.36). A junction is seen between sills 6 and 7 and another between sills 7 and 8.

Fig. 3.37a shows a contour map of sills 6 and 7. The line of junction between the two sills is slightly irregular, but shows an overall NE-SW strike. The full length of the line of junction is approximately 5 km. Along most of the line of junction the junction point is seen between the southern tip of sill 6 and the base of sill 7 (Fig. 3.37b). There is an abrupt change in the junction geometry towards the east, where the two sills are almost inseparable. Here, the junction point between them is marked by a kink in the reflection (Fig. 3.37c). Within the same compound sill there is a junction between sills 7 and 8 (Fig. 3.38a). The contour pattern and cross-sectional geometry of the mappable part of sill 8 suggests that it is a circular saucer with a diameter of approximately 2.5 km and a vertical relief of less than 300 m. The line of junction is at least 1.5 km long and strikes NNE-SSW. Sill 8 cross-cuts sill 7 and the tip of sill 7 is as a result detached from the main sill body. The detached tip region of sill 7 is structurally elevated and is rotated slightly backwards (Fig. 3.38b).

3.4.2.2 Compound sill 2

Junctions are also seen between sills 10, 11, and 12 within a compound sill located in the south-eastern part of the survey area (Fig. 3.39). Sill 12 was described and classified as a curved transgressive sheet above. Sill 10 has an elongated geometry with the longest axis oriented NE-SW. It measures 15 by 7 km and covers an area of almost 80 km^2 (Fig. 3.40). The intrusion is intruded at a present-day depth of approximately 5100 to 5850 m and has an overall concave cross-sectional geometry with a vertical relief of more than 700 m. Sill 11 is a large, slightly elongated intrusion with a smooth

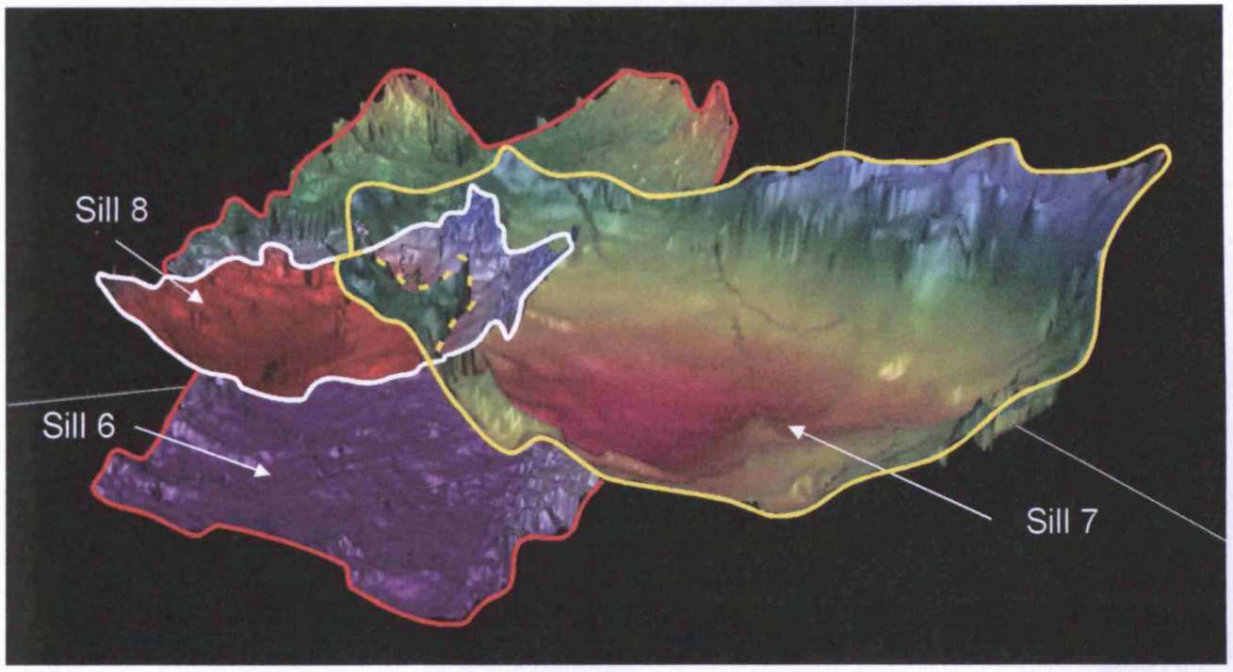

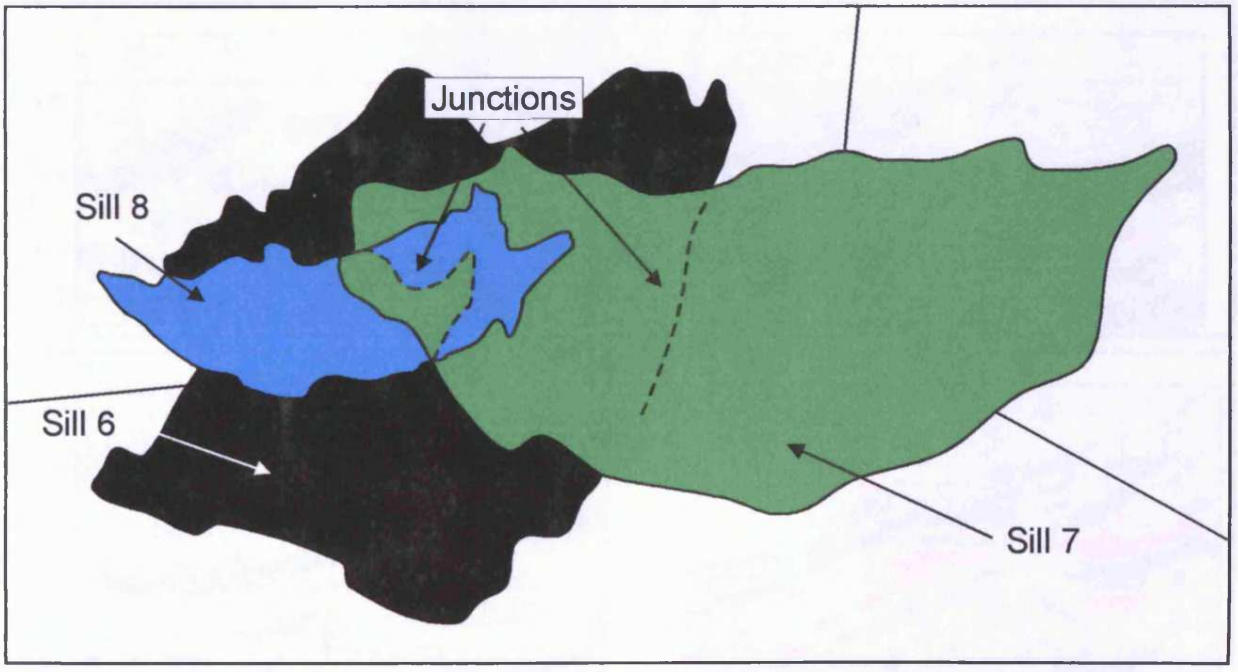

Fig. 3.36 Three-dimensional displays showing three intersecting sills. Sill 6 intersects sill 7 and sill 7 intersects sill8. Lines of junction are shown in dashed lines.

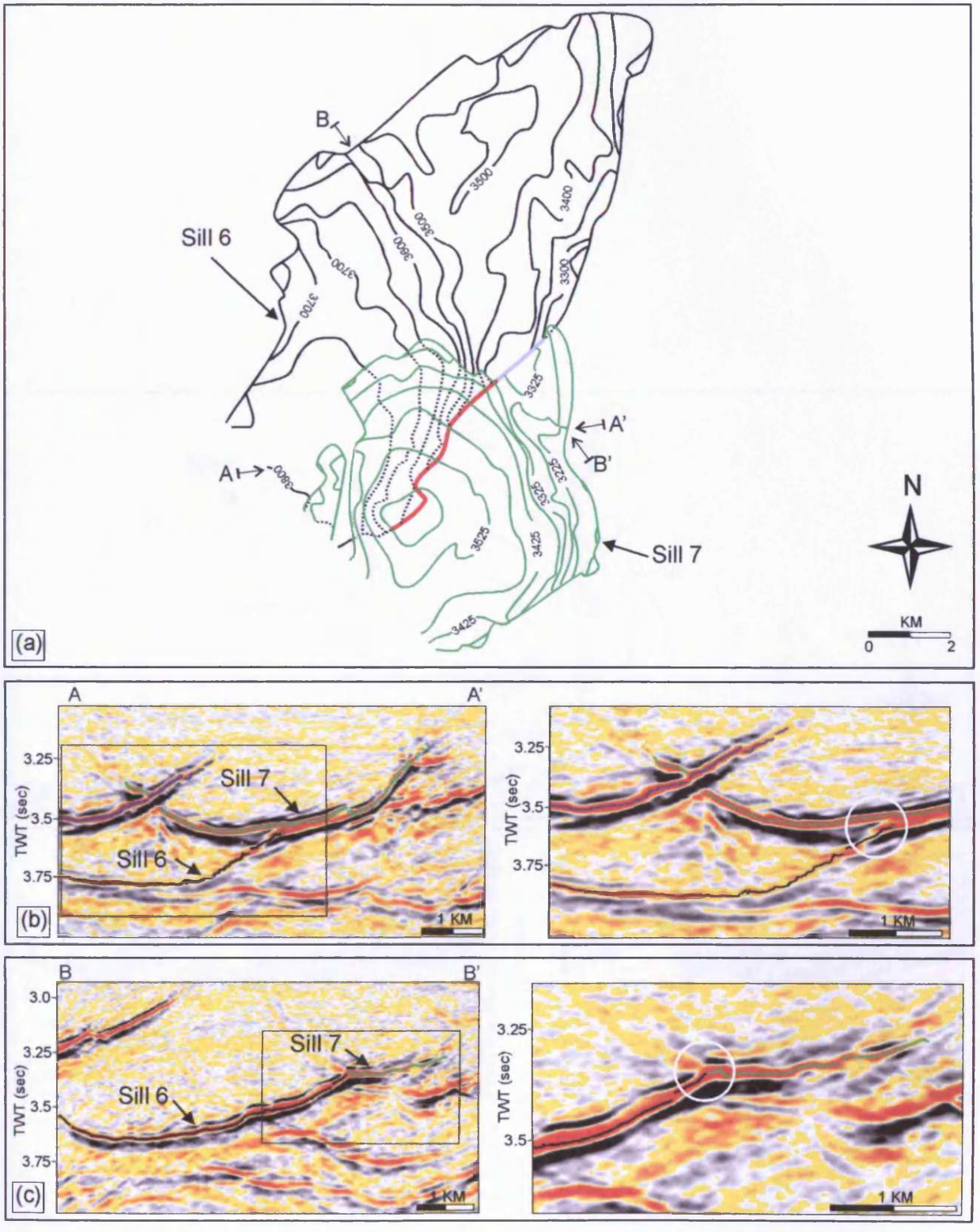

Fig. 3.37 (a) Contour map showing the junction between sill 6 (black contours) and sill 7 (green contours) of compound sill 1 in the T67 survey area. (b) Along most of the line of junction, sill 6 abuts against sill 7 (shown in red on the contour display). (c) Towards the east there is an abrupt change in the geometry of the junction and the tips of sill 6 and sill 7 intersect (shown in purple on the contour map.

In areas of uncertainty or lack of data the contours are left open and where two sills partly or fully overlie one another the contours of the underlying sill are dashed. The sills are colour coded with contours and seismic pick shown in the same colour. The line of junction is drawn with a thicker line. All contour annotations are in ms TWT. This also applies to Figs. 3.38, 3.42, and 3.43.

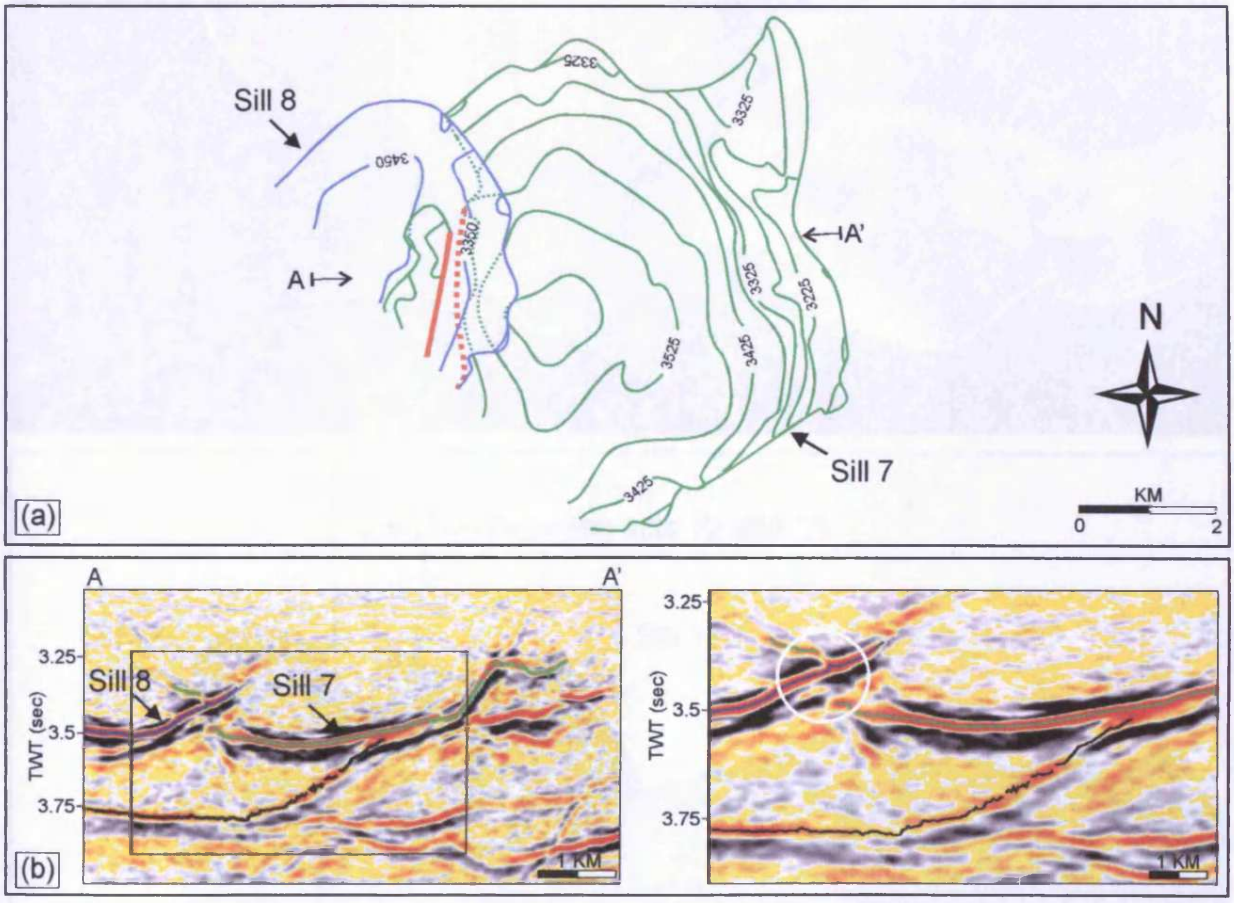

Fig. 3.38 (a) Contour map showing the junction between sill 7 (green contours) and sill 8 (blue contours) of compound sill 1 in the T67 survey area. (b) Sill 7 is cross-cut by sill 8 and the tip of sill 7 is detached from the main sill body and is slightly structurally elevated and backwards rotated.

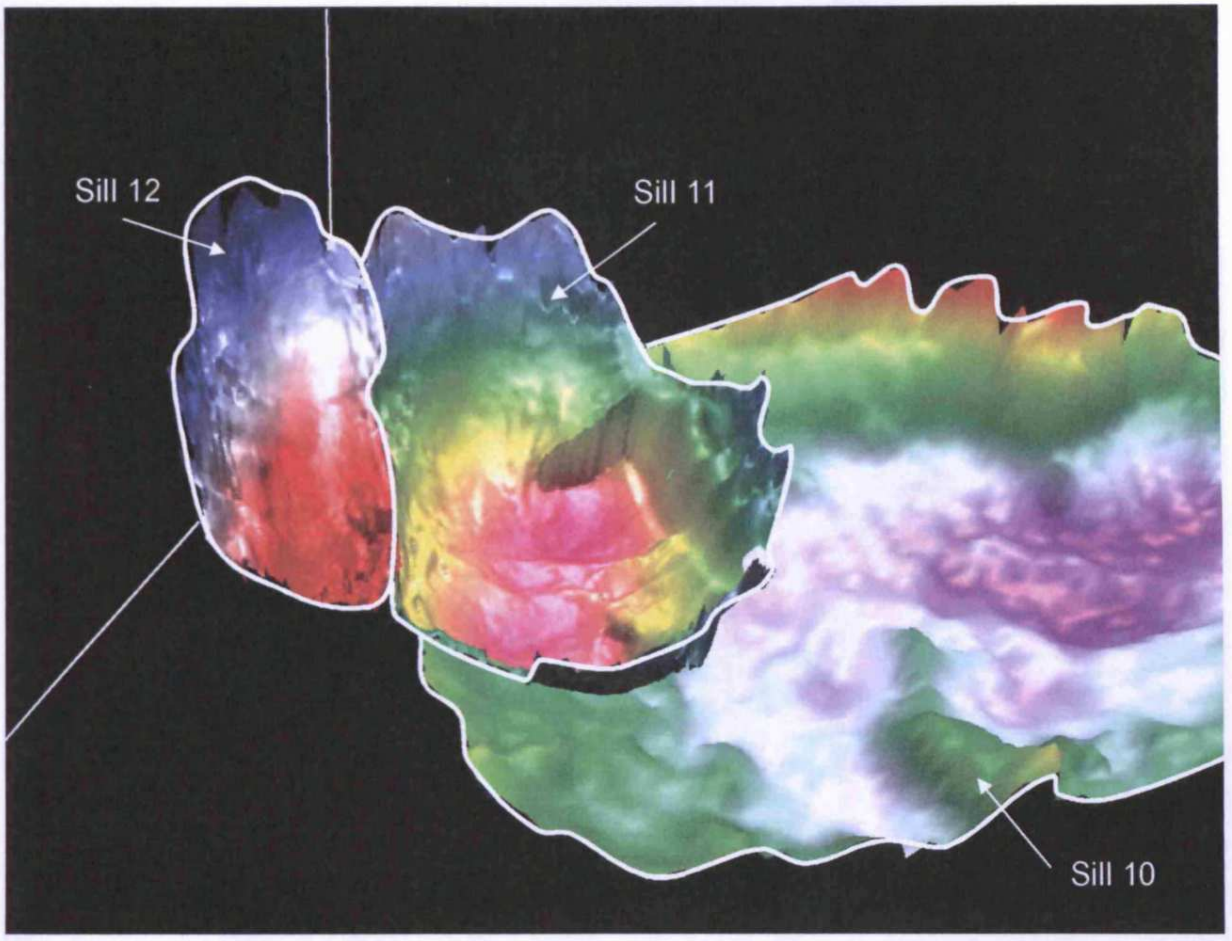

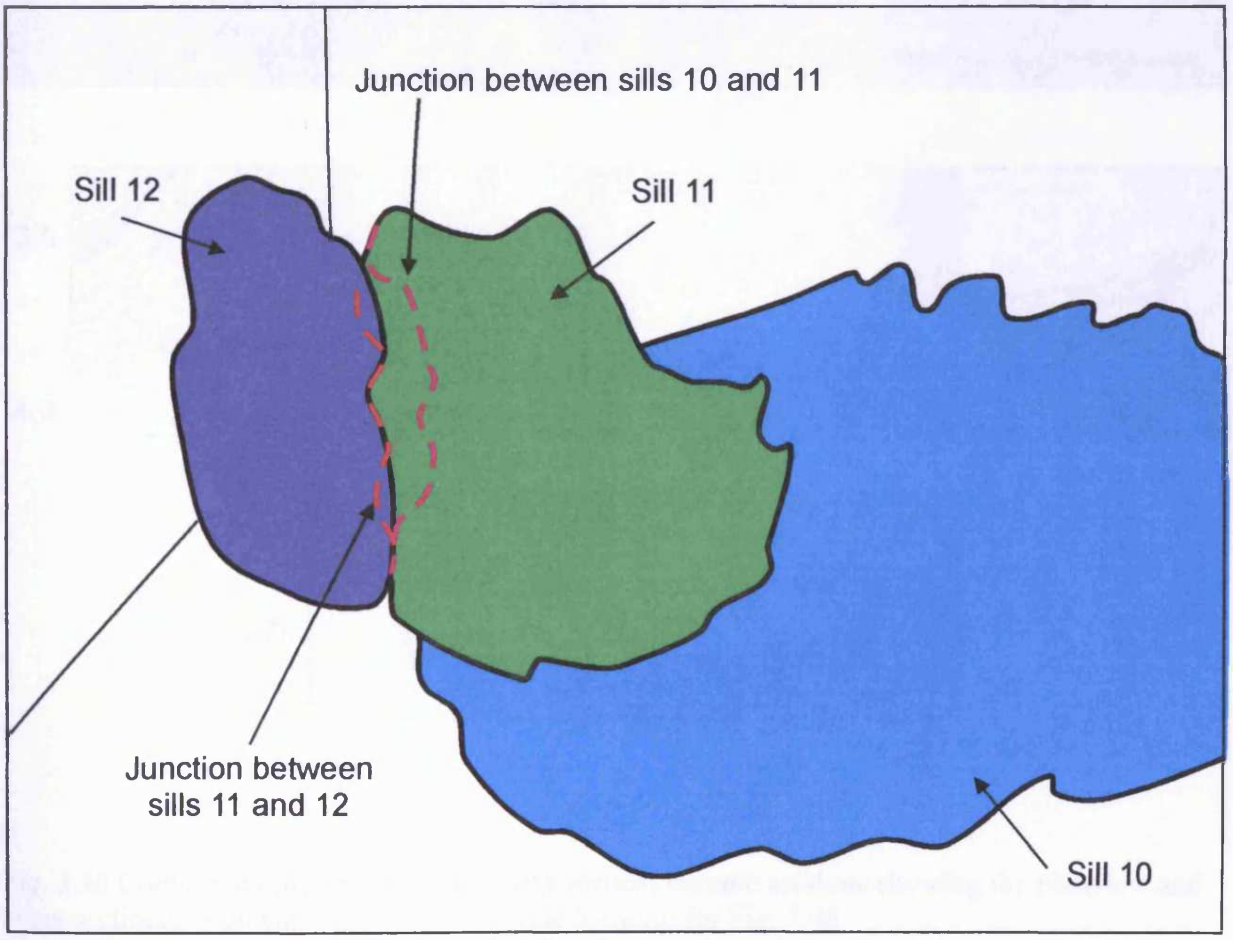

Fig. 3.39 Three-dimensional displays showing the junction relationships between sills 10, 11, and 12.

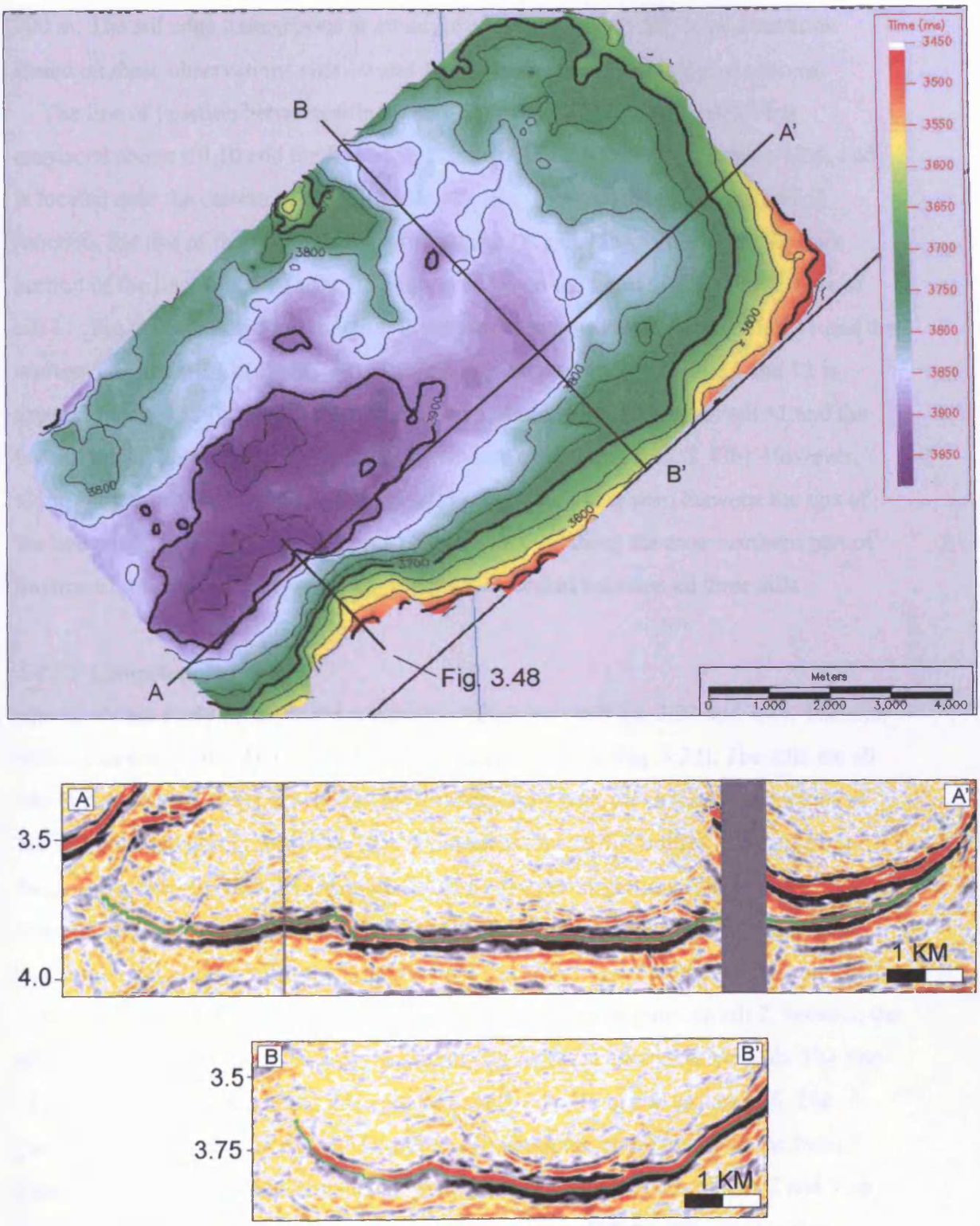

Fig. 3.40 Contoured time-structure map and vertical seismic sections showing the planview and cross-sectional geometry of sill 10. Note line location for Fig. 3.48.

periphery, which is seen at a present-day depth of 4650-5550 m (Figs. 3.41). It measures 4 by 6 km, covers an area of 21 km^2, and has a vertical relief of approximately 900 m. The sill edge transgresses at an angle of approximately 10° in all directions. Based on these observations sills 10 and 11 are both classed as elongated saucers.

The line of junction between sills 10 and 11 is shown in Fig.3.42a. Sill 11 is emplaced above sill 10 and the line of junction strikes NNW-SSE, measures 4 km, and is located near the eastern peripheries of both sills. Towards the tips of the line of junction, the tips of the two sills appear to merge (Fig. 3.42b), while along the mid-section of the line of junction the junction is between the tip of sill 10 and the base of sill 11 (Fig. 3.42c). A second junction is seen between the eastern edge of sill 11 and the western edge of sill 12 (Fig. 3.43a). The line of junction between sills 11 and 12 is approximately 3 km long and the junction is located between the tip of sill 11 and the base of sill 12 along most of the extent of the line of junction (Fig. 3.43b). However, along shorter segments of the line of junction, the junction is seen between the tips of the two sills (Fig. 3.43c). For a short distance < 500 m along the most northern part of the line of junction a highly complex junction is formed between all three sills.

3.4.2.3 Compound sill 3

The third case study involves the compound sill shown in Figs. 3.22 and 3.44. The sills within this compound sill (sills 1-5) all belong to Group B (Fig. 3.22). The sills are all interlinked and junctions are seen between them, however, the detailed geometries of the junctions are poorly resolved. This is primarily due to difficulties in confidently locating the true tips of individual sills because of over-migration. It is further complicated due to resolution problems below the Group C sills and the lava plateau.

On the section (Fig. 3.45) the junction between sills 1 and 2 is between the tip of sill 1 and the base of sill 2. The junction is located at the deepest point on sill 2, between the slightly northward dipping base of the sill and its northern transgressive limb. The line of junction between sills 1 and 2 is approximately 2 km long and strikes N-S. The junction geometry seen in Fig. 3.45 can be seen along the entire length of the line of junction. Another junction is located between the transgressive tips of sills 2 and 3 on the section shown in Fig. 3.45, but slightly further towards the south, the junction geometry changes and the junction point is seen between the tip of sill 3 and the base of sill 2 (Fig. 3.46a). The line of junction is only about 1 km long and strikes ENE-WSW. A third junction is seen between the base of sill 3 and the northern tip of sill 4. The tip

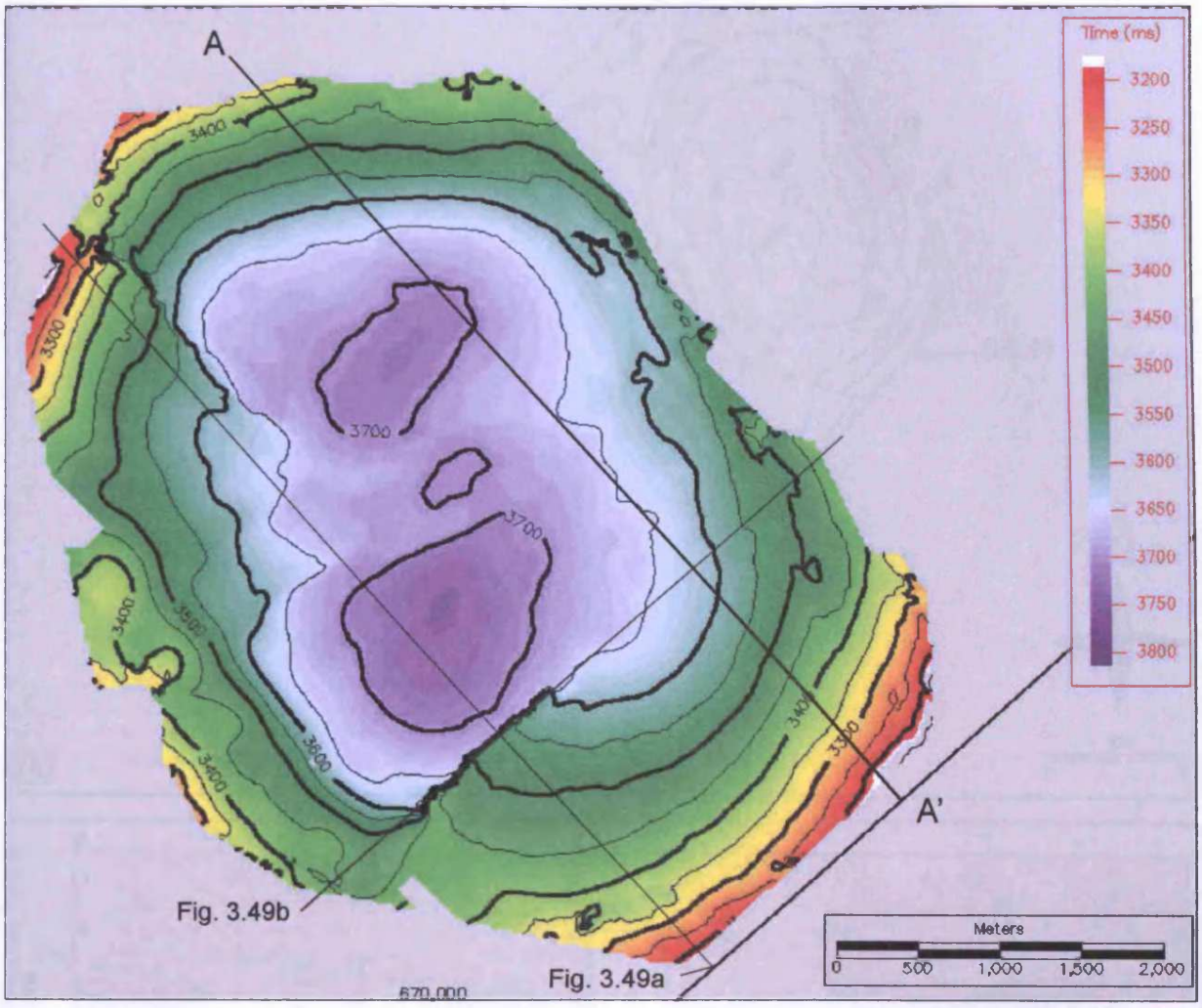

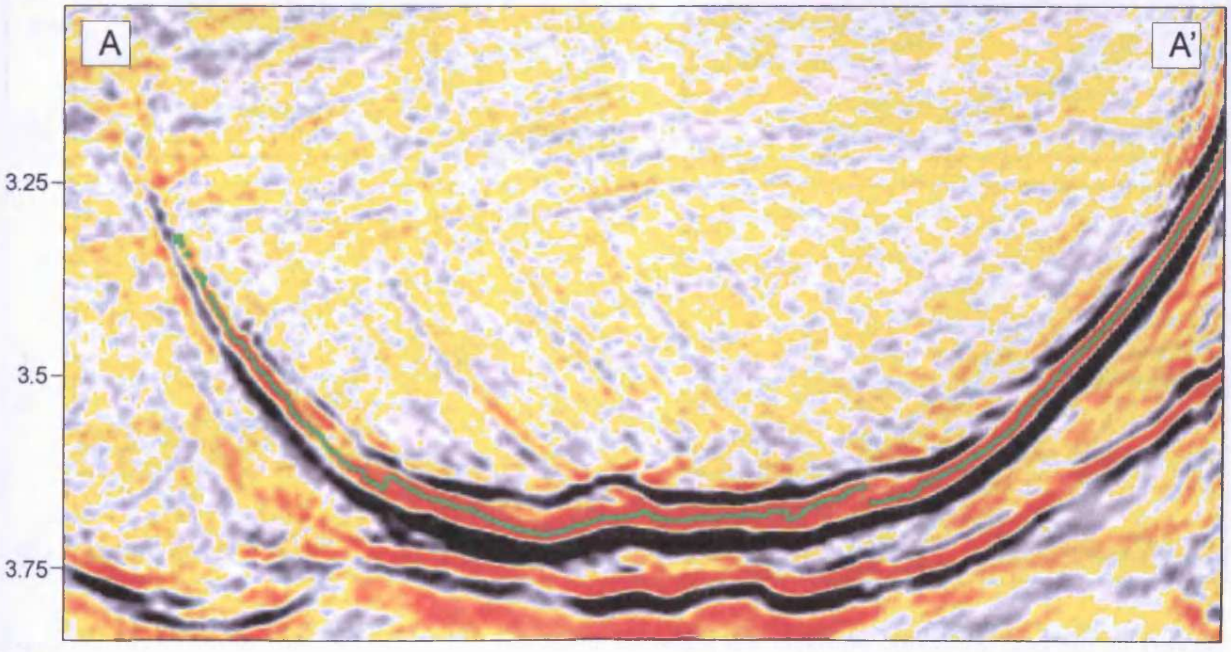

Fig. 3.41 Contoured time-structure map and vertical seismic sections showing the planview and cross-sectional geometry of sill 11. Note line location for Fig. 3.49.

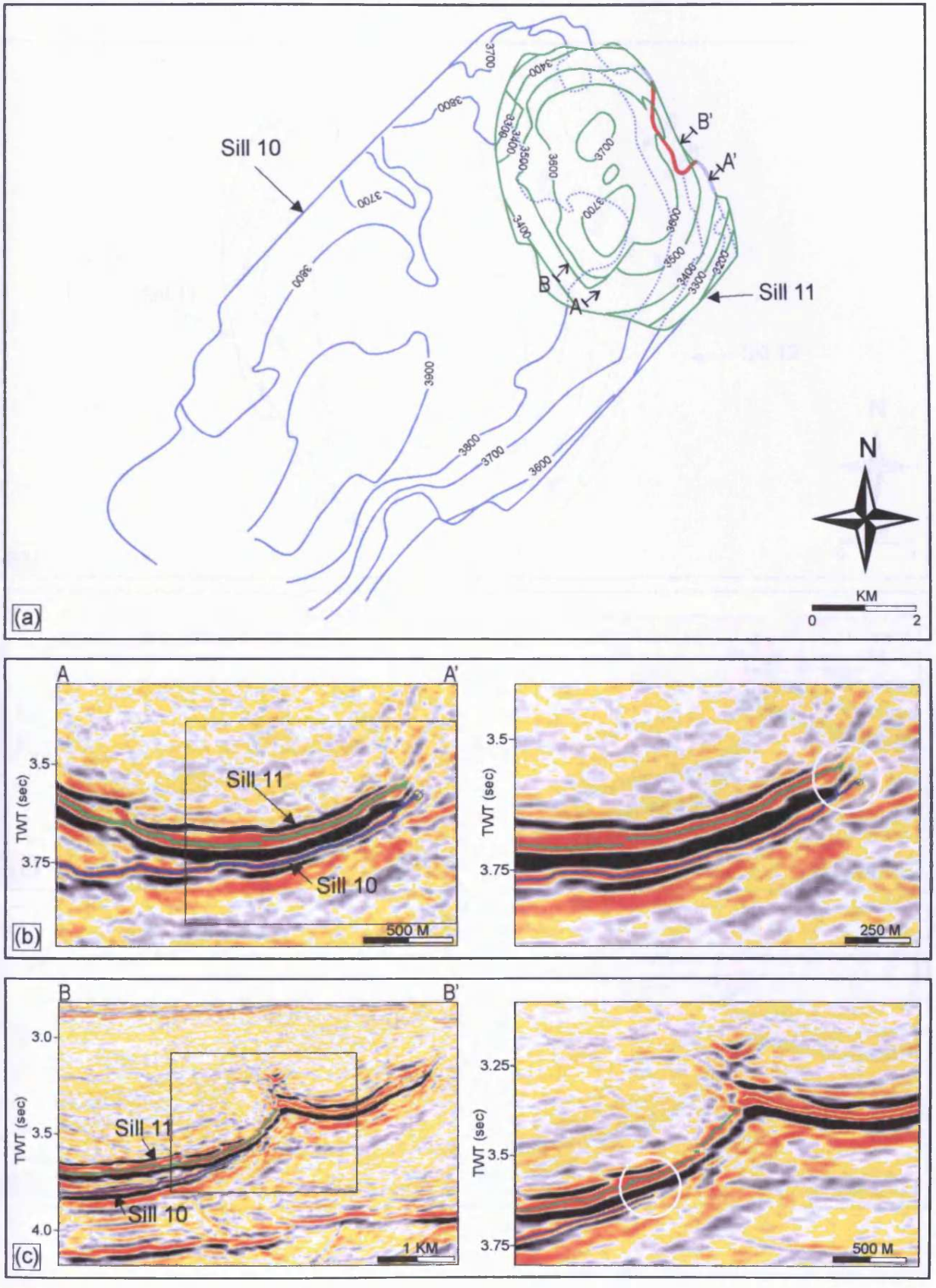

Fig. 3.42 (a) Contour map showing the junction between sill 10 (blue contours) and sill 11 (green contours) of compound sill 2 of the T67 survey area. The line of junction between the two sills is 4 km long and strikes NNW-SSE (b) Towards the tips of the line of junction the tips of the two sills merge (shown in purple on the contour display). (c) Along the mid-section of the line of junction sill 10 abuts against sill 11 (shown in red on the contour display).

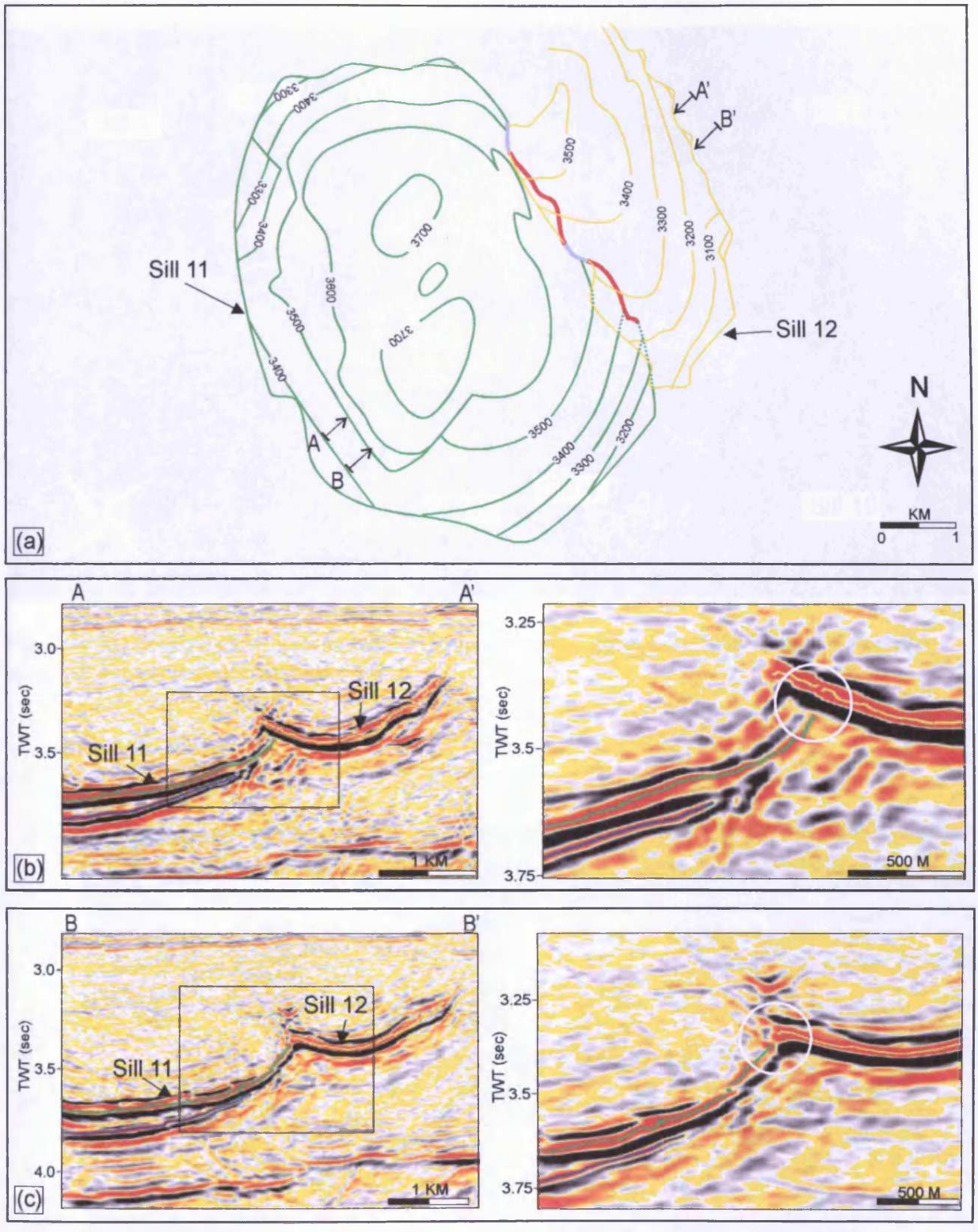

Fig. 3.43 (a) Contour map showing the junction between sill 11 (green contours) and sill 12 (yellow contours) of compound sill 2 of the T67 survey area. The line of junction is 3 km long and strikes NW-SE. (b) Along most of the line of junction sill 11 abuts against sill 12 (shown in red on the contour display). (c) Locally the junction is seen between the tips of the two sills (shown in purple on the contour display).

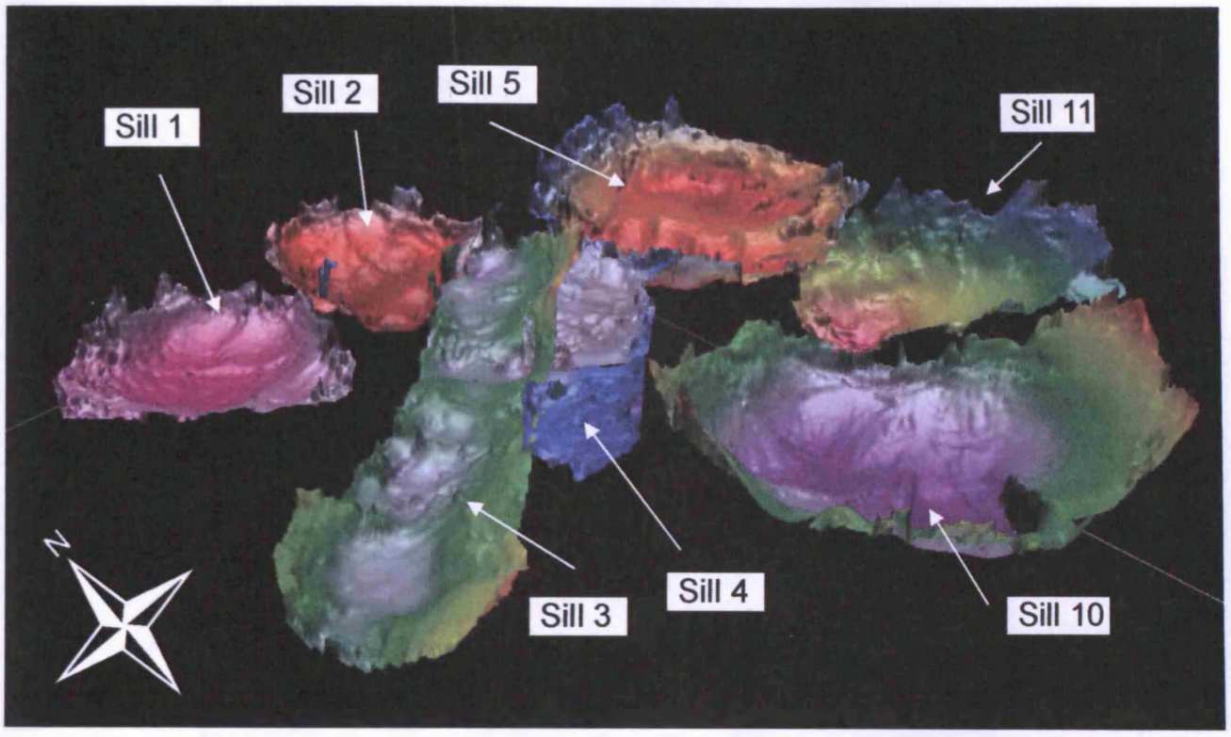

Fig. 3.44 3D display showing sills within compound sill 3 (sills 1-5). Sills 10 and 11 are also seen, but are not part of compound sill 2.

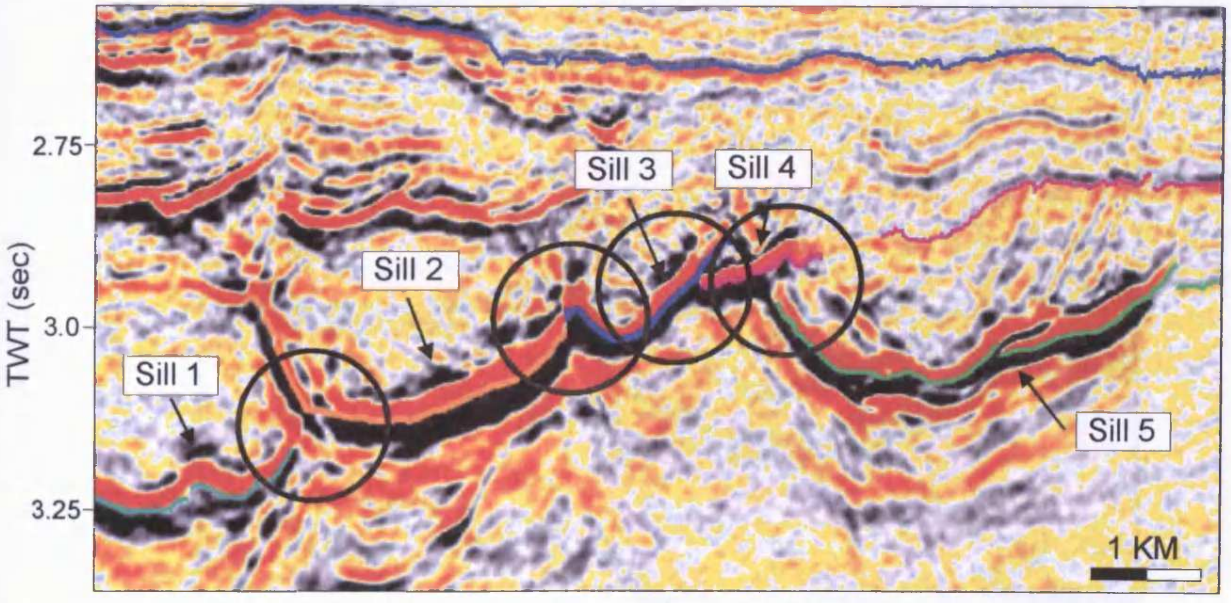

Fig. 3.45 Vertical seismic section showing junctions (within circles) between sills of compound sill 3.

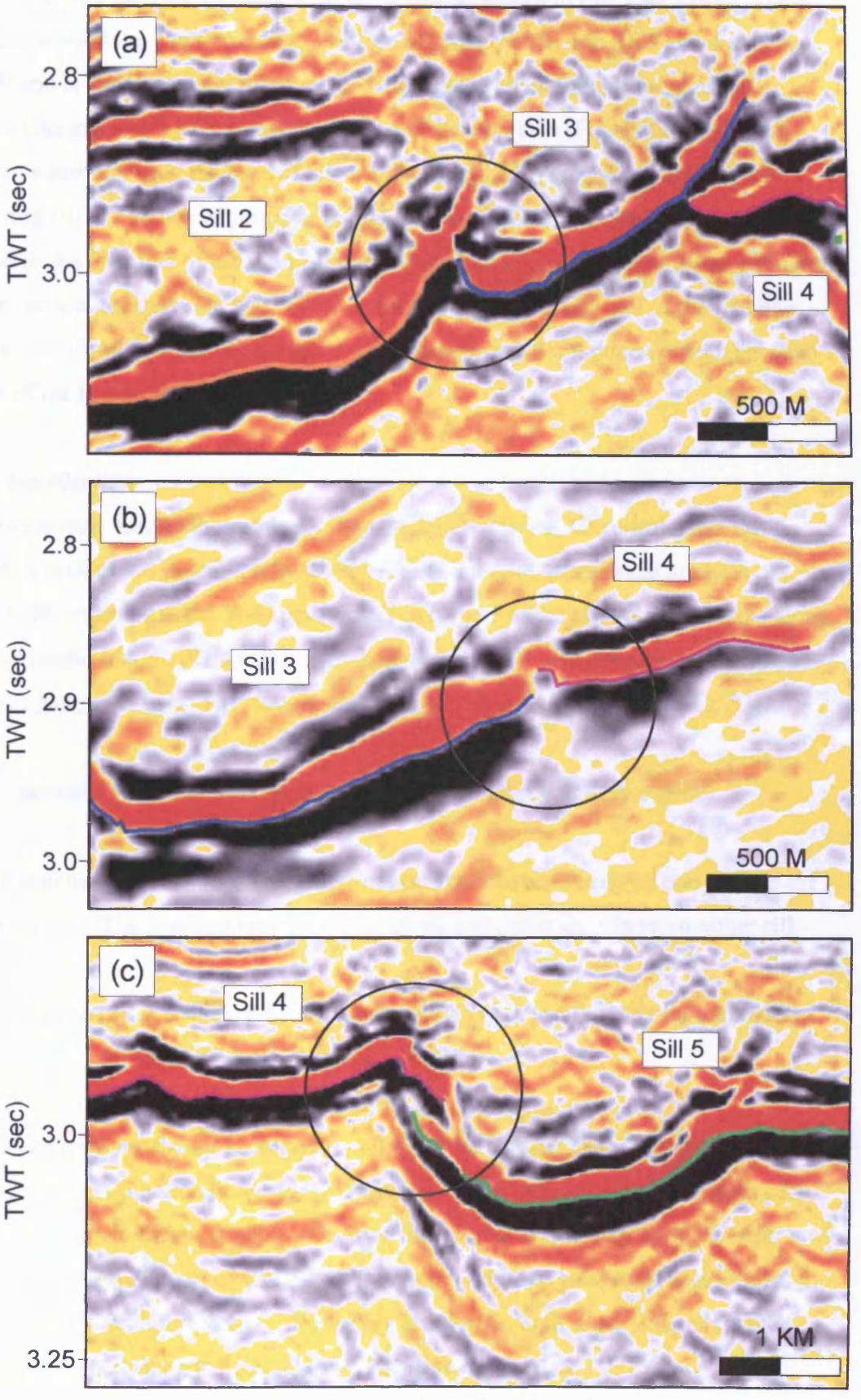

Fig. 3.46 Seismic sections illustrating local junction relationships between sills within compound sill 3.

of sill 3 is poorly defined, but on the specific section shown in Fig. 3.45 it does appear to extend beyond the junction point. The line of junction between sill 3 and 4 strikes NE-SW and is approximately 4 km long. Towards the south the geometry of the junction changes and is seen between the tips of the two sills (Fig. 3.46b). Finally, a junction is seen between the base of sill 4 and the northern, transgressive tip of the underlying sill 5. The line of junction is highly irregular, but it exhibits an overall N-S oriented strike. The line of junction is approximately 2 km long. The junction geometry seen on the section shown in Fig. 3.45 is seen along the northern half of the line of junction, but towards the south the geometry changes and the junction is seen between the tips of the two sills (Fig. 3.46c).

3.4.3 Classification

As shown above, careful interpretation of compound sills on 3D seismic data has revealed a suite of sill junction relationships. Based on the geometrical analysis of junction relationships in the T67 survey area, and more widely in volcanic basins along the NE Atlantic Margin (Chapters 4 and 5), these junction geometries can be grouped into three distinct classes. The three main junction classes are defined in Fig. 3.47.

Class A junction (Fig. 3.47a): The junction is between the tips of two sills.

Class B junction (Fig. 3.47b): The junction point is between the tip of one sill and the base of another. The junction may be at any angle and occur anywhere on either sill.

Class C junction (Fig. 3.47c): One sill cross-cuts another leaving the two segments of the earlier sill displaced by the continuous, later sill.

Class B junctions are the most common and form the longest lines of junction. In no case has a class A junction between two sills been observed along the full length of a line of junction but always appears to evolve into a class B junction, with the latter extending for the main part of the line of junction. Only two good examples of class C junctions have been interpreted in the survey area and in both cases is the class of junction developed along the full length of the line of junction.

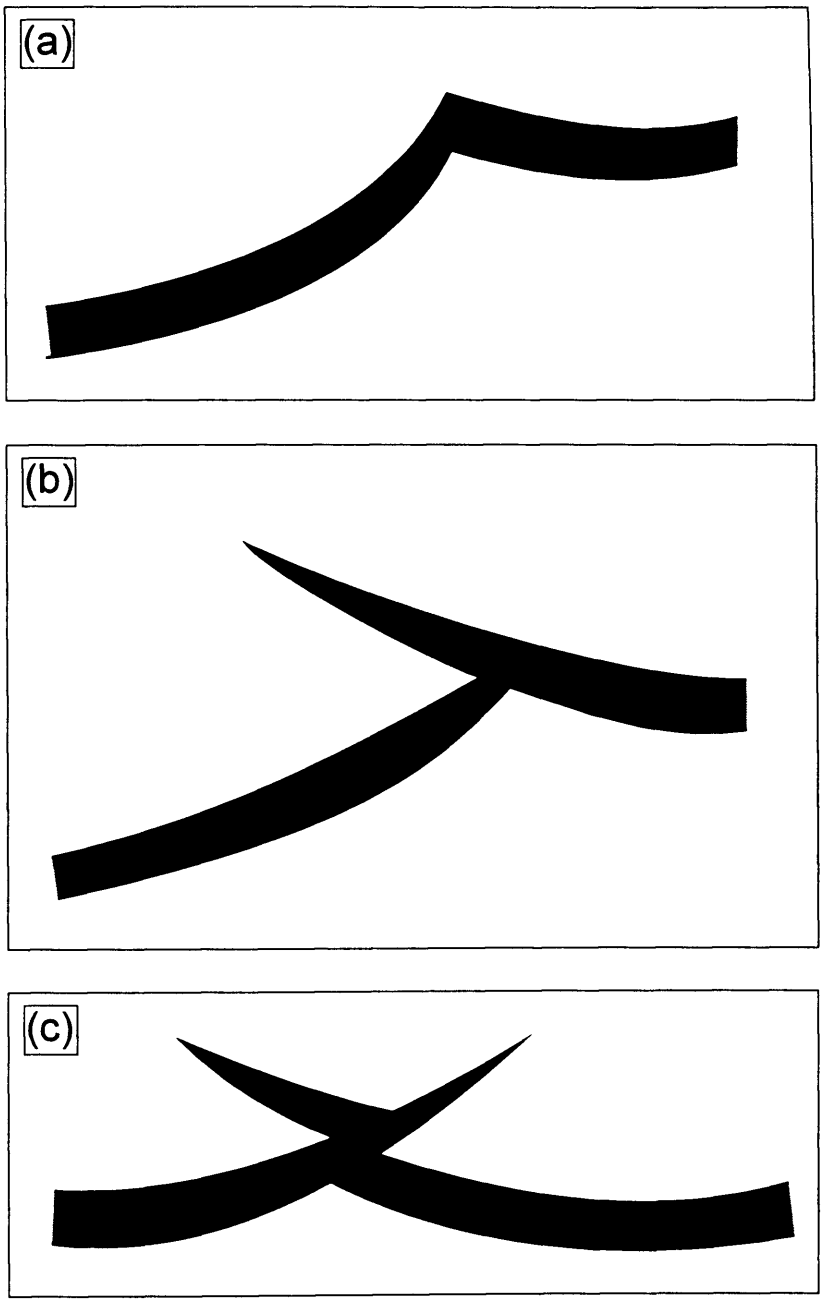

Fig. 3.47 Classification of sill junction relationships: (a) Class A junctions form where the tips of two sills are linked. (b) Class B junctions form where one sill abuts against another. (c) Class C junctions form where one sill cross-cuts another.

3.4.4 Outcrop analogues

Since the fully three-dimensional geometry of igneous systems cannot be visualised at outcrop, a direct comparison of junctions observed on 3D seismic data and outcrop analogues is not possible. However, junction relationships comparable to the class A and B junctions defined above have previously been described and inferred from in classical field areas such as the Karoo of South Africa.

Almost a century ago, du Toit (1920) recognised that many sills intruded into Carboniferous-Permian sediments of the Karoo Basin, South Africa, during the Early Jurassic had a concave shape and formed circular outcrop patterns. Due to erosion, however, the rims of the outcropping sills are never fully preserved. Following this pioneering work, Bradley (1965) developed a model for sill development in which adjacent saucer-shaped sills, in a manner similar to that shown here as class A junctions, connected to form undulating sheets (Fig. 1.7b).

The class B junction is the dominant type of junction in the T67 survey and two-dimensional sections through this type of junction have been recognised in many field descriptions of sills. Field sketches by du Toit (1920) and Lombard (1952) show highly interconnected networks of sills in which sills abut against one another (Fig. 1.9). Other field studies have shed light on the significance of certain junction geometries using special techniques to establish the sequence of intrusion. Tweto (1951), for example, used mineral orientation as an indicator of flow direction and described examples of sill splitting and sill merging in the Pando area in Colorado. Where the splitting or merging involves one sill splitting into two or two sills merging to one the resultant geometries can be regarded as comparable to class B junctions. Outcrop analogues to class B junctions have also been described in detail from Jurassic sills near Hobart in Tasmania (Leaman, 1975). Intrusion geometries varying from Y- to T-shaped are here developed near feeder sources of dolerite sills intruded into Permian and Triassic sedimentary rocks.

3.4.5 Internal junctions

The above description and classification of sill junctions was based on junctions between two interlinked sills. Similar junction geometries have been observed within individual saucers. Sill bifurcations and sill intersections are difficult to distinguish on seismic data because they are geometrically very similar and indicators of magma flow direction resolvable at the seismic scale, such as flow ridges (Chapter 6 and Trude,

2004) and lobes (Chapter 5), are rarely observed. However, where the junction can be seen to be between segments that are clearly part of the same saucer they are almost certainly the result of bifurcation. Where internal junctions are found within circular or elongated saucers these intrusions are, according to the flow-chart (Fig. 3.34), more correctly classified as complex circular saucers and complex elongated saucers. Several examples of internal junction have been observed in the survey area and two examples (sills 10 (Fig. 3.48) and 11 (Fig. 3.49)) are described in detail in the following section. Prior to considering the internal geometry of these two intrusions they were both classed as elongated saucers in section 3.4.2.2.

3.4.5.1 Sill 10

Three junctions are seen along the transgressive southern tip of sill 10 on the cross-section shown in Fig. 3.48. These junctions are interpreted as internal junction because they do not influence the overall geometry of the sill. The first internal junction occurs at the base of the transgressive segment, approximately 800 m before tip A. The sill bifurcates with one segment forming a natural continuation of the horizontal base of the sill (tip A) while the other transgresses at an angle of 12°. The sill transgresses approximately 200 m and then bifurcates a second time. Approximately 250 m before the second internal junction the angle of transgression decreases slightly. Beyond the point of bifurcation one of the segments transgresses at an angle of 30° to the horizontal while the other can be interpreted for just less than 400 m beyond the bifurcation along the trajectory of the first transgressive segment (tip B). The second transgressive segment climbs approximately 280 m and is capped by an approximate 600 m wide segment that gently transgresses at an angle of 12° (relative to the horizontal) towards the SE.

The intrusion has a smooth periphery, an elongated plan geometry, a concave overall cross-sectional geometry, and a complex internal geometry. Based on this it is best classed as a complex elongated saucer. The internal junctions within sill 10 are interpreted as class B junctions.

3.4.5.2 Sill 11

The second example involves sill 11. On crosslines through the eastern part of sill 11 like the one shown in Fig. 3.49 it has a 6 km wide and perfectly smooth concave shape with a relatively flat base and gently transgressing limbs. Towards the western sill

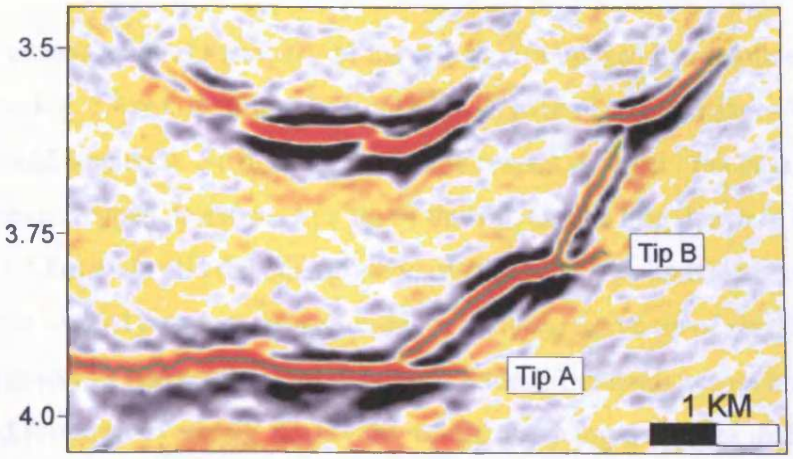

Fig. 3.48 Internal junction along the south-eastern transgressive tip of sill 10. See Fig. 3.40 for line location.

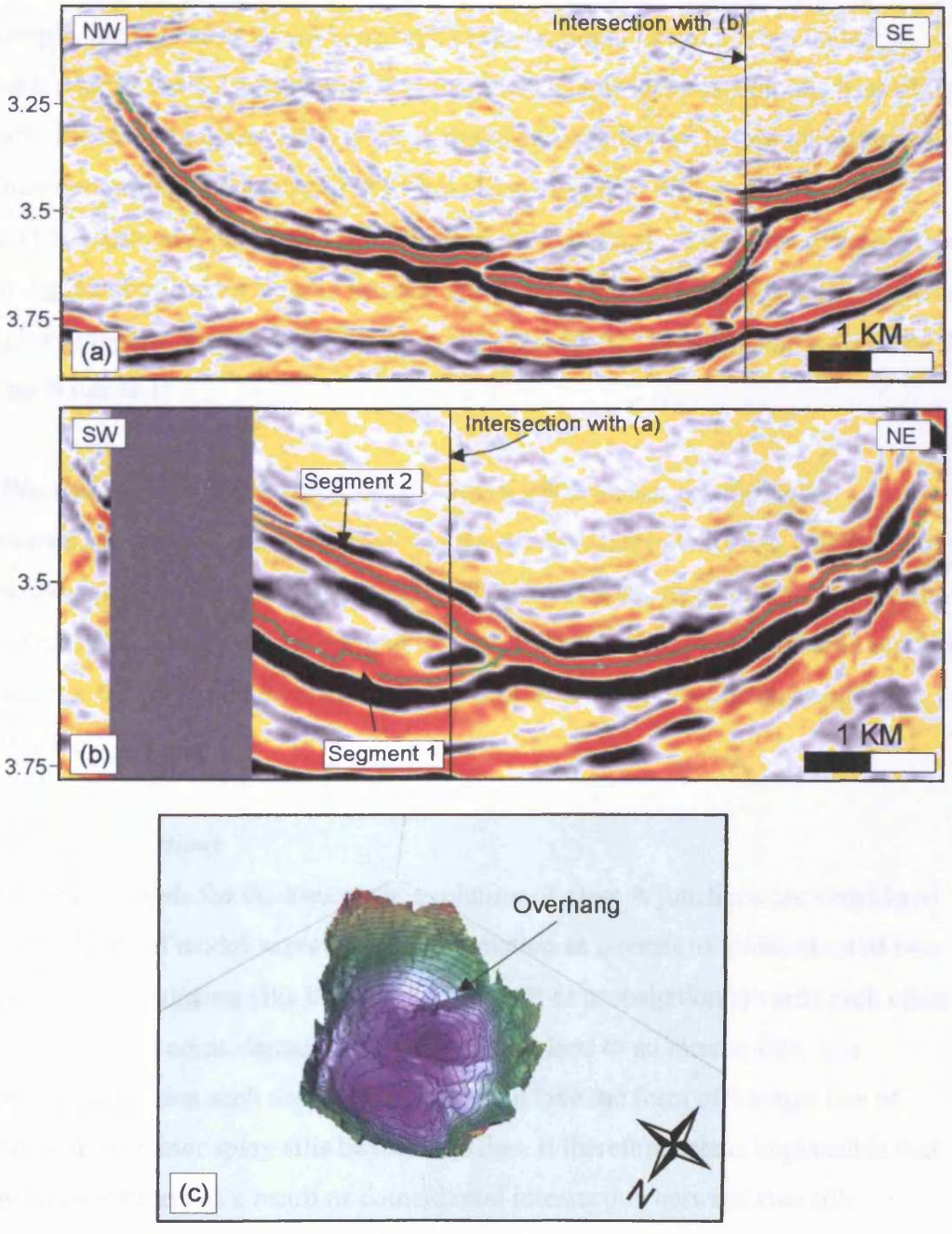

Fig. 3.49 Internal junction within sill 11. (a) Inline. (b) Cross-line. (c) 3D display of sill 11 showing overhang. See Fig. 3.41 for line locations.

boundary the cross-sectional geometry of the sill, as it is imaged by crosslines, becomes more complex (Fig. 3.49a). It continues to exhibit an overall concave shape but consists of two interlinked segments. Segment 1 forms the central relatively flat basal part and the north-western stepped, transgressive tip of the sill. On the line shown in Fig. 3.49a segment 2 is 1.5 km wide and dips gently towards the NW. The junction between the two segments is located between the south-eastern transgressive tip of segment 1 and the base of segment 2. The north-western tip of segment 2 extends across the underlying segment 1 and forms an overhang. The width of the overhang decreases in the north-eastern direction where the two segments gradually merge. The geometry of the junction is also imaged on a narrow range of inlines. On the inline shown in Fig. 3.49b, for example, the sill has an overall concave cross-sectional geometry, but it clearly bifurcates near its base. The upper branch (segment 2) transgresses from the base of the sill whilst the lower (segment 1) is slightly downwards deflected before transgressing. The three-dimensional geometry of sill 11 is shown in Fig. 3.49c.

Sill 11 has a smooth periphery, an elongated plan geometry, a concave overall cross-sectional geometry, and a complex internal geometry. Based on this it is best classed as a complex elongated saucer. The internal junction geometry between segments 1 and 2 is a class B junction.

3.4.6 Discussion: The kinematic development of sill junction relationships

The detailed seismic analysis presented has revealed the complexity and variability of sill junction relationships. As shown in the previous sections, three distinctly different sill junction relationships can be defined and classified. This section provides a number of models for the possible kinematic development of each of these three junction geometries.

3.4.6.1 Class A junctions

Three possible models for the kinematic evolution of class A junctions are considered (Fig. 3.50). The first model explains class A junction as a result of intersection of two independently propagating sills that meet as a result of propagation towards each other (Fig. 3.50a). Whilst coincidental propagation might lead to an intersection, it is extremely unlikely that such an intersection would take the form of a single line of junction, with no minor splay sills beyond the line. It therefore seems implausible that class A junctions form as a result of coincidental intersection between two sills.

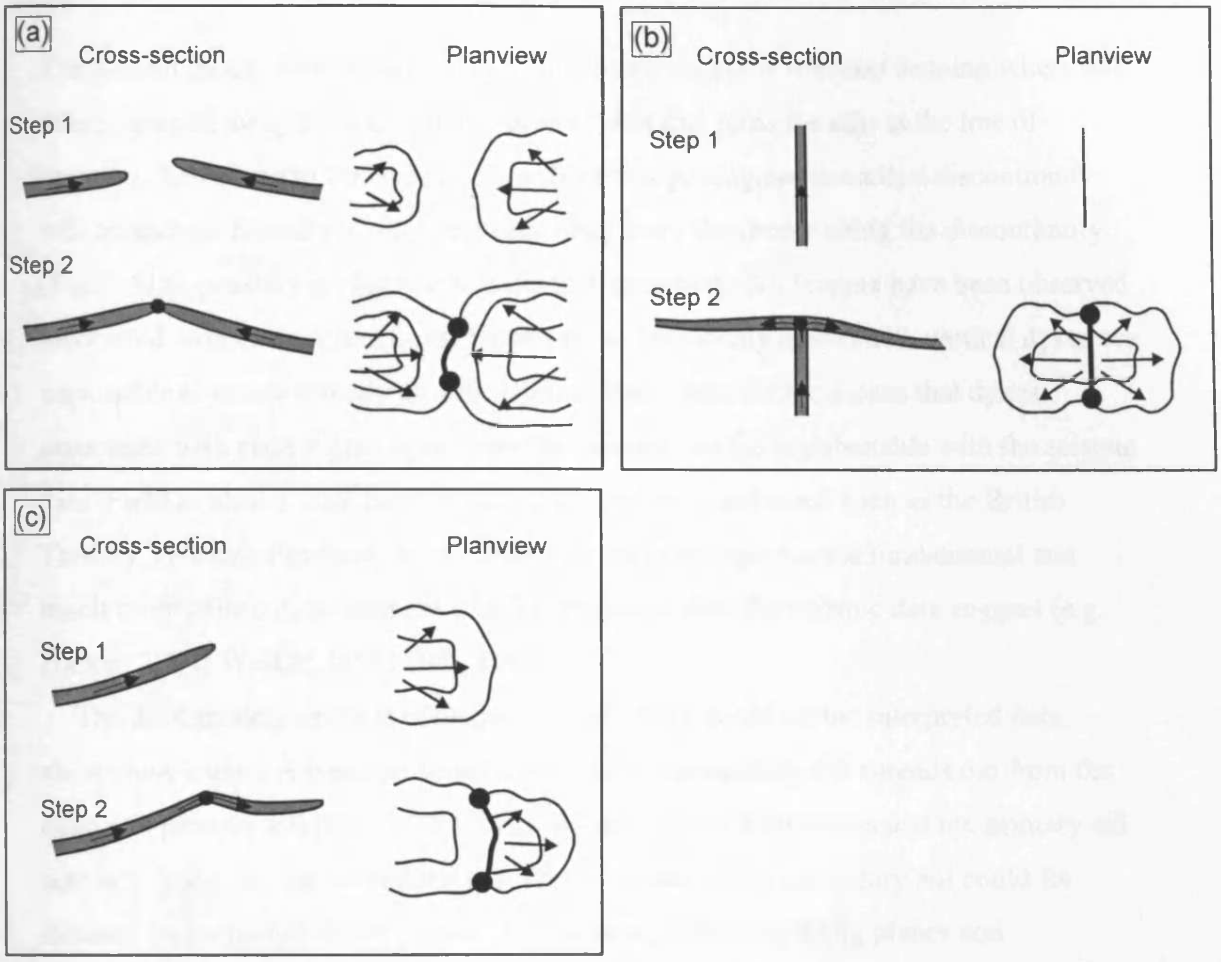

Fig. 3.50 Kinematic models for the development of class A junctions.

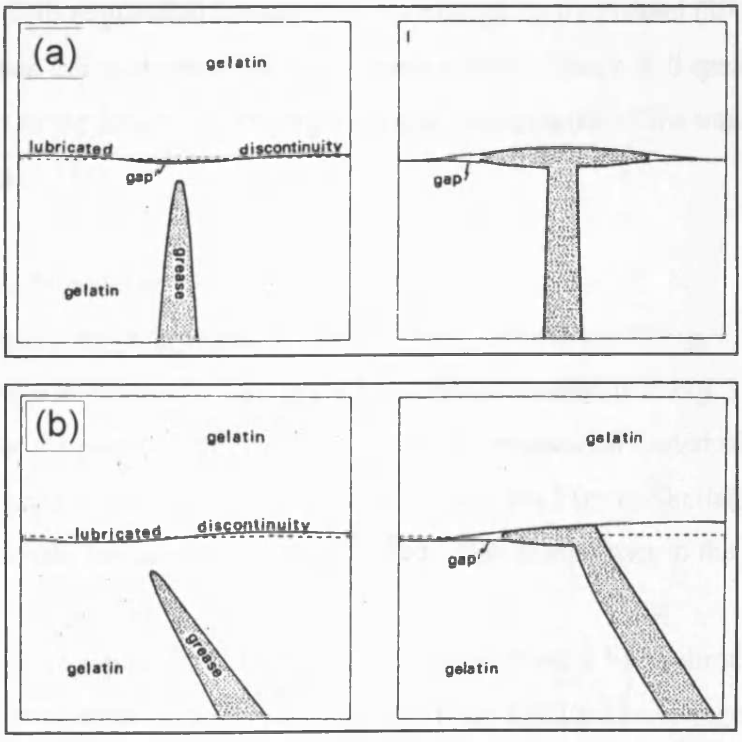

Fig. 3.51 Sketches of experiments involving grease intruding towards a lubricated discontinuity within gelatin. (a) Grease is intruded at right angle to the lubricated discontinuity and spreads out laterally, in all directions along the discontinuity. (b) Grease is intruded at an angle to the lubricated discontinuity and intrudes along the discontinuity in one direction. After Pollard (1973).

The second model illustrated in Fig. 3.50b shows a class A junction forming where two sills propagate away from a feeder source (dyke) that joins the sills at the line of junction. According to Pollard (1973) a dyke that propagates towards a discontinuity will spread out laterally in all directions away from the feeder along the discontinuity (Fig. 3.51a), possibly giving rise to a class A geometry. No feeders have been observed associated with class A junctions. However, as previously mentioned, vertical dykes are impossible to image directly on reflection seismic data, which means that dykes associated with class A junctions could be present but are undetectable with the seismic data. Field evidence from heavily intruded, well-exposed areas such as the British Tertiary Volcanic Province, does certainly imply that dykes are a fundamental and much more common component of sill complexes than the seismic data suggest (e.g. Harker, 1904; Walker, 1975; Bell, 1984).

The third model, which is considered most likely based on the interpreted data, shows how a class A junction could form where a secondary sill spreads out from the edge of a primary sill (Fig. 3.50c). This is a case of sill bifurcation and the primary sill acts as a feeder for the secondary sill. The initiation of the secondary sill could for instance be promoted where planes of weakness, such as bedding planes and unconformities, or local lithological barriers, re-direct the propagation path of the primary sill. This suggestion is supported by modelling by Pollard (1973) who found that an inclined intrusion propagating towards a discontinuity will spread out along the discontinuity in the direction forming a natural continuation of the transgressive segment (Fig. 3.51b).

3.4.6.2 Class B junctions

Class B junctions are interpreted to form in three distinct ways (Fig. 3.52). The first way in which a class B junction is interpreted to form is illustrated in Fig. 3.52a and involves obstruction of the propagation path of a sill by a previously intruded sill. This is very likely to happen in densely intruded basins, such as the Faeroe-Shetland Basin, and probably accounts for many of the interpreted Class B junctions in the T67 seismic survey area.

The second way in which class B junction might form is by bi-directional lateral propagation away from a transgressive sill tip (Fig. 3.52b). The change from transgressive to lateral propagation could occur as a result of exploitation of a plane of weakness or due to the presence of a lithological barrier. This kinematic explanation for

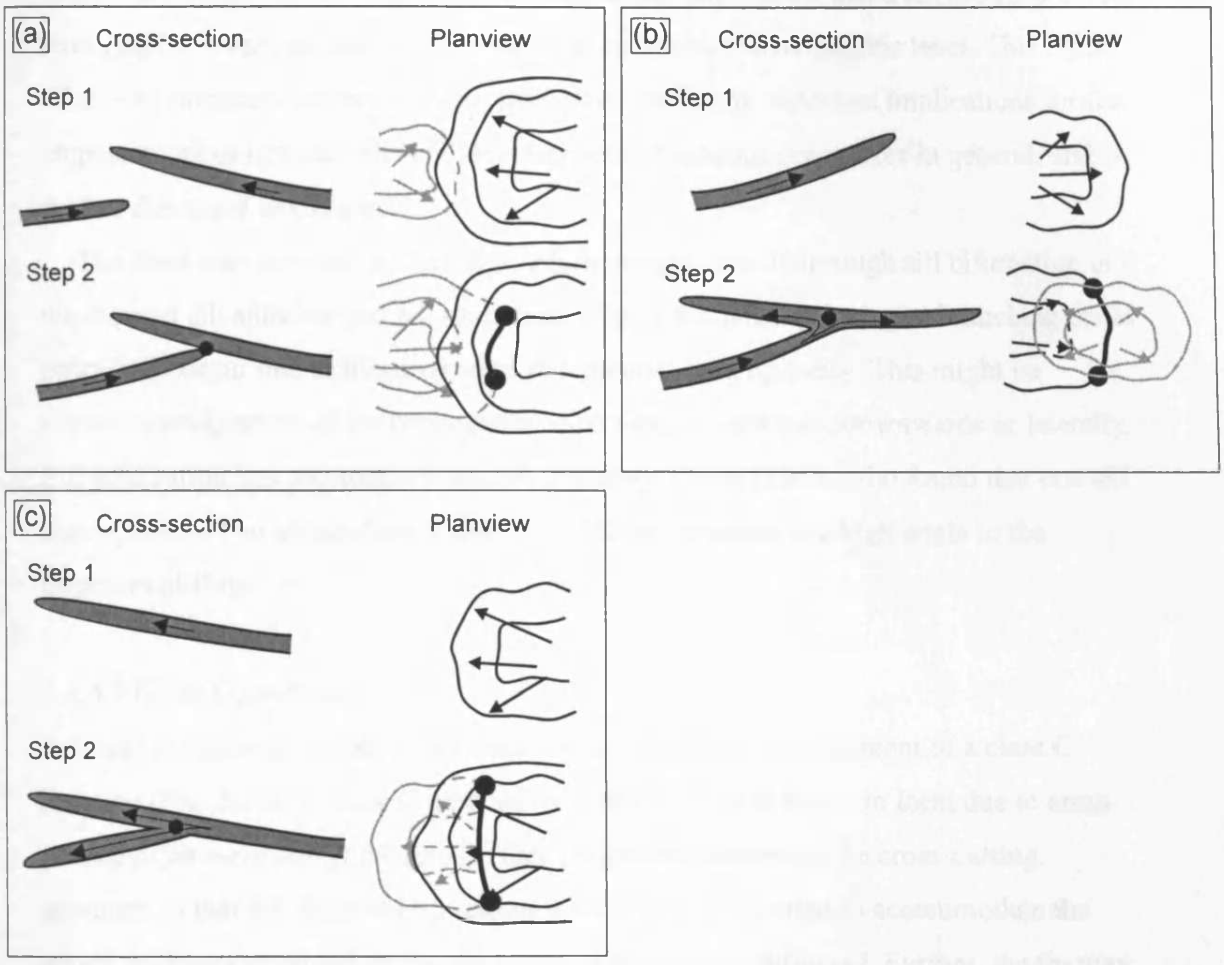

Fig. 3.52 Kinematic models for the development of class B junctions.

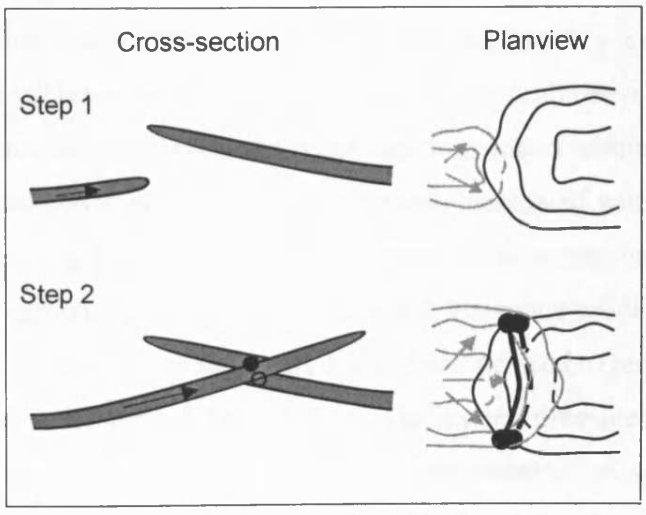

Fig. 3.53 Kinematic model for the development of a class C junction.

class B junctions carries with it the very important implication that a sill intruded at one stratigraphic level can feed a sill intruded at a shallower stratigraphic level. This mode of sill-fed intrusions at successively shallower levels has important implications for the emplacement of igneous sills and development of igneous complexes in general, and is further discussed in Chapter 7.

The third way in which a class B junctions might form is through sill bifurcation in the form of sill splitting and sill branching (Fig. 3.52c). Sill splitting or branching could potentially occur due to lithological or mechanical heterogeneity. This might be expected irrespective of the propagation direction i.e. upwards, downwards or laterally. Sill bifurcation has previously been described by Tweto (1951) who found that one sill may split into two along along a line of 'splitting' oriented at a high angle to the direction of flow.

3.4.6.3 Class C junctions

A single model is presented to account for the kinematic development of a class C junction (Fig. 3.53). A class C junction is considered most likely to form due to cross-cutting of an early sill by a later sill. One diagnostic feature of the cross-cutting geometry is that the detached tip region is structurally elevated to accommodate the added thickness provided by the thickness of the cross-cutting sill. Further, the tip may be rotated slightly backwards as a result of drag induced during the forcible intrusion of the cross-cutting sill.

3.4.7 Reconstructing the intrusion history of compound sills

From the above discussion of the kinematics of sill junctions it is evident that sill intersections and sill bifurcations play an important role in the development of compound sills and sill complexes. Once the junctions found within a given sill complex have been classified, the kinematic models associated with each junction class can be used as building blocks in the reconstruction of the compound sill or sill complex. In this section it is demonstrated how the kinematic models for the interpreted junctions between sills of compound sills 1 and 2 can be used to reconstruct their likely three-dimensional development through time. The models presented are not the only possible ways of reconstructing the geometry of compound sills 1 and 2, but they are relatively simple and are considered more plausible than a number of alternative propagation patterns that have been considered, but that are not described.

Reconstruction of the intrusion history of compound sill 3 has not been attempted because of the uncertainties in the classification of the junction geometries.

3.4.7.1 Compound sill 1

Two possible models for the development of compound sill 1 are considered. Both models involve four time-stages and these are illustrated in Figs. 3.54 and 3.55 (pages 70 and 71). For each stage the contour pattern of the compound sill at that stage as well as the temporary cross-sectional geometry of the final junctions are illustrated.

During *stage 1* of the ***first model*** (Fig. 3.54a) only sill 6 exists. Based on the mapped geometry of sill 6 it is considered most likely that the sill propagated from the south-west towards the north-east. It is suggest that during the early stages of its development it gently transgressed from the south-west towards the north-east exhibiting a greater length to width ratio than the final sill 6. Cross-sections A-A' and B-B' are very similar both illustrating the slightly upward concave geometry of the central part of sill 6. Continued feeding of sill 6 during *stage 2* (Fig. 3.54b) results in further spread of sill 6. A weakness (possibly a bedding surface or some local heterogeneity) along a kilometre long segment of the eastern boundary of sill 6 is exploited by the magma and sill 7 is initiated. Sill 7 spreads away from the edge of sill 6 in a south-easterly direction forming a class A junction as illustrated in model 3 for class A junctions (Fig. 3.50c). Cross section A-A' shows the class A junction between sill 6 and sill 7 and cross-section B-B' the concave upwards cross-sectional geometry of sill 6. Sill 7 is mainly developed during *stage 3* (Fig. 3.54c). The magma fed into sill 6 is further feed into sill 7, and sill 6 only spreads out slightly during this stage. Sill 7 on the other hand spreads out towards the south and adopts its saucer-shaped geometry. Sill 8 is also developing at this stage. Cross section A-A' has not changed much between stage 2 and 3, but sill 7 is shown to have inflated slightly as a result of the continued flow of magma from sill 6 into sill 7. On cross-section B-B' sill 6 and sill 7 are seen as separate concave upward bodies. Sill 7 is propagating towards the south (out of the paper). Sills 6, 7, and 8 are all seen as separate bodies on cross-section C-C'. During *stage 4* (Fig. 3.54d) the sills only grow slightly. The south-eastern tip of sill 6 continuous to transgresses and abuts against the overlying sill 7 forming a class B junction in accordance with model 1 for class B junctions (Fig. 3.52a). Sill 8 is also propagating at this time and cross-cuts the tip of sill 7 forming a class C junction as illustrated in Fig. 3.53. Cross-section A-A' has not changed between stages 3 and 4 and shows the class A junction relationship

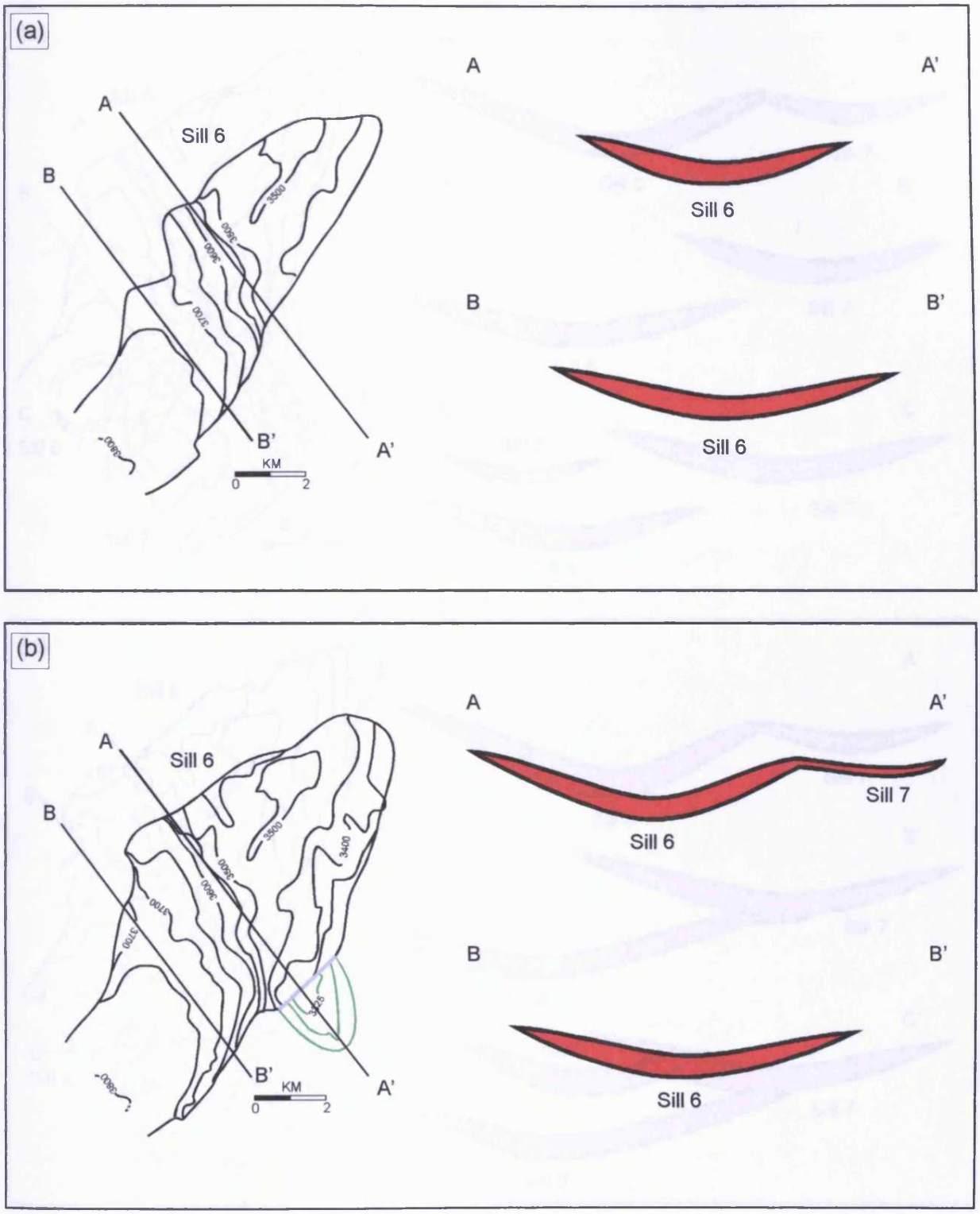

Fig. 3.54 Kinematic model 1 for the development of compound sill 1. The model comprises four stages and these are illustrated with contour maps and schematic cross-sections. (a) Stage 1. (b) Stage 2. (Sill 6: black contours, sill 7: green contours, sill 8: blue contours).

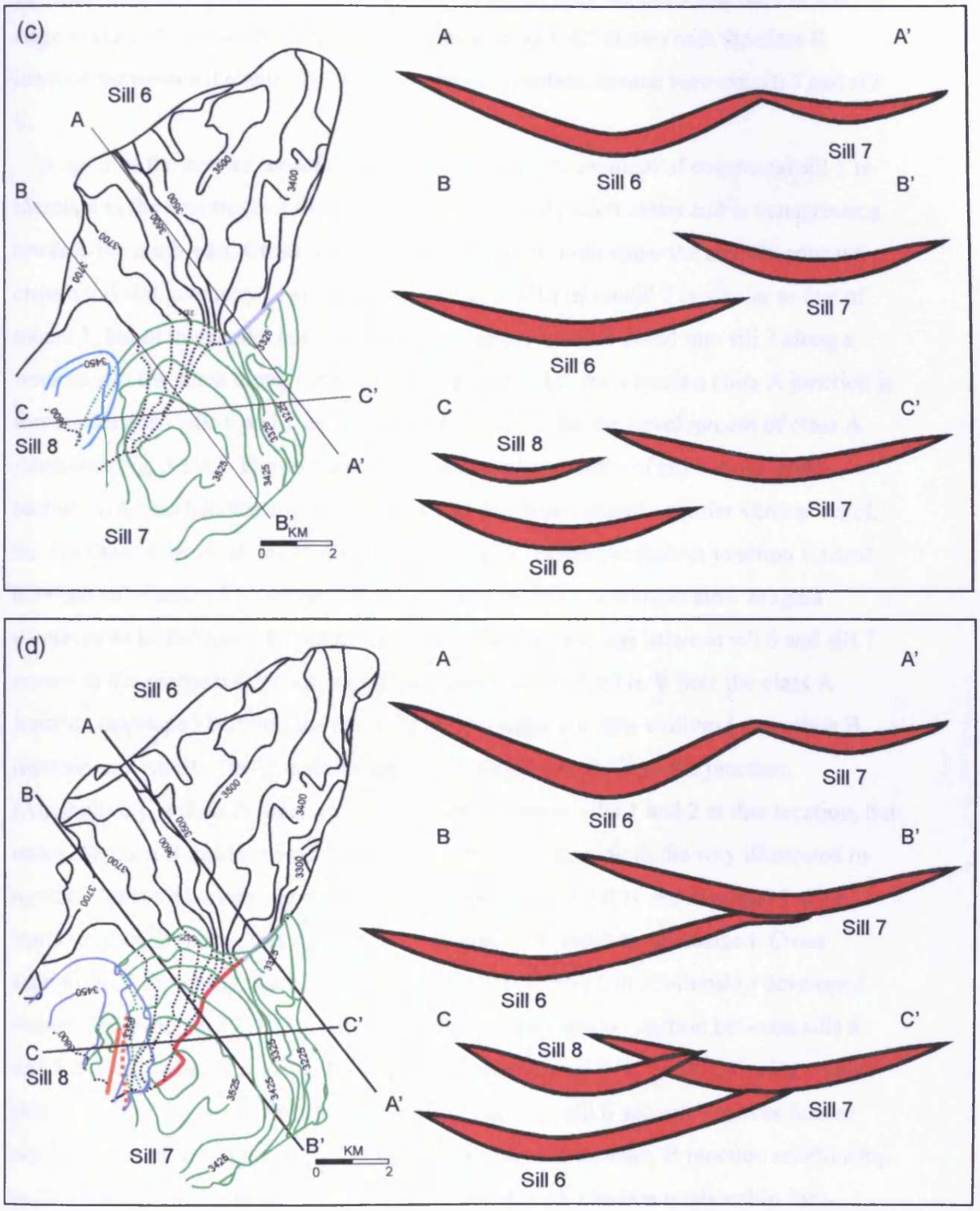

Fig. 3.54 (continued) Kinematic model 1 for the development of compound sill 1. (c) Stage 3. (d) Stage 4. (Sill 6: black contours, sill 7: green contours, sill 8: blue contours).

between sill 1 and sill 2. The class B junction formed between sill 6 and sill 7 at this stage is seen on cross-section B-B' and cross-section C-C' shows both the class B junction between sill 6 and sill 7 and the class C junction formed between sill 7 and sill 8.

Stage 1 of the ***second model*** (Fig. 3.55a) for the development of compound sill 1 is identical to the first stage of the first model where only sill 6 exists and is transgressing towards the north-east. Cross-sections A-A' and B-B' both show the slightly concave cross-sectional geometry of sill 6. *Stage 2* (Fig. 3.55b) of model 2 is similar to that of model 1, but in this model continued magma supply to sill 6 is fed into sill 7 along a weakness to the south along the eastern margin of sill 6. As a result a class A junction is formed between sills 6 and 7 as illustrated in model 3 for the development of class A junctions (Fig. 3.50c). The concave cross-sectional geometry of sill 6 along cross-section A-A' has become slightly broader and exhibits a slightly greater vertical relief, but has otherwise not changed. Cross-section B-B' shows the class A junction formed between sill 6 and sill 7. *Stage 3* (Fig. 3.55c) of model 2 is complicated. Magma continues to be fed into sill 7 from sill 6. The class A junction between sill 6 and sill 7 moves in the northern direction along the eastern edge of sill 6. Where the class A junction developed between the two sills during stage 2 it now evolves into a class B junction as a result of bi-directional spread of magma away from the junction. (Alternatively, a class A junction never existed between sills 1 and 2 at this location, but rather the class B junction was developed from the beginning in the way illustrated in model 2 for the development of class B junctions (Fig. 3.52b)). As in model 1 sill 8 starts to develop during this stage. Cross-section A-A' remains unchanged. Cross section B-B' has changed and now shows the class B junction relationship developed between sill 6 and sill 7. Cross-section C-C' shows a class B junction between sills 6 and 7 and the cross-sectional geometry of the separate sill 8 to the east. During *stage 4* (Fig. 3.52d) of the model the class A junction between sill 6 and sill 7 moves further north and the length of the line of junction along which the class B junction relationship is developed, expands to the north replacing the class A junction relationship fore-runner. Sill 8 continues to spread out and eventually cross-cuts the tip of sill 7 resulting in a class C junction relationship between the two sills (Fig. 3.53). The final cross-sections for model 2 are identical to those derived from stage 4 in model 1 and illustrate the geometrical junction relationships between the three sills seen on the seismic data.

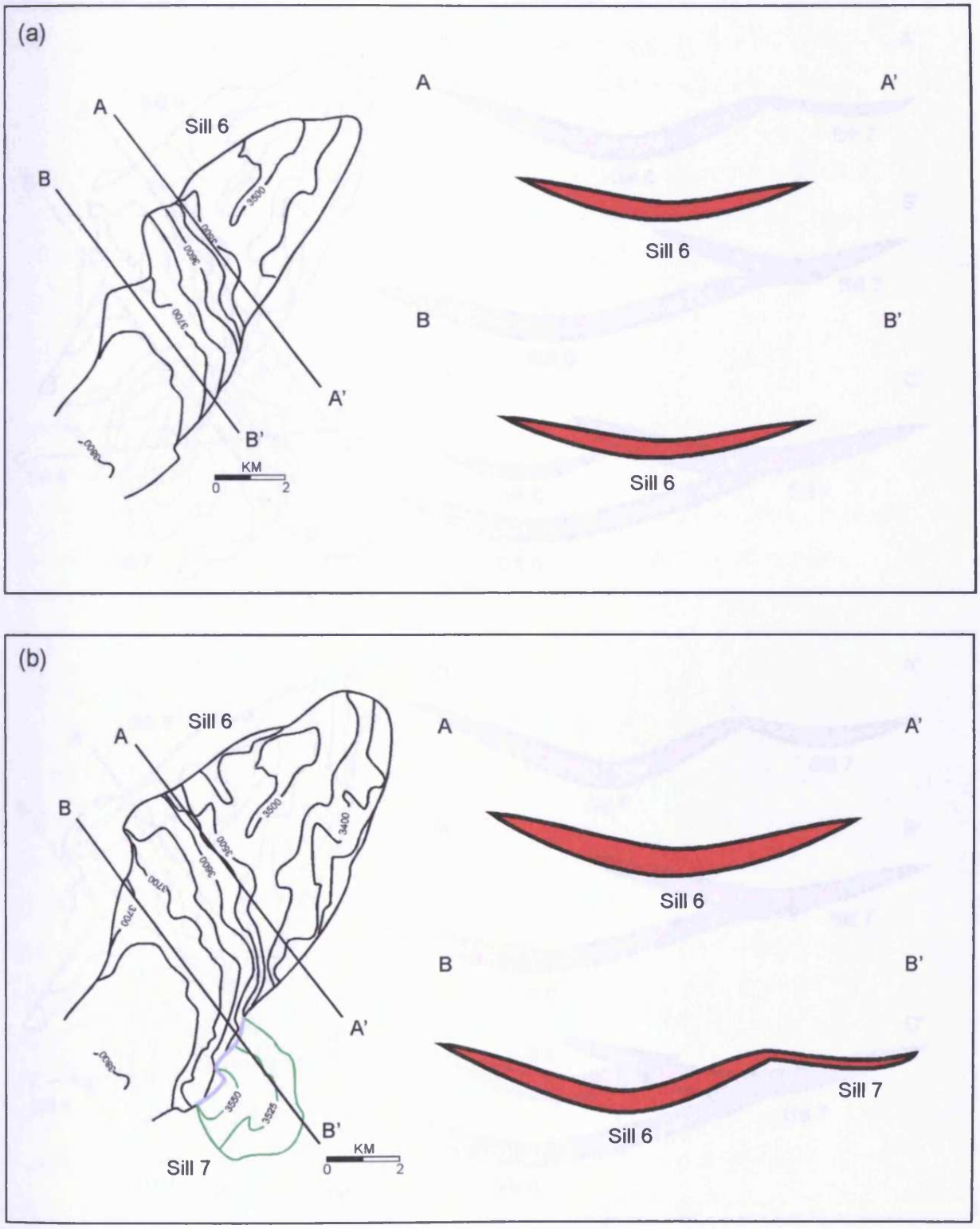

Fig. 3.55 Kinematic model 2 for the development of compound sill 1. The model comprises four stages and these are illustrated with contour maps and schematic cross-sections. (a) Stage 1. (b) Stage 2. (Sill 6: black contours, sill 7: green contours, sill 8: blue contours).

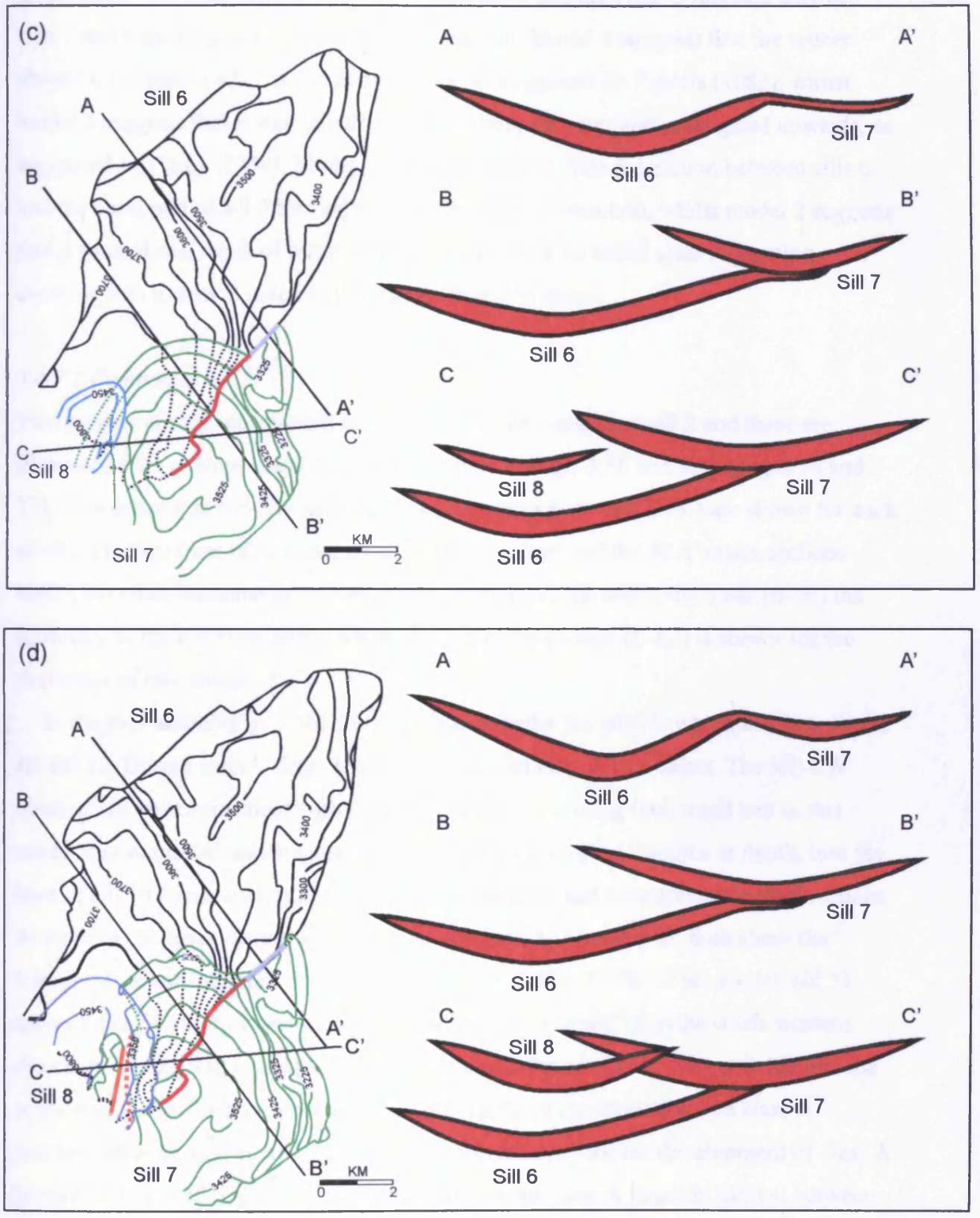

Fig. 3.55 (continued) Kinematic model 2 for the development of compound sill 1. (c) Stage 3. (d) Stage 4. (Sill 6: black contours, sill 7: green contours, sill 8: blue contours).

The proposed models both have implications for the mechanics of sill emplacement. Both models show sill 6 acting as a feeder for sill 7 and the class C junction between sills 7 and 8 forming as a result of sill intersection. Model 1 suggests that the saucer-shaped main part of sill 7 is fed peripherally, as suggested by Francis (1982), whilst model 2 suggests that it was initially fed at its deepest point and propagated upwards, as suggested by Carey (1958). Model 1 suggests that the class B junction between sills 6 and the basal part of sill 7 formed as a result of sill intersection, whilst model 2 suggests that it formed as a result of bifurcation, possibly, with an initial class A junction evolving into a class B junction through time and in space.

3.4.7.2 Compound sill 2

Two models are also considered for the build-up of compound sill 2 and these are illustrated with contour maps and cross-sections in Figs. 3.56 and 3.57 (pages 76 and 77). Two schematic NE-SW striking cross-sections (A-A' and B-B') are shown for each model. The two lines of junction are almost coincident and the A-A' cross-sections shows the cross-sectional geometry of the junctions to the north, the other (B-B') the geometry of the junctions to the south. A third cross-section (C-C') is shown for the first stage of the models.

In the ***first model*** (Fig. 3.56) sill 10 acts as a feeder for sill 11, which acts as a feeder for sill 12. During *stage 1* (Fig. 3.56a) of the model only sill 10 exists. The NE-SW trend of sill 10 is coincident with the strike of the underlying fault trend and in this model it is suggested that magma is fed along the fault, from a source at depth, into the base of sill 10 (cross-section C-C'). Sill 10 propagates and transgresses in all directions away from the basal, central feeder. Cross-sections A-A' and B-B' both show the transgressive north-eastern tip of sill 10. In *stage 2* (Fig. 3.56b) of the model, sill 11 spreads away from the north-eastern transgressive tip of sill 10 in the south-western direction. During this initial phase in the development of sill 11, magma is fed into the near-basal, central part of the final sill. This results in the formation of a class A junction between sills 10 and 11 as described in model 3 for the development of class A junctions (Fig. 3.50c). Cross-section A-A' shows the class A junction formed between the tips of sills 10 and 11. Sills 10 and 11 are both seen on the B-B' cross-section, but they are not linked. They are seen as separate bodies, with sill 11 overlying sill 10. During *stage 3* (Fig. 3.56c) of this model, sill 11 spreads further and turns transgressive. Sill 11 transgresses slightly along its north-eastern boundary across the tip of the

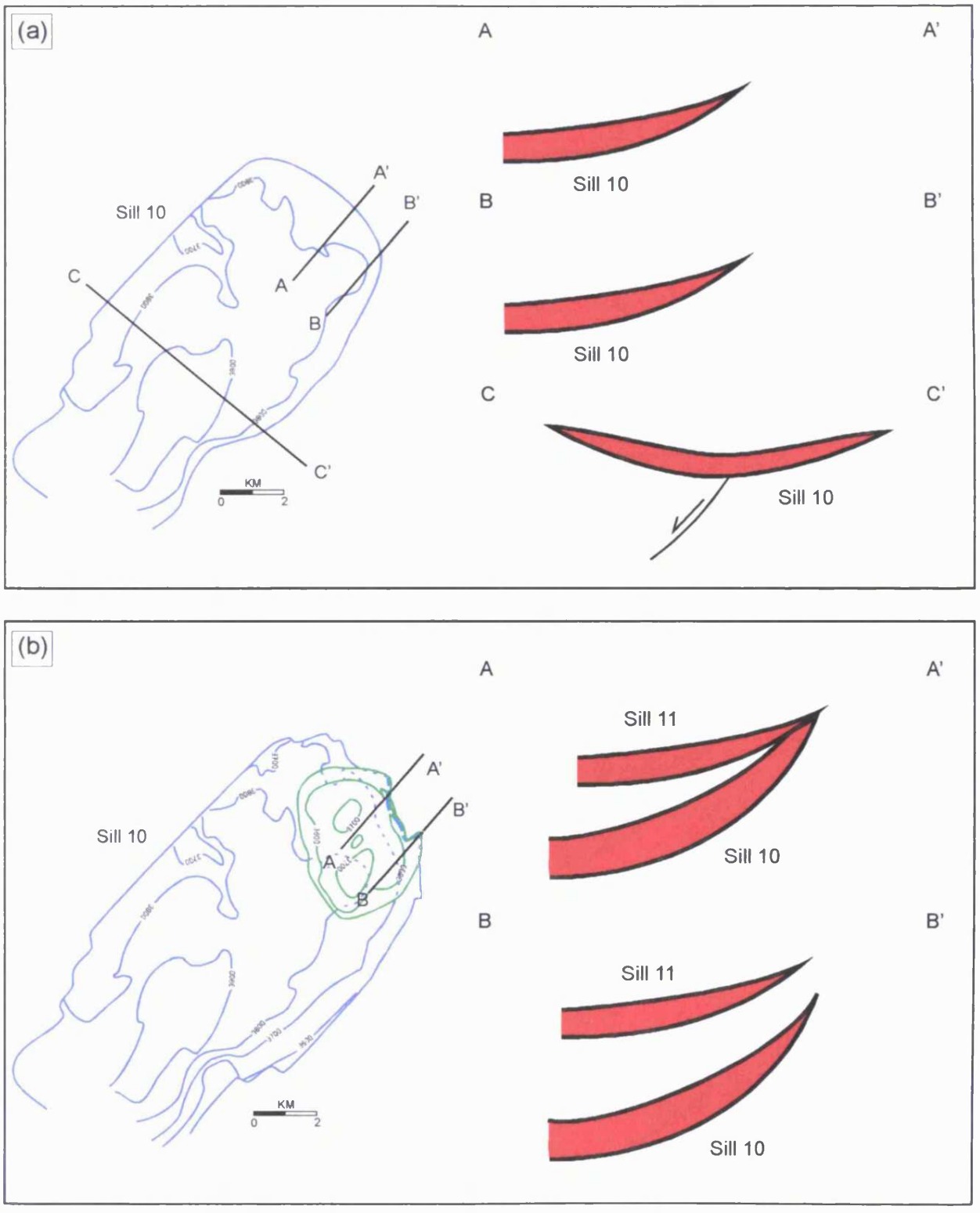

Fig. 3.56 Kinematic model 1 for the development of compound sill 2. The model comprises four stages and these are illustrated with contour maps and schematic cross-sections. (a) Stage 1. (b) Stage 2. (Sill 10: blue contours, sill 11: green contours, sill 12: yellow contours).

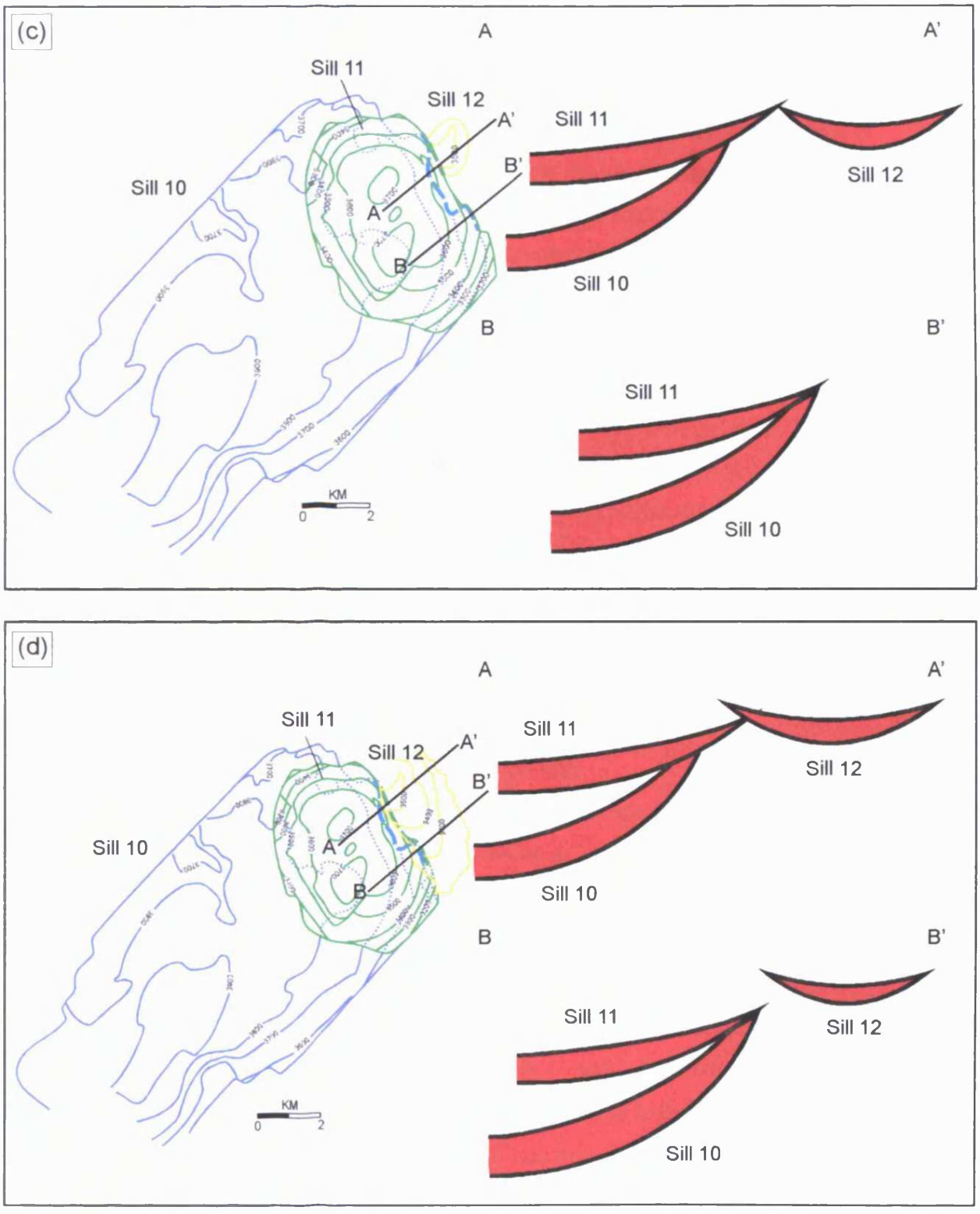

Fig. 3.56 (continued) Kinematic model 1 for the development of compound sill 2. (a) Stage 3. (b) Stage 4. Thick dashed blue and green lines indicate lines of junction. (Sill 10: blue contours, sill 11: green contours, sill 12: yellow contours).

underlying sill 10. As a result the class A junction developed between sill 10 and 11 during stage 2 evolves into a class B junction. During stages 2 and 3 sill 10 has only transgressed slightly along its north-eastern margin. As sill 11 transgresses to the north-east sills 10 and 11 intersect, north and south of the initial line of junction and a class A junction forms between them in the way described for model 1 for the development of class A junctions (Fig. 3.50a). Sill 12 starts to develop during this third stage of the model. It spreads out from the edge of sill 11 along a short segment of the final line of junction between the two sills. This leads to the development of a class A junction between sills 11 and 12 as described in model 3 for the development of class A junctions (Fig. 3.50c). At this stage cross-section A-A' shows a class B junction between sills 10 and 11 and a class A junction between sills 11 and 12, whilst cross-section B-B' shows a class A junction between sills 10 and 11. During *stage 4* (Fig. 3.56d) of this model sill 12 spreads and transgresses to the south-east. As it transgresses it locally slightly overshoots the tip of sill 11, forming class B junctions (model 1 for the development of class B junctions; Fig. 3.52a), and elsewhere intersects the tip of sill 11 giving rise to a class A junction relationship between the two (model 1 for the development of class A junctions; Fig. 3.50a). The final A-A' cross-section shows class B junctions between both sills 10 and 11 and sills 11 and 12. Cross-section B-B' still shows a class A junction between sills 10 and 11. Sill 12 is also seen on the cross-section, but is shallower and separate from the other sills.

The ***second model*** (Fig. 3.57) for the development of compound sill 2 only involves three stages of which *stage 1* (Fig. 3.57a) is the same as in the first model. During *stage 2* (Fig. 3.57b) in the second model both sills 11 and 12 start to develop and both are fed by sill 10. Sill 11 propagates away from sill 10 along a relatively long segment, whilst the initial spread of sill 12 is limited to the northern part of the final line of junction between sills 11 and 12. As a result a complex triple junction kinematically comprised of class A junctions between sills 10 and 11 and sills 10 and 12 is developed along the most northern part of the lines of junction. A class A junction is developed between sills 10 and 11 along the full length of the final line of junction. The class A junctions are both formed in the way described in model 3 for the development of class A junctions (Fig. 3.50c). Cross-section A-A' shows a class A junction between sills 10 and 11 and the cross-sectional geometry of sill 12, which is separated from sills 10 and 11 (the complex triple junction mentioned above is located to the north of section A-A'). The southern cross-section B-B' shows the more simple class A junction between sills 10

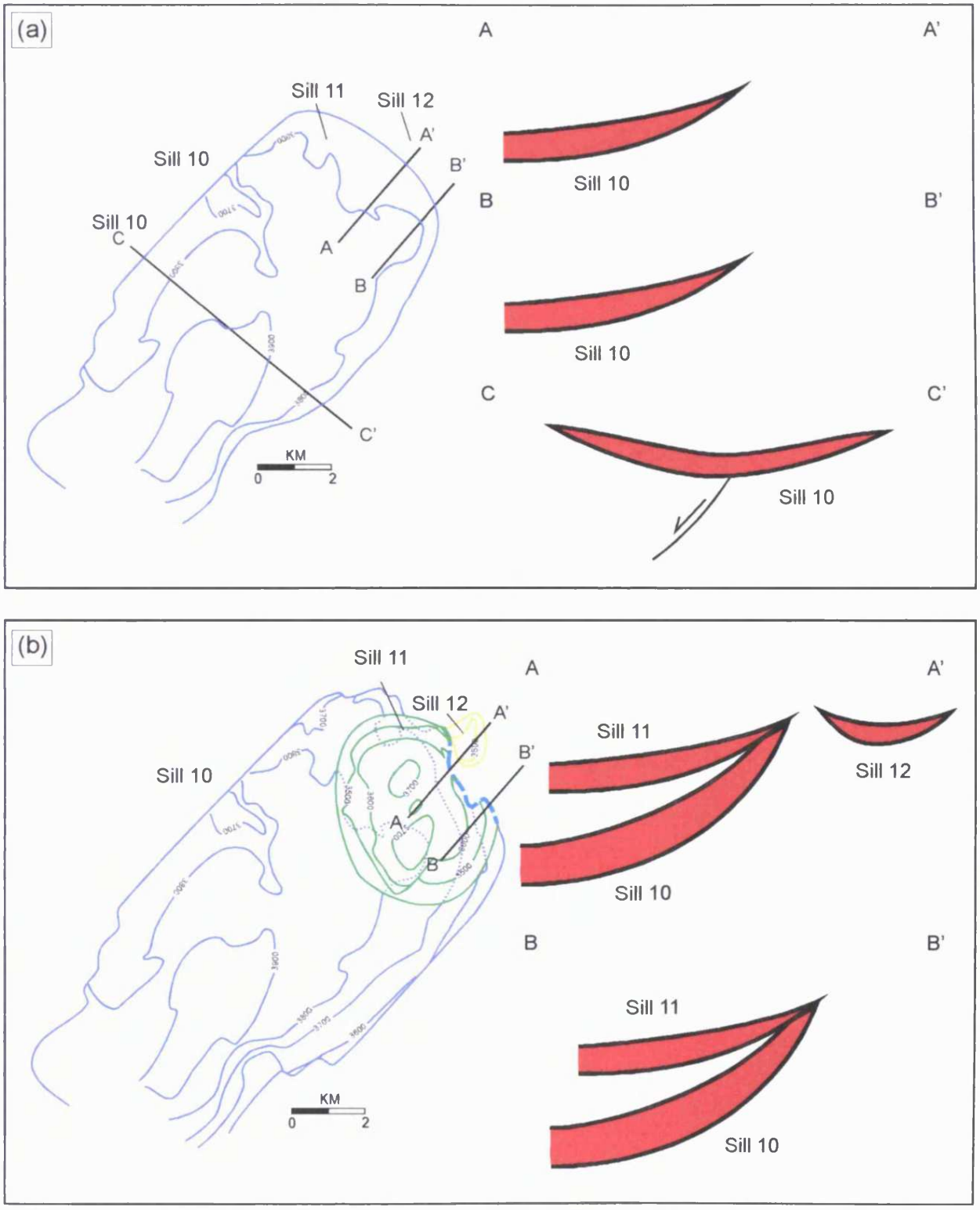

Fig. 3.57 Kinematic model 2 for the development of compound sill 2. The model comprises three stages and these are illustrated with contour maps and schematic cross-sections. (a) Stage 1. (b) Stage 2. Thick dashed blue and green lines indicate lines of junction. (Sill 10: blue contours, sill 11: green contours, sill 12: yellow contours).

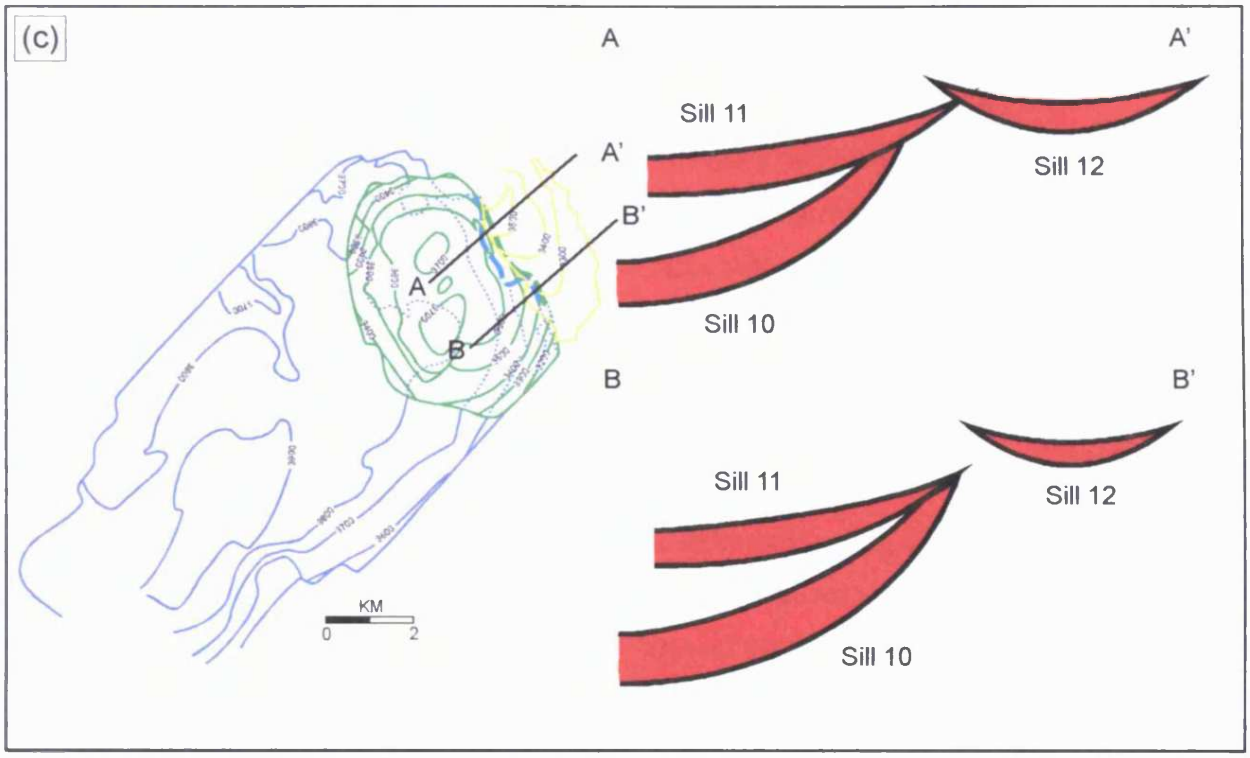

Fig. 3.57 (Continued) Kinematic model 2 for the development of compound sill 2. (a) Stage 1. (b) Stage 2. Thick dashed blue and green lines indicate lines of junction. (Sill 10: blue contours, sill 11: green contours, sill 12: yellow contours).

and 11. During the final *stage 3* (Fig. 3.57c) of this second model for the development of compound sill 2, sills 11 transgresses in all directions, locally overshooting the line of junction formed between sill 10 and 11 during stage 2, forming local class B junctions (model 1 for the development of class B junctions; Fig. 3.52a). Sill 12 transgresses towards the south-east during this stage, locally slightly overshooting the edge of sill 11 and forming local class B junctions (model 1 for the development of class B junctions; Fig. 3.52a). The final cross-sections show the same geometry as those from model 1 and reflect the geometry observed on the seismic data.

Sills 11 and 12 both have asymmetrical NE-SW concave cross-sectional geometries. For both sills the limb opposite the junction has transgressed to a shallower level than the one nearest to the junctions. Along most of the line of junction between the two sills, sill 12 overlies sill 11 and blockage of the transgressive tip of sill 11 by sill 12 could possibly explain the observed asymmetry of this sill. However, this does not explain why sill 12 has only propagated slightly beyond the line of junction in the western direction. The line of junction between sills 11 and 12 is almost perfectly coincident with the north-eastern boundary of the underlying sill 10. An elongated seismic chimney is seen extending upwards from the triple junction between sills 10, 11, and 12 towards the north (Fig. 3.58). It can be traced to the level of horizon B, which is clearly distorted by the chimney, but it does not appear to influence horizon C. The chimney is clearly linked to the intrusions and it is likely to be either a dyke or a hydrothermal chimney. Regardless of whether it is one or the other it could constitute a barrier and this barrier may have inhibited magma flow and thus the fuller lateral spreading of the sills.

The two models for the development of compound sill 2 share some of the implications for the general mechanics of sill emplacement as the models proposed for the development of compound sill 1. Like the models for compound sill 1, the two models proposed for compound sill 2 imply that sills can act as feeders for other sills (e.g. sill 10 acts as a feeder for sill 11). Both models also suggest that the saucer-shaped sill 11 was fed near its base as it was suggested for sill 7 in model 2 for the development of compound sill 1. In addition model 1 suggests that class A junctions can evolve into class B junctions through time and in space along the line of junction. Model 2 suggests that the class B junction geometry seen between sills 11 and 12 formed partly through sill bifurcation and partly through sill intersection.

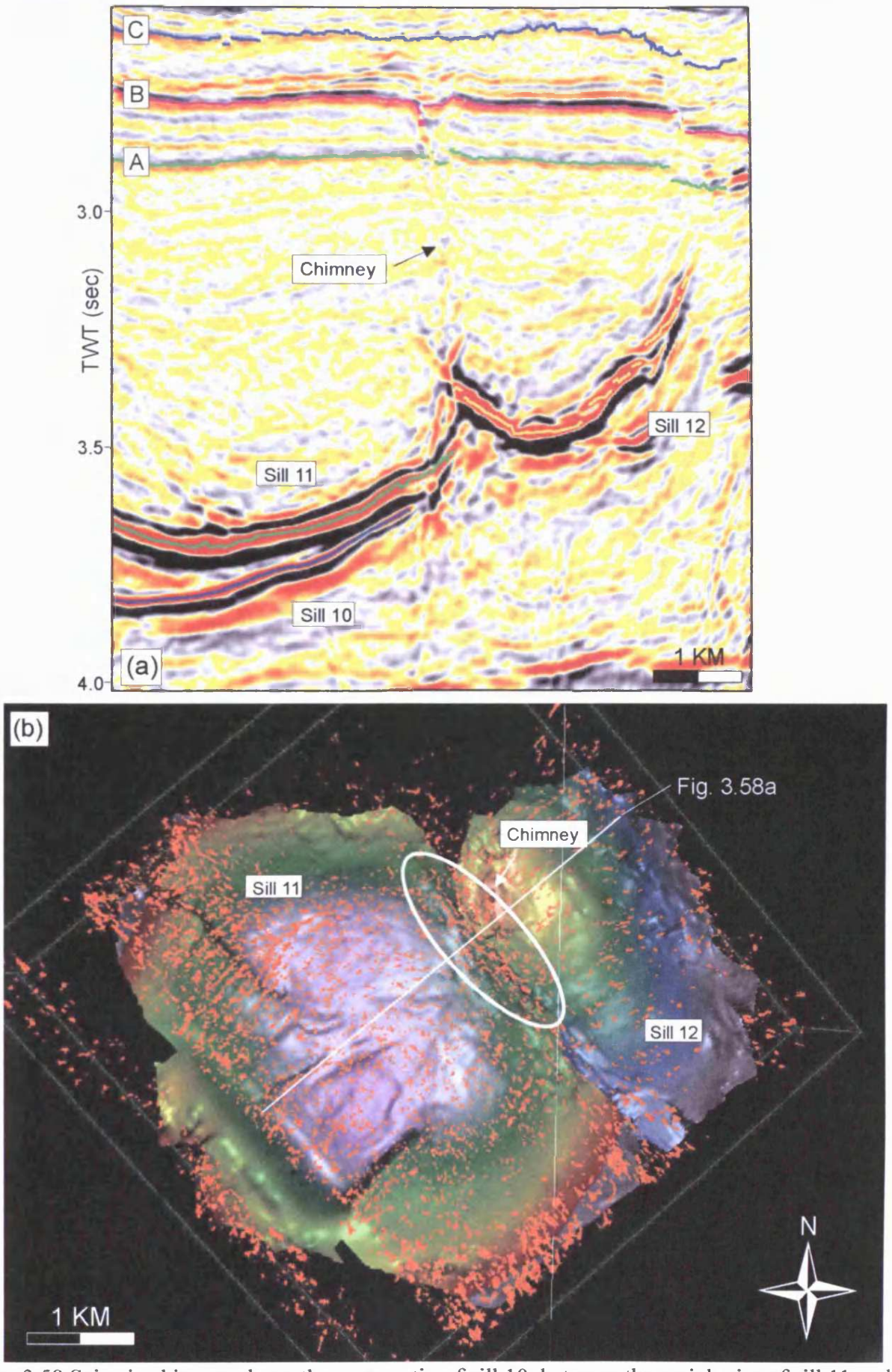

Fig. 3.58 Seismic chimney above the eastern tip of sill 10, between the peripheries of sill 11 and sill 12. (a) Seismic cross-section showing the vertical appearance of the seismic chimney that rises from the junction between sills 11 and 12. (b) 3D display showing sills 11 and 12 and opacity rendered variance cube of a 2952-3400 ms time-window. The display shows that the

3.4.7.3 Synthesis

Each of the above presented models could explain the development of compound sills 1 and 2, however, 'model 2' are in both cases considered to be more likely than 'model 1'. In the case of compound sill 1 the preference of model 2 over model 1 is based on a general observation made throughout this study, that saucer-shaped sills are fed in their basal region and propagate outwards and upwards rather than being fed peripherally and propagating downwards, as proposed by Francis (1982; see Chapter 7). Model 2 is also preferred in the case of compound sill 2 and this is based on the geometry of sill 11 and its line of junction with sill 10. The full line of junction between the two sills is almost perfectly coincident with their 3600 ms contour lines and it is considered most likely that such a horizontal line of junction would develop if it represents the original feeder between sill 10 and 11 as suggested in model 2 as oppose to having formed partly as a feeder and partly as a result of coincidental intersection between sills 10 and 11 along the southern part of the line of junction.

3.4.8 Spatial and temporal changes along lines of junction

It is commonly observed that there is a change from a class A junction into a class B junction along the line of junction between two neighbouring sills (e.g. Fig. 3.37). There are several ways in which the change from a class A junction to a class B junction along a line of junction can be explained. Such a change in junction geometry could, for example, occur along sections of the line of junction where bi-directional magma propagation away from the feeder (transgressive sill tip) as illustrated in Fig. 3.52b was locally obstructed and the magma, as a result, only propagated away from the feeder in one direction (Fig. 3.50c). Alternatively, sill branching and splitting (Fig. 3.52c) may only occur locally along a line of junction, in areas where pre-existing heterogeneities such as faults are present. It is also possible that sill branching might even be induced by local stress perturbations in the region around the line of junction that are associated with sill propagation.

The above reconstructions of both compound sill 1 (model 2) and compound sill 2 (models 1 and 2) suggests that a class A junction can evolve into a class B junction through time. The present-day junction geometry along a line of junction is a record of the geometry at the time when the propagation of the sill was arrested and thus reflects the evolutionary stage at that particular time. Had the sill propagation not been arrested the recorded junction geometries might have changed and the geometry along segments

showing a class A junction, such as the northern part of the line of junction between sills 6 and 7 (compound sill 1), might have evolved into a class B junction.

It is kinematically feasible that a class B junction can evolve in space to a class C junction. Although this mode of junction development has not been observed in the study area, it might occur if local weaknesses along a line of junction allow an otherwise blocked sill (class B junction; Fig. 3.52a) to penetrate and breach the blocking sill (class C junction; Fig. 3.53). This could occur either when the two sills first intersect or later when a certain pressure had been allowed to build up in the tip of the, eventually, penetrating sill.

3.4.9 The development of internal junctions

From the above sections it is evident that sills may feed other sills and that the geometries of individual intrusions change markedly through the full period of intrusion of compound sills. The interpreted internal bifurcations within sills 10 and 11 (Section 4.4.5) resemble class B junctions and are purely distinguished from these because they occur within circular or elongated saucers. However, if these complex saucers had been left to propagate further the internal bifurcations might have evolved into genuine junctions between the original sills (e.g. sills 10 and 11) and new sills formed by the splay segments. The resultant intrusions would then be classified as compound sills. The near-horizontal splay segments (tips A and B) seen beyond the junctions along the transgressive segment of sill 10 (Fig. 3.48) might have developed further if the sill had been fed more magma. This would have given the intrusion a layered geometry with three near-horizontal layers linked by transgressive segments. Such a geometry is known from sill complexes in the Karoo, South Africa (du Toit, 1920; Lombard, 1952; Fig. 1.9). The internal geometry within sill 11 could simply be an early stage in the evolution of a class B junction as illustrated in model 2 for the development of class B junctions (Fig. 3.52b). If the development of the splay segment (segment 2) had not been arrested, the overhang might have developed into a separate sill, which would be interlinked with segment 1 by a true class B junction.

3.4.10 Summary

The detailed interpretation and analysis of sill junction relationships presented in this chapter have provided much new insight into the three-dimensional geometry and development of igneous sill complexes. Three classes of sill junctions have been

defined and a number of kinematic models for each of these have been proposed. This has allowed for the three-dimensional development of a number of compound sills to be reconstructed. This has not previously been possible due to lack of three-dimensional insight available at outcrop and it has lead to a major discovery:

The kinematic models and the reconstruction provide strong evidence to suggest that sills act as feeders for other sills and that compound sills and sill complexes build up from deeper to shallower stratigraphic levels through a succession of sill-fed emplacement events.

3.5 Host-rock deformation above sills

A clear spatial relationship between the distribution of some sills and deformation of the overlying strata is seen in the T67 survey area. Towards the east and west on the section shown in Fig. 3.11b, horizons A, B, and C are clearly elevated relative to the central part of the section. The magnitude of the elevation is greatest at the level of horizon A and decreases upwards with horizon D and E showing only very limited relief as a result. The elevated areas coincide exactly with the lateral extent of some of the underlying sills.

A similar relationship between sills and their host-rock is exceptionally well imaged in the T38 survey area (Chapter 5) and the mechanics and implications of this type of sill emplacement-related deformation are discussed in detail in Chapters 5 and 7.

Here, two examples of local upward vertical host-rock displacement above sills are described. The first example shows elevation of horizons A, B, and C above two concave shaped sills (sills 11 and 12; Group A) in the eastern corner of the survey area (Fig. 3.59). The elevated area forms a well-defined broad fold and the limbs of this fold are clearly coincident with the extent of the two underlying sills 11 and 12 on the vertical section (Fig. 3.59a). A maximum elevation of 165 m has been measured across the western limb at the level of horizon A. The outlines of Sills 11 and 12 have been superimposed on a time-structure map of horizon B in Fig. 3.59b. The map shows good spatial coincidence between the extent of the sills and the elevated area particularly towards the south-eastern survey boundary where the 4125 m contour is almost perfectly coincident with the sill boundaries.

The second example (Fig. 3.60) is also from the eastern part of the survey area. sill 5 (Group B) is intruded along horizon A and has been classed as a complex circular

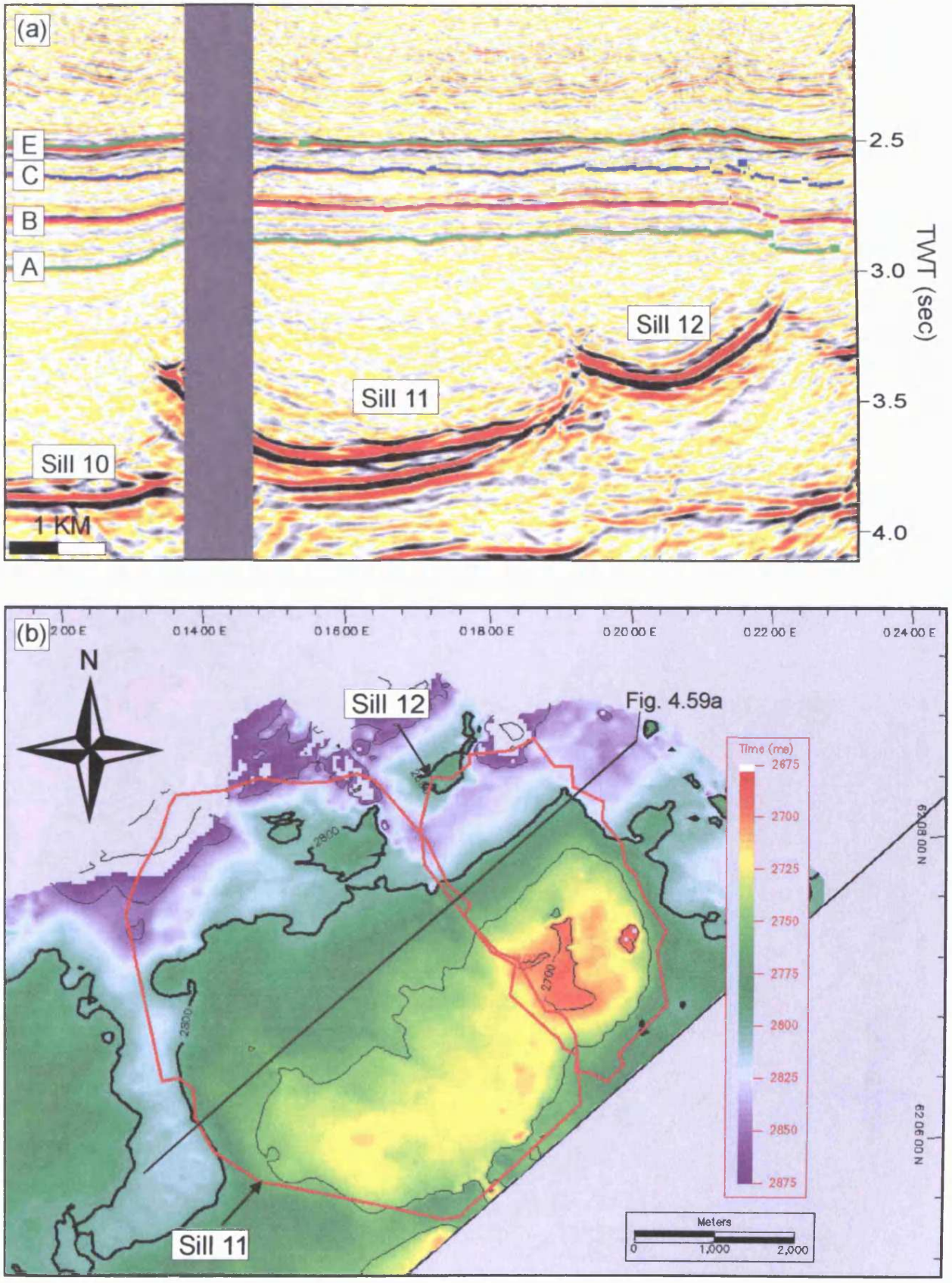

Fig. 3.59 Host-rock deformation above sills 11 and 12. (a) Vertical seismic section showing vertical upward displacement of horizons A-C above sills 11 and 12. (b) The outlines of sill 11 and 12 superimposed upon a time-structure map of horizon B (Fig. 3.13). The outlines are coincident with an elevated area on the map, particularly towards the south-east where the outlines are almost perfectly coincident with the 2750 ms contour line.

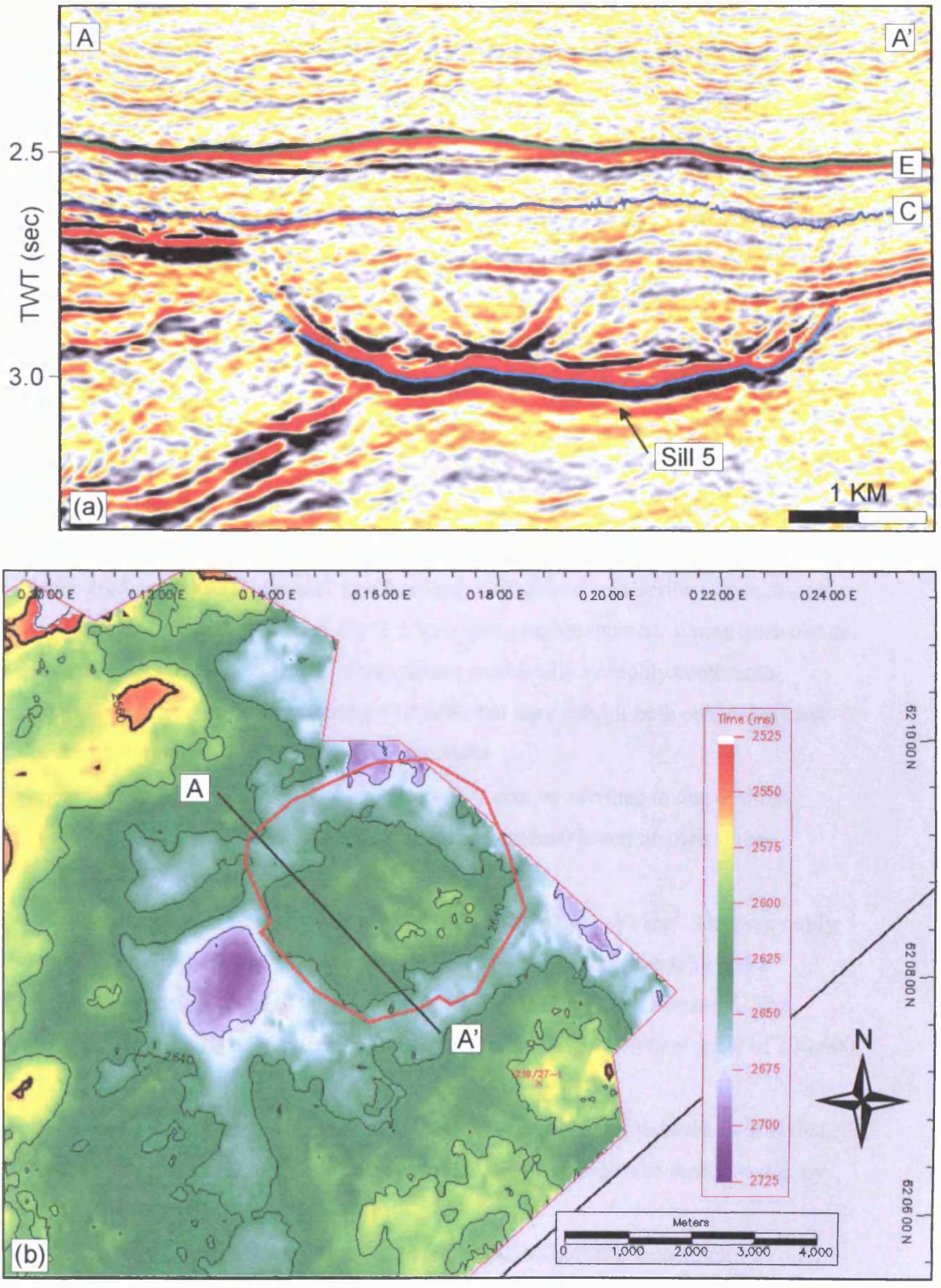

Fig. 3.60 Host-rock deformation above sill 5. (a) Vertical seismic section showing vertical upward displacement of horizons C and E above sill 5. (b) The outline of sill 5 superimposed upon a time-structure amp of horizon C (Fig. 3.14). The outline is clearly coincident with a circular elevated area on the map.

saucers. Horizon C is elevated 90 m above sill 5 and by superimposing the outline of sill 5 on the time-structure map of horizon C it is evident that the extent of the sill and the elevated area are coincident (Fig. 3.60b).

3.6 Conclusions

This case-study has focused on two major themes: (1) the geometry of igneous sills and (2) the role of sill-sill junction relationships in the development of compound sills and sill complexes. The major findings related to these two themes are summarised below. The order of conclusions is thematically ordered rather than ranked according to significance.

The geometry of igneous sills:

- The traditional definition of a sill as a intrusive igneous body with concordant surfaces of contact has been found inadequate to describe the sills mapped in this case-study area and in general. The term ***sill*** is here used to describe any continuous igneous body spanning a limited (<1.5 km) stratigraphic interval. It may have one or more feeders. Sills are generally recognised seismically as highly continuous, smooth, and very high amplitude reflections that may exhibit both concordant and discordant relationships with stratal reflections
- Igneous sills in the survey area, and in general, can be ascribed to one of three different sill classes (saucers, sheets, and sill segments) based on their three-dimensional geometry
- The sills in the survey area range in size from a few km^2 to 80 km^2. They are rarely fully concordant with stratigraphy but generally cross-cut stratigraphy and a maximum vertical relief of approximately 900 metres has been measured. The majority of the sills have intermediate sizes (10-30 km^2 and vertical relief of 300-600 m)
- A sill complex is here used to refer to a highly interconnected network of sills that may develop through a succession of repeated intrusive events to form a vertically extensive system of interlinked sills
- Within the sill complex there is moderate correlation between maximum emplacement depth and vertical relief, but only poor correlation between sill area and maximum emplacement depth and between sill area and vertical relief

- Many of the sills intruded at intermediate depth (Group B) are intruded along bedding planes (horizons A and B)
- A number of sills have been seen to cause upwards vertical displacement of the overburden. This will be further discussed in Chapters 5 and 7

The role of sill-sill junction relationships in the development compound sills and sill complexes:

- Sills act as feeders for other sills and compound sills and sill complexes build-up vertically as well as laterally through a succession of sill-fed emplacement events from deeper to shallower levels
- Individual sills and compound sills are interlinked and separated by sill junctions and three distinctively different classes of sill junction geometries have been classified. These different sill junctions invoke different emplacement kinematics
- The junction relationship between two sills may change in space and through time

CHAPTER 4: THE IGNEOUS COMPLEX OF THE SOLSIKKE SURVEY AREA (NORTH-EASTERN MØRE BASIN)

4.1 Introduction

4.1.1 Aims of chapter

This chapter aims at describing the three-dimensional geometry and context of an intrusive igneous complex interpreted on the Solsikke 3D seismic dataset from the north-eastern Møre Basin (Fig. 4.1). In the Solsikke survey area high amplitude reflections interpreted as igneous sills form a vertically extensive sill complex within the Cretaceous and Paleogene sediments. This chapter provides a three-dimensional interpretation of the Solsikke igneous complex. The main emphasis has been placed on a detailed interpretation of a particularly well imaged sill, the Solsikke Sill. The Solsikke Sill exhibits an intriguing morphology, expressed partly in the form of a complex lobate bifurcating system of sill segments (the Solsikke lobe system). Models for the emplacement and kinematic development of the Solsikke Sill and the Solsikke sill lobe system are discussed in detail in this chapter.

Following an introduction to the database (section 4.1.2) and the geological setting of the case study area (sections 4.2 and 4.3) the main part of this chapter is sub-divided into three main sections: the Solsikke sill complex (section 4.4), the Solsikke Sill (section 4.5), and the Solsikke sill lobe system (section 4.6). Each of these sections comprises a discussion and the main points of these are summarised in section 4.7. Finally, the conclusions of the interpretation of the Solsikke case study are listed in section 4.8.

4.1.2 Database

4.1.2.1 3D seismic data

The Solsikke 3D seismic survey covers an area of approximately 1050 km^2 and has an inline (NW-SE) and crossline (NE-SW) spacing of 25 m (Fig. 4.2). Two different seismic volumes have been provided by the operator for research purposes. The first volume is limited to data in the TWT range 0-3700 ms, while the second volume includes data to a maximum TWT value of > 8000 ms. The first volume shows slightly higher resolution than the second volume and has been used to interpret the details of the Solsikke Sill, the Solsikke sill lobe system (this chapter), and extrusive mound structures (Chapter 6). The second volume shows the full vertical extent of the Solsikke

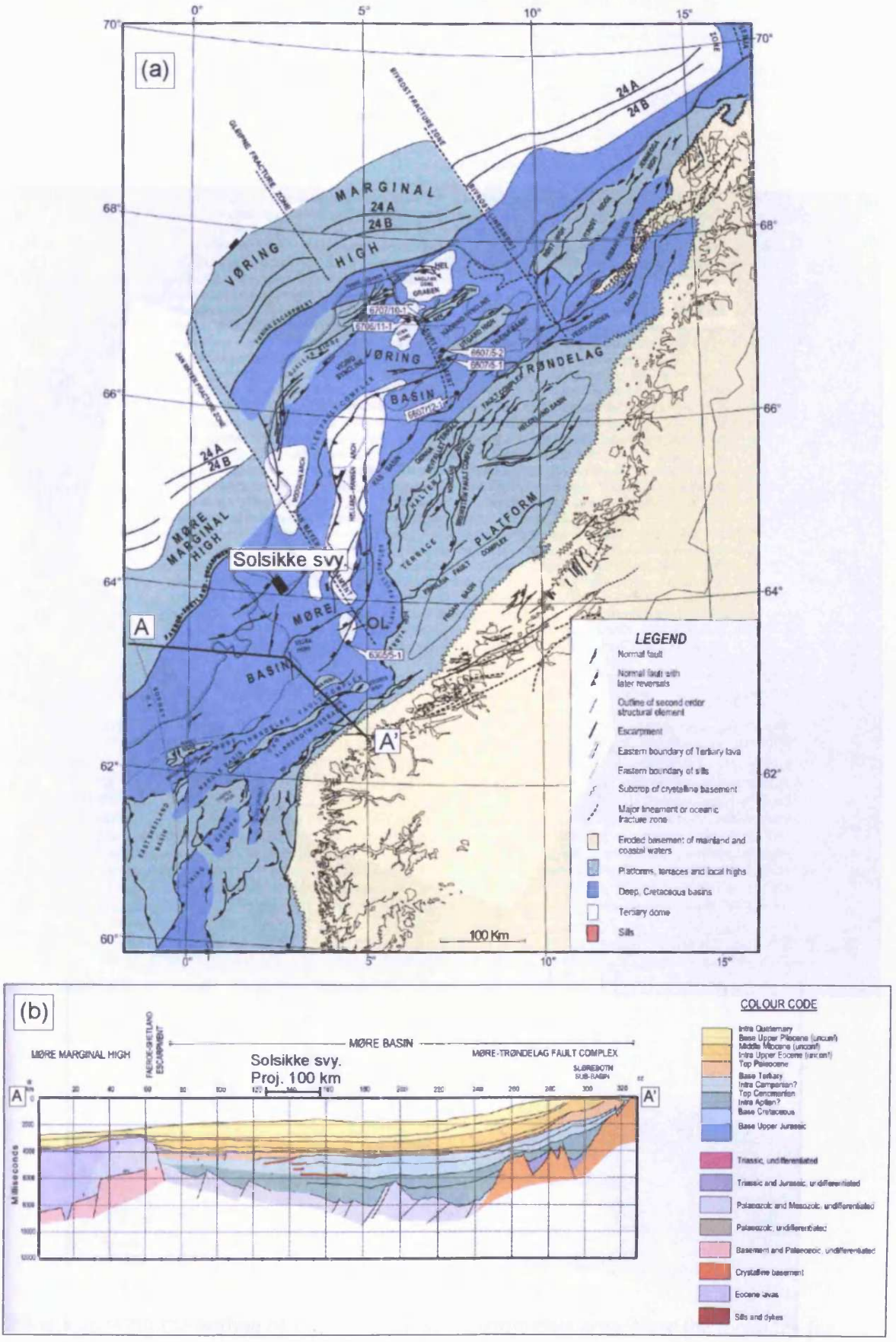

Fig. 4.1 (a) Map showing the location of the Solsikke survey within the north-eastern part of the Moere Basin on the Norwegian continental margin. From Brekke (2000). (b) Geoseismic section of the Moere Basin. The location of the Solsikke survey area (located 100 km to the north of the line) has been projected onto the line. From Brekke et al. (1999).

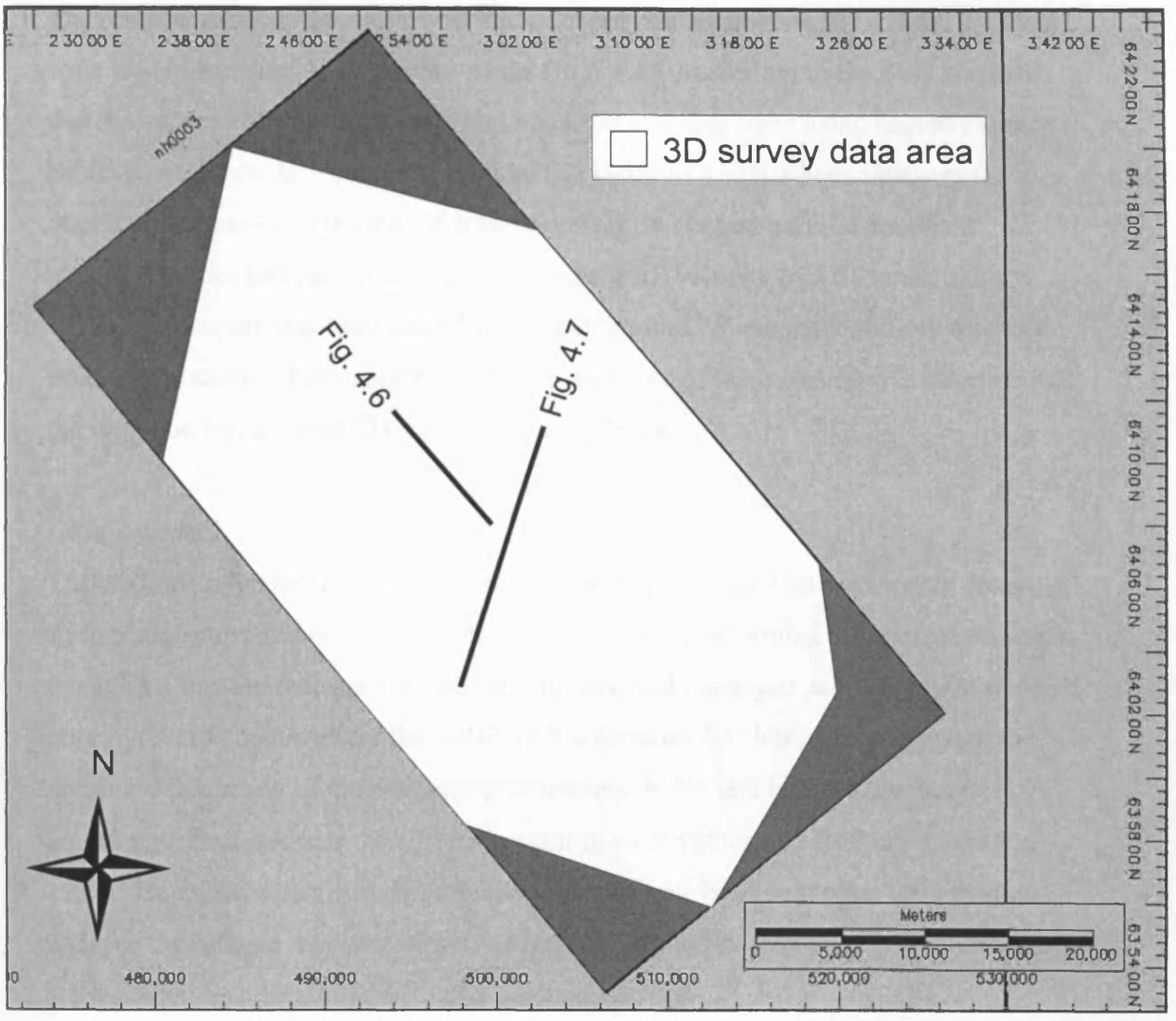

Fig. 4.2 Map showing the outline of the Solsikke 3D seismic data area. Note the locations for Figs. 4.6 and 4.7.

sill complex, which is not imaged by the first volume, and it has been used to interpret the geometry of the Solsikke igneous complex (this chapter).

Data volume 1

The seafloor reflector (positive acoustic boundary) is imaged on the seismic data as a wide trough surrounded by narrow peaks (Fig. 4.4). According to the SEG standards this means that the data are zero-phase migrated and displayed using negative standard polarity. At the depth where the Solsikke Sill (section 4.5) has been interpreted the dominant frequency of the data is approximately 38 Hz and half the dominant wavelength thus just less than 75 m (assuming a sill velocity of 5.55 km/s; Skogly, 1998). This means that intrusions thinner than around 75 m cannot be fully resolved because the seismic responses from the top and base of the intrusion will interfere and the intrusion be represented by a composite reflection.

Data volume 2

The seafloor reflector (positive acoustic boundary) is imaged on the seismic data as a wide trough surrounded by narrower peaks (Fig. 4.3). According to the SEG standards this means that the data are zero-phase migrated and displayed using negative standard polarity. At the depth where the Solsikke Sill (section 4.5) has been interpreted the dominant frequency of the data is approximately 40 Hz and half the dominant wavelength thus just less than 70 m (assuming a sill velocity of 5.55 km/s; Skogly, 1998). This means that intrusions thinner than around 70 m cannot be fully resolved because the seismic responses from the top and base of the intrusion will interfere and the intrusion be represented by a composite reflection.

The Solsikke igneous sill complex is layered and spans a wide vertical interval. The quality and resolution of the seismic data is reduced underlying the shallowly emplaced sills, as shown in Fig. 2.1.

4.1.2.2 Well data

Exploration well 6403/10-1 was drilled in the survey area in 2002 in a water depth of 1712 m. The well has been available to the study, but permission to use it in this thesis has not been obtained. However, the Base Tertiary pick (horizon B, section 4.2.2) has been released. The well achieved a total depth of 3400 m (~3950 ms) and reached its TD in Upper Cretaceous sediments. Many of the sills mapped in the survey area

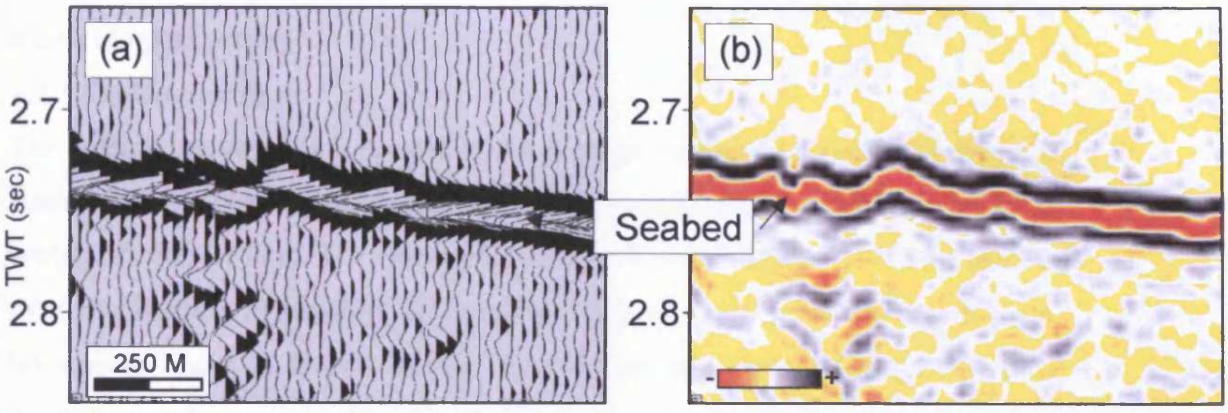

Fig. 4.3 Dataset 1 seabed reflection. (a) Variable area (VA) display. (b) Variable intensity (VI) display.

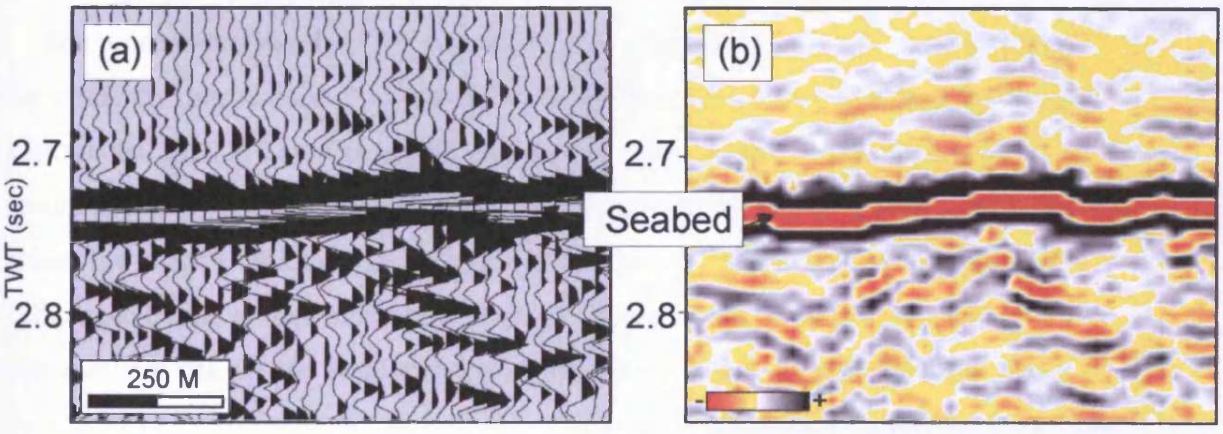

Fig. 4.4 Dataset 2 seabed reflection. (a) Variable area (VA) display. (b) Variable intensity (VI) display.

(section 4.4) are intruded into Upper Cretaceous sediments of the Shetland Group that is dominated by claystones with minor amounts of carbonates and sandstones (Dalland et al., 1988).

4.2 Geological setting

4.2.1 Regional setting

The Solsikke survey area is located in the northern part of the NE-SW trending Møre Basin (Fig. 4.1a) on the Norwegian continental margin in a present-day deep-water setting of 1600-2150 m. The Norwegian Margin is dominated by a NE-SW structural trend that is offset by two NW-SE trending lineaments, the Jan-Mayen and Bivrost lineaments (Fig. 4.1a; Brekke, 2000). These lineaments divide the margin into three main structural provinces. The most southern of these, delineated to the north-east by the Jan-Mayen lineament, comprises the Møre Basin. The overall NE-SW trend on the margin is constituted by faults and basin axes that probably originated in the Paleozoic and subsequently became re-activated during later tectonic phases (Brekke, 2000; Dore et al., 1999). The transverse NW-SE trending lineaments are thought to reflect the Precambrian grain of the basement (Brekke, 2000; Dore et al., 1999). Much of the structural development of the Norwegian Margin is thus closely linked to the basement structure, with Precambrian and Paleozoic lineaments becoming selectively re-activated according to the extension direction during each subsequent tectonic event.

The present-day structural configuration of the Norwegian Margin is the result of three main rifting periods: (1) Carboniferous to Permian, (2) late Mid-Jurassic to Early Cretaceous, and (3) Late Cretaceous to Early Eocene (Brekke, 2000). Extensional tectonics in the Carboniferous to Early Cretaceous was related to continental rifting, whilst the later tectonics of the Late Cretaceous and the Tertiary were more directly influenced by movement along plate boundaries immediately prior to and during continental break-up and continental spreading in the North Atlantic (Brekke, 2000).

A number of inversion events both pre- and post-dating seafloor spreading have been recorded along the Norwegian Margin (Fig. 4.1a). The main compressional events are of Late Paleocene-Early Eocene and Oligocene-Miocene ages. These events resulted in the development of impressive elongated dome structures, including the Helland-Hansen Arch and the Ormen Lange Dome (Roberts et al., 1999; Dore et al., 1999). The Møre Basin (Figs. 4.1 & 4.5; Brekke, 2002) is flanked to the north by the Møre Marginal High, which is capped by Eocene lavas. To the south and south-east it is

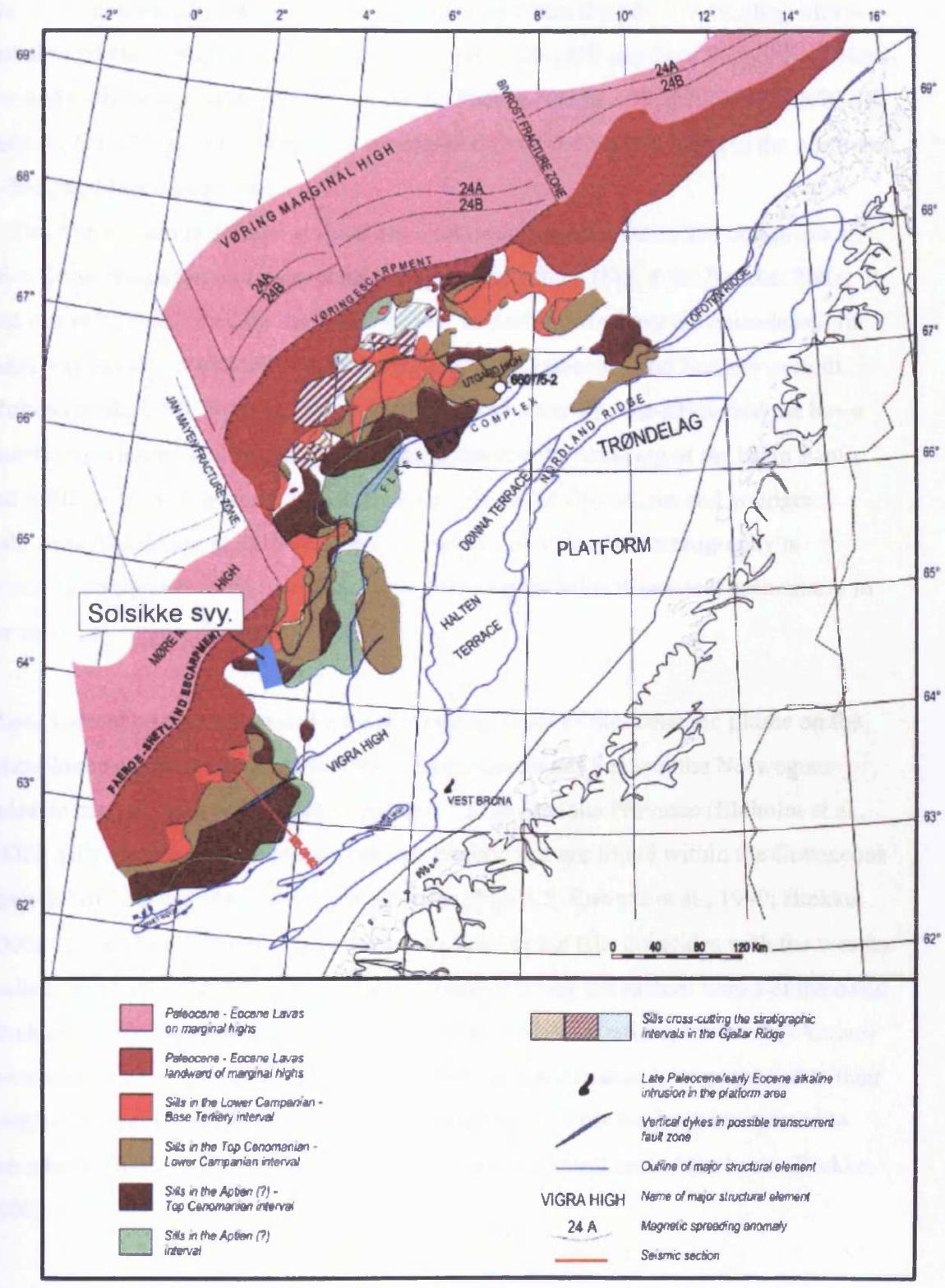

Fig. 4.5 Map showing the extent and ages of extrusive and intrusive volcanics on the Norwegian Margin. The sills intrude younger sediments along the western basin margins than in the more central basin areas. The outline of the Solsikke survey is superimposed on the map and is seen to primarily contain sills intruded into pre-Tertiary sediments. From Brekke (2000).

defined by the eroded Norwegian mainland and the Trøndelag Platform, respectively. The south-eastern boundary of the basin is located where the NE-SW trending Møre-Trøndelag Fault Complex truncates the N-S and NNE-SSW trends of the northern North Sea and to the south-west it borders upon the Faeroe-Shetland Basin along the NW-SE trending Erlend Platform. The basin is separated from the Vøring Basin to the north-east by the Jan-Mayen lineament.

The Møre Basin is defined at the Base Cretaceous unconformity and comprises a thick Cretaceous sedimentary succession up to 6 km thick (Fig. 4.1b; Brekke, 2002). It was primarily influenced by the Mid-Jurassic to Early Cretaceous rift episode and the basin was largely tectonically quiet throughout the Cretaceous and Tertiary periods (Roberts et al., 1999; Brekke, 2002). During the Cretaceous post-rift period the basin mainly experienced continuous passive subsidence with flexuring of the basin flanks and infilling of the sag-basin with a thick succession of Cretaceous and younger sediments (Roberts et al., 1999). The Cretaceous and Paleogene stratigraphy is primarily comprised of marine clays, with some sands being deposited, particularly in the early Paleogene (Roberts et al., 1999).

Major volcanism was associated with the impingement of the Icelandic plume on the lithosphere and the break-up in the Norwegian-Greenland Sea and the Norwegian volcanic margin is part of the North Atlantic Large Igneous Province (Eldholm et al., 2002). Sills of probably Paleocene-earliest Eocene age are found within the Cretaceous basin-fill of both the Møre and Vøring Basins (Fig. 4.5; Roberts et al., 1999; Brekke, 2000). In the Møre Basin the general eastern limit of the sills coincides with the western faults in the broad Møre-Trøndelag Fault Complex along the eastern flanks of the basin (Brekke, 2000). They are generally found at their deepest stratigraphic level (?Aptian) towards the east and from this position they are commonly seen to step upward to their shallowest level (Mastrichtian) towards the north-west. This has been interpreted to indicate that the sills were fed by feeder dykes in the central part of the basin (Brekke, 2000).

The hydrocarbon potential in the basin is considered to be mainly in the Cretaceous and the Paleocene, because the Jurassic is too deeply buried. The nature of the source rock in the basin is uncertain, but there are indications of Upper Cretaceous oil source intervals (Brekke et al., 1999). Thermogenic gas has been found in good quality Upper

Cretaceous and Lower Paleocene reservoir sands (Brekke et al., 1999). The complexity of the tectonic history of the basin combined with magmatism during the Paleocene and earliest Eocene means that basin modelling of the thermal history of the basin is unreliable (Brekke et al., 1999).

4.2.2 Stratigraphic context

A number of horizons (horizons A-I) have been interpreted within the Solsikke survey area (Figs. 4.6 & 4.7). Horizons A-F are of particular interest to the study of the Solsikke sill complex and these are described in the following section and illustrated in Figs. 4.8-4.13. The two cross-sections shown in Figs. 4.6 & 4.7 illustrate the characters of the horizons and the main structural elements in the survey area.

Horizon A (Fig. 4.8) is Upper Cretaceous in age and marks an increase in acoustic impedance and has been picked in a minimum trough. The reflection is continuous and of moderate amplitude. The horizon has been mapped over an area of 740 km^2 at a TWT depth of approximately 3200-3675 ms, covering the central part of the survey area. The reflection could not be mapped in the northern part of the survey area where it underlies a complex high amplitude reflection interpreted as a large igneous intrusion (the Solsikke Sill; section 4.5). The reflector is intensely faulted and the time-structure map shows a complex fault pattern with three dominant fault trends that trend (1) N-S, (2) E-W, and (3) smaller faults that intersect the others orthogonally. Some of these faults display a throw of up to 225 m at the level of horizon A. The time-structure map also shows a NW-SE trending dome (here informally referred to as the Solsikke Dome) running across the survey area. This dome is also clearly imaged on horizons B-H and accounts for the majority of the structural relief on these horizons.

Horizon B (Fig. 4.9) has been tied to exploration well 6403/10-1 and marks the ***Base Tertiary***. It represents an increase in acoustic impedance and is imaged as negative reflection (trough) that has been mapped at a TWT range of 3025-3500 ms over 910 km^2 of the survey area. The reflection is high in amplitude and continuous to the south, but becomes increasingly lower in amplitude and discontinuous to the north. The horizon could not be mapped to the north where a large igneous intrusion (the Solsikke intrusion) has been emplaced approximately at the level of the horizon. The horizon is not as intensely faulted as the underlying horizon A and the time-dip map of the horizon

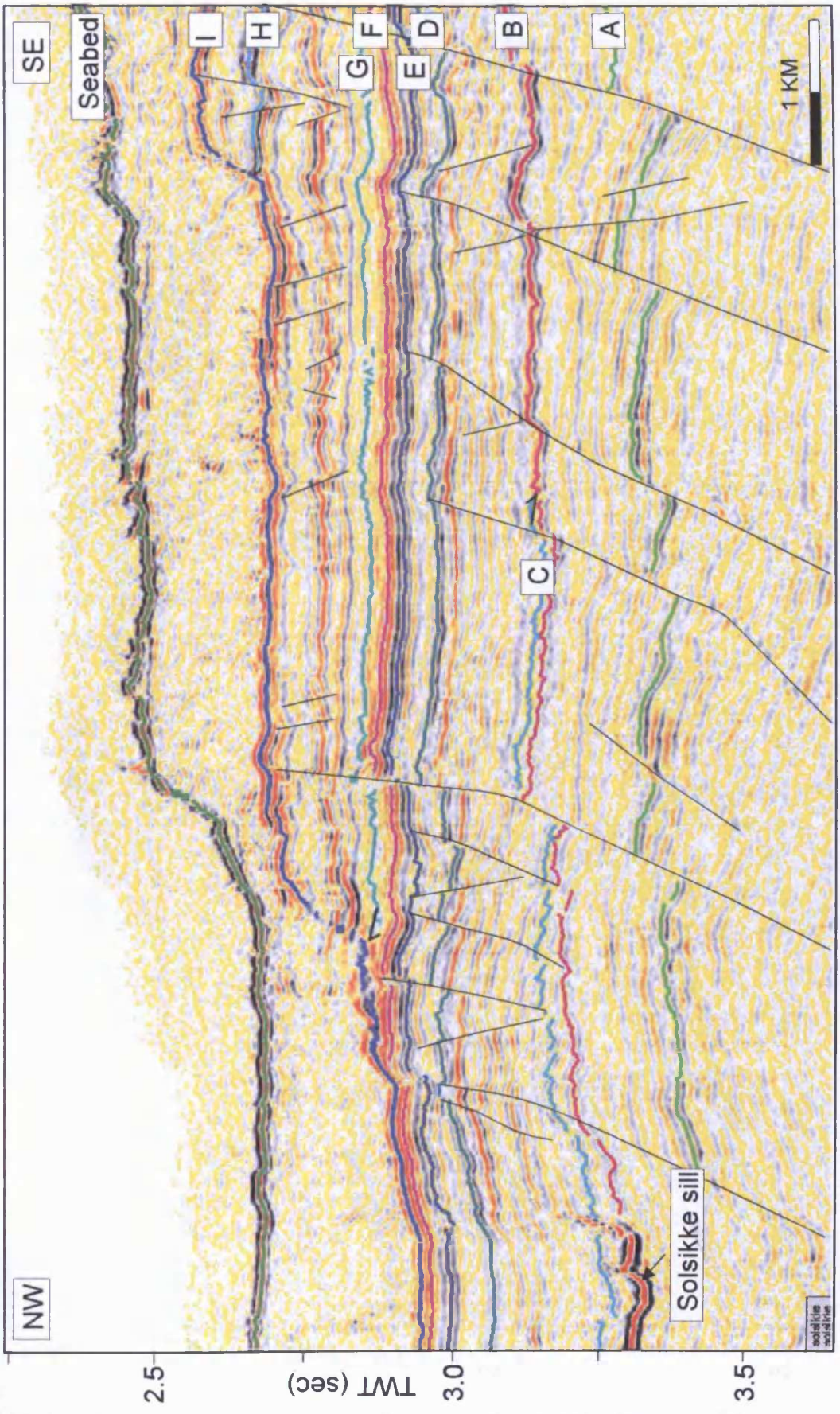

Fig. 4.6 NW-SE striking seismic section (inline) illustrating the seismic character of the central part of the survey area and the mapped horizons. See Fig. 4.2 for line location.

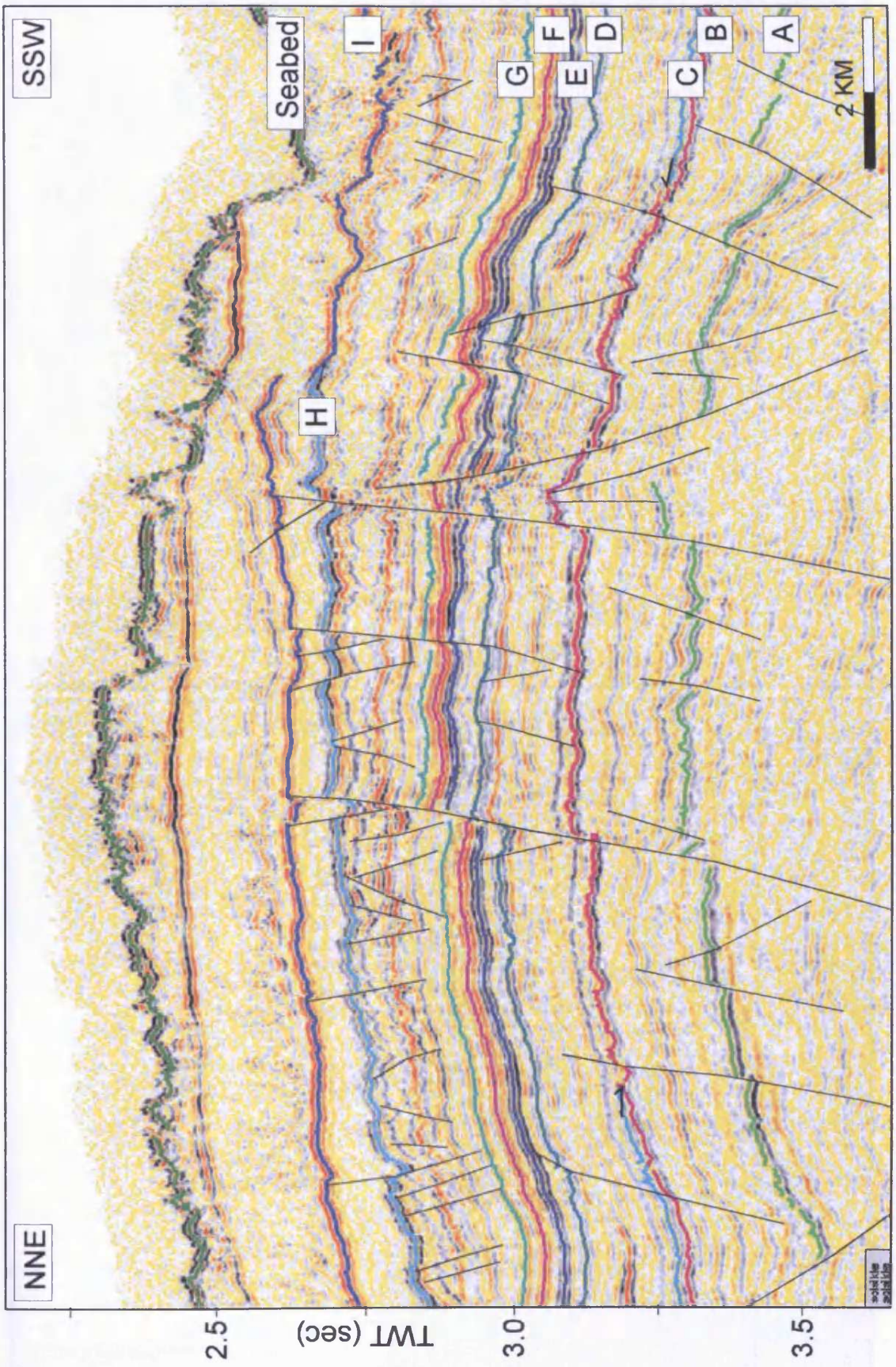

Fig. 4.7 NNE-SSW striking seismic section illustrating the seismic character of the survey area and the mapped horizons. The line shows doming (Solsikke Dome) most likely related to inversion during the Late Paleocene-Early Eocene compressional event. See Fig. 4.2 for line location.

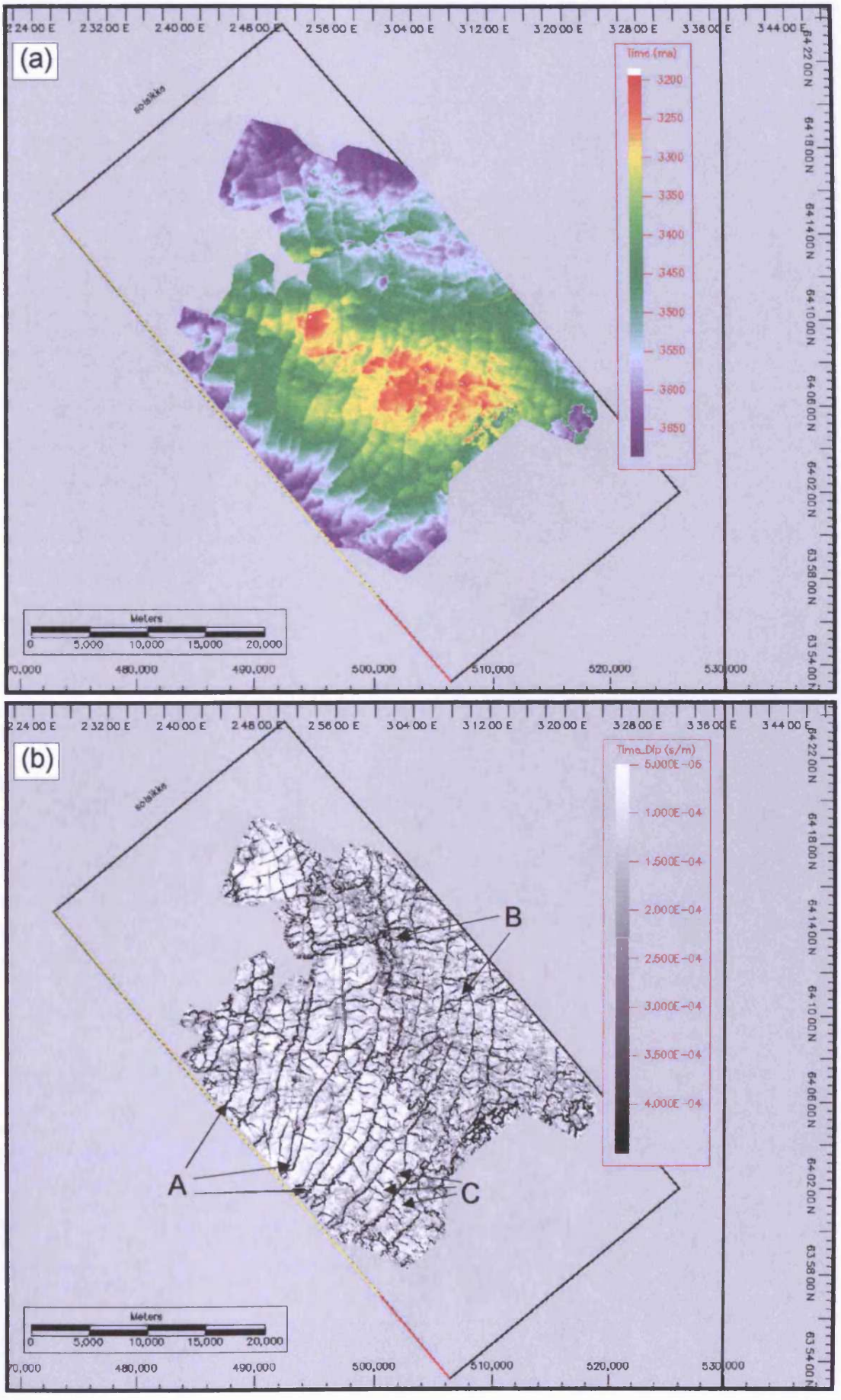

Fig. 4.8 (a) Time-structure map of horizon A. (b) Time-dip map ofhorizon A. Examples of faults of the three main fault sets (fault sets A-C) are indicated on the time-dip map.

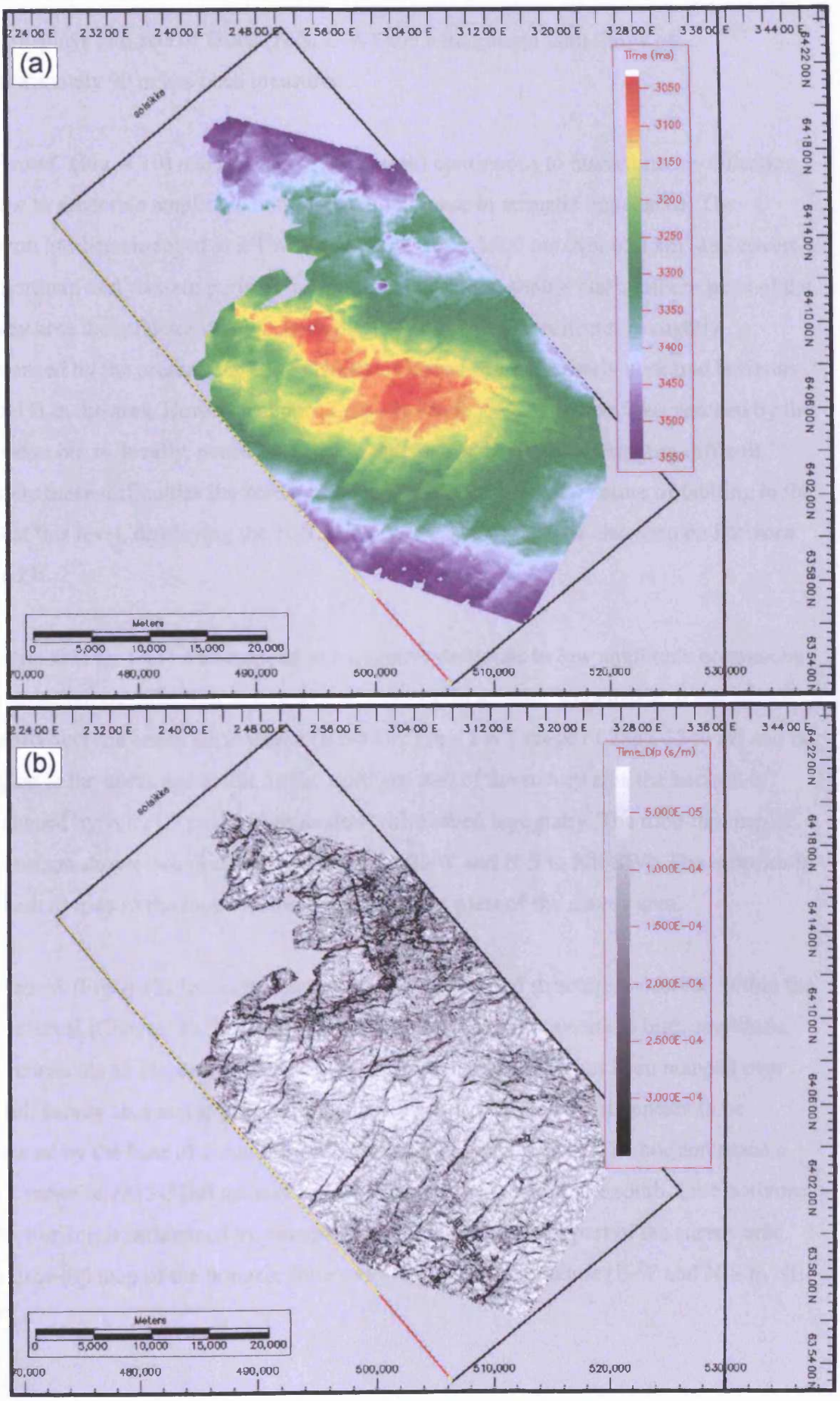

Fig. 4.9 (a) Time-structure map of horizon B. (b) Time-dip map ofhorizon B

only displays two sets of faults (N-S, E-W) and a maximum fault throw of approximately 90 m has been measured.

Horizon C (Fig. 4.10) marks a negative (trough) continuous to discontinuous reflection of low to moderate amplitude that marks an increase in acoustic impedance. The horizon has been mapped at a TWT interval of 3000-3500 ms over 630 km^2 and covers the northern and western parts of the survey area. In the central and southern parts of the survey area the reflector onlaps horizon B. To the north the reflector is slightly influenced by the presence of the Solsikke intrusion that completely obscured horizons A and B in the area. Horizon C approximately marks the shallowest level reached by the intrusion but is, locally, penetrated by igneous intrusions making mapping difficult. Despite these difficulties the resultant maps clearly illustrate the nature of faulting in the area at this level, displaying the N-S and E-W trending fault sets also seen on horizons A and B.

Horizon D (Fig. 4.11) was mapped at a negative moderate to low amplitude continuous to discontinuous reflection that marks an increase in acoustic impedance. It has been mapped over the entire survey area (1050 km^2) at a TWT range of 2865-3340 ms and is deepest to the north and south. In the northern part of the survey area the horizon is influenced by velocity pull-up associated with seabed topograhy. The time-dip map of the horizon shows two dominant fault trends (E-W and N-S to NE-SW). The reflector is difficult to map in the most northern and southern parts of the survey area.

Horizon E (Fig. 4.12) forms the base to a series of mound structures observed within the E-F interval (Chapter 6). The reflection is negative, has a moderate to high amplitude, and represents an increase in acoustic impedance. The horizon has been mapped over the full survey area and is generally continuous, however, locally it appears to be truncated by the base of a number of lensoidal mound structures. The horizon spans a TWT range of 2815-3280 ms and is deepest to the north and to the south. Like horizons D the horizon is influenced by velocity pull-up in the northern part of the survey area. The time-dip map of the horizon shows two dominant fault trends (E-W and N-S to NE-SW).

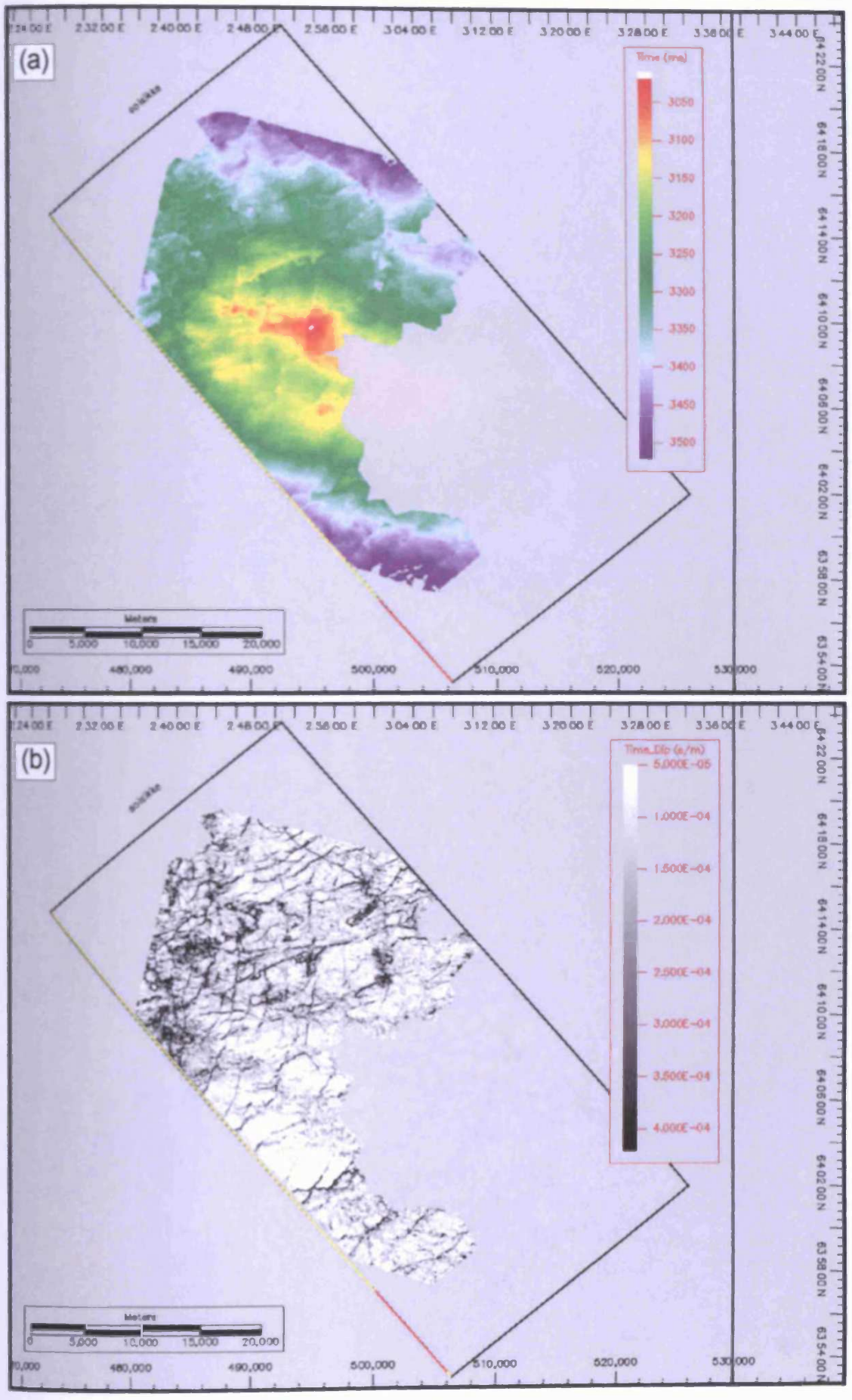

Fig. 4.10 (a) Time-structure map of Horizon C. (b) Time-dip map of Horizon C

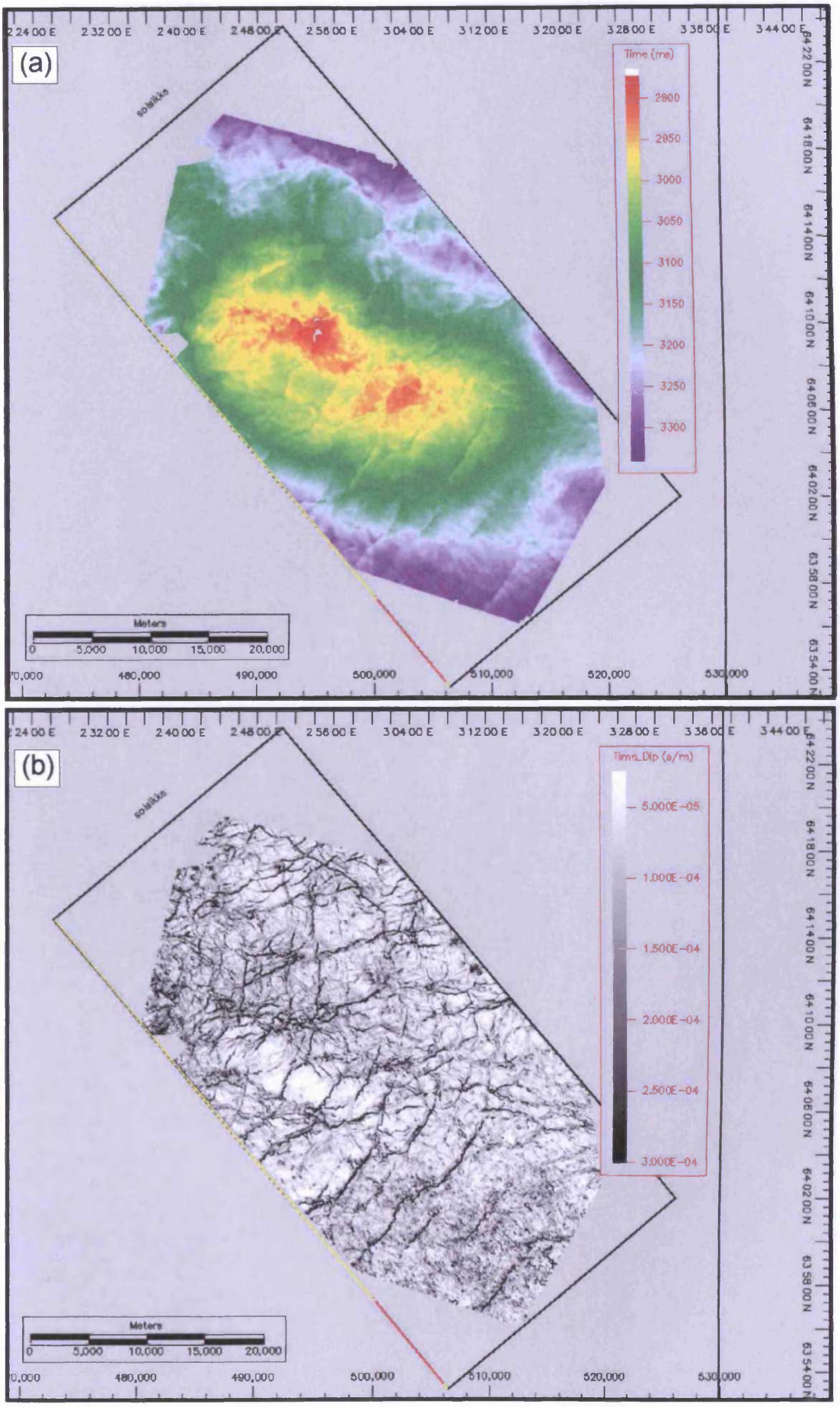

Fig. 4.11 (a) Time-structure map of horizon D. (b) Time-dip map of horizon D.

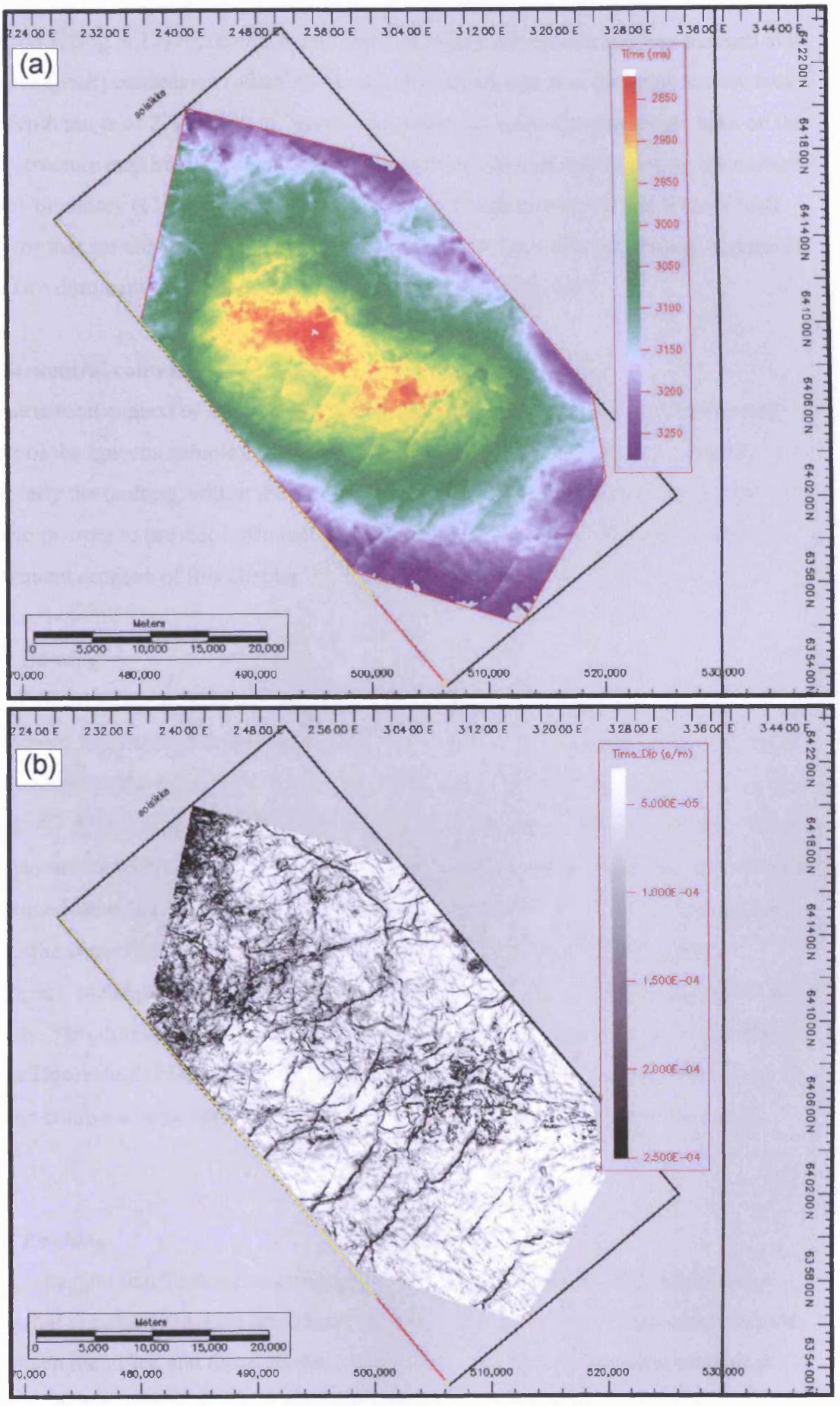

Fig. 4.12 (a) Time-structure map of horizon E. (b) Time-dip map of horizon E.

Horizon F (Fig. 4.13) represents a decrease in acoustic impedance and was mapped at a positive (peak) continuous reflection of moderate amplitude over the entire survey area at a depth range of 2790-3240 m. Several near-circular mound structures are seen on the time-structure map in the northern part of the survey area and midway along the eastern survey boundary (Chapter 6). The time-dip maps of both horizons E and F show fault patterns that are almost identical to the one seen on the time-structure map of horizon D, with two dominant fault trends oriented E-W and N-S to NE-SW.

4.3 Structural context

The structural context of the Solsikke survey area has influenced the distribution and shape of the igneous complex and individual sills within it. The structural context, especially the faulting, within the Solsikke survey area is described in detail in this section in order to provide sufficient supporting evidence to justify interpretations in subsequent sections of this chapter.

4.3.1 Doming

A NW-SE trending anticlinal dome (the Solsikke Dome) influences the imaged Cretaceous and Paleogene strata in the survey area. The Solsikke Dome is clearly seen on the time-structure map of horizon A shown in Fig. 4.8a and is shown in cross-section in Fig. 4.7. It is approximately 35 km long, has a vertical relief of approximately 400 m, and has shallowly dipping flanks (E-W: 2-3°; N-S: 1-2°). The timing of the formation of the dome is poorly constrained. Horizon C onlaps horizon B (Figs. 4.6 & 4.7), which marks the Base Tertiary, and this suggests that doming occurred in the earliest Paleogene, but shallower horizons are also affected and this suggests a long period of activity. This dome is one of many observed along the Norwegian margin (e.g. Ormen Lange Dome) and is likely to be related to inversion during the Late Paleocene-Early Eocene compressional event (Stuevold et al., 2003; Roberts et al., 1999; Dore et al., 1999).

4.3.2 Faulting

The Cretaceous and Tertiary sediments in the survey area are intensely deformed by faults that are clearly imaged on vertical sections and in planview. Three main fault sets have been identified and these are described in this section. The locations of vertical seismic section used to illustrate the faults are shown in Fig. 4.14.

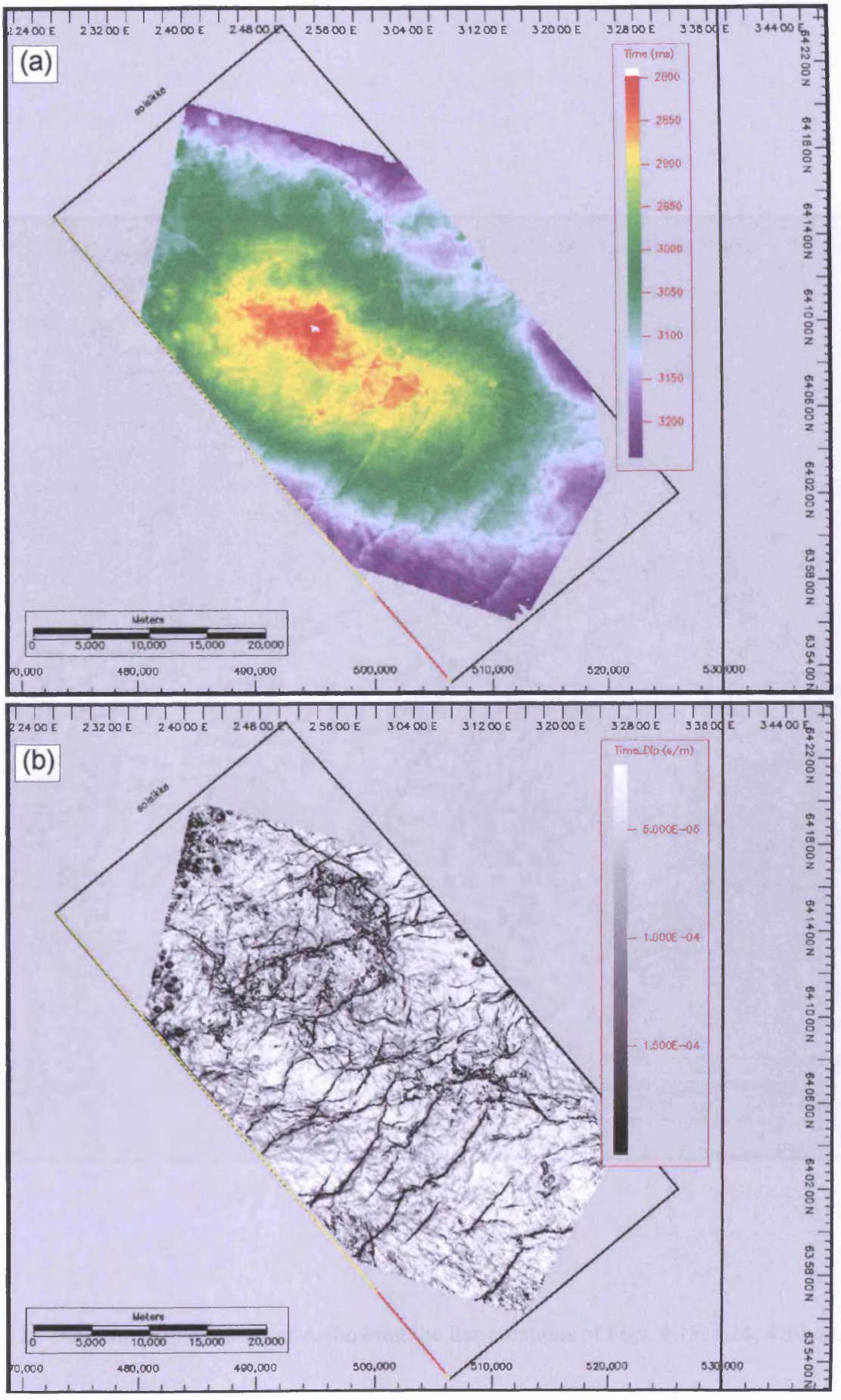

Fig. 4.13 (a) Time-structure map of horizon F. (b) Time-dip map of horizon F.

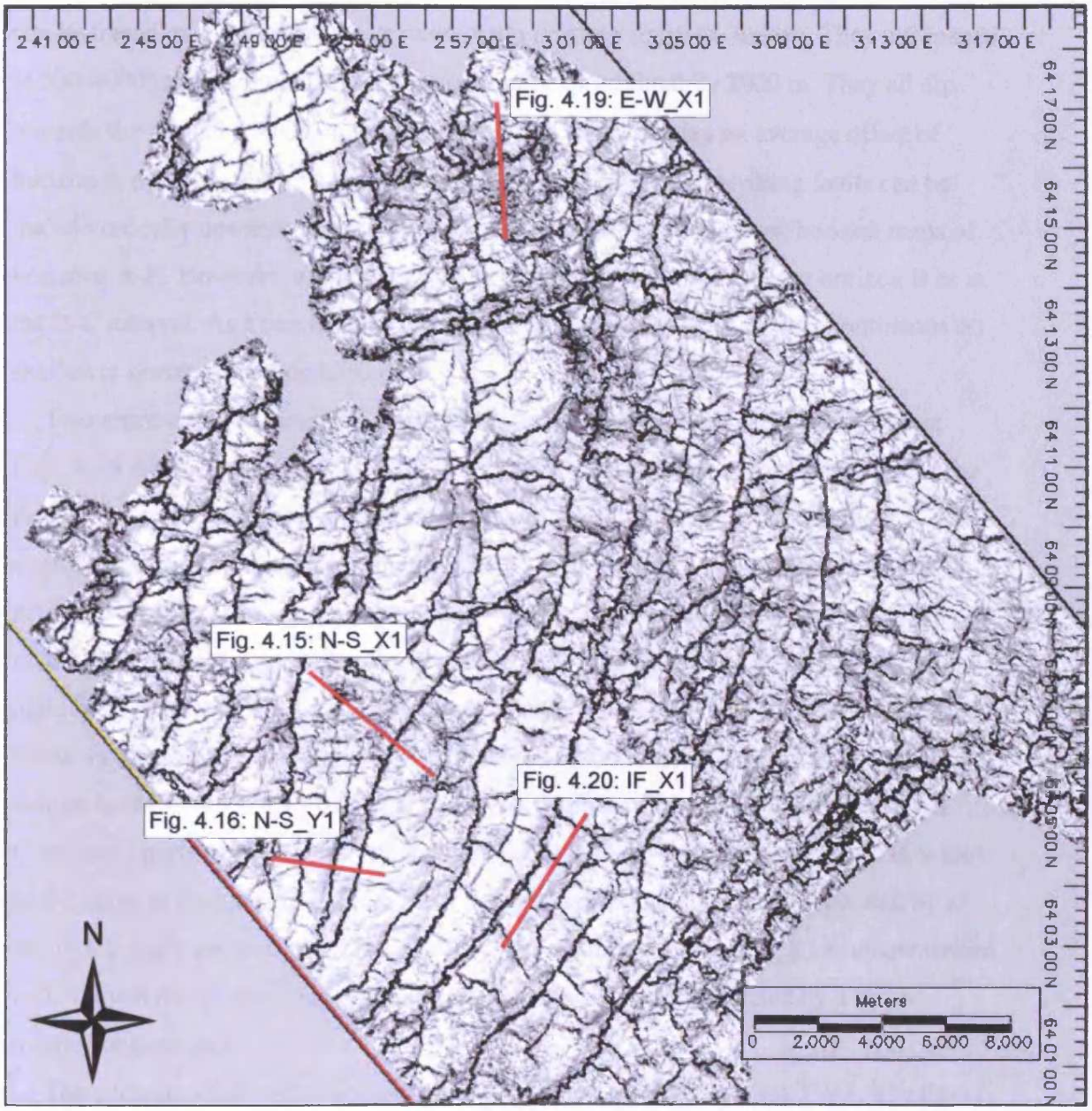

Fig. 4.14 Time-dip map of Horizon A showing the line locations of Figs. 4.15, 4.16, 4.19, and 4.20.

4.3.2.1 Fault set A: N-S striking faults

The most dominant set of faults (*fault set A*) forms continuous curved fault traces with an overall N-S strike. These are clearly imaged by the horizon A attribute maps (Fig. 4.8). In the southern part of the survey area the fault traces have a NE-SW trending strike, but become N-S oriented towards the north. The fault traces are continuous and can be traced over the entire survey area from north to south (> 30 km). They are spaced at 500-4000 m, with most faults being spaced at approximately 2000 m. They all dip towards the west and have an average dip of 31°. They display an average offset of horizon A of 67 ms TWT. Along most of their lengths the N-S striking faults can be traced vertically upwards to horizon I and they can be seen clearly on horizon maps of horizons A-H. However, along parts of their lengths the faults tip out at horizon B or in the B-C interval. As a result, the traces of the N-S striking faults are less continuous on shallower horizons than on horizon A.

Two representative throw vs. depth profiles for faults of fault set A are shown in Figs. 4.15 & 4.16 (see Fig. 4.14 for line locations). The profile in Fig. 4.15b shows the throw vs. depth profiles for a segment of a fault (N-S_X1) that influences the stratigraphic interval from below horizon A to near horizon I, whilst the profile in Fig. 4.16b shows the throw vs. depth curve for a segment of the fault (N-S_Y1) that tips out at horizon B. The throw vs. depth profile for fault N-S_X1 can be sub-divided into two main parts, namely a Cretaceous part and a Tertiary part separated by horizon B. The throw vs. depth profile for fault N-S_Y1, which tips out below horizon B, is very similar to the Cretaceous part of the throw vs. depth profiles for faults N-S_X1. The Cretaceous parts of the curves are characterised by a throw minima at horizon B, a kink in the curve at horizon A, and two local throw maxima (labelled max) separated by a throw minima (labelled min). The Tertiary part of the curve for N-S_X1 is characterised by two local throw maxima (G-H interval and at horizon D) separated by a throw minima at horizon F.

The average offset of horizon A by the N-S striking faults is 67 ms TWT. The throw vs. frequency histogram for the N-S striking faults does not show a normal distribution (Fig. 4.17a), but has two peaks one in the 40-50 ms bin (17.82 %) and a second in the 70-80 bin (12.38 %). A more detailed analysis of fault throw at the level of horizon A shows that the peak in the 40-50 ms bin is associated with the N-S striking fault segments that tip out around the level of horizons B and C (average fault throw of 54 ms at horizon A), whilst the second peak is associated with the N-S striking fault segments

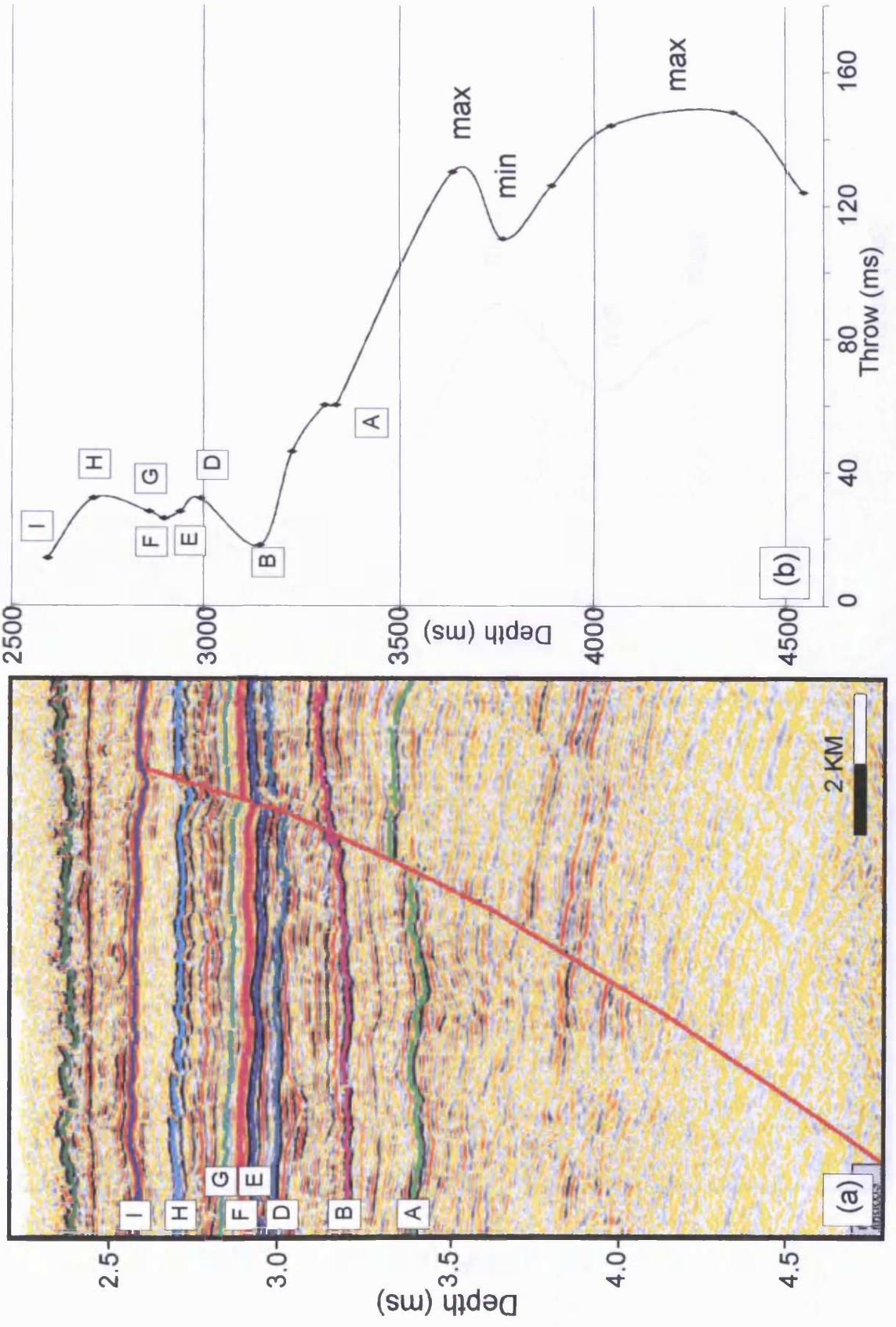

Fig. 4.15 (a) Cross-section showing the seismic expression of the N-S trending fault N-S_X1. See Fig. 4.14 for line location. (b) Throw vs. depth curve for fault N-S_X1. The fault was active during the Cretaceous and re-activated in the Tertiary.

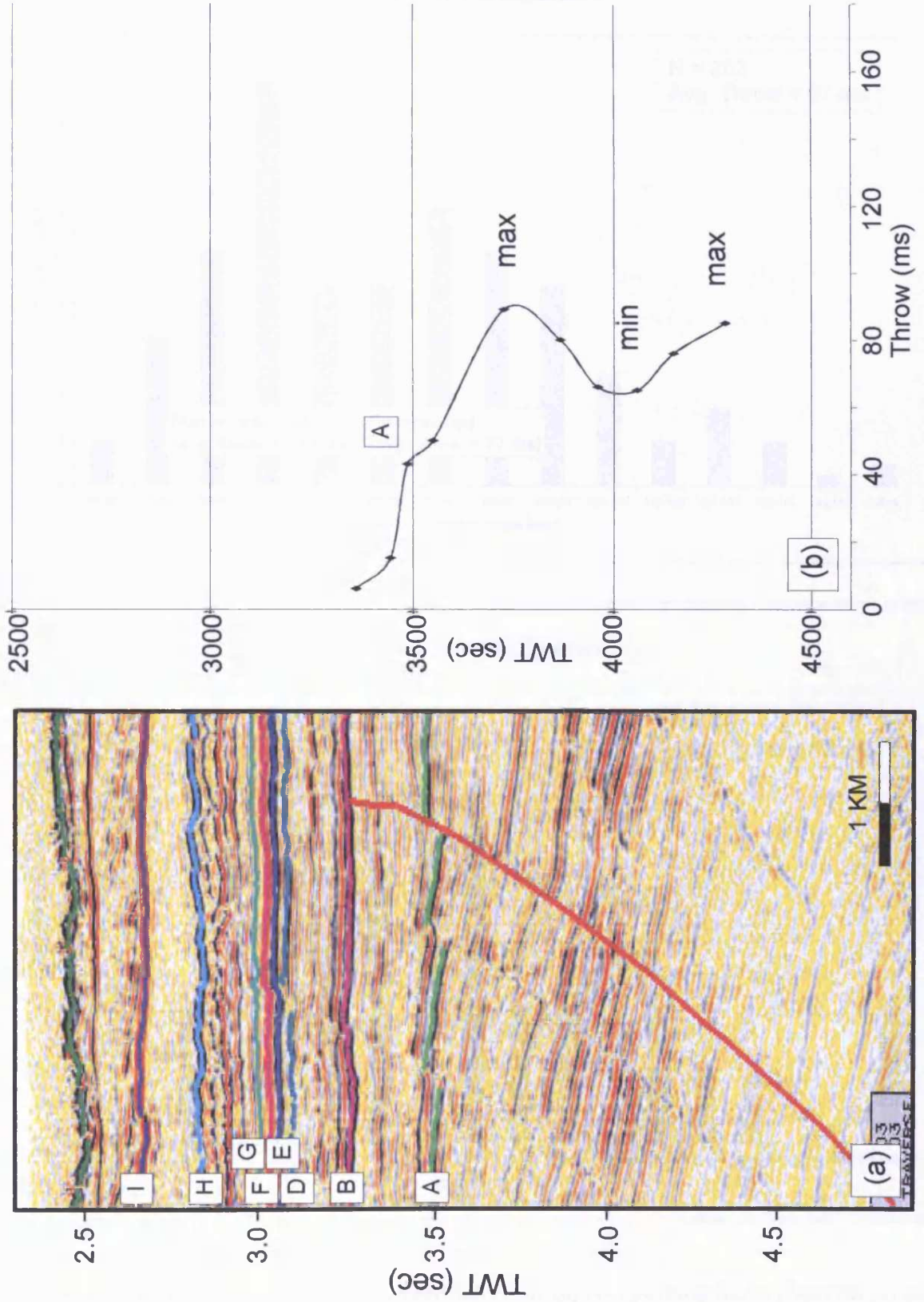

Fig. 4.16 (a) Cross-section showing the seismic expression of the N-S trending fault N-S_Y1. See Fig. 4.14 for line location. (b) Throw vs. depth curve for fault N-S_Y1. The fault was active during the Cretaceous and died out around the end of the Cretaceous.

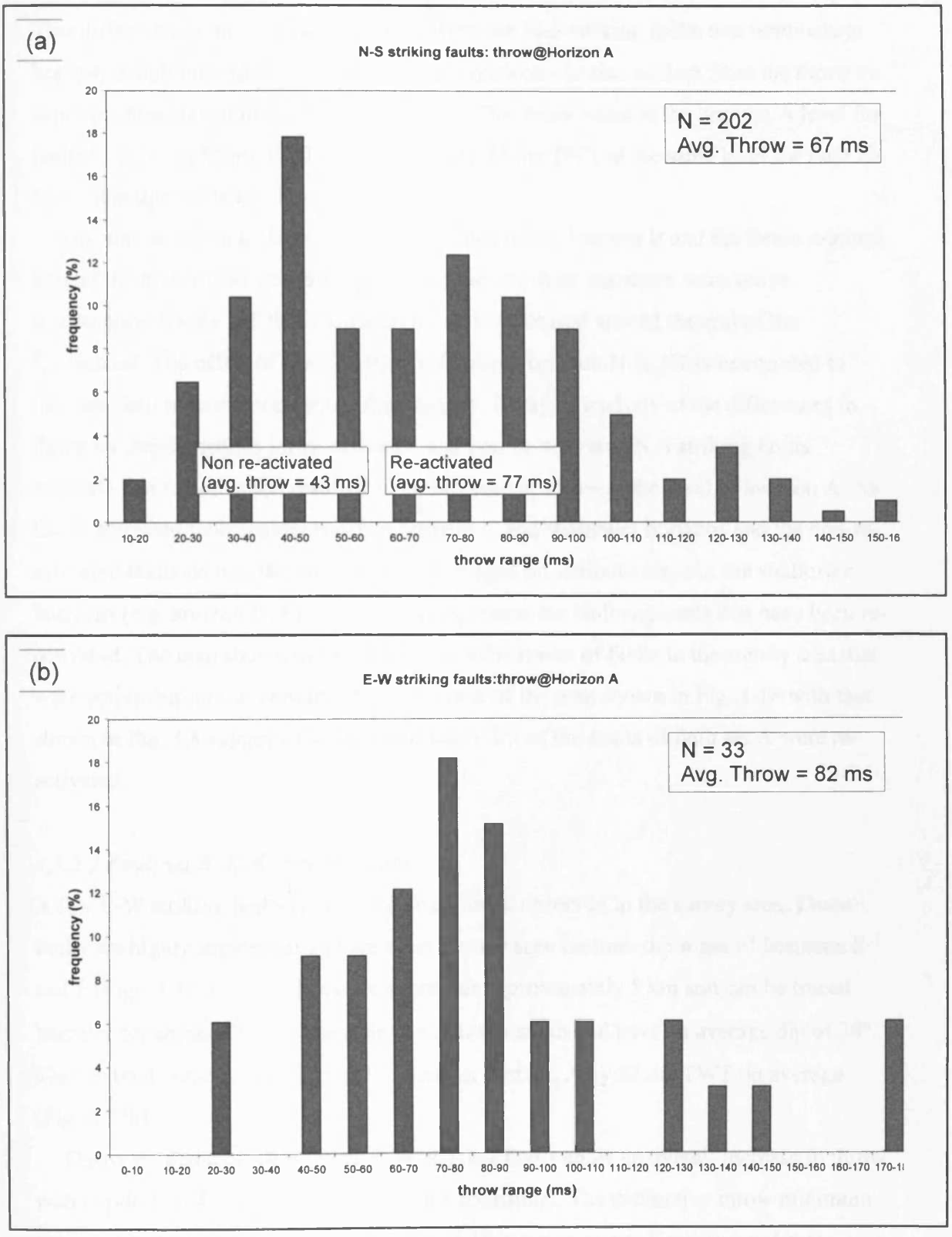

Fig. 4.17 Throw distribution at the level of Horizon A for (a) N-S striking faults (fault set A) and (b) E-W striking faults (fault set B).

that extend vertically to horizon I (average fault throw of 77 ms TWT at horizon A). This difference in throw at horizon A between the N-S striking faults that terminate at horizon B and those that extend vertically to horizon I is also evident from the throw vs. depth profiles shown in Figs. 4.15b & 4.16b. The throw value at the horizon A level for faults N-S_X1 is 82 ms TWT, while it is only 43 ms TWT at the same level for fault N-S_Y1 that tips out below horizon B.

The almost identical throw vs. depth profiles below horizon B and the throw minima around the level of horizon B suggests that the two fault segments were active contemporaneously and that fault activity on both ceased around the end of the Cretaceous. The offset of post-Tertiary reflections on fault N-S_X1 is interpreted to indicate fault re-activation during the Tertiary. Detailed analysis of the differences in throw vs. depth profiles for re-activated and non-re-activated N-S striking faults suggests that re-activation resulted in an increase of throw at the level of horizon A. As the re-activated fault segments offset horizon C and shallower horizons and the non-re-activated faults do not, the fault segments imaged on attribute maps of the shallower horizons (e.g. horizon D; Fig. 4.11) must represent the fault segments that have been re-activated. The map shown in Fig. 4.18 shows the traces of faults in the survey area that were active during the Tertiary. A comparison of the map shown in Fig. 4.18 with that shown in Fig. 4.8 suggests that approximately 2/3 of the faults of fault set A were re-activated.

4.3.2.2 Fault set B: E-W striking faults

A few E-W striking faults (*fault set B*) have been observed in the survey area. These faults are highly segmented and are most clearly seen on time-dip maps of horizons E and F (Figs. 4.12 & 4.13). They are spaced at approximately 5 km and can be traced laterally for around 20 km. They dip towards the south and have an average dip of 30°. They extend vertically to horizon I and offset horizon A by 82 ms TWT on average (Fig. 4.17b).

Throw vs. depth profiles of the E-W striking faults show an overall increase in throw with depth (Fig. 4.19, see Fig. 4.14 for line locations). The distinctive throw minimum seen immediately below horizon B in Fig. 4.19 is not seen on all profiles and may represent a local lithological effect. Evidence for growth in the form of growth wedges is seen on these faults, particularly immediately above horizon B and in the D-E

Fig. 4.18 Trace map of horizon D (Fig. 4. 11) showing re-activated fault traces.

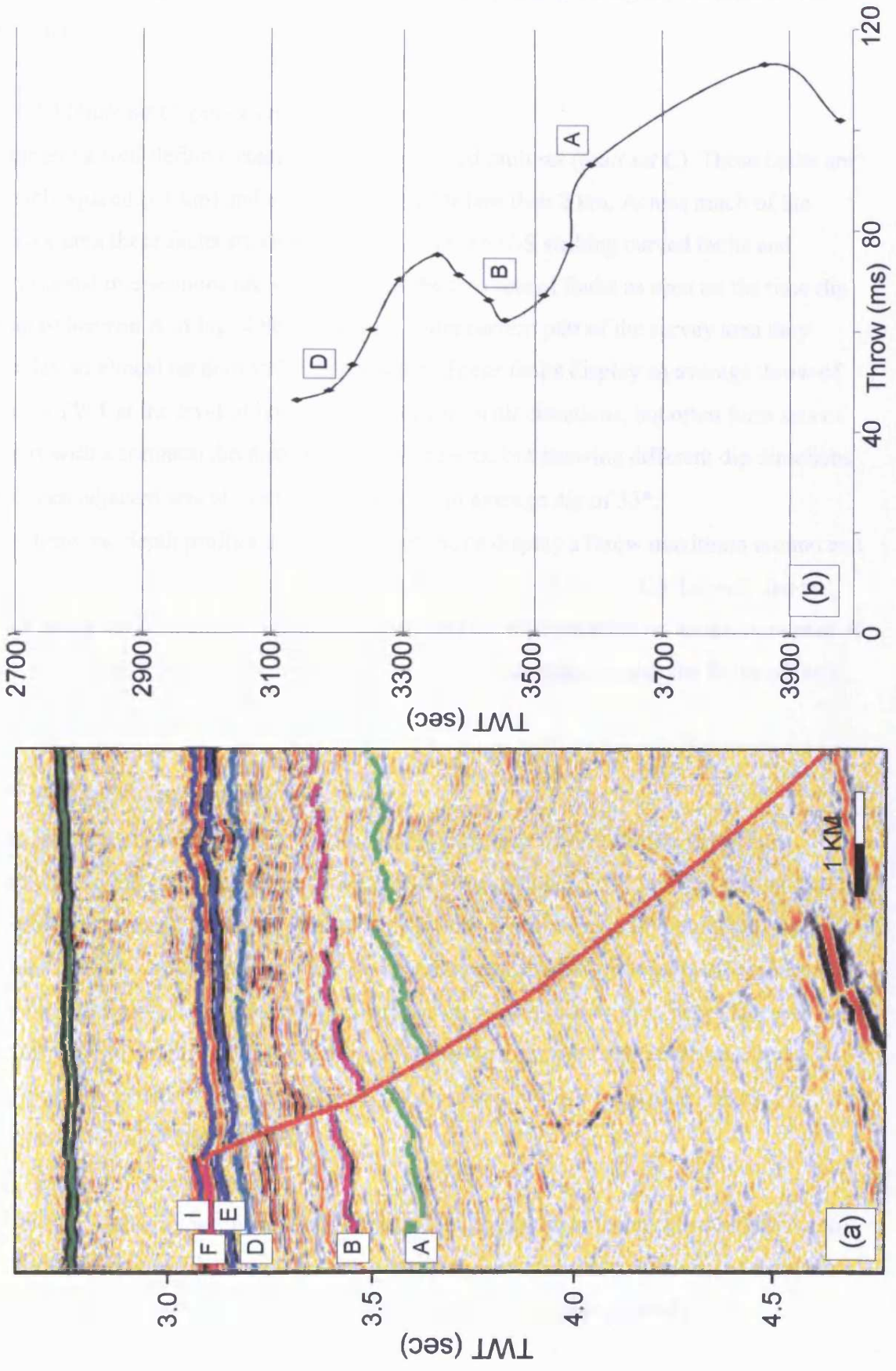

Fig. 4.19 (a) Cross-section showing the seismic expression of the E-W trending fault E-W_X1. See Fig. 4.14 for line location. (b) Throw vs. depth curve for fault E-W_X1. The fault was intermittently active during the Cretaceous and Tertiary.

interval. This suggests that they were intermittently active during the Cretaceous and Tertiary.

4.3.2.3 Fault set C: Intersecting faults

Numerous well-defined, small faults form a third fault set (*fault set C*). These faults are closely spaced (~1 km) and extend laterally for less than 2 km. Across much of the survey area these faults strike perpendicular to the N-S striking curved faults and orthogonal intersections are seen between the two sets of faults as seen on the time-dip map of horizon A in Fig. 4.8b. However, in the eastern part of the survey area they display an almost random strike distribution. These faults display an average throw of 46 ms TWT at the level of horizon A. They dip in all directions, but often form sets of faults with a common dip direction within the sets, but showing different dip directions between adjacent sets of faults. They exhibit an average dip of 33°.

Throw vs. depth profiles of this group of faults display a throw maximum around and just below the level of horizon A, decreasing downwards (Fig. 4.20). Growth can be seen along the fault within the A-B interval and is clearly imaged on an isochore map of the interval between the two horizons (Fig. 4.21). This suggests that the faults of fault set C were active during the Cretaceous.

4.3.2.4 Interpretation of fault pattern

The fault pattern recognised in the Solikke survey area is very similar to the fault pattern recognised in the Ormen Lange field (Stuevold et al., 2003) to the east of the Solsikke case-study area. The Ormen Lange fault system occurs in dominantly fine-grained Upper Cretaceous and Paleogene sediments, similar to the affected sediments in the Solsikke survey area, and was interpreted as a polygonal fault system (Stuevold et al., 2003). Such fault systems are thought to form as a result of three-dimensional compaction, possibly through the process of syneresis (Cartwright et al., 2003; Cartwright & Dewhurst, 1998).

Fault sets A and C are the two dominant fault sets that affect the intruded sediments in the Solsikke survey area and they share many of the same characteristics and there are several lines of evidence suggesting that they grew contemporaneously:

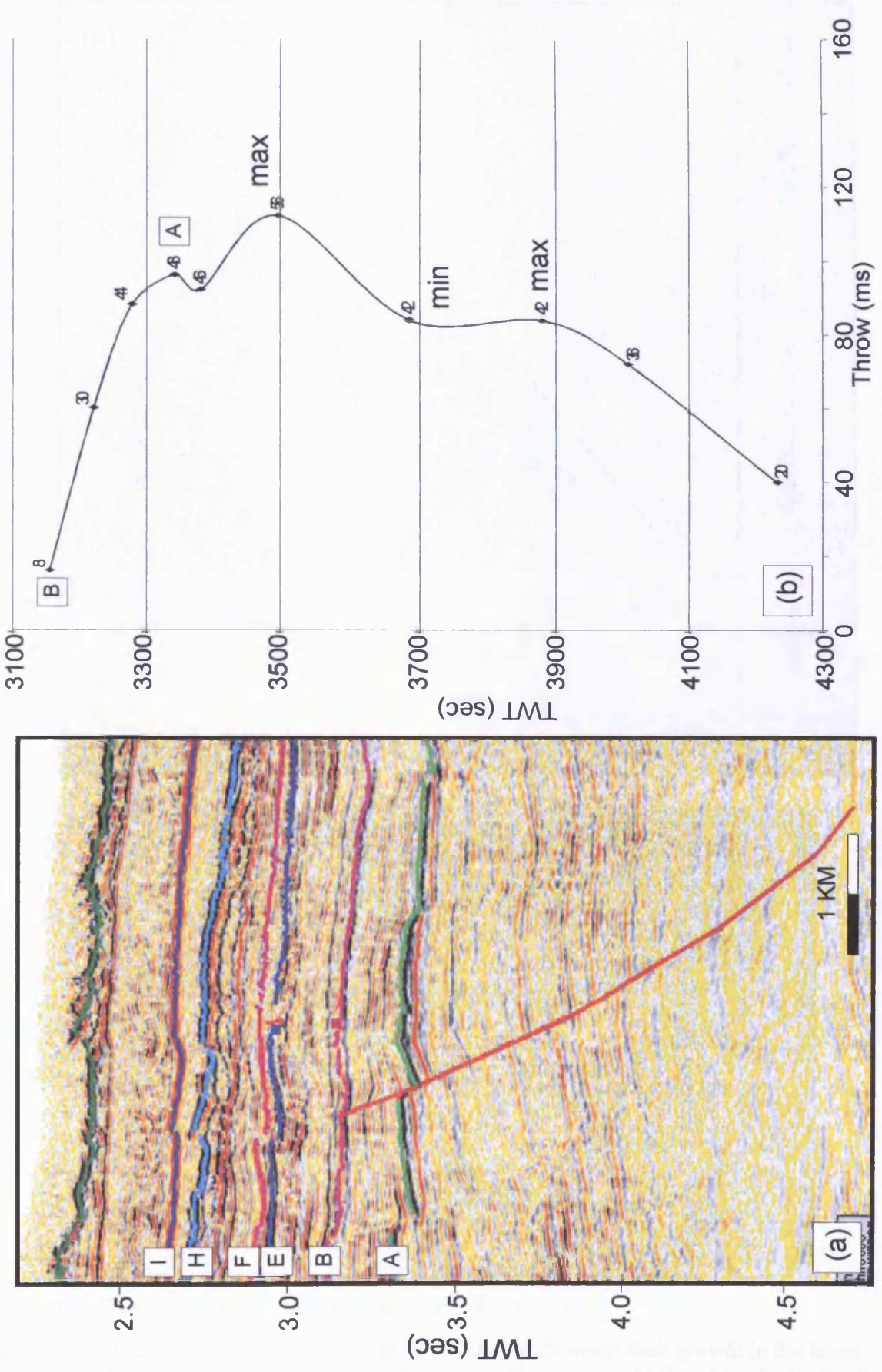

Fig. 4.20 (a) Cross-section showing the seismic expression of the intersecting fault IF_X1. See Fig. 4.14 for line location. (b) Throw vs. depth curve for fault IF_X1. The fault was active during the Cretaceous and died out around the end of the Cretaceous.

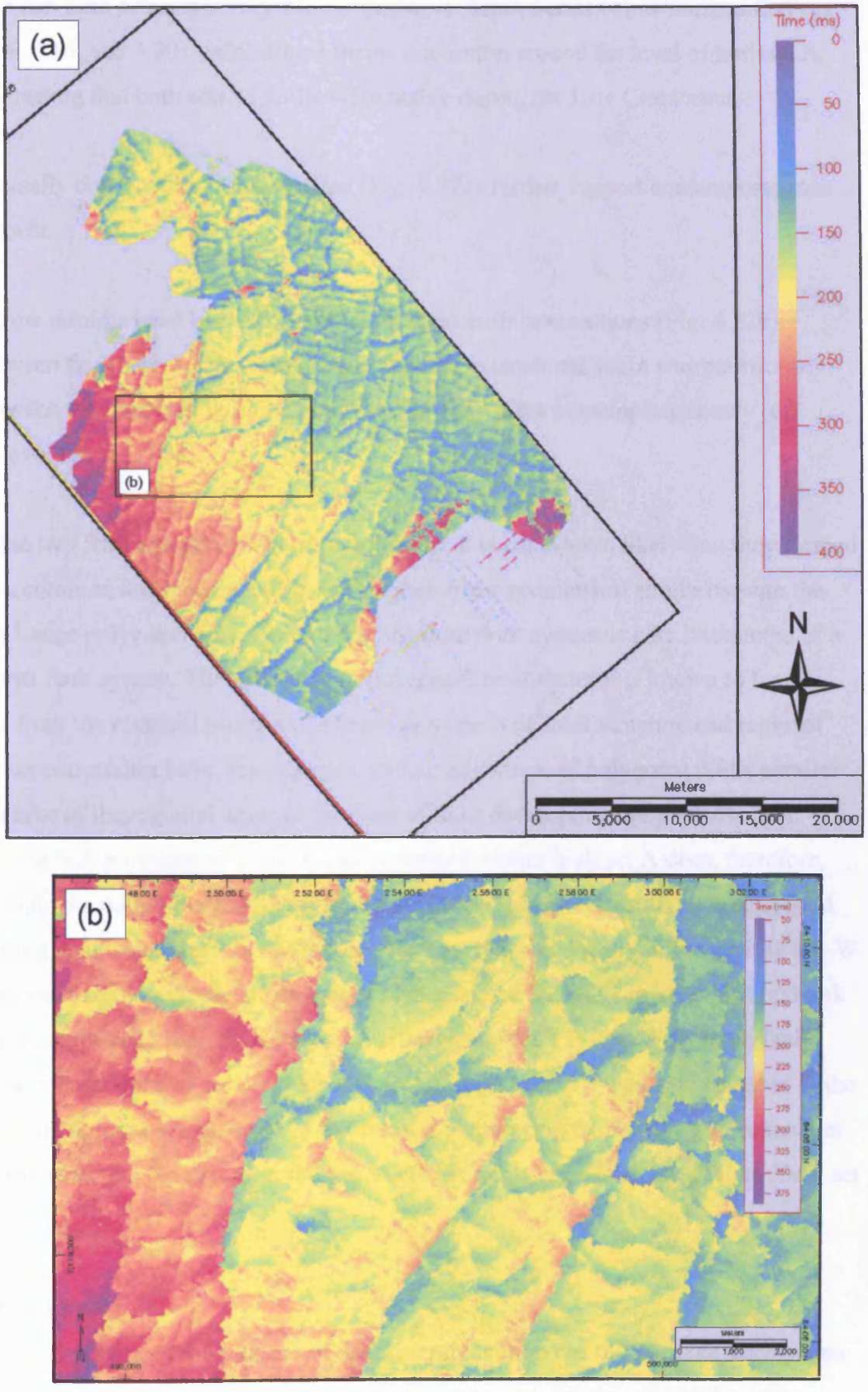

Fig. 4.21 (a) Isochore map of the Horizons A- B interval showing fault growth in the latest Cretaceous. (b) Close up of isochore map showing fault growth on N-S striking faults (fault set A) as well as on intersecting faults (fault set C).

(1) The two fault sets show very similar throw vs. depth trends below horizon C (Figs. 4.15, 4.16, and 4.20), exhibiting a throw maximum around the level of horizon A, suggesting that both sets of faults were active during the Late Cretaceous.

(2) Mutually cross-cutting relationships (Fig. 4.22a) further support contemporaneous growth.

(3) Throw minima have been observed associated with intersections (Fig. 4.22b) between fault sets A and C suggesting that the extensional strain was partitioned between the intersecting faults and thus that they grew contemporaneously (cf. Stuevold et al., 2003).

Since the two fault sets grew contemporaneously it is considered likely that they formed due to a common mechanism and based on their clear geometrical similarity with the Ormen Lange polygonal fault system, the Solsikke fault system is here interpreted as a polygonal fault system. The geometry of polygonal fault systems is known to locally deviate from the classical polygonal pattern as a result of local structure and regional slope. Several studies have, for example, shown alignment of polygonal faults parallel to the strike of the regional slope at the time of fault development (e.g. Cartwright, 1994). The N-S polarisation of the faults contained within fault set A does, therefore, not exclude the possibility that these faults are indeed polygonal faults. It is suggested that during its development this polygonal fault system was locally influenced by a E-W oriented extensional tectonic stress that caused many of the faults to align N-S and link to form exceptionally long fault traces for a polygonal fault system. Polygonal faults form under conditions of radial stress and part of the strain that was not expressed in the N-S striking faults was expressed in the smaller intersecting faults with a more random dip distribution that developed in the gaps between adjacent N-S striking faults (fault set C).

4.3.3 Summary

The above description and analysis of the structural context of the Solsikke survey area shows that the survey area underwent extensive structural deformation particularly during the Late Cretaceous prior to intrusion of the sills, but also during the Tertiary, both during and after intrusion of sills.

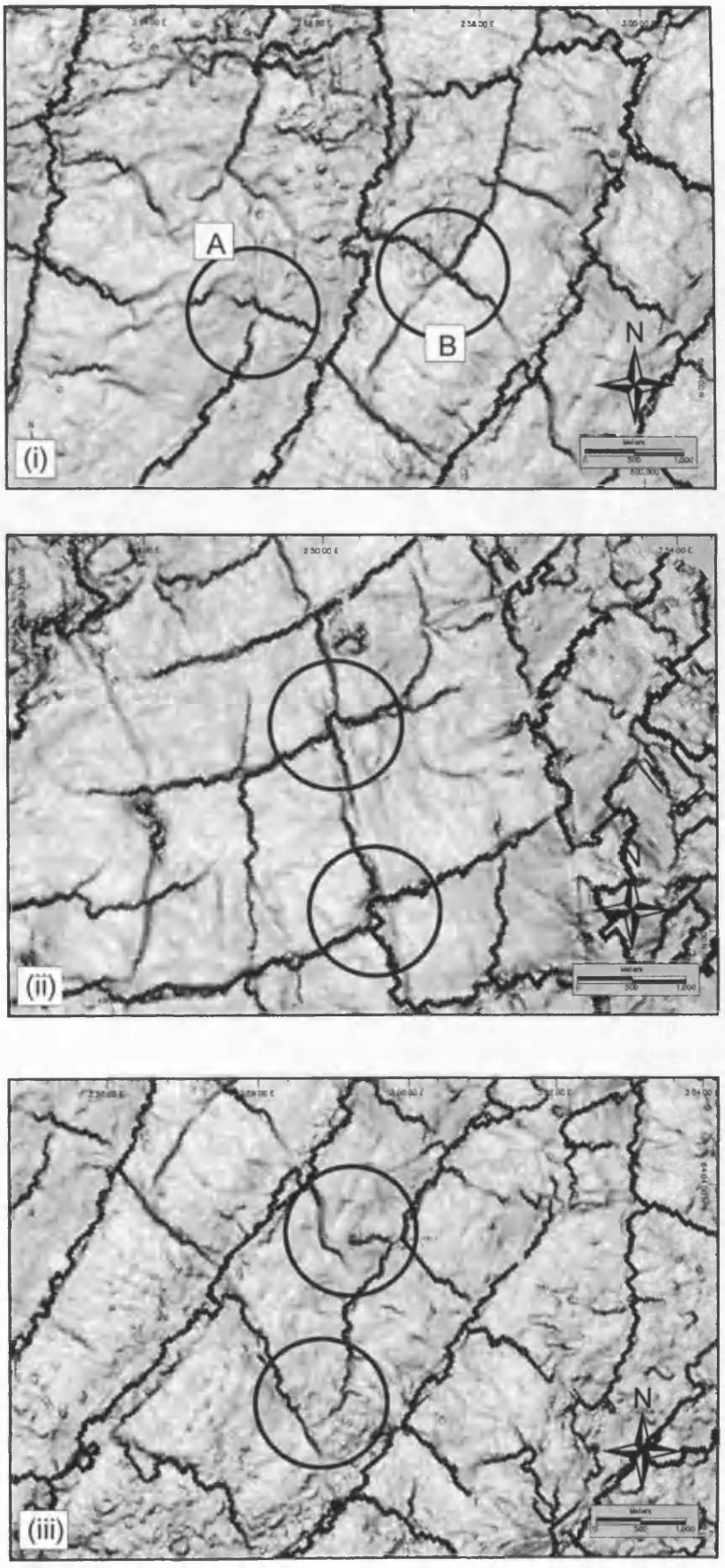

Fig. 4.22a Cross-cutting relationships between faults of fault sets A and C indicating contemporaneous growth in the Late Cretaceous. (i) (A) Fault set A terminates at junction with fault set C. (B) Cross-cutting relationship. (ii) Fault set C is offset by fault set A. (iii) Fault tip deflections due to stress field interference between contemporaneously propagating fault tips.

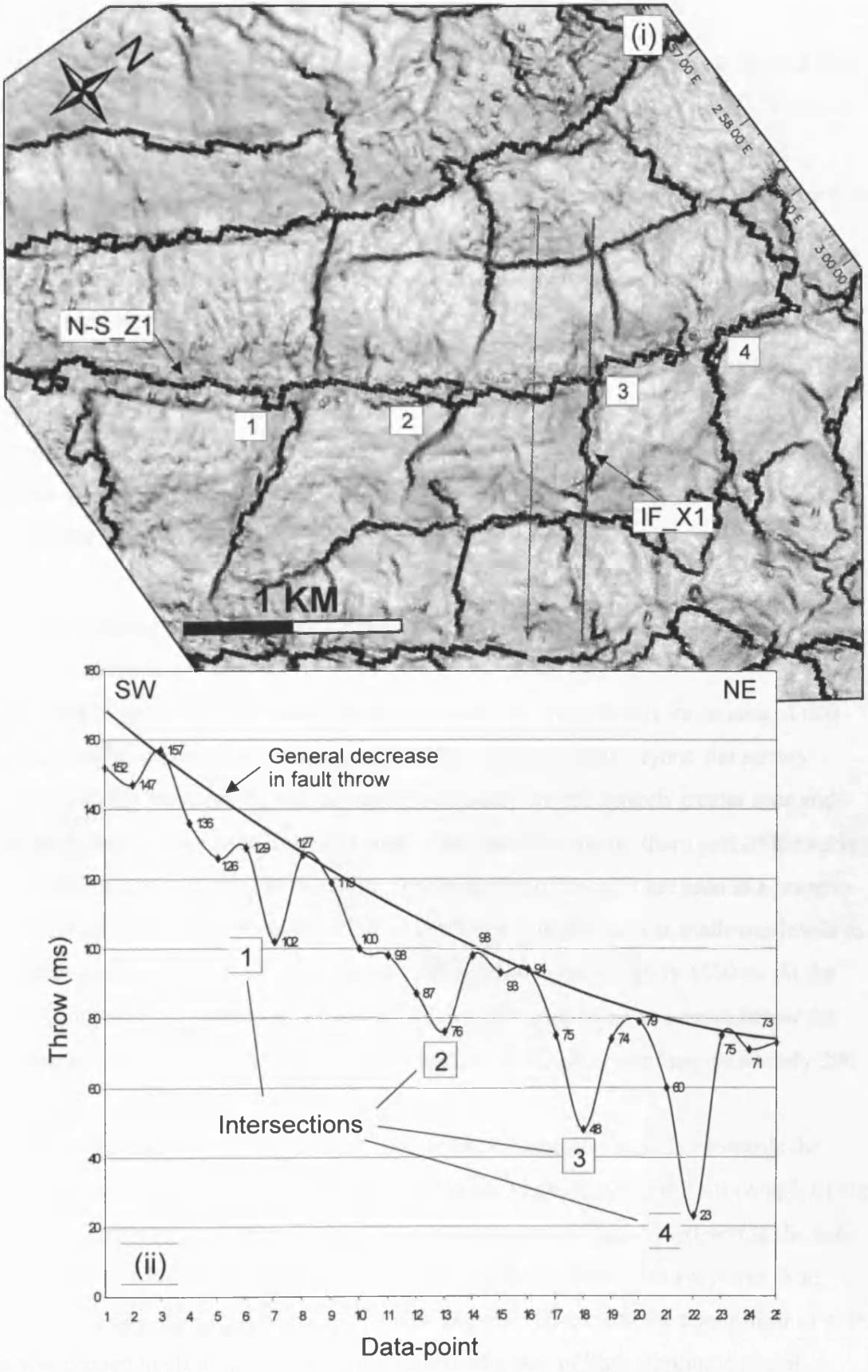

Fig. 4.22b (i) Sub area of time-dip map of horizon A showing orthogonal intersections between fault sets A and C. (ii) Throw profile measured along fault N-S_Z1 showing throw minima at intersections. See Fig. 4.14 for location.

4.4 The Solsikke intrusive igneous complex

4.4.1 Introduction

Many high amplitude concordant and discordant reflections interpreted as igneous sills are seen in the northern part of the Solsikke survey area (Figs. 4.23 & 4.24). They are intruded into Cretaceous and Paleogene sediments and span a vertical section of approximately 5 km of compacted sediments. Extrusive mound structures interpreted to have formed at the seabed at the time of intrusion (Chapter 6) have been mapped on horizon E and suggest that intrusion took place at the time represented by this surface.

The interpretation of the Solsikke sill complex is complicated because of the density of intrusions. The sills form a highly interconnected network with many junctions and layers of intrusion. This means that it is difficult to separate individual sills and the deeper sills are poorly resolved due to loss of resolution in the region underlying the shallow sills (Fig. 2.1). In this section the distribution and geometry of the Solsikke sill complex is described and its emplacement and history discussed.

4.4.2 Description of the Solsikke intrusive igneous complex

4.4.2.1 Distribution of sills

The Solsikke sill complex is made up of more than 30 sills and covers an area of 600 km^2 within the survey area. However, the sill complex extends beyond the survey boundary to the west, north, and east and most likely covers a much greater area and comprises many more sills. The sill complex is limited to the northern part of the survey area with no sills occurring to the south. The majority of the sills are seen at a present-day depth of approximately 6000-9750 m, but a few sills are seen at shallower levels to the north and the shallowest upper tip of a sill reaches approximately 4500 m. At the time of intrusion the shallowest sills would have been emplaced at a depth below the contemporaneous seabed (approximate by horizon E; Chapter 6) of approximately 300 m.

Seismic cross-sections suggest that the density of intrusion is higher towards the northern than towards the southern boundary of the imaged part of the sill complex (Fig. 4.23). This increase in sill density has been imaged in map-form by extracting the sum of negative amplitudes within a 4100-6500 ms window across the survey area. This window does not capture the shallowest sills above 4100 ms, but the upper limit of 4100 ms was chosen to eliminate the acoustic effects of a unit of high amplitude stratal reflections in the 3500-4100 ms interval. The resultant map (Fig. 4.25) shows that the

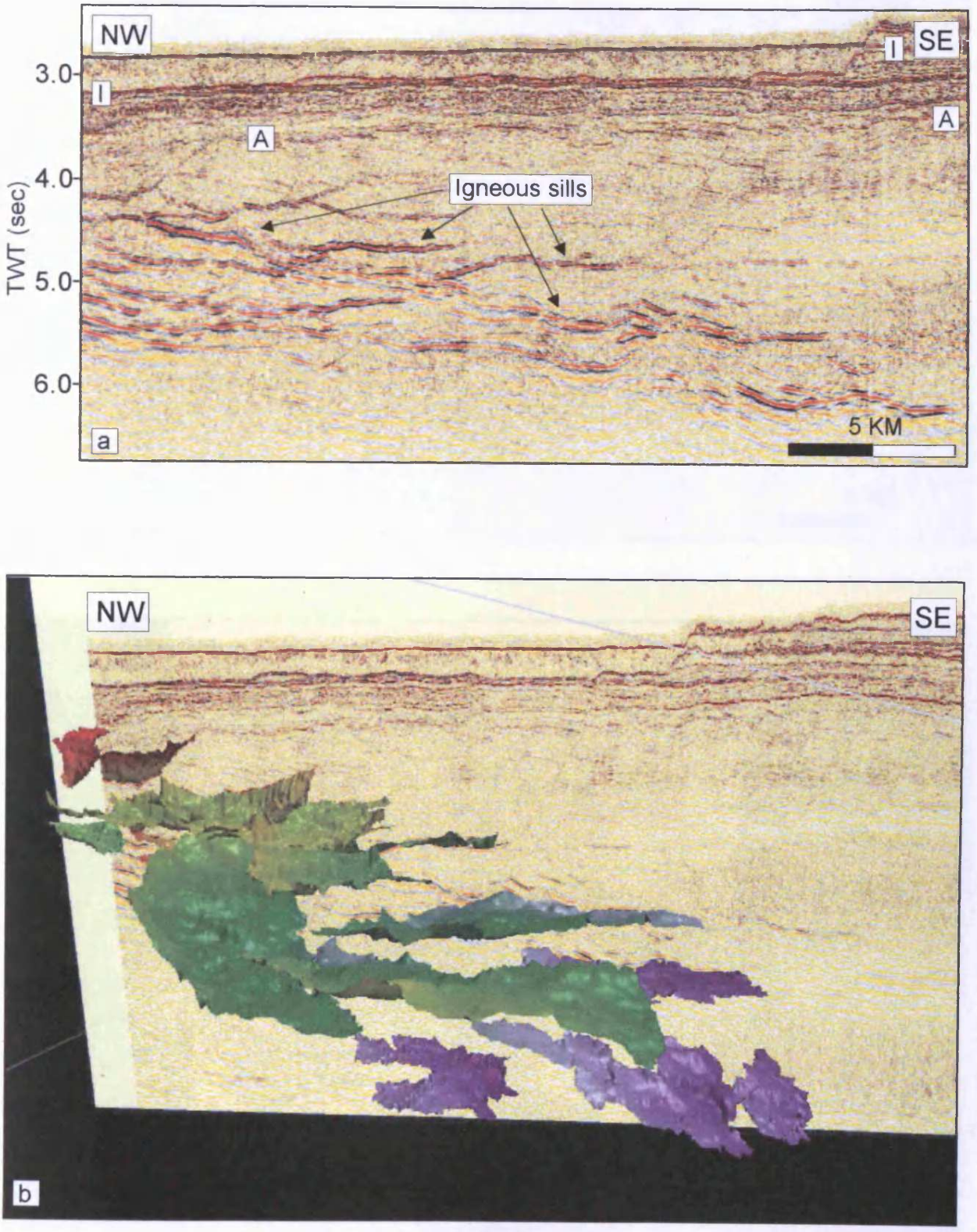

Fig. 4.23 (a) Seismic section showing stacking of sills towards the northern part of the survey area. (b) Three-dimensional display showing the seismic section shown in Fig. 4.23a and stacking of sills towards the north. See Fig. 4.25 for line location.

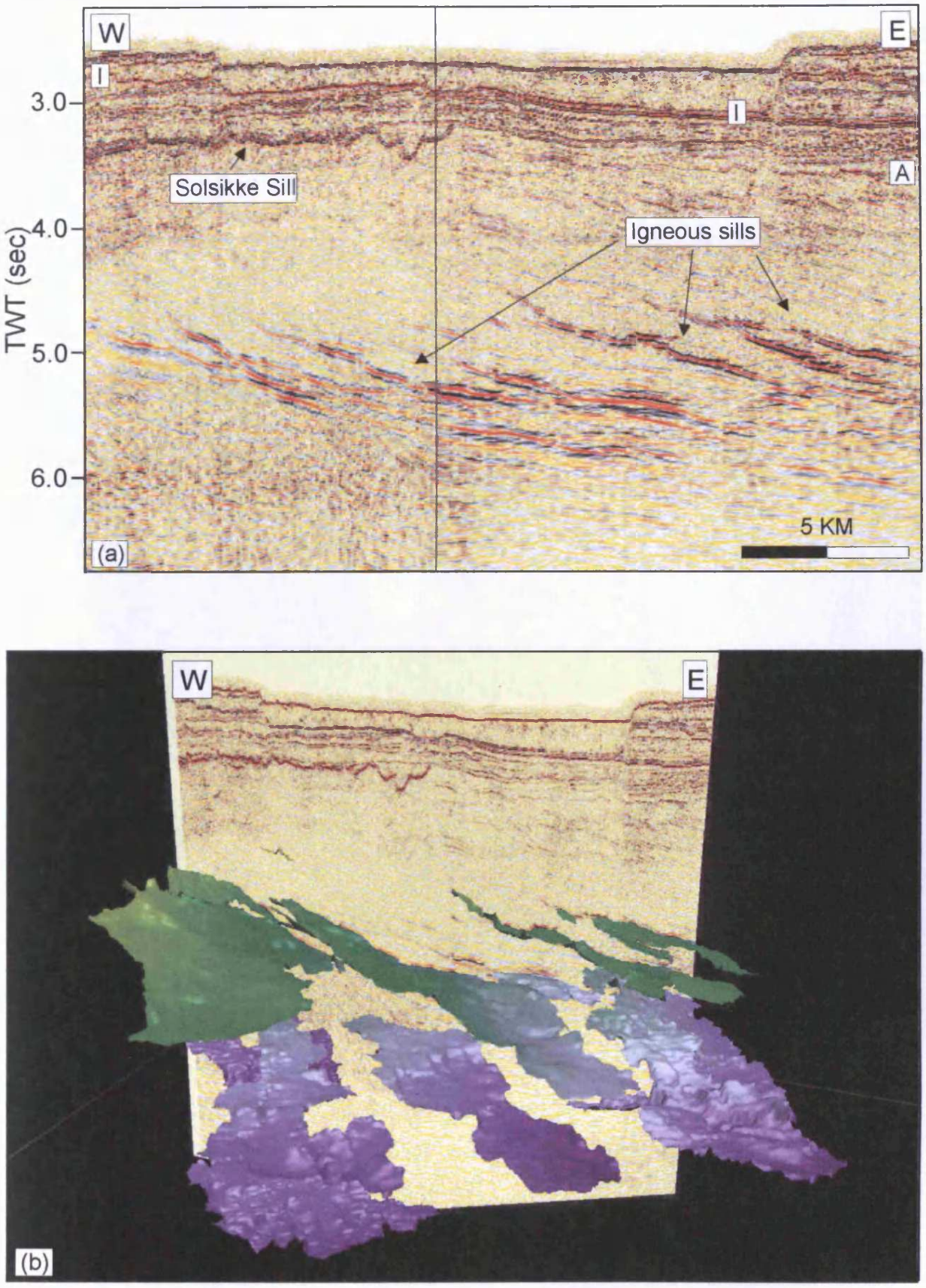

Fig. 4.24 (a) Seismic section showing eastward dipping sills. (b) Three-dimensional display showing seismic section shown in Fig. 4.24a and eastward dipping sill horizons. See Fig. 4.25 for line location.

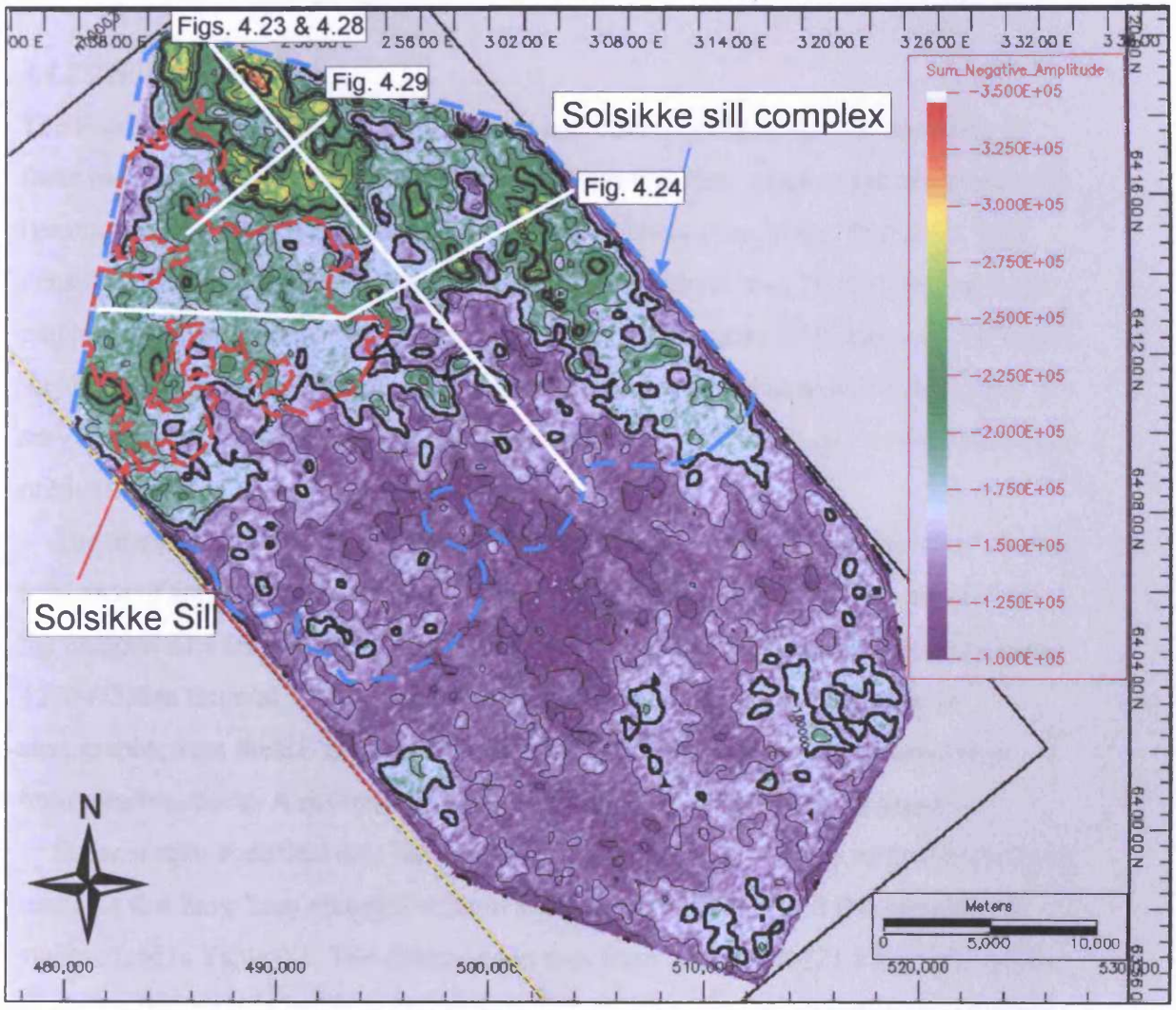

Fig. 4.25 Map showing extraction of maximum negative amplitude in a 4100-6500 ms window across the full survey area. The outline of the Solsikke Sill and the approximate outline of the Solsikke sill complex are superimposed on the map. The locations of the lines shown in Figs. 4.23, 4.24, 4.28 & 4.29 are shown on the map.

sum of negative amplitudes is greatest towards the north and east. The outline of the sill complex as it has been mapped from vertical sections has been superimposed on the map and there is good correlation between the extent of the sill complex and the area of high negative value. Variations in the magnitude of the value are interpreted to show areas of relatively high (high negative values) and relatively low (low negative values) density of sills suggesting that the density of sills is greatest towards the north and east.

4.4.2.2 Sill geometries

The Solsikke sill complex comprises many interconnected igneous sills and thirty of these have been mapped in detail in order to determine their geometrical characteristics (geometrical style, size, vertical relief) and spatial interconnectivity. Due to the high density of sills in the survey area it has not been possible to map all the sills, but those mapped are considered to be representative of the sill complex. The majority (19/30) of the mapped sills are not fully defined within the survey area, but extend beyond the survey boundary. This means that the obtained values for sill size and vertical relief are minimum values.

The mapped sills vary in size from a few km^2 to more than 100 km^2 and they cover a total area of approximately 600 km^2 within the Solsikke survey area. The majority of the mapped sills are seen below 6000 m and only a few of the mapped sills occur in the 4500-6000 m interval. The majority of the deeper sills transgress discordant to stratigraphy from the SE towards the NW (Fig. 4.23) and many can be classified as transgressive sheets. A maximum vertical relief of 2025 m has been measured.

Some simple statistical data have been collected for the thirty sills of the Solsikke sill complex that have been mapped in detail and these are described in this section and summarised in Table 4.1. The sills range in area from 3.5 km^2 to 121.8 km^2 and exhibit vertical relief ranging between 485 m and 2025 m. The average fully defined sill covers approximately 40 km^2 and has a vertical relief of 1050 m. The total mapped area of sills covers more than 1200 km^2. The sills are consistently thinner than the thickness of separability, i.e. < 70-75 m. If an average sill thickness of 50 m is assumed, the volume of the mapped part of the intruded complex would be 60 km^3. Using the same assumption it is estimated that individual sills range in magma volume between 0.18-6.1 km^3, with the average sill comprising a maximum volume of magma of 2 km^3. As mentioned above many of the sills are inclined sheets and these transgress at 4-7°. The deepest mapped sill transgresses from a present-day depth of more than 9 km and the

sill	area (km2)	volume (km3)	max Z (ms)	min Z (ms)	v. r. (ms)	v. r. (m)	cont. seabed (ms)	empl. depth (ms)	empl. depth (m)
1	102.5	5.13	5489	4159	1330	1995	2996	2493	3739.5
2	76.5	3.83	5218	4359	859	1288.5	3076	2142	3213
3	11.7	0.59	5082	4343	739	1108.5	3068	2014	3021
4	61.8	3.09	5307	4274	1033	1549.5	3164	2143	3214.5
5	34.9	1.75	4471	4096	375	562.5	3092	1379	2068.5
6	24	1.20	5121	4141	980	1470	3164	1957	2935.5
7	41.8	2.09	4548	3959	589	883.5	3160	1388	2082
8	33.8	1.69	4992	4014	978	1467	3076	1916	2874
9	8	0.40	4444	4257	187	280.5	3184	1260	1890
10	22.2	1.11	4273	3592	681	1021.5	3236	1037	1555.5
11	46.8	2.34	5610	4576	1034	1551	3256	2354	3531
12	5.9	0.30	3865	3475	390	585	3224	641	961.5
13	75.8	3.79	5703	4353	1350	2025	3088	2615	3922.5
14	20.9	1.05	5379	4751	628	942	3216	2163	3244.5
15	9.5	0.48	5081	4655	426	639	3256	1825	2737.5
16	86	4.30	5392	4406	986	1479	3164	2228	3342
17	31	1.55	5177	4736	441	661.5	3244	1933	2899.5
18	4.9	0.25	4844	4375	469	703.5	3272	1572	2358
19	54.4	2.72	6250	5394	856	1284	3008	3242	4863
20	49.8	2.49	6166	5384	782	1173	2956	3210	4815
21	28.5	1.43	6276	5684	592	888	2876	3400	5100
22	102	5.10	5671	4402	1269	1903.5	3056	2615	3922.5
23	17.2	0.86	6144	5770	374	561	2976	3168	4752
24	51	2.55	6188	5251	937	1405.5	3112	3076	4614
25	62.7	3.14	6108	5282	826	1239	3200	2908	4362
26	9.6	0.48	5694	5340	354	531	3272	2422	3633
27	6.9	0.35	4726	4403	323	484.5	3208	1518	2277
28	3.5	0.18	4555	4138	417	625.5	3284	1271	1906.5
29	7.5	0.38	3867	3405	462	693	3104	763	1144.5
solsikke sill	121.8	6.09	3519	3109	410	615	2952	567	850.5
average	40.43	2.02	5172	4469	703	1053.9	3131	2041	3061

Table 4.1 Summary of statistical data for 30 sills of the Solsikke sill complex. Depth conversion done using Vsed = 3.0 km/s, see Chapter 2. Max Z: maximum emplacement depth, min Z: shallowest emplacement depth, v.r.: vertical relief, cont. seabed: depth of seabed at time of intrusion, empl. depth: emplacement depth below contemporaneous seabed.

uppermost tip of the shallowest mapped sill (Solsikke Sill, section 4.5) reaches a minimum present-day depth of approximately 4.5 km, which means that the sill complex covers more than 4.5 km of compacted vertical section. At the time of intrusion (approximated by horizon E, see Chapter 6) the deepest mapped sill intruded at a depth of 4.8 km (compacted), whilst the shallowest intrusion reached a minimum depth of just over 200 m below the contemporaneous seabed. The graph shown in Fig. 4.26a shows sill area plotted against vertical relief on the sills mapped within the Solsikke survey area. The graph shows moderate correlation (R^2 = 43%) between area and vertical relief, with the larger sills also exhibiting the greatest vertical relief. The graphs shown in Figs. 4.26b & 4.26c suggest that there is very poor correlation between sill area and maximum depth of emplacement (R^2 = 6%) and between maximum depth of emplacement and vertical relief (R^2 = 23%). The correlations between sill area and vertical relief and between sill area and maximum emplacement depth are both affected by a point that plots off trend (labelled X in Fig. 4.26). This point represents the Solsikke Sill (section 4.5), which exhibits a very large area compared to other sills with similar vertical relief and emplacement depth. Eliminating the Solsikke Sill from the plots causes a large increase in the correlation values between sill area and vertical relief (new R^2 = 70%) and between sill area and maximum emplacement depth (new R^2 = 25%). The correlation between maximum emplacement depth and vertical relief remains practically the same (new R^2 = 21%). The implications of this will be further discussed in section 4.5.5.2 and in Chapter 7.

4.4.2.3 Sill complex geometry

The map shown in Fig. 4.27 shows the planview geometry of 29 of the sills that have been mapped in the survey area. The outline of the Solsikke Sill (section 4.5.3.2) has been superimposed on the map, but the time-structure map of the sill itself is not shown because it covers a very large area (122 km^2) and would cover up much of the underlying sill complex. A high degree of overlap is seen within the sills complex, particular to the north and east where the sill density appears to be greatest (section 4.4.2.1).

The vertical seismic sections shown in Figs. 4.23 & 4.24 illustrate the cross-sectional geometry of the sill complex. The section shown in Fig. 4.23 is an inline and trends NNW-SSE it shows an increase in the number of sills towards the north. The increase in sills is seen both as an increase in the density of sills and as an expansion of the vertical

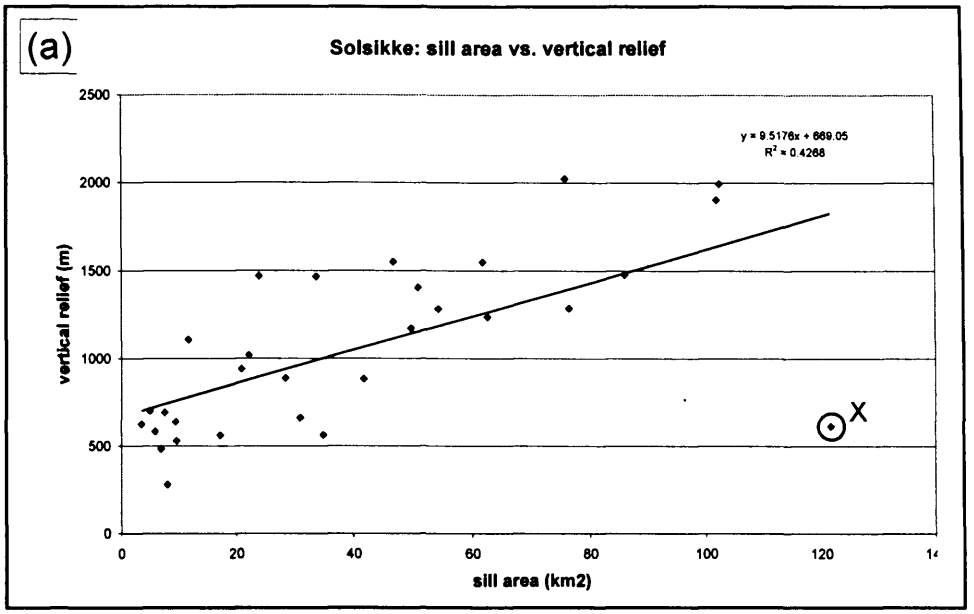

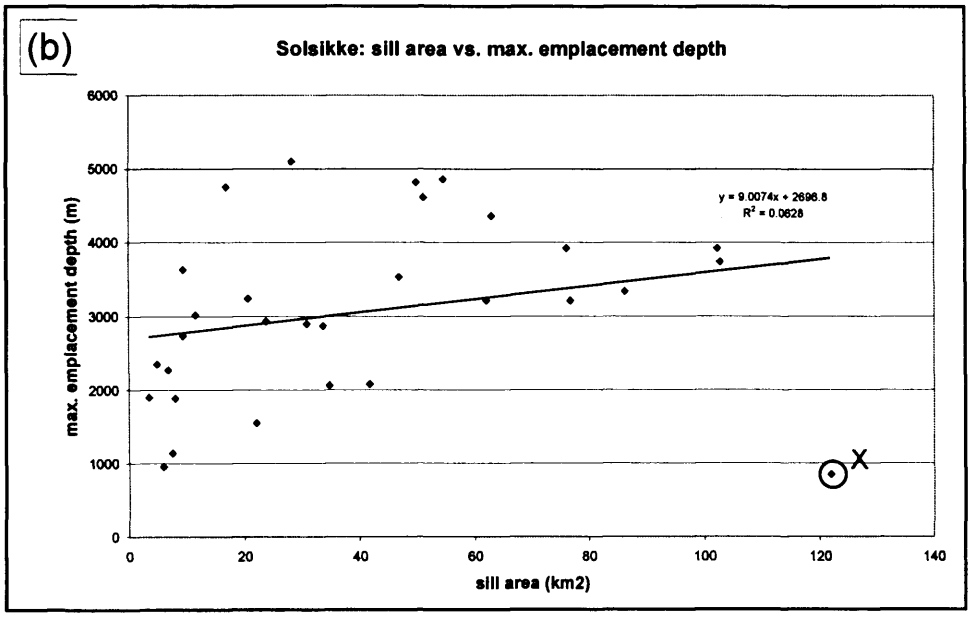

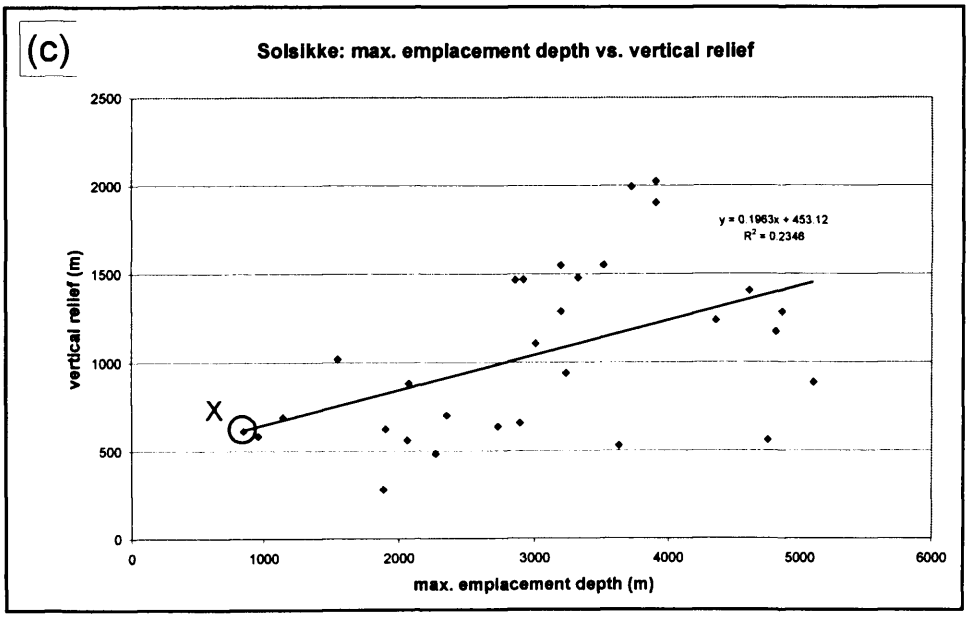

Fig. 4.26 Graphs illustrating statistical data for 30 sills of the Solsikke sill complex. (a) sill area vs. vertical relief. (b) sill area vs. maximum emplacement depth. (c) maximum emplacement depth vs. vertical relief. Depth conversion done using Vsed = 3.0 km/s, see Chapter 2.

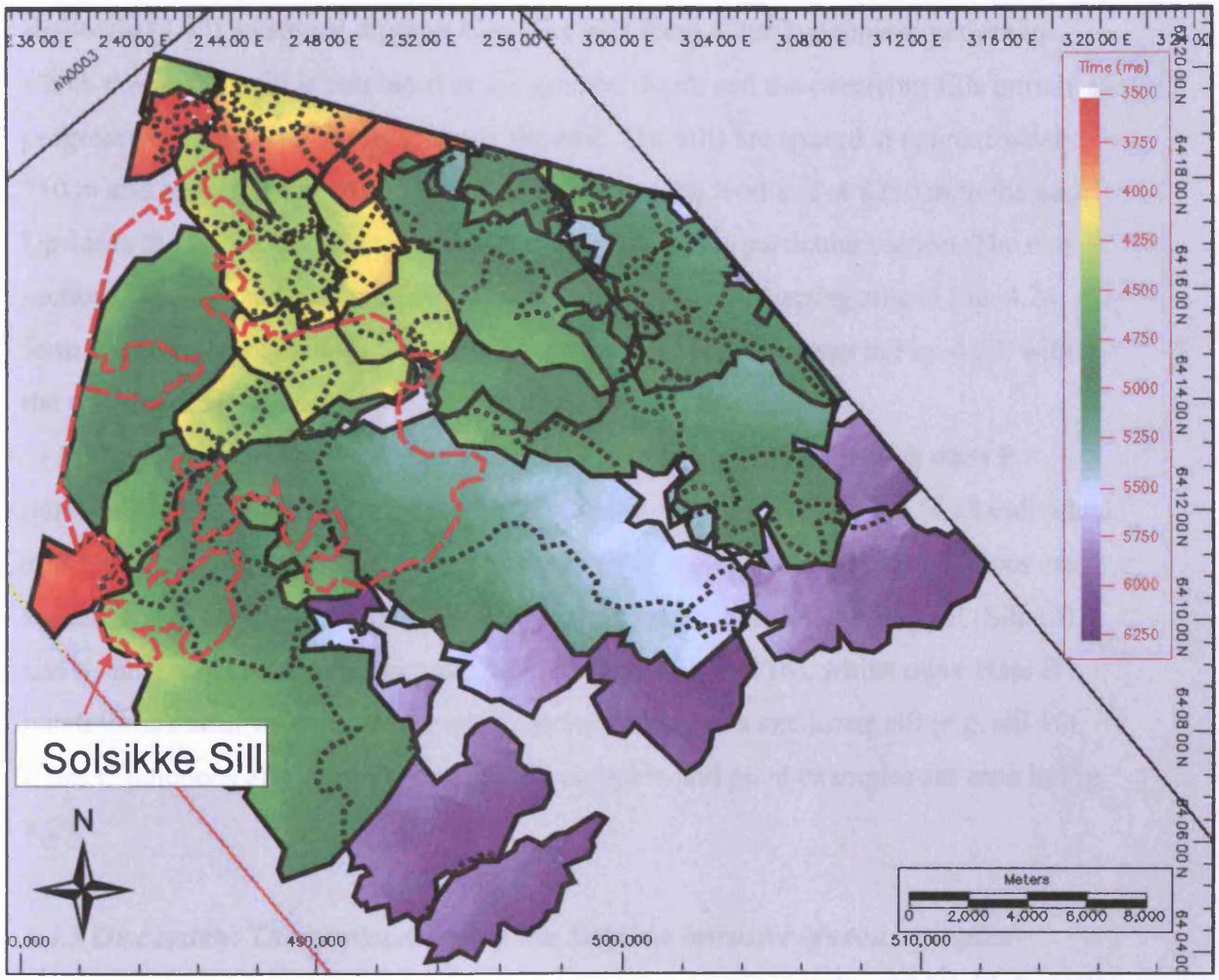

Fig. 4.27 Map showing the distribution of 29 sills of the Solsikke sill complex. The outline of the shallowly emplaced Solsikke Sill has been superimposed on the map.

section where sills occur. Towards the south the sills are seen in the 9750-8250 m interval, whilst further north they span the 8625-5250 m interval. The sills are interlinked and organised into layers. The layers are spaced at approximately 750 m and are slightly asymmetrically organised around a shallowly (5°) south-dipping central axis represented by a sill. The E-W trending traverse section shown in Fig. 4.24 has a contrasting appearance compared to the NNW-SSE trending section. It shows at least 7 shallowly (4-7°) westward dipping sills. The sills form a 'back-stepping' pattern in which the western sill is emplaced at the greatest depth and the overlying sills intrude at progressively shallower levels towards the east. The sills are spaced at approximately 750 m and appear to tip out at a depth of 9000 m to the west and at 8250 m to the east. Upwards the sills tip out at approximately 6750 m on this particular section. The two sections intersect and a comparison of them shows that the dipping sills in Fig. 4.24 form progressively shallower layers within the layered system seen in Fig. 4.23, with the western-most sill forming the deepest layer.

Many sill-sill junctions are seen within the Solsikke sill complex with class B junctions being the most abundant. On the seismic section shown in Fig. 4.28 individual sills have been traced and form a stacked pattern in which many class B junctions are seen. Some of these class B junctions are seen between an axial, dipping sill (Sill 13) and a number of sills that appear to branch off this (e.g. sill 16), whilst other class B junctions are seen where a deeper sill links to the base of a shallower sill (e.g. sill 11). Class C junctions also occur within the sill complex and good examples are seen in Fig. 4.29.

4.4.3 Discussion: The emplacement of the Solsikke intrusive igneous complex

As shown above, the Solsikke igneous complex comprises more than 30 interlinked sills that cover an area of 600 km^2 within the survey area, and span a vertical section of more than 4.5 km of compacted sediments. In this section some of the likely controls upon the geometry, emplacement, and build-up of the Solsikke sill complex are discussed and relevant outcrop analogues are briefly described.

The majority of the deeper sills, especially those mapped in the eastern part of the survey area, transgress towards the north-west (Fig. 4.24). This could be related to the presence of the Solsikke Dome, with the sills rotating and adopting their dip towards the SE as the dome evolved.

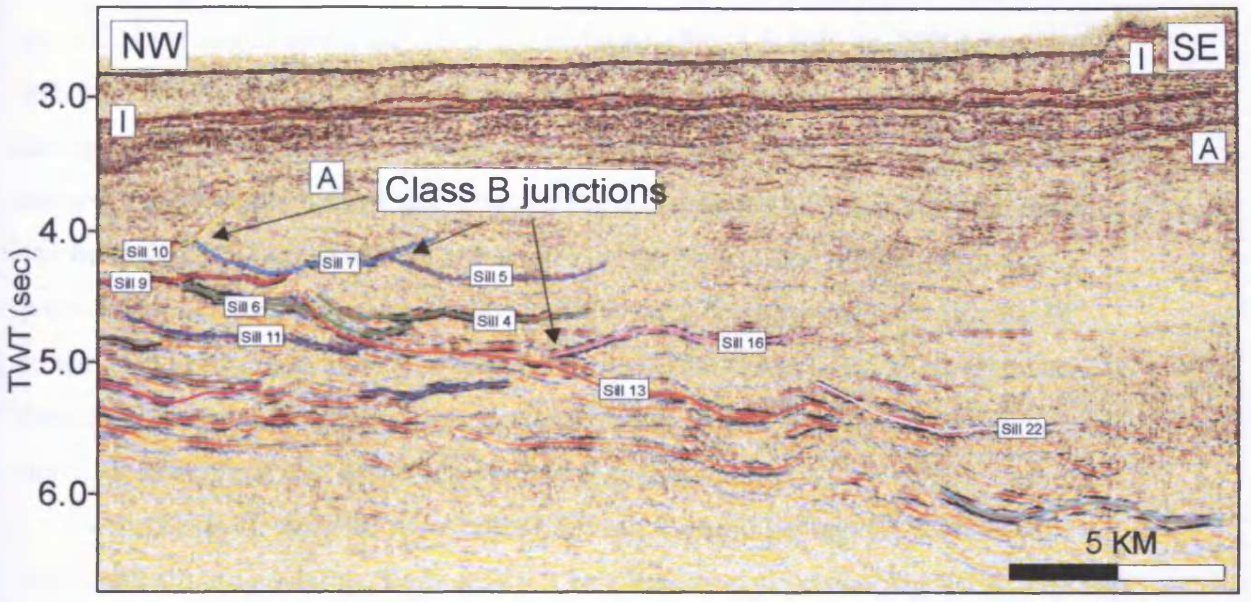

Fig. 4.28 Seismic section showing class B junctions between sills of the Solsikke sill complex. See Fig. 4.25 for line location.

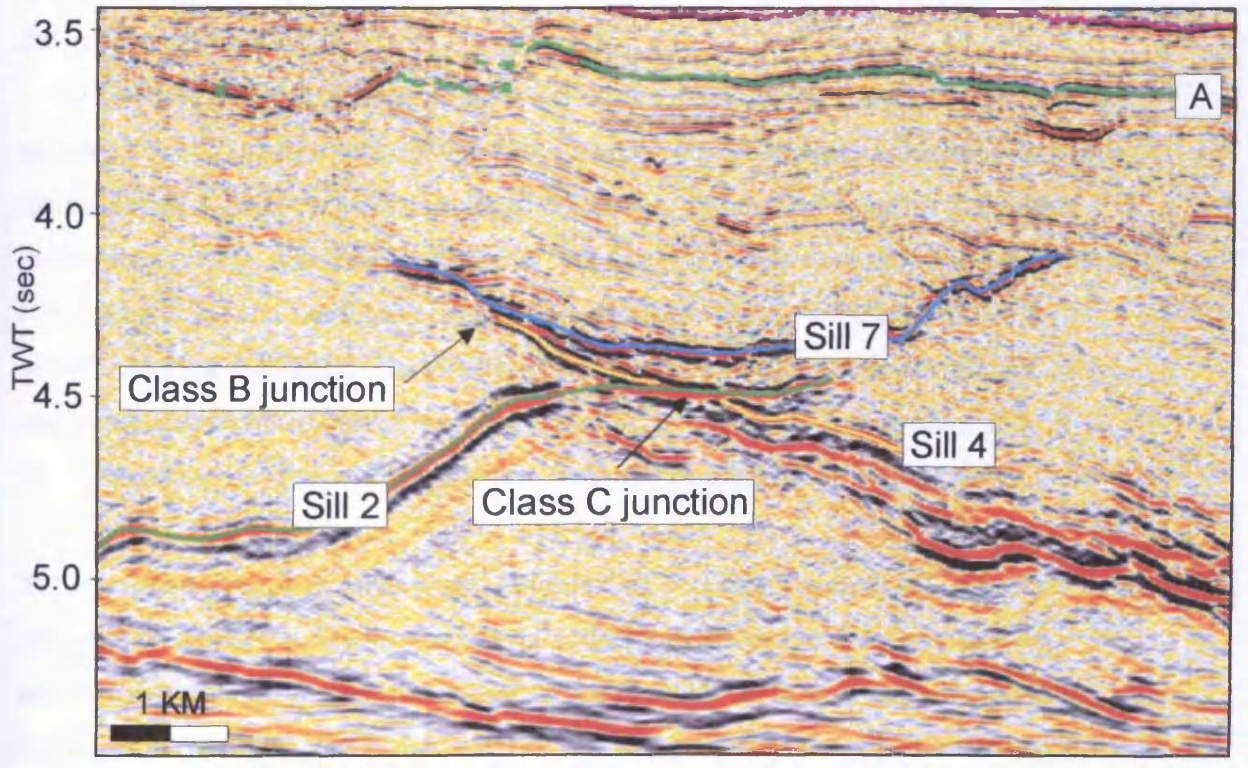

Fig. 4.29 Sill 2 cross-cuts sill 4 forming a class C junction. Sill 4 is linked to sill 7 through a class B junction. See Fig. 4.25 for line location.

The source of the sill complex is poorly constrained. The upwards stepping from east to west of the igneous sills within the Solsikke sill complex is in agreement with more general observations along the Norwegian Margin (Fig. 4.5; Brekke, 2000), where sills in both the Møre and Vøring Basins are seen to step upwards from their stratigraphically deepest point (?Aptian) to the east to their highest level (Maastrichtian) towards the north and north-west. This has been interpreted to suggest that the sills were fed from a source located in the central parts of the basins. The limited coverage provided by the 3D seismic data does not allow for this suggestion to be rigorously tested. However, in a later section it will be shown that dykes are likely to be present directly underlying the imaged part of the sill complex and these are suggested to have played at least some role in feeding parts of the sill complex.

The Solsikke sill complex has a highly complex spatial geometry with multiple layers and sill-sill junctions, leading to a 'Christmas tree' structure (Fig. 4.28). The high level of interconnectivity within the sill complex and the lack of any clearly imaged vertical dykes suggests that the build up of the sill complex relied heavily on deeper sills acting as feeders for shallower sills. Surfaces of easy parting in the form of pre-existing structures and lithological boundaries most likely played an important part in the development of layers and transgression of the sill complex (see Chapter 7 for further discussion).

The layered and interconnected geometry of the Solsikke sill complex is not unique to this particular igneous intrusive complex and similar geometries have been described from classical igneous provinces such as the Karoo, South Africa, and in classical textbook examples, e.g. Press & Siever, 1993. Field sketches from the Karoo by du Toit (1920; Fig. 1.9a) and Lombard (1952; Fig. 1.9b) show highly interconnected sill complexes from the Karoo. These sketches show a complex geometry in which dykes and transgressive sill segments connect layers of concordant and discordant sills. A similar geometry is seen in the schematic textbook example shown in Fig. 1.9c.

The interpretation of the Solsikke sill complex has revealed a typical sill complex geometry in which multiple layers of concordant and discordant sills are linked by transgressive sills and probably near-vertical dykes. The geometry of the sill complex may have been influenced by the Solsikke Dome that formed as a result of inversion that was initiated prior to intrusion and continued during the emplacement of the sill complex. The feeder for the sill complex is poorly constrained, but it has been

suggested that the main feeder for the sill complex was located in the central part of the Møre Basin and that the sill complex build upwards towards the north and north-west.

4.5 The Solsikke Sill

4.5.1 Introduction

The Solsikke Sill dominates the shallow section of the northern part of the Solsikke survey (Figs. 4.25 & 4.30). The sill is seen at a present-day depth of approximately 4665-5275 m, is large, covering an area of more than 120 km^2, and has a maximum volume of approximately 6 km^3 (assuming a maximum average thickness of 50 m). It is clearly discordant with the intruded stratatigraphy and has a vertical relief of approximately 600 m. In the northern and western part of the survey area the Solsikke Sill is, locally, linked to underlying deeper sills of the Solsikke sill complex through discordant and steeply transgressing sill reflections that are seen to intersect the base of the Solsikke Sill reflection (Fig. 4.31). Based on the presence of sill emplacement related extrusive mounds at horizon D (see Chapter 6) it is estimated that the sill was intruded at a depth of 850-225 m below the contemporaneous seafloor into Upper Cretaceous and Lower Paleogene sediments during the Paleocene. The seismic appearance, geometry, and stratigraphic and structural context of the Solsikke Sill are described in the following sections.

4.5.2 Seismic appearance of the Solsikke Sill

4.5.2.1 Acoustic character

The Solsikke Sill reflector gives rise to a high amplitude seismic reflection that is easily distinguished from the surrounding stratal reflections. The sill reflector appears as a peak-trough-peak reflection configuration in which the central trough displays a higher amplitude than the surrounding peaks. Considering the resolution of the data it is estimated that the sill is < 50 m thick.

The sill reflection exhibits hardly any visible changes in amplitude across its extent. However, locally, the reflection configuration (peak-trough-peak configuration) varies slightly in width and this is interpreted to indicate slight variations in sill thickness. Also, where the reflection is steeply dipping (near-vertical) or slightly offset the amplitude is reduced and it can be difficult to determine whether the reflector is present or not.

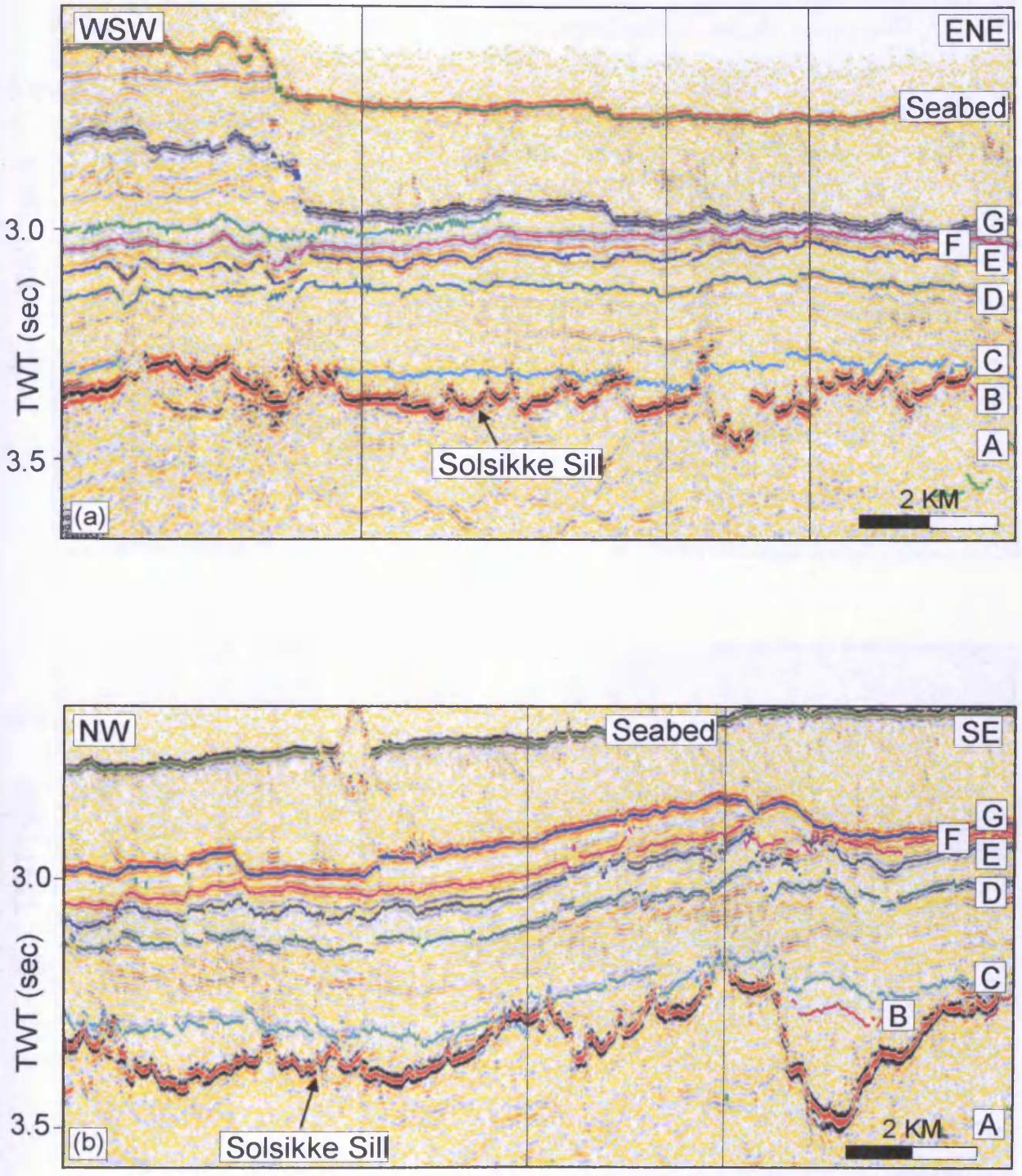

Fig. 4.30 Seismic sections illustrating the cross-sectional geometry of the Solsikke Sill. (a) WSW-ENE trending section. (b) NW-SE trending section. See Fig. 4.32 for line locations.

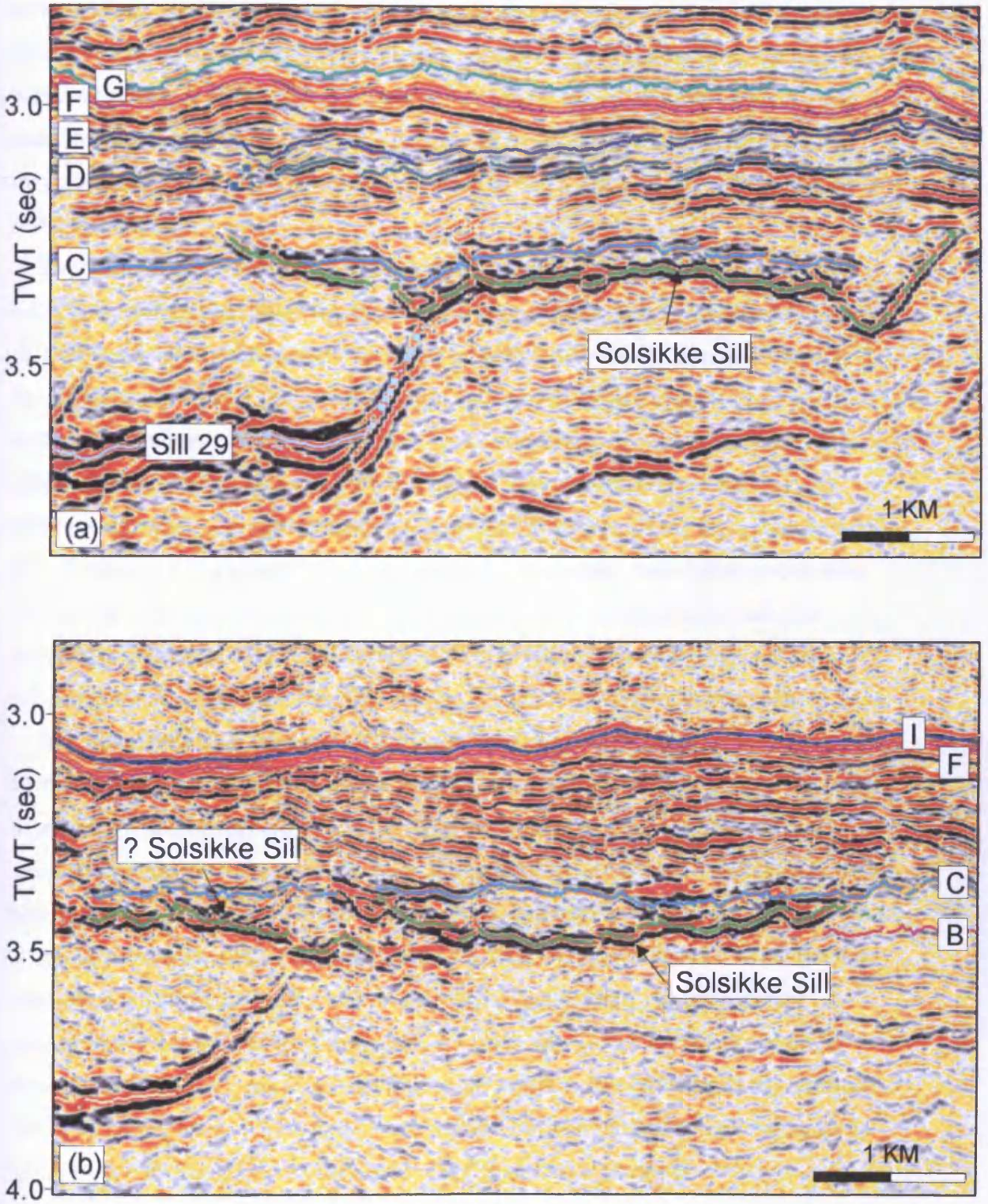

Fig. 4.31 The Solsikke Sill is linked to deeper sills of the underlying Solsikke sill complex. (a) To the west the Solsikke Sill is linked to the underlying sill 29. On the section shown in (b) two high amplitude reflections are seen. The upper reflection forms part of the Solsikke Sill. The lower reflection may also be part of the Solsikke Sill, but the reflection is not link to the Solsikke Sill within the survey area. See Fig. 4.32 for line locations.

4.5.2.2 Appearance on vertical seismic profiles

The Solsikke Sill has a highly segmented cross-sectional geometry that is distinctively different from the simple, smooth, and concave upwards cross-sectional sill geometries, interpreted in T67 (Chapter 3). This section provides a general description of the cross-sectional geometry of the Solsikke Sill and introduces a number of descriptive terms to assist in the description of complex igneous sills in vertical profiles, in general. The more detailed and three-dimensional geometry of the Solsikke Sill will be described later in this section.

The Solsikke Sill appears as a number of interlinked concordant and discordant reflection segments separated by discontinuities on vertical seismic profiles. Three different types of discontinuities have been interpreted between adjacent segments of the sill reflector; class A junctions (often in the form of steps that show some vertical juxtaposition without showing vertical reflection separation), class B junctions, and offset. The latter term, offset, is here used to describe the relationship between two adjacent segments of the sill reflection that are unlinked and clearly separated vertically. Offset adjacent sill segments often overlap in a lateral sense. Adjacent segments may also be fully separated laterally by horizontal gaps where the high amplitude sill reflection is not seen. Along the boundary between two adjacent segments of the sill reflection a class A junction may change into a class B junction or into an offset.

Individual reflection segments of the Solsikke Sill are distinguished, in cross-section, by the three types of discontinuities described above and these segments constitute sill segments of the Solsikke Sill. The sill segments display a range of cross-sectional geometries and sizes as seen on the seismic sections shown in Fig. 4.30. Many of the sill segments have symmetrical concave upwards cross-sectional geometries that vary in width between 200-1000 m and have cross-sectional vertical relief of 10-150 m. Other discordant sill segments have more asymmetrical, transgressive cross-sectional geometries. The concordant sill segments are generally more continuous and more laterally extensive than the more discordant sill segments on vertical seismic profiles. Adjacent sill segments are commonly linked and form larger, often, concave upwards geometries with vertical cross-sectional relief of several 100 metres.

4.5.3 Seismic mapping and general map description

The high degree of segmentation of the Solsikke Sill evident from the vertical appearance of the sill reflection described above, is unusual and suggests that the sill

has an exceptionally complex three-dimensional geometry that differs from the commonly observed simple saucer-shaped geometrical form recognised on other 3D seismic datasets (e.g. T67: Chapter 3) and in the Karoo Basin. In this section the process of mapping the Solsikke Sill is first described, followed by a description of the detailed planview and three-dimensional geometry and morphology of the Solsikke Sill and individual sill segments.

4.5.3.1 Seismic mapping of the Solsikke Sill

Interpreting the segmented Solsikke Sill reflection required a careful and systematic picking approach in order to resolve the three-dimensional geometrical complexity of the sill. The sill reflection (central trough of the peak-trough-peak configuration) was interpreted on every 10^{th} crossline and inline across the area covered by the sill. This picking interval was chosen because it provided a good coverage of the sill and ensured that most sill segments were interpreted on several lines, both in the inline and crossline direction. However, locally, more detailed interpretation was required, due to an increase in the complexity of the segmentation of the reflection, and the line spacing was reduced.

Within the Solsikke Sill there are many examples where adjacent offset sill segments slightly overlap (e.g. Fig.4.30a). This provides an interpretational challenge because the seismic interpretation software does not allow two different Z-values to be ascribed to one XY-coordinate on the seismic grid. In order to overcome the problem of overlapping reflections it was decided to follow the more dominant of the overlapping reflections during interpretation. In most cases the shallower of the overlapping reflections was the dominant reflection. This is likely to be related to loss of frequency and thus ability of the seismic data to resolve deeper sill segments underlying the shallower segments (Chapter 2). The zones of overlap are narrow relative to the width of the sill segments and the simplification of the geometry of the sill introduced during the mapping is not thought to greatly distort the overall geometrical style adopted by the sill.

Following the line-based interpretation the resultant interpreted seismic grid was autotracked and any obvious autotracking errors corrected. The edge of the sill is clearly defined by sudden termination of the high amplitude sill reflection (Fig. 4.31), and it was mapped in detail through line-by-line correction of the autotracked map. The resultant time-structure map of the Solsikke Sill shows the outline of the sill and reflects

the internal geometry as accurately as it is possible when mapping the reflection as a single horizon and considering the limitations of the software.

4.5.3.2 Map description: Sill outline and sub-division

The overall shape and geometrical style exhibited by the Solsikke Sill is clearly defined by seismic attribute maps. The time-structure map of the Solsikke Sill (Fig. 4.32) shows a generally north-westward dipping surface with a vertical relief of approximately 600 m that extends beyond the survey boundary in areas towards the north and west.

The periphery of the sill is highly irregular and displays several small, elongated protrusions, measuring approximately 1 by 1.5 km that extend away from a more regularly shaped outline. Locally, the outline displays linear segments oriented NNW-SSE and NE-SW, which is parallel to the dominant trends adopted by fault sets A and B in the survey area.

The mapview geometry of the sill forms a semi-continuous body that comprises four irregularly shaped subareas (A-D; Fig. 4.32) that are separated by neck regions where the sill is narrow compared to the immediately adjacent much larger and broader regions that form the subareas. The sill reflection is generally continuous across the neck regions between adjacent subareas. However, between subareas A and C the sill reflection is locally slightly offset. The neck region between subareas A and D forms a narrow ridge with a vertical relief of approximately 100 m. The four subareas vary is shape and size, however, only subarea A is fully defined within the survey area. *Subarea A* forms the south-eastern and central part of the Solsikke Sill imaged by the seismic data. It has an irregular periphery and is linked to subarea C to the west and subarea D to the north. The sub-area measures 6 by 8 kilometres, with the longest axis oriented NW-SE, and covers approximately 65 km^2. The imaged part of *subarea B* is relatively small, slightly E-W elongated, measuring 3 by 5.5 kilometres, and covers an area of 15.5 km^2. It forms the south-western part of the sill and is linked to subarea C to the north. *Subarea C* is located to the west and the western boundary of the sub-area extends to the western periphery of the seismic survey. It measures 6 by 4 kilometres, is elongated N-S, and covers an area of 20 km^2. It is linked to subarea B to the south and subarea A to the east. *Subarea D* is the most northern of the four sub-areas and is linked to subarea A to the south. It extends to the survey boundary to the north and west. The mapped part of the subarea measures 5 by 6 kilometres and covers 24.5 km^2.

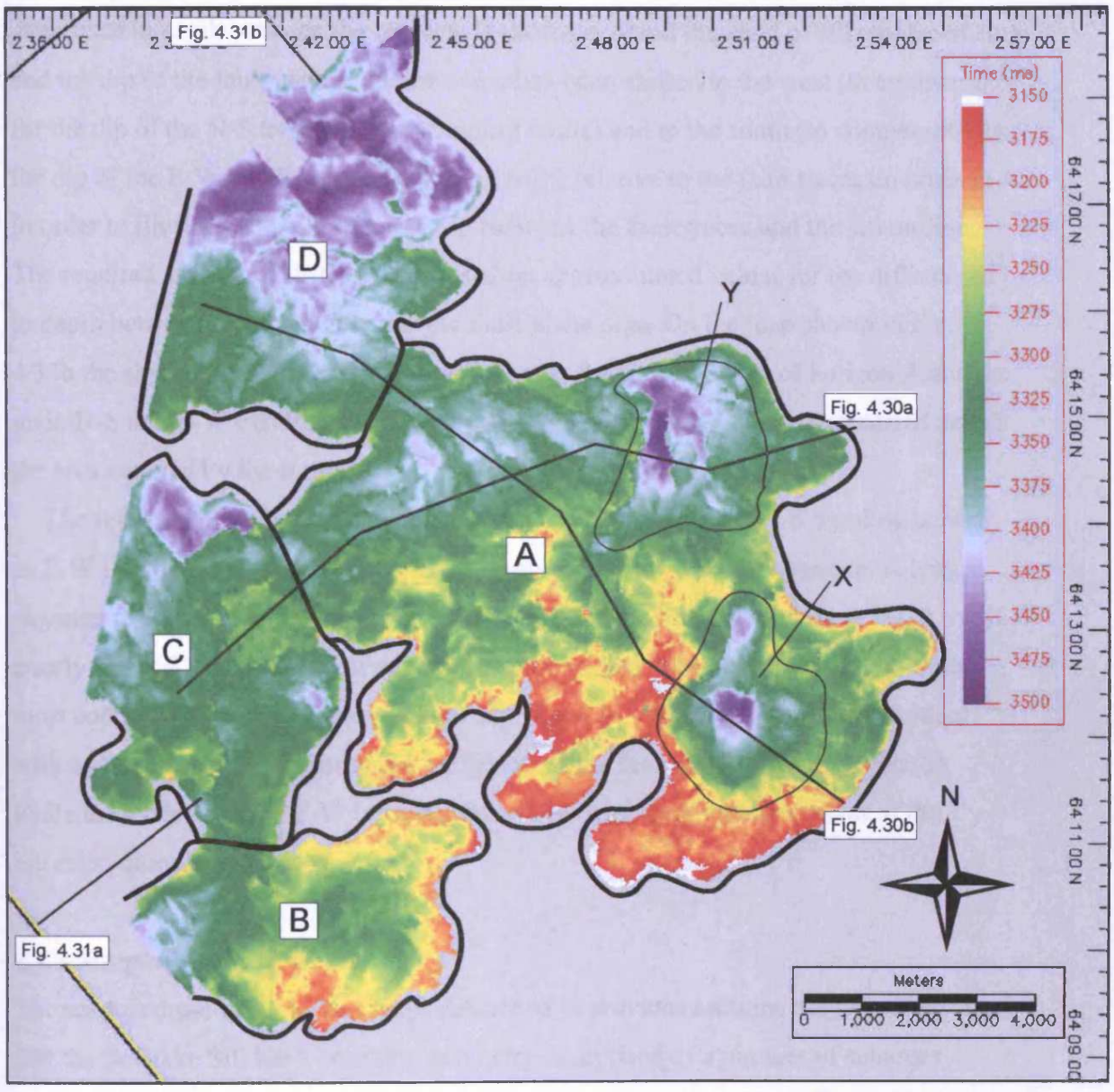

Fig. 4.32 Time-structure map of the Solsikke sill. The sill has been sub-divided into four sub-areas (A-D) separated by narrow neck regions. Two saucer-shaped depressions within the Solsikke Sill are labelled X and Y. Note line locations for Figs. 4.30 & 4.31.

In Fig. 4.33a, the Solsikke Sill has been superimposed on a time-dip map of horizon A. The intrusion is not emplaced at the level of horizon A, but at a depth of 4665-5275 m and thus approximately 300 m above horizon A. Because the faults are dipping the location of the intrusion relative to the fault traces as they are seen on horizon A differ from the true relationship at the level of intrusion. In order to compensate for the difference in depth between the two levels (horizon A and the level of sill emplacement) and the dip of the fault planes, the intrusion has been shifted to the west (to compensate for the dip of the N-S trending, west dipping faults) and to the south (to compensate for the dip of the E-W trending, south dipping fault) relative to the fault traces on horizon A in order to illustrate the true relationship between the fault traces and the sill outline. The required amount of shifting was based on approximated values for the differences in depth between the two levels and the fault plane dips. On the map shown in Fig. 4.33b the shifted intrusion is superimposed upon the time-dip map of horizon A and the main N-S and E-W trending faults seen in the area have based been extrapolated across the area covered by the intrusion.

The resultant map shows local correspondence of fault traces (N-S trending as well as E-W trending) and linear trends in the periphery of the sill. For example: A long segment of the eastern periphery of the intrusion is coincident with fault D (1). A very poorly defined fault to the west of fault A is coincident with the eastern extent of the most south-western part of the intrusion (2). The E-W trending fault Y is coincident with a long segment of the northern periphery of the main part of the intrusion (3), while the more southern E-W trending fault X is coincident with the extent of the intrusion more locally (4a & 4b).

4.5.4 Morphological elements

The seismic cross-sections and maps described in previous sections not only illustrate that the Solsikke Sill has a complex geometry comprised of a number of subareas connected by narrow necks, but also suggest that the Solsikke Sill exhibits a highly irregular internal morphology. In this section the cross-sectional and planview geometry of the Solsikke Sill are compared in order to better illustrate the three-dimensional complexity of the sill and highlight its dominant morphological sub-elements.

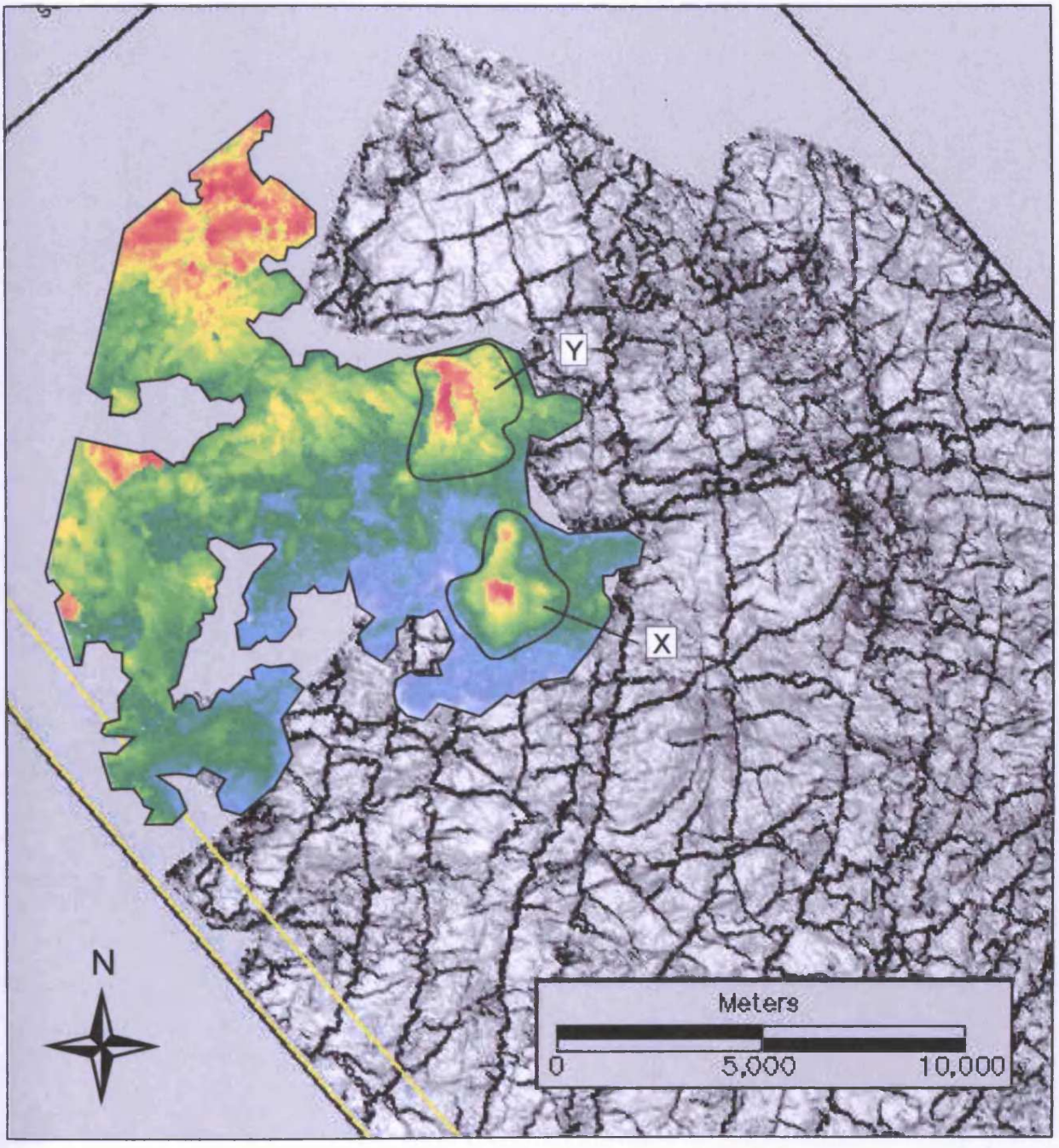

Fig. 4.33a Solsikke Sill time-structure map superimposed on a time-dip map of Horizon A. X and Y indicate two saucer-shaped depressions within the Solsikke Sill.

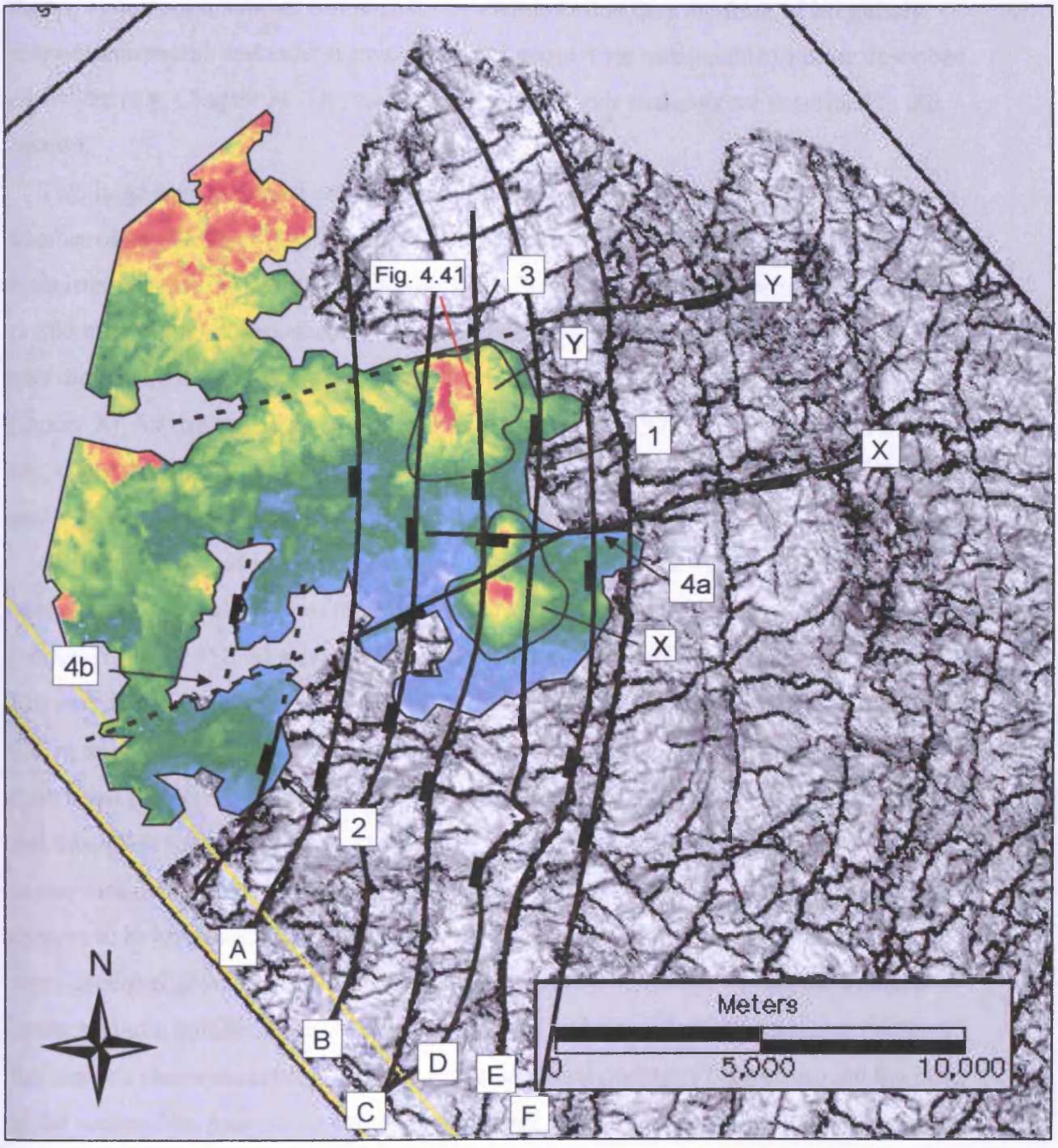

Fig. 4.33b Solsikke Sill time-structure map superimposed on a time-dip map of Horizon A. The map shows some correspondence between linear segments on the periphery of the sill and the fault trends. The saucer-shaped depressions X and Y are indicated and seen to have their deepest points near fault intersections. Note the line locations for Fig. 4.41.

4.5.4.1 Saucer-shaped depressions

From the above descriptions of the cross-sectional and mapview geometries of the Solsikke Sill it is evident that it has a highly complex geometry that differs from that of the more simple saucer-shaped geometries described from T67 (Chapter 3). However, the sill comprises a number of internal sub-elements that take the form of irregularly shaped depressions that exhibit saucer-shaped geometries comparable to those described elsewhere (e.g. Chapter 3). The main saucer-shaped sub-elements are described in this section.

Two large saucer-shaped sub-elements (location X and Y; Figs. 4.33 and 4.34) and a number of smaller ones (e.g. location Q and P) can be seen on the Solsikke Sill. They have irregular outlines, vary in width between 2-4 km, and exhibit vertical relief of 100 to 280 m with the saucers-shaped elements that have the greatest diameters (X and Y) also displaying the greatest vertical relief (plot: X, Y, Q, P). The saucer at location X (saucer X), for example, has a vertical relief of more than 375 m and a diameter of 4 km, while the smaller circular saucer at location Q (saucer Q) has a diameter of 2 km and only exhibits a vertical relief of less than 150 m.

Saucer X is located in the southern part of subarea A and is the most well defined saucer-shaped sub-element of the Solsikke Sill. It consists of a main central depression (vertical relief of 450 m) with a second minor localised low (vertical relief of 225 m). The two depressions are separated by a narrow (<300 m) ridge with a vertical relief of 225 m as shown on the north-south trending section seen in Fig. 4.35a. This figure also shows that the northern limbs of the two depressions are coincident with fault planes and transgress the stratigraphy. The southern limb of the main depression (to the south) is also discordant with startigraphy, while the southern limb of the northern depression appears to be concordant with the relatively poorly resolved stratigraphy. The NE-SW cross-sectional geometry of the saucer is shown in Fig. 4.35b shows that the saucer is comprised of a number of interlinked concordant and discordant sill segments that give the saucer a near-symmetrical stepped cross-sectional geometry centred around the base of the saucer. The base of the saucer is flat-lying and is flanked by two transgressive segments that transgress the stratigraphy at approximately 20° for 150 m before turning concordant. These concordant segments intrude for approximately 300 m before the reflection changes dip again and transgress, cross-cutting 120 m of stratigraphy. This pattern is repeated three times. The three-dimensional geometry of saucer X is shown in Fig. 3.36.

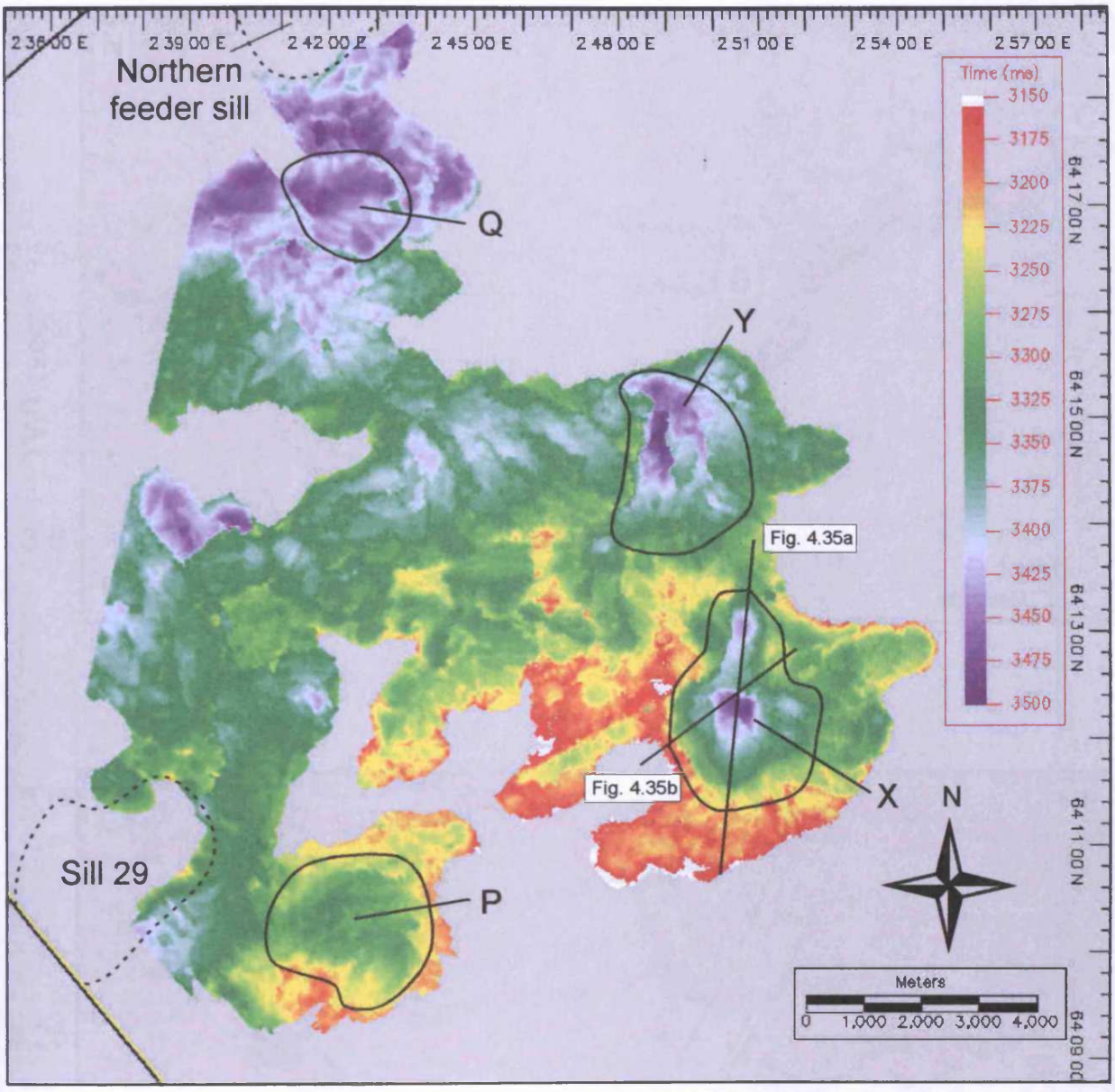

Fig. 4.34 Time-structure map of the Solsikke Sill showing the locations of saucer-shaped depressions X, Y, P, and Q. Note line locations for Fig. 4.35.

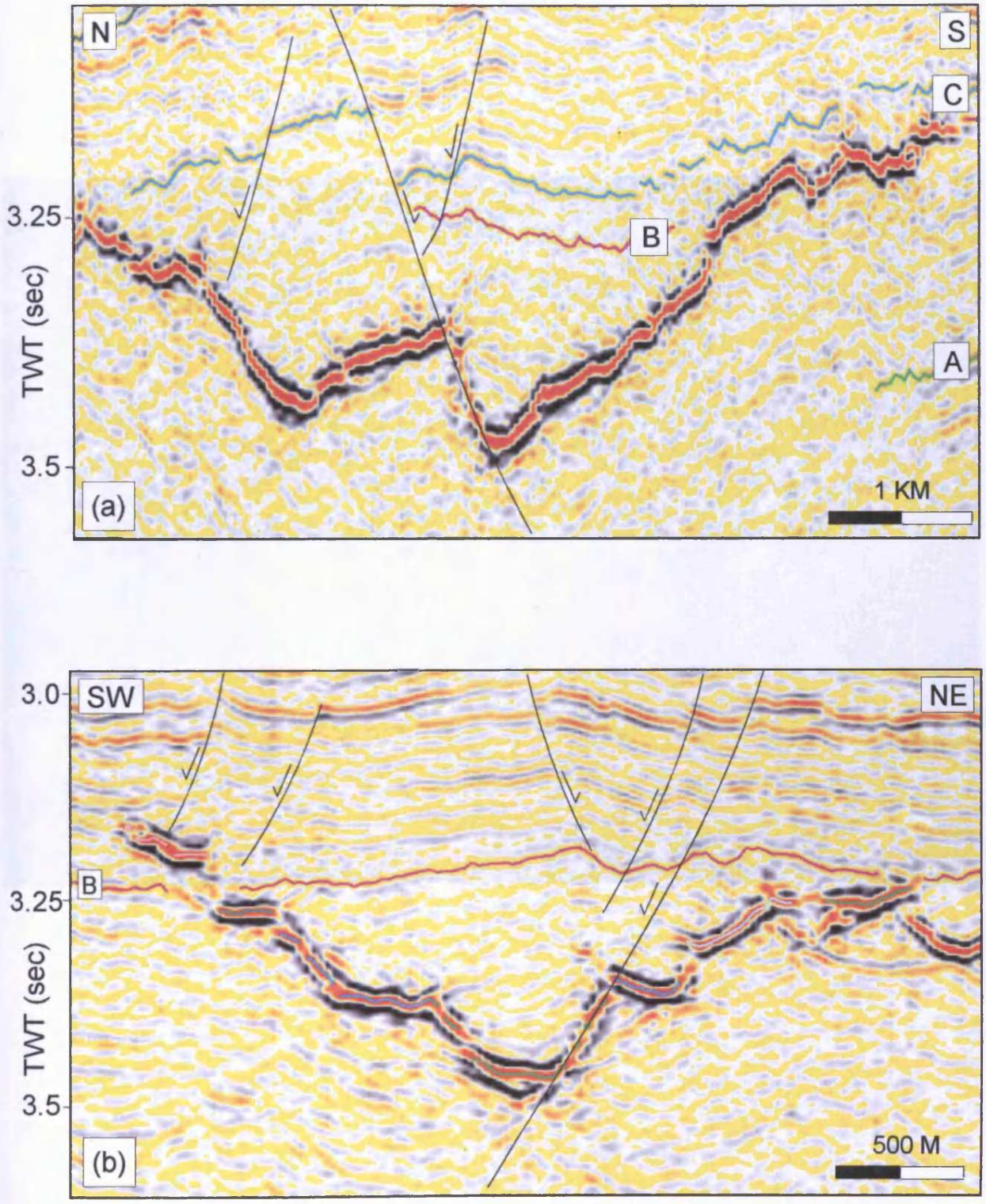

Fig. 4.35 Cross-sections through saucer X of the Solsikke sill. (a) Inline showing the two depressions of the saucer and the fault defined ridge that separates them. (b) Crossline showing stepped transgression of the saucer. See Fig. 4.34 for line locations.

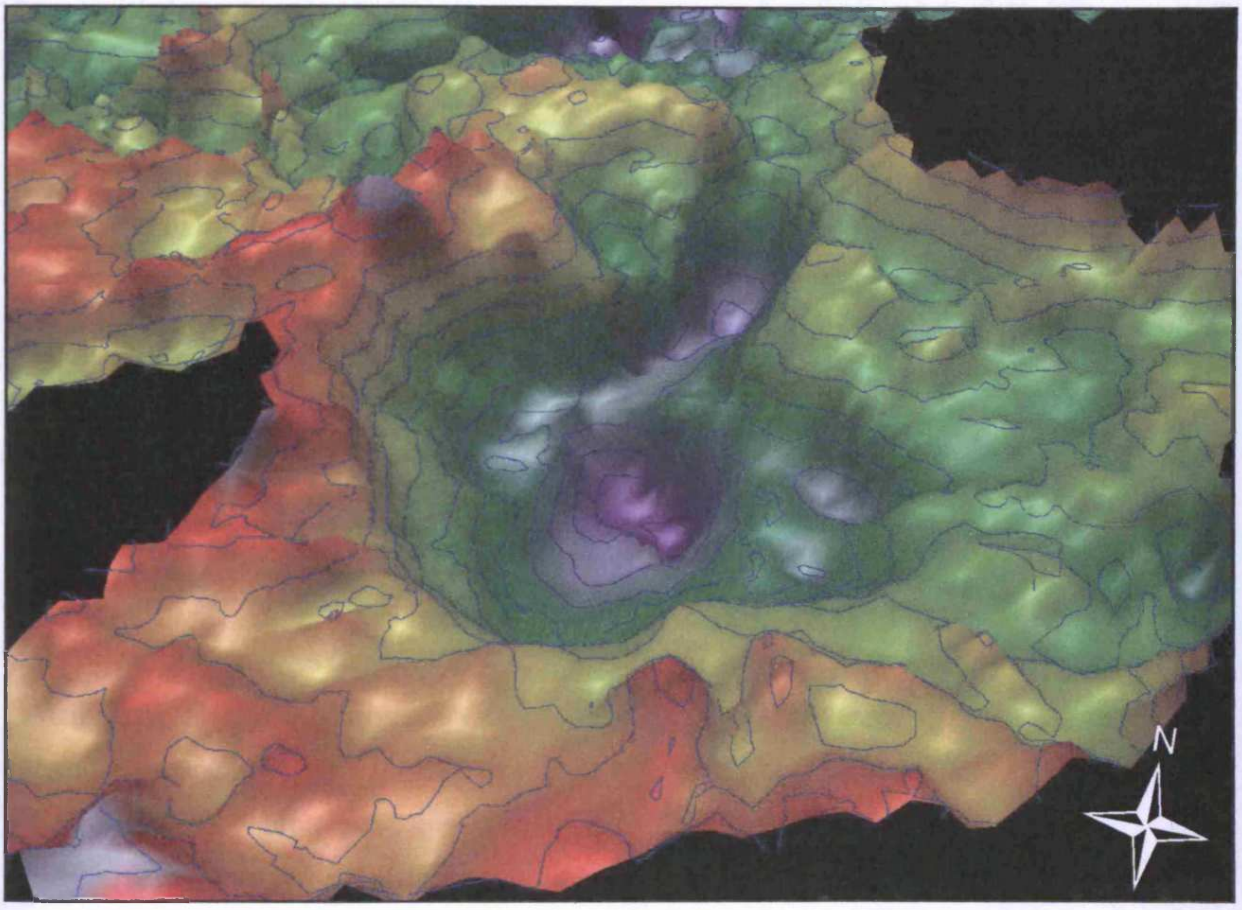

Fig. 4.36 Three-dimensional image of saucer X.

Saucer Y is less distinct than saucer X, but in cross-section it exhibits a clear concave upwards cross-sectional geometry and has a vertical relief of 375 m. The sill reflection is highly segmented and the saucer is asymmetrical around the deepest point on the saucer which is located to the north. The more detailed internal morphology of this saucer will be described in section 4.6.

The map shown in Fig. 4.33b places saucers X and Y in a structural context. The deepest points of the two depressions of saucer X and that of saucer Y are all located near fault intersections in the hangingwall of an E-W trending fault and the footwall of N-S trending fault. The main depression of saucer X is located near the intersection between fault X (south) and fault C while the smaller northern depression of saucer X is located near the intersection between fault X (north) and fault C. The deepest point on saucer Y is located close to the intersection between fault Y and fault B. The possible significance of this relationship will be discussed in section 4.5.5.2 and the development of saucer-shaped sill, in general, will be discussed in Chapter 7.

4.5.4.2 Linear discontinuities

Numerous linear to slightly curved discontinuities are seen in many places on attribute maps of the Solsikke Sill (Fig. 4.37), particularly in the northern part of subarea A and in subareas C and D. They are characterised by low negative amplitude, high dip, and they often mark changes in depth of a few 10s of metres. The discontinuities vary in length from less than a kilometre to approximately 6 kilometres and show a wide range of strike orientations.

One particularly prominent, long N-S trending discontinuity that measures 6 kilometres is seen in subarea C on the attribute maps shown in Fig. 4.37. It has an irregular trace that appears to be comprised of a number of linear sub-segments measuring 1-2 kilometres and shows two clear orthogonal intersections with smaller linear discontinuities. In cross-section the discontinuity can be linked to a clear fault-related offset of more than 50 m in the sill reflection (Fig. 4.38a). In subarea D, less distinctive linear discontinuities can also be linked to faults- related offsets and steps in the sill reflection (Fig. 4.38b).

Towards the northern periphery of subarea A two systems of parallel to slightly divergent linear discontinuities are seen (Figs. 4.34 and 4.37). The discontinuities vary in length from approximately 500-3000 m and are spaced at a few 100s of metres. They appear to radiate away from two locations near the northern boundary of subarea A. The

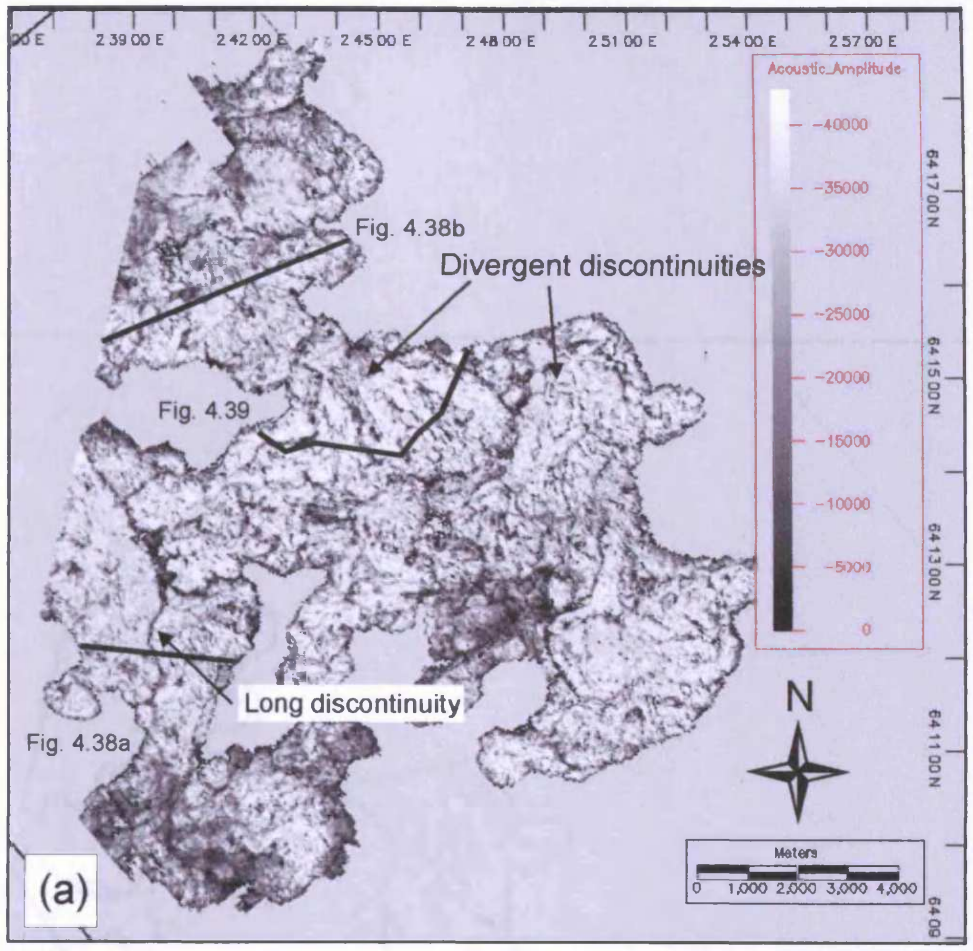

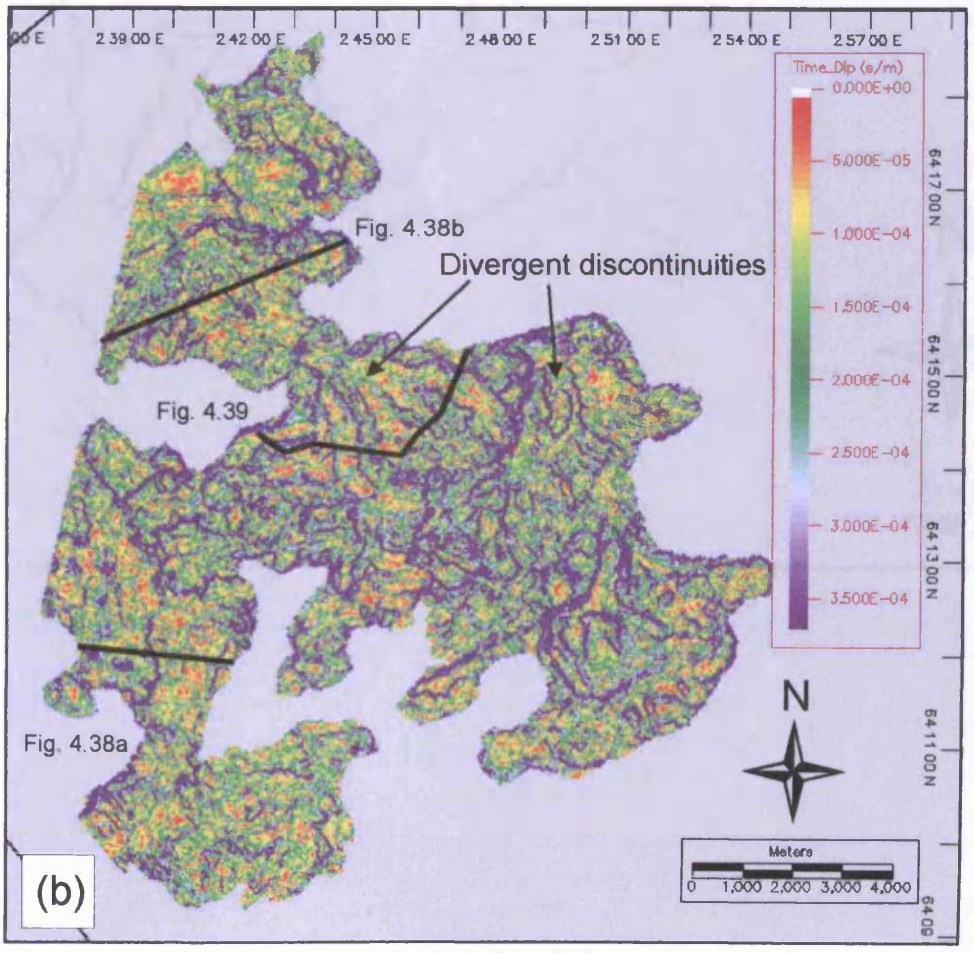

Fig. 4.37 Attribute maps of the Solsikke Sill. (a) Amplitude map. (b) Time-dip map. Note line locations for Figs. 4.38 and 4.39.

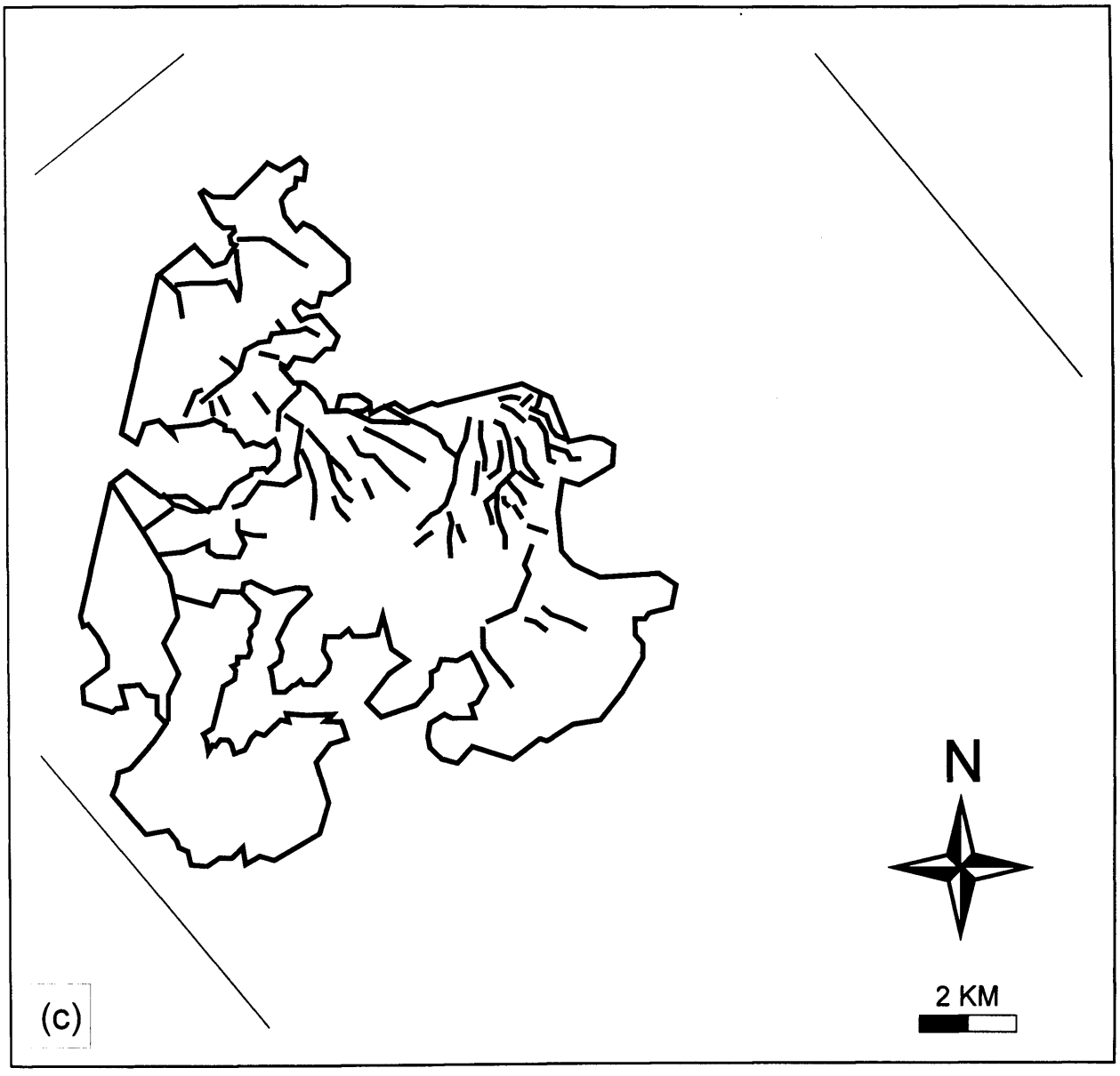

Fig. 4.37 (continued) (c) Trace map of the Solsikke Sill showing main linear discontinuities.

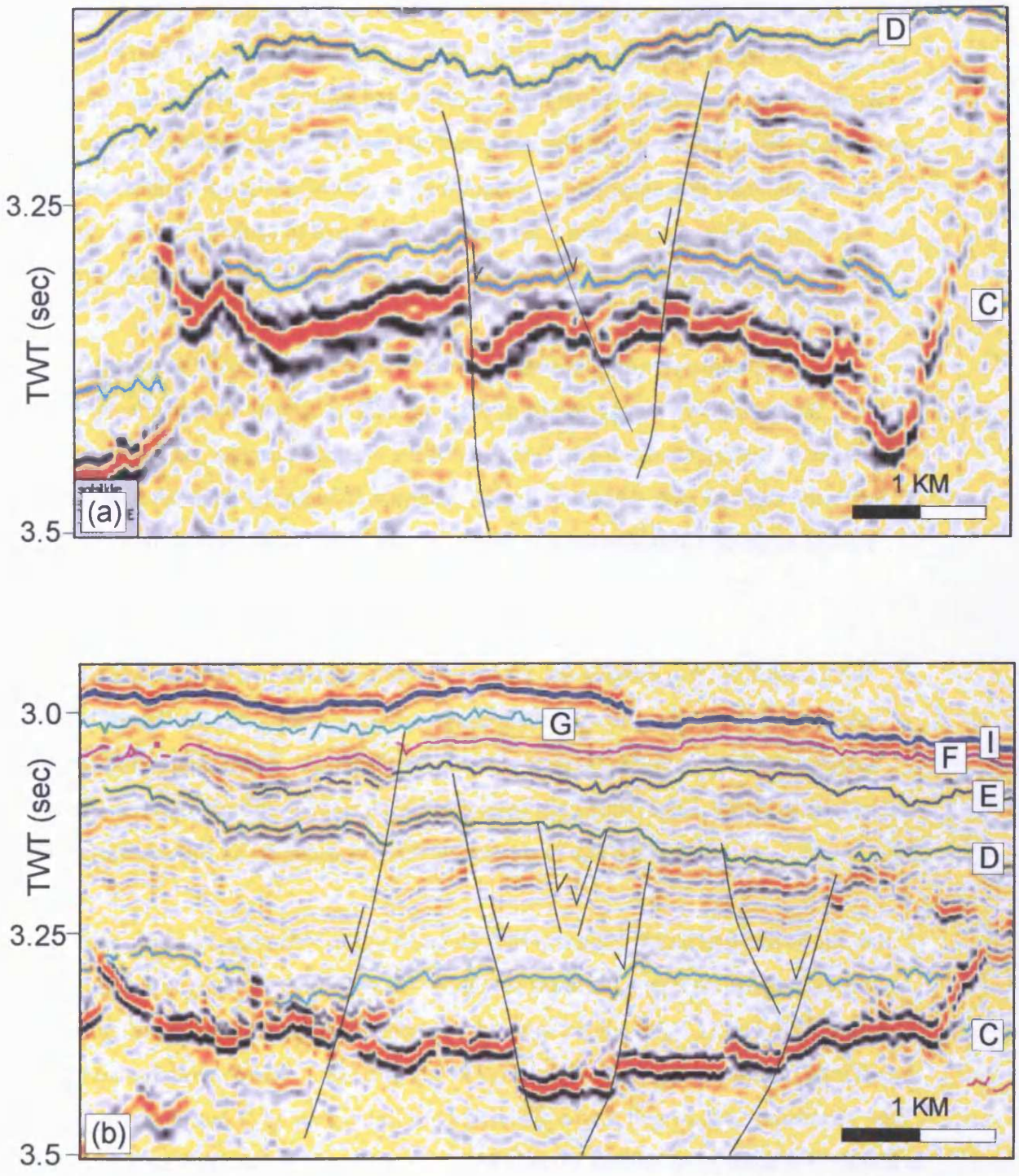

Fig. 4.38 Seismic sections illustrating the cross-sectional geometry of the Solsikke sill in (a) subarea C and (b) subarea D. In these areas the sill reflection shows a high degree of concordance with Horizon C and is offset by several faults. See Fig. 4.37 for line locations.

most western system radiates away from a linear trend at the neck region between subareas A and D whilst the more eastern system seems to radiate away from a point location near the periphery of the sill. Fig. 4.39 shows a cross-section that transects the western of these systems of discontinuities. On this section the sill reflection is highly discontinuous and the discontinuities recognised on the attribute maps are coincident with steps and offsets between adjacent discordant sill segments. However, contrary to subareas C and D the sill reflection discontinuities do not appear to be related to faulting. The significance of the discontinuities seen in subarea A, particularly the eastern-most system, will be described and discussed in detail in section 4.6.

4.5.5 Discussion: The emplacement and development of the Solsikke Sill

As shown above the Solsikke Sill has a highly complex geometry and internal morphology. This suggests that this sill has undergone a more complex emplacement process than the more simple sills mapped in the T67 survey area. In this section the possible controls upon the general emplacement and growth of the Solsikke Sill are discussed.

4.5.5.1 Stratigraphic and structural controls upon the geometry of the Solsikke Sill

Parts of the sill are concordant with the intruded stratigraphy, closely following the trend of horizons B and C, whilst elsewhere it is clearly discordant and transgresses along fault planes. In this section the influence of the stratigraphic and structural context of the Solsikke Sill on its geometry and development are discussed.

The cross-sectional geometry of the Solsikke Sill is highly segmented and comprises numerous sill segments (e.g. Fig. 4.30). Many of these sill segments are partially or fully concordant with the intruded stratigraphy (e.g. Figs. 4.30, 4.31 and 4.38) and in some places follow clearly imaged stratal reflections including those of horizons B and C. In subareas C and D, in particular, the sill shows a high degree of concordance with the intruded stratigraphy as shown in Fig. 4.38. On the section from subarea C shown in Fig. 4.38a the sill reflection closely follows the trend of horizon B intruding at a nearly constant depth of approximately 75 m below it over a distance of > 3 km. On the section from subarea D (Fig. 4.38b) the sill reflection is discontinuous displaying offsets and steps coincident with fault planes. However, adjacent segments of the sill reflection are largely concordant with horizon B although the depth below horizon B at which they

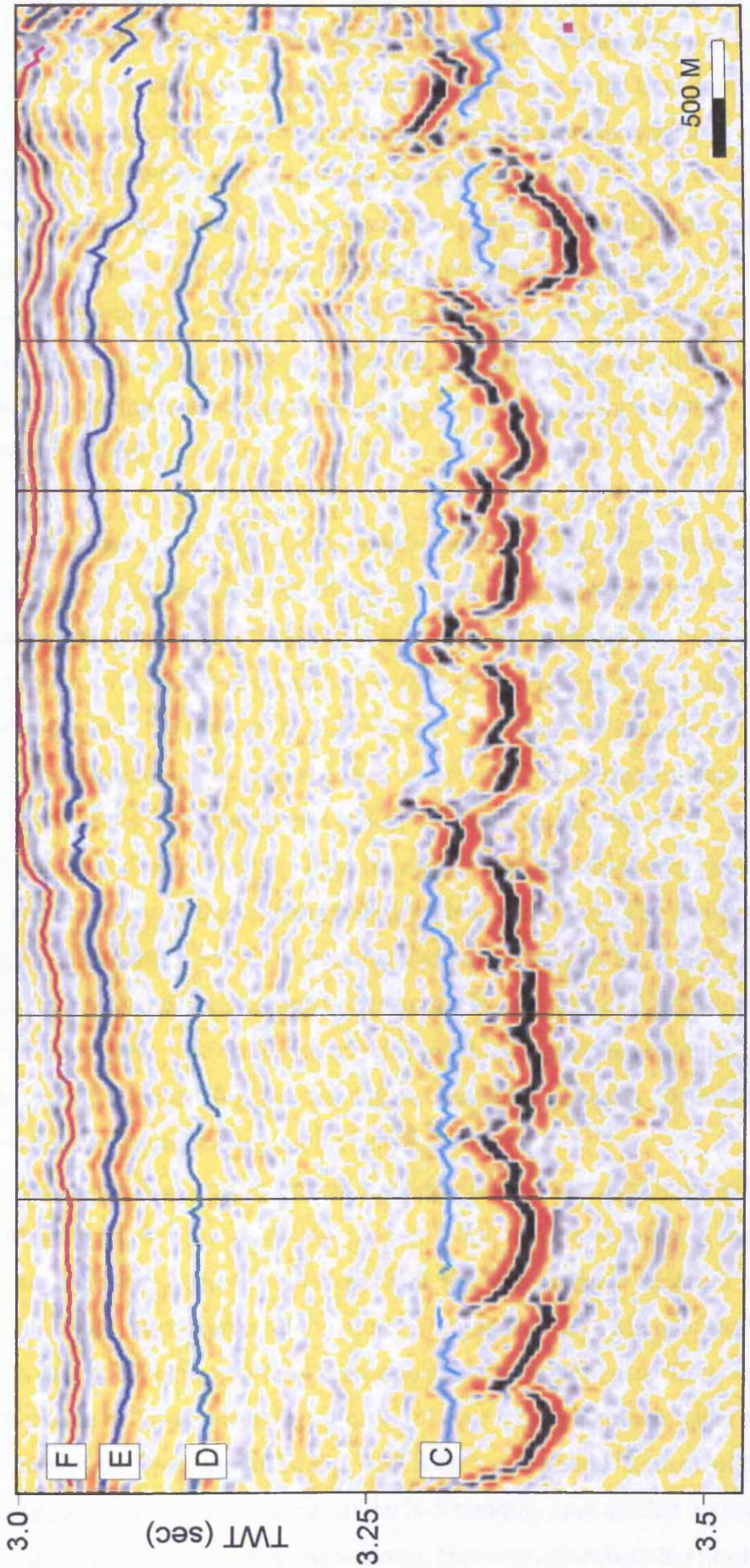

Fig. 4.39 Seismic section illustrating the cross-sectional geometry of the most western divergent system of linear discontinuities within subarea A. See Fig. 4.37 for line location.

are intruded varies across the section. In Fig. 4.40 the seismic sections shown in Fig. 4.38 have been flattened on horizon E, which marked the seabed at the time of intrusion (see Chapter 6). The concordant segments of the sill largely follow the stratal reflections, but they are not always concordant with the seabed.

These observations suggest that the emplacement of the sill was partly determined by the stratigraphy, with much of the sill preferentially intruding along seismic reflectors (formation and stratigraphic boundaries) and along less distinct seismic reflectors parallel to these (bedding planes). The observations also suggest that the sill intruded concordant to stratigraphy even where the stratigraphy was discordant with the contemporaneous seabed.

In section 4.5.3.2 the outline of the sill was superimposed on a time-dip map of horizon A (Fig. 4.33). Horizon A is the mapped horizon that best illustrates the structural template that existed at the time of intrusion. The comparison showed that in several places the periphery of the sill was coincident with fault traces. This relationship between fault planes and the edge of the sill is also evident from vertical seismic sections. The seismic section shown in Fig. 4.41 transects the northern periphery of subarea A. On this section the imaged part of the sill shows a high degree of concordance with stratal reflections towards the south whilst its northern tip clearly transgresses and cross-cuts 250 m of stratigraphy before terminating. The transgression occurs along the fault plane of the E-W trending and southward dipping fault Y. This confirms that there is a close relationship between the tip geometry of the sill and the presence of the fault plane. The fault existed prior to intrusion and the relationship is interpreted to arise due to the sill exploiting the mechanical weakness in the cover sediments provided by a pre-existing fault plane (Chapter 7).

Coincidence between fault planes and sill transgression has also been observed internally within the sill. It was, for example, described in relation to saucer X in section 4.5.4.1 and imaged in Fig. 4.35. This relationship is also interpreted to arise as a result of sill exploitation and transgression along pre-existing fault planes. Many of the linear discontinuities described in section 4.5.4.2 are coincident with steps and offsets some of which can be seen to be fault related (e.g. Fig. 4.38). The long N-S discontinuity seen on attribute maps of the Solsikke Sill in Fig. 4.37 is fault related and the trend of the discontinuity suggests that the fault is part of the N-S trending fault set that is clearly imaged in the more eastern parts of the survey area. However, elsewhere the linear

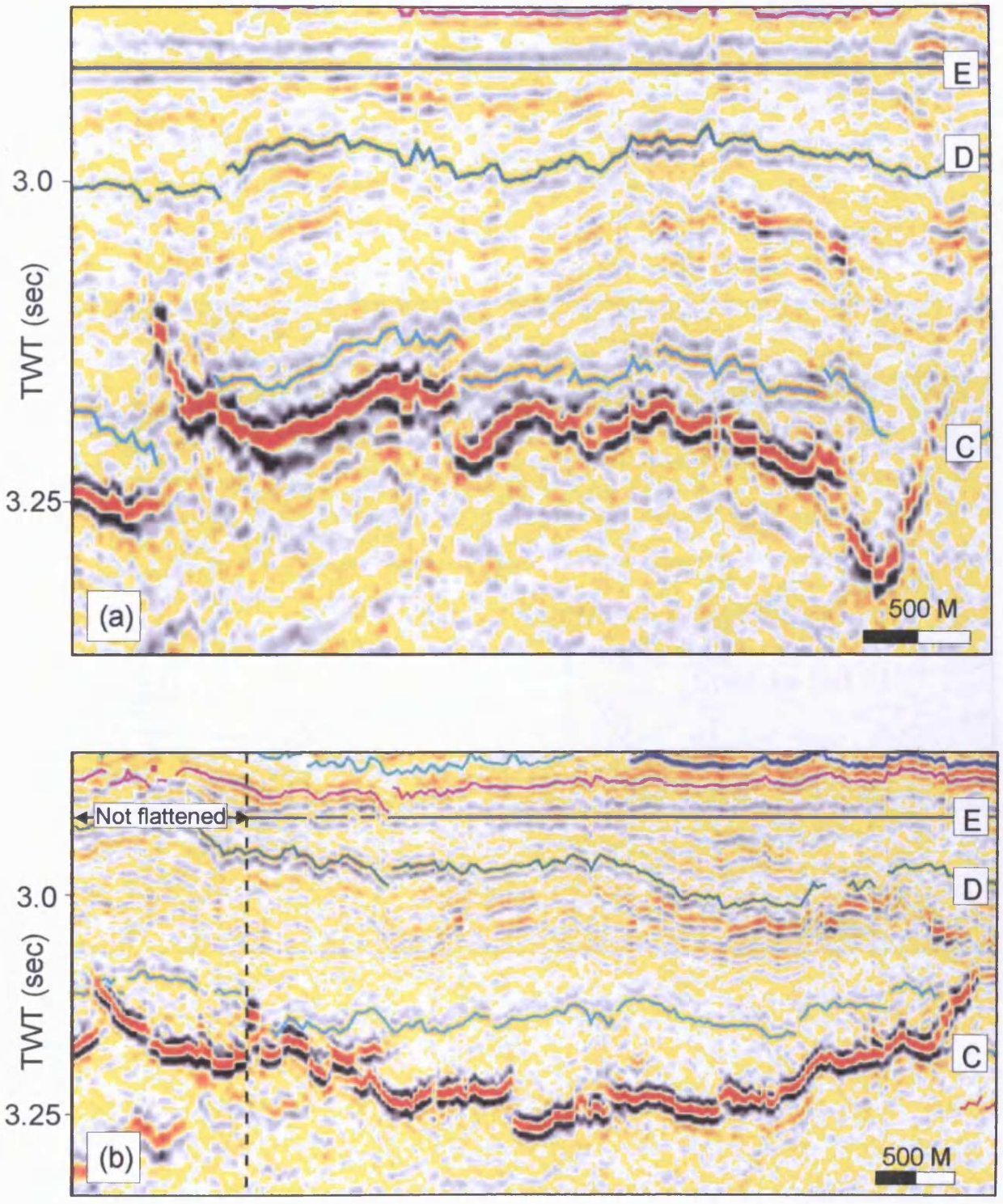

Fig. 4.40 Seismic sections (also shown in Fig. 4.38) from subarea C (a) and subarea D (b) flattened on Horizon E. Horizon E formed the seabed at the time of intrusion (Chapter 6) of the Solsikke Sill and the figures show that the sill was discordant to the seabed at the time of intrusion. See Fig. 4.37 for line locations.

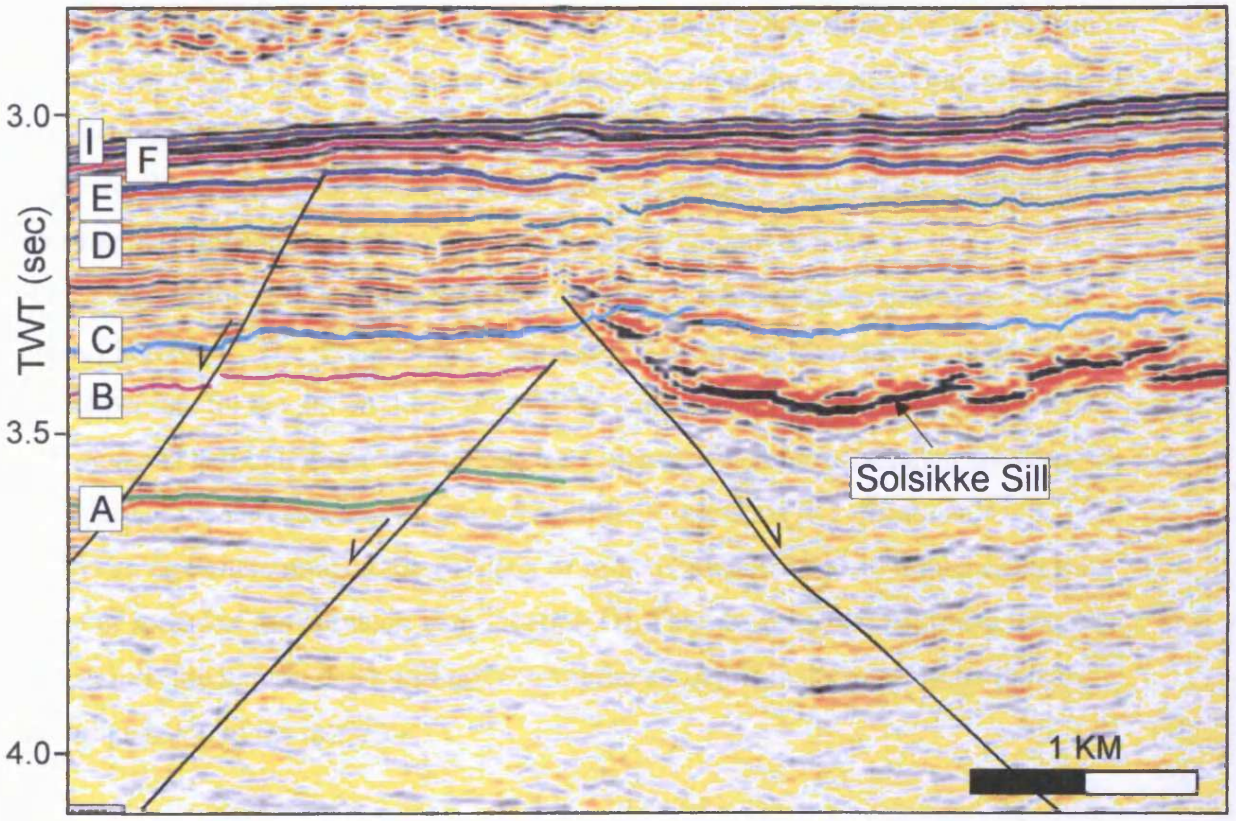

Fig. 4.41 The Solsikke Sill transgresses and terminates against the E - W trending fault Y. See Fig. 4.33b for line location.

discontinuities are not related to faulting and these will be described and discussed in more detail in section 4.6.

In spite of there being numerous examples of sill exploitation or arrest coincident with the presence of fault planes there are also examples where the presence of fault planes has had no influence on the spread of the intrusion. This could imply that re-activation and the associated increase in fault throw (section 4.3.2) play a role in determining whether or not the propagation of the intrusion is hindered by the presence of the fault. The detailed throw analysis described in section 4.3.2.1 showed that the throw vs. depth profiles for the N-S striking fault segments that had been re-activated displayed higher maximum throw values below horizon C than those that had not been re-activated (Fig. 4.17a). This means that a comparison of the extent of the periphery of the intrusion and the location of fault segments on horizon D (re-activated faults; Fig. 4.18) should reveal if re-activation and the amount of throw on the faults controlled whether the intrusion was able to propagate across the fault or not.

In Fig. 4.42 the outline of the Solsikke intrusion has been superimposed on a trace map of horizon D. The intrusion has been shifted (north and east) relative to the horizon to compensate for the dip on the faults and the difference in depth between the level of intrusion and that of horizon D. The resultant map shows some correlation between the boundary of the intrusion and re-activation of fault segments (e.g. locations A-C). However, elsewhere re-activation or lack of re-activation has had no influence on the arrest or spread of the intrusion (e.g. location D). This suggests that fault re-activation and an increase in fault throw did not control the ability of faults to act as barriers for the propagation of the intrusion.

Structural and stratigraphic controls upon the development and geometry of igneous sills are also known from outcrop (Tweto, 1951; Pollard & Johnson, 1973; Leaman 1975; Francis, 1982; Francis & Walker, 1987). Sills of the Pando area, Colorado, are seen to change stratigraphic position without actually transgressing the bedding due to the character of the hostrock (Tweto, 1951) and palinspastic reconstruction of the Whin Sill carried out in order to eliminate effects of post-intrusion deformation has revealed a clear correspondence between the sill geometry and the sedimentary template at the time of intrusion (Francis, 1982). In the Karoo Basin doleritic sills were intruded into undeformed near-horizontal strata and the deeper sills are largely concordant with stratigraphy and often follow argillaceous horizons of easy parting (Walker &

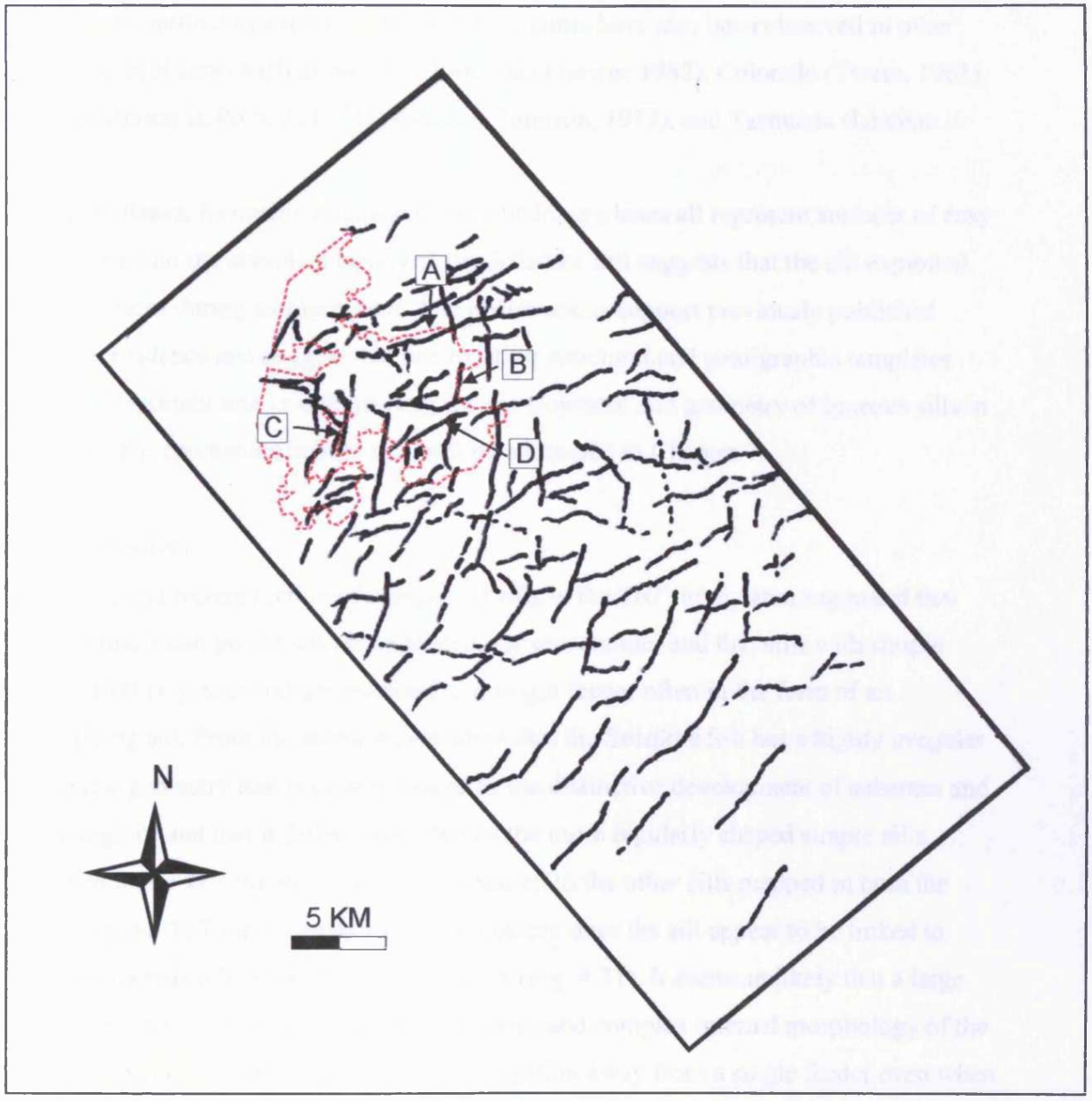

Fig. 4.42 Outline of the Solsikke Sill superimposed on fault trace map of Horizon D (Fig. 4.18). The map shows the relationship between the outline of the Solsikke Sill and re-activated faults of fault set A as well as faults of fault set B.

Poldervaart, 1949). There are also numerous examples of intrusions, which utilise fault planes to transgress to higher stratigraphic levels. Francis & Walker (1987) described the Poakley-Kinneddar-Parklands Sill intruded into Carboniferous sediments in Fife, Scotland, which transgresses as much as 400 m along the Alloa Fault. Good examples of doleritic intrusions exploiting pre-existing faults have also been observed in other classical field areas such as northern England (Francis, 1982), Colorado (Tweto, 1961), Utah (Johnson & Pollard, 1973; Pollard & Johnson, 1973), and Tasmania (Leaman 1975).

Fault planes, formation boundaries, and bedding planes all represent surfaces of easy separation and the seismic analysis of the Solsikke Sill suggests that the sill exploited such surfaces during emplacement. The observations support previously published outcrop evidence and suggest that pre-existing structural and stratigraphic templates play an important role in determining the development and geometry of igneous sills in general. The mechanics behind this will be addressed in Chapter 7.

4.5.5.2 Feeders

Mapping and reconstruction of compound sills in the T67 survey area suggested that sills within a compound sill act as feeders for one another and that sills with simple geometries (e.g. saucers) are attached to a single feeder often in the form of an underlying sill. From the above it is evident that the Solsikke Sill has a highly irregular mapview geometry that is closely linked to the distinctive development of subareas and neck regions and that it differs from that of the more regularly shaped simple sills mapped in the T67 survey. It is large compared to the other sills mapped in both the Solsikke and T67 survey areas and in two places does the sill appear to be linked to underlying sills of the Solsikke sill complex (Fig. 4.31). It seems unlikely that a large sill exhibiting the irregular mapview geometry and complex internal morphology of the Solsikke Sill could form as a result of propagation away from a single feeder even when considering the influences of the stratigraphic and structural templates. It is proposed that the geometrical observations suggest that the Solsikke Sill was fed by more than one feeder and formed as a result of amalgamation of a number of intrusive bodies emplaced at a common stratigraphic level. Such an interpretation could also explain the anomalous relationships between sill area and vertical relief and sill area and emplacement depth exhibited by the Solsikke Sill (section 4.4.2.2). In the following the possible locations and nature of the Solsikke Sill feeders are discussed.

The Solsikke Sill is linked to sills of the underlying Solsikke sill complex towards the west (subarea C; Fig. 4.31a) through a Class B junction (section 3.4.3). A number of possible kinematic models for the development of Class B junctions were provided in section 3.4.6.2 (Fig. 3.52). The second kinematic model suggests that a Class B junction may form as a result of bi-directional lateral propagation away from a transgressive sill tip with the transgressive sill tip acting as a feeder for the shallower sill. If this model applies in the case of the Solsikke Sill it suggests that the Solsikke Sill was fed by the underlying sill 29 (Fig. 4.31a). There is some evidence to suggest that the Solsikke Sill was also fed by an underlying sill towards the north (subarea D; Fig. 4.31b). However, in this area mapping of the sill was very difficult due to the close proximity to the survey edge and it was not possible to determine whether the junction between the underlying transgressive tip links upwards to connect with the Solsikke Sill itself or to a separate sill emplaced at a similar stratigraphic level. It does, however, seem likely that the reflections are part of the same igneous body in space.

Several saucer-shaped sub-elements have been identified within the Solsikke Sill. In section 4.5.4.1 the relationship between the location of the deepest points on saucers X and Y and fault intersections was described (Fig. 4.33b). Zones of fault intersection have been identified as areas of increased fluid and heat flow due to fracturing, or weakening, of the crust to great depth and have been found to localise the phenomena of intrusion and volcanism (Mayo, 1958; Sibson, 1996). Fault intersections form a preferential focus for fluid flow because they are areas of low shear strain and a zone of high dilation may form surrounding an intersection as a result of only minor deformation (Gartrell et al., 2003). The observed relationship may, based on this, suggest that upward magma flow from the deeper source was favoured in a damage zone surrounding the fault intersection. The intersections underlying saucers X and Y are poorly defined on the time-dip map of horizon D, however, the map does appear to suggest that the intersections were re-activated during the Early Cretaceous. Such a re-activation of the intersections would, according to Gartrell et al. (2003), have led to dilation surrounding the intersection and thus have increased permeability and encouraged magma emplacement in this area.

The two sets of intersecting faults are both shallow dipping (< 35°) and the resultant branch line would, therefore, also be shallowly dipping. If magma transport was focused within a zone of increased dilation surrounding the branchline it should, therefore, be possible to resolve it with seismic data provided that: (1) magma was still present in the

paleo-conduit, (2) the attenuation underlying the Solsikke Sill did not overprint the seismic response from the magma-filled conduit, and (3) the conduit was vertically extensive enough to be resolved by the seismic data given the lateral resolution limitations. These potential conduits have not been imaged as zones of anomalously high reflection amplitude on vertical seismic sections or time-slices and nor are they revealed by variance displays. It is, therefore, not possible to determine whether they were present or not and whether fault intersections played a role in feeding the Solsikke Sill.

4.5.5.3 Summary and conclusions

The above analysis of the Solsikke Sill has shown that the pre-existing startigraphic and structural templates influenced the geometry and development of the sill and suggest that the sill formed as a result of amalgamation of a number of sills with separate feeders that were emplaced at a similar stratigraphic level. Concordant and discordant segments of the sill have in many places been shown to relate to exploitation of surfaces of easy separation in the form of bedding and fault planes. The Solsikke Sill is linked to the Solsikke sill complex and subarea C of the sill was most likely fed by the transgressive tip of sill 29. There is also some evidence to suggest that the sill was fed by a sill to the north. Elsewhere coincidence between the deeper parts of saucer-shaped sub-elements of the sill (e.g. saucers X and Y) and fault intersections suggests that fault intersections may have acted as magma conduits. Fault re-activation does not appear to have had a significant influence on the geometry of the sill, however, re-activation of fault intersections is likely to have promoted magma ascent in these areas.

4.6 The Solsikke sill lobe system

4.6.1 Introduction

From the above it is clear that the Solsikke Sill has a very complex morphology and that linear discontinuities are one of the main morphological elements of this sill. Whilst many of these can be shown to be related to faulting those seen in the northern part of subarea A (Figs. 4.32 and 4.37) cannot be explained in this way. In this section the detailed geometry of the north-eastern part of subarea A is described and the significance of linear discontinuities and the kinematic development of this part of the Solsikke Sill is discussed.

4.6.2 General mapview and cross-sectional geometry

Seismic attribute maps of the north-eastern part of subarea A has revealed an overall saucer-shaped sub-element with a vertical relief of approximately 300 m that comprises a number of N-S to NNW-SSE trending linear discontinuities (Fig. 4.43). The linear discontinuities form a fan-shaped system of slightly divergent linear discontinuities that radiate away from a common location to the north. This location is coincident with a fault intersection as described in sections 4.5.4.1 and 4.5.5.2 and it is suggested that the sub-element of the Solsikke Sill described in this section was fed at this location. The system bifurcates from the north towards the south over a distance of approximately 5 km covers an area of approximately 20 km^2. Assuming that the intrusion is 50 m thick this means that this sub-element of the sill has a maximum volume of approximately 1 km^3.

Two cross-sections are shown in Fig. 4.44 and these illustrate the cross-sectional complexity of the sill in this area, parallel and orthogonal to the direction of the dominant N-S to NNW-SSE trending lineaments. Section A (Fig. 4.44a) shows the cross-sectional geometry of the sill parallel to the linear discontinuities. It reveals an overall concave upwards shape with a vertical relief of 375 m defined by a continuous reflection that can be subdivided into smaller, sometimes concave upwards and discordant sill segments linked by class A junctions. The geometry clearly transgresses discordant to stratigraphy towards the north, but in the southern direction the transgression towards shallower level is largely concordant with the overall dip of the stratigraphy. The two most southern sill segments seen on the section have concave upward cross-sectional geometries that is also seen on underlying stratal reflections. Section B (Fig. 4.44b) intersects the linear discontinuities orthogonally. It shows an overall concave upwards cross-sectional geometry with a vertical relief of < 300 m defined by a discontinuous reflection that is comprised of many smaller concordant and discordant sill segments with planar, inclined, and concave shapes that overlap and in many places link through class B junctions.

4.6.3 Lobe geometry

Detailed analysis of the junction relationships between adjacent sill segments has allowed the geometry of individual segments to be defined in three-dimensional space. Ten interlinked sill segments (labelled A-J in Fig. 4.45) have been mapped in considerable detail on a line-by-line basis in order to clearly illustrate the geometry and

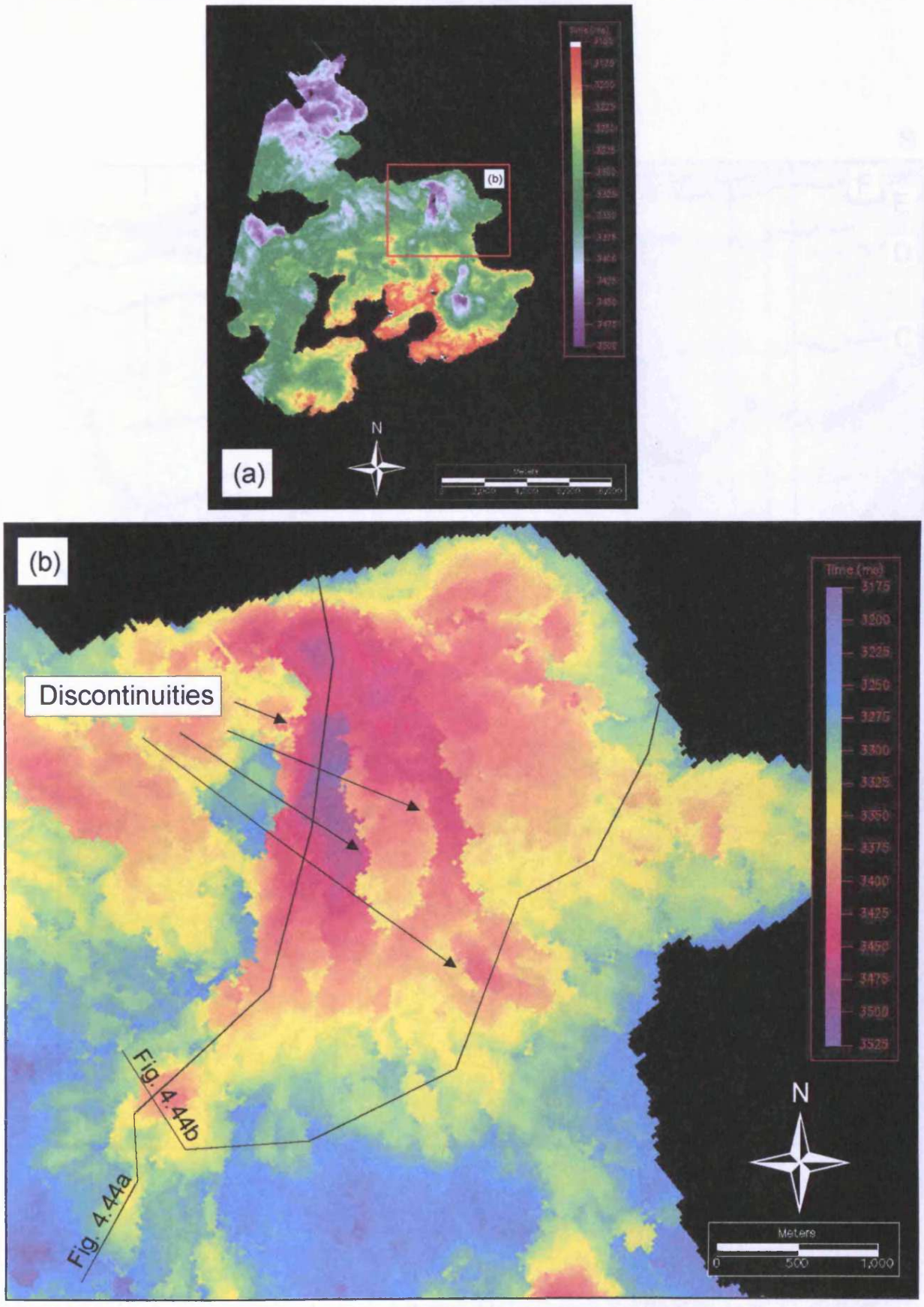

Fig. 4.43 (a) Time-structure map of the Solsikke Sill showing outline of Fig. 4.43b. (b) The north-eastern part of subarea A is characterised by a system of divergent N-S to NW-SE trending discontinuities. This system is referred to as the Solsikke sill lobe system. Note line locations for Fig. 4.44.

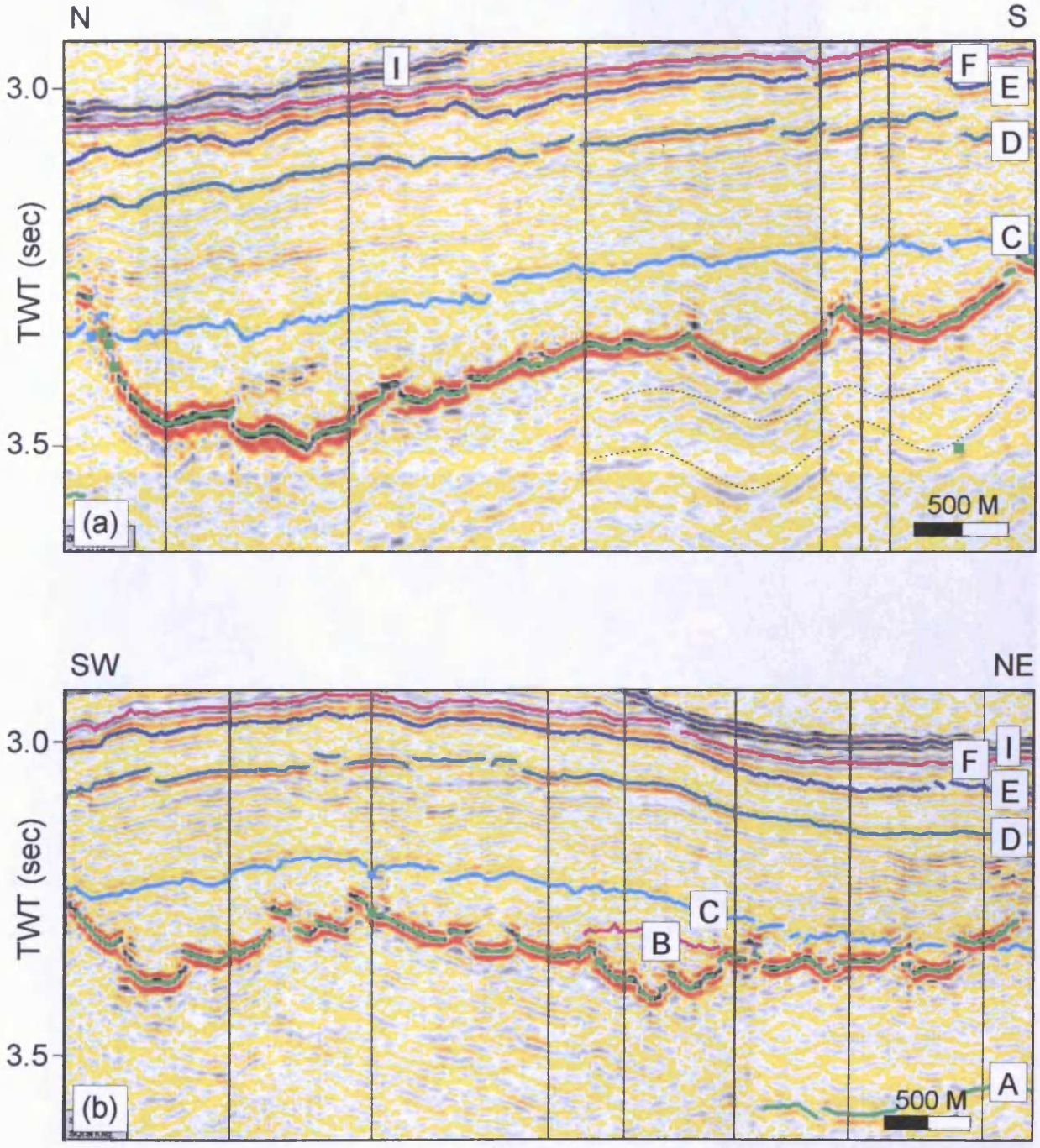

Fig. 4.44 Seismic section through the Solsikke sill lobe system. (a) Section A: N-S trending section showing the cross-sectional geometry parallel to the N-S trending linear discontinuities in the north-eastern part of subarea A. (b) Section B: NE-SW trending section showing the cross-sectional geometry perpendicular to the trend of the discontinuities. See Fig. 4.43 for line locations

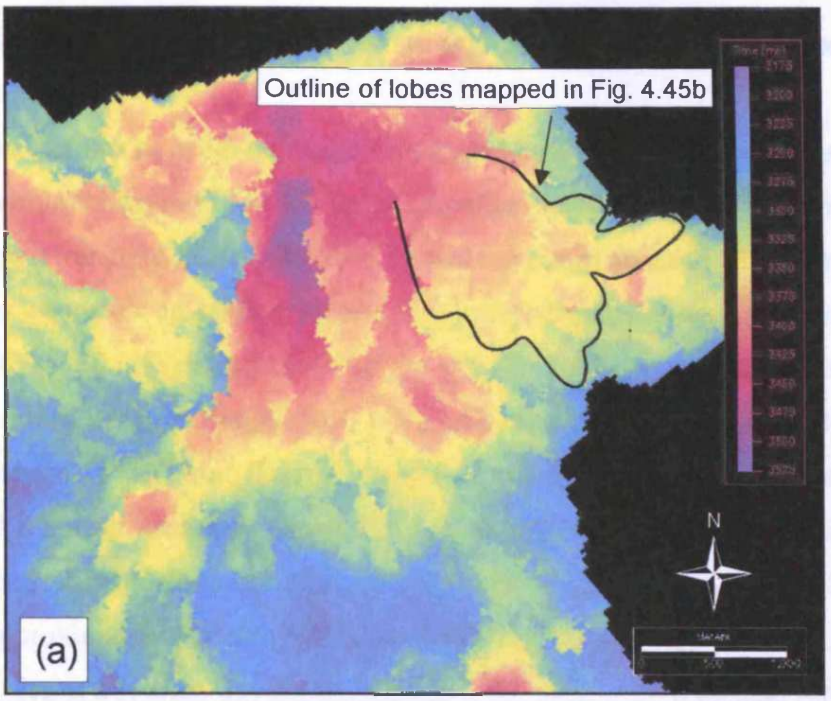

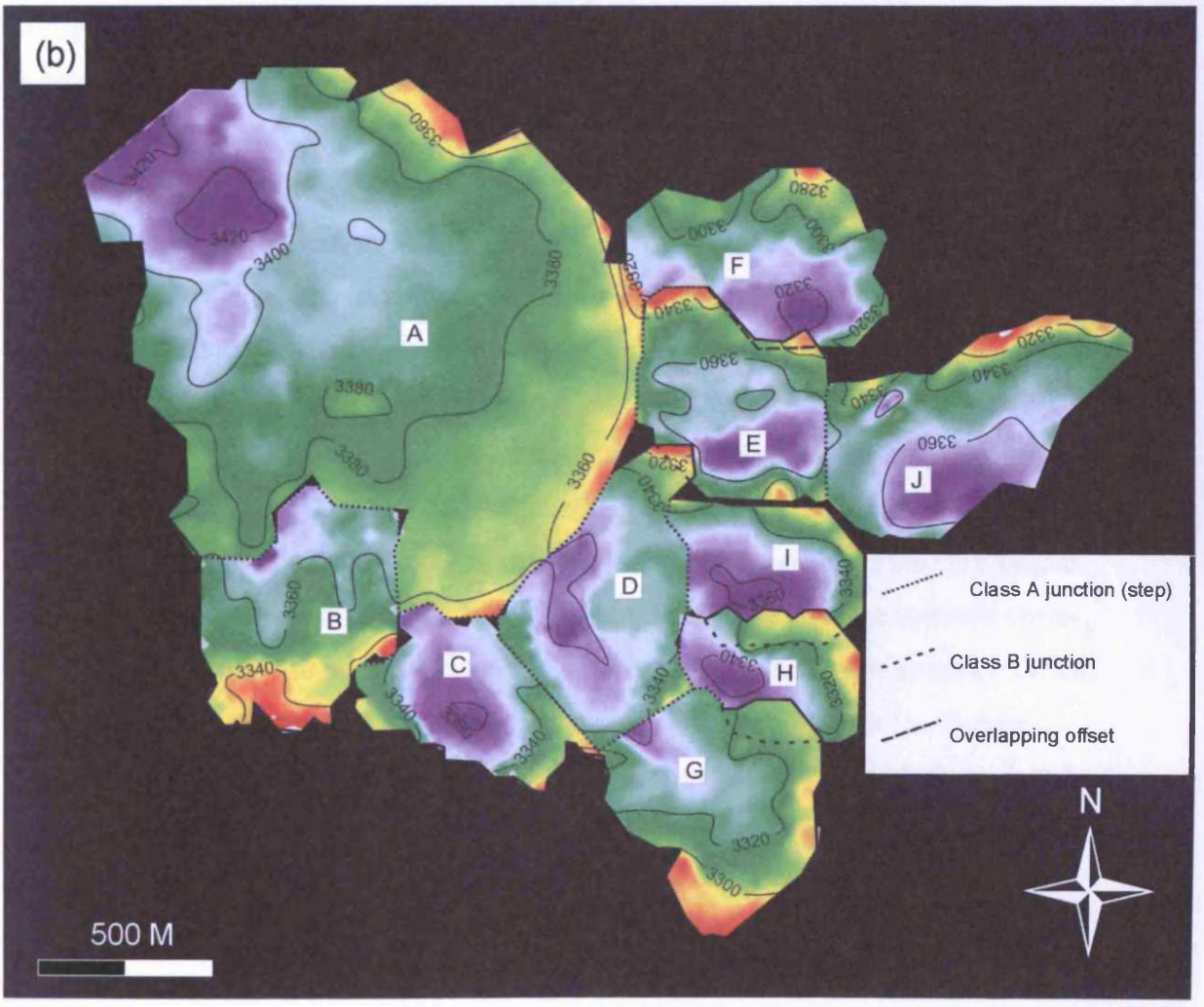

Fig. 4.45 Detailed mapping of lobes of the Solsikke sill lobe system. (a) Time-structure map of the Solsikke sill lobe system showing the outline of the area that has been mapped in detail, using multiple horizons. (b) Time-structure maps of ten individual lobes of the Solsikke sill lobe system. Note that the colour spectrum varies between the different lobes.

junction relationships between individual sill segments in a representative part of the lobe system.

Sill segment A has an irregular shape dominated by a large bulbous southern part (only this part is shown in Fig. 4.45b) and a smaller NE-SW trending northern part. It measures approximately 1250 m by 1000 m and covers an area of $94*10^{-2}$ km^2. The sill segment has a concave upwards cross-sectional geometry and is seen at a present-day depth of 5025-5130 m (vertical relief (v.r.) = 105 m). *Sill segment B* has a near-circular geometry with an irregular periphery. It measures approximately 500 m by 350 m and covers an area of $15*10^{-2}$ km^2. This sill segment is seen at a present-day depth of 4995-5070 m and it transgresses approximately 75 m towards the south. *Sill segment C* has a saucer-shaped, slightly elongated geometry with the long axis oriented NW-SE. It measures approximately 500 m by 250 m and covers an area of $11*10^{-2}$ km^2. The sill segment is seen at a present-day depth of 4965-5040 m and has a vertical relief of 75 m. *Sill segment D* has a saucer-shaped geometry with an irregular periphery. It measures approximately 600 m by 400 m and covers an area of $16*10^{-2}$ km^2. It is seen at a present-day depth of 4965-5055 m and has a vertical relief of 90 m. *Sill segment E* is saucer-shaped and measures approximately 500 m by 350 m, covering an area of $14*10^{-2}$ km^2. It is seen at a present-day depth of 4995-5070 m and has a vertical relief of 75 m. *Sill segment F* is elongated and measures 500 m by 250 m and has its longest axis oriented E-W. It has an irregular saucer-shaped geometry, covers an area of approximately $14*10^{-2}$ km^2, and is seen at a present-day depth of 4905-4995 m (v.r. = 90 m). *Sill segment G* is a curved transgressive sheet with a vertical relief of 90 m. It measures approximately 400 m by 400 m, covers an area of $15*10^{-2}$ km^2, and is seen at a present-day depth of 4935-5025 m. *Sill segment H* and *Sill segment I* are very similar. They are both slightly elongated, (E-W) lobe-shaped and have concave upwards cross-sectional geometries. Sill segment H measures 400 m by 250 m, covers an area of $9*10^{-2}$ km^2, and is seen at a present-day depth of 4950-5025 m. Sill segment I is slightly larger. It measures approximately 450 m by 250 m, covers an area of $10*10^{-2}$ km^2, and is seen at a slightly shallower present-day depth, than sill segment H, of 3310-3360. Finally, *Sill segment J* is E-W trending, elongated, and concave upwards. It measures approximately 650 m by 250 m and covers an area of $18*10^{-2}$ km^2. It is seen at a present-day depth of 4950-5070 m and it has a vertical relief of 120 m.

The ten sill segments are linked through class A and class B junctions (Fig. 4.45b). Sill segment A is linked to sill segments B, C, D, E, and F through class A junctions

along its eastern and southern periphery. The eastern periphery of sill segment B is linked to the western periphery of sill segment C through a class A junction. Sill segment D is linked by class A junctions to sill segment C to the south-west and sill segments G, H, and I to the east and to sill segment E through a Class B junction to the north. Sill segment E abuts against sill segment D to the south and is linked to sill segment J to the east through a class A junction, and is linked to sill segment F to the north through a class A junctions that develops into an overlapping, but unlinked offset to the south-east. The junction relationship between sill segments G and H and between sill segments H and I both evolve from class A junctions to the west into class B junctions to the east.

The above detailed interpretation shows that when viewed in planview, individual sill segments exhibit near-circular to elongated, lobe-shaped geometries. Within the interpreted system this appears to be a fundamental geometrical style and this specific style of sill segment is here informally termed a ***lobe***.

The mapped lobes range in *shape* from near-circular to elongated and they often adopt a saucer-shaped geometry with an internal low. The *orientation* of individual lobes has been measured parallel to the longest axis of each of the lobes. The lobes span the full range of orientations, but are preferentially oriented N-S and ENE-WSW. The lobes vary in *size* from approximately $4*10^{-2}$ km^2 to almost $94*10^{-2}$ km^2 with the average lobe covering an area of just less than $20*10^{-2}$ km^2 (Fig. 4.46a). The lobes were intruded at *depths* of 355-700 m below the contemporaneous seafloor (approximated by horizon E), with an average emplacement depth of 510 m. Their *vertical relief* ranges between 20 m and 200 m, with an average of 95 m (Fig. 4.46b). The graph in Fig. 4.46c shows moderate correlation (R^2 = 50%) between the depth to the base of the lobes at the time of intrusion and the amount of vertical relief on the lobes, with the deeper lobes exhibiting greater vertical relief than the shallower lobes.

4.6.4 Lobe orders

The detailed interpretation above suggests that the linear discontinuities within the north-eastern part of subarea A represent junctions between adjacent lobes. In Fig. 4.47 the discontinuities of the saucer-shaped sub-element in the north-eastern part of subarea A have been interpreted from attribute maps and, to a lesser extent, vertical sections. The map suggests that the sub-element is comprised of more than forty interlinked lobes. This system of interlinked lobes is here referred to as a ***lobe system***.

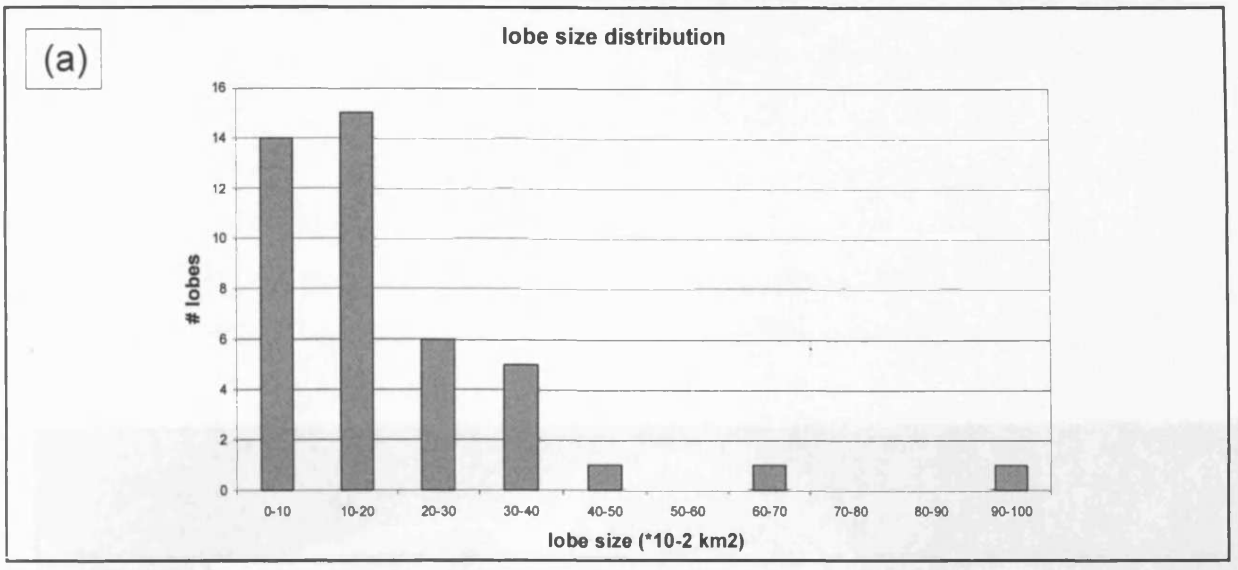

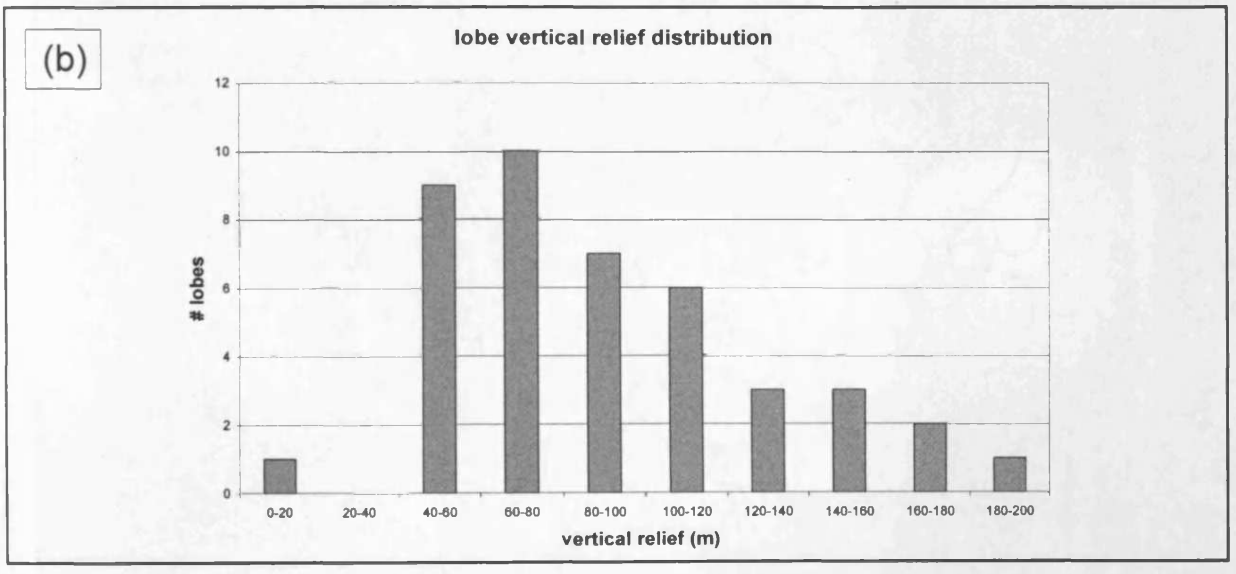

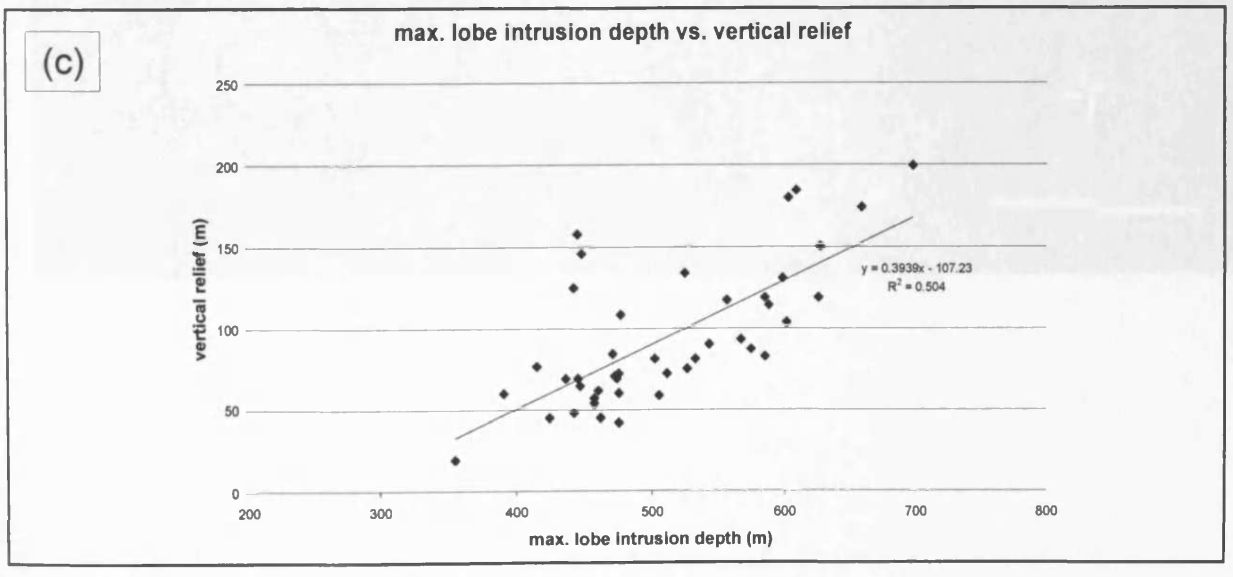

Fig. 4.46 Statistical data for the Solsikke sill lobe system; (a) lobe size distribution, (b) lobe vertical relief distribution, and (c) max lobe intrusion depth vs. vertical relief. N = 43. Depth conversion done using Vsed = 3.0 km/s, see Chapter 2.

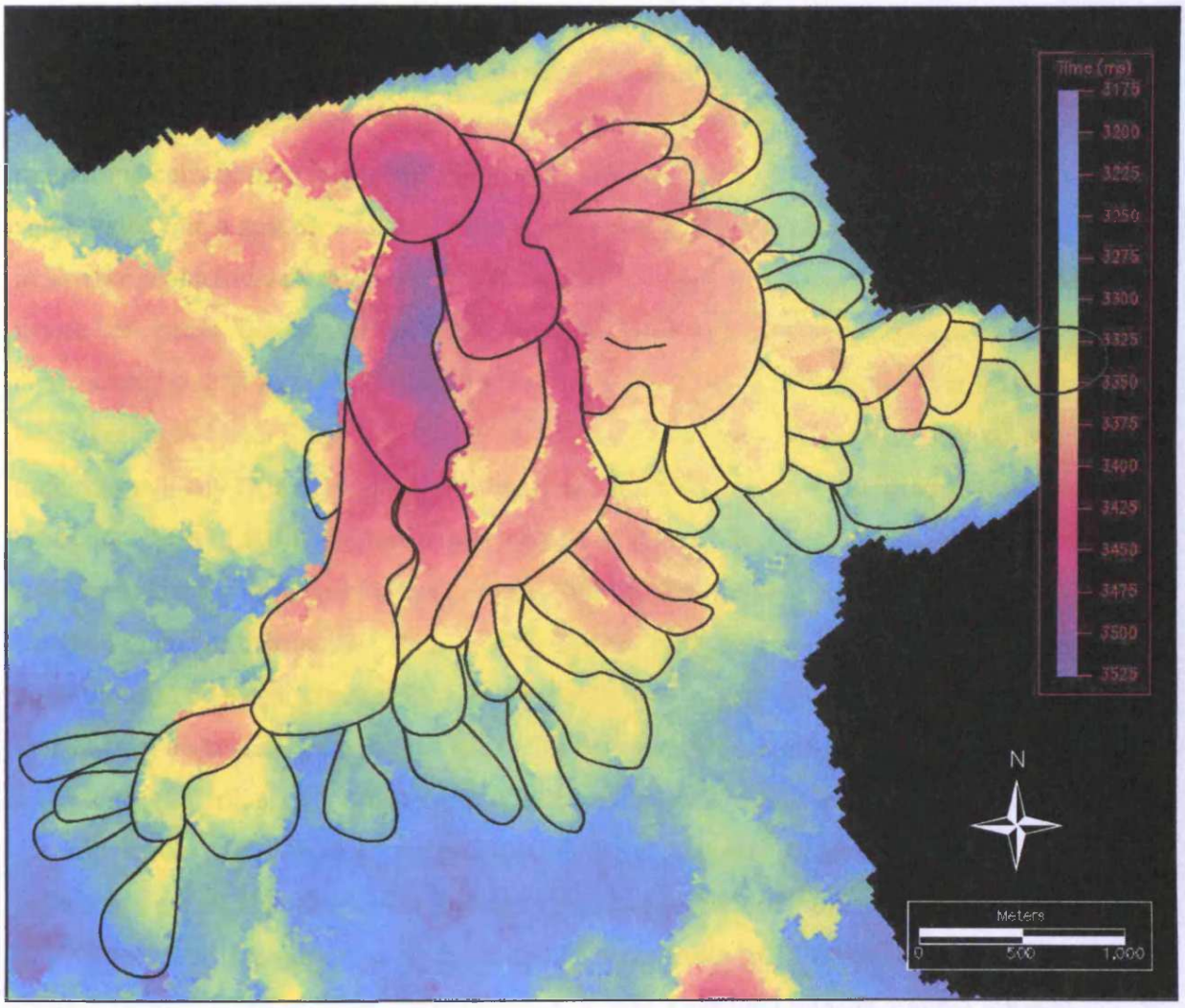

Fig. 4.47 Time-structure map of the Solsikke sill lobe system showing the approximate outline of individual lobes. The lobe system appears to bifurcate towards the south and east away from a common location to the north-west.

The edge of the lobe system is poorly defined, particularly towards the west and south. It appears that the number of lobes increases towards the south and east, away from a common location to the north-west that is interpreted to mark the feeder location for the saucer-shaped sub-element (sections 4.5.4.1 and 4.5.5.2). In addition, the size of the proximal lobes is greater than the area of the distal lobes. This gives the lobe system a bifurcating appearance in which rings with an increasing number of lobes are arranged concentrically around the inferred feeder.

Like other naturally occurring bifurcating systems (e.g. drainage networks) the lobe system shows a degree of internal organisation. Lobes that are located in similar geometrical positions, relative to the inferred feeder, within the lobe system are morphologically similar (e.g. size, shape, and vertical relief). The lobe system has been sub-divided into a number of ***lobe orders***. Lobes within the same lobe order are located in similar geometrical positions relative to the inferred feeder and each lobe order forms a near-concentric ring around the feeder. The similarities in geometrical positions are constrained by their junction relationships. A lobe of order *n* is connected to at least one lobe of order *n-1* by a Class A junction. It may also be connected to other lobes of any order through any type of junction geometry and is likely to be connected to several lobes of order *n+1* through Class A junctions (Fig.4.48a). The lobe system has been sub-divided into six orders of lobes and each lobe within the lobe system has been assigned to one of these orders (Fig. 4.48b). The location of the inferred feeder is approximated by a near-circular lobe in the north-western part of the lobe system. This lobe has not been assigned to a lobe order. The lobe system is comprised of four 1st order lobes (1a-1d), six 2nd order lobes (2a-2f), nineteen 3rd order lobes (3a-3s), eleven 4th order lobes (4a-4j), three 5th order lobes (5a-5c), and one 6th order lobe (6a). The 1st order lobes are all linked to lobe x through Class A junctions, 2nd order lobes are linked to 1st order lobes through Class A junctions, 3rd order lobes to 2nd order lobes through Class A junctions and so forth. Lobe orders 1, 2, and 3 are well imaged, but the lobes of the higher lobe become increasingly difficult to map because of their limited areal extent and increased linkage complexity and the seismic resolution limitations. This probably means that the higher lobe orders are under-represented on the map shown in Fig. 4.48b. Based on the lower lobe orders it appears that each *n* order lobes bifurcates into two or three *n+1* order lobes.

In addition to the statistical data compiled for the lobes some statistical data have been compiled for the lobe system. 1st and 2nd order lobes are larger (average area/ lobe

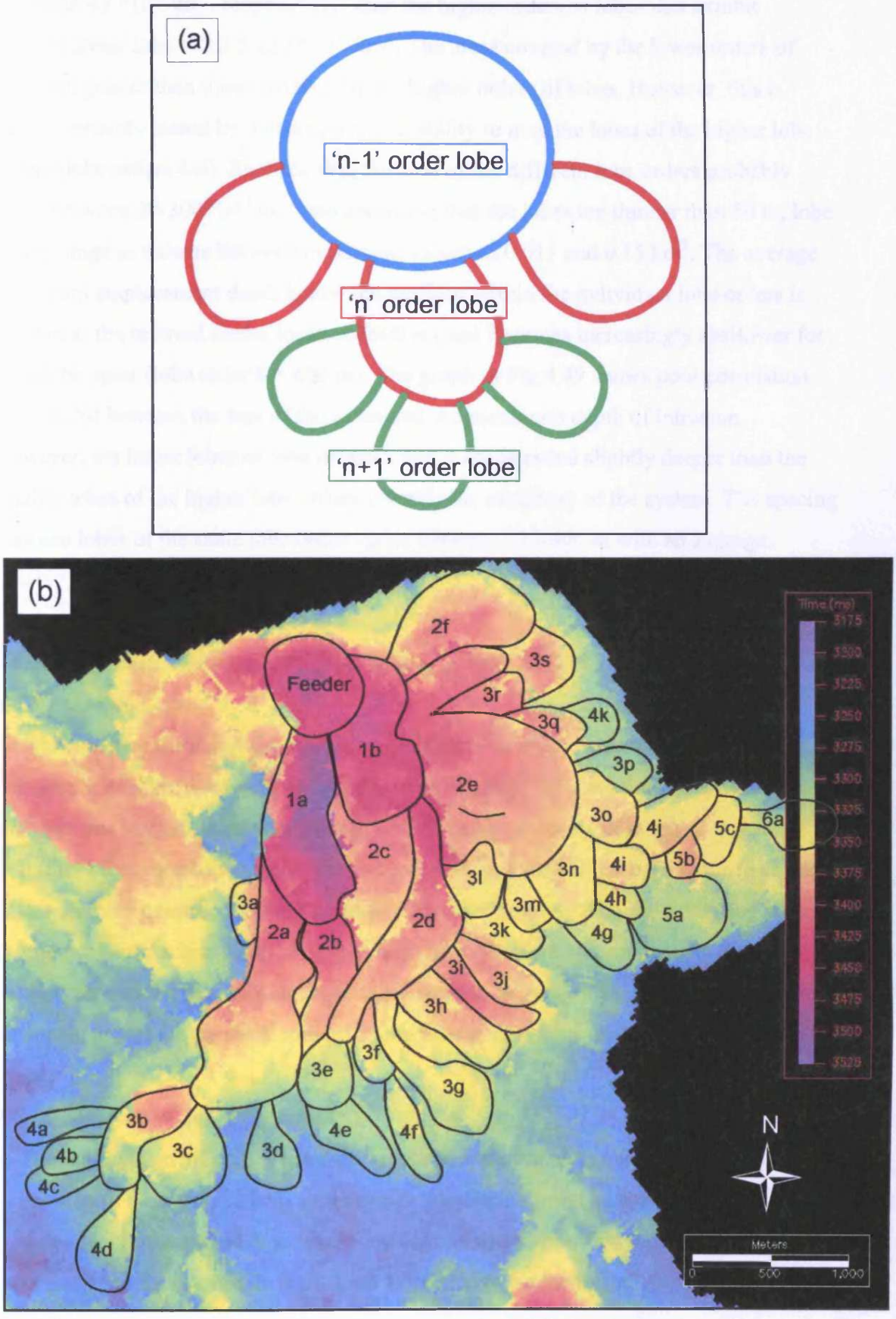

Fig. 4.48 Lobe orders. (a) Schematic illustration of lobe orders. (b) Time-structure map of the Solsikke sill lobe system with labels indicating the lobe order of each lobe (e.g. '3') and the number of the lobe within the lobe order (e.g. 'd')

of 27 and 49 $*10^{-2}$ km^2, respectively) than the higher orders of lobes that exhibit average areas/ lobe of 10.5-13.5$*10^{-2}$ km^2. The areas covered by the lower orders of lobes are greater than those covered by the higher orders of lobes. However, this is almost certainly biased by a decrease in the ability to map the lobes of the higher lobe orders (lobe orders 4-6). Realistically, the area of the different lobe orders probably range between 30-300$*10^{-2}$ km^2 and assuming that the lobes are thinner than 50 m, lobe orders range in volume between maximum values of 0.015 and 0.15 km^3. The average maximum emplacement depth below the seafloor within the individual lobe orders is greatest at the inferred feeder location (600 m) and becomes increasingly shallower for each lobe order (lobe order 6 = 400 m). The graph in Fig.4.49 shows poor correlation (R^2 = 12%) between the size of the lobes and the maximum depth of intrusion. However, the larger lobes of lobe orders 1 and 2 are intruded slightly deeper than the smaller lobes of the higher lobe orders towards the periphery of the system. The spacing between lobes of the same lobe order varies between 125-460 m with an average spacing of 270 m.

4.6.5 Discussion: The kinematic development of the Solsikke sill lobe system

4.6.5.1 Introduction

As shown above the discontinuities seen in the north-eastern part of subarea A of the Solsikke Sill define a fan-shaped lobe system comprised of more than 40 lobe shaped sill segments termed lobes. The geometry of the lobe system is unique and no other examples of an equivalent geometrical style of an igneous sill has been mapped as part of this study or described in the literature. However, igneous features exhibiting some geometrical similarities with the lobe system have previously been described. In this section these analogues are described and discussed in relation to the lobe system and a kinematic model for the development of the lobe system is proposed.

4.6.5.2 Summary of key observations

- The lobe system bifurcates towards the south and south-east away from a common location to the north. This location marks the deepest point on the overall saucer-shaped lobe system and is located very near a fault intersection that may have acted as a conduit for magma. It is suggested that this is the feeder location for the lobe system

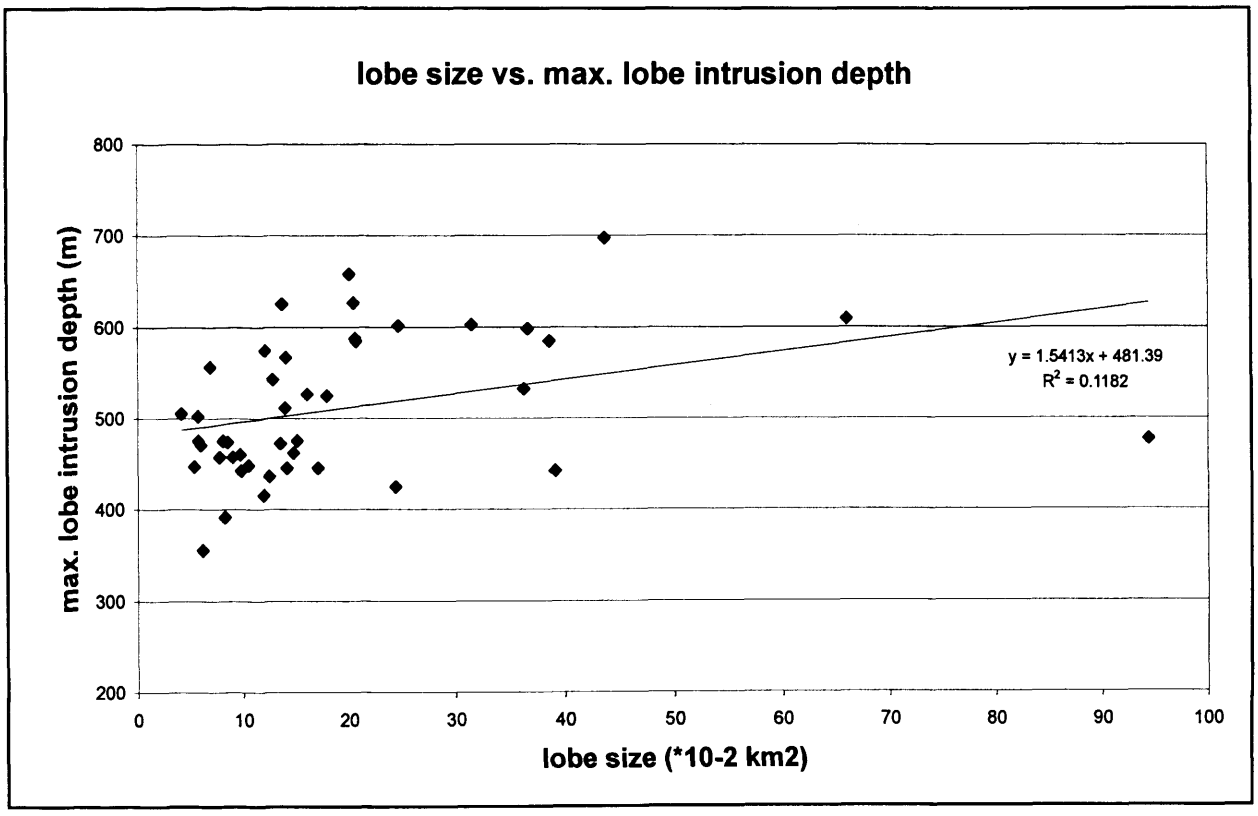

Fig. 4.49 Graph showing poor correlation (R2 = 12%) between lobe size and maximum lobe intrusion depth. N = 43. Depth conversion done using Vsed = 3.0 km/s, see Chapter 2.

- The lobe system has an overall saucer-shaped geometry and is comprised of more than 40 interlinked lobe shaped sill segments termed lobes
- The lobes are linked through class A junctions on lines perpendicular to the main N-S to NW-SE trending discontinuities and primarily through class B junctions on lines oriented perpendicular to these
- The lobes are organised into six lobe orders that form concentric rings around the inferred feeder, with the lowest lobe order located proximal to the inferred feeder and the higher lobe orders located distally
- The lobes nearest to the inferred feeder location are larger than those located further away from the inferred feeder
- The number of lobes increases 2-3 times between lobe order *n* and lobe order *n+1*

4.6.5.3 Lobe system feeder relationship

As shown in previous sections the lobe system bifurcates away from a common location located near the northern periphery of the lobe system. In section 4.6.2 it was suggested that this common location marked the feeder for the lobe system and that the feeder was likely to be associated with an underlying fault intersection. The more detailed analysis of the lobe system seems to support the interpretation of the feeder location. This supporting interpretation is based on the argument that it seems much more probable that the lobe system formed as a result of bifurcation during outwards and upwards magma propagation away from a common location than through downwards merger of multiple lobes towards a common location. In Chapter 3 it was argued that that magma migration is generally upward with deeper sills feeding shallower sills. Hence the assumption carried here, that the feeder for the lobe system is likely to be located close to the deepest part of the lobe system.

The often near-saucer shaped geometry of individual lobes could be taken as evidence to suggest an alternative model for the lobe system whereby each lobe is fed by its own individual source of magma, either through a dyke, or a pipe, possibly exploiting the underlying fault network (Fig. 4.50). However, this model is considered highly unlikely for a number of reasons. These include: (1) there is no evidence for the presence of dykes underlying any of the lobes, (2) the organisation of the lobe system into lobe orders seems incompatible with multiple independent feeders, (3) the class A junctions seen between adjacent lobes are unlikely to form as a result of the independent

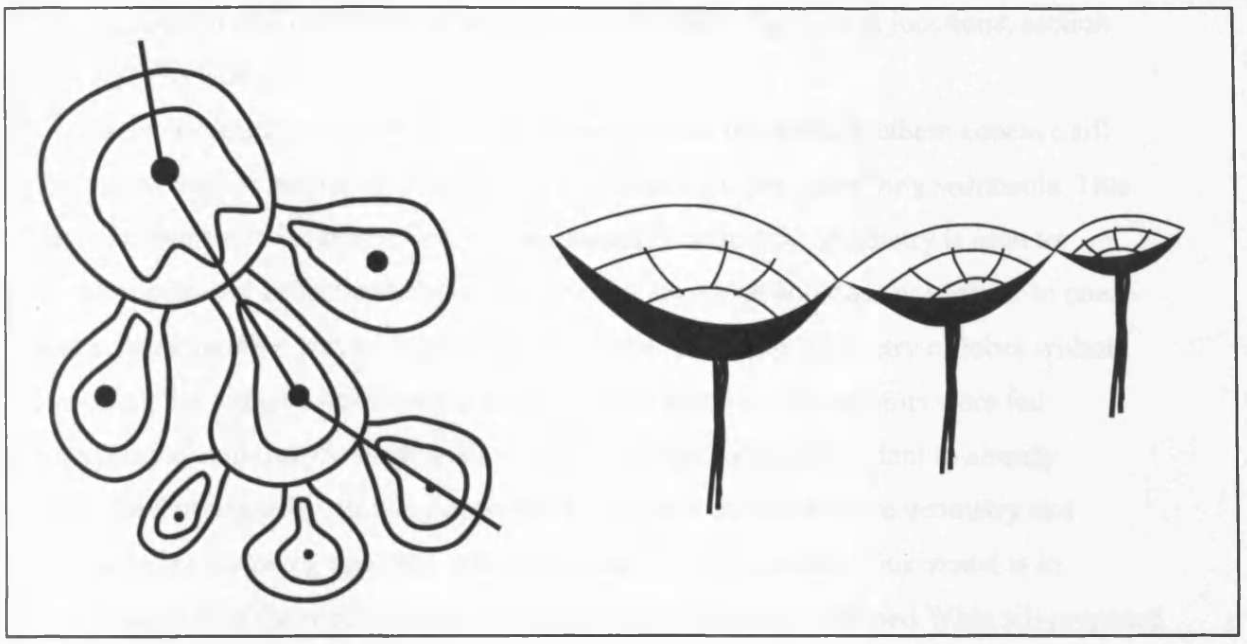

Fig. 4.50 Possible model for the feeder relationship of the Solsikke sill lobe system. In this model each individual lobe is fed by an underlying magma pipe.

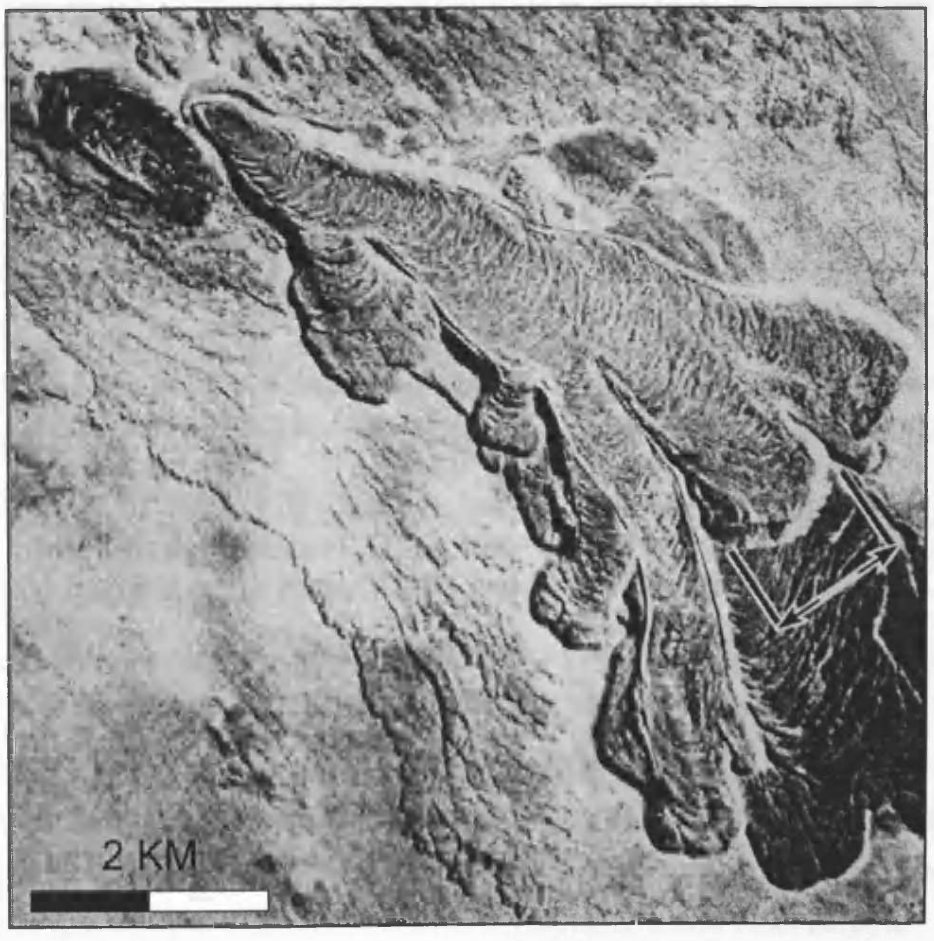

Fig. 4.51 Aerial photography of a lobate lava flow (Farallon de la Portada) on the southern flank of Volcan Payun Matru in Argentina. From Wadge & Lopes, 1991.

propagation of two individual igneous bodies (model 1 for class A junctions; section 3.4.5.1; Fig. 3.50a).

As mentioned in section 4.6.2 the geometry of the two most southern concave sill segments seen on section A (Fig. 4.44a) is also seen in the underlying sediments. This does not appear to be an artefact (e.g. multiples) because the geometry is seen to influence several reflections underlying the sill segments and does not appear to cross-cut reflections. One way of explaining the concave upward geometry of lobes without invoking individual feeders would be to suggest that the sill segments were fed peripherally and that the magma subsequently propagated concordant to already deformed stratigraphy, flowing downdip to the base of the concave geometry and thereafter propagating upwards, still following the stratigraphy. This model is in accordance with the model for the development of the saucer-shaped Whin sill proposed by Francis (1982), but differs from the majority of models for the development of saucer-shaped sills and the general observation made in the case-study areas in this study that saucers are fed at the base (see Chapter 7 for further description and discussion of saucer-shaped sills). Alternatively, the concave geometry could have formed following intrusion due to a density difference between the intruding magma and the host-rock causing soft-sediment deformation (further described in section 7.6.5; 'basal settling').

4.6.5.4 Analogues

The lobe system is unique and no direct analogues are described in the literature. There are, however, a number of both intrusive and extrusive igneous features that exhibit geometrical components that are of interest in relation to the Solsikke sill lobe system and these are described in this section.

Inflated pahoehoe lava flows

A flow pattern very similar to that of the lobe system has been documented from several extrusive igneous systems; e.g. Mauna Ulu, Kilauea Volcano, Hawaii (Hon et al., 1994; Peterson et al., 1994) and Volcan Payun Matru, Argentina (Fig. 4.51; Wadge & Lopes, 1991). These flows develop forms referred to as lava flow lobes and Wadge & Lopes (1991) provide a summary of a range of flow lobe measurements including thickness and widths. According to their measurements terrestrial lava flow lobes range in thickness between 5-300 m with the average thickness being 38 m and have widths

(average width of lobes on individual flows) of 20-1300 m with an average width of 270 m.

Hon et al. (1994) and Peterson et al. (1994) describe the process of pahoehoe lobe extension forming inflated pahoehoe sheet flows that are very similar in appearance to the Solsikke sill lobe system. In this process a system of lobes develop as a result of successive outbreaks along inflated fronts of prior sheet flow lobes in the manner illustrated in Fig. 4.52. As the hot magma is brought into contact with cooler surroundings a crust forms on the outer surface of the flow. As a result the tensile strength of the flow increases and the spread of the flow decelerates. Continued input of magma leads to inflation of the flow and eventually the tensile strength of the flow is exceeded and the inflated front ruptures at one or more locations and new lobes are formed. Repetition of the process leads to the development of an interlinked lobe system. The process of pahoehoe lobe formation, as well as other tube-forming processes, are favoured by low to moderate volume-rates (<5 m^3/s) of flow for sustained periods of time emplaced on subhorizontal slopes of no more than 2° and often less than 1° (Hon et al., 1994; Peterson et al., 1994).

Hon et al. (1994) suggested that the difference in emplacement behaviour between inflated sheet flows and more continuously advancing flows is likely to be linked to an interplay between pre-existing slope gradients, small-scale topography, and lava supply rate. Although the discontinuities seen in the lobe system area of the Solsikke Sill cannot be directly linked to faulting, it should be kept in mind that the intruded sediments are heavily faulted. The faulting would have introduced heterogeneity that may have had a similar effect on sill intrusion as the controls listed by Hon et al (1994) and thus have encouraged inflated multi-lobate intrusion rather than more continuous intrusion.

Fingered intrusion

A less obvious intrusive analogue that occurs at a smaller scale was described by Pollard et al. (1975) and briefly outlined in section 1.5.4.3. Pollard et al. (1975) studied a sill emanating from the Shonkin Sag laccolith in Montana and found that it had propagated along a series of separated protruding oval to elliptical fingers rather than along one smooth front (Fig. 1.15). The individual fingers are about 100 m long, 3-5 m wide, and 0.6-1.2 m thick and become increasingly wide and thick towards the line of coalescence where they merge into one continuous sheet. The fingers are separated by

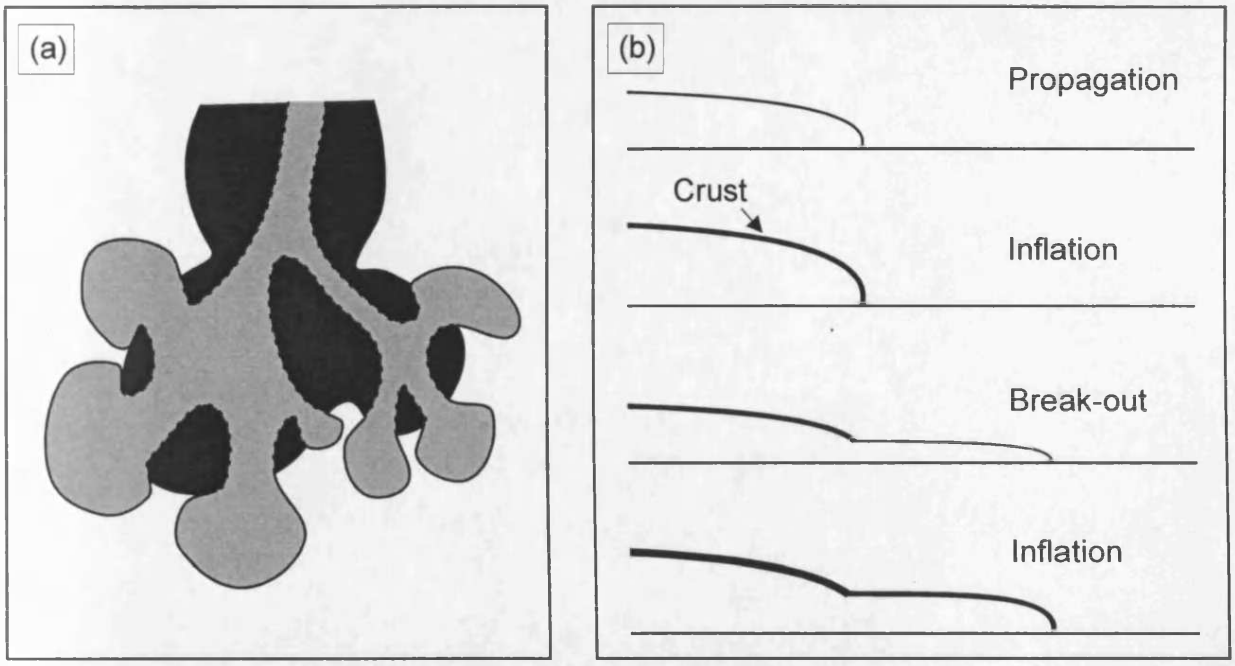

Fig. 4.52 Schematic illustrations of the formation of inflated pahoehoe flows. (a) The planview geometry of a lobate flow showing two orders of lobes. The second order of lobes (light grey) form around the edge of the first order lobes (dark grey). (b) The cross-sectional geometry of a developing lobate system. As a crust forms on the intial lobe forward propagation is arrested and the lobe starts to inflate. Eventually the strength at the lobe front is overcome and a second lobe breaks out. After Peterson et al., 1994.

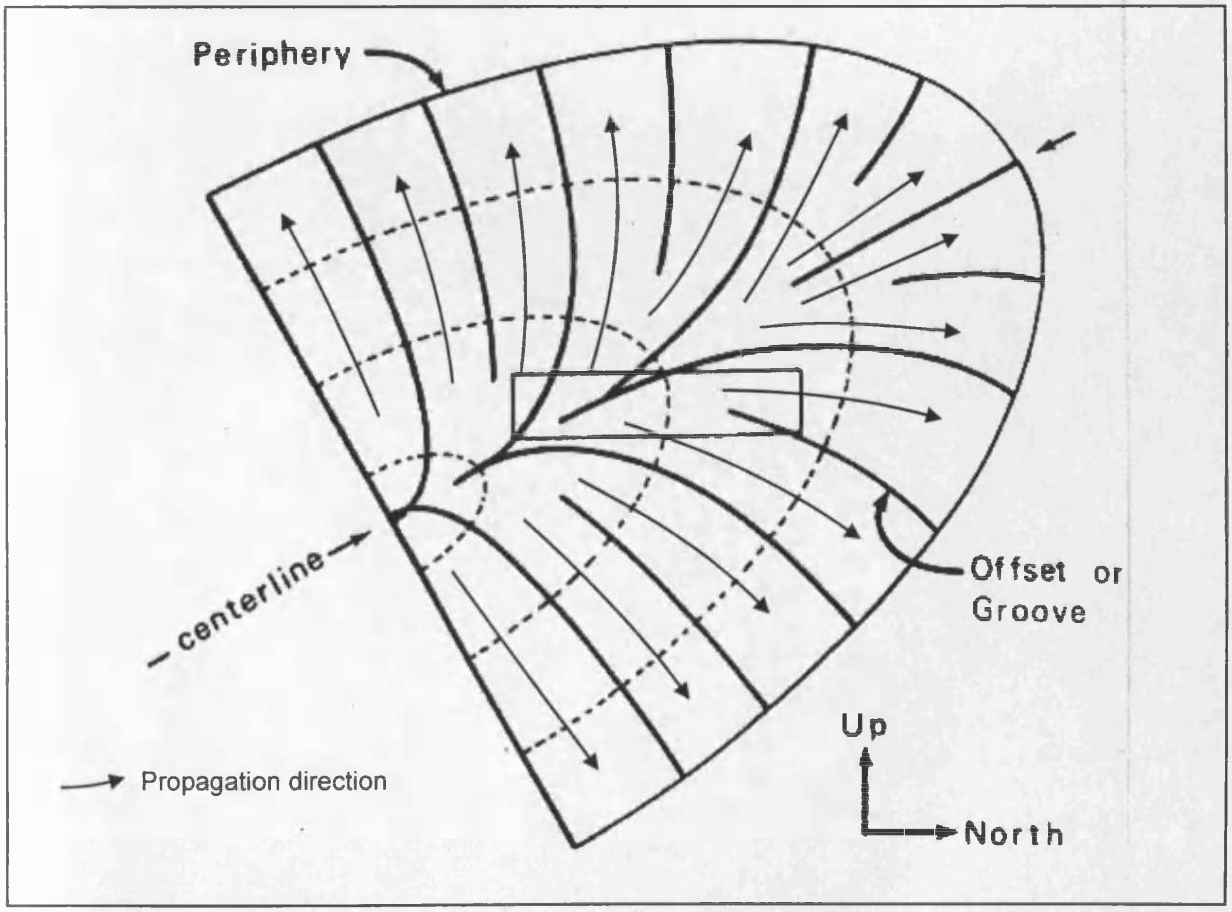

Fig. 4.53 Planview of fingered flow with grooves and offset indicating the propagation direction. After Pollard et al., 1975.

grooves and offsets that Pollard et al. (1975) interpreted to have formed parallel to finger lengths and thus to indicate the propagation direction of the intrusion (Fig. 4.53). The offsets between fingers are interpreted to form as host-rock heterogeneities and anisotropy cause adjacent fingers to propagate out of a single plane or as a result of local changes in the orientation of the principal stresses along the propagation path (Fig. 1.15b). The latter of these explanations can lead to the development of curved sheets and the development of rotated en echelon fingers. The fingers described by Pollard et al (1975) and the lobes of the Solsikke sill lobe system differ in size and in planform geometry, but in cross-section they adopt similar geometries comprised of linked and offset segments.

Segmented dykes (and faults)

Segmented dykes (Delaney & Pollard, 1981; Rickwood, 1990; Baer & Beyth, 1990) offer another analogue to the geometries seen within the Solsikke sill lobe system. Dykes often occur as a number of segments that may be unconnected at any specific erosional level, but which are somewhere interconnected and injected from a common magma source (Fig. 4.54). The planview geometry of a segmented dyke will appear as a number of apparently isolated offset dyke segments that may overlap and form an en echelon pattern. This geometry is very similar to the cross-sectional geometries seen within the lobe system. Baer & Beyth (1990) suggest that the dyke segmentation observed in Har Timna, Israel, occurs due to the presence of pre-existing fractures with major segments of the dyke terminating along ancient planes of weakness in the form of joints. They argue that segmentation is caused by the instantaneous decrease in the stress intensity factor at the tip of dyke segments as they reach the freely-slipping joints or dykes. Delaney & Pollard (1981) acknowledge that pre-existing regional joints in the host-rock may supply anisotropy capable of causing dyke segmentation, however, in the case of the north-eastern dyke they describe from an area near Ship Rock in New Mexico the regional joints exhibit a wrong orientation to be able to explain the segmentation. This leads Delaney & Pollard (1981) to propose an alternative model in which the segmentation is interpreted to occur due to rotation of the least principal stress axis during upward propagation, i.e. a similar process to that of rotated fingers in sills described above.

A similar geometry has recently also been proposed for the growth of segmented normal faults (Childs et al. 1995; Walsh et al., 2002; Walsh et al., 2003). In these

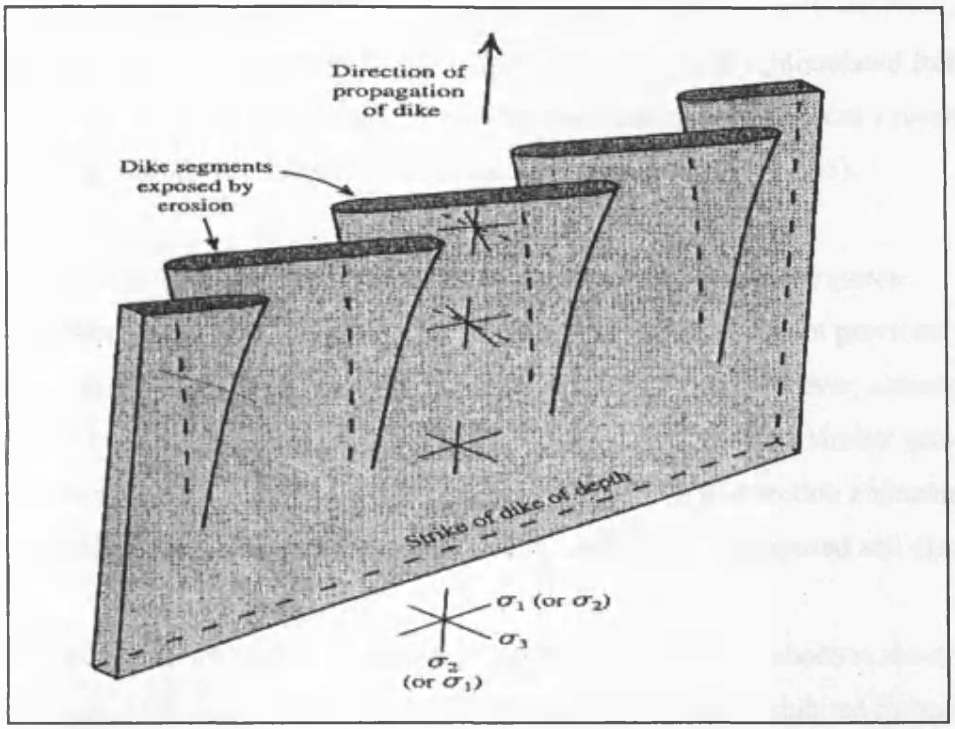

Fig. 4.54 Schematic illustration of sub-vertical en echelon dyke segments. After Delaney and Pollard, 1981.

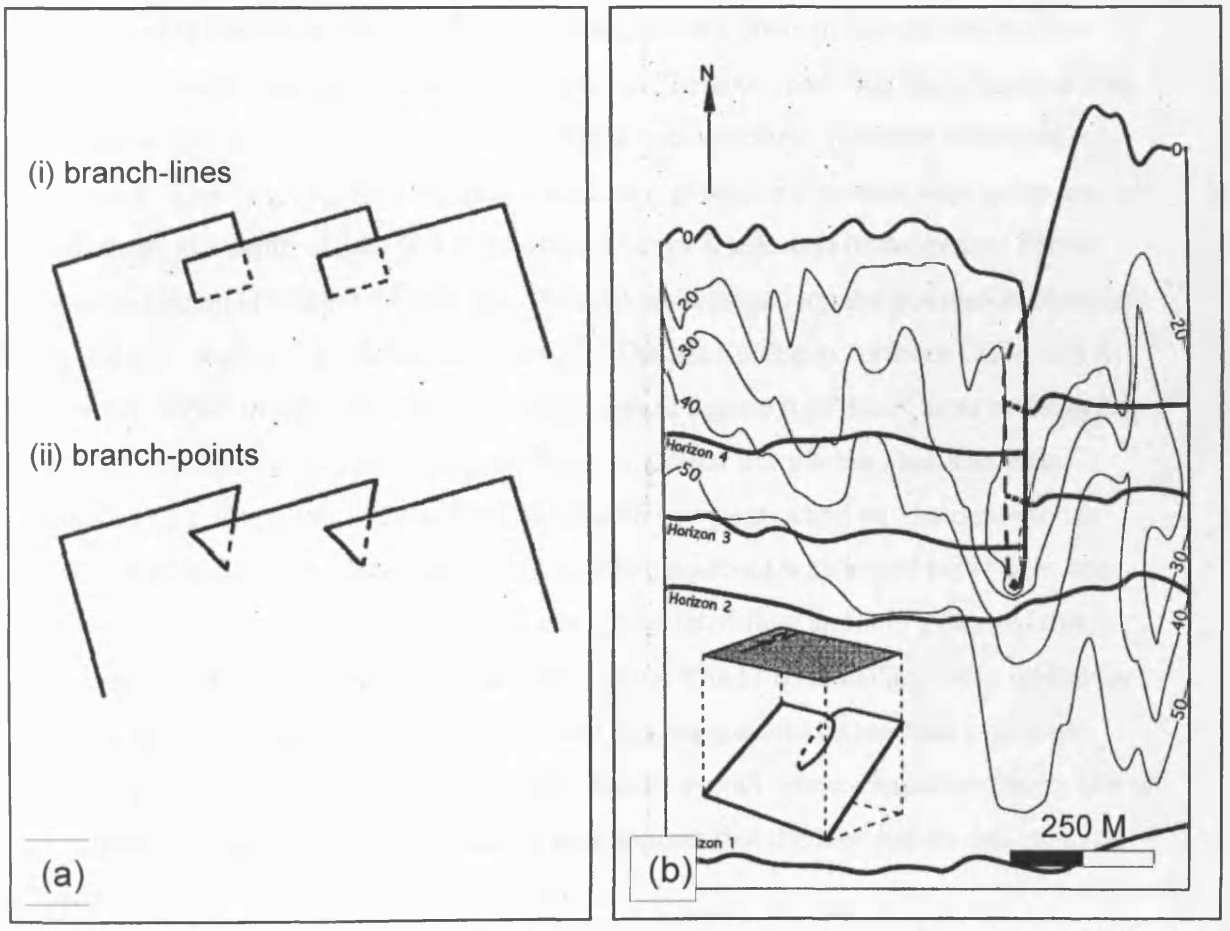

Fig. 4.55 Segmented faults. (a) Schematic illustration of segmented faults. The faults are linked at depth at (i) branch-lines or (ii) branch-points. (b) Horizontal projection and schematic illustration of a segmented faults from the Gulf of Mexico. The fault surface splits upwards at a branch-point into two overlapping fault segments. Both figures from Childs et al., 1995.

models segments of fault arrays are thought to be kinematically interrelated from their initiation and to be linked at depth. The fault bifurcates into segments as a result of propagation through mechanically heterogeneous sediments (Fig. 4.55).

4.6.5.5 Kinematic model for the development of the Solsikke sill lobe system

The Solsikke sill lobe system exhibits a unique geometry that has not previously been described in the literature from either field or seismic studies. However, although there appears to be no direct analogue a number of igneous features with similar geometrical components are known and have been described above. In this section a kinematic model for the development of the Solsikke sill lobe system is proposed and discussed.

The Solsikke sill lobe system is similar in geometry to inflated pahoehoe sheet flows and individual lobes are within the thickness and width ranges exhibited by terrestrial lava flow lobes. Based on the similarities between the lobe system of the Solsikke Sill and extrusive igneous systems it is suggested that the lobe system developed through a process very similar to that of inflated pahoehoe sheet flows. It has previously been inferred that sills emplaced at shallow depth may behave much like flows because they intrude sediments that are poorly consolidated and therefore offer little resistance to intrusion. Trude (2004), for example, studied an igneous sill intruded into water-logged sediments at a depth of 340-610 m of in the Corona Ridge area of the central Faeroe-Shetland Basin (Tranches 61 and 62). This sill has a ridged top surface almost identical to that of pahoehoe lave flows, e.g. the Chao Dacitic Coulee in northern Chile, and it was interpreted to have formed by compression of a more rigid outer layer of magma in the sill, retarded by the solidifying sill front. A similar morphology has also been mapped on a sill (sill 44) in the T38 3D seismic survey area and will be described in detail in Chapter 5. The Solsikke Sill is clearly discordant with stratal reflections and this confirms that it is an intrusion and not an extruded flow and it is estimated that it was emplaced at a depth of approximately 300 m. The Solsikke lobe pattern resembles that of an inflated pahoehoe sheet flows and this suggests that it may have behaved much as a flow. However, the lobe system has an overall saucer-shaped geometry that is commonly adopted by sill intrusions. It thus appears that the lobe system has behaved partly as a flow and partly as an intrusion.

A simple schematic model for the proposed emplacement model of the lobe system of the Solsikke Sill is illustrated in Fig. 4.56. In this model the lobe system propagates

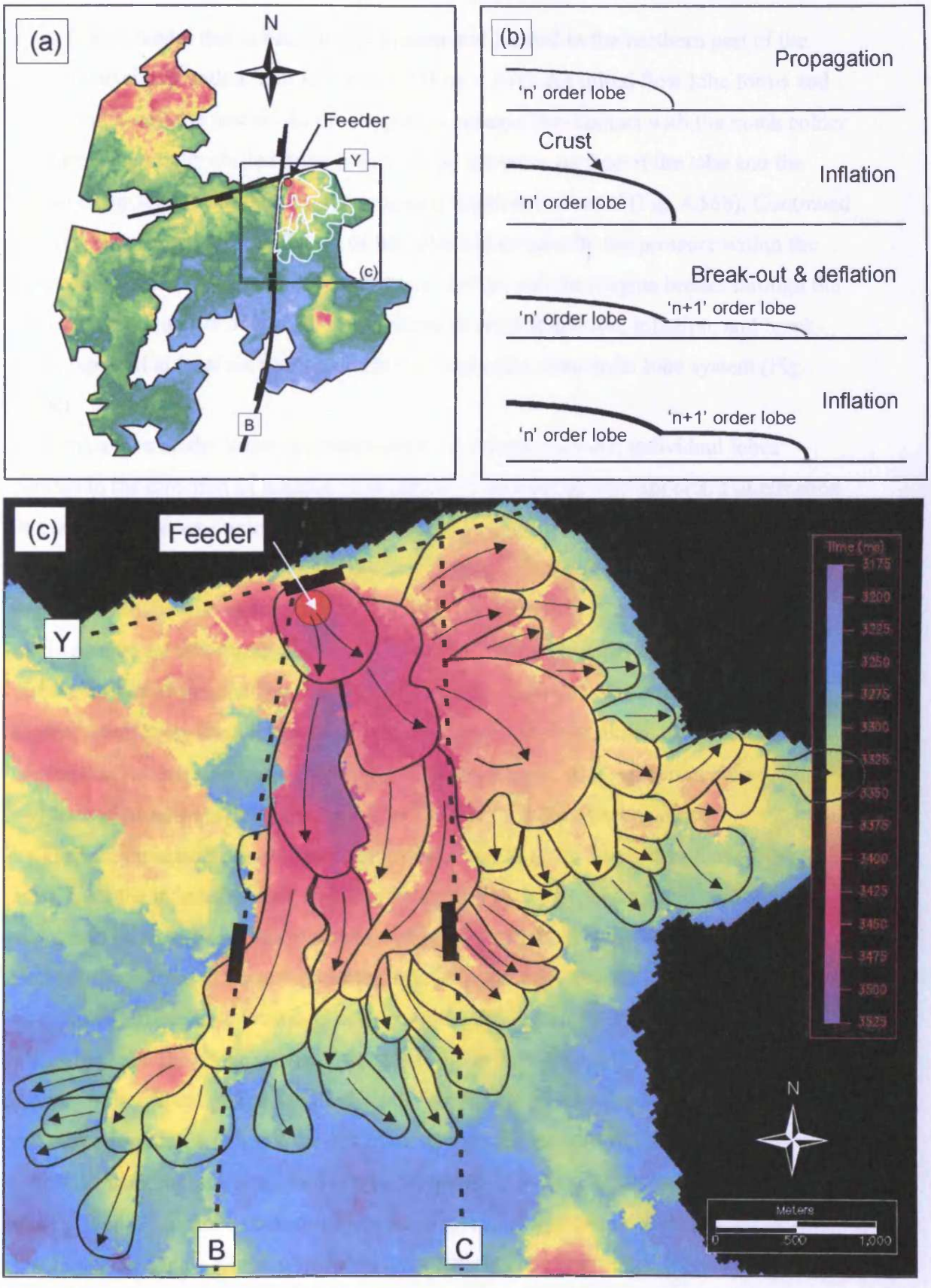

Fig. 4.56 Model for the development of the Solsikke sill lobe system. (a) The lobe system is seen in the north-eastern part of subarea A of the Solsikke Sill and propagates south and south-eastwards away from a feeder that is near-basal to the system and located northern part of the system coincident with a fault intersection. (b) The lobes form as a result of successive episodes of lobe inflation, lobe front rupture and magma break-out, and subsequent deflation. (c) Detailed time-structure map of the lobe system showing the inferred flow pattern away from the feeder.

away from a feeder that is basal to the system and located in the northern part of the system coincident with a fault intersection (Fig. 4.56a). An initial flow lobe forms and spread out above the feeder. As the magma is brought into contact with the much colder sediments a partially chilled crust is formed on the outer surface of the lobe and the spread of the lobe is inhibited as the tensile strength is increased (Fig. 4.56b). Continued input of magma promotes inflation of the lobe and eventually the pressure within the lobe overcomes the tensile strength of the lobe crust and the magma breaks through the lobe front in a number of places. The process of crust formation, inflation, and break-out is repeated at least six times to form the final multi-lobe order lobe system (Fig. 4.56c).

In the above model linear discontinuities are formed between individual lobes parallel to the direction of magma propagation. This has the very important implication that such linear discontinuities mapped internally within sills and not directly linked to offsets on faults can be used as indicators of magma flow direction. This is of great importance in seismic-based studies of igneous intrusions because these are only very rarely penetrated and sampled during exploration drilling. The use of these linear discontinuities as magma flow indicators is similar to the use of bifurcation and segmentation away from feeders and nucleation points in the analogues presented in section 4.6.5.4. In these cases the offsets between fingers, and separation between dyke and fault segments are developed parallel to the direction of propagation.

The lobes located nearest the inferred feeder location are larger than those located away from the inferred feeder, towards the periphery of the lobe system, and there appears to be an increase in the number of lobes away from the inferred feeder. Breakouts occurred in several locations on the initial lobe, suggesting that any lobe is likely to fail in multiple locations as the continued input of magma raises the pressure within the lobe above the tensile strength of the chilled lobe crust. The location and spacing of break-out points are likely to be controlled by local host-rock heterogeneities and stress conditions (cf. Wadge & Lopes, 1991). The number of lobes increases following each rupture event and it was estimated in section 4.6.4 that any lobe of lobe order n is likely to fail in two or three places giving rise to two or three $n+1$ order lobes. The break-out points where new lobes form appear to be fairly evenly spaced and preferentially located in the flow direction (Fig. 4.56).

The decrease in lobe size away from the feeder (section 4.6.4) can be explained in at least two different ways. The first way in which it can be explained is if, through time,

the magma supply rate decreases and the more distal lobes, as a result, have less time to grow before cooling increases the tensile strength at the lobe front and promotes inflation rather than continued spread of the lobe. Alternatively, the decrease in lobe size could be the result of an increase in the size of the sill and thus that the magma supply is feeding a larger body and therefore is feeding individual areas of the body more slowly than if it was smaller. Although the data are sparse there is some evidence suggesting that the total area (volume) of the different lobe orders remains relatively constant, which would support the latter of these two explanations.

In the model for inflated pahoehoe lava flows presented in section 4.6.5.4 the lobate system is suggested to be fed continuously and the development of the system is primarily controlled by the relationship between magma supply and cooling rates. Similarly the Solsikke sill lobe system could have developed during a single phase of intrusion with the lobate geometry being mainly controlled by the supply rate, magma temperature and thermal conductivity of the host-rock. Alternatively, the individual lobe orders could have formed as a result of consecutive pulses of magma injection, with each lobe order forming as a result of one injected pulse. Such magma pulses may be quite regular and typically occur on a time-scale of months to several years (Barmin et al., 2002)

As mentioned earlier no direct analogues to the Solsikke sill lobe system has been observed in any of the other case-study areas used in this study or described in the literature. However, the western part of subarea A west of the Solsikke sill lobe system appears to exhibit a comparable geometrical style. This area is characterised by a number of N-S trending linear discontinuities that radiate away from a linear trend within the neck region between sub-areas A and D (Figs. 4.32, 4.37, and 4.57). A cross-section through this system of linear discontinuities was shown in Fig. 4.39 and from this section it is clear that the cross-sectional geometry of the Solsikke Sill within this region is very similar to that exhibited by the Solsikke sill lobe system. This suggests that this part of the sill has a similar lobate geometry and formed in a similar way to the lobe system to the east. The planview geometry of the western lobe system is shown in Fig. 4.57. The lobes have been mapped based on their appearance on attribute maps (Fig. 4.57b). They form a divergent system of elongated lobes that shows less bifurcation than the Solsikke sill lobe system described above. It is proposed that this lobe system formed in a similar way to the Solsikke sill lobe system and that it was fed,

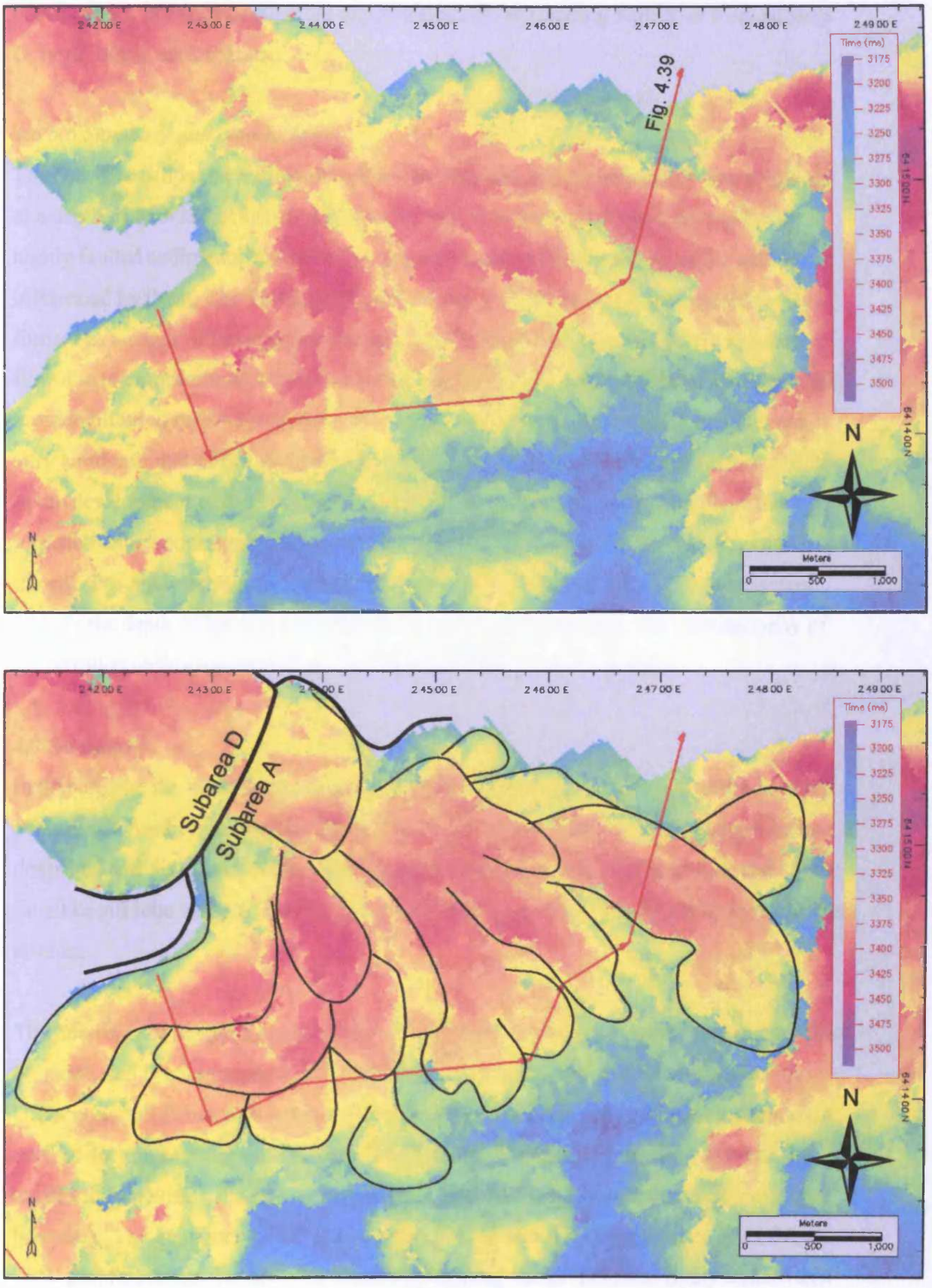

Fig. 4.57 Time-structure map showing lobe-like geometry in the western part of subarea A. A number of N-S to NW-SE oriented elongated lobate segments radiate away from a NE-SW trending lineament to the north, which defines the boundary between subareas A and D. Note line location for Fig. 4.39.

possibly by a linear dyke segment exploiting the E-W trending fault Y or from subarea D, north of the neck region.

4.6.5.6 Summary and conclusions

The Solsikke Sill is the shallowest sill in the Solsikke survey area and it was emplaced at a depth of 850-225 m below the contemporaneous seabed. It was emplaced into highly faulted sediments and both the shape and internal morphology of the sill are influenced by them. The Solsikke sill lobe system is unique and is interpreted to have formed as a result of the magma behaving partly as an intrusion and partly as a lava flow due to emplacement at relatively shallow depth into unconsolidated sediments that provided limited resistance to flow. It is suggested that the sill intruded in a manner very similar to that of inflated pahoehoe flows where cooling of the sill surface results in the development of a crust on the flow that increases the tensile strength of the intrusion and encourages inflation of the intrusion rather than forward propagation of the sill. The analysis suggests that controls upon the development of the lobe system include the depth of intrusion and the properties of the host-rock, the heterogeneity of the intruded sediments, as well as the magma pressure and properties,

4.7 Summary

In this chapter the intrusive igneous system of the Solsikke survey area of the northern Møre Basin has been analysed. Three different levels of intrusive systems have been described and discussed: (1) the Solsikke sill complex, (2) the Solsikke Sill, and (3) the Solsikke sill lobe system. The main points of this chapter are briefly summarised in this section.

The *Solsikke sill complex* is comprised of more than 30 sills, covers an area greater than 600 km^2, and is comprised of at least 60 km^3 of magma. The sills were intruded into Cretaceous and Paleocene sediments during the early Paleogene and span a compacted vertical section of more than 4.5 km. The density of intrusion is greatest towards the north and east within the survey area and no sills are seen towards the southern survey boundary. The geometry of the sill complex is influenced by the presence of a NNE-SSW trending dome feature with shallowly dipping flanks that most likely formed as a result of inversion during the late Cretaceous.

The *Solsikke Sill* is the shallowest sill of the Solsikke sill complex and was emplaced at a depth of 850-225 m below the contemporaneous seafloor. It covers an area of 120 km^2 and has a vertical relief of approximately 600 m. It is estimated that it may comprise up to 6 km^3 of magma. The Solsikke Sill has been sub-divided into 4 sub-areas that are separated by narrow neck regions. It is proposed that the individual sub-areas were fed by one or more feeders and that they initially propagated independently and amalgamated to form the Solsikke Sill. It exhibits an exceptionally complex geometrical style. The geometry of the Solsikke Sill has been influenced by pre-existing faulting of the intruded sediments and this is reflected both in the shape of the sill and in its internal morphology. The morphology of the sill exhibits saucer-shaped sub-elements and numerous linear discontinuities that are partly related to the pre-existing faulting and the stratigraphic context.

The *Solsikke sill lobe system* is found in the north-eastern part of subarea A of the Solsikke Sill. It covers an area of 20 km^2, has a vertical relief of 300 m, and comprises an estimated volume of less than 1 km^3 of magma. It is characterised by numerous N-S to NE-SW trending discontinuities that give the lobe system a highly segmented cross-sectional geometry. When mapped in three-dimensions individual segments have been found to be lobe-shaped and more than 40 interlinked lobes have been mapped. The overall geometry of the lobe system exhibits that of inflated pahoehoe lava flow and it is proposed that the lobe system formed through a process very similar to that of inflated pahoehoe flows. It is suggested that the lobe system is most likely to have been fed by a feeder that exploited the damage zone surrounding a fault intersection that underlies the northern and deepest part of the lobe system.

4.8 Conclusions

This case-study has provided a detailed analysis of different scales of an igneous intrusive system. The main findings with implications for sill complexes in general are summarised below. The conclusions are thematically ordered under the two main headings: (1) the Solsikke sill complex and (2) the Solsikke Sill, rather than ranked.

The Solsikke sill complex:

- Sills have acted as feeder for other sills within the Solsikke survey area and this has given rise to a highly interconnected sill complex that has built up over more than 4.5 km of compacted vertical section
- The intruded Upper Cretaceous and Paleocene host-rocks are intensely deformed by pre-existing and contemporaneously active polygonal faults and these have clearly influenced the geometry and propagation of the sills in general and of the Solsikke Sill in particular
- The dominant sill classes are sill segments and transgressive sheets. No perfect saucers shave been mapped in the survey area
- Compilation of statistical data for sills within the Solsikke sill complex shows moderate correlation between sill area and vertical relief and between maximum emplacement depth and vertical relief, but poor correlation between sill area and maximum emplacement depth. The Solsikke Sill plots off trend and the correlation values increase when the Solsikke Sill is discarded. This is suggested to support an interpretation that the Solsikke Sill was fed by multiple feeders.

The Solsikke Sill:

- The Solsikke Sill is a large compound sills with highly complex geometries that is interpreted to have formed as a result of amalgamation of a number of sills emplaced at a similar stratigraphic level at the same time by multiple contemporaneous feeders
- The Solsikke Sill is emplaced at relatively shallow depth between 850-225 m and has behaved partly as a sill and partly as a lava flow. This is suggested to relate to the low resistance to flow offered by the poorly consolidated host-rock at the shallow intrusion depth
- A fault intersection has been identified as a likely location favourable to upwards magma flow. Two saucer-shaped sill segments of the Solsikke Sill are located above fault intersections, with the intersection being coincident with the basal part of the sill segments
- Some linear discontinuities represent boundaries between adjacent sill segments and these can be used as magma flow indicators.

CHAPTER 5: THE IGNEOUS COMPLEX OF TRANCHE 38 (NORTH-EASTERN ROCKALL BASIN)

5.1 Introduction

5.1.1 Aims of chapter

This chapter aims at describing the igneous complex of the T38 3D seismic survey area located in the NE Rockall Basin (Figs. 1.1 and 5.1). In the T38 survey area many high amplitude reflections are imaged. The majority of these are discordant with stratal reflections and are interpreted as intrusive igneous sills. However, a number of shallow reflections that show a high degree of concordance are also imaged and these are interpreted as shallow sills and in one case as an extrusive lava flow. This chapter provides a three-dimensional interpretation of the T38 igneous complex and, in particular, aims at discussing the geometrical and timing relationship between deep and shallow sills and their timing relationship with lava flow extrusion in the survey area. The chapter also illustrates thickness variations within sills and host-rock deformation associated with sill emplacement.

Following an introduction to the database (section 5.1.2) and the geological setting of the case study area (section 5.2), the three-dimensional geometry of the deepest part of the T38 igneous complex (below horizon B) is described in section 5.3 and the shallowest part of the T38 igneous complex (at and above horizon B) is described in section 5.4. Host-rock deformation associated with sill emplacement is described and discussed in section 5.5. Finally, the main findings of the T38 case study are summarised in section 5.6, whilst the main conclusions of the case study are listed in section 5.7.

5.1.2 Database

5.1.2.1 Seismic data

This chapter is based on interpretation of the T38 3D seismic dataset from the NE Rockall Basin. 2D seismic data have not been available for this case-study. The T38 3D seismic survey covers an area of almost 1400 km^2 and has an inline (NE-SW) and crossline (NW-SE) spacing of 25 m (Fig. 5.2). The data reach a maximum TWT of 7500 ms. Detailed interpretation of the seafloor reflection (positive acoustic boundary) suggests that this dataset displays an increase in acoustic impedance as a wide peak surrounded by troughs (Fig. 5.3). This indicates that the data are zero-phase migrated

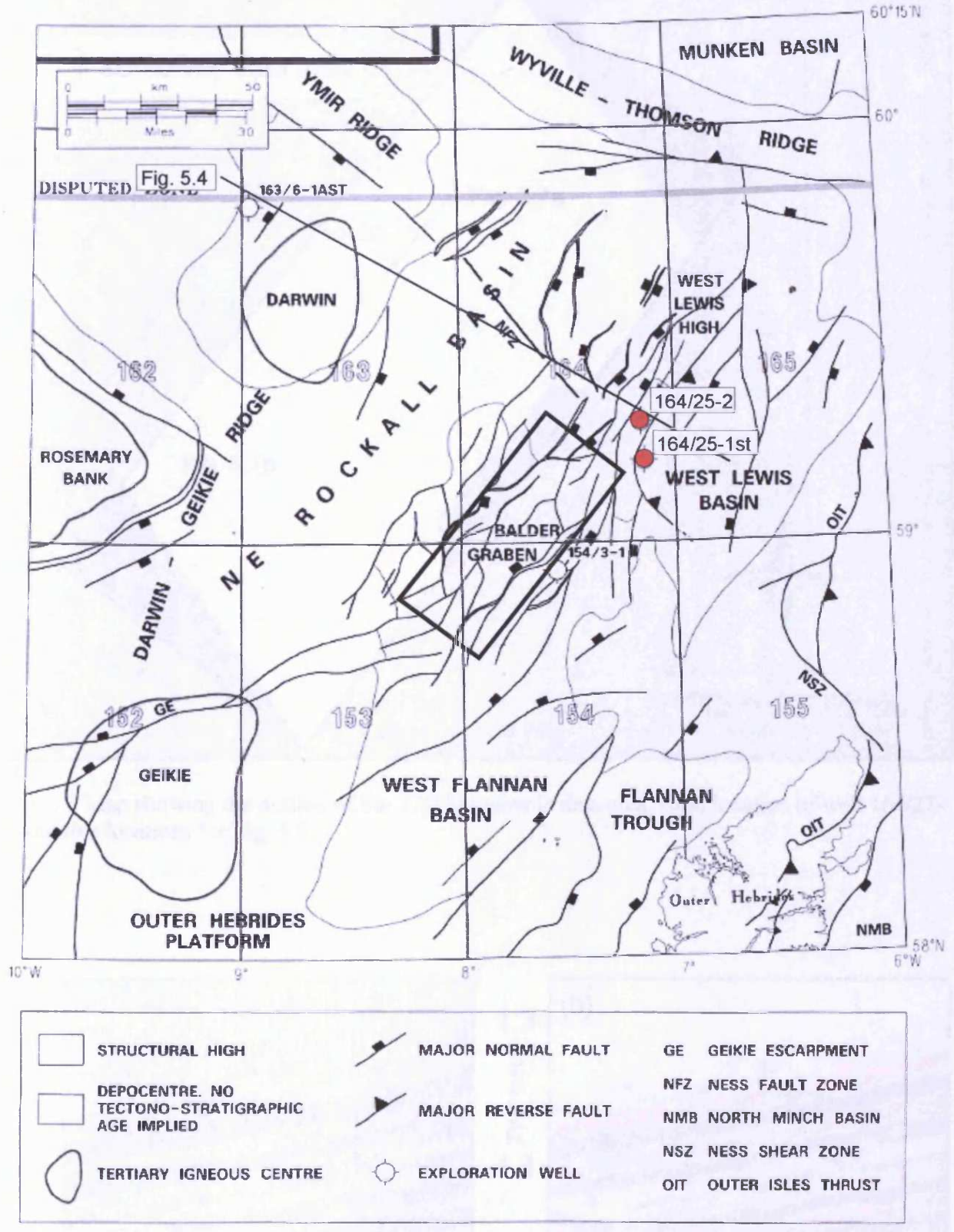

Fig. 5.1 Location map showing the location of the T38 3D seismic dataset in the NE Rockall Trough. Note line location for Fig. 5.4 and locations of wells 164/25-1st and 164/25-2. After Waddams & Cordingley (1999).

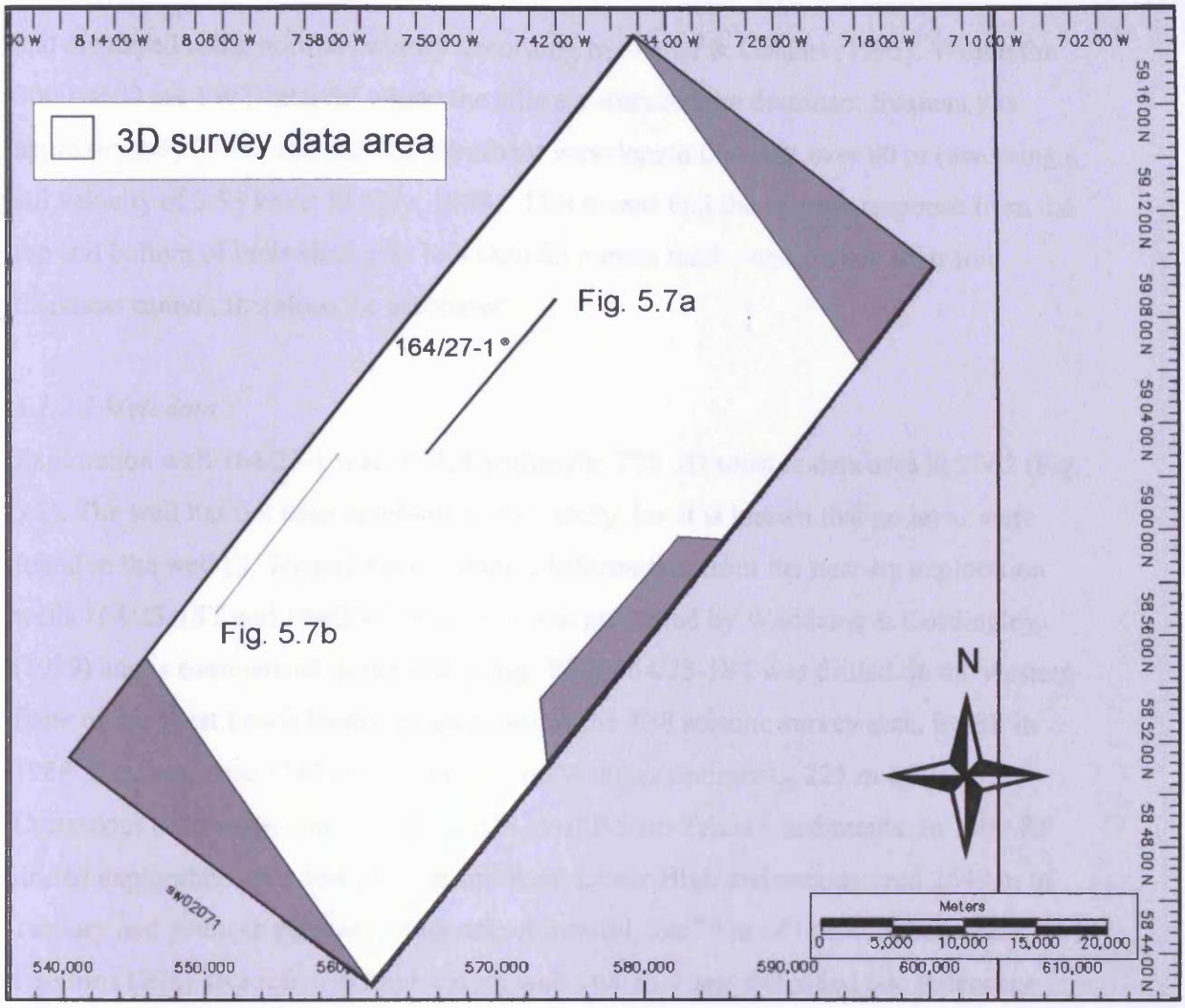

Fig. 5.2 Map showing the outline of the T38 3D seismic data area. Note location of well 164/27-1 and line locations for Fig. 5.7.

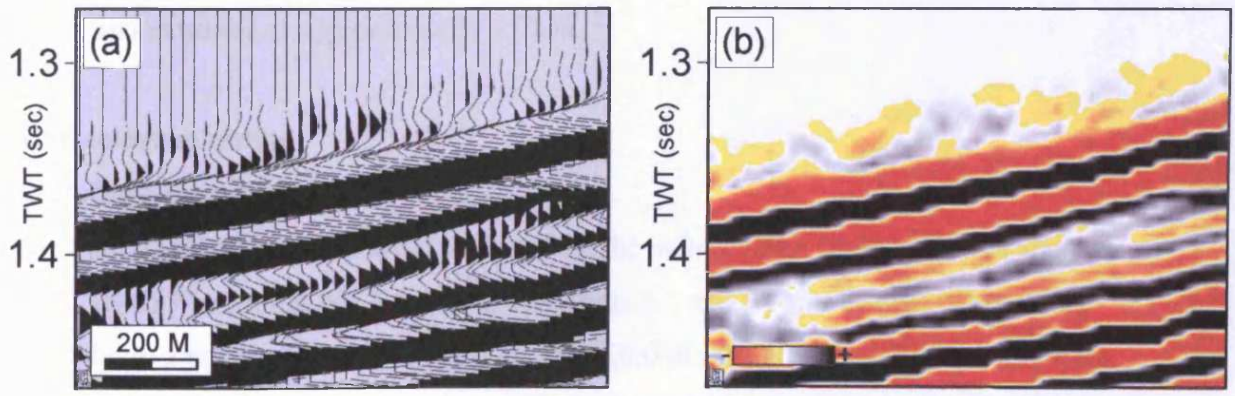

Fig. 5.3 Seabed reflection. (a) Variable area (VA) display. (b) Variable intensity (VI) display. The data are zero phase migrated and displayed using normal polarity (SEG standards).

and displayed using normal polarity according to Sheriff & Geldart (1995). Within the 3000-4500 ms TWT interval where the sills are intruded the dominant frequency is approximately 35 Hz and half the dominant wavelength thus just over 80 m (assuming a sill velocity of 5.55 km/s; Skogly, 1998). This means that the seismic response from the top and bottom of individual sills less than 85 metres thick interfere and their true thickness cannot, therefore, be estimated.

5.1.2.2 Well data

Exploration well 164/27-1 was drilled within the T38 3D seismic data area in 2002 (Fig. 5.2). The well has not been available to this study, but it is known that no lavas were found in the well (S. Wright, Pers. comm.). Information from the near-by exploration wells 164/25-1ST and 164/25-2 (Fig. 5.1) was presented by Waddams & Cordingley (1999) and is summarised in the following. Well 164/25-1ST was drilled on the western flank of the West Lewis Basin, located east of the T38 seismic survey area, by BP in 1988. It encountered 3149 m of Tertiary and younger sediments, 225 m of Late Cretaceous sediments, and more than 675 m of Permo-Triassic sediments. In 1990 BP drilled exploration well 164/25-2 on the West Lewis High and encountered 2649 m of Tertiary and younger section resting unconformably on 79 m of Lewisian basement. Egerton (1998) also refers to exploration well 164/25-1 and described late Paleocene shallow-marine or coastal clastic deposits interbedded with basaltic volcanic rocks. Morton et al. (1988) provided a detailed study of volcanic rocks in exploration well 163/6-1A, located north-west of the Darwin Igneous Centre (Figs. 1.1 and 1.4). The well encountered a thick sequence of extrusive igneous rocks below Upper Paleocene sediments. Based on K-Ar dating it was suggested that the lavas were latest Paleocene in age and extruded at approximately 55 Ma.

5.2 Geological setting

5.2.1 Regional setting

The T38 3D seismic survey area is located on the eastern flank (Balder Graben area) of the NNE-SSW trending NE Rockall Basin (Figs. 5.1 and 5.4) north-west of the Outer Hebrides in a present-day water depth of 350-1300 m. The NE Rockall Basin forms the north-eastern part of the Rockall Trough and is bounded to the north by the Wyville-Thomson Ridge, to the east by the West Lewis High and the Outer Hebrides platform and by the Geikie Igneous Centre and escarpment to the south (Waddams &

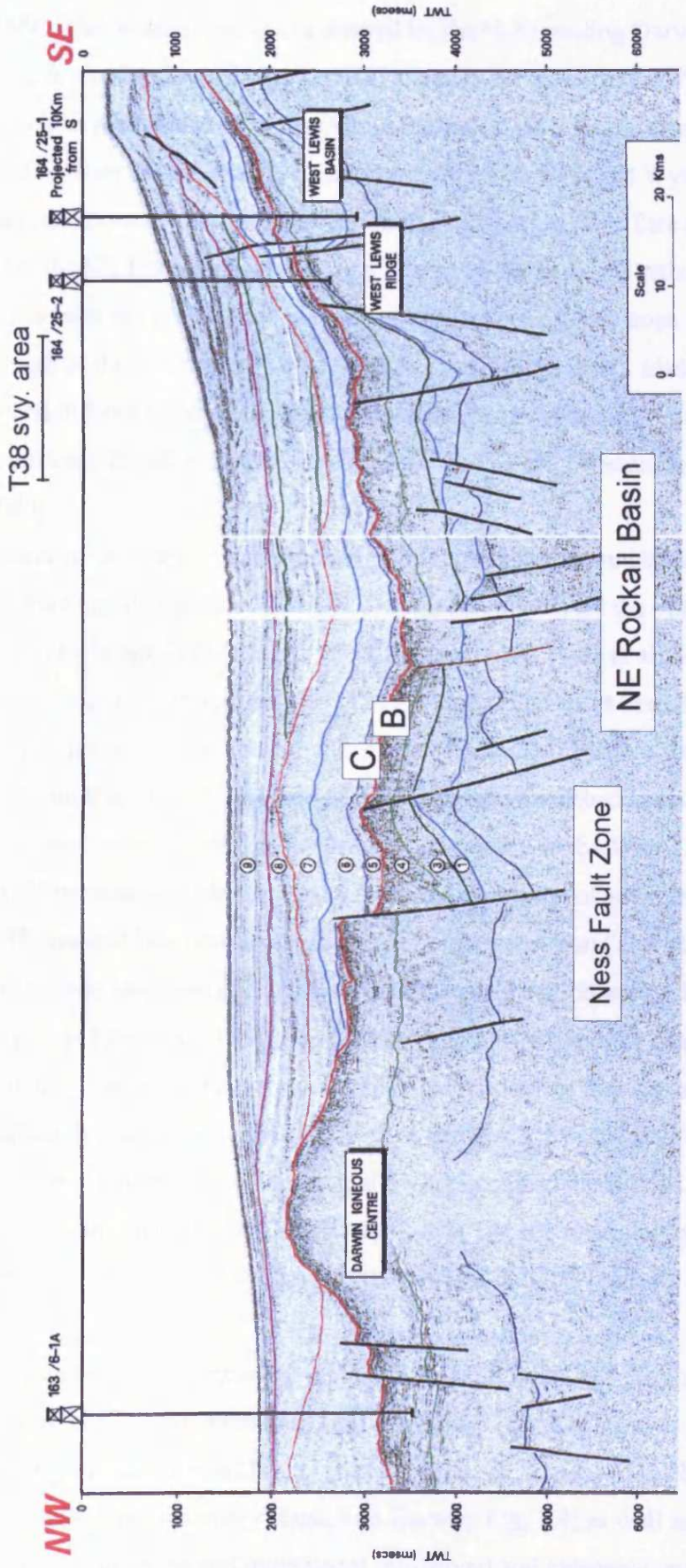

Fig. 5.4 Regional NW-SE trending section extending from the West Lewis Basin to the SE to the Darwin Igneous Centre to the NW. The horizons B and C (section 5.2.2) equivalents have been labelled. Note location of the T38 3D seismic survey area. See Fig. 5.1 for line location. After Tate et al. (1999).

Cordingley, 1999). The western margin is formed by the N-S trending Darwin-Geikie Ridge (Waddams & Cordingley, 1999). The basin area is dominated by a NNE-SSW structural trend that is recognised in basins along the entire NE Atlantic margin. Although separated from the Faeroe-Shetland Basin to the north by the Wyville-Thomson Ridge (late Eocene - Oligo-Miocene fault-propagation fold; Tate et al., 1999) a Jurassic age for the NE Rockall Basin, similar to that of the Faeroe-Shetland Basin to the north-east, has been suggested for the basin as opposed to a Cretaceous origin for the Rockall Trough to the south-west (Waddams & Cordingley; 1999). Mid-Tertiary episodes of inversion have affected the post-Lower Eocene stratigraphy and several inversion structures are found within the basin (Tate et al., 1999; Waddams & Cordingley, 1999).

The basalt cover of the NE Rockall appears to be thinner and more transmissive to acoustic energy than that of the main Rockall Trough and allows for the syn-rift succession to be to be imaged (Tate et al., 1999). Seismic data (Tate et al., 1999) and gravity modelling (Waddams & Cordingley, 1999) suggest that more than 6000 m of Mesozoic section is present in the central part of the NE Rockall Basin. Data from exploration wells, such as 164/25-1ST and 164/25-2 briefly described above, show that Triassic, Jurassic, and Early Cretaceous sediments are present in the West Lewis Basin and West Lewis High areas and this suggests that a similar range of sediments are present in the NE Rockall Basin underneath the Tertiary succession (Tate et al., 1999). The post-rift succession has been divided into nine intervals that broadly follow sequence boundaries (Tate et al., 1999). These nine intervals will not be described in detail herein, but they are mainly comprised of basinal mudstones that contain some scattered basinal sands and slump units (Fig. 5.5; Waddams & Cordingley, 1999). The Paleocene stratigraphy suggests large-scale shallowing occurred during this time most likely due to regional thermal doming, whilst the Lower Eocene stratigraphy suggests a deepening probably in response to collapse of the thermal dome (Waddams & Cordingley, 1999).

Extensive magmatic activity occurred in the NE Rockall Basin and North Rockall Trough from at least the latest Cretaceous until the Early Eocene (Tate et al., 1999). This resulted in the emplacement of large igneous centres in the axis of the Rockall Trough (e.g. Anton Dohrn, Rosemary Bank, and Darwin; Fig. 1.4) as well as smaller centres (that sourced volcanoes and hypabyssal intrusions) and extensive lava flows. The Anton Dohrn and Rosemary Bank igneous centres are thought to be late Upper

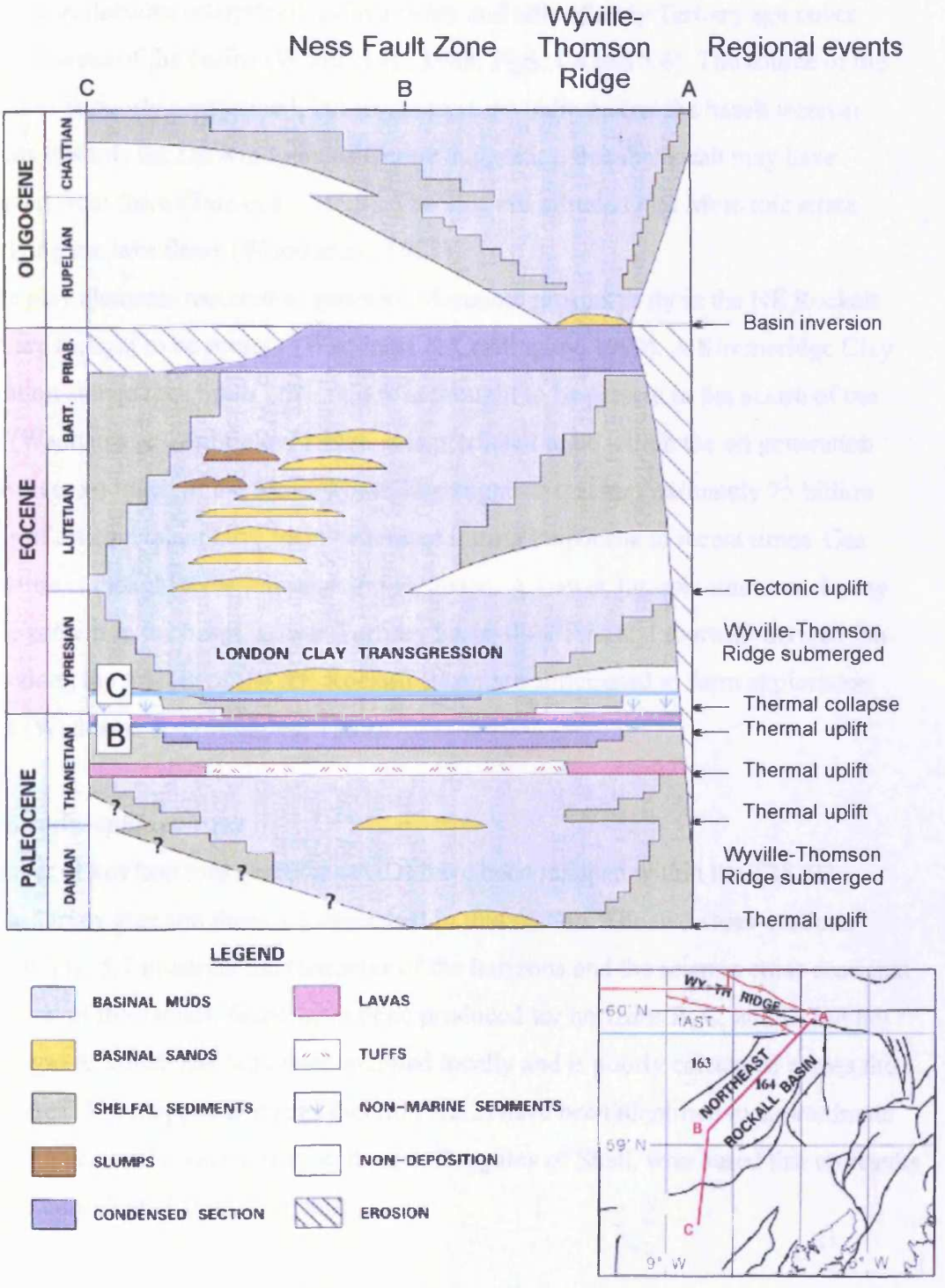

Fig. 5.5 Schematic chronostratigraphic diagram for the NE Rockall Basin. The approximate locations of horizons B and C have been marked. After Waddams & Cordingley (1999)

Cretaceous in age, whilst the Darwin Centre, adjacent to the NE Rockall Basin, is likely to be slightly younger in age, yielding Paleocene dates (Tate et al., 1999). High amplitude reflections interpreted as lava flows and sills of early Tertiary age cover extensive areas of the basins (Wood et al., 1988; Figs. 1.4 and 5.6). The source of the lava flows is poorly constrained, but isochore maps indicate that the basalt interval thickens towards the Darwin Igneous Centre suggesting that the basalt may have emanated from there (Tate et al., 1999). The sills are intruded into Mesozoic strata underlying the lava flows (Wood et al., 1988).

The play elements required to generate Mesozoic prospectivity in the NE Rockall Basin are thought to be present (Waddams & Cordingley, 1999). A Kimmeridge Clay Formation source rock up to 250 m thick is thought to be present in the centre of the basin (Waddams & Cordingley, 1999). It is predicted to be within the oil generation window across much of the basin. Modelling suggests that approximately 75 billion barrels of oil equivalent have been generated during Paleocene to recent times. Gas generation is thought to be minimal and localised. A Lower Jurassic source rock may also be present in the basin. Lower Tertiary basin-floor fans and footwall-derived fan-deltas along the margin of the NE Rockall Basin are anticipated to form exploration targets (Waddams & Cordingley, 1999).

5.2.2 Stratigraphic context

A number of key horizons (horizons A-D) have been mapped within the T38 3D seismic survey area and these are described in this section. The two cross-sections shown in Fig. 5.7 illustrate the character of the horizons and the seismic cross-sectional expression of the dataset. Maps have been produced for horizons B, C, and D, but not for horizon A, which has only been mapped locally and is poorly correlated across the survey area. The mapped horizons (section 5.2.2) have been identified in approximate terms by a personal communication from J. Bagguley of Shell, who based this on results from the confidential 164/27-1 well.

Horizon A has been picked locally as a continuous positive reflection of moderate amplitude. The seismic package immediately below horizon A is characterised by low amplitude discontinuous to moderately continuous reflections. The horizon is close to Base Tertiary (J. Bagguley, pers. comm.). Numerous high amplitude reflections interpreted as igneous sills are seen to terminate at the horizon (Fig. 5.7a).

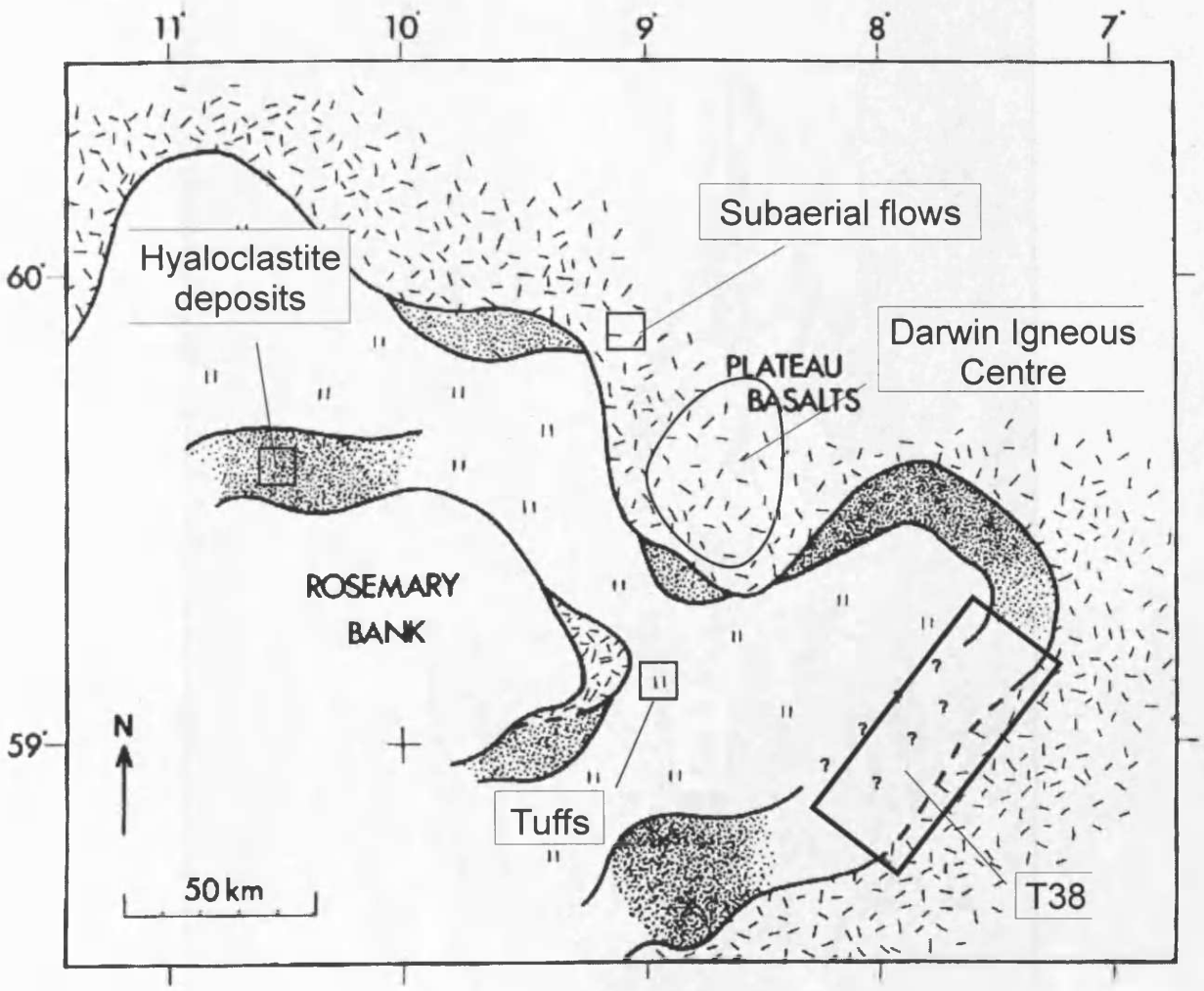

Fig. 5.6 Distribution of subaerial flows, hyaloclastites, and tuffs of early Tertiary age in the NE Rockall Basin. The T38 3D seismic survey area is located in a poorly understood part of the basin near the western edge of the plateau basalts. The approximate location of the Darwin Igneous Centre has been added to the map (based on Waddams & Cordingley, 1999). After Wood et al. (1988).

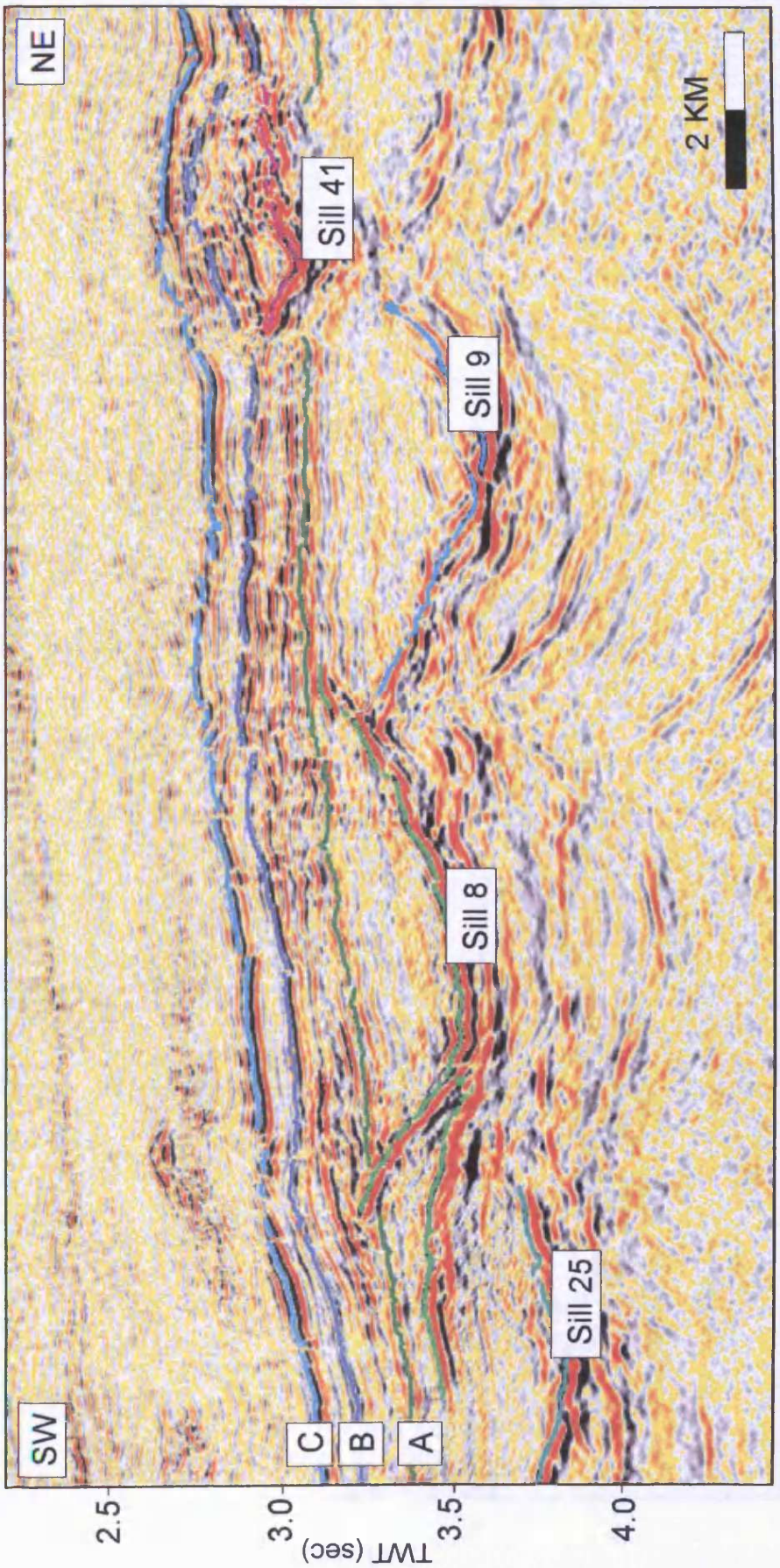

Fig. 5.7a Seismic section illustrating the character of horizons A-C. Note sill termination at both horizons A (sill 8) and B (sill 41) and deformation of horizons B and C overlying sill 41. See Fig. 5.2 for line location.

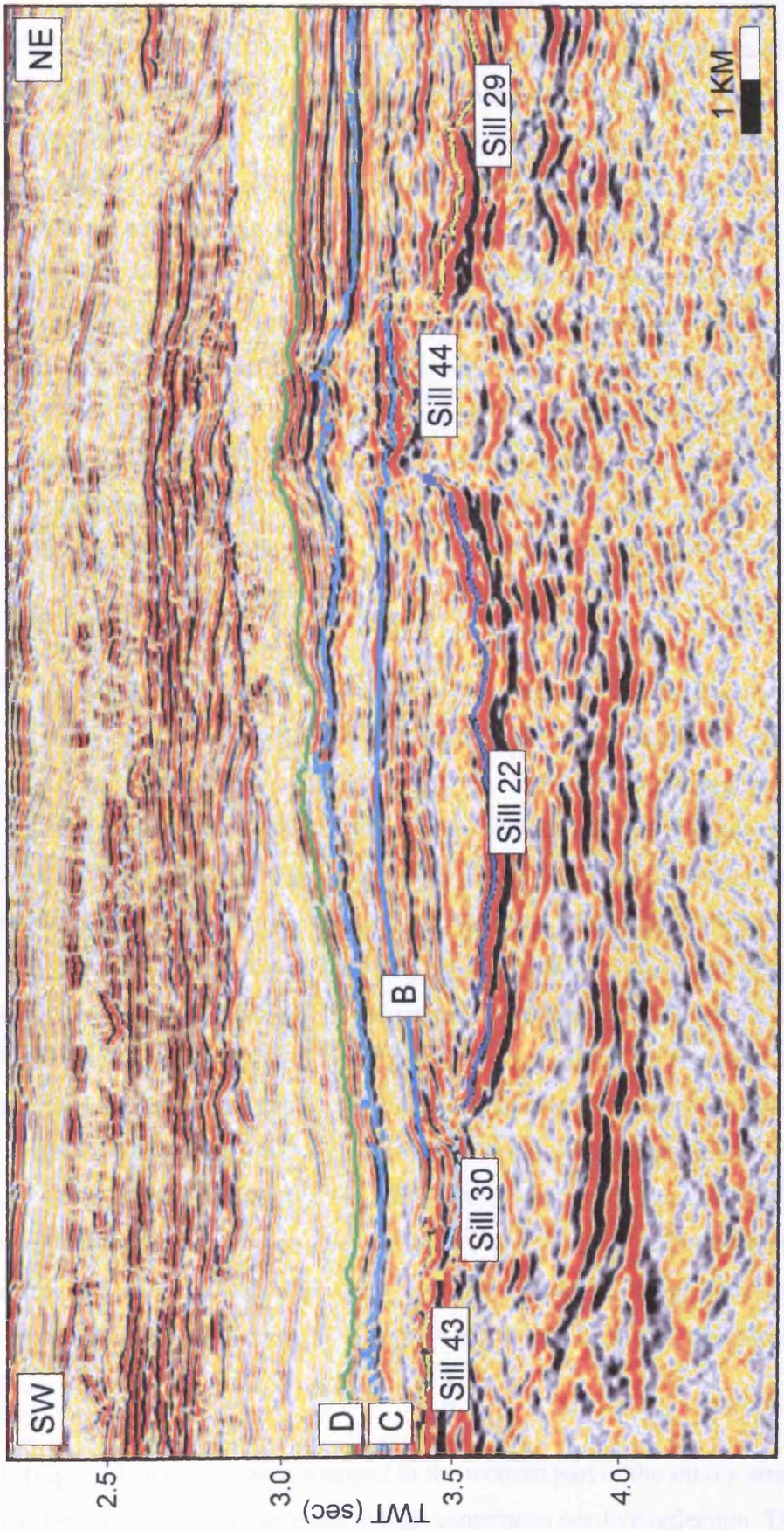

Fig. 5.7b Seismic section illustrating the character of horizons B and C. Note termination of sills at the approximate level of horizon B (sills 22 and 30) and sills 43 and 44 that are continuous with horizon B.

Horizon B (Fig. 5.8) marks the Top Faeroe Group (J. Bagguley, pers. comm.) and has been mapped as a moderate to high amplitude continuous negative reflection. It has been mapped across most of the survey area, but it has not been interpreted along the eastern survey boundary. The horizon is Late Paleocene in age and is approximately equivalent to the top of unit 4 shown in Fig. 5.4, which is interpreted to mark the Top Basalt reflector. The A-B unit exhibits moderately continuous to continuous moderate to high amplitude reflections corresponding to sandstone and claystone lithologies (J. Bagguley, pers. comm.). Several sills are seen to terminate at approximately the horizon B level (Fig. 5.7b). Elsewhere the horizon is interpreted to have been deformed during intrusion of deeper sill (Fig. 5.7a) and the horizon, locally, appears to be onlapped by the overlying strata within the B-C interval. A number of concordant and near concordant high amplitude reflections are seen to be continuous with the horizon (Fig. 5.7b).

Horizon C (Fig. 5.9) has been interpreted across most of the survey area as a moderate to high amplitude negative reflection. It marks the Top Balder Formation (J. Bagguley, pers. comm.) of earliest Eocene age (Tate et al., 1999). The B-C unit is characterised by low amplitude moderately continuous reflections and is dominated by claystones and volcaniclastic claystones (J. Bagguley, pers. comm.). The horizon is offset by many closely spaced faults that are seen to form a polygonal fault pattern, particularly in the central part of the survey area (Fig. 5.9b). No igneous sills are seen to cross-cut this reflection, but the horizon is locally deformed above underlying sills (Fig. 5.7a) and is onlapped by the overlying strata. In the north-eastern corner of the survey area, two mound structures are clearly imaged on the time-structure map of the horizon (Fig. 5.10). The resolution of the data and the low acoustic impedance contrast between these mounds and the overburden makes it very difficult to determine the true relationship between them and horizon C. On the map shown in Fig. 5.9 horizon C has been mapped across the mounds, however, it is considered likely that horizon C onlaps the mounds and that the mounds pre-date horizon C. These structures will be further described and discussed in Chapter 6.

Horizon D (Fig. 5.11) has only been mapped in the western part of the survey area. The reflector has been mapped as a moderate to high continuous positive reflection. The horizon has a mounded morphology and downlaps onto horizon C suggesting a non-

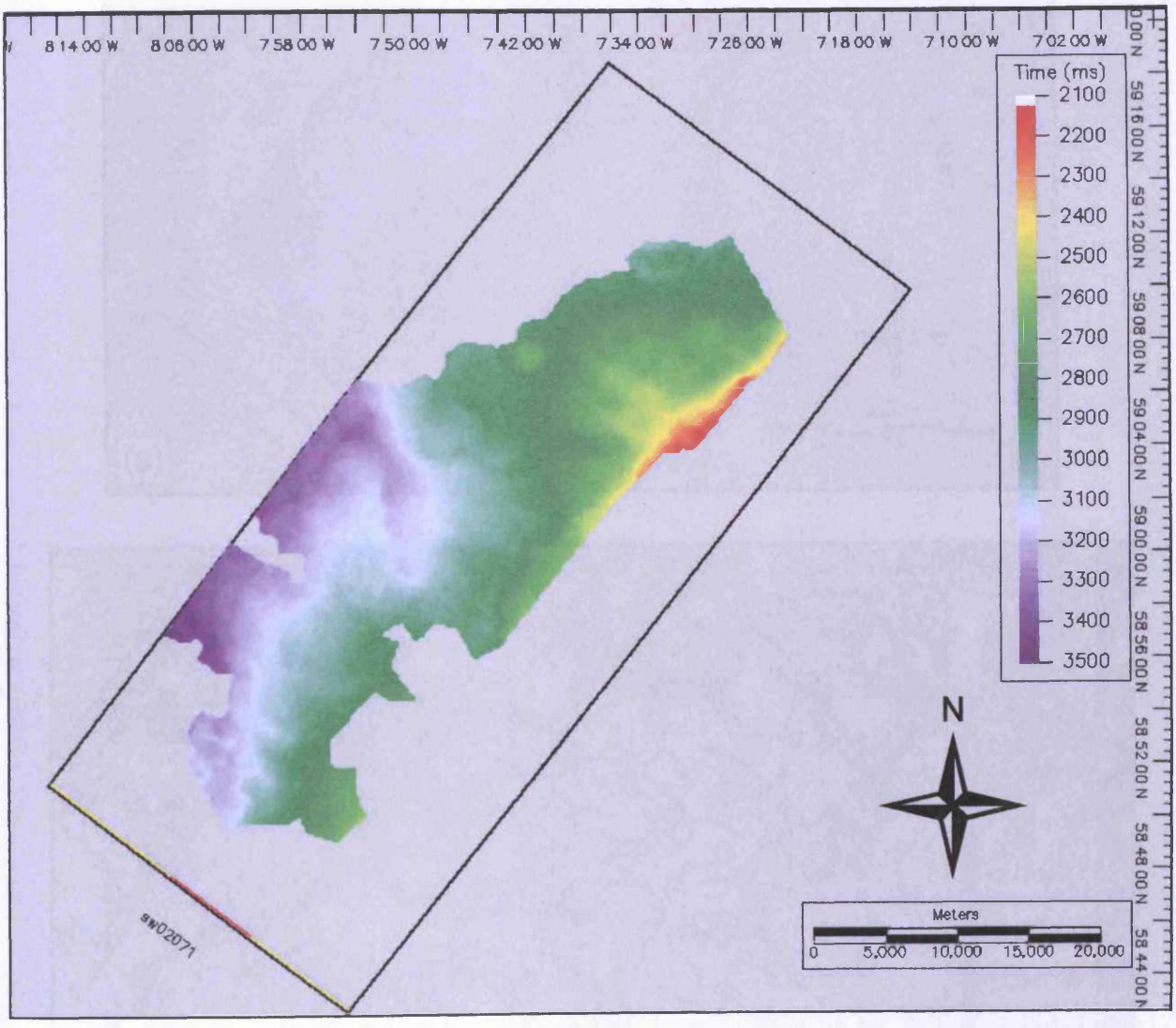

Fig. 5.8 Time-structure map of horizon B.

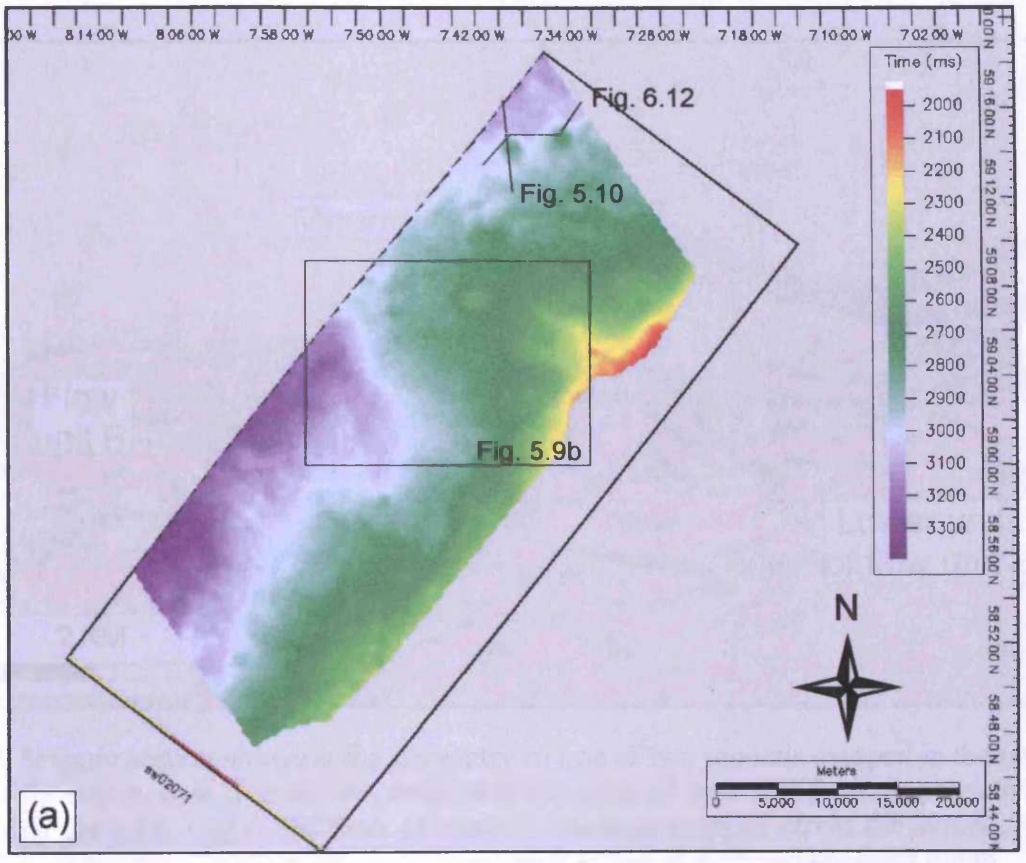

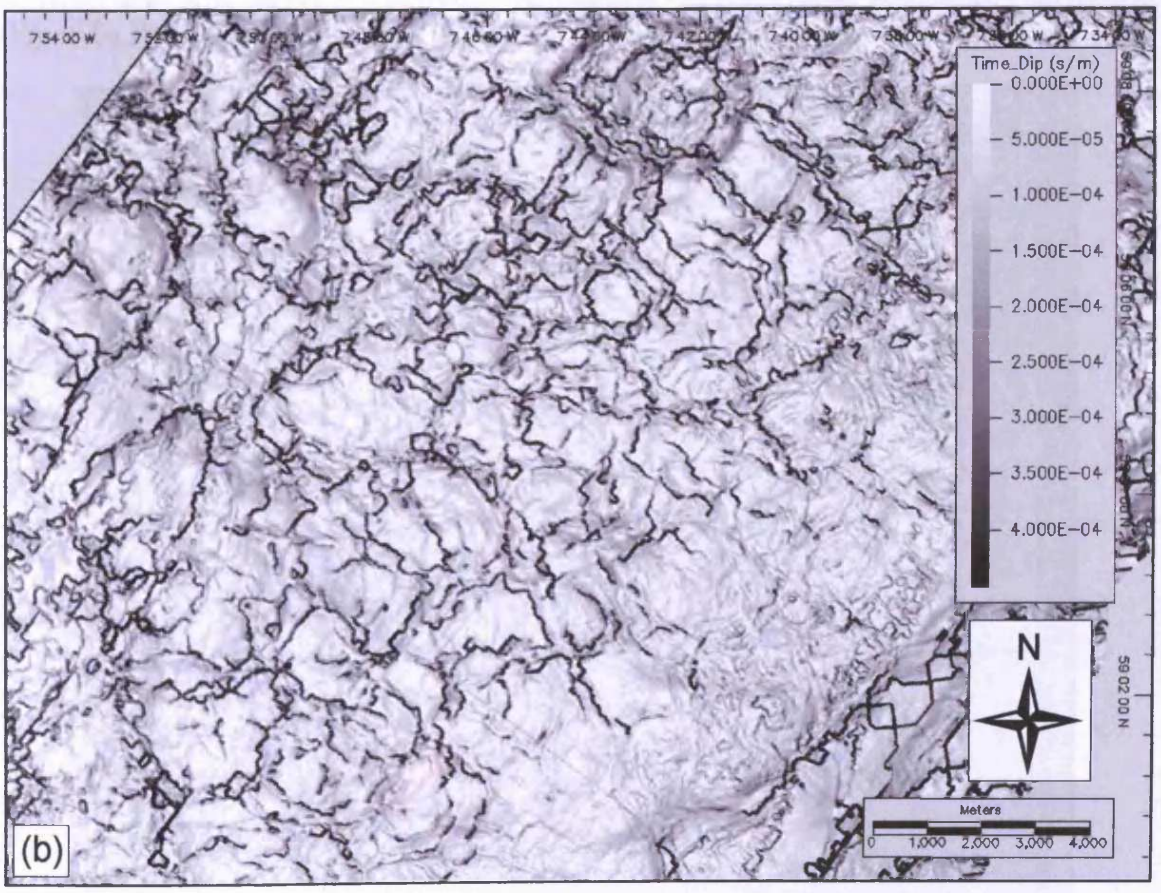

Fig. 5.9 Horizon maps of horizon C. Note line location for Fig. 5.10. (a) Time-structure map. (b) Time-dip map showing polygonal faulting.

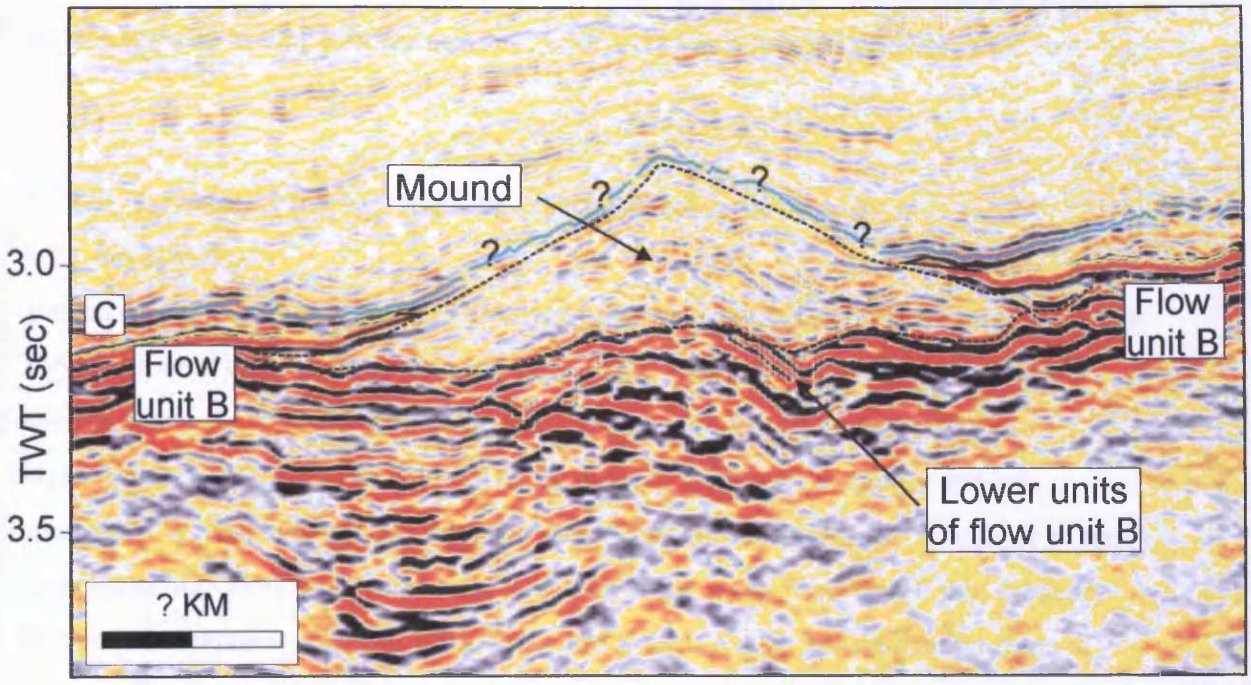

Fig. 5.10 Seismic section showing the geometry of one of two mounds mapped in the northern corner of the survey area. The mound rests on lower units of flow unit B and appears to be onlapped by the upper unit of the flow. Horizon C has been mapped across the mound. However, mapping is very difficult and based on the geometry of the mound and apparent onlap relationship with flow unit B it is possible that horizon C onlaps rather than drapes the mound. See Fig. 5.9a for line location.

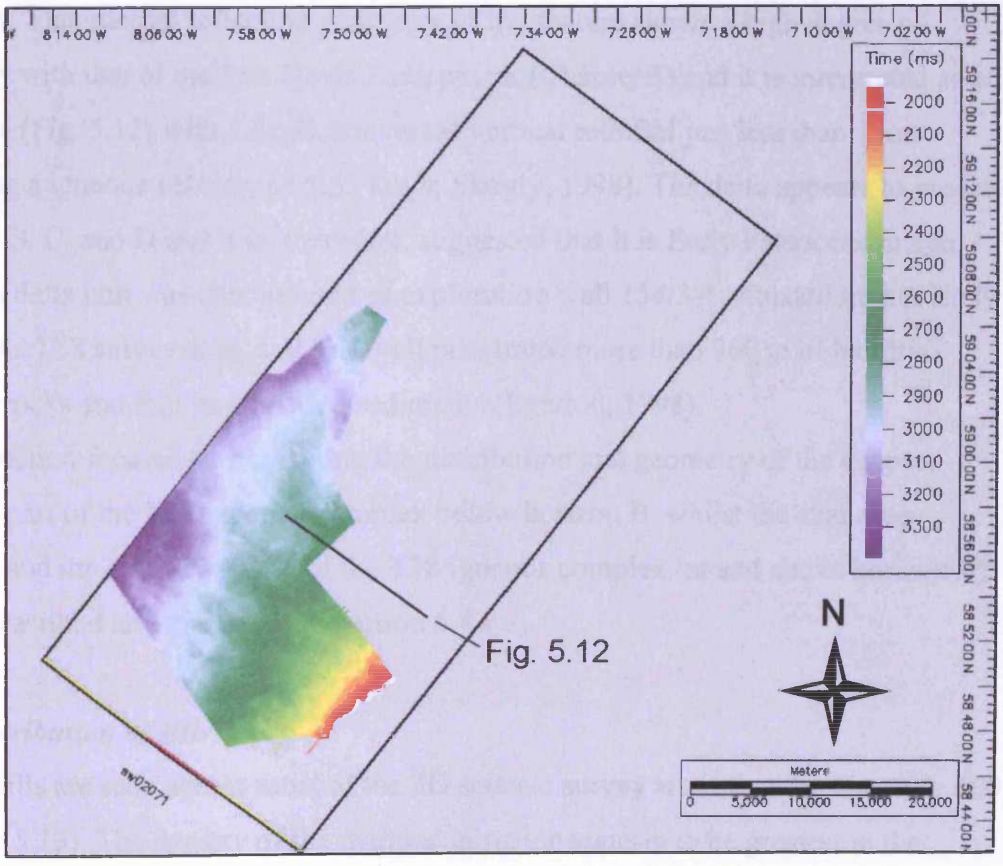

Fig. 5.11 Time structure map of horizon D. Note line location for Fig. 5.12.

pelagic origin and probably rapid deposition. The age of the horizon is unknown. The horizon appears to drape an escarpment, interpreted as a lava delta towards the east (Fig. 5.12).

5.3 The Tranche 38 intrusive igneous complex below horizon B

5.3.1 Introduction

Numerous high amplitude reflections interpreted as igneous in origin are imaged by the T38 3D seismic dataset. They occur within Upper Cretaceous and Lower Paleogene sediments and the mapped sills in the survey area span a vertical section of approximately 2300 m. The majority of these reflections are discordant and are interpreted as intrusive igneous sills and are described in this section. A number of near-concordant high amplitude reflections are seen at the level of horizon B and these are interpreted as shallow sills (sections 5.4.3 and 5.4.4). A fully concordant package of high amplitude reflections has also been mapped at the level of horizon B and this has been interpreted as a lava flow unit (section 5.4.2). Towards the eastern boundary of the survey area, interpretation within the laterally extrapolated Upper Cretaceous and Paleogene interval becomes very difficult. In this area this interval is dominated by a progradational unit that is upwards defined by a high amplitude positive acoustic boundary. The internal reflection geometry of the feature shows a high degree of similarity with that of the Ben Nevis Escarpment (Chapter 3) and it is interpreted as a lava delta (Fig. 5.12) with a depth converted vertical relief of just less than 1 km (assuming a igneous velocity of 5.55 km/s; Skogly, 1998). The delta appears to predate horizons B, C, and D and it is, therefore, suggested that it is Early Paleocene in age. This lava delta unit was encountered in exploration well 154/3-1, situated immediately outside the T38 survey area, and this well penetrated more than 900 m of basaltic volcanic rocks and thin interbedded sediments (Egerton, 1998).

This section focuses on describing the distribution and geometry of the deepest intrusive part of the T38 igneous complex below horizon B, whilst the shallower intrusive and the extrusive parts of the T38 igneous complex (at and above horizon B) will be described and discussed in section 5.4.

5.3.2 Distribution of sills

Igneous sills are seen across most of the 3D seismic survey area covering an area > 600 km^2 (Fig. 5.13). The density of the mapped intrusion appears to be greatest in the

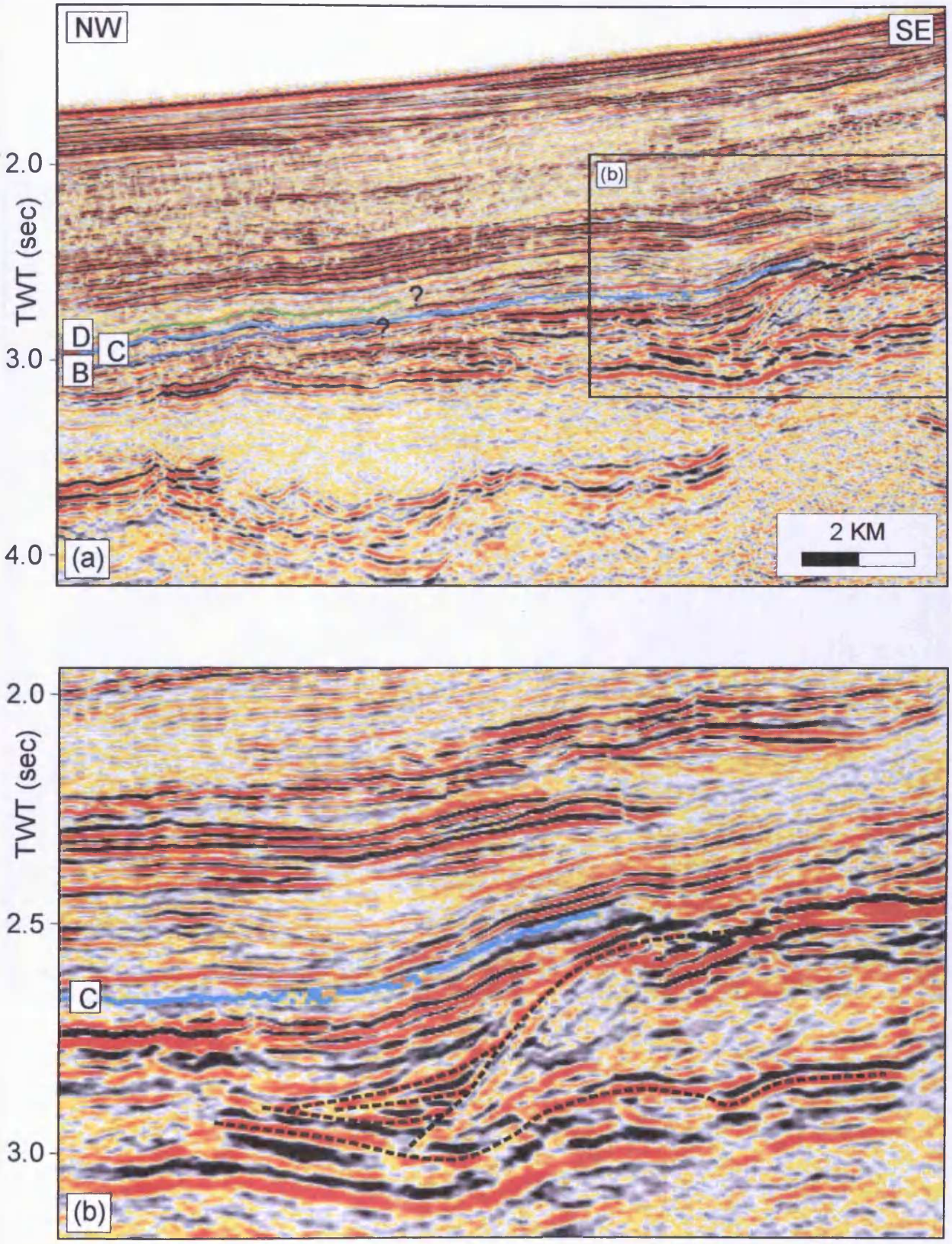

Fig. 5.12 Seismic sections showing the cross-sectional and internal geometry of a progradational unit upwards defined by a high amplitude positive acoustic boundary. The feature is interpreted as a lava delta. See Fig. 5.11 for line location.

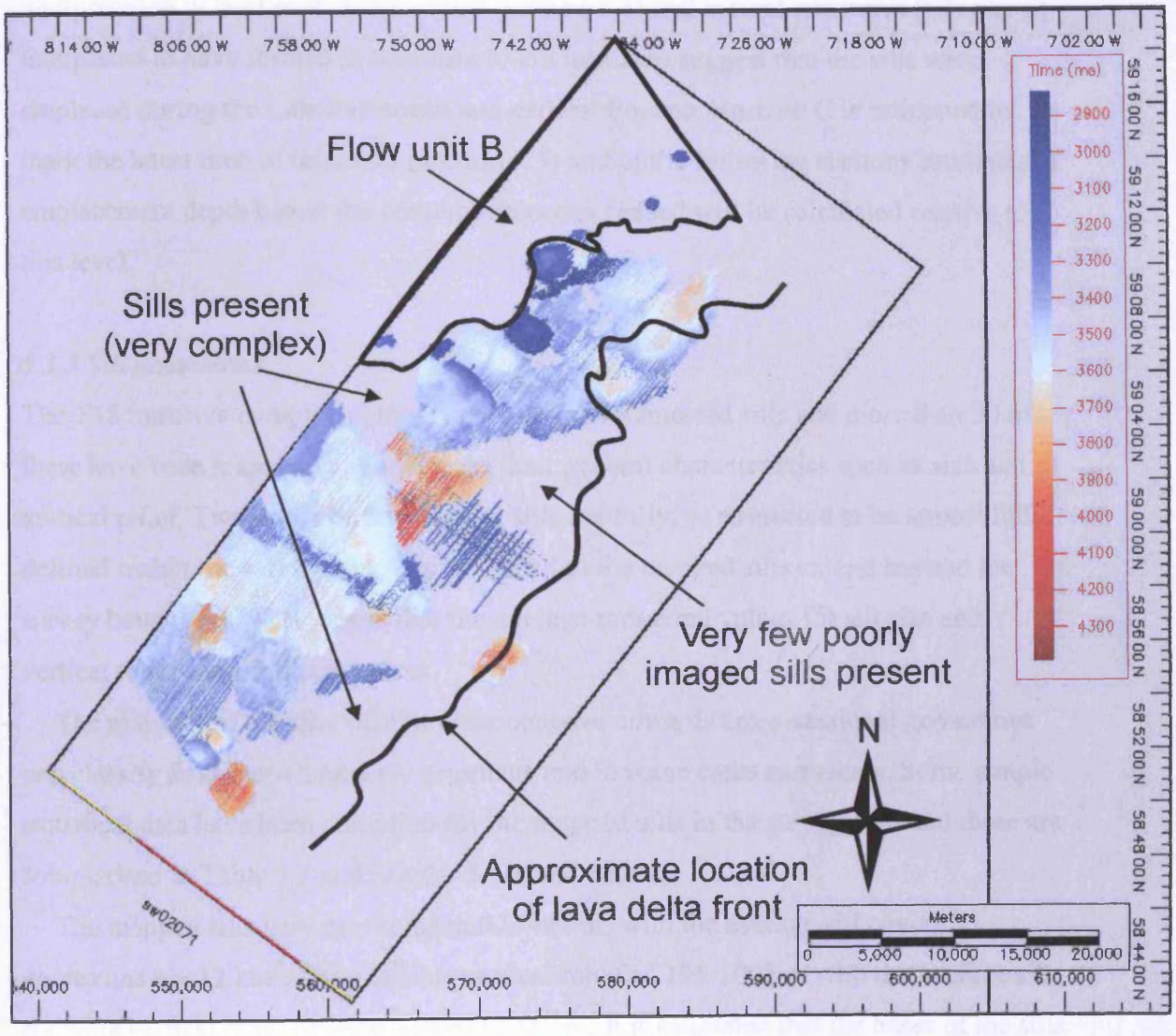

Fig. 5.13 Map showing the distribution of sills in the T38 3D seismic survey area. Sills are not imaged in the northern part of the survey area and along the eastern survey boundary. This is, at least partly, due to the presence of magmatic extrusives in these areas.

western and northern parts of the survey area. This is likely to be due to the presence of magmatic extrusives along the eastern survey boundary and in the northern corner of the survey area limiting the ability of the data to image the sills (Fig. 5.13). The sills have been mapped at a present-day depth of 4320-6585 m spanning a vertical section of just over 2250 m with the shallowest sills terminating within the B-C interval. Detailed interpretation of host-rock deformation (section 5.5) and mound structures (Chapter 6) interpreted to have formed in response to sill intrusion suggest that the sills were emplaced during the Late Paleocene and earliest Eocene. Horizon C is estimated to mark the latest time of intrusion (section 5.5) and in the following sections estimates of emplacement depth below the contemporaneous seabed will be calculated relative to this level.

5.3.3 Sill geometries

The T38 intrusive complex comprises many interconnected sills and more than 30 of these have been mapped to characterise their general characteristics such as size and vertical relief. Two thirds of the mapped sills are fully, or suspected to be almost fully, defined within the survey area, whilst a third of the mapped sills extend beyond the survey boundaries. This means that the average measured values for sill size and vertical relief are minimum values.

The majority of the sills exhibit clear concave upwards cross-sectional geometries and classify as saucer-shaped sill segments and in some cases as saucers. Some simple statistical data have been compiled for the mapped sills in the survey area and these are summarised in Table 5.1 and briefly described below.

The mapped sills vary in size from 0.6-49 km^2 with the average sill covering approximately 12 km^2. They exhibit vertical relief of 195-1005 m with the average sill showing vertical relief of approximately 450 m. It is estimated that the bases of the sills were emplaced between 300-1990 m below the contemporaneous seabed, with an average emplacement depth of approximately 925 m. The graphs shown in Fig. 5.14 show moderate correlation between sill area and vertical relief (R^2 = 51 %; Fig. 5.14a), poor correlation (R^2 = 8 %; Fig. 5.14b) between sill area and maximum emplacement depth, and moderate correlation between the maximum emplacement depth and vertical relief (R^2 = 52 %; Fig. 5.14c). The significance of these statistical relationships will be further discussed in Chapter 7.

sill	area (km2)	max Z (ms)	min Z (ms)	v. r. (ms)	v. r. (m)	cont. seabed (ms)	empl. depth (ms)	empl. depth (m)
sill1	4.5	3559	3234	325	487.5	3048	511	766.5
sill2	5.2	3724	3360	364	546	3100	624	936
sill3	6.8	3278	3065	213	319.5	2840	438	657
sill4	11	3445	3295	150	225	3244	201	301.5
sill5	25.6	3875	3402	473	709.5	3028	847	1270.5
sill6	2.5	3590	3349	241	361.5	2868	722	1083
sill7	14.9	4072	3610	462	693	3056	1016	1524
sill8	29.3	3560	3069	491	736.5	2884	676	1014
sill9	25.5	3627	3238	389	583.5	2828	799	1198.5
sill12	49.4	3688	3018	670	1005	2580	1108	1662
sill13	42.7	3793	3146	647	970.5	2572	1221	1831.5
sill14	18.7	3648	3274	374	561	2712	936	1404
sill15	3	3342	3201	141	211.5	2808	534	801
sill16	2.2	3324	3160	164	246	2744	580	870
sill17	19	3678	3389	289	433.5	2972	706	1059
sill18	2.9	3715	3385	330	495	3056	659	988.5
sill19	7.9	4038	3702	336	504	3076	962	1443
sill20	13.9	3489	3229	260	390	2720	769	1153.5
sill21	5.4	3942	3640	302	453	3300	642	963
sill22	43.1	3656	3351	305	457.5	3072	584	876
sill23	4.2	3672	3379	293	439.5	2892	780	1170
sill24	2.9	3627	3482	145	217.5	3248	379	568.5
sill25	13.6	3949	3635	314	471	3104	845	1267.5
sill26	5.1	4390	3890	500	750	3132	1258	1887
sill27	5.2	4390	3890	500	750	3080	1310	1965
sill28	7.8	3935	3535	400	600	2608	1327	1990.5
sill29	10.2	3600	3431	169	253.5	3216	384	576
sill30	11	3775	3453	322	483	3268	507	760.5
sill31	2.2	3552	3397	155	232.5	3268	284	426
sill32	17.1	3527	3258	269	403.5	3044	483	724.5
sill33	3.7	3371	3190	181	271.5	3012	359	538.5
sill34	0.7	3297	3168	129	193.5	3028	269	403.5
sill35	1.6	3361	3216	145	217.5	2928	433	649.5
sill36	7	3614	3440	174	261	3088	526	789
sill37	1.6	3066	2936	130	195	2832	234	351
sill38	0.6	3139	2930	209	313.5	2772	367	550.5
sill39	0.9	3023	2891	132	198	2748	275	412.5
sill40	6.6	3275	2931	344	516	2704	571	856.5
sill41	7.2	3124	2881	243	364.5	2552	572	858
sill43	48	3560	3069	491	736.5	3220	340	510
sill44	31.5	3422	2983	439	658.5	3272	150	225
sill45	1	3184	2998	186	279	2816	368	552
sill46	0.9	3147	3002	145	217.5	2868	279	418.5
sill47	1.1	3250	3099	151	226.5	2976	274	411
average	12	3575	3277	298	446	2959	616	924

Table 5.1 Summary of statistical data for 44 sills of the T38 sill complex. Depth conversion done using Vsed = 3.0 km/s, see Chapter 2. Max Z: maximum emplacement depth, min Z: shallowest emplacement depth, v.r.: vertical relief, cont. seabed: depth of seabed at time of intrusion, empl. depth: emplacement depth below contemporaneous seabed.

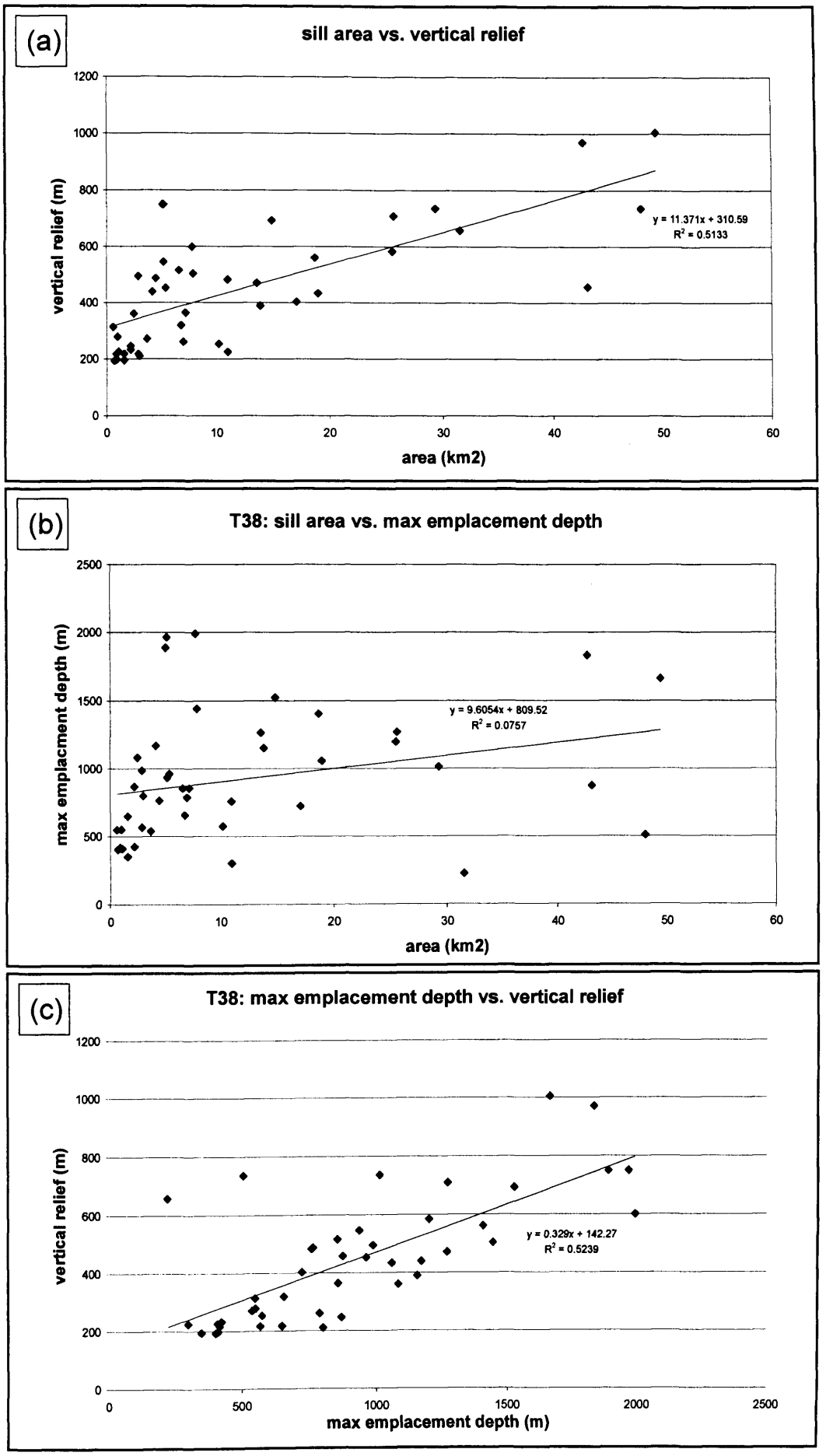

Fig. 5.14 Graphs illustrating statistical data for sills of the T38 sill complex (n = 44). (a) sill area vs. vertical relief. (b) sill area vs. maximum emplacement depth. (c) maximum emplacement depth vs. vertical relief.

5.3.4 Thickness variation within sills

Imaging the top and base of individual sills and thus determining sill thickness variations within sills has been a problem in the 3D survey areas described in previous chapters. However, in the T38 survey area a few sills (e.g. sills 40 and 41) exhibit thicknesses that are greater than the thickness of separability (i.e. 85 m; section 5.1.2.1) and it has been possible to do a detailed study of their thickness variation.

In Figs. 5.15 and 5.16 the depth converted thicknesses (using a sill velocity of 5.55 km/s; Skogly, 1998) of sills 40 and 41 along sets of perpendicular intersecting lines through the two sills are shown. The thickness has been estimated by measuring the true thickness approximately perpendicular to the sill - host-rock contacts.

Sill 40 measures 3.2*2.7 km, covering an area of 6.6 km^2 and it is emplaced at a present-day depth of 4395-4910 m and has a vertical relief of just over 500 m. It exhibits a clear change in thickness between the central basal part of the sill and the sill edge (Fig. 5.15). The central basal part of the sill measures approximately 1200-1500 m in width and exhibits a thickness of approximately 350 m, decreasing towards the sill edges at gradients between 0.3-0.4. The volume of sill 40 (and sill 41) has been estimated by approximating the thickness distribution graph to a cylinder as shown in Fig. 5.17. Sill 40 is slightly elongated and the volume estimates obtained from the two different cross-sections vary with iln20738 (Fig. 5.15a) yielding a volume of 1.3 km^3 and xln15804 (Fig. 5.15b) suggesting a sill volume of 1.8 km^3. Based on this it is suggested that the sill probably has a volume of approximately 1.5 km^3.

Sill 41 is emplaced at a present-day depth of 4320-4685 m and thus has a vertical relief of approximately 365 m. It measures 3 * 2.5 km and covers an area of 7.2 km^2. This sill also exhibits a clear decrease in thickness between the central basal part and the sill edge (Fig. 5.16). The sill has a maximum thickness of approximately 400 m, which is reasonably constant across a central area, approximately 1 km in width. Away from this area the thickness of the sill decreases gradually towards the edge at gradients of 0.3-0.4. Sill 41 has an estimated volume of approximately 1.3 km^3.

From the above it is evident that the two sills both show a clear decrease in thickness between their central, basal parts and their edges. Previous studies have observed a similar decrease in thickness away from the basal parts of the sill towards the sill edge (e.g. Pollard & Johnson, 1973; Francis, 1982). It has been proposed that sills thicken in the source direction (Tweto, 1951), which in the case of sills 40 and 41 places their

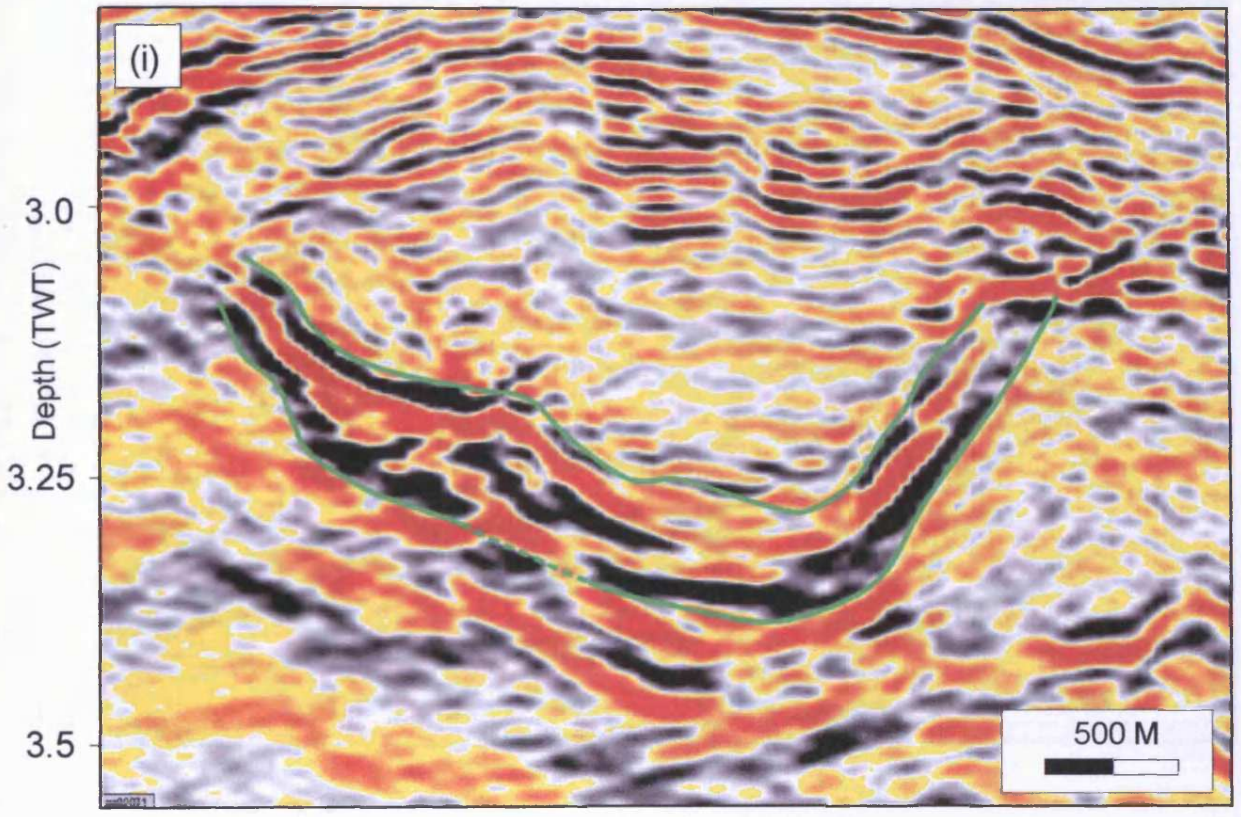

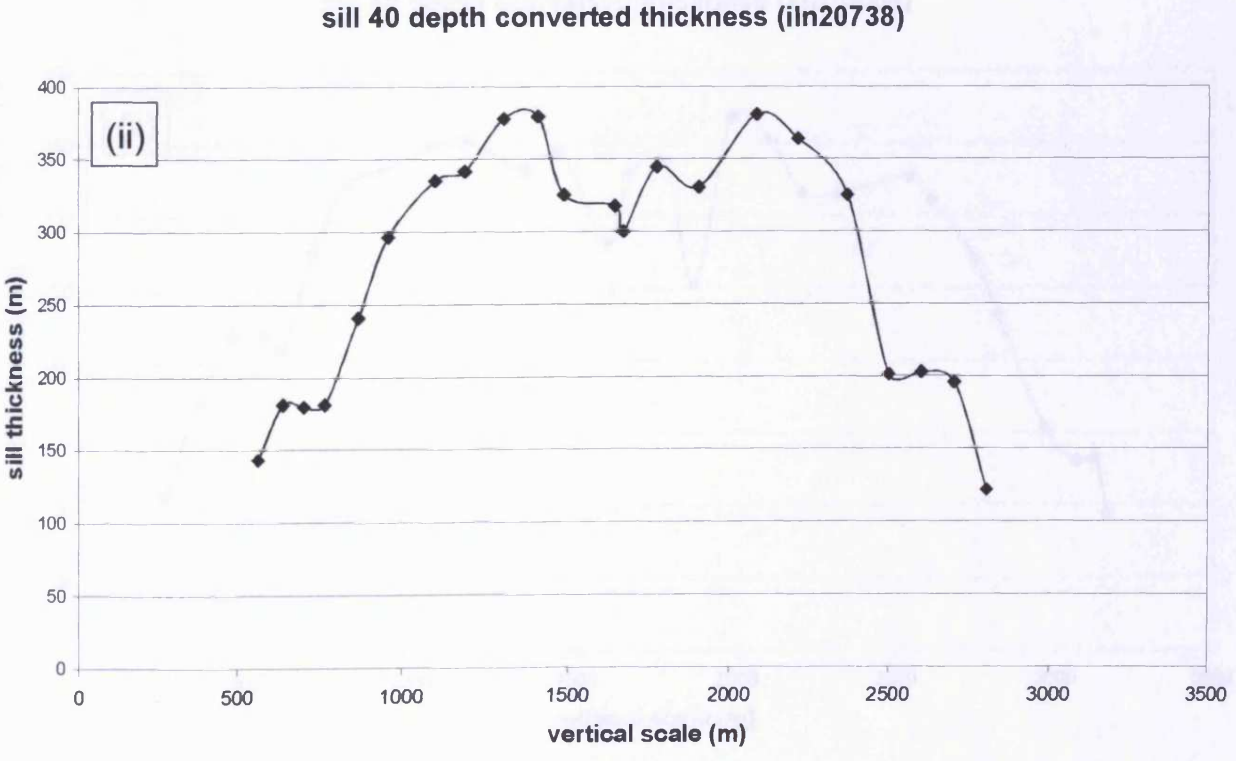

Fig. 5.15a (i) Seismic section (iln20738) showing the cross-sectional geometry of sill 40. Green lines mark the interpreted top and base of the sill. (ii) Graph showing the depth converted thickness of the sill as it is interpreted on the seismic section in (i). The sill thickness has been estimated using a sill velocity of 5.55 km/s. The graph shows that the sill is thickest in its central region and thins towards its edges.

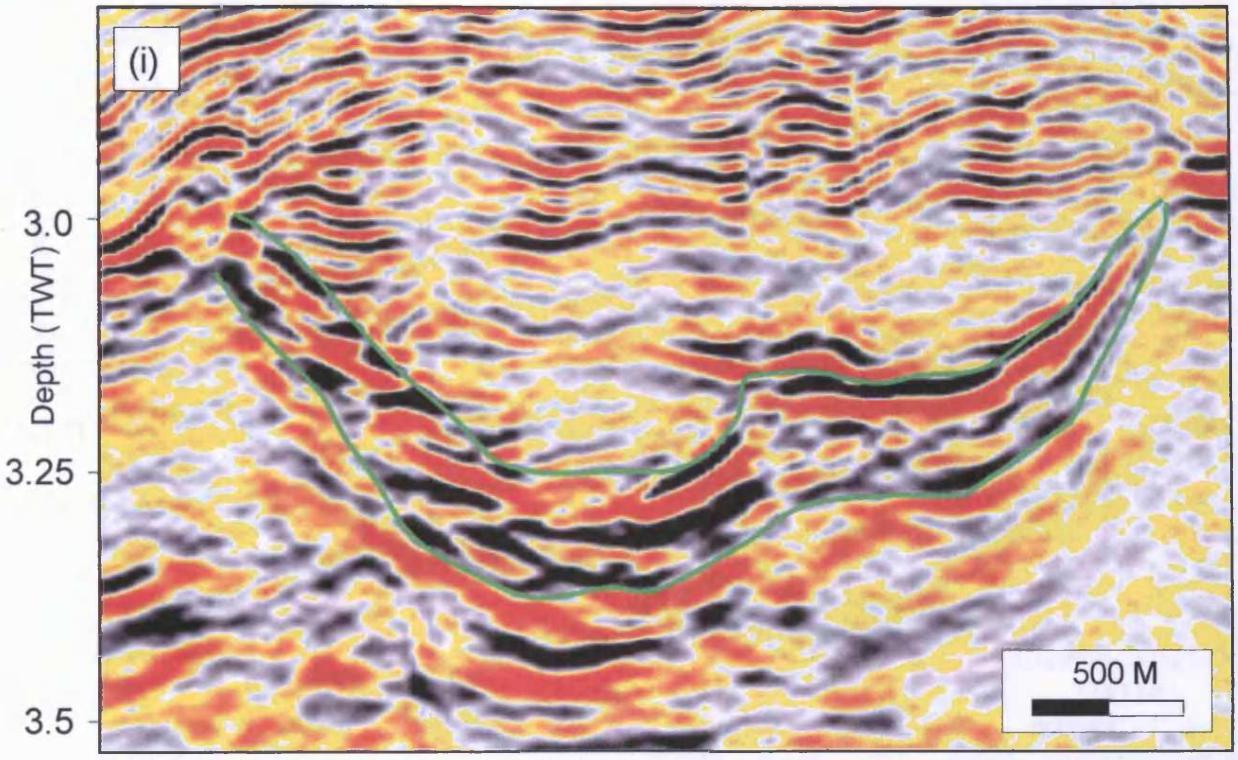

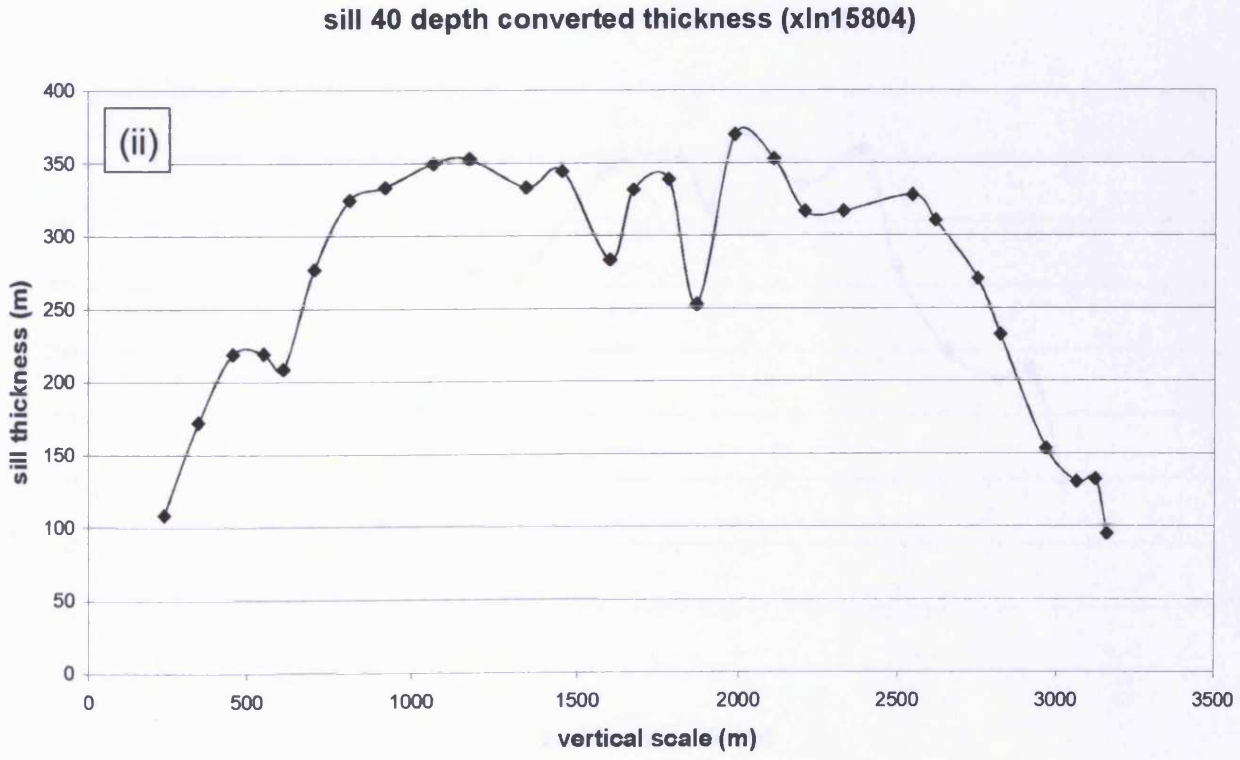

Fig. 5.15b (i) Seismic section (xln15804) showing the cross-sectional geometry of sill 40. Green lines mark the interpreted top and base of the sill. (ii) Graph showing the depth converted thickness of the sill as it is interpreted on the seismic section in (i). The sill thickness has been estimated using a sill velocity of 5.55 km/s. The graph shows that the sill is thickest in its central basal region and thins towards its edges.

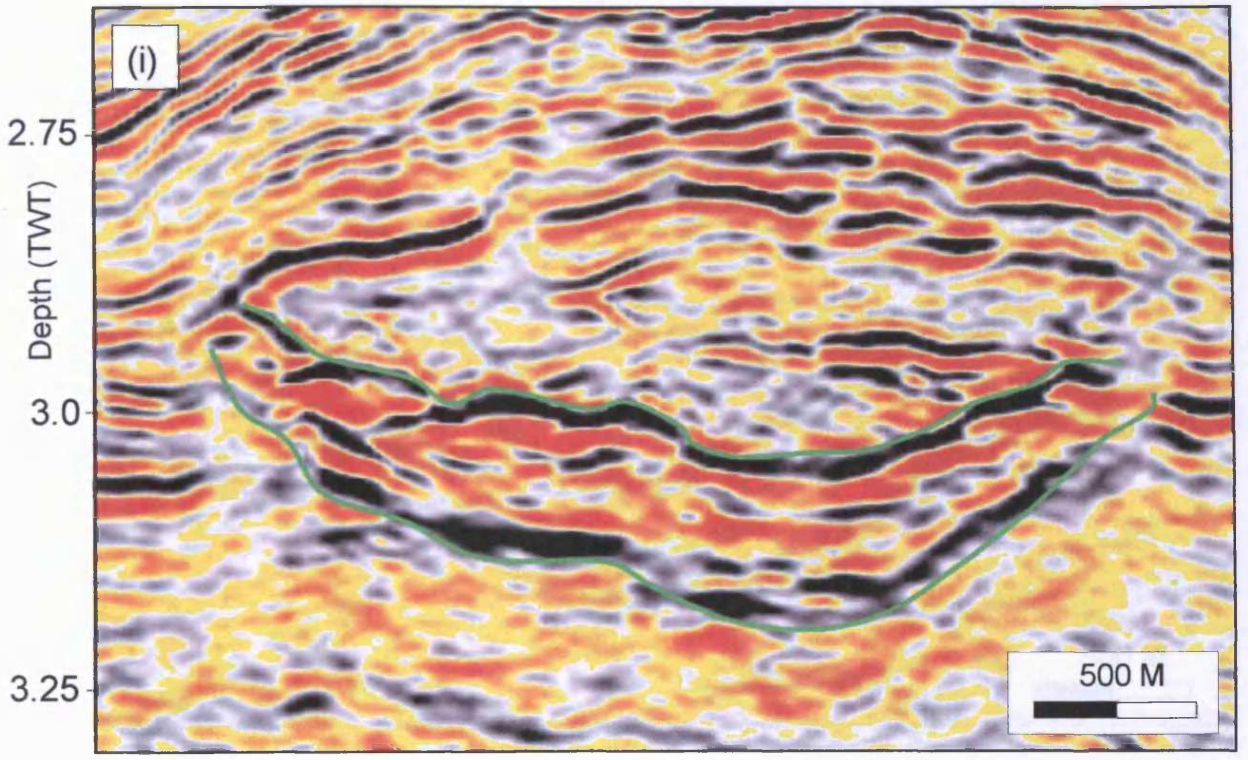

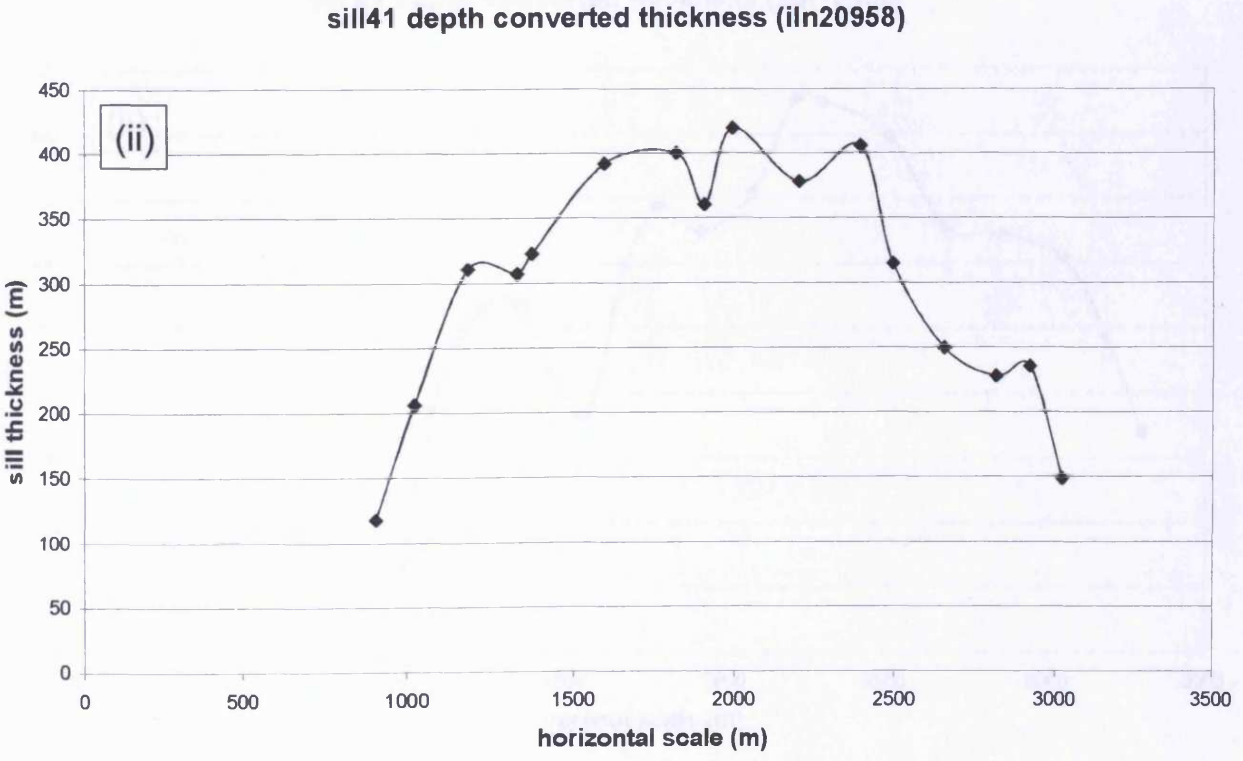

Fig. 5.16a (i) Seismic section (iln20958) showing the cross-sectional geometry of sill 41. Green lines mark the interpreted top and base of the sill. (ii) Graph showing the depth converted thickness of the sill as it is interpreted on the seismic section in (i). The sill thickness has been estimated using a sill velocity of 5.55 km/s. The graph shows that the sill is thickest in its central region and thins towards its edges.

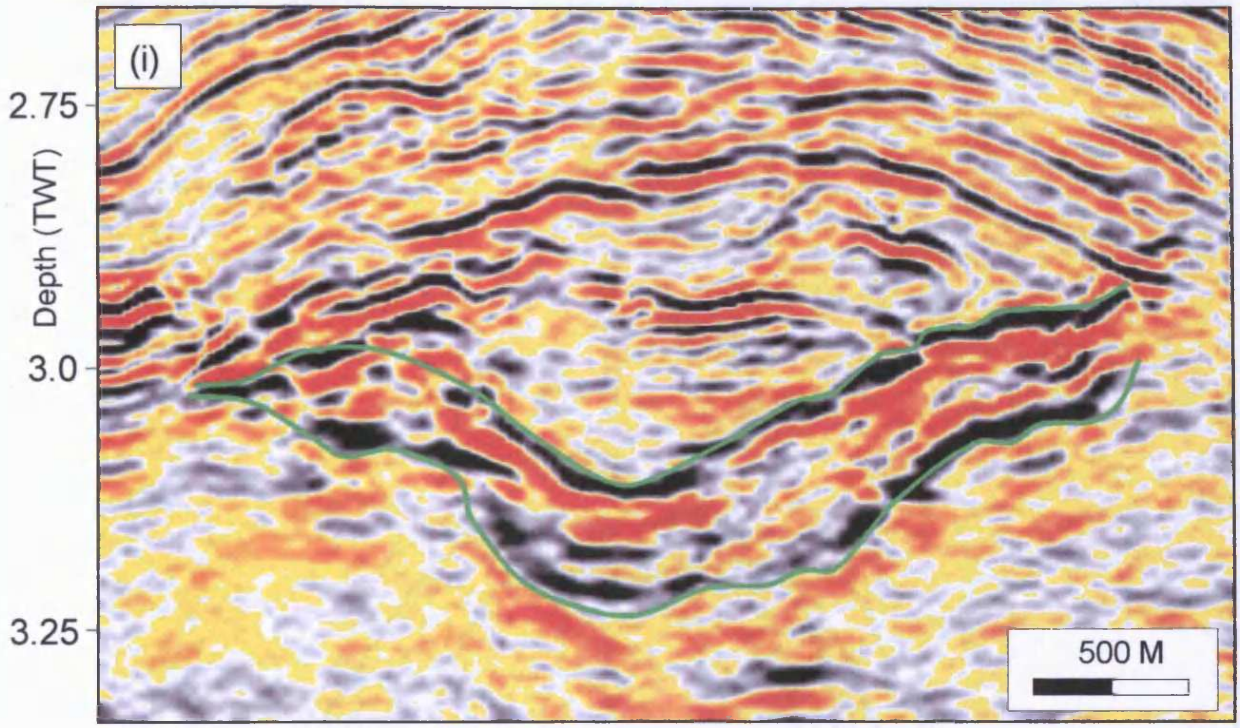

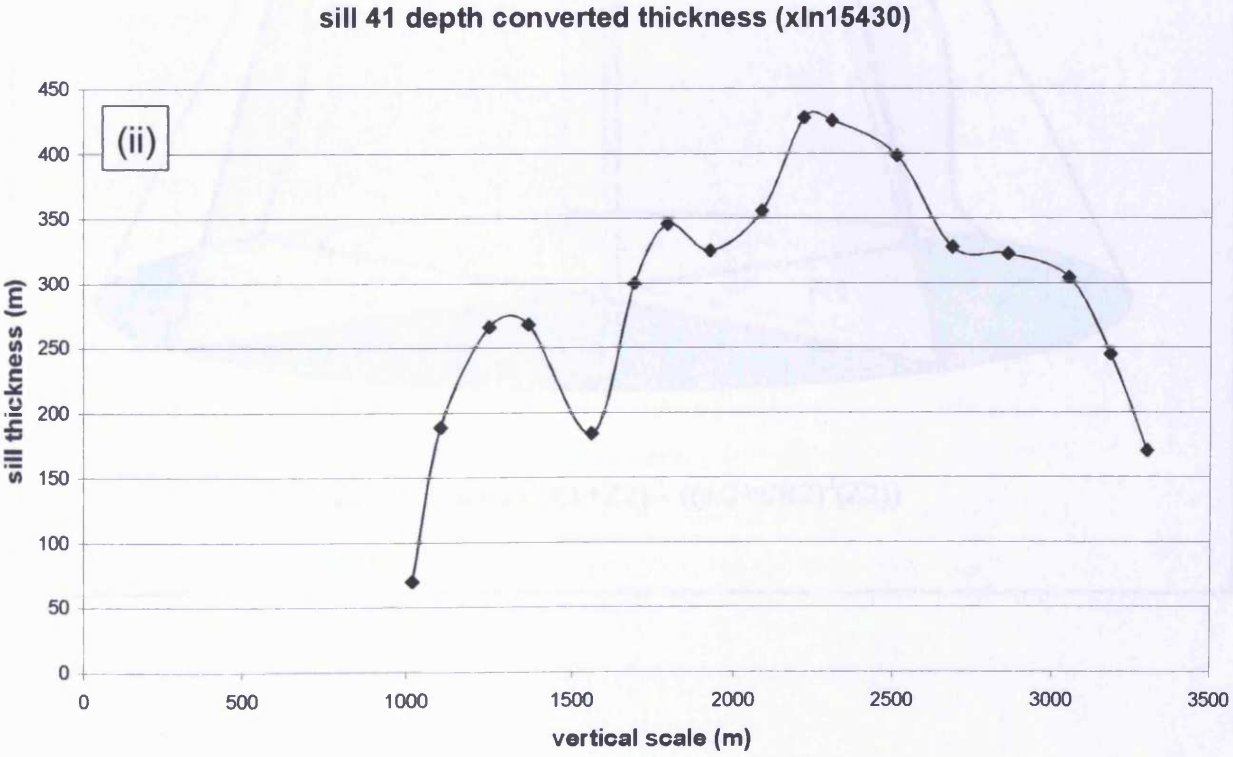

Fig. 5.16b (i) Seismic section (xln15430) showing the cross-sectional geometry of sill 41. Green lines mark the interpreted top and base of the sill. (ii) Graph showing the depth converted thickness of the sill as it is interpreted on the seismic section in (i). The sill thickness has been estimated using a sill velocity of 5.55 km/s. The graph shows that the sill is thickest in its central region and thins towards its edges.

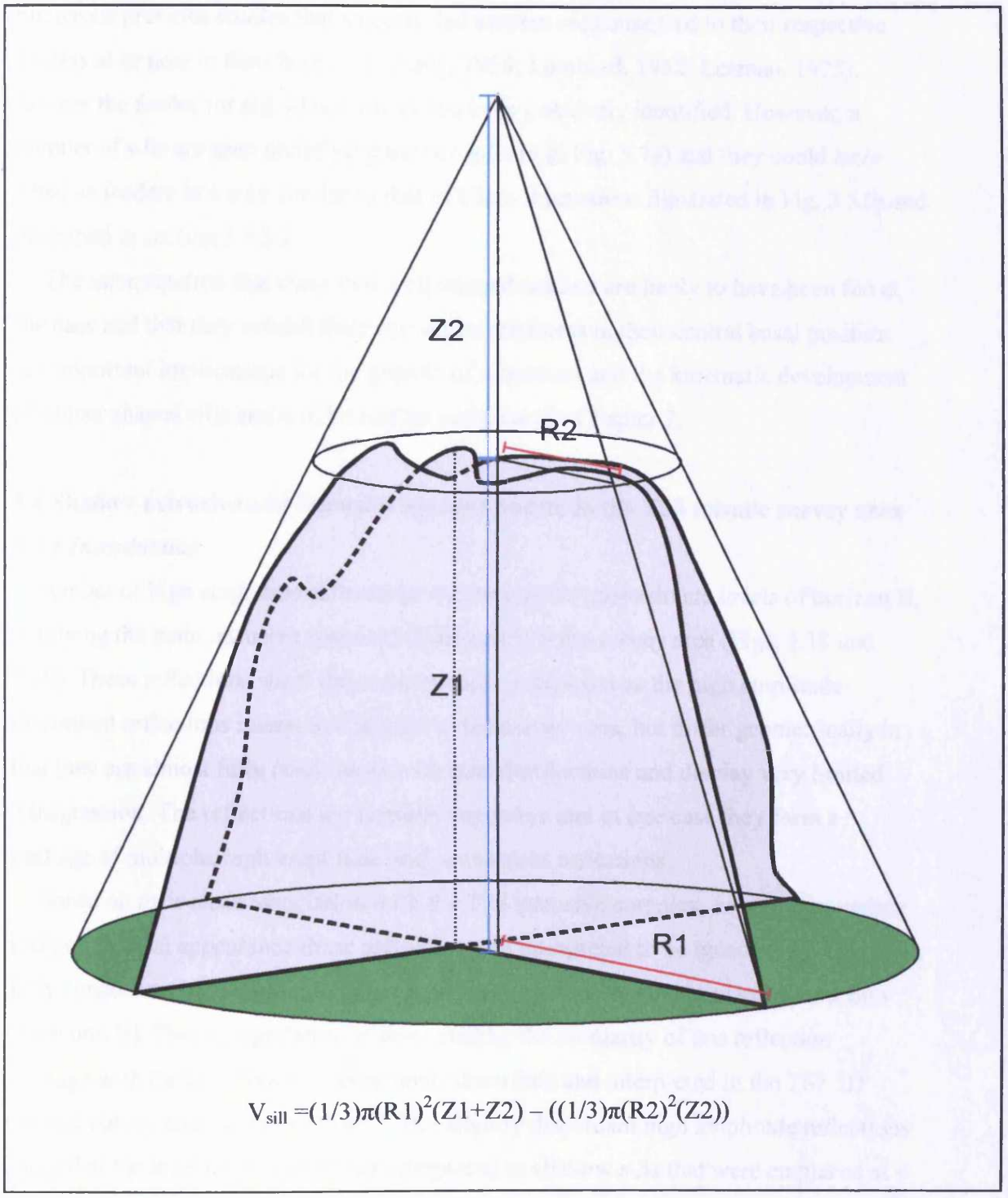

$$V_{sill} = (1/3)\pi(R1)^2(Z1+Z2) - ((1/3)\pi(R2)^2(Z2))$$

Fig. 5.17 Sill volume is calculated by approximating the thickness distribution graphs to a cone. The volume of the sill is calculated by subtracting the volume of the small cone (defined by Z2 and R2) from the volume of the large cone (defined by Z1+Z2 and R1).

feeders at the base of the saucers. This is in agreement with observations made by numerous previous studies that suggest that saucers are connected to their respective feeders at or near to their base (e.g. Carey, 1958; Lombard, 1952; Leaman, 1975). Neither the feeder for sill 40 nor sill 41 has been positively identified. However, a number of sills are seen underlying the two sills (e.g. Fig. 5.7a) and they could have acted as feeders in a way similar to that of Class B junctions illustrated in Fig. 3.52b and described in section 3.4.5.2.

The interpretation that these two well imaged saucers are likely to have been fed at the base and that they exhibit their maximum thickness in their central basal position has important implications for the growth of intrusions and the kinematic development of saucer shaped sills and will be further addressed in Chapter 7.

5.4 Shallow extrusive and intrusive igneous bodies in the T38 seismic survey area

5.4.1 Introduction

A number of high amplitude reflections are seen at the approximate levels of horizon B, overlying the main intrusive igneous sill complex in the survey area (Figs. 5.18 and 5.19). These reflections share the same acoustic properties as the high amplitude discordant reflections interpreted as sills in the survey area, but differ geometrically in that they are almost fully concordant with stratal reflections and display very limited transgression. The reflections are laterally extensive and in one case they form a package of multiple, high amplitude and concordant reflections.

Based on their close association with the T38 intrusive complex, acoustic properties and geometrical appearance these reflections are interpreted to be igneous in origin. The fully concordant high amplitude reflection package is interpreted as stacked lava flow (flow unit B). This interpretation is supported by the similarity of this reflection package with the lava flow unit previously described and interpreted in the T67 3D seismic survey area (section 3.2.4.2). The slightly discordant high amplitude reflections imaged at the level of horizon B are interpreted as shallow sills that were emplaced at < 450 m below the contemporaneous seabed.

The geometry and origin of flow unit B and shallow sills are described and discussed in the following sections.

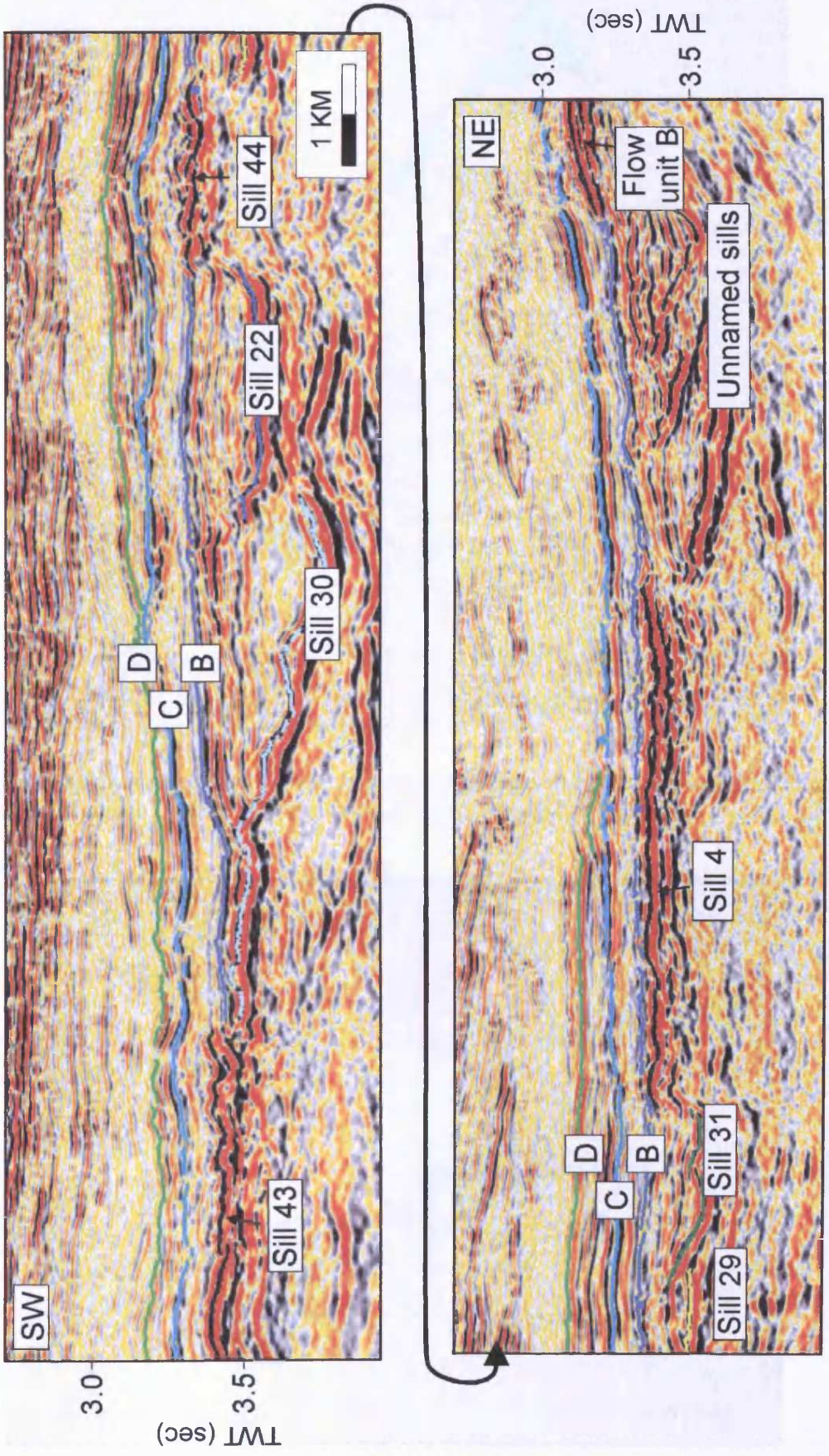

Fig. 5.18 Seismic cross-section showing four highly concordant reflections along the western survey boundary. The three most southern are interpreted as shallow sills (Sills 43, 44, and 4), whilst the most northern is interpreted as a lava flow (flow unit B). See Fig. 5.19 for line location.

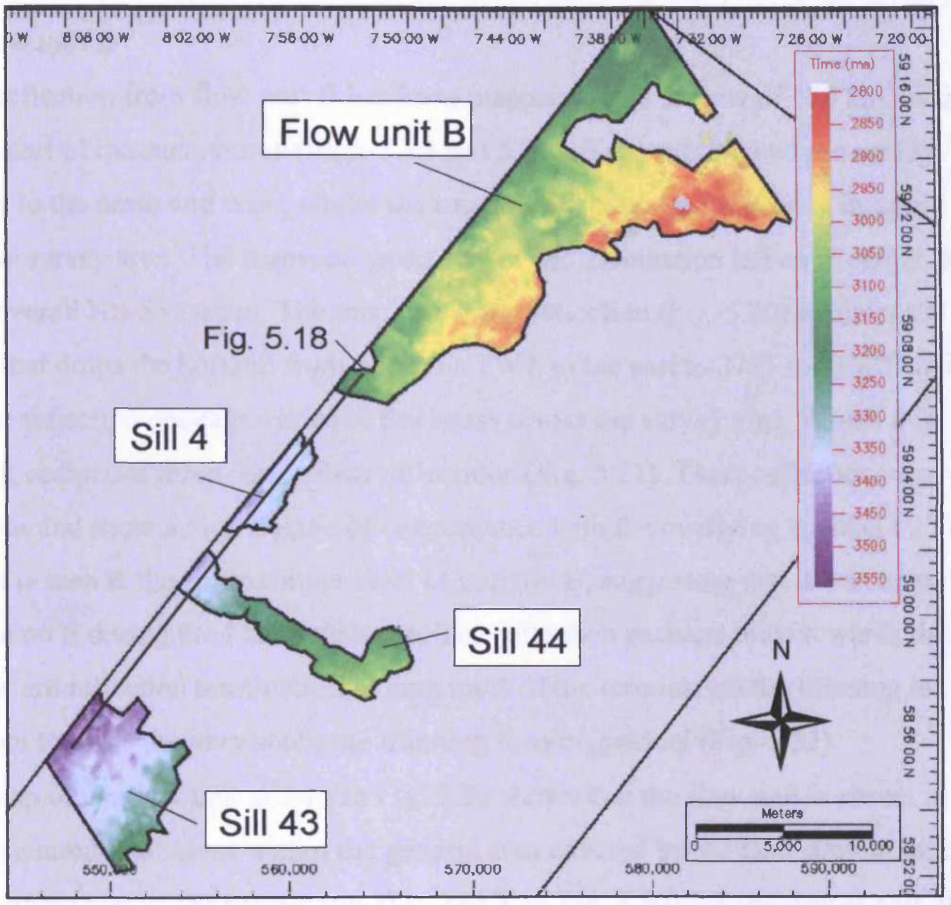

Fig. 5.19 Time-structure maps of high amplitude concordant and near-concordant reflections seen at the approximate level of horizon B. Note line location for Fig. 5.18.

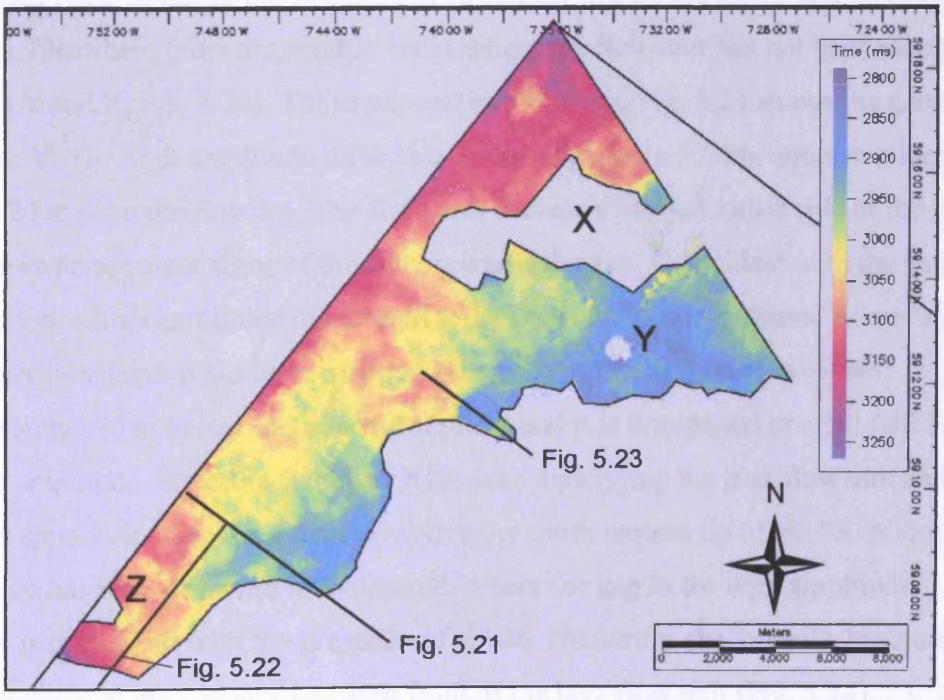

Fig. 5.20 Time-structure map of the top reflection from flow unit B. Note line locations for Figs. 5.21, 5.22, and 5.23.

5.4.2 Flow unit B

The top reflection from flow unit B has been mapped across an area of 160 km^2 in the northern part of the survey area (Figs. 5.19 and 5.20). It extends beyond the survey boundary to the north and west, whilst the eastern reflection termination is imaged within the survey area. The mapview geometry of the termination has an irregular shape with an overall NE-SW trend. The map of the top reflection (Fig. 5.20) exhibits a N to NW dip that drops the horizon from 3267 ms TWT to the east to 2787 ms TWT to the west. The reflection package varies in thickness across the survey area. Where it is thickest it comprises three concordant reflections (Fig. 5.21). These reflections are continuous and show a high degree of concordance with the overlying horizon C. The flow unit is seen at the approximate level of horizon B, suggesting that it was extruded onto horizon B during the Late Paleocene. The reflection package thins towards the south-eastern reflection termination. Along most of the termination the thinning is abrupt, but towards the very south the thinning is more gradual (Fig. 5.22).

The map of the flow unit shown in Fig. 5.20 shows that the flow unit is absent in absent in a number of areas within the general area covered by the flow unit. In an area in the northern part of the survey area (marked X in Fig. 5.20) the uppermost part of flow unit B onlaps two large mound structures. The mound structures appear to rest on a couple of the deeper high amplitude reflections that are comprised within flow unit B. The geometry and origin of the two mound structures will be described and discussed in Chapter 6. Elsewhere there are smaller areas where the flow unit has not been mapped (locations Y and Z; Fig. 5.20). The cross-section shown in Fig. 5.23 shows the geometry at location Y. The high amplitude reflection is missing over a 1.5 km wide area located less than 2 km from the flow tip. The flow unit is clearly imaged either side of the gap and it shows no apparent signs of thinning towards the gap. Coincident with the gap in the reflection, a high amplitude discordant reflection with a saucer-shaped geometry in three-dimensional space has been mapped. The base of this reflection is located approximately 300 m below the level of the flow and it is interpreted as a sill (sill 38). A moderate amplitude reflection (labelled X) is seen underlying the lava flow unit and this reflection appears to have been bent up above the south-eastern tip of sill 38. A similar relationship has been observed at location Z, where the gap in the high amplitude reflection is coincident with the presence of sill 46. Numerous shallow sills have also been interpreted along the south-eastern front of the lava flow unit (Fig. 5.24).

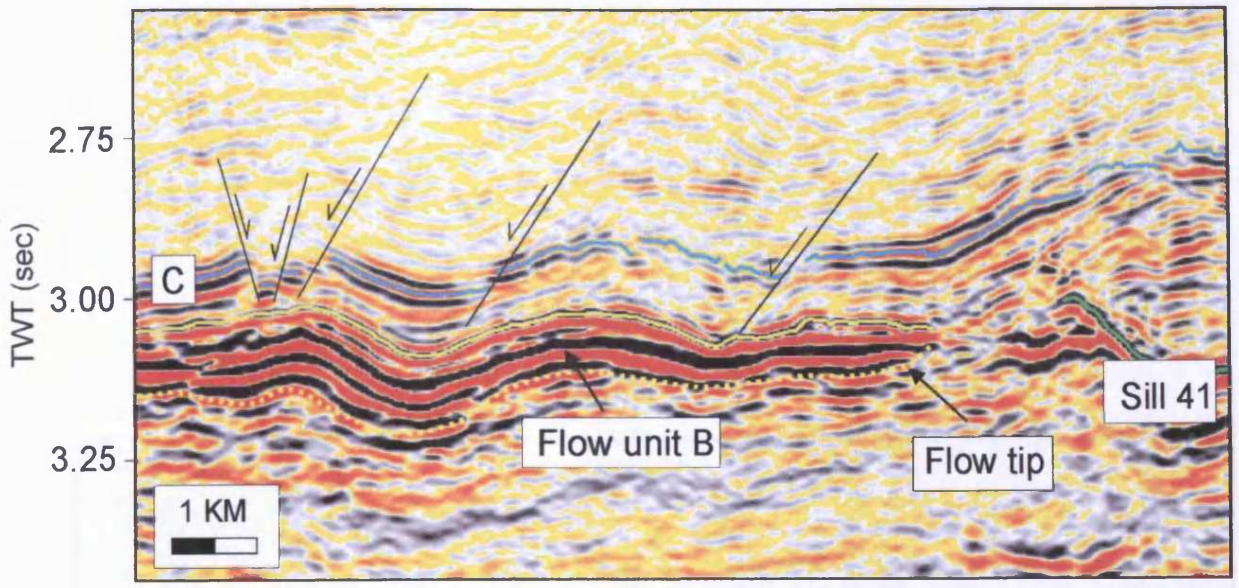

Fig. 5.21 Seismic section showing multiple internal reflections within flow unit B. The flow is concordant with the overlying horizon C and it is seen to thin over a short distance before terminating. See Fig. 5.20 for line location.

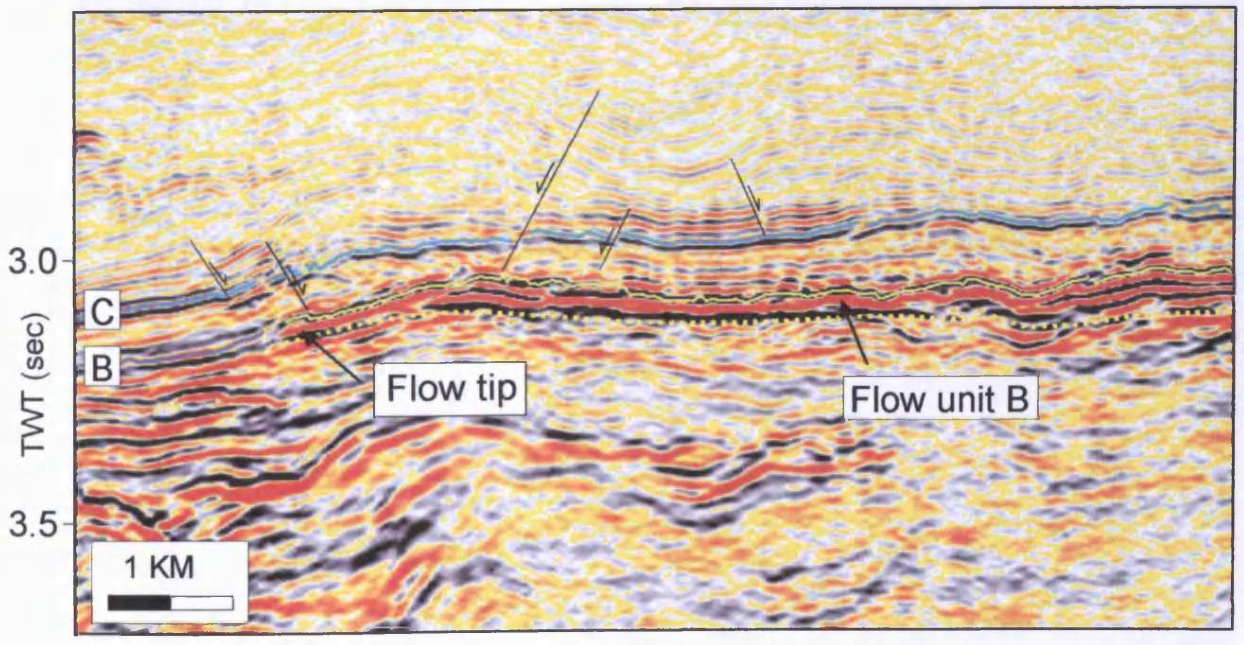

Fig. 5.22 Seismic cross-section showing gradual thinning of flow unit B towards its southern edge. The flow is concordant with the overlying horizon C and it is continuous with horizon B. See Fig. 5.20 for line location.

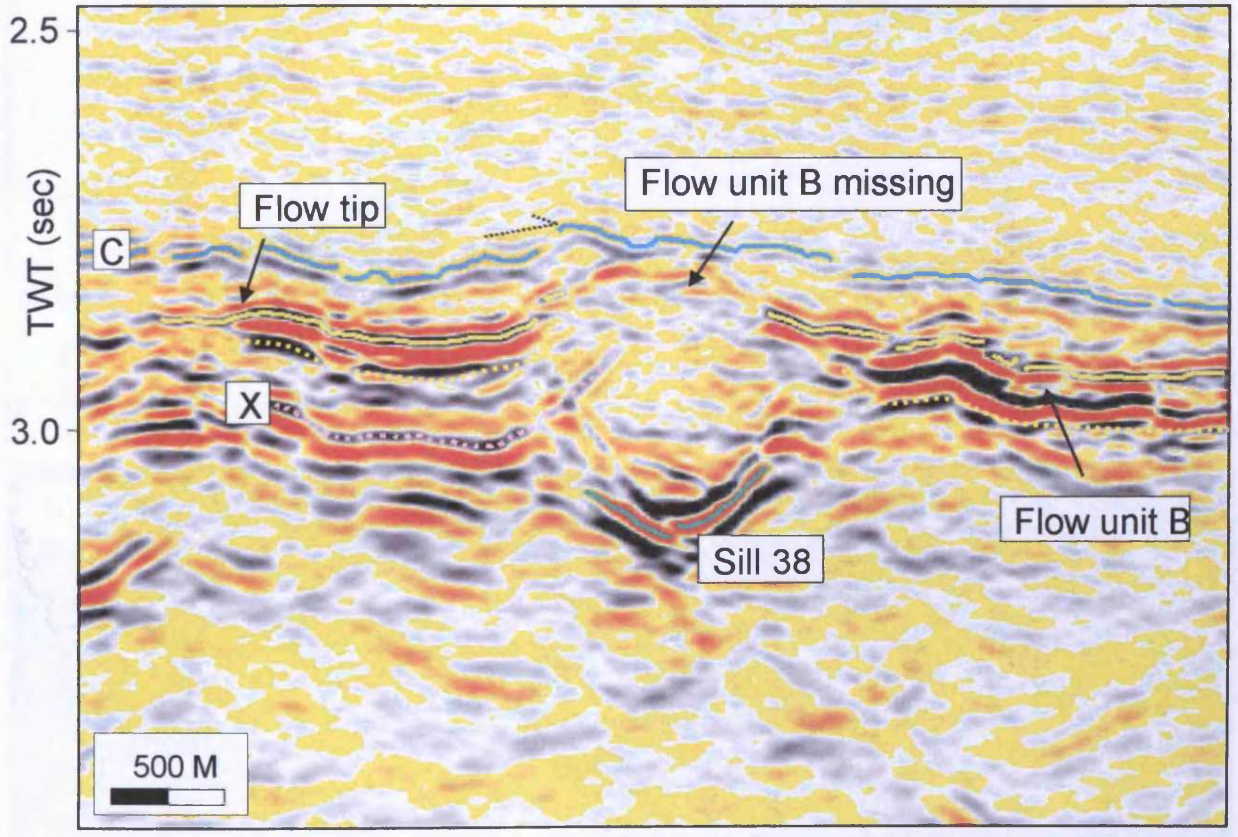

Fig. 5.23 Seismic section showing flow unit B missing overlying sill 38. Flow unit B is present either side of the sill. See Fig. 5.20 for line location.

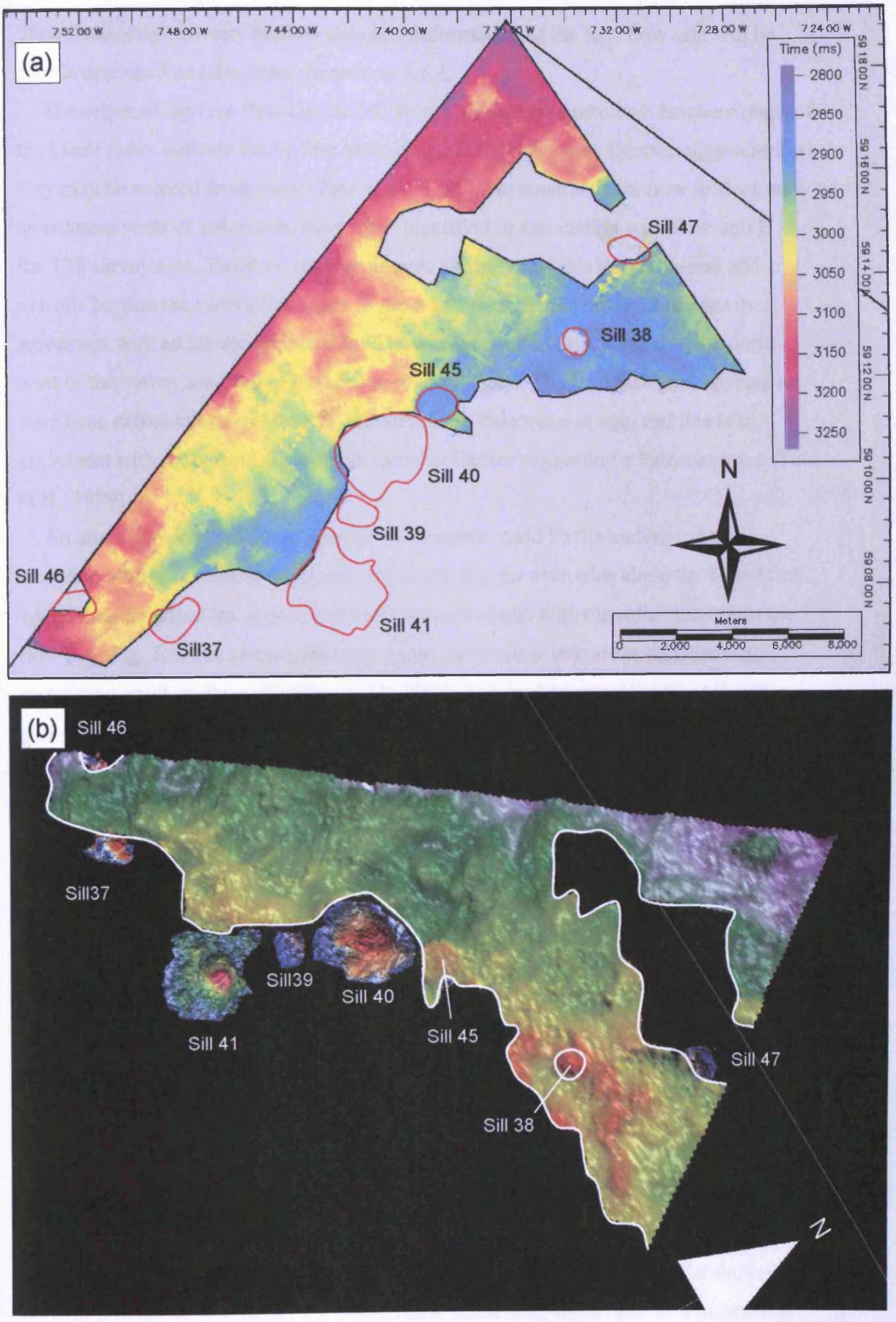

Fig. 5.24 Time-structure maps showing flow unit B and eight relatively shallow sills located along the south-eastern flow front or underlying the flow unit. (a) Basemap display. (b) Three-dimensional display.

The relationship between shallow sills and deformation of the lava flow unit will be further described and discussed in section 5.5.6.

The origin of the lava flows in the NE Rockall Basin is unresolved. Isochore maps of the basalt flows indicate thickening towards the Darwin Igneous Centre, suggesting that they may be sourced from there (Tate et al., 1999). No apparent lava flow feeders, such as volcanic vents or volcanoes, have been identified in association with flow unit B in the T38 survey area. The flow unit terminates abruptly towards the south-east and extends beyond the survey boundary to the north-west. These observations are in agreement with an interpretation of the Darwin Igneous Centre, located to the north-west of the survey area, being the source of the magma. The lava flow unit appears to have been extruded onto horizon B, which is Late Paleocene in age, and this is in agreement with dates from the Darwin Igneous Centre suggesting a Paleocene age (Tate et al., 1999).

An alternative view of the source for the magma could be the underlying sill complex, with sills feeding the flows. There are several examples along the flow front where the sill reflections appear to be almost continuous with the reflections from the flow (e.g. Fig. 5.22) and examples where gaps in the flow unit are coincident with underlying small shallow sills (Fig. 5.23). These observations could suggest that the sills fed the flow unit at multiple locations. However, it will be shown in a later section (section 5.5) that the sills located at the front of the flow unit and underlying the flow unit (Fig. 5.24) post-date the timing of the extrusion of the flow unit and thus could not have fed it and hence the preferred source for the flows is the Darwin Igneous Centre.

The onlap relationship between the top flow unit reflections and the mounds seen in the northern part of the survey area (Fig. 5.10) suggests that the mounds were formed prior to the extrusion of the uppermost lava flow. The mounds rest on high amplitude reflections that are interpreted to represent the younger flows within the flow unit. This implies that the mounds formed following extrusion of parts of the lava flow unit, but prior to the last extrusion event at this time. The origin of the mounds will be further discussed in Chapter 6.

5.4.3 A linear shallow sill (sill 44) in the T38 3D seismic survey area

5.4.3.1 Introduction

A number of discordant igneous bodies have been mapped approximately at the level of horizon B in the survey area (Fig. 5.18). These differ from the deeper sills mapped in

the survey area in shape (Fig. 5.19) and most noticeably in being largely concordant, only exhibiting limited vertical relief. One of these shallow sills (sill 44) is particularly interesting and shows many characteristics resembling those of lava flows. In this section this sill will be described in detail and a model for it emplacement presented. An additional two shallow sills have also been mapped and these will be briefly described and discussed in section 5.4.4.

5.4.3.2 Description of sill 44

Sill 44 has a characteristic elongated NNW-SSE shape (Fig. 5.25). It dips towards the NNW, from a TWT of 2983 ms to the east to 3422 ms TWT to the west (Figs. 5.25 and 5.26). The sill covers an area of 31.5 km^2 and extends beyond the survey boundary to the west. The mapped part of the sill is 12 km long and 2 km wide across most of its extent, but towards its eastern periphery the sill is wider and reaches a width of almost 5 km.

Sill 44 transgresses across horizon B from the SE towards the NW (Fig. 5.26), exhibiting a vertical relief of approximately 120 m relative to horizon B. Towards the south-east the sill appears approximately 125 m below horizon B and shows discordance with stratal reflections on NE-SW trending cross-sections. On the section shown in Fig. 5.27, for example, the north-eastern edge of the sill transgresses approximately 60 m, showing clear discordance. Towards the north-western end of the imaged part of the sill, the NE-SW trending cross-sectional geometry of the sill is apparently concordant with horizon B (Fig. 5.28), showing no discordance. However, from the length profile shown in Fig. 5.26 it is evident that the sill does indeed exhibit some discordance with stratigraphy, hence the interpretation that this body is a sill.

The section shown in Fig. 5.29 appears to show deformation above sill 44. The sill is seen approximately 300 m below horizon C. Horizon C is bent up overlying the flow and exhibits a relief of 150 m. The high is onlapped by several reflections within the C-D interval. However, this trend is not seen along the full length of the flow and thickness variations in the B-C interval have been observed across the survey area and it is possible that the deformation is unrelated to the presence of the sill. Thickening within the B-C interval apparently unrelated to sill intrusion is, for example, seen in Fig. 5.29 (location X) slightly south-west of the possible deformation structure described above.

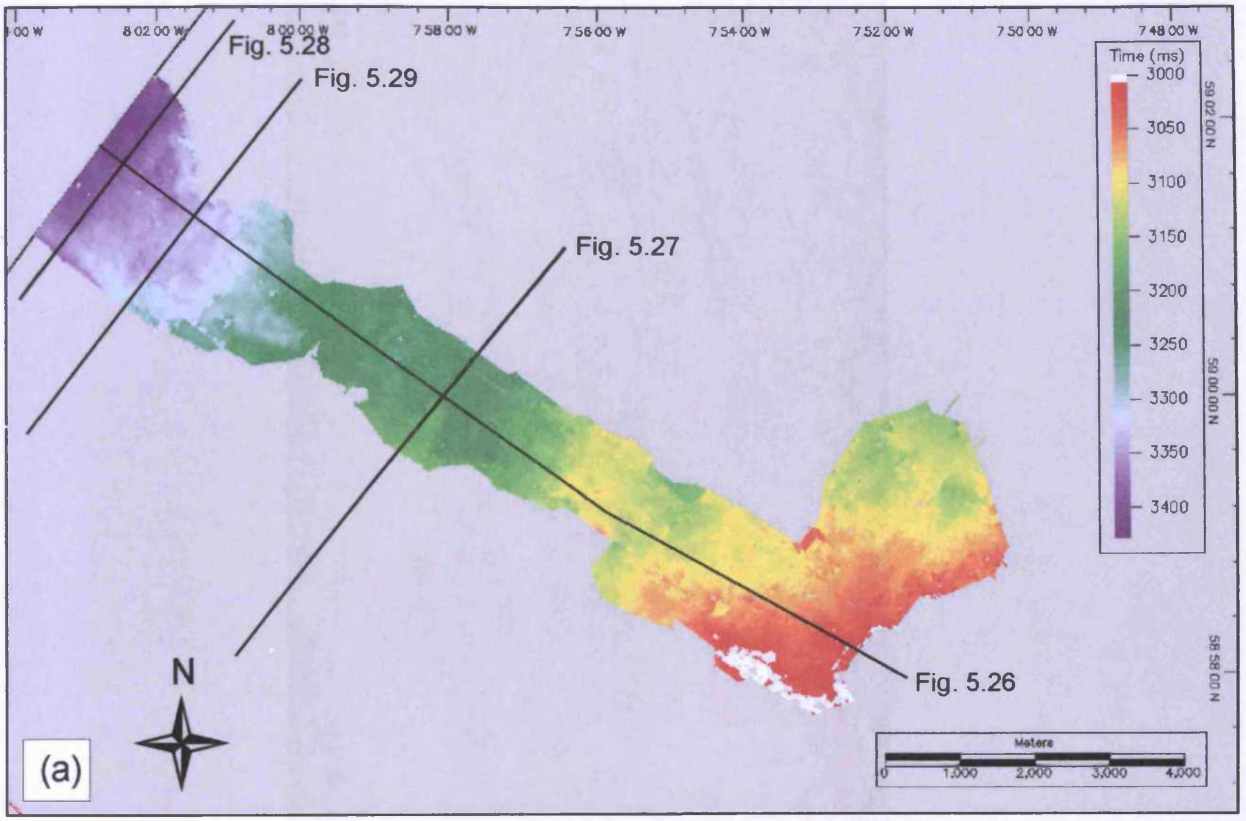

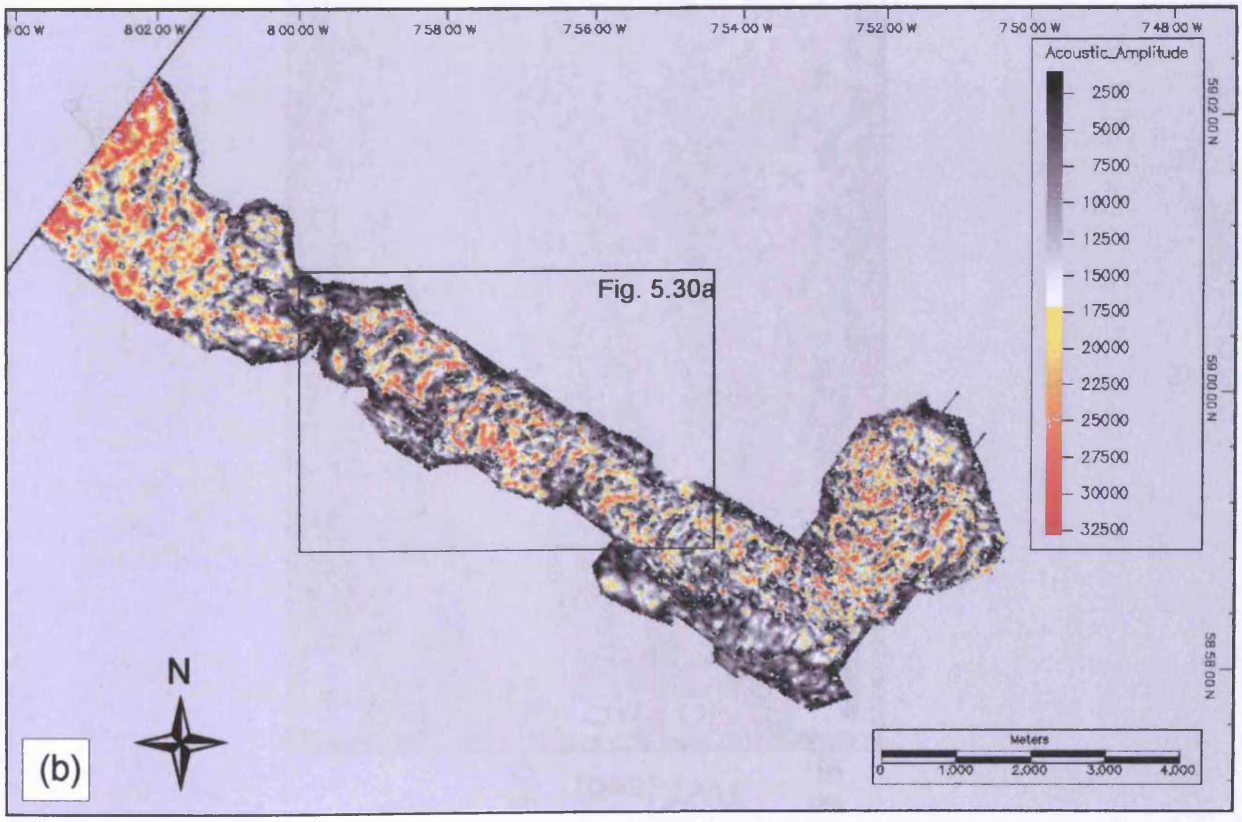

Fig. 5.25 Sill 44. (a) Time-structure map of sill 44. Note line locations for Figs. 5.26, 5.27, 5.28, and 5.29. (b) Amplitude map of sill 44. Note location for Fig. 5.30a. See Fig. 5. 19 for location within survey area.

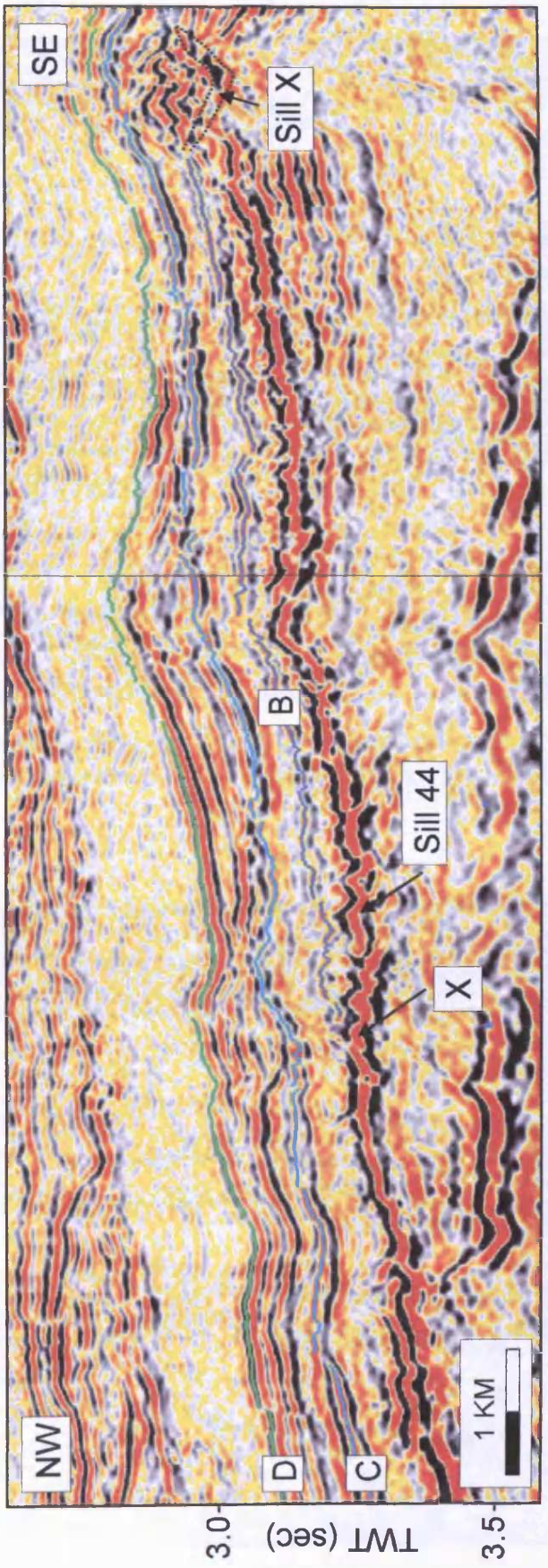

Fig. 5.26 Seismic section showing a length profile of sill 44. The sill dips towards the north-west and transgresses across horizon B at location X. See Fig. 5.25a for line location.

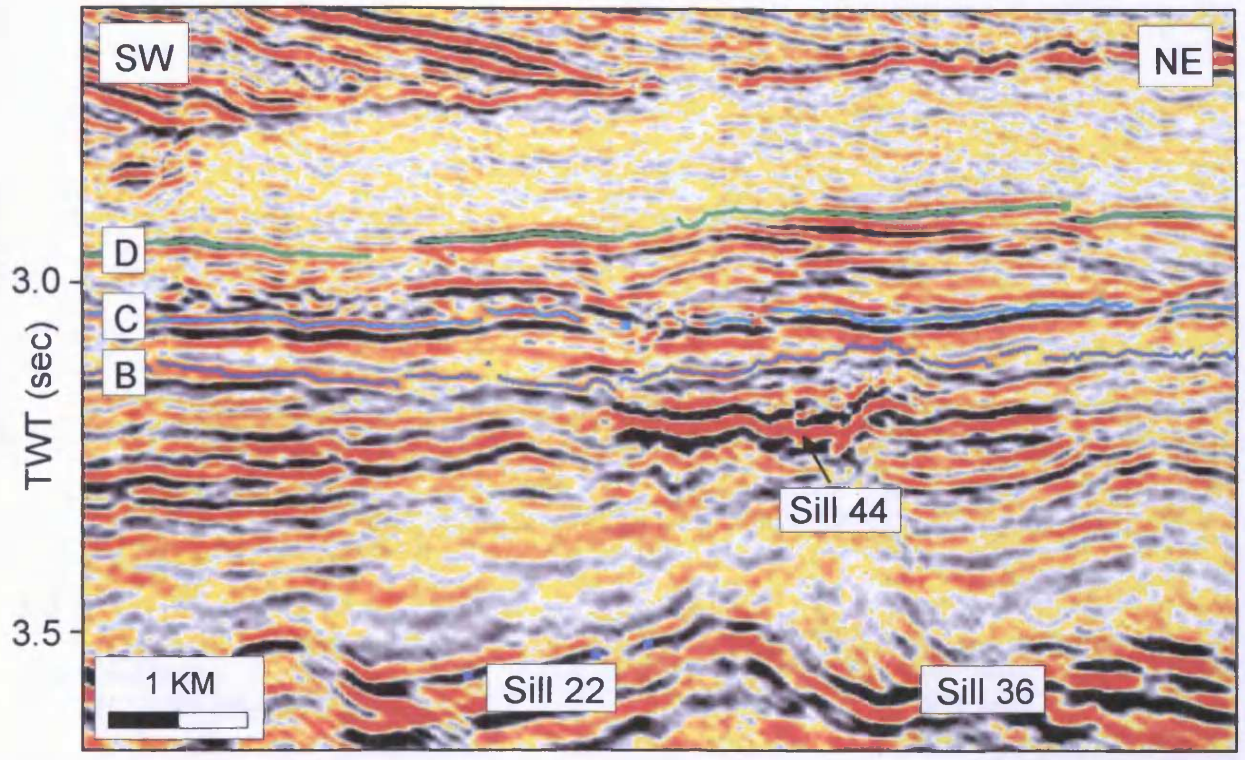

Fig. 5.27 Seismic section showing discordant cross-sectional geometry of sill 44. The north-eastern edge of the sill transgresses 42 ms discordantly. See Fig. 25a for line location.

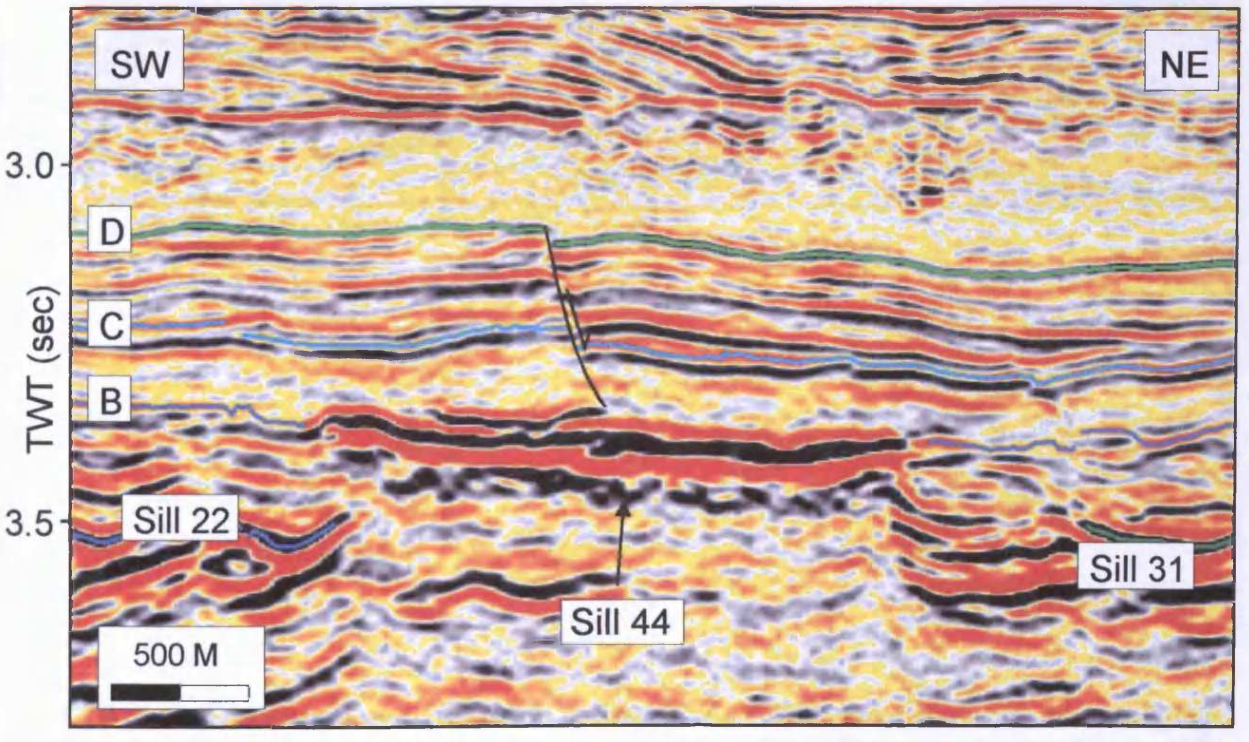

Fig. 5.28 Cross-sectional geometry of sill 44 showing perfect concordance between the sill and horizon B. Note the underlying sills 22 and 31. See Fig. 5.25a for line location.

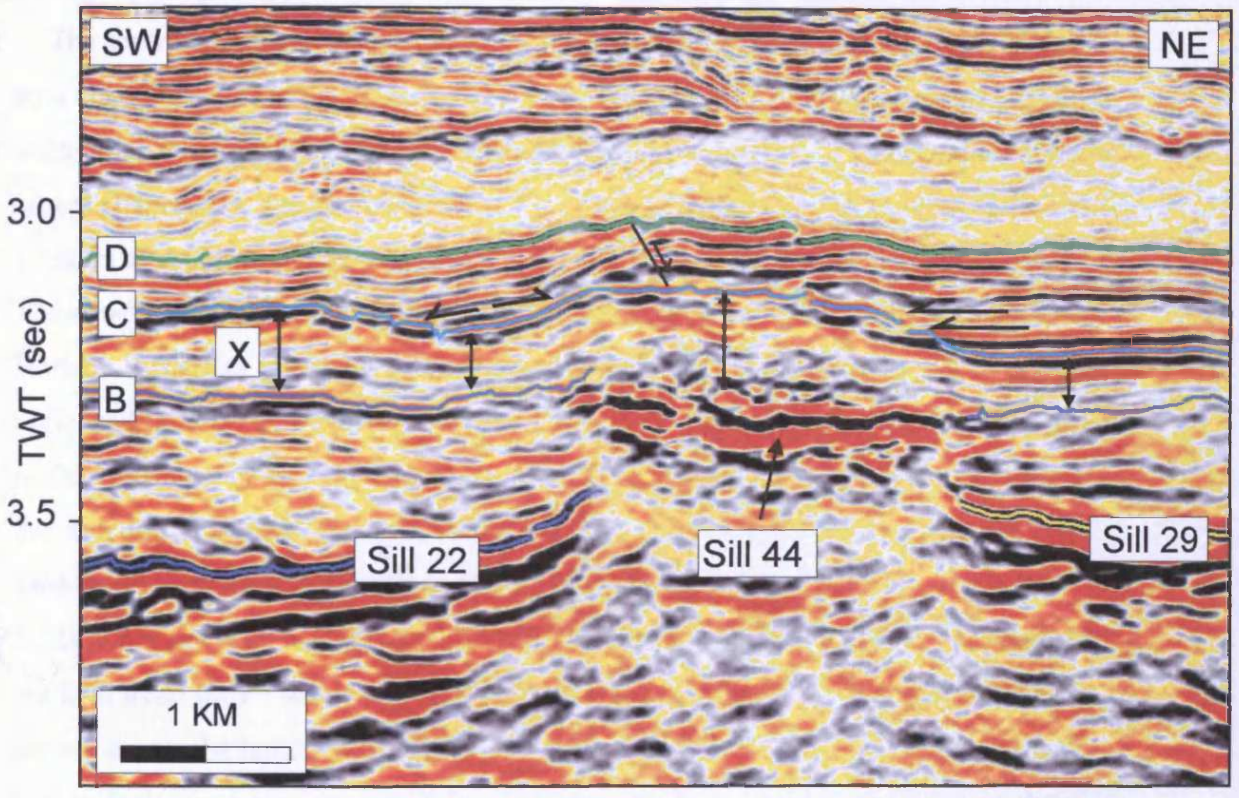

Fig. 5.29 Seismic section showing apparent deformation of overburden above sill 44. Overlying the sill horizon C is bent upwards and the created high is onlapped by reflections within the C-D interval. Similar deformation of horizon C unrelated to sill 44 is seen at location X, suggesting that the deformation is unrelated to sill intrusion. Note the underlying sills 22 and 29. See Fig. 5.25a for line location.

The sill has an irregular top surface that exhibits a poorly defined pattern of curved structures that are convex towards the north-west (Fig. 5.30). These are particularly well imaged on the amplitude map of the sill on which the curved structures appear as low amplitude anomalies (Fig. 5.30a). A comparison with a vertical seismic profile (Fig. 5.30b) shows that the curved planview geometry corresponds to a set of ridges on the sill (cf. Trude, 2004), with the lows being imaged as the low amplitude curved anomalies seen on the amplitude map. The ridges are spaced at 200-400 metres with an average spacing of approximately 300 m and range in height between 15-30 m.

The south-eastern end of the sill is coincident with a high amplitude poorly defined structure (Figs. 5.31 and 5.32). The structure consists of a conical basal high amplitude continuous feature that exhibits a cross-sectional geometry that is comparable to that of saucer-shaped sills mapped elsewhere (Fig. 5.31). This basal concave upward feature is overlain by an upward doming package of high amplitude discontinuous reflections. The structure is slightly N-S elongated and measures approximately 1050 m by 800m. Horizon B is either truncated or displaced upwards across the structure. The overlying horizons C and D can be mapped continuously across the structure and both are clearly pushed up above it. The C-D interval (possibly B-D interval) thins across the crest of the structure. It is located on a N-S oriented linear fault trend (Fault A) imaged on a time-structure map of horizon B to the north of the outline of sill 44 (Figs. 5.8 and 5.32). It has not been possible to map the fault underlying the sill, but extrapolation of the fault trend shows that it is coincident with the fault trace. The vertical seismic section across the fault shown in Fig. 5.33 shows that horizon B is offset by the fault, but the fault tips out at horizon C. There is clear growth across the fault within the B-C interval. A throw profile for the imaged part of the fault at the level of horizon B (Fig. 5.34) shows throw maxima towards the northern tip of the fault and a decrease towards the south.

A number of sills have been mapped underlying sill 44 (Fig. 5.35). The map shows five sills that all terminate along a linear trend that is coincident with the location of sill 44. Sills 22 and 17 are seen to the south of sill 44, whilst on the northern side of sill 44, sills 29, 36, and 5 are seen.

5.4.3.3 Discussion: The emplacement of sill 44

Sill 44 is discordant to stratigraphy, which means it cannot be a surface lava flow. However, the sill exhibits several characteristics usually associated with extruded lava

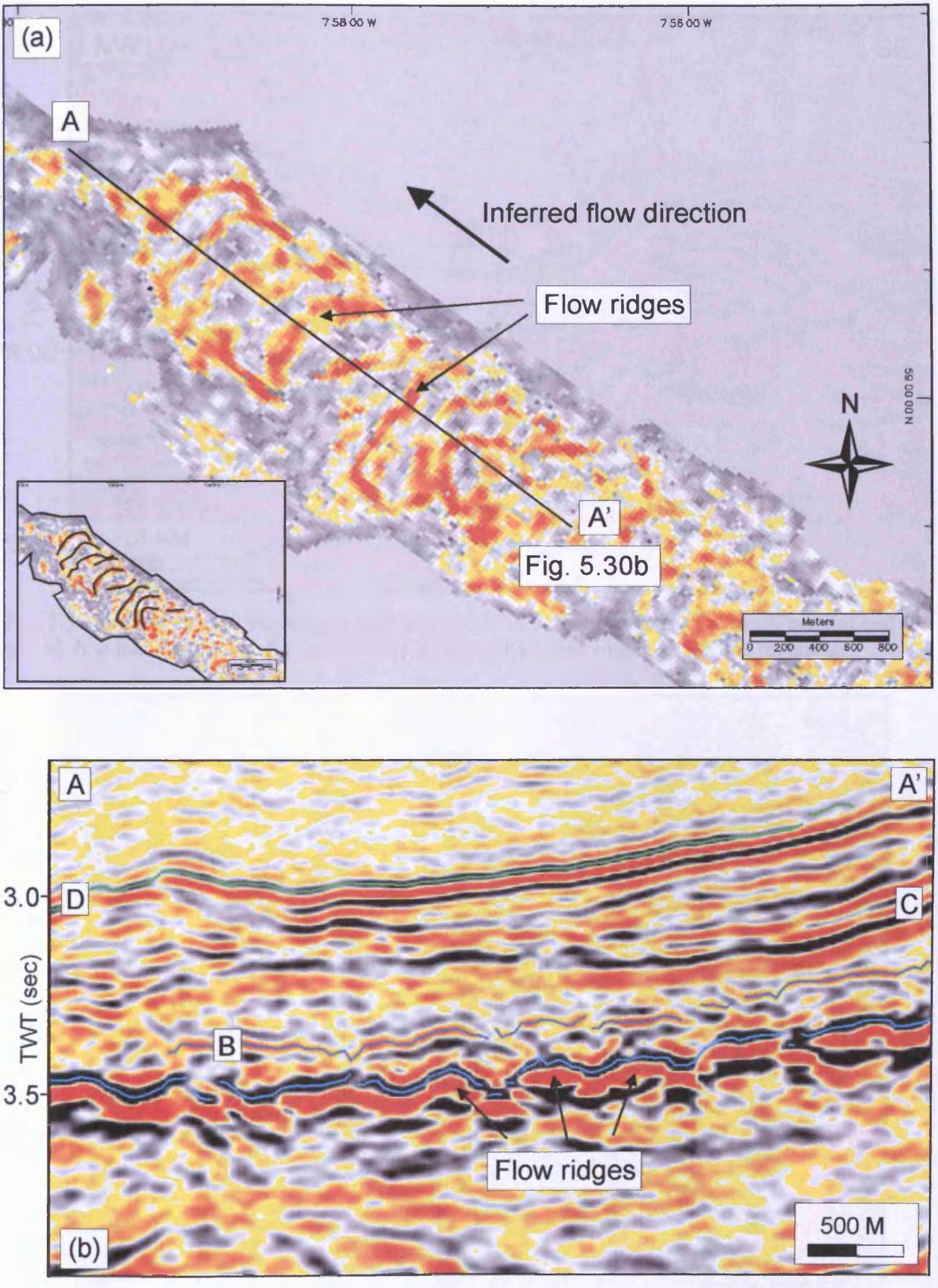

Fig. 5.30 (a) Amplitude map of central part of sill 44 showing low amplitude convex structures interpreted as flow ridges. The structures are convex towards the NW suggesting that the sill propagated from the SE towards the NW. See Fig. 5.25b for location. (b) Seismic section showing the cross-sectional geometry of the flow ridges. The ridges are spaced at 200-400 m and range in height between 15-30 m.

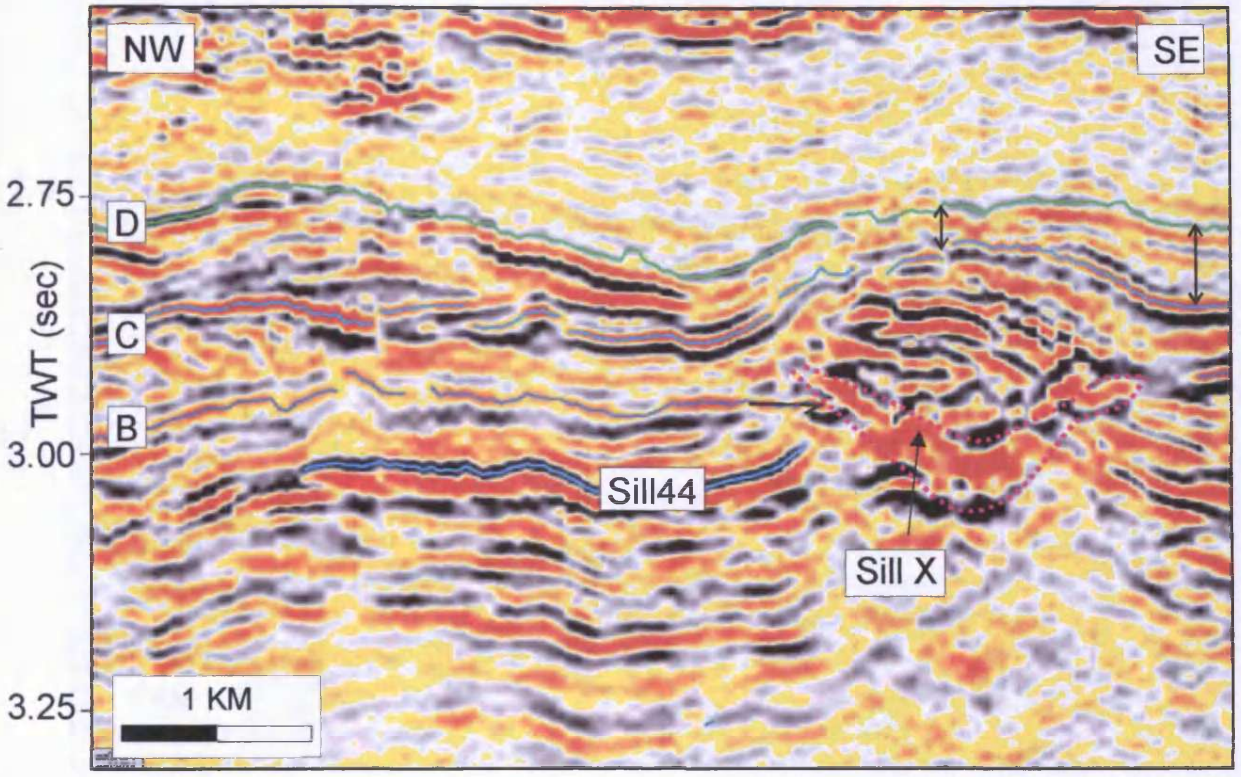

Fig. 5.31 Seismic section showing a high amplitude structure located at the south-eastern end of sill 44. It is interpreted as a feeder sill (sill X) for sill 44. See Fig. 5.32 for line location.

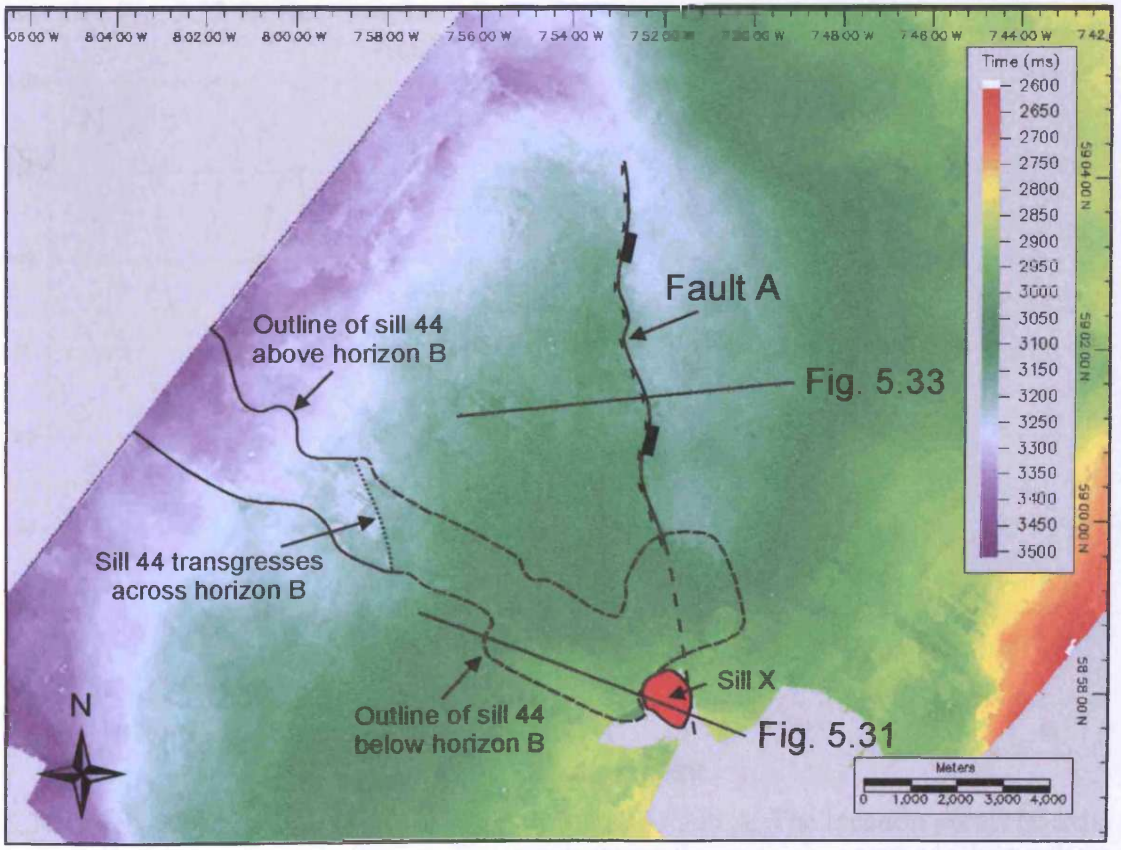

Fig. 5.32 Outline of sill 44 superimposed on time-structure map of horizon B. The map shows that sill X is located along the continuation of the trend of Fault A, which offsets horizon B. Note line locations for Figs. 5.31 and 5.33.

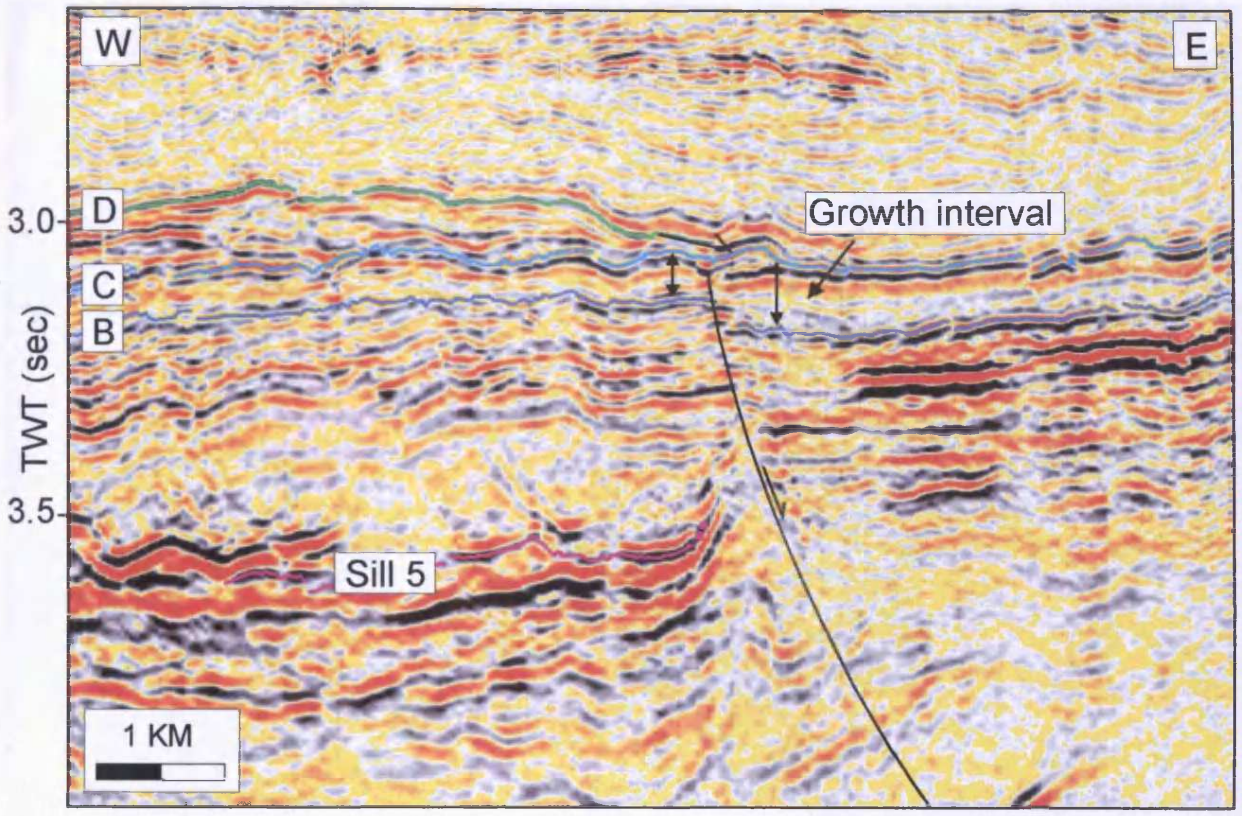

Fig. 5.33 Seismic section across Fault A showing clear displacement of horizon B and tip out and horizon C. A growth wedge is seen in the hangingwall of the fault within the B-C interval, indicating active fault propagation at this time. Sill 5 is seen to terminate in the hangingwall of the fault. See Fig. 5.32 for line location.

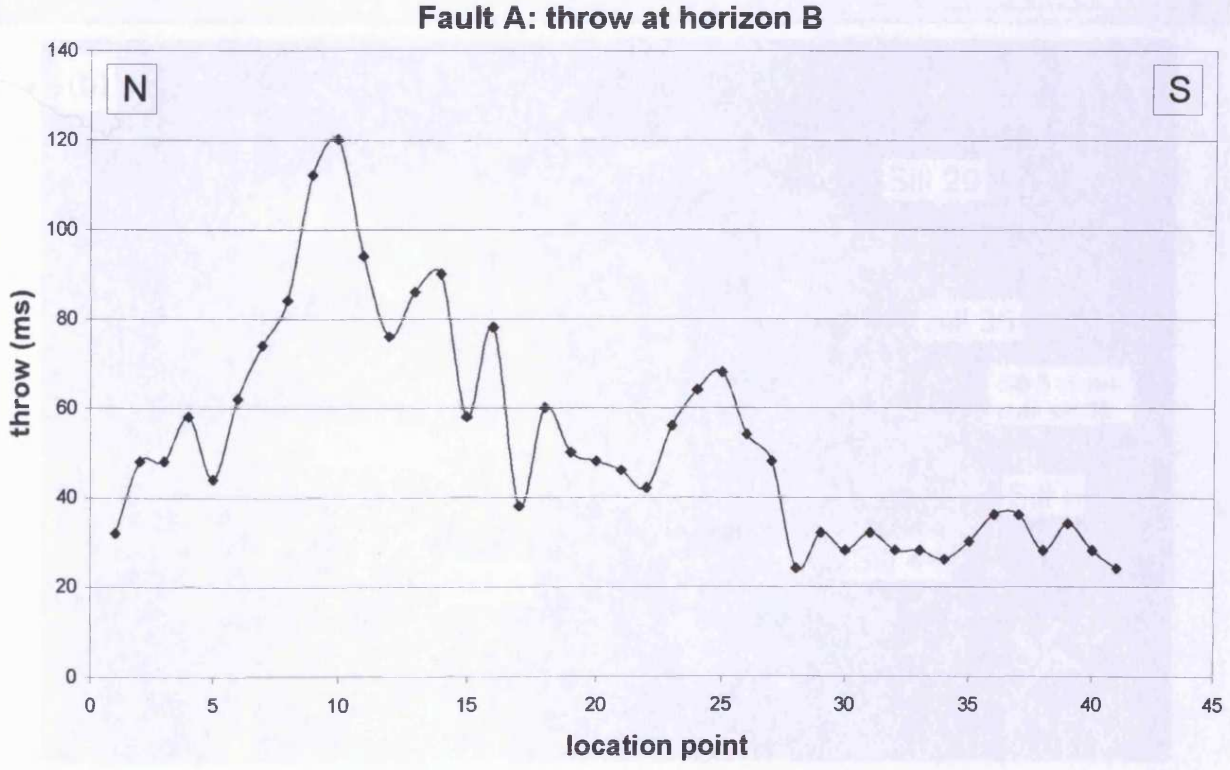

Fig. 5.34 Graph showing fault throw at horizon B along Fault A. The location points (x-axis) are evenly spaced at approximately 200 m. The graph shows throw minima towards the northern fault tip and towards the south and a central (skewed towards the north) throw maximum. The fault cannot be mapped underlying sill 44 to the south, but the throw profile is interpreted to indicate that the southern lateral tip is likely to be located near the location of sill X.

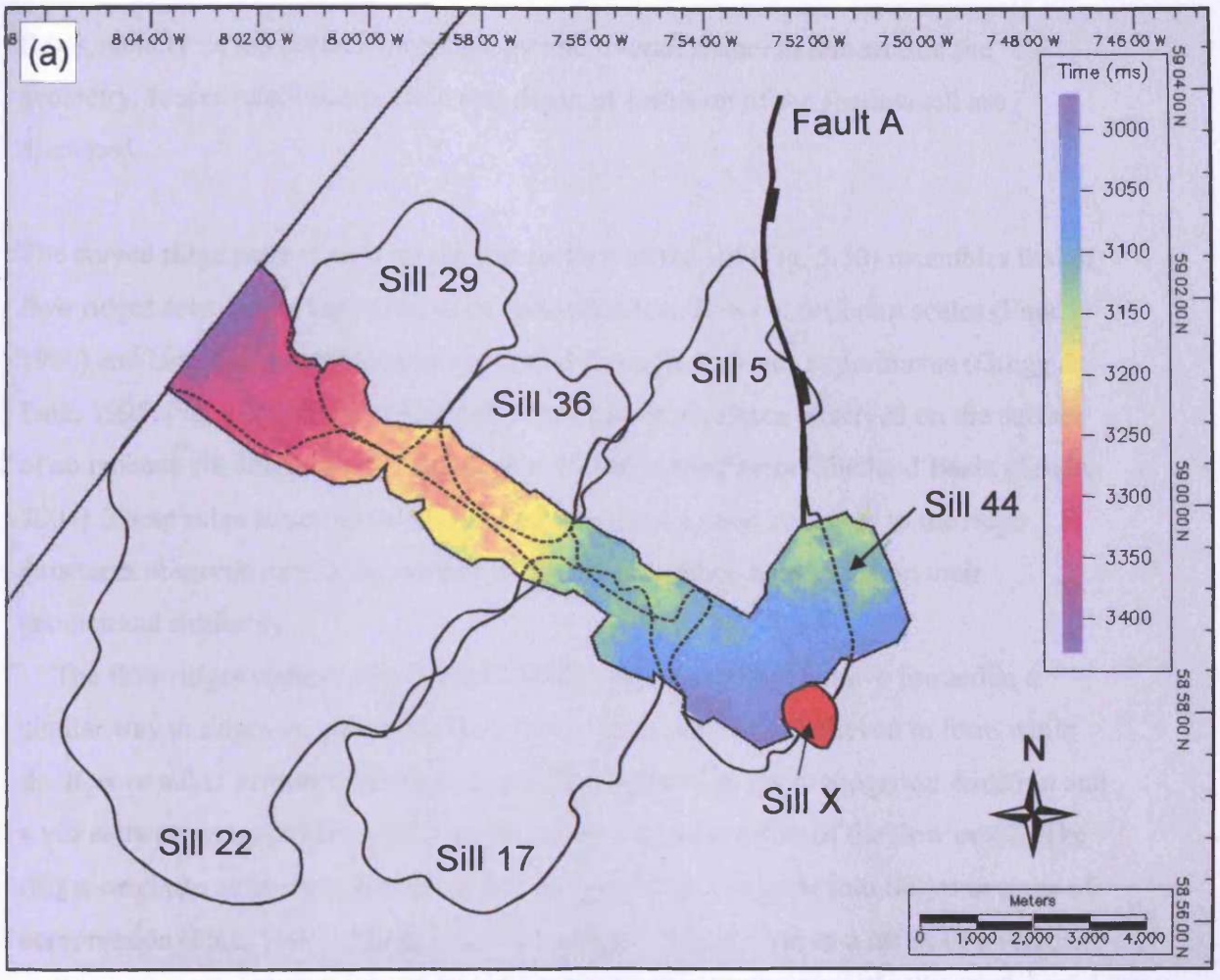

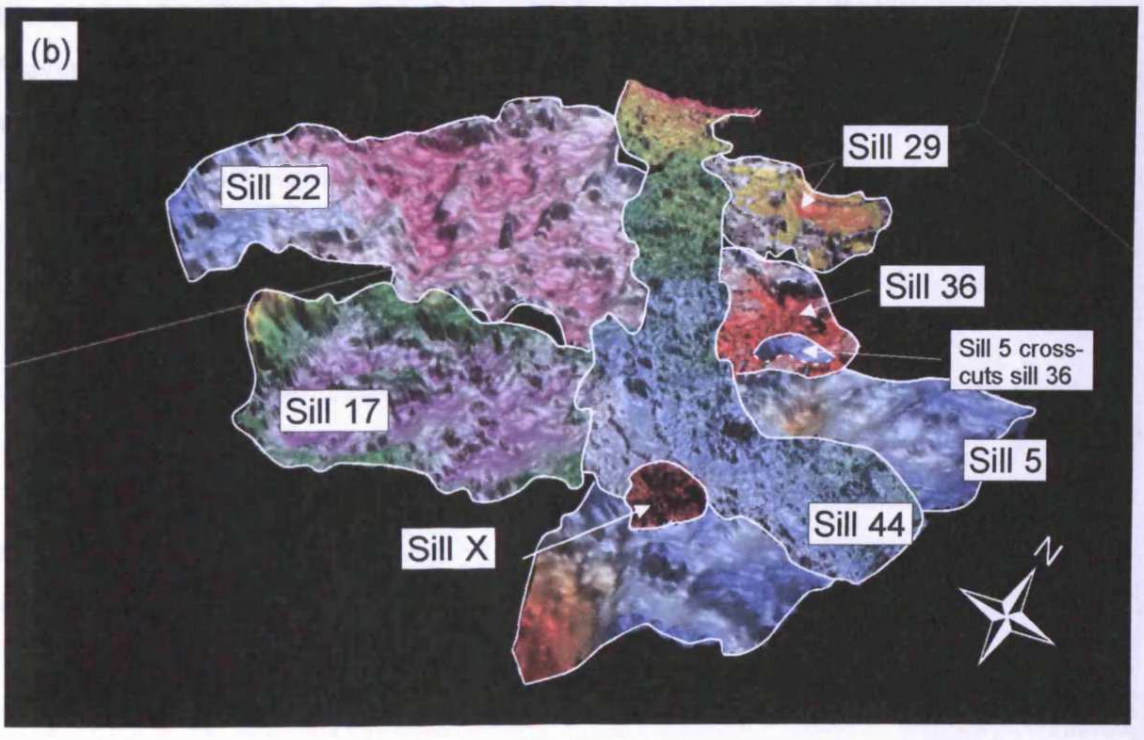

Fig. 5.35 (a) Map showing the outline of five sills underlying sill 44. The sills all terminate along a linear trend that is coincident with the sill 44. Sills 22 and 17 are seen south of sill 44, whilst sills 29, 36, and 5 are seen to the north of the sill. The eastern periphery of sill 5 is coincident with fault A. (b) Three-dimensional view of sill 44 and the underlying sills and the feeder sill (sill X).

flows, namely its top surface morphology and overall shape. In this section the geometry, feeder relationship, time and depth of intrusion of the shallow sill are discussed.

The curved ridge pattern seen on the top surface of the sill (Fig. 5.30) resembles that of flow ridges seen on the top surfaces of pahoehoe lava flows at different scales (Fink, 1980) and lava flow morphologies generated through analogue experiments (Gregg & Fink, 1995; Fig. 5.36). Similar ridge structures have also been observed on the surface of an igneous sill emplaced at a depth of < 400 m in the Faeroe-Shetland Basin (Trude, 2004). These ridge structures are considered to offer a good analogue to the ridge structures observed on the top surface of the sill described here based on their geometrical similarity.

The flow ridges observed by Trude (2004) were interpreted to have formed in a similar way to ridges on pahoehoe lava flows. Such ridges are believed to form while the flow or sill is in motion due to compression parallel to the propagation direction and a viscosity decrease downwards from the surface to the interior of the flow or sill. The ridges originate as low amplitude surface irregularities and grow into ridges in areas of compression (Fink, 1980). These initial irregularities may form as a result of a viscosity difference between the interior and exterior of the flow or sill (Fink, 1980). Compression, and thus ridge amplification, may be imposed as a result of higher viscosity at the flow front retarding the forward advance of the flow, as suggested by Fink (1980) for the development of flow ridges on rhyolites. Considering this and previous studies, it is suggested that the ridges seen on the top surface of sill 44 formed as a result of amplification of surface irregularities, formed due to a viscosity difference between the surface and interior of the sill, as a result of retardation of forward propagation related to a combination of increased viscosity at the sill front and the shear strength of the host-rock.

Flow ridges adopt a convex geometry due to a difference in flow rate and friction between the centre and edges of the flow (Ramsay & Lisle, 2000). At the edges, the flow rate is lower than in the central part of the flow due to friction and higher viscosity related to increased cooling. The sense of convexity of the flow ridges can, therefore, be used to determine flow direction with the ridges adopting a shape that is convex in the direction of flow (Ramsay & Lisle, 2000). In the case of sill 44 this suggests that the sill propagated from the south-east towards the north-west transgressing across horizon B.

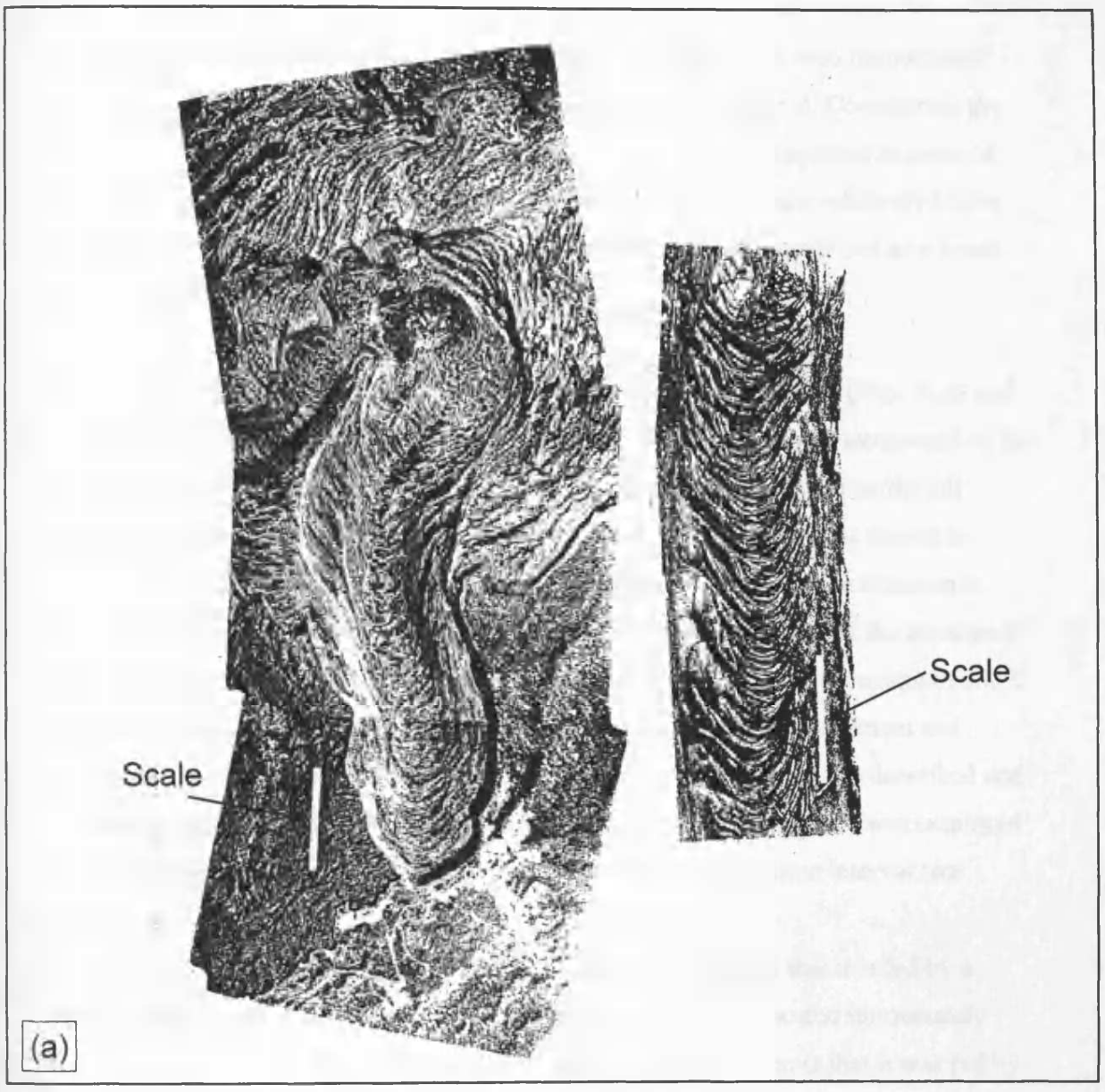

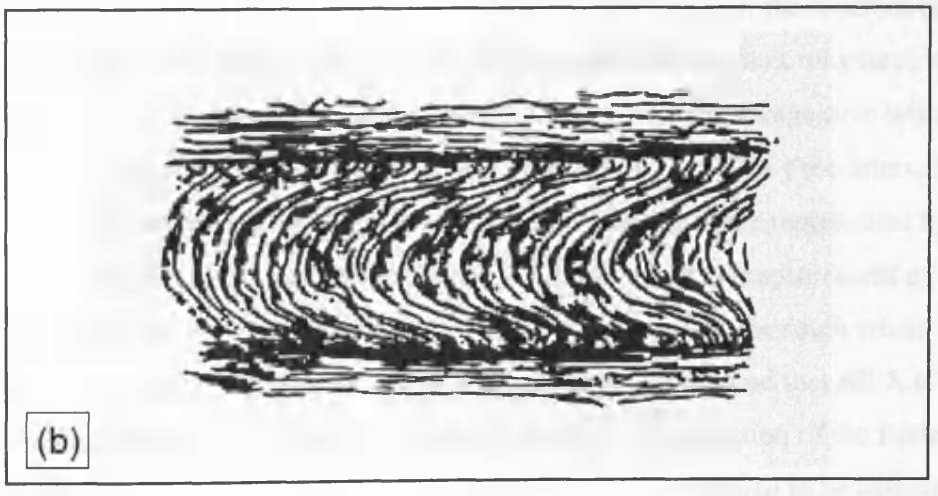

Fig. 5.36 Examples of ridge morphology on lava flows. (a) Field examples of ridges on lava flow at different scales. Left: North Lobe, Big Glass Mountain, Medicine Lake Highlands Volcano, California. Scale bar represents 500 m. Right: Ropy Pahoehoe structure, Kilauea Volcano, Hawaii. Scale bar represents 2 m. After Fink (1980). (b) Schematic showing the geometry of folds on a submarine flow produced in a laboratory. After Gregg & Fink (1995).

It is particularly interesting to note that the imaged flow ridges are seen immediately upflow from the location where sill 44 transgresses across horizon B. Considering the model for development of flow ridges, particularly that they are amplified in areas of compression, this may suggest that the horizon B boundary offered a relatively higher resistance to the propagation of the sill than the surrounding sediments and as a result induced a local area of compression.

The high amplitude structure that is located at the eastern end of sill 44 (Figs. 5.26 and 5.31) exhibits amplitude anomalies similar to those of the igneous sills interpreted in the survey area. Based on the flow ridge geometry it was suggested above that the sill propagated away from the direction of the structure, which indicates that the sill is likely to have been fed by the structure. Based on these observations the structure is interpreted to be igneous in origin. The geometry of the concave upward the basal part of the structure is interpreted as a saucer-shaped sill (sill X). The emplacement of sill X appears to have affected the overlying horizons causing upward displacement and thinning across the crest of the structure (this type of deformation will be described and discussed in detail in section 5.5). This interpretation suggests that sill X was emplaced around the time of represented by horizon B and during the B-D time interval (see section 5.5).

There is no sign of a conduit underlying sill X, which suggests that it is fed by a vertical feeder that is not resolved by the seismic data. Sill X is located immediately above the edge of sill 5 (Fig. 5.35a) and one possible interpretation is that it was fed by a magma pipe that emanated from the edge of sill 5. Alternatively, the location of sill X along the trend of Fault A (Figs. 5.32 & 5.35a) suggests that the fault may have been important in relation to the emplacement of sill X. The growth package seen within the B-C interval on Fault A suggests that the fault was active during the time interval represented by these two reflectors, but inactive following the time represented by horizon C. Hence, the fault was active during the initial stage of emplacement of sill X. The throw profile for fault A shows a decrease in throw towards the south where sill X is located. This suggests that the fault tips out towards the south and that sill X is located near a fault tip. Based on this a second possible interpretation of the feeder for the plug is proposed. In this model the feeder for sill X is interpreted to be associated with the tip of fault A. The fault forms the north-eastern boundary to sill 5 and it is possible that magma migrated from sill 5 at depth along the plane of Fault A.

The geometry of sill 44 is very different from that of any other sills interpreted in the survey area. The majority of the sills are irregular saucer-shaped sill segments, whilst sill 44 is clearly elongated. It is interesting that the path of the sill is coincident with a line defined by the peripheries of underlying sills. In Fig. 5.7 a cross-section across the south-western edge of sill 22 is shown and it shows that the sediments overlying the sill are displaced upwards by approximately 100 m and a monocline is formed at the level of horizon B across the edge of the sill. Similar deformation is seen above the south-western edge of sill 30 in Fig. 5.18. This type of deformation is attributed to forced folding during intrusion and will be described and discussed in detail in section 5.5. It is reasonable to suggest that a comparable monoclinal structure was formed at the northern periphery of the sill, although there is no direct evidence to support this suggestion. The deformation of horizon B suggests that emplacement post-dates the time represented by this horizon. If all of the five sills mapped underlying sill 44 were to have caused upward vertical displacement of the overburden a trough exhibiting the same trend as that of sill 44 would possibly have formed at the seabed and the underlying stratigraphy boundaries, including horizon B, would have adopted synclinal forms along the same trend (Fig. 5.37). One way of explaining the linear path of sill 44 is to suggest that it was emplaced after the emplacement of the underlying sills and that its intrusion path was constrained to the synform between the surrounding forced fold structures related to the underlying, earlier emplaced sills.

The timing and depth of intrusion of sill 44 are poorly constrained. The sill transgresses and deforms horizon B and must, therefore, have been emplaced later than the time represented by this horizon (Late Paleocene). The overlying horizon C is locally deformed and onlapped above the sill (Fig. 5.29) suggesting that intrusion occurred at this time. However, as mentioned above, based on the nature of horizon C, it cannot be excluded that the deformation is unrelated to the emplacement of the sill. The interpreted feeder sill X (Fig. 5.31) appears to have been emplaced during the early phase of the C-D interval (approximately Early Eocene). The data are not conclusive, but based on the above it is suggested that the timing of emplacement is around the time represented by horizon C, i.e. Early Eocene, following the emplacement of the underlying sills, which were interpreted to be Late Paleocene in age. This interpretation is further supported by the more confident interpretation of the emplacement of other

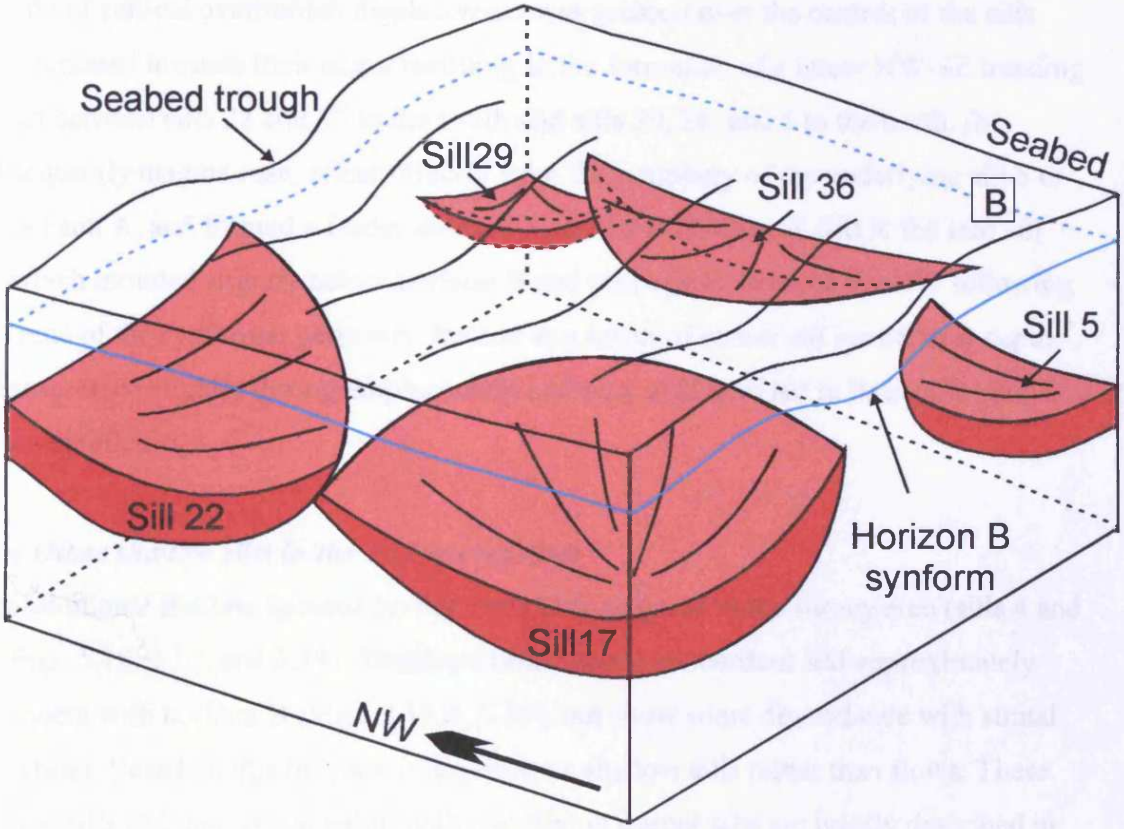

Fig. 5.37 Schematic illustration showing deformation of overburden above five sills. The upwards displacement of the overburden overlying the sills results in the formation of a NW-SE trending trough at the seabed and is seen as a synform on underlying horizons (e.g. horizon B).

relatively shallow intrusions in the survey area within this time interval, described in section 5.5. This suggests that the sill was emplaced at a depth of between 225-425 m below the contemporaneous seabed.

5.4.3.4 Model for the emplacement of sill 44

A model for the emplacement of sill 44 is illustrated in Fig. 5.38 and summarised in this section. (a) Sills 22, 17, 29, 36, and 5 were emplaced initially and led to forcible uplift of the overburden and deformation of horizon B and the contemporaneous seabed. The amount of vertical overburden displacement was greatest over the centres of the sills and decreased towards their edges resulting in the formation of a linear NW-SE trending trough between sills 22 and 17 to the south and sills 29, 36, and 5 to the north. (b) Subsequently magma rose, either directly from the periphery of the underlying sill 5 or along Fault A, and formed a feeder sill (sill X) in the B-D interval. Sill X fed into sill 44, which intruded slightly below horizon B and propagated towards the NW following the trend of the synformal geometry formed as a result of earlier sill intrusion at depth. It transgressed slightly during emplacement and may also have led to limited folding of the overburden.

5.4.4 Other shallow sills in the T38 survey area

Two additional shallow igneous bodies have been mapped in the survey area (sills 4 and 43; Figs. 5.18, 5.19, and 5.39). These are both largely concordant and approximately coincident with horizon B (Figs. 5.18 & 5.39), but show some discordance with stratal reflections. Based on this they are interpreted as shallow sills rather than flows. These shallow sills and their relationship with underlying deeper sills are briefly described in this section.

Sill 4 is located at the western periphery of the survey area (Figs. 5.19 and 5.40). The imaged part of the sill measures 7 km by 2 km and covers an area of just less than 11 km^2. The sill dips towards the west and spans a TWT range of 3445 ms to 3295 ms. Sill 43 has been mapped in the north-western corner of the survey area (Figs. 5.19 and 5.40). It extends beyond the northern and western survey boundaries. The mapped part of the sill measures approximately 6 km by 9 km. It dips towards the NW dropping from 3560 ms TWT to 3070 ms TWT. Both sills have irregular top surfaces, but neither exhibits an ordered flow pattern comparable to the pattern seen on the top surface of the shallow sill described in detail above.

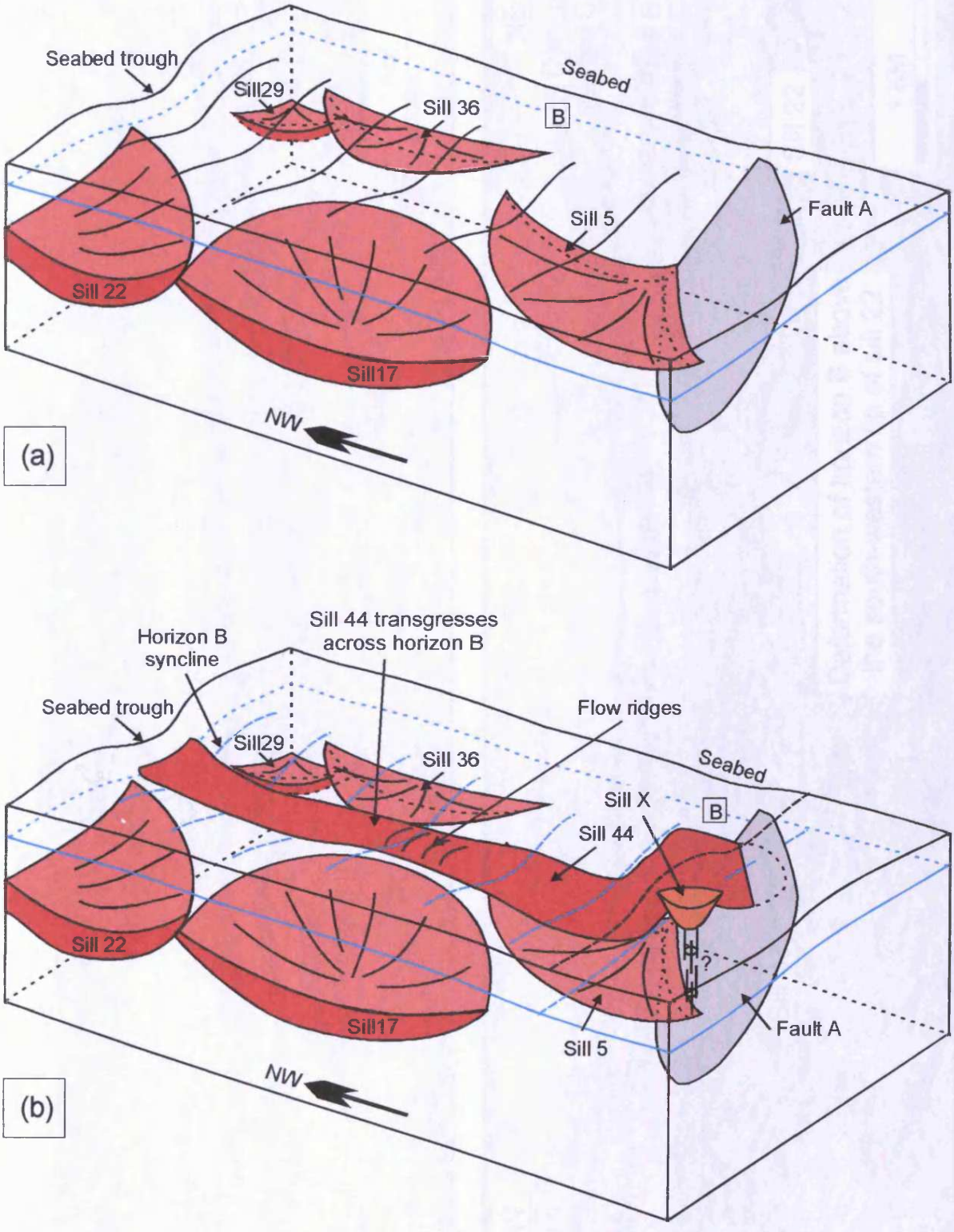

Fig. 5.38 Schematic showing sill 44 emplacement model. (a) Sills 22, 17, 29, 36, and 5 are emplaced and cause uplift of the overburden and deformation of horizon B and the contemporaneous seabed. The vertical displacement of the overburden overlying the sills results in the formation of a linear NW-SE trending trough between sills 22 and 17 to the south and sills 29, 36, and 5 to the north. (b) Subsequently magma rises from below and sill X forms within the B-C interval. Sill X feeds into sill 44, which intrudes slightly below horizon B and propagates towards the NW following the trend of the horizon B synform.

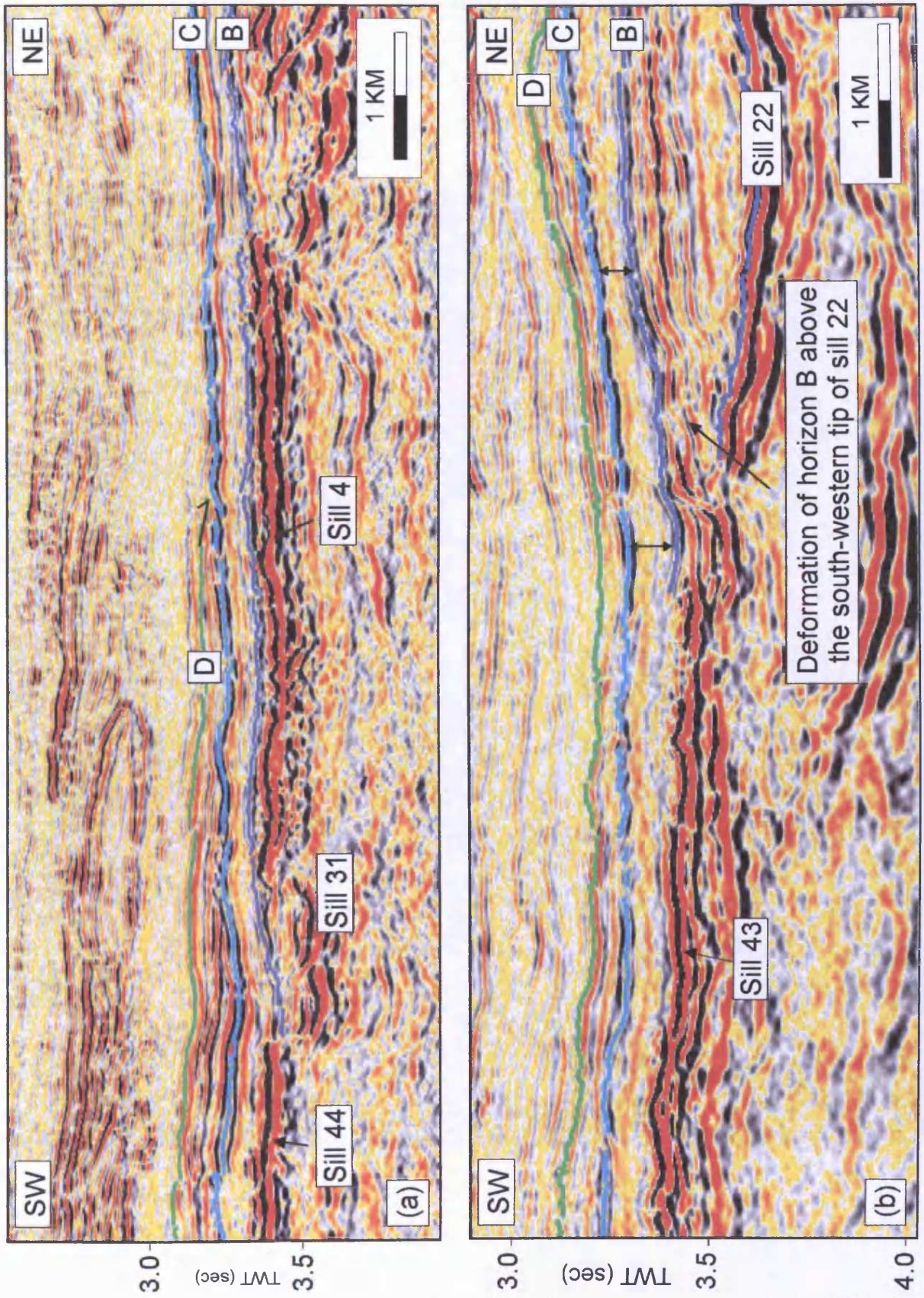

Fig. 5.39 Seismic sections showing the cross-section geometry of the shallow and near-concordant sills 4 (a) and 43 (b). See Fig. 5.40 for line locations.

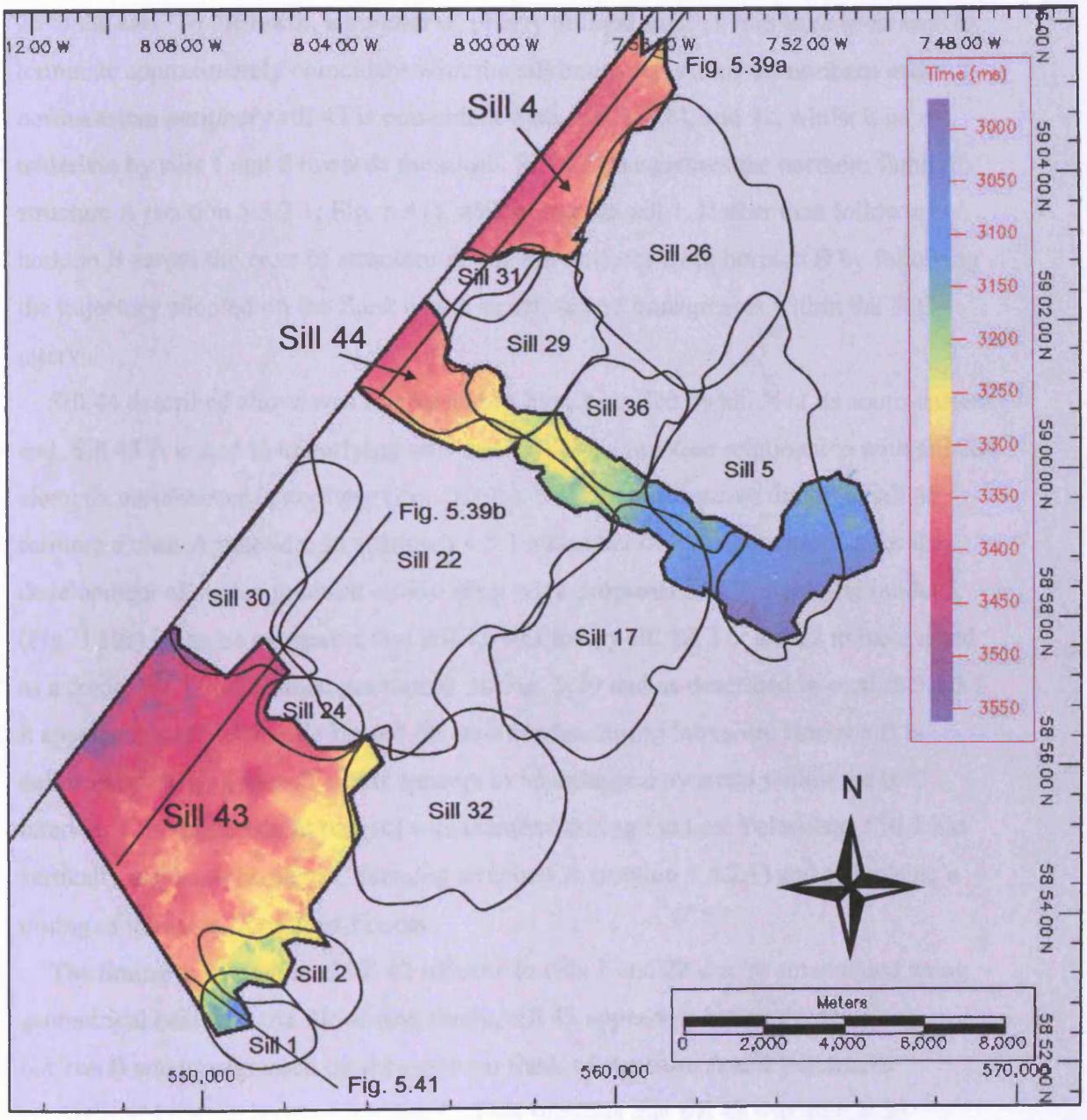

Fig. 5.40 Time-structure maps of sills 4, 43, and 44 showing the outline of underlying sills. There is a high degree of coincidence between the boundaries of the underlying sills and the outlines of shallow sills. Note line location for Figs. 5.39 and 5.41.

It was suggested above that sills underlying sill 44 had influenced the trend of sill 44. The map shown in Fig. 5.40 illustrates the distribution of sills in the north-western part of the survey area underlying sills 4, 43, and 44. It shows that the area is heavily intruded and the boundaries of the deeper sills show a high degree of coincidence with the outlines of the shallow sills. Sill 4 is underlain by sills 29 and 31 to the south and sill 26 to the east. To the north, a number of poorly defined smaller sills have been seen to terminate approximately coincident with the sill boundary. Along its northern and north-eastern periphery sill 43 is coincident with sills 30, 24, and 32, whilst it is underlain by sills 1 and 2 towards the south. Sill 43 transgresses the northern flank of structure A (section 5.5.2.1; Fig. 5.41), which overlies sill 1. Rather than following horizon B across the crest of structure A, the sill deviates from horizon B by following the trajectory adopted on the flank of the structure and transgresses within the B-C interval.

Sill 44 described above was interpreted to have been fed by sill X at its south-eastern end. Sill 43 is linked to underlying sills and exhibits a junction relationship with sill 22 along its north-eastern periphery (Fig. 5.39b). Sill 22 abuts against the tip of sill 43 forming a class A junction. In section 3.4.5.1 a number of kinematic models for the development of such a junction relationship were proposed and by invoking model 3 (Fig. 3.50c) it can be suggested that sill 43 was fed by sill 22. For sill 22 to have acted as a feeder for sill 43 it must pre-date it. In Fig. 5.39 and as described in section 5.4.3.3 it appears that sill 22 has deformed the overburden during intrusion. Horizon B is deformed overlying the sill and it appears to be onlapped by strata within the B-C interval. This suggests that this sill was intruded during the Late Paleocene. Sill 1 has vertically displaced horizon C forming structure A (section 5.5.2.1) and suggesting a timing of intrusion of earliest Eocene.

The timing of intrusion of sill 43 relative to sills 1 and 22 can be constrained using geometrical evidence. As illustrated above, sill 43 appears to have intruded along horizon B and transgressed up the northern flank of structure A and terminates approximately at the level of horizon C. This suggests that sill 43 was emplaced following horizon B and at the earliest immediately prior to horizon C in the earliest Eocene. Sill 22 was found to have been intruded in the Late Paleocene and thus prior to sill 43. Sill 1 is interpreted to have been intruded during the earliest Eocene and Sill 43 could either have been (1) intruded prior to it and have been vertically displaced upwards during the deformation above sill 1 or (2) have intruded already deformed

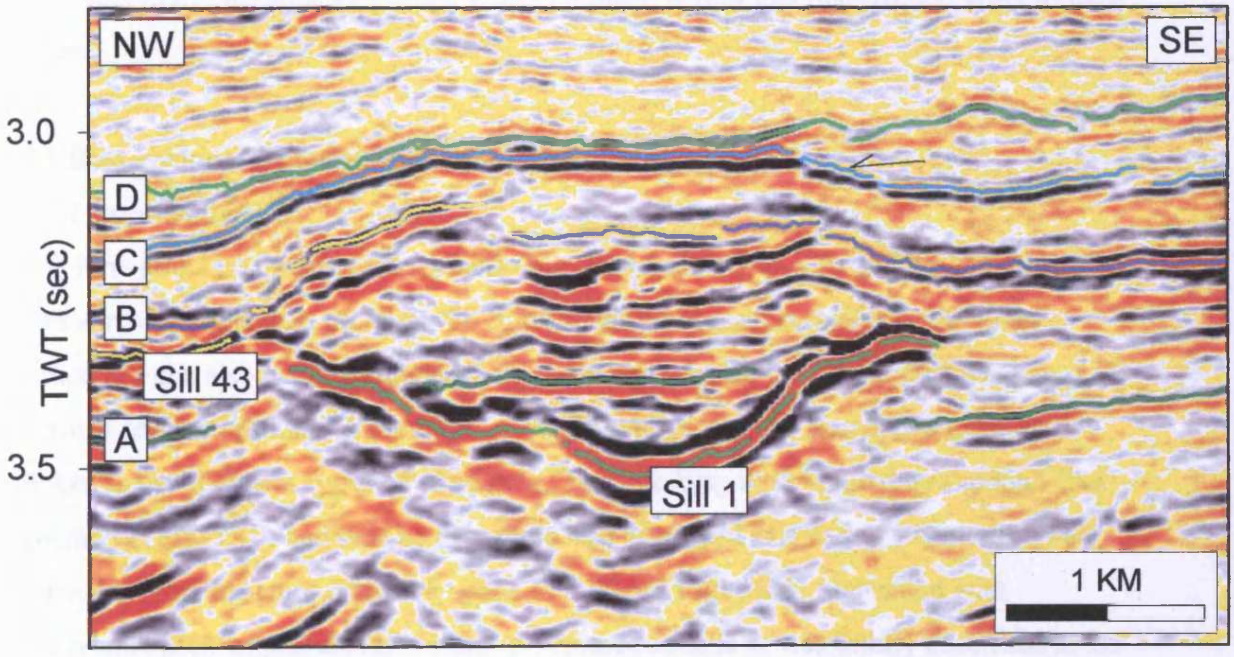

Fig. 5.41 Seismic section showing the cross-sectional geometry of structure A overlying sill 1. Horizons A, B, and C are displaced upwards overlying sill 1 forming a forced fold. The C-D interval is thinned across the crest of the structure and reflections within the interval onlap horizon C. Sill 43 transgresses along the northern flank of structure A and terminates within the B-C interval. See Fig. 5.40 for line location.

strata following the emplacement of sill 1. It is suggested that the geometry of sill 43 and, in particular, its deviation from concordance above the northern limb of structure A is best explained by invoking that intrusion of sill 43 followed on from the intrusion of and deformation above sill 1. Such an interpretation further suggests that sill 43 was intruded following the emplacement of both sill 1 and sill 22, during the Early Eocene. The duration of the time interval between the emplacement of sill 22 in the Late Paleocene and sill 43 in the earliest Eocene is poorly constrained. However, for sill 22 to have acted as a feeder for sill 43 it is unlikely that it was fully solidified at the time sill 43 was intruded (section 1.5.4.3). If the interpretation that sill 43 was fed by sill 22 is correct these two sills were most likely emplace within less than 10,000 years of each other.

5.5 Host-rock deformation associated with sill intrusion

5.5.1 Introduction

The time-structure maps of horizons B (Fig. 5.8) and C (Fig. 5.9) exhibit a number of near-circular highs (e.g. location X). Similar structures, not revealed by the time-structure map, also occur elsewhere in the survey area and have been identified on vertical seismic sections. A comparison with vertical sections shows that these are linked to two different types of structures. The first type of structure has a mound-like geometry (Fig. 5.10) and will be described and discussed in detail in Chapter 6. The second type of structure takes the shape of a forced fold and is associated with underlying high amplitude reflections interpreted as sills as was briefly described in the preceding section and shown in Fig. 5.41. The geometry and origin of these structures are described in this section. Similar deformation, although less pronounced, was also observed and described in the T67 case study overlying sills 5, 11, and 12 (section 3.5).

5.5.2 Description of host-rock deformation structures

Four main deformational structures (A-D) have been interpreted and will be described in this section. One of these (structure A) is located near the western survey boundary, whilst the other three are located in the mid to northern part of the survey area at the eastern limit of the horizon B lava flow.

5.5.2.1 Structure A

Structure A is located near the western survey boundary and appears on the horizon B time-structure map as a poorly defined, near circular high with a diameter of 5 km and a vertical relief of approximately 150 m. The cross-sectional geometry of the structure is shown in Fig. 5.41.

Underlying the structure a high amplitude concave upwards, discordant reflection interpreted as a sill (sill 1) is seen. Sill 1 measures 3.2*2.2 km and covers an area of 4.5 km^2. It is emplaced at a present-day depth of 4850-5340 m and exhibits a vertical relief of 490 m. The top and base of the sill cannot be distinguished and the thickness of the sill cannot, therefore, be estimated. Above the sill, horizons A, B, and C have been deformed. Horizon A is cross-cut by the sill and the reflector segment that is nested within the concave shape of the sill is displaced upwards relative to the reflector segment seen outside the sill. Horizon B is continuous above the sill. The horizon is bent up above the sill and exhibits a folded geometry with fold limbs that coincide precisely in three dimensions with the sill tips. The overlying horizon C is deformed in a similar way, exhibiting a folded geometry with a vertical relief of 150 m. The C-D unit is thinned across the crest of the fold and reflections within the unit clearly onlap horizon C.

5.5.2.2 Structure B

Structure B (Fig. 5.42 and 5.43) is approximately 4 km in diameter and is the most clearly imaged of the structure on the horizon C time-structure map. It is located in the northern part of the survey area at the edge of the horizon B lava flow, in close proximity to structures C and D (Fig. 5.42). This structure is further described and discussed in section 5.5.5. The cross-sectional geometry of the structure is shown in Fig. 5.43. The structure is upwards defined by horizon C, which is onlapped by the overlying strata. Like structure A, structure B is characterised by updoming of the stratigraphy above an igneous sill (sill 41; Figs. 5.16 and 5.43). Sill 41 was described in detail in section 5.3.4. It was estimated that it had a maximum thickness of 420 m in its central part and thinned towards its edges. At the edge, the sill is abruptly terminated particularly along its north-eastern, eastern, and southern periphery. A number of poorly defined sills are seen immediately underlying sill 41 (Figs. 5.7 and 5.43), but the data do not allow for a definite link between these sills and sill 41 to be established. In Fig. 5.43a the north-western sill tip is almost

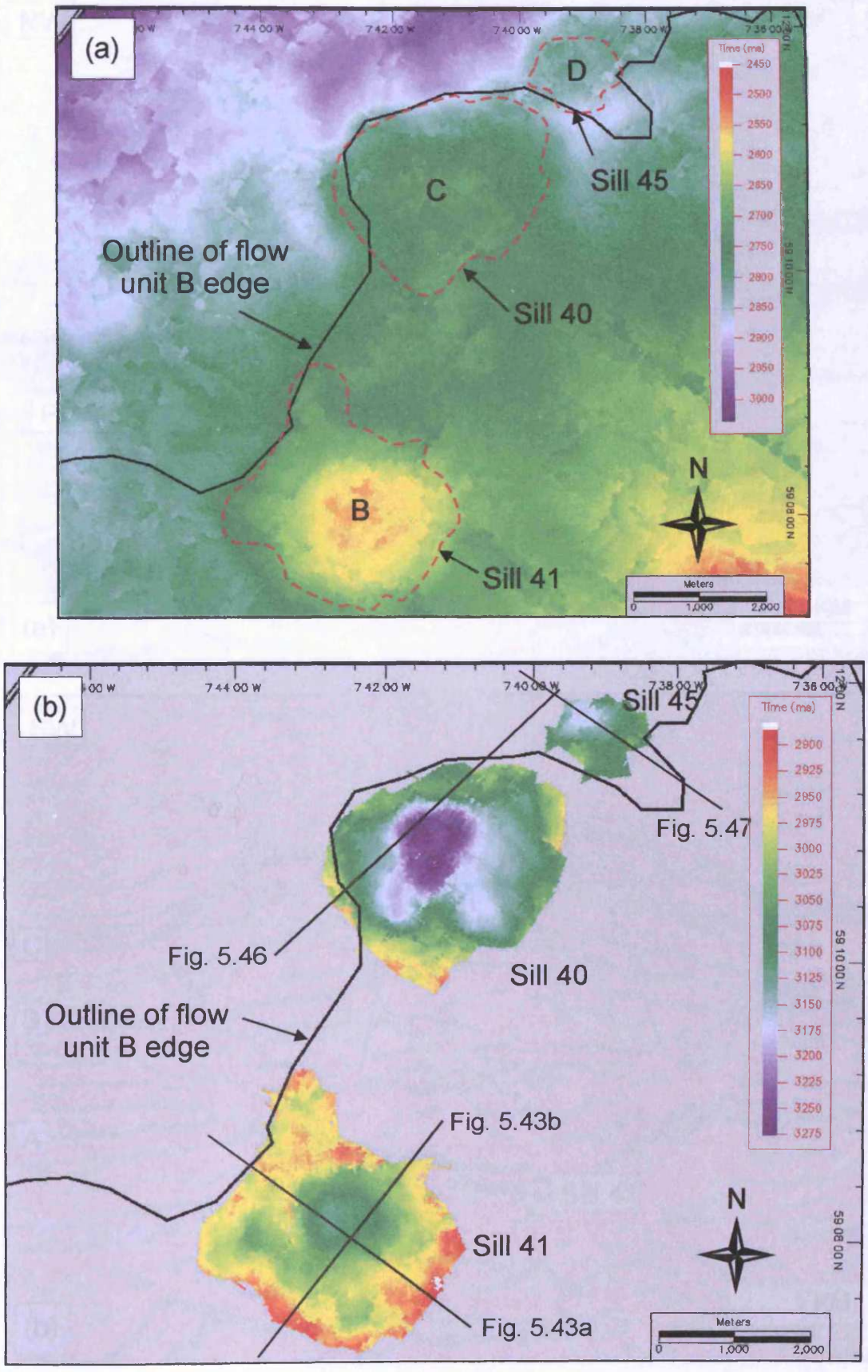

Fig. 5.42 (a) Time-structure map of horizon C. The outlines of sills 40, 41, and 45 are and the edge of flow unit B are superimposed on the map. The three sills are located near the edge of flow unit B and coincident with local highs (structures B, C, and D) seen on horizon C. (b) Time-structure maps of sills 40, 41, and 45. Note line locations for Figs. 5.43, 5.46, and 5.47.

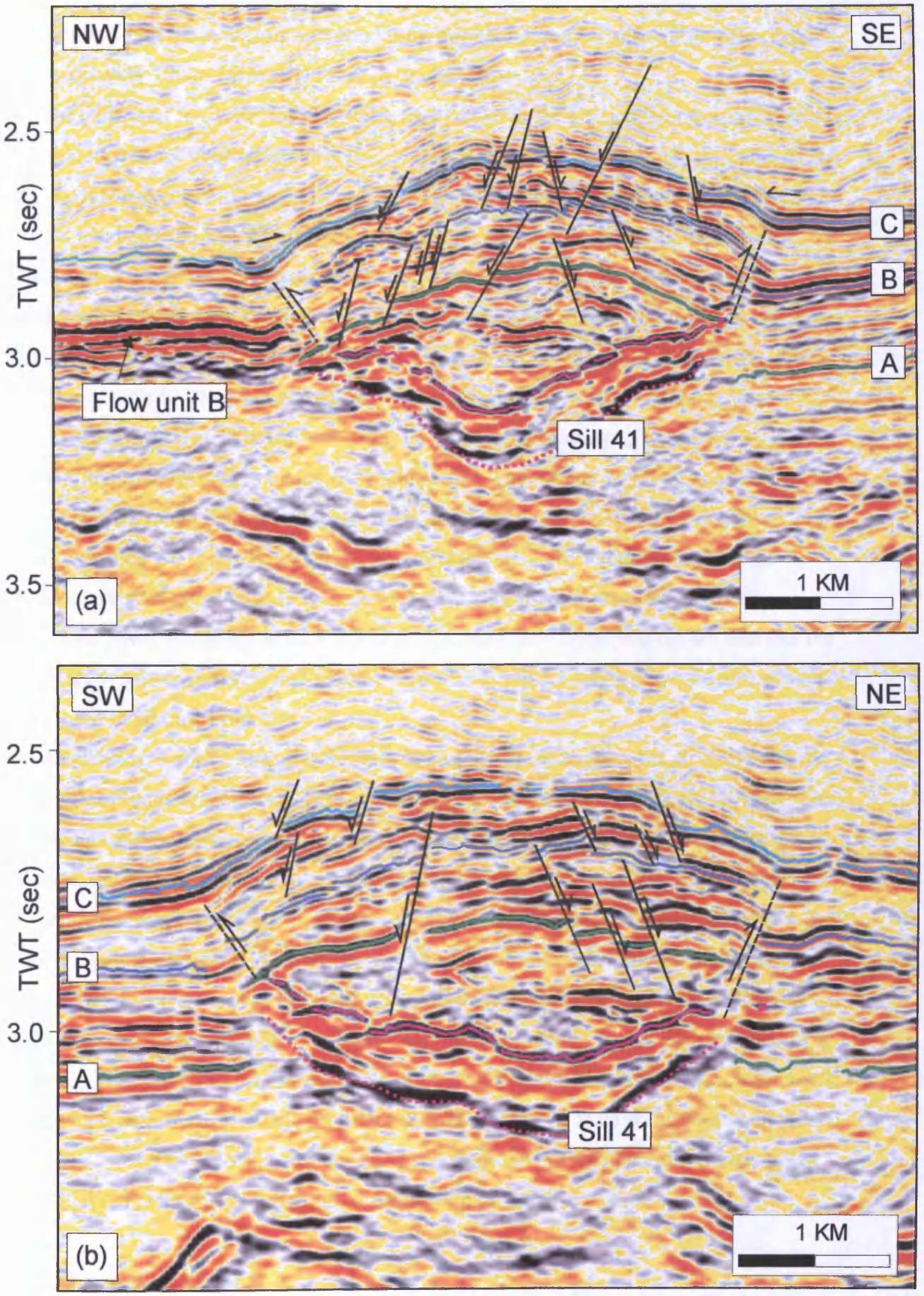

Fig. 5.43 Seismic sections ((a) cross-line; (b) inline) showing the cross-sectional geometry of structure B and the underlying sill 41. Horizons A, B, and C are upwards vertically displaced above the sill and the deformed sediments are intensely faulted. Thrust faults are interpreted overlying the sill tips. The edge of flow unit B is seen immediately beyond the north-western tip of sill 41 in (a). See Fig. 5.42b for line locations.

continuous with the lava flow extruded onto horizon B and the base of the sill is found approximately 300 m below the level of the lava flow.

The deformed A-C interval is heavily faulted above the sill and interpretation and confident correlation of reflections is difficult. However, the interpreted horizons A, B, and C shown in Fig. 5.43 are believed to be good approximations to the true reflector trends overlying the sill. Above the sill, horizons A and B are detached from, and displaced upwards relative to, the level of the reflector away from the sill. The displacement appears to have occurred along fault planes that tip out immediately below horizon C. Horizon C is more continuous across the structure and it is not offset above the tips of the sill. The horizon exhibits a folded geometry with a vertical relief of approximately 300 m. The vertical relief on horizon C decreases gradually from the crest of the fold towards the edge of the structure. The outline of sill 41 has been superimposed on an isochore map of the vertical relief of structure B (Fig. 5.44a) constrained by the mapped horizon C and a interpolation of the base-level of the structure relative to horizon C (Fig. 5.44b). The map (Fig. 5.44a) shows that the structural relief is greatest in the central part immediately overlying the sill and that the structure is axio-symmetric and extends approximately 1.5 km beyond the area covered by the sill in all directions.

As mentioned above, the A-C interval is heavily faulted across the structure and the majority of faults exhibit a synthetic sense of dip relative to the adjacent fold limb. The sediments overlying horizon C are intensely faulted by a polygonal fault system, with most of these faults tipping out approximately at the level of horizon C. The time-structure map shown in Fig. 5.45a and schematically illustrated in Fig. 5.45b shows the fault pattern at horizon C. The outline of sill 41 has been superimposed on the map to allow for any differences in the fault pattern immediately above the sill and the adjacent area to be distinguished. The area found within the outline of the sill is dominated by a near-circular, concentric fault that is close (<500 m) to the sill outline towards the north, south-east, and south, whilst being more distant (~1000 m) from the western periphery of the sill. Outside the outline of the sill the pattern is very different and characterised by radial faults that are orthogonal to the outline of the sill.

5.5.2.3 Structures C and D

Two less pronounced structures (structures C and D) have also been mapped in the survey area, immediately north-east of structure B very near the flow front of Flow B

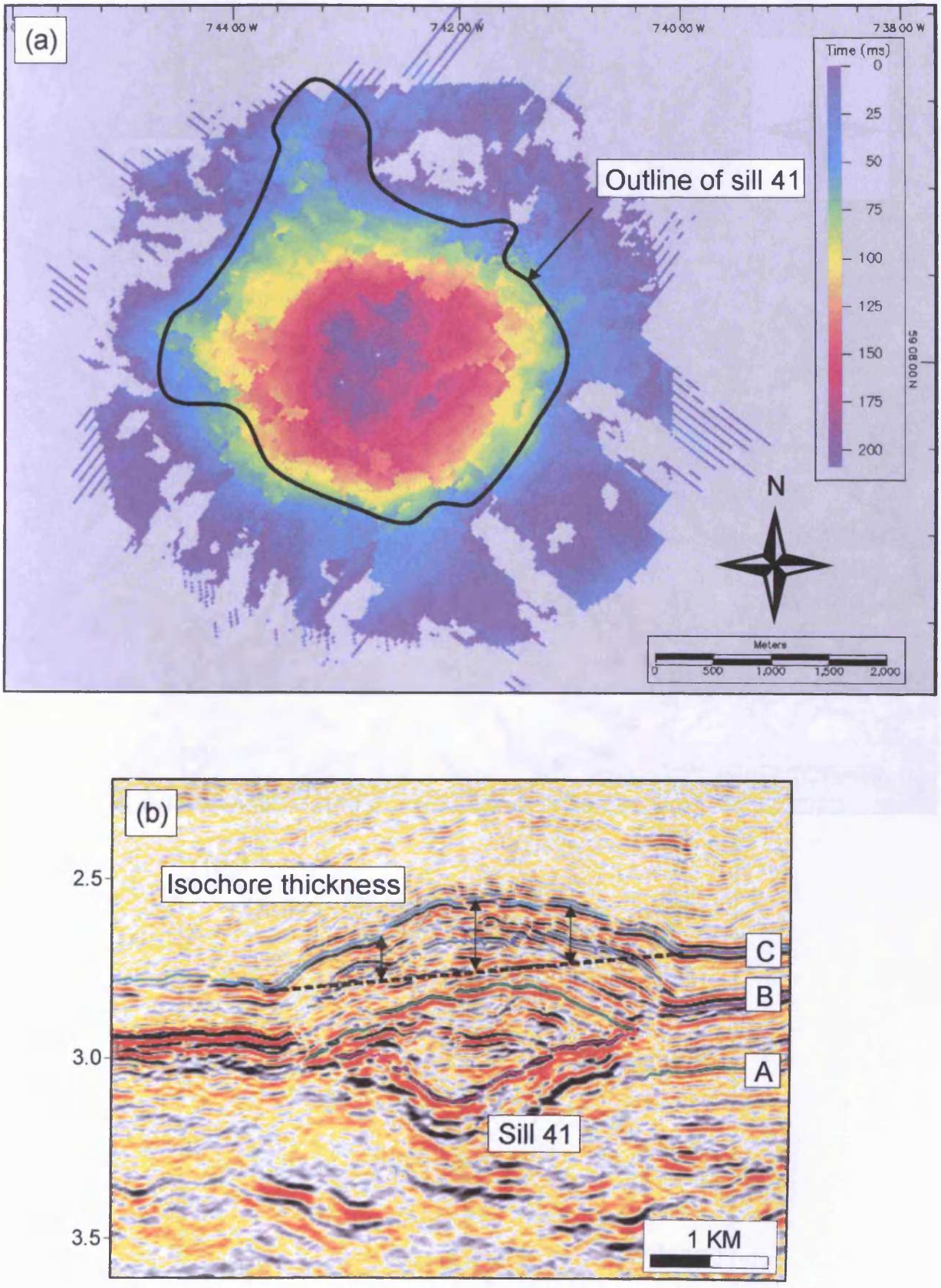

Fig. 5.44 (a) The outline of sill 41 superimposed on isochore map (TWT) of structure B. (b) Cross-section through structure B illustrating isochore thickness. See Fig. 5.42b for line location (labelled Fig. 5.43a).

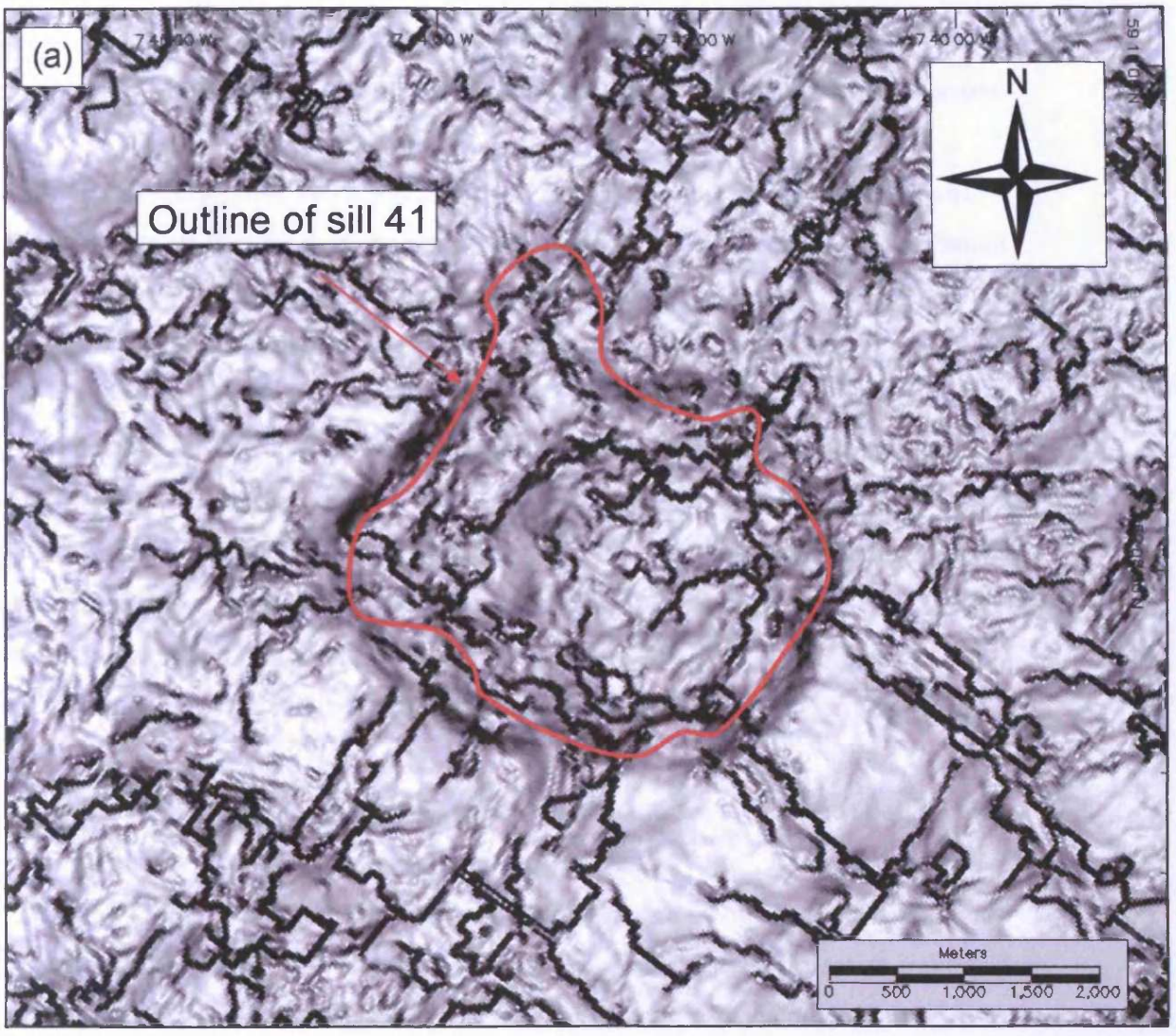

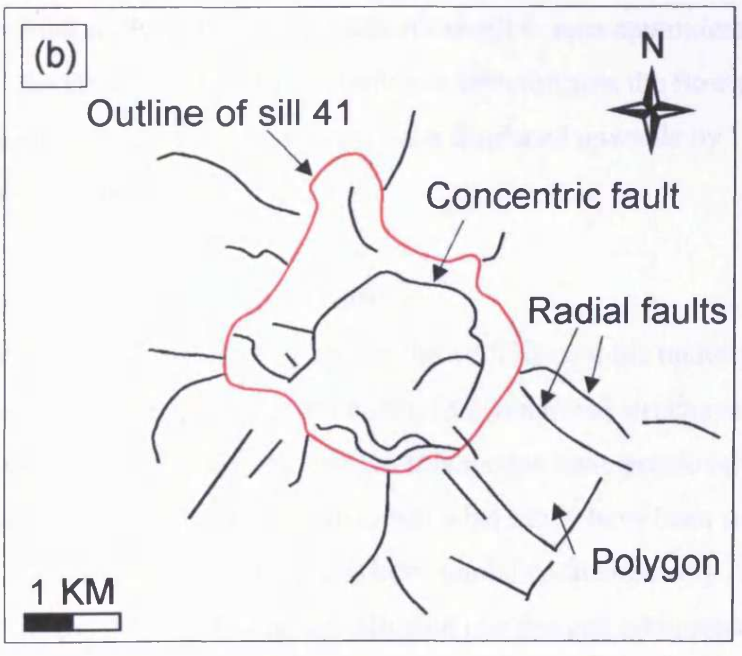

Fig. 5.45 (a) Time-dip map of horizon C showing the geometry of a polygonal fault system across and around structure B. The outline of sill 41 is superimposed on the map. (b) Trace map of Fig. 5.45a showing the outline of sill 41 and main faults. The area seen within the outline of the sill is characterised by a near-circular concentric fault. Outside the outline of the sill the polygonal faults form a radial pattern that is orthogonal to the outline of the sill.

(Fig. 5.42). Both structures are characterised by deformation of the stratigraphic interval overlying igneous sills and are delimited upwards by horizon C, which is onlapped.

Structure C (Figs. 5.42 and 5.46) is formed above sill 40 (Fig. 5.15), which was described in section 5.3.4. It covers an area of 6.6 km^2, has an estimated maximum thickness of 370 m, and appears to gently thin towards its tips. Horizons C has been mapped across the structure, but it has not been possible to map horizons A and B. Horizon C has a domed geometry across the extent of sill 40 that exhibits a vertical relief of 345 m. The northern and western periphery of sill 40 is approximately coincident with the flow front of Flow B. The vertical section shown in Fig. 5.46 shows the relationship between the sill, structure C and the surrounding lava flow. The base of the sill is seen approximately 300 m below the level of the lava flow. To the north of the sill the lava flow thins and tips out approximately 1 km from the northern sill tip, whilst to the south-west the thinned sill tip is bent upwards above the underlying sill tip.

Structure D (Figs. 5.42 and 5.47) overlies a relative small sill (sill 45). Sill 45 measures approximately 1 by 1 km and covers an area of around 1 km^2. It is seen at a present-day depth of 4775-3180 m and exhibits a vertical relief of 240 m. Horizon C exhibits a dome geometry above sill 45 with a vertical relief of 300 m. A reflection immediately overlying horizon C is onlapped by the overlying strata on the dome flanks. Sill 45 underlies the flow front of Flow B and the base of the sill is seen approximately 300 m below the level of the lava flow. Gradual thinning is seen towards the flow tip, which has been detached from the main flow and has been displaced upwards by approximately 300 m above the sill.

5.5.3 Analogues for forced folding above sills

The coincidence between the described positive forced folds and the underlying sills suggests a causative relationship between the two. Deformational structures that are considered to be analogues to those described in this section have previously been described from field studies as well as seismic data where they have been seen in close association with igneous sills. They have also been modelled theoretically. The structures have generally been linked to the intrusion process and interpreted to form overlying igneous sills in order to accommodate the added thickness provided by the

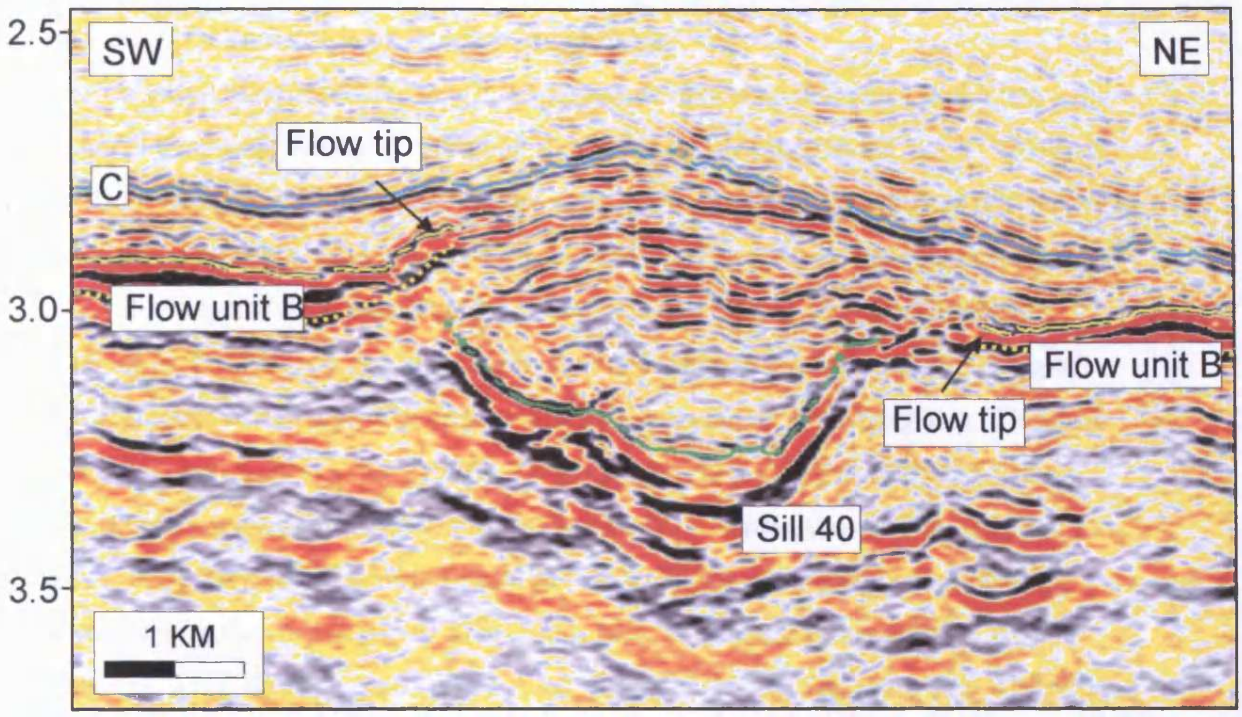

Fig. 5.46 Seismic section showing deformation of flow unit B overlying the south-western tip of Sill 40. See Fig. 5.42b for line location.

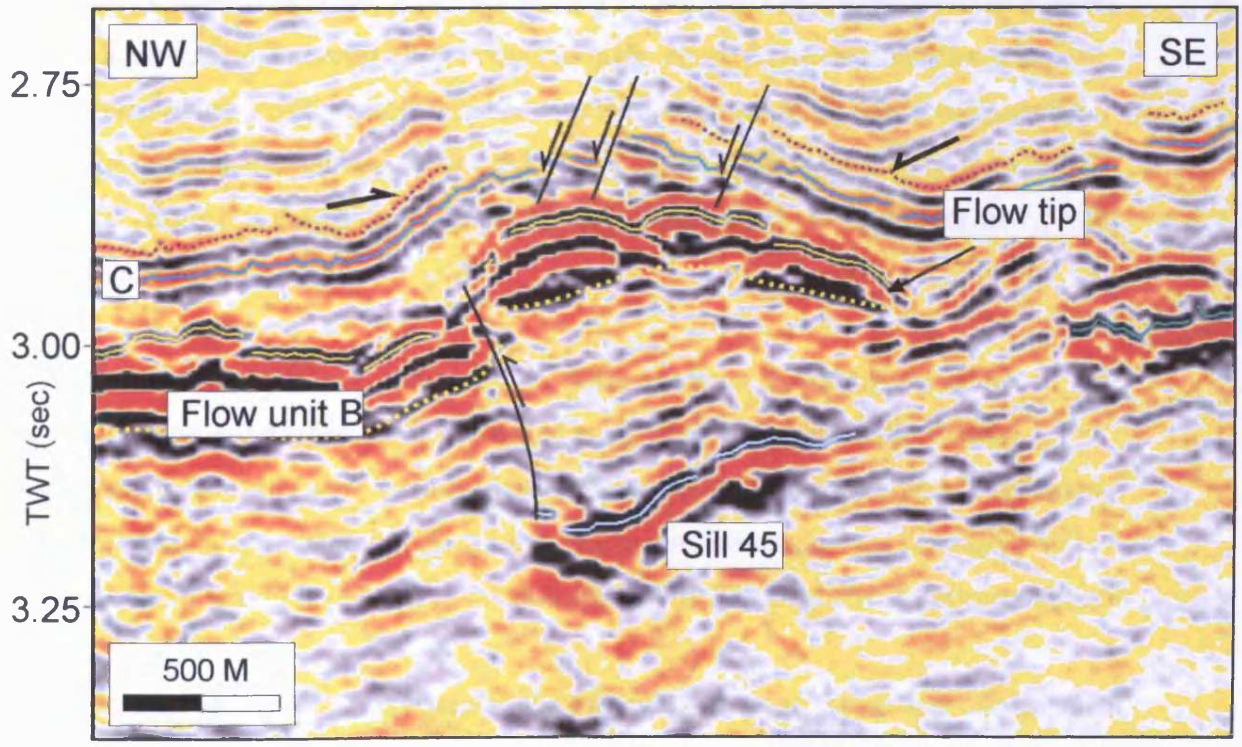

Fig. 5.47 Seismic section showing upward vertical displacement of the south-eastern tip of flow unit B overlying sill 45. See Fig. 5.42b for line location.

forcible intrusion of the sill. A short summary of the previously published examples of such 'jack-up' structures is provided in this section.

Deformation of overburden by sill emplacement has been described in the literature for almost a century. An early reference to the concept is made by du Toit (1920) who speculated that the intrusion of the Karoo sills had caused vertical uplift of the overlying strata equivalent to the thickness of the intrusion. Early field evidence supporting du Toit's (1920) speculation was later described by Hotz (1952) who studied diabase intrusions of Triassic age in southeastern Pennsylvania and found evidence for uplift and disturbance of sediments overlying diabase sheets in the Dillsburg area. Classical papers by Loewinson-Lessing (1936), Tweto (1951), and Carey (1958) also discuss ways of creating space for igneous intrusions through overburden deformation and Carey (1958) showed a schematic example of vertical displacement of a roof-block associated with the emplacement of an irregularly shaped cone sheet (Fig. 5.48). Lombard (1952), Bradley (1965), Pollard & Johnson (1973), Schirnick et al. (1999), and Zenri & Kerr (2001) all describe uplift and bending of overburden above sills and find that the overburden is likely to become fractured to accommodate the strain developed during the 'jack-up' process (Fig. 5.49).

Seafloor studies from the Gulf of California (Lonsdale & Lawyer, 1980; Gieskes et al., 1982; Einsele, 1986) and East Pacific Rise (Lonsdale, 1983) have revealed positive relief dome structure several 100s of metres high. These dome structures have been interpreted as the seafloor expression of overburden 'jack-up' formed above igneous sills and laccoliths. It has been proposed that in extreme cases, the flanks of seafloor 'jack-up' structures may be over-steepened and lead to flank collapse (McBirney, 1963; Lonsdale, 1983).

Pollard & Johnson (1973) conducted a theoretic mechanical study of the effects of intrusion upon overburden geometry based on field observations in the Henry Mountains where sills were intruded into horizontally stacked rock layers. They found that the bending is induced by the driving pressure of the magma and is resisted by internal forces within layers of the overburden and by frictional forces between adjacent layers.

Pollard & Johnson (1973) presented the following equation for vertical displacement associated with sill intrusion assuming a non-uniform pressure distribution acting on a layer overlying an intrusion (Fig. 5.50):

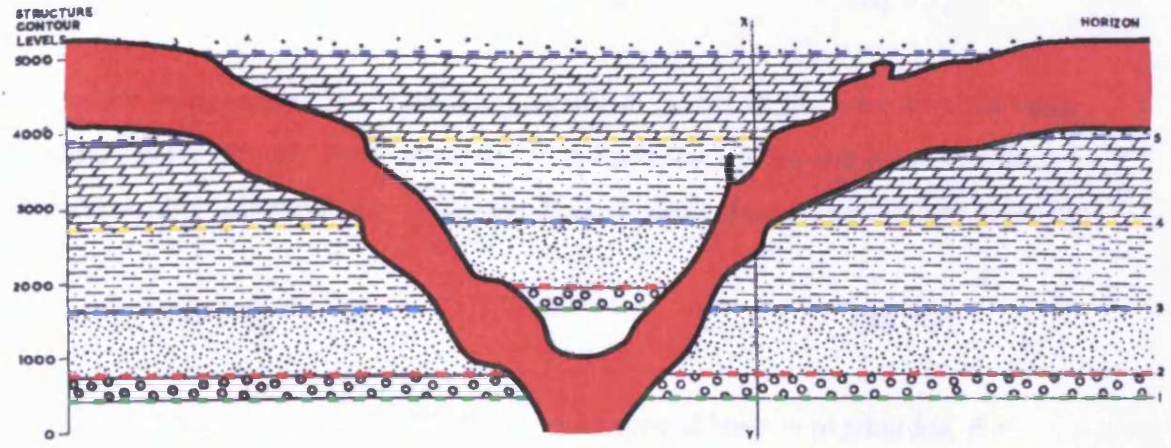

Fig. 5.48 Schematic illustration of 'jack-up' above a cone sheet. Layer boundaries are upwards vertically displaced inside the cone-sheet structure to accommodate the added thickness provided by the intrusion of the cone-sheet. After Carey, 1958.

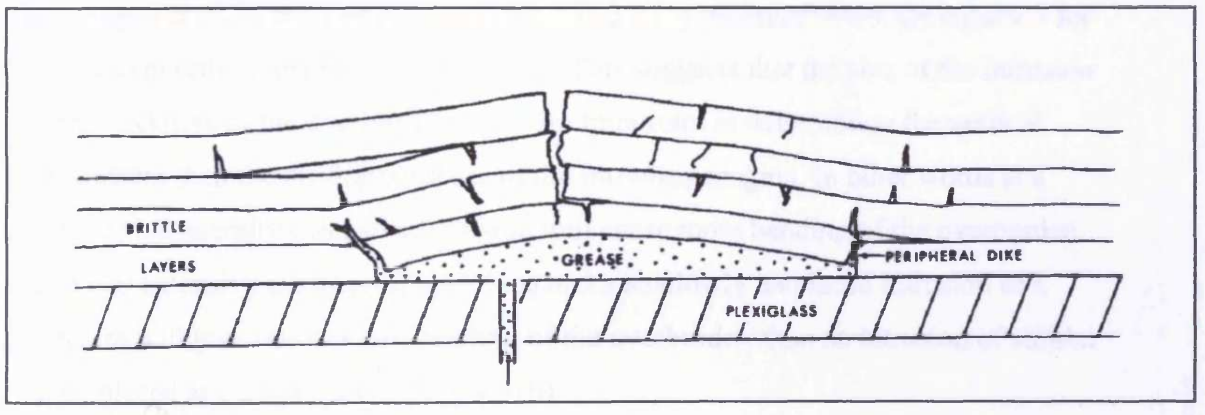

Fig. 5.49 Experimental model of intrusion showing fracturing of semi-brittle overburden overlying intrusion. After Pollard & Johnson (1973).

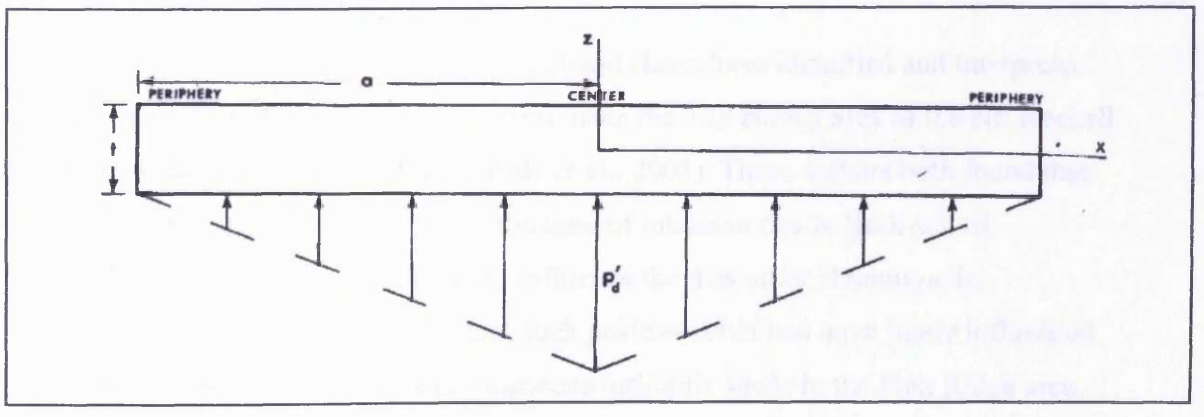

Fig. 5.50 Schematic illustration of a non-uniform pressure distribution action on overburden above an intrusion. The driving pressure *p*'d is distributed linearly along the layer with a maximum *p*'d, at the centre and a minimum at the periphery. After Pollard & Johnson (1973).

$w = (p'_d / 240R) * (10x^4 - (2|x|^5 / a) - 15a^2x^2 + 7a^4)$ (eq. 5.1)

Where: w = displacement, p'_d = driving pressure at the feeder, $|x|$ is the absolute value of x, and a is the distance from the centre to the periphery of the intrusion. R is the 'flexural rigidity' (or resistance to deformation of layers above the intrusion) given by:

$R = Bt^3 / 12 = Et^3 / 12 * (1-\nu^2)$ (eq. 5.2)

Where: B = Elastic modulus = $E/(1-\nu^2)$, t = thickness of layer in overburden, E = Young's modulus, and ν = Poisson's ratio.

From these equations it is seen that the amount of upward displacement increases as the fourth power of the distance the magma spreads (eq. 1), the layer resists deformation as the third power of its thickness (eq. 2), and the driving pressure enters the equation for displacement only as the first power (eq. 1). This suggests that the size of the intrusion and the thickness of the overburden are more important in determining the vertical displacement than the driving pressure of the intruding magma. In other words at a given depth a laterally extensive intrusion will cause more bending of the overburden than a less extensive intrusion (Fig. 5.51a) and a shallowly emplaced intrusion of a given size will give rise to more bending of the overburden than an intrusion of similar size emplaced at a deeper level (Fig. 5.51b).

Pollard & Johnson (1973) also found that a multi-layered host-rock offered less resistance to bending than a uniform host-rock because sliding of adjacent layers reduces the resistance to bending (Fig. 5.51c).

Recent seismic studies from the Faeroe-Shetland Basin have identified and interpreted similar structures to the ones described here from the T38 survey area of the NE Rockall Basin (Smallwood & Maresh, 2002; Trude et al., 2003). These authors both found that positive relief created at the seabed, at the time of intrusion due to 'jack-up' of overburden above an igneous sill, could influence the depositional topography. Smallwood & Maresh (2002) found that such positive relief had most likely influenced the distribution of deepwater Lower Paleocene turbiditic sands in the Flett Ridge area, whilst Trude et al. (2003) showed that 'jack-up' above a series of sills in the T61/62 survey area has led to the formation of a 5 km wide and >20 km long mini-basin that

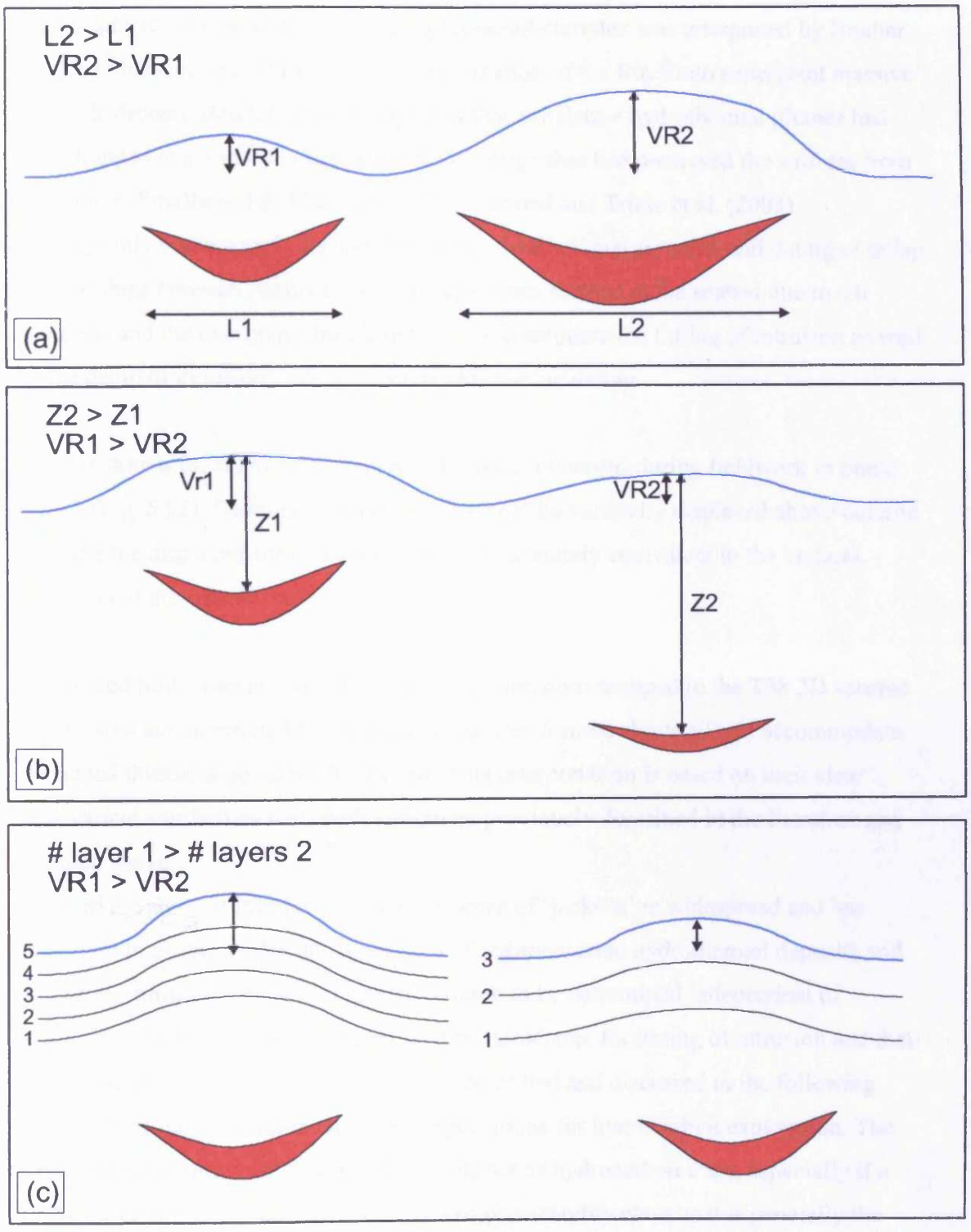

Fig. 5.51 Schematic illustrations of predicted jack-up magnitude. (a) Laterally extensive sills give rise to a greater amount of jack-up than smaller sills intruded at the same depth. (b) Sills intruded at shallow depth give rise to a greater jack-up than a sill of the same size intruded at greater depth. (c) A sill intruded underneath a multi-layered overburden gives rise to a greater jack-up than a sill of similar size, intruded at a similar depth but underneath an overburden consisting of less layers.

exhibited a 250 m thick onlap fill. The formation of such mini-basins in the seafloor topography due to 'jack-up' above an igneous sill complex was interpreted by Boulter (1993) to have played a large role in the formation of the Rio Tinto supergiant massive sulphide deposit. Boulter (1993) suggested that exhalative hydrothermal plumes had been trapped in a ~ 400 m deep basin-floor trough that had preserved the sulfides from dispersion. Smallwood & Maresh (2002) suggested and Trude et al. (2003) subsequently convincingly demonstrated that detailed interpretation and dating of onlap relationships between positive 'jack-up' structures formed at the seabed due to sill intrusion and the overlying strata can be used to estimate the timing of intrusion as well as the depth of intrusion, independent of radiometric dating.

Similar structures, albeit on a smaller scale were, observed during fieldwork in South Africa (Fig. 5.52). Bedding surfaces were seen to be vertically displaced above dolerite sills and the displacement was seen to be approximately equivalent to the vertical thickness of the sills.

The forced folds seen in association with sill intrusions mapped in the T38 3D seismic survey area are interpreted as 'jack-up' structures formed above sills to accommodate the added thickness occupied by the sill. This interpretation is based on their clear geometrical similarities with such structures previously described in the literature and outlined above.

From the above it is evident that the process of 'jack-up' is widespread and has important implications for the deposition of sediments and hydrothermal deposits and allows for intrusion timing and intrusion depth to be determined independent of radiometric dating. The implications of these structures for timing of intrusion and their usefulness in constraining sill thickness is described and discussed in the following section. 'Jack-up' structures also have implications for hydrocarbon exploration. The structures form anticlinal closures that could act as hydrocarbon traps, especially if a folded reservoir sequence is overlain by low permeability clays as it is generally the case in the NE Atlantic igneous province.

5.5.4 Discussion: Determining timing of intrusion

As mentioned above the onlap relationship onto this type of structure can be used to estimate the timing of intrusion independent of radiometric dating, which has previously

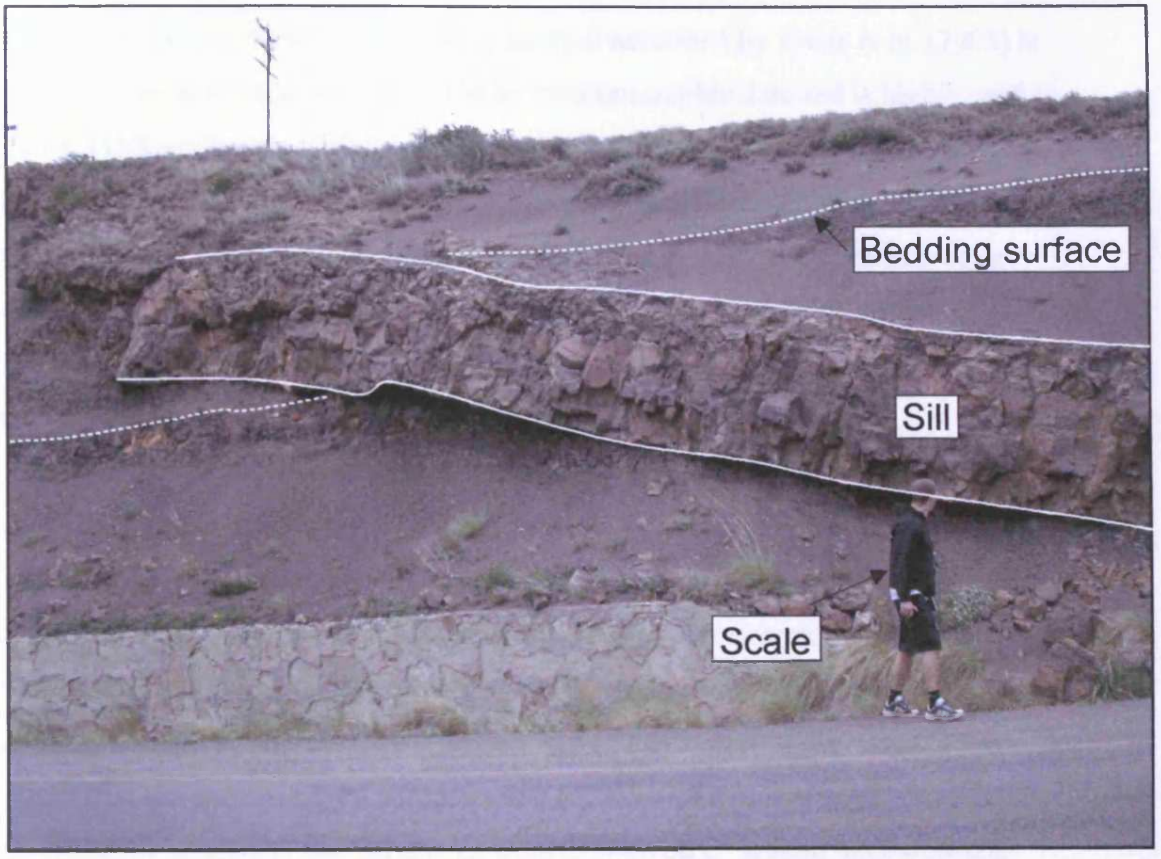

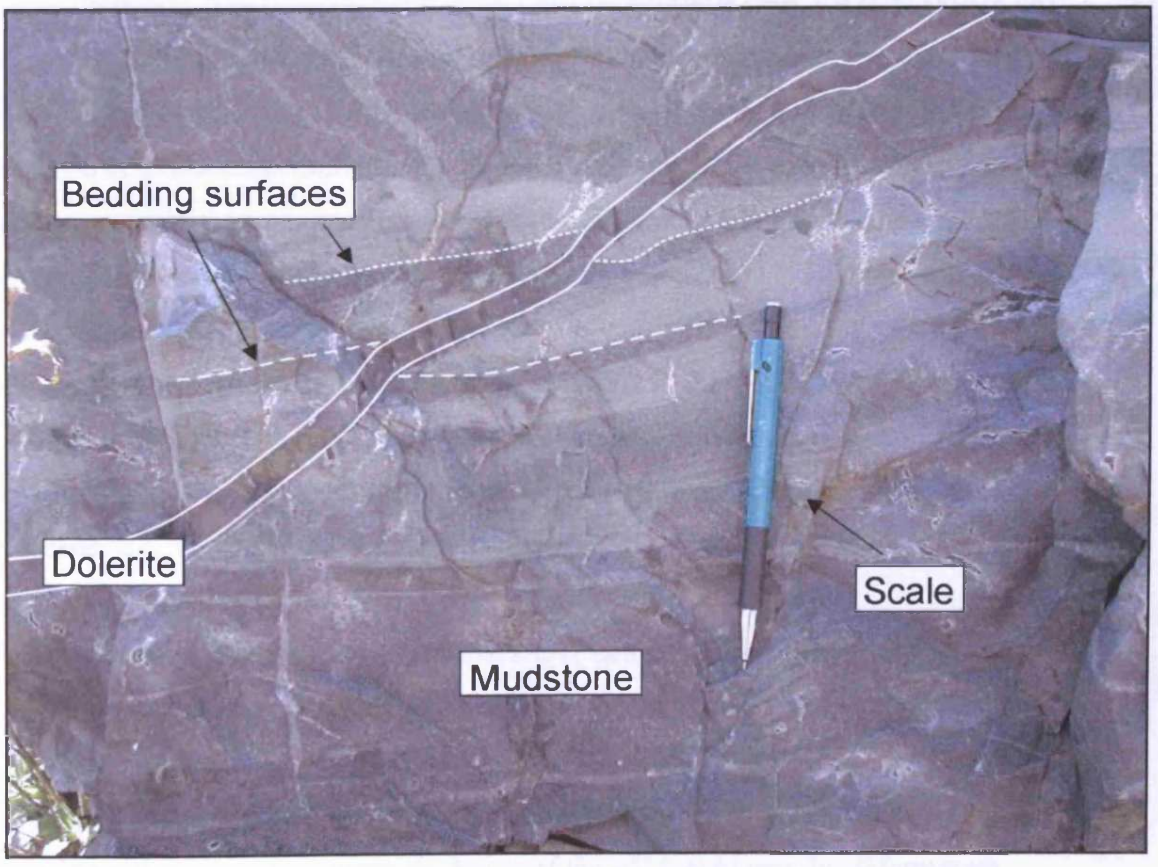

Fig. 5.52 Field examples of vertical displacement of sediments above dolerite intrusions, Karoo, South Africa.

been the main dating method. The dating method described by Trude et al. (2003) is based on 3D seismic data and calibrated by biostratigraphic data and is highly useful because: (1) Radiometric dating is related with a high degree of uncertainty due to alteration and poor sampling, as is often seen in borehole data (Gibb & Kanaris-Sotiriou, 1988). (2) Only a very limited number of sills have been encountered in boreholes and the age data available are, therefore, sparse and highly scattered. (3) Even when biostratigraphic data are not available for calibration the method still allows for the relative timing of intrusion to be constrained.

Age data from boreholes are not available for the sills mapped in the T38 3D seismic survey area and the method presented by Trude et al. (2003) has, therefore, been applied to sills 1, 40, 41, and 45 in the survey area and the results are described in this section. Across sill 1 (Fig. 5.41), horizons B and C are clearly bent upwards indicating that the sill was intruded after these horizons were established. Stratal reflections within the C-D unit onlap horizon C, and horizon D appear to be undeformed across the structure. This suggests that the structure grew and thus that the sill was emplaced following the date represented by horizon C and before the time of horizon D, around the Paleocene-Eocene transition. The onlap relationships onto structures B (Fig. 5.43), C (Fig. 4.46), and D (Fig. 5.47) are less well constrained due to intense faulting of the strata overlying horizon C and of horizon C itself. However, in all three cases, it does appear that horizon C or a reflection immediately above it is onlapped by the overlying strata. As with the case of sill 1 and structure A the interpretation of sill emplacement timing in the more northern part of the survey area suggests that intrusion occurred at or close to the Paleocene-Eocene transition.

In the case of the host-rock deformation observed in the T67 3D seismic survey area described in Chapter 3 (section 3.5) there is a large decrease in the amount of jack-up between horizons C and E suggesting that the sills were emplaced during the Late Paleocene.

5.5.5 Discussion: Comparison of sill thickness and sill volume with vertical relief and volume of displaced sediment of jack-up structure B

5.5.5.1 Introduction

Another important implication of the development of jack-up structures is that they can be used to estimate the minimum thickness of the sill that causes the deformation structure to form (Smallwood & Maresh, 2002; Trude et al., 2003). This is particularly

useful in cases where the resolution of the data does not allow for the seismic response from the top and base of the sill to be separated and thus does not allow for the actual sill thickness to be constrained seismically. In this section the depth converted and decompacted vertical relief and volume of structure B will be compared with the estimated thickness and volume of sill 41, which underlies the structure.

5.5.5.2 Depth conversion

Jack-up structure B and the underlying sill 41 are both very well imaged. Sill 41 was depth converted in section 5.3.4 (Fig. 5.16) to illustrate the change in thickness across the sill. The depth conversion was based on the true thickness of the sill, measured perpendicular to the sill - host-rock boundaries. In relation to the type of host-rock deformation described here it is the vertical thickness of the sill that is of interest not the true thickness. A second depth conversion of sill 41 based on inline 20958 (Figs. 5.16a and 5.43b) has been performed using an estimated sill velocity of 5.55 ± 0.56 km/s in order to illustrate the vertical thickness change along the sill (Fig. 5.53).

The vertical relief on structure B as measured on horizon C on the section has been depth converted using an estimated average velocity in the sediments in the seabed-horizon C interval overlying the structure of 2.0 ± 0.2 km/s. In Fig. 5.53 the thickness of the sill and the depth converted relief on structure B are both shown. The shape of the two curves exhibit a similar form, but the sill thickness is consistently greater (by a factor of approximately 2) than the depth converted relief on the jack-up structure. Structure B has a maximum depth converted vertical relief of approximately 180 m and an estimated volume of approximately 0.5 km^3 compared with an estimated sill thickness of approximately 400 m and sill volume of 1.3 km^3 (section 5.3.4).

Sedimentary units undergo compaction during burial, whilst an igneous intrusive does not. Compaction of the sedimentary overburden following intrusion should, therefore, be considered when comparing the thickness and volume of an intrusive sill and the vertical relief and volume of the jack-up structure formed above it. In the following sections the estimated thickness of the sill and the approximated decompacted vertical relief on the jack-up structure as it is expressed on horizon C are compared. This comparison will provide an estimate of the shape of structure B and the volume of displaced material at the time of intrusion.

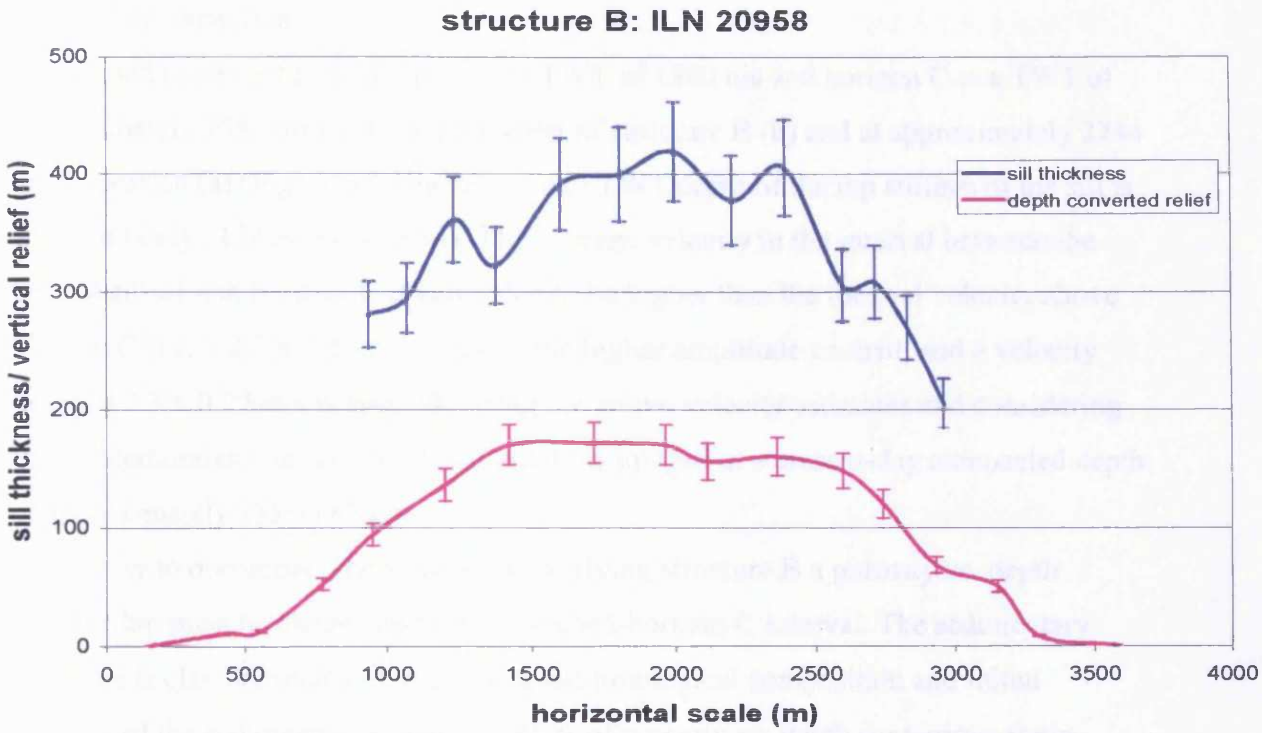

Fig. 5.53 Graph showing depth converted (vertical) sill thickness and depth converted vertical relief on structure B. The graphs exhibit similar trends but the sill thickness is consistently greater than the vertical relief on the structure by a factor of ~2.

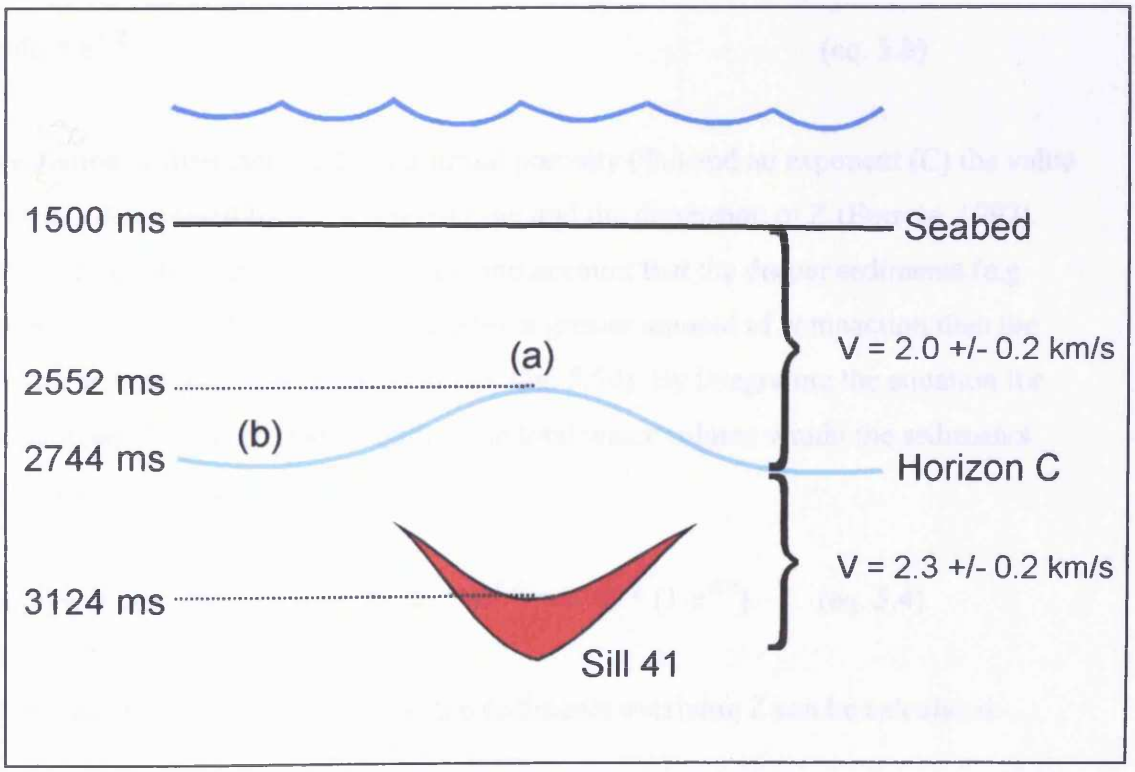

Fig. 5.54 Simplified schematic illustration of the cross-sectional geometry of structure B and the underlying sill 41. The illustration shows TWT depths and velocity estimates used to depth convert and decompact the seabed-horizon C interval.

5.5.5.3 Decompaction

The seabed is imaged at an approximate TWT of 1500 ms and horizon C at a TWT of approximately 2552 ms overlying the crest of structure B (b) and at approximately 2744 ms at location (a) (Fig. 5.54). The maximum TWT depth of the top surface of the sill is approximately 3124 ms (Fig. 5.54). The average velocity in the interval between the base of sill 41 and horizon C is estimated to be higher than the interval velocity above horizon C (i.e. > 2.0 ± 0.2 km/s), due to the higher amplitude content, and a velocity range of 2.3 ± 0.2 km/s is applied. Using the above velocity estimates and considering their uncertainties it is estimated that sill 41 is imaged at a present-day compacted depth of approximately 1550-1870 m.

In order to decompact the sediments overlying structure B a porosity vs. depth relationship must be established for the seabed-horizon C interval. The sedimentary sequence is clay dominated, but the detailed lithological composition and initial porosity of the sediments is unknown. Plots of porosity vs. depth for various shale sequences show considerable scatter, but when generalised exhibit an exponential decrease in porosity with depth (Sclater & Christie, 1980). Athy (1930) proposed calculating porosity at depth (Z) according to:

$$\Phi_z = \Phi_0 * e^{-CZ} \qquad \text{(eq. 5.3)}$$

This equation is characterised by the initial porosity (Φ_0) and an exponent (C) the value of which is determined by the sediment type and the dimension of Z (Einsele, 1992).

When decompacting it must be taken into account that the deeper sediments (e.g. sediments at (b); Fig. 5.54) have undergone a greater amount of compaction than the shallower sediments (e.g. sediments at (a); Fig. 5.54). By integrating the equation for porosity in eq. 3 between 0 and depth Z the total water volume within the sediments overlying Z can be calculated:

$$\text{Total pore water volume above Z: } \Phi_0 * e^{-CZ} = \Phi_0/C * (1-e^{-CZ}) \qquad \text{(eq. 5.4)}$$

and from this the average porosity of the sediments overlying Z can be calculated:

$$\text{Average porosity above Z} = \Phi_0/C * ((1-e^{-CZ})) / Z \qquad \text{(eq. 5.5)}$$

Using this average porosity the decompacted thickness of a sediment column between the seabed and depth Z can be calculated and this allows for the vertical relief formed at the seabed at the time of intrusion to be reconstructed.

Sclater & Christie (1980) found the following parameters of the exponential relationship between porosity and depth for various normal pressured North Sea shales: $\Phi_0 = 0.63$ and $C = 0.51$ (where Z is measured in km). Lacking detailed lithological constraints on the sediments overlying horizon C in the survey area a rough estimate of the decompacted thickness of the relief on structure B will be estimated using the porosity-depth relationship from equation (3) and the Φ_0 and C values of Sclater & Christie (1980). Applying these parameters to the T38 3D seismic survey area is associated with a high degree of uncertainty. In order to try and compensate for this uncertainty the parameters are assigned an uncertainty of ± 25 %. This means that $\Phi_0 = 0.63 \pm 0.1575$ and $C = 0.51 \pm 0.1275$.

Using the equations above and substituting for Z, Φ_0, and C the vertical relief on structure B has been calculated considering the effects of the added uncertainties. The calculated vertical relief is shown in Fig. 5.55 along with the depth converted, but compacted, relief on structure B and the depth converted sill thickness. The decompacted structure is characterised by moderately dipping flanks surrounding a flat central section. The flank dips range between 13-35° and the maximum vertical relief on the structure between 200-580 m. The structure is estimated to comprise a sediment volume of 0.6-1.7 km^3. The maximum thickness of sill 41 is estimated to be approximately 400 m and its volume was estimated to be approximately 1.3 km^3 in section 5.3.4. These estimates of sill thickness and sill volume are both within the range of the calculated decompacted vertical relief and volume of structure B. This suggests that vertical relief on jack-up structures can provide an approximate measure of sill thickness and volume. The better constraint the lithological parameters (v_{sed} or Z, Φ_0, and C) are the better the estimate is likely to be.

5.5.5.4 Pitfalls

From the above detailed analysis of jack-up structure B and the underlying sill 41 it is evident that the emplacement of the sill caused vertical displacement of the overburden. The deformation formed a positive structure at the contemporaneous seabed approximated by horizon C that was subsequently onlapped by younger strata. Tentative decompaction of the present-day overburden has shown that the vertical relief on

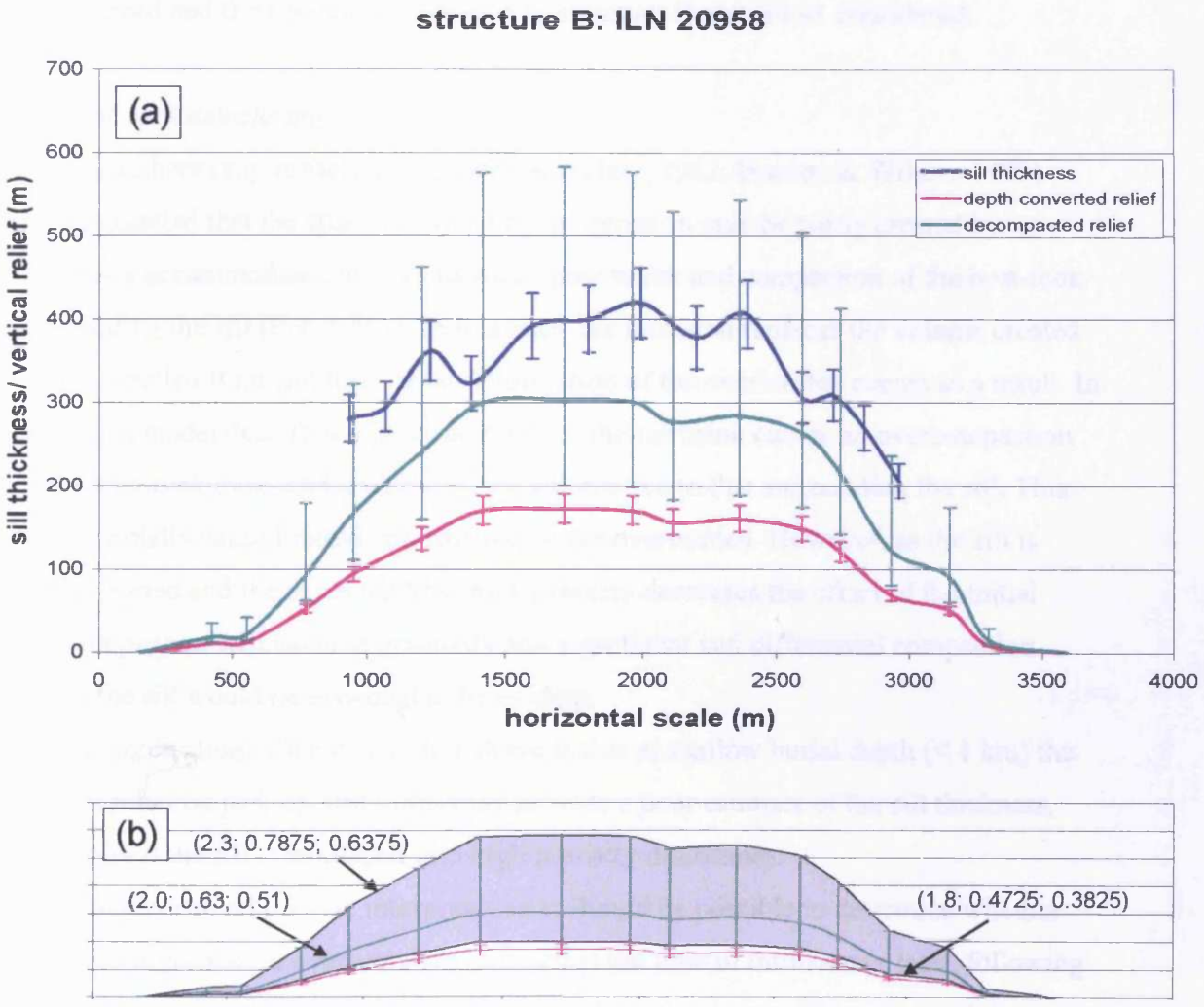

Fig. 5.55 (a) Graph showing depth converted (vertical) sill thickness and vertical relief on structure B and decompacted vertical relief on structure B. The depth converted sill thickness falls within the range of decompacted vertical relief on structure B. This suggests that vertical relief on jack-up structures can provide a crude estimate of sill thickness. (b) Graphs showing depth converted and decompacted vertical relief on structure B with no vertical exaggeration. Numbers in brackets show parameters (Vsed; initial porosity; and C) used for decompaction.

horizon C provides a crude estimate of the thickness and volume of sill 41. However, the analysis is not sufficiently accurate to confidently discern whether the space for the sill is fully accommodated by vertical displacement of the overburden or if some additional mechanism is involved. In the following sections a number of limitations to the use of vertical relief on jack-up structures to estimate sill thickness and volume are summarised and their possible relevance to structure B and sill 41 considered.

(1) Host-rock dewatering

Several authors (e.g. Einsele et al., 1980; Kokelaar, 1982; Hanson & Wilson, 1993) have suggested that the space occupied by an intrusion may be partly created by, or even fully accommodated by, expulsion of pore water and compaction of the host-rock surrounding the sill (Fig. 5.56a). In this case, the intrusion replaces the volume created by the expelled fluid and little or no deformation of the overburden occurs as a result. In effect this model describes a process in which the intrusion causes an overcompaction of the host-rock over- and underlying the sill relative to that surrounding the sill. This would initially cause limited deformation of the overburden. However, as the sill is further buried and the expected host-rock porosity decreases the effect of the initial overcompaction will become gradually less significant and differential compaction across the sill would be expected to be evident.

One implication of the discussion above is that at shallow burial depth (< 1 km) the vertical relief on jack-up structures may provide a poor estimate of the sill thickness, especially if the sill is emplaced into high porosity mudstones.

Through detailed seismic interpretation it should be possible to determine whether host-rock deformation overlying sills formed at the time of intrusion or later, following burial. If the overburden was deformed during intrusion to provide accommodation space for the sill it should be possible to identify onlaps onto the deformation structure (Fig. 5.56b), whereas the emplacement process proposed by Einsele et al. (1980) and others would give rise to a differential compaction effect where thinning, but no onlap would be seen in the sediments overlying the sill (Fig. 5.56a). This distinction presumes, of course, that the appropriate depositional systems are active such that onlap of topography would be expected to occur.

Structure B is well defined by horizon C (Fig. 5.41), which is clearly onlapped by the overlying strata. This strongly suggests that a positive structure was formed at the

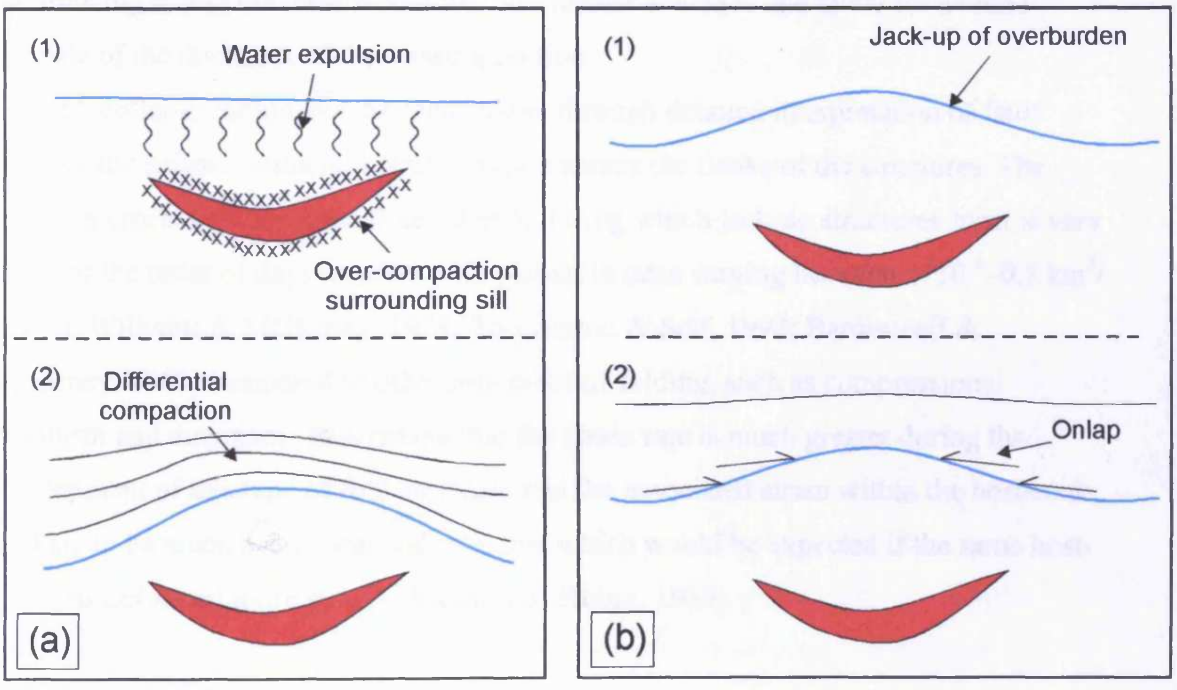

Fig. 5.56 Models for sill emplacement. (a) Space for the intruding sill is created through fluid expulsion and over-compaction of sediments surrounding the sill without causing deformation of the seabed. During burial the sediments overlying the sill are differentially compacted. (b) Space for the intruding sill is created by upward displacement of the overburden creating positive relief on the seabed. The structure is onlapped by post-intrusion deposits.

contemporaneous seabed, approximated by horizon C, during intrusion. The decompaction study suggests that the space for the intrusion may have been fully accommodated by vertical displacement of the overburden.

(2) Seabed processes

Jack-up structures formed positive structure at the seabed at the time of intrusion and it may have been eroded or partially collapsed (McBirney, 1963; Lonsdale, 1983) prior to deposition of the overlying strata. From the seismic data it should be possible to determine whether such erosion or collapse has taken place. If erosion has modified the relief on the structure it should be possible to identify truncations overlying the structure and thinning across the crest would provide further evidence and allow for a crude estimate of the thickness of the missing section.

Flank collapse should also be identifiable through detailed interpretation of fault patterns and seismic reflection configuration across the flanks of the structures. The intrusion process and thus the time interval during which jack-up structures form is very short (of the order of days to years with plausible rates varying between $4*10^{-4}$–0.7 km^3/ day; cf. Williams & McBirney, 1979; Thordarson & Self, 1993; Bardintzeff & McBirney, 2000) compared to other processes of folding, such as compressional tectonism and diapirism. This means that the strain rate is much greater during the development of this type of fold structure and the associated strain within the host-rock is likely to be much more localised than that which would be expected if the same host-rock was deformed more slowly (Ramsay & Huber, 1983).

Faulting both above and below horizon C (Fig. 5.43) makes it difficult to determine whether structure B has been modified by erosion, since apparent truncations in many cases can be seen to be associated with faults. The A-C interval is thinned across the structure suggesting that erosion may have taken place, but it should also be kept in mind that confident interpretation across the structure is very difficult and some interpretational error may have been introduced.

A comparison of the fault pattern seen across structure B (Fig. 5.45) with vertical seismic sections shows that the central concentric fault downthrows in an outward direction with respect to the structure. Additional faults within the A-C interval with a similar sense of dip have also been observed. These faults were almost certainly formed during intrusion and may have formed partly due to the strain associated with the jack-

up process (Pollard & Johnson, 1973; Fig. 5.49) and partly due to subsequent collapse of the flanks of the structure as envisioned by McBirney (1963) and Lonsdale (1983).

(3) Intrusion depth and lateral extent of intrusion

As described above, Pollard & Johnson (1973) found that the lateral extent of the sill, the depth of intrusion, and the stratification in the overburden greatly influenced the magnitude of vertical displacement of the overburden (Fig. 5.51). It is thus important to consider the lateral extent of the sill and its depth of intrusion when using the vertical relief on the jack-up structure to estimate the sill thickness.

Vertical displacement of overburden has only been observed overlying sills 1, 40, 41, 45 and possibly above sill 44 and across the western periphery of sill 22. These sills are all emplaced at relatively shallow depth compared to the majority of sills in the T38 survey area (Table 5.1), which according to Pollard & Johnson (1973) would encourage upward vertical displacement of the overburden because of limited resistance to bending. In addition sills 40 and 41 are exceptionally thick, although not particularly extensive laterally, which is likely to have further encouraged deformation.

(4) Multi-layered sill complexes

In a densely intruded sedimentary section individual sills have been seen to form highly interconnected and multi-layered sill complexes (e.g Chapters 3 and 4). In such complexes overburden deformation associated with individual intrusions is highly unlikely to form discrete distinguishable structures. It is thus considered possible that where a sill complex that exhibits an approximate uniform lateral distribution of sills, the overburden deformation may not be identified.

Apart from the relatively shallow sills mentioned in the preceding paragraph no sill-related jack-up structures have been interpreted in the survey area. This could be because the deeper sills are reasonably evenly distributed and give rise to a near-uniform vertical displacement of the overburden. The deeper sills in the survey area appear to have been emplaced prior to the more shallow sills, most likely within the time span represented by the B-C interval. The B-C interval is characterised by low amplitude, moderately continuous reflections and this combined with the apparently limited thickness of the deeper sills (below thickness of separability) may further

explain why jack-up is generally not observed in association with the deeper parts of the sill complex.

(5) Thermal aureoles

The sediments immediately surrounding a sill are likely to be indurated as a result of baking during intrusion (e.g. Einsele et al., 1980; Raymond & Murchison, 1988; Krynauw et al., 1994; Johnson & Dunham, 2001) and thus less compactable than the surrounding unaffected sediments. Thermal aureoles have generally been found to only influence the sediments within a few 10's of metres and often only metres of the sill-sediment interface and are thus unlikely to introduce a large error into a decompaction calculation. However, subsequent hydrothermal circulation may influence a much greater volume of sediments surrounding the sill (e.g. Gieskes et al., 1982; Einsele, 1986) and could introduce a significant compaction anomaly.

The A-C interval appears to be thinned across structure B (Fig. 5.43), but erosion cannot be confidently identified. Immediately overlying sill 41 the reflection amplitudes within the A-C interval are greater than within the same interval in the surrounding area. This amplitude anomaly could be indicative of hydrothermal alteration and induration of the sediments. Such alteration would most likely have lead to an increase in the A-C interval velocity. Based on this it is suggested that the apparent thinning of the A-C interval across structure B could be a result of a higher interval velocity immediately overlying the sill compared to the same interval away from the sill. This would not affect the sill thickness estimate based on the vertical relief on the structure at the level of horizon C because this estimate is based purely on the properties of the sediments overlying horizon C.

5.5.6 Jack-up of flow unit B

Structures B, C, and D are all located in close proximity to the eastern edge of flow unit B that is Paleocene in age (section 5.5.2). From the above analysis of jack-up structures the timing of intrusion of the sills underlying the four structures has been constrained to the time equivalent to horizon C, which is of earliest Eocene age. This means that the extrusion of the lava flow predates the timing of intrusion. In this section the effects of the emplacement of sills, and the overburden deformation they have been shown to cause, on the already extruded flow unit B are described and the implications discussed.

Sill 41 is located just beyond the edge of the lava flow (Fig. 5.24). In Fig. 5.43a the flow is seen to tip out some distance from the western transgressive tip of the sill. The intrusion of sill 41 does not appear to have had any influence on flow unit B at this location. Sill 40 and sill 45, in particular, are partly emplaced underlying the edge of flow unit B (Figs. 5.46 and 5.47). Fig. 5.46 shows that the tip of flow unit B is upturned at the south-western flank of structure C that overlies sill 40, whilst the flow tips out slightly away from the north-eastern sill periphery. The upturned tip of flow unit B is concordant with the stratal reflections that have been deformed overlying sill 40 and rises approximately 150 m above the undeformed level of the flow before terminating. Sill 45 almost fully underlies Flow unit B (Fig. 5.24) and the flow is highly deformed across the crest of structure D formed above the sill (Fig. 5.47). The flow reflection is discontinuous and clearly offset above the western periphery of the sill. flow unit B appears to be concordant across the crest of structure D and is displace vertically by approximately 200 m.

From the above it is evident that flow unit B has been deformed overlying sills 40 and 45. The deformed flow reflection is concordant with stratal reflections and it is suggested that it has been vertically displaced during the process of sill emplacement as part of the jack-up deformation induced to create space for the intruding sills. This interpretation is in accordance with the previously established timing relationship between the two magmatic events.

Flow unit B was seen to be missing overlying two small sills (sills 38 and 46; Figs. 5.23 and 5.24) towards the eastern and northern survey boundaries. At both locations there is evidence in the form of folded stratal reflections and thinning of the B-C interval overlying the sills that suggests that the sediments overlying the sills have been jacked up to accommodate the intrusion of the sills. The timing of the intrusion of sills 38 and 46 is poorly constrained, but based on the well constrained timing of intrusion of nearby sills intruded at a similar level (e.g. sills 40, 41, 45) it is suggested that sills 38 and 46 are also early Eocene in age and thus emplaced following lava flow extrusion. The areas overlying the two sills where flow unit B is missing are fully surrounded by the flow and there appears to be no thinning of the flow indicating natural flow tips towards the areas in which flow unit B is missing. Considering this and the illustrated ability of sills to vertically displace the lava flow it is suggested that in the regions overlying sills 38 and 46, flow unit B was vertically displaced upwards and subsequently removed prior to post-deformation deposition.

The coincidence between the edge of the lava flow unit and the location of numerous relatively shallow sills (Fig. 5.24) may be of mechanical significance and will be further discussed in Chapter 7.

5.6 Summary

In this chapter the igneous complex of the T38 3D seismic survey area of the NE Rockall Basin has been analysed. This has allowed for the relative timing of and development of the T38 igneous complex to be constrained. Several themes have been addressed in this chapter: (1) the general characteristics of sills of the T38 sill complex, (2) thickness variations within sills, (3) the geometry, morphology, and emplacement of a lava flow and a number of shallow sills have been described, and (4) large-scale host-rock deformation associated with sill emplacement. The key findings of the T38 case study are summarised in this section.

More than 40 sills have been mapped in the survey area and the majority of these classify as saucer-shaped sill segments. The average sill covers an area of 12 km^2 and has a vertical relief of approximately 450 m. Compiled statistical data shows good correlation between sill area and vertical relief and between maximum emplacement depth and vertical relief, with larger sills exhibiting greater vertical relief and sills emplaced at greater depth exhibiting greater vertical relief than more shallowly emplaced sills. The statistical data also show poor correlation between emplacement depth and sill size.

Detailed interpretation of saucer-shaped sills that exhibit greater thickness than the thickness of separability (> 80 m) have been studied in detail. The interpretation suggests that these sills show that they are thickest in their central basal part and gradually thin towards their tips. Although no feeders have been confidently identified it has been suggested that these sills were fed by underlying sills in their basal region and transgressed and thinned towards their edges.

A series of lava flows (flow unit B) and a number of near-concordant shallow sills have been studied in detail. The lava flow was extruded onto Horizon B in the Late Paleocene and was most likely fed from the NW, possibly by the Darwin Igneous Centre. The near-concordant sills have intruded near the level of horizon B and share many geometrical similarities with extrusive lava flows. They are interpreted to have been intruded during the Early Eocene. The interpretation suggests that these near-

concordant shallow sills were fed either directly by the underlying sills or by conduits emanating from them. The underlying sills are interpreted to have been emplaced slightly earlier than the shallow sills in the latest Paleocene. The interpretation suggests that the geometry of the shallow sill has been partly determined by overburden deformation above the deeper sills.

Several examples of host-rock deformation, in the form of upward vertical displacement of the sediments (jack-up structures) overlying relatively shallow sills, have been described in detail and their origin discussed. The deformation is interpreted to be induced in order to accommodate the added thickness introduced by the forcible intrusion of sills. Detailed depth conversion and decompaction studies of the vertical relief and volume of displaced sediment overlying a relatively shallowly emplaced saucer-shaped sill has shown that the vertical relief and volume of a forced fold structure created at the seabed at the time of intrusion is comparable with thickness and volume estimates for the underlying sill.

A number of relatively shallow sills have been interpreted along the periphery and underlying flow unit B. The sills have been interpreted to have been intruded in the Early Eocene and thus following the extrusion of flow unit B in the Late Paleocene. The emplacement of the sills has deformed flow unit B. The flow edge has locally been jacked-up during intrusion of the underlying sills and elsewhere, internally, the flow appears to have been upwards displaced and subsequently removed leaving gaps in the otherwise continuous lava flow.

5.7 Conclusions

This case-study has addressed many different themes related to sill emplacement. The main findings of this case-study are summarised below. The conclusions are not ranked.

- The T38 igneous sill complexes built up from deeper to shallower levels with the deeper sills being emplaced prior to and acting as feeders for the shallower sills
- Sills were emplaced during the Late Paleocene and earliest Eocene
- Lava flow extrusion, most likely linked to the Darwin Igneous Centre, partly pre-dated sill intrusion in the survey area
- The sills within the sill complex show moderate correlation between maximum emplacement depth and vertical relief (R^2 = 52%) and between sill area and vertical

relief (R^2 = 51%), but poor correlation between sill area and maximum emplacement depth (R^2 = 8%)

- The thickness variation along two exceptionally well imaged saucers has shown that these are thickest in their central basal part and thin towards their edges
- Space for intrusions has been created by vertical displacement of overburden forming 'jack-up' structures. The vertical relief and decompacted volume of displaced sediments of 'jack-up' structures provide a good estimate of the thickness and volume of the sill that caused the deformation
- A number of shallow sills emplaced approximately 300 m below the contemporaneous seabed have been found to have behaved partly as flows and partly as sills

CHAPTER 6: EXTRUSIVE MOUND STRUCTURES ASSOCIATED WITH THE EMPLACEMENT OF SILL COMPLEXES

6.1 Introduction

6.1.1 Aims of chapter

This chapter aims at describing the geometry and context of a number of mound structures found associated with each of the igneous sill complexes interpreted in this study. A detailed three-dimensional description of these mound structures based on data from all four case-study areas (T67, Solsikke, T38, and T4; Fig. 6.1) is provided and based on these observations they are classified and compared with previously described comparable mound structures observed on 2D and 3D seismic data (Fig. 6.1) and in the field. Based on this their origin is discussed.

Reference to the mound structures described in this chapter has already been made in Chapter 3 (T67), Chapter 4 (Solsikke), and Chapter 5 (T38) where they have been used to date the timing of intrusion. The use of these mound structures as indicators of emplacement timing is further explained in this chapter and in Chapter 7.

6.1.2 Database

This chapter uses data from the Faeroe-Shetland Basin (Tranches 67 and 4), the NE Rockall Basin (T38), and the Solsikke survey area of the northern Møre Basin. The T67, Solsikke, and T38 surveys have been described in previous chapters (Chapters 3, 4, and 5, respectively), whilst the T4 3D seismic survey is introduced for the first time. An introduction to the T4 3D seismic dataset and the geological context of the survey area will be given in section 6.2.3.1.

6.2 Mound structures

6.2.1 Introduction

Numerous mound structures with diameters of up to 3.5 km and up to 550 m high have been mapped in the strata immediately overlying the sill complexes interpreted in the previous chapters (Chapters 3, 4, and 5) as well as in T4 of the central Faeroe-Shetland Basin. These mound structures share many of the same characteristics, but differ slightly in geometrical style and stratigraphic context within and between the different surveys. The following sections provide a description and classification of the mound structures interpreted in the four case-study areas. The implications of these mounds for

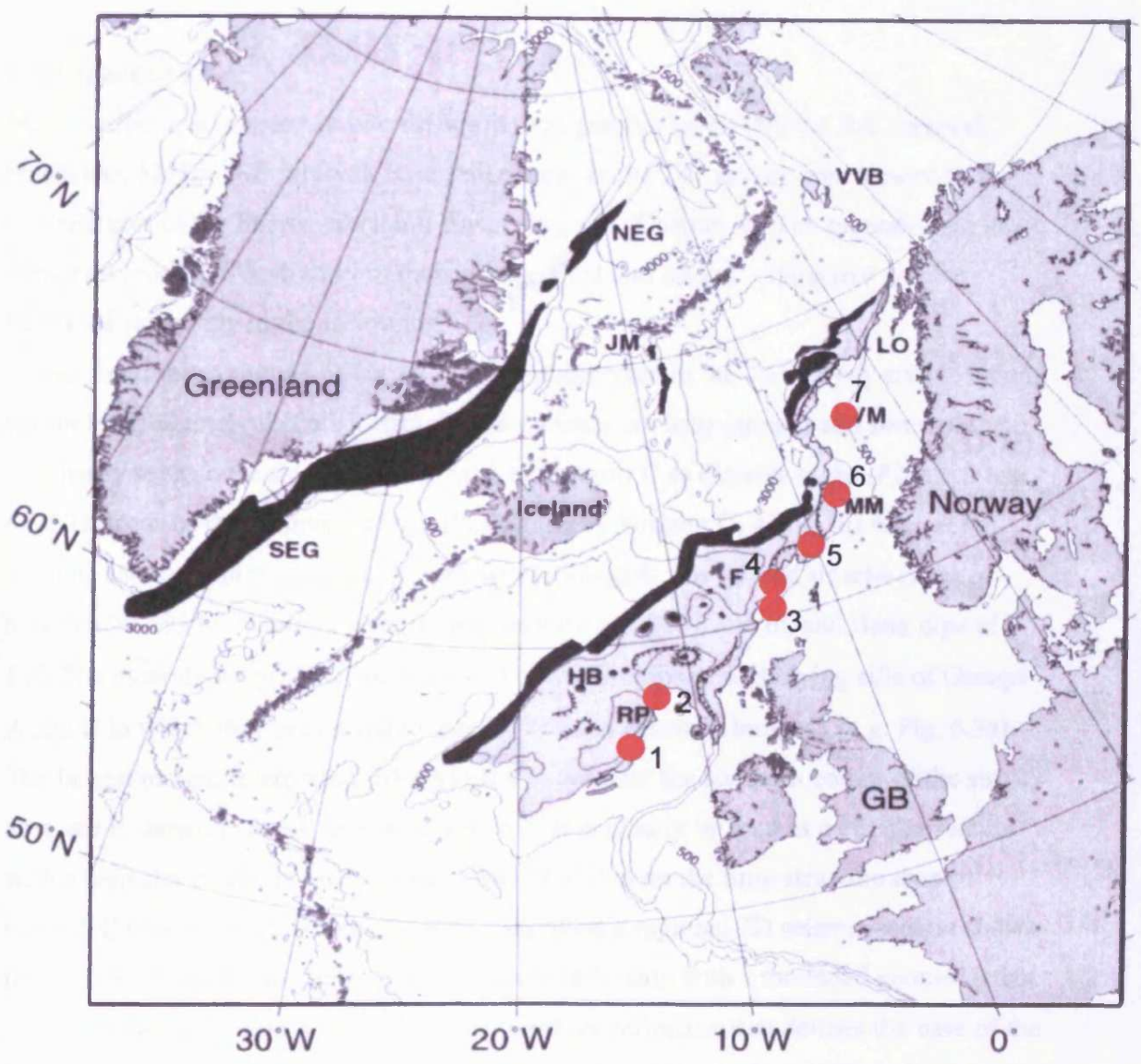

1. Rockall Trough: Joppen & White (1990)
2. NE Rockall Basin: **T38**
3. Faeroe-Shetland Basin: **T4**
4. Faeroe-Shetland Basin: T61/62; Davies et al. (2002)
5. Faeroe-Shetland Basin: **T67**; Hodges et al. (1999); Bell & Butcher (2002)
6. Moere Basin: **Solsikke**; Svensen et al. (2004)
7. Voering Basin: Skogseid et al. (1992), Svensen et al. (2004)

Fig. 6.1 Map of the NE Atlantic Margin showing areas where mounds associated with sill emplacement have been observed during this study and by previous studies. After Berndt (2000).

determining the timing of intrusive events in the case-study areas will be discussed in section 7.4.

6.2.2 Tranche 67

Mound structures are seen at two different stratigraphic levels (M*67*a: B-C interval, Paleocene; M*67*b: D-E interval, Late Paleocene) in the T67 survey area located in the northern part of the Faeroe-Shetland Basin (Fig. 6.1; Chapter 4). The mounds seen at these two levels differ slightly in their geometrical and seismic characters and are described separately in the following.

The first type of mound structure (M*67*a) interpreted in the T67 survey area is found within the B-C interval (Paleocene). These mounds are near-circular and some of them are clearly seen on the time-structure map of horizon C as discrete highs (Figs. 6.2 and 6.3). The tops of the mounds are clearly defined by horizon C, whilst the base of the mounds and their internal geometry are poorly imaged. The mound structures range between 90-195 m in height, have diameters between 800-1300 m, and flank dips of 9-16°. The mounds are preferentially located above the tips of underlying sills of Groups A and B to which they are linked by poorly defined seismic chimneys (e.g. Fig. 6.3a). The largest mound interpreted (M*67*a1) is located near the southern corner of the survey area and is shown in cross-section in Fig. 6.3. It is clearly imaged as a circular feature with a diameter of 950 m and vertical relief of 120 m on the time-structure map of horizon C (Fig. 6.2). The mound is also imaged on a regional 2D seismic section shown in Fig. 6.3b. The mound comprises an internal reflection with a mounded geometry that appears to downlap onto a high amplitude positive reflection that defines the base of the mound. The top of the mound is marked by a positive acoustic boundary (horizon C) above which the seismic character changes. There is no change in amplitude of horizon C across the crest of the mound. Horizons A and B become lower in amplitude and more poorly defined directly underlying M*67*a1. The mound is located directly above the tip of sill 7 of Group A (Fig. 6.2) to which it is connected by a seismic chimney (Fig. 6.3a). The chimney is a pipe-like structure that disrupts the seismic reflection pattern. The C-E interval is thinned across the crest of the mound (Fig. 6.3).

Two mound structures (M*67*b1 and M*67*b2) have been mapped at a shallower stratigraphic level (D-E interval; Late Paleocene) in the T67 survey area and are shown on the vertical seismic section seen in Fig. 6.4. They appear as near-circular features on the time-structure map of horizon E and are located on the lava plateau, 2.5 km in front

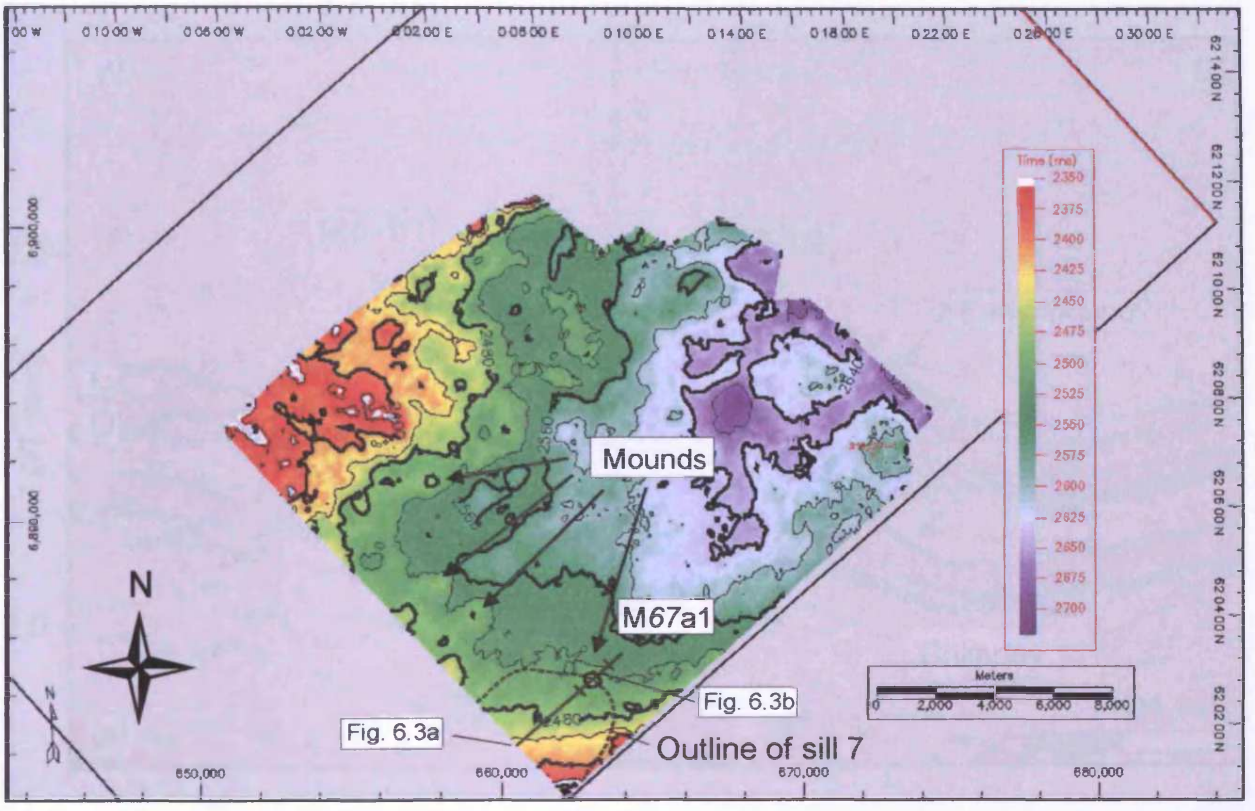

Fig. 6.2 Time-structure map of horizon C showing locations of a number of M67a mounds. Note location of M67a1 and the underlying sill 7. Note line location for Fig. 6.3.

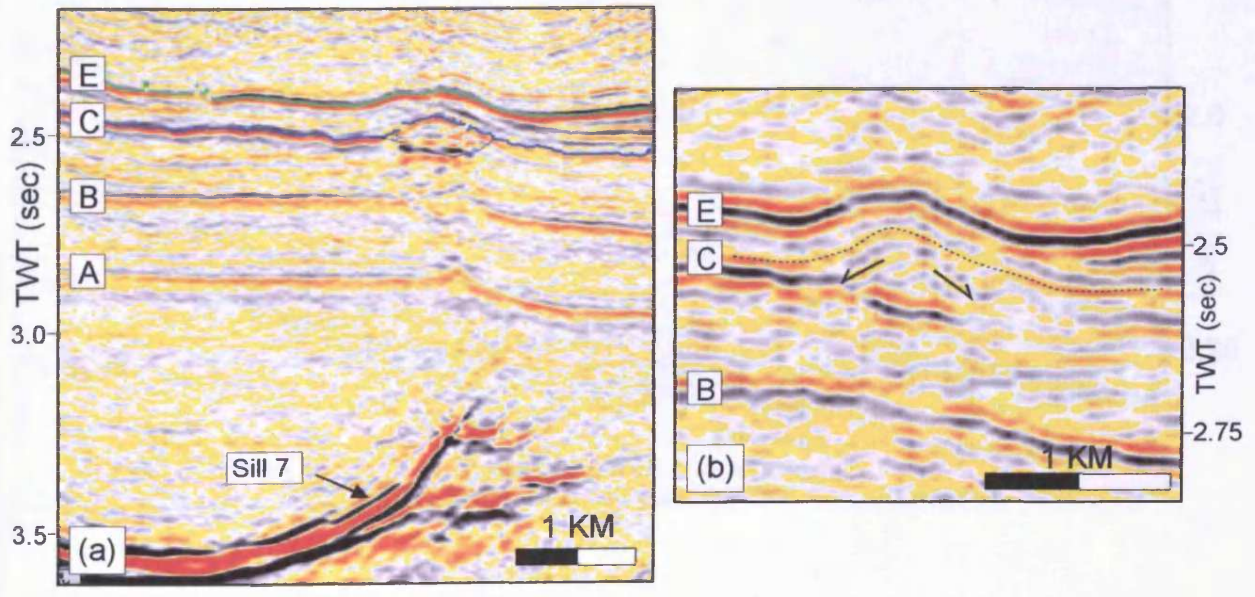

Fig. 6.3 Mound M67a1. (a) 3D seismic display showing the linkage between M67a1 and the underlying sill 7. (b) 2D seismic display showing the internal downlapping structure of M67a1. See Fig. 6.2 for line locations.

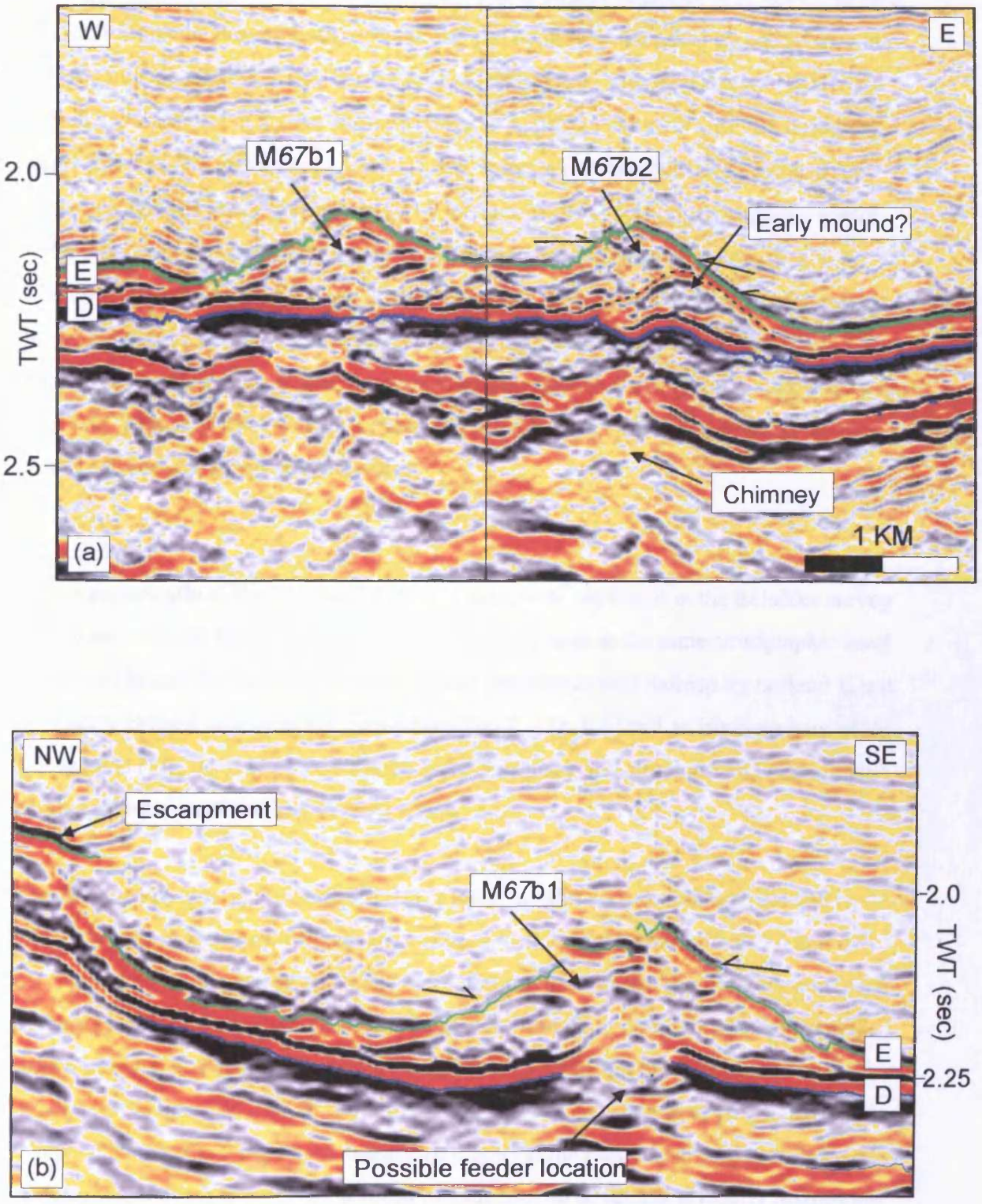

Fig. 6.4 (a) Seismic section showing the cross-sectional geometry of M67b1 and M67b2. (b) Seismic section showing the cross-sectional geometry of M67b2 indicating possible feeder location. See Fig. 6.5b for line locations.

of the escarpment (Fig. 6.5). Upwards the mounds are delimited by a positive acoustic boundary (horizon E) of moderate amplitude that is clearly onlapped (Fig. 6.4). The lava flow unit forms the base to both mounds and the boundary is marked by an increase in acoustic impedance (Fig. 6.4). The base of mound M*67*b1 measures 1.3 by 1.8 km and it has a vertical relief of 276 m and flank dips of approximately 20°. M*67*b2 is slightly bigger than M*67*b1 measuring 2.2 by 1.4 km. It has a vertical relief of 273 m and its flanks are inclined at approximately 17°. On some vertical sections through the centre of the mounds it appears that they are connected to central basal chimneys (Fig. 6.4) that link to the underlying shallow sills of Group C. The internal geometry of these mounds shows an overall chaotic reflection configuration. However, within M*67*b2, a high amplitude reflection is seen towards the north-eastern flank of the mound structure (Fig. 6.4). This reflection defines a mounded geometry that could represent an early phase in the development of the mound.

6.2.3 Solsikke

Two geometrically different types of mound structures are found in the Solsikke survey area of the northern Møre Basin (Fig. 6.1). They are seen at the same stratigraphic level (M*ss*a and M*ss*b: E-F interval, Paleocene) and are downwards defined by horizon E and are clearly imaged on a time-dip map of horizon F (Fig. 6.6) and an isochore map of the E-F interval (Fig. 6.7). The three-dimensional geometry and structural and stratigraphic context of these are described in this section.

The first type of mound structure (M*ss*a) is near-circular and conical in shape and is primarily seen in the north-western part of the Solsikke survey area (Figs. 6.6 and 6.7). More than 20 closely spaced mounds (500-2500 m) are found in the north-western part of the survey area and a representative vertical section that cross-cuts three of them is shown in Fig. 6.8. The mounds are defined downwards by horizon E and are clearly imaged on the time-dip map of horizon F shown in Fig. 6.6. The overlying horizon G is onlapped by the overlying strata and above this level the relief on the mounds decreases rapidly (Fig. 6.8a). The internal geometry of the mound structures is clearly imaged and can be divided into two main units separated by horizon X (Fig. 6.8a), which is a moderate amplitude reflection that has been mapped locally in areas where the mound structures are present. Horizon X downlaps onto horizon E and defines a lower package of downlapping reflections. The unit overlying horizon X and upwards bound by

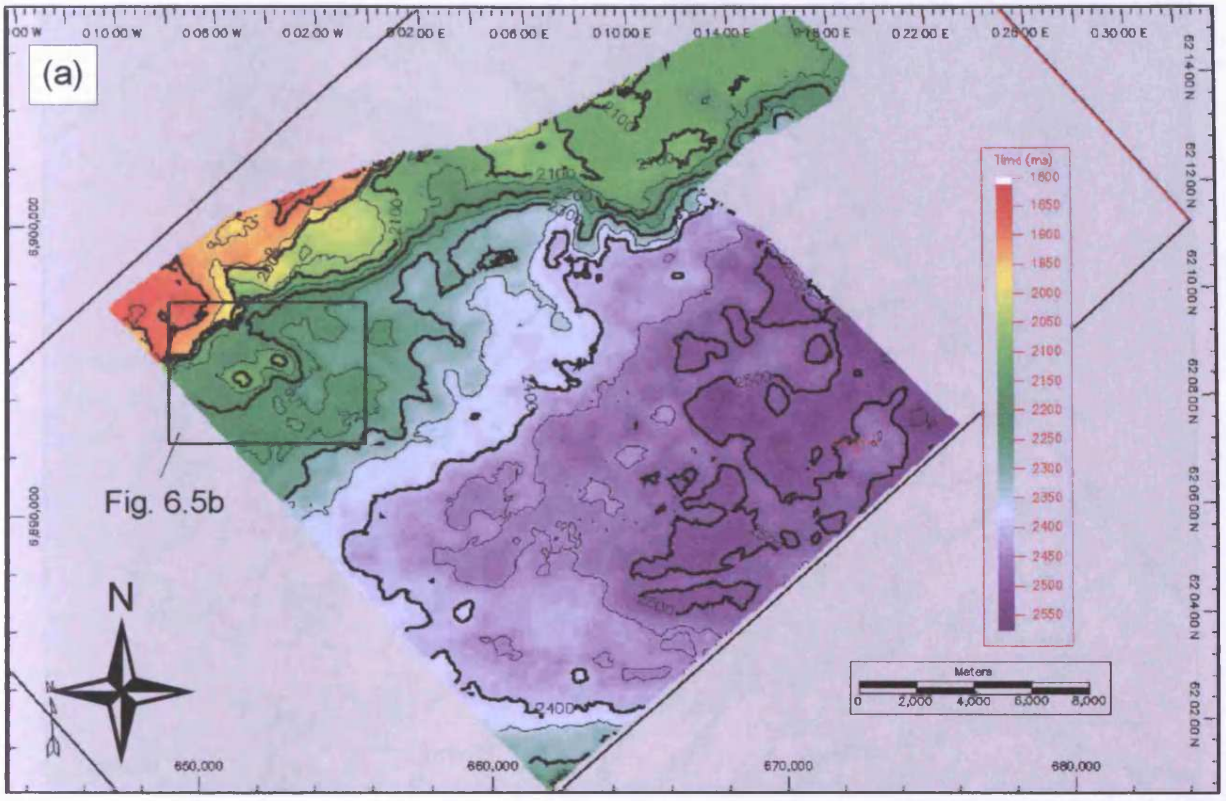

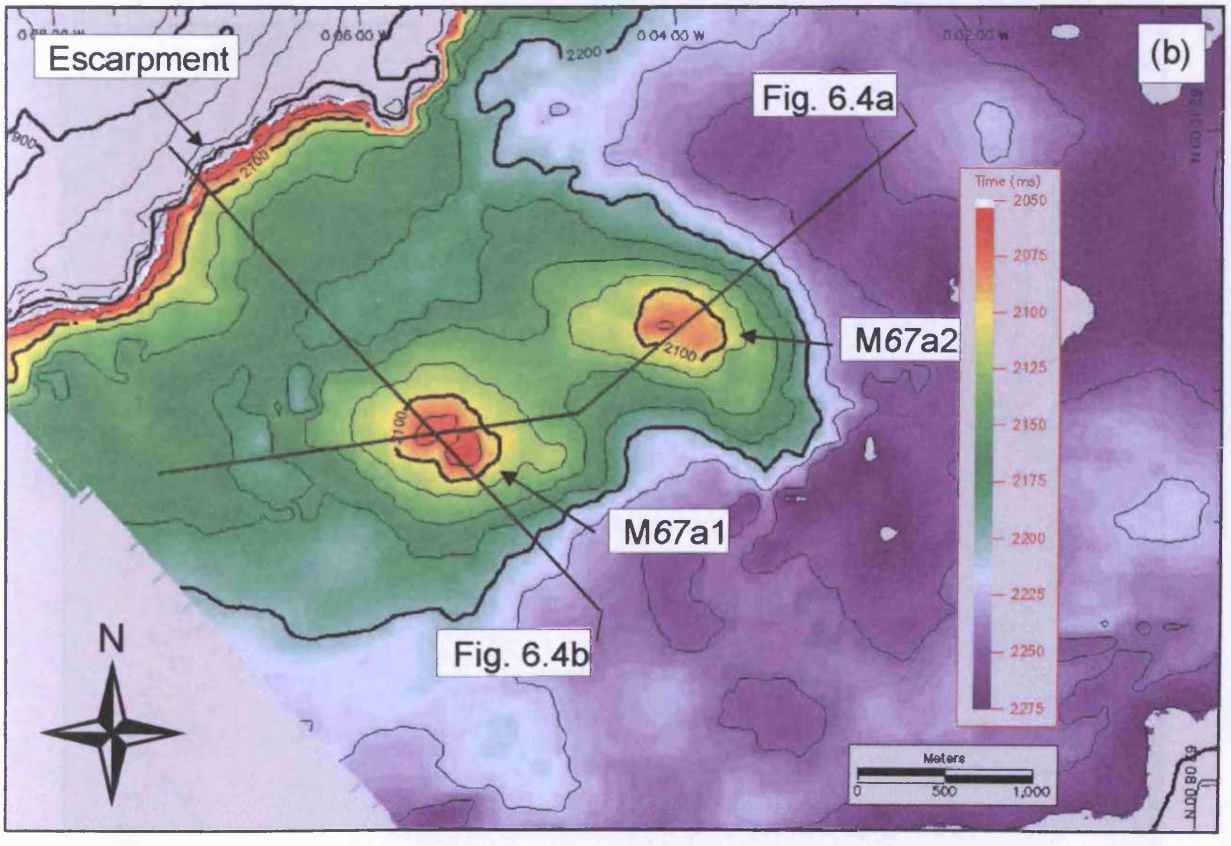

Fig. 6.5 (a) Time structure map of horizon E showing location of Fig. 6.5b. (b) Conical mound structures M67b1 and M67b2 imaged on time-structure map of horizon E. Note line location for Fig. 6.4.

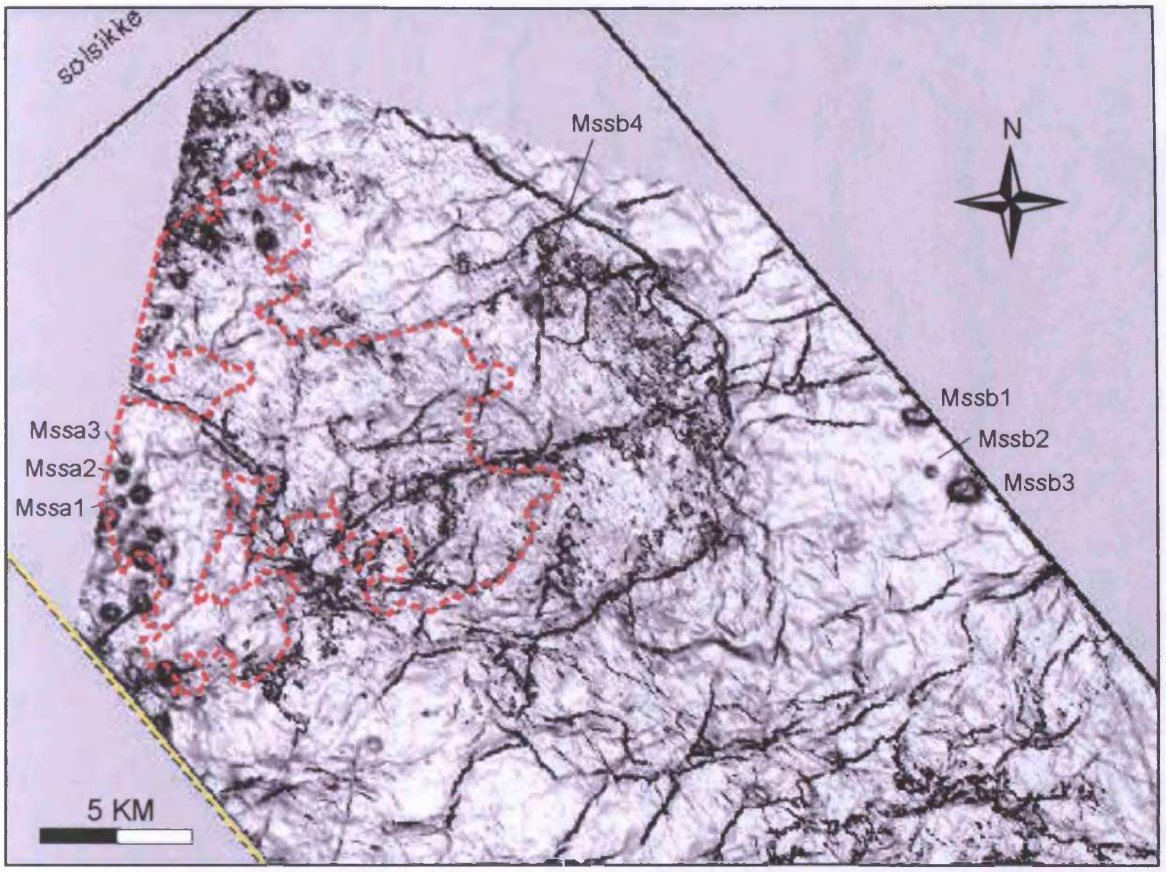

Fig. 6.6 Time-dip map of horizon F showing the distribution of mounds within the Solsikke survey area. The outline of the Solsikke Sill has been superimposed on the map to illustrate the relationship between this sill and moundsin the western and northern part of the survey area.

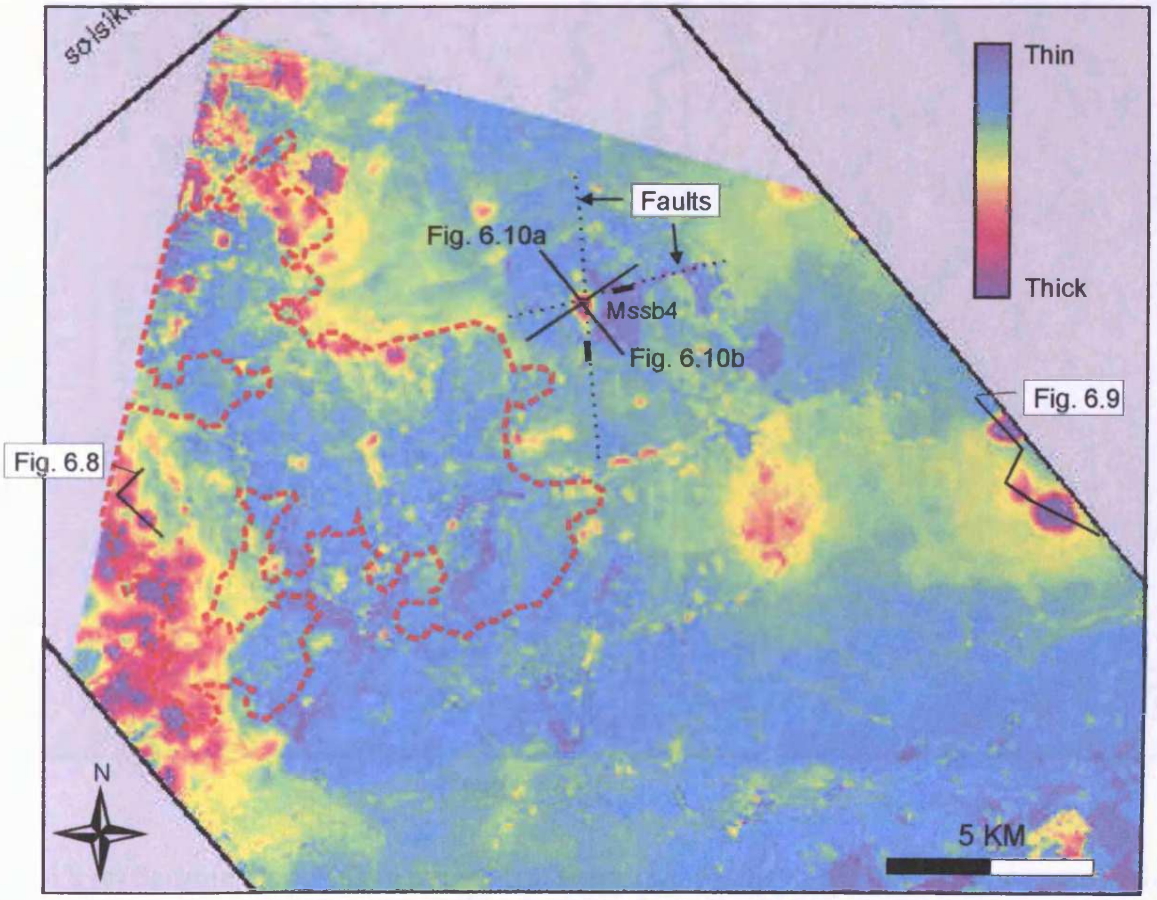

Fig. 6.7 Isochore map of the E-F interval with isochore maxima indicating mounds. Note line locations for Figs. 6.8, 6.9, and 6.10.

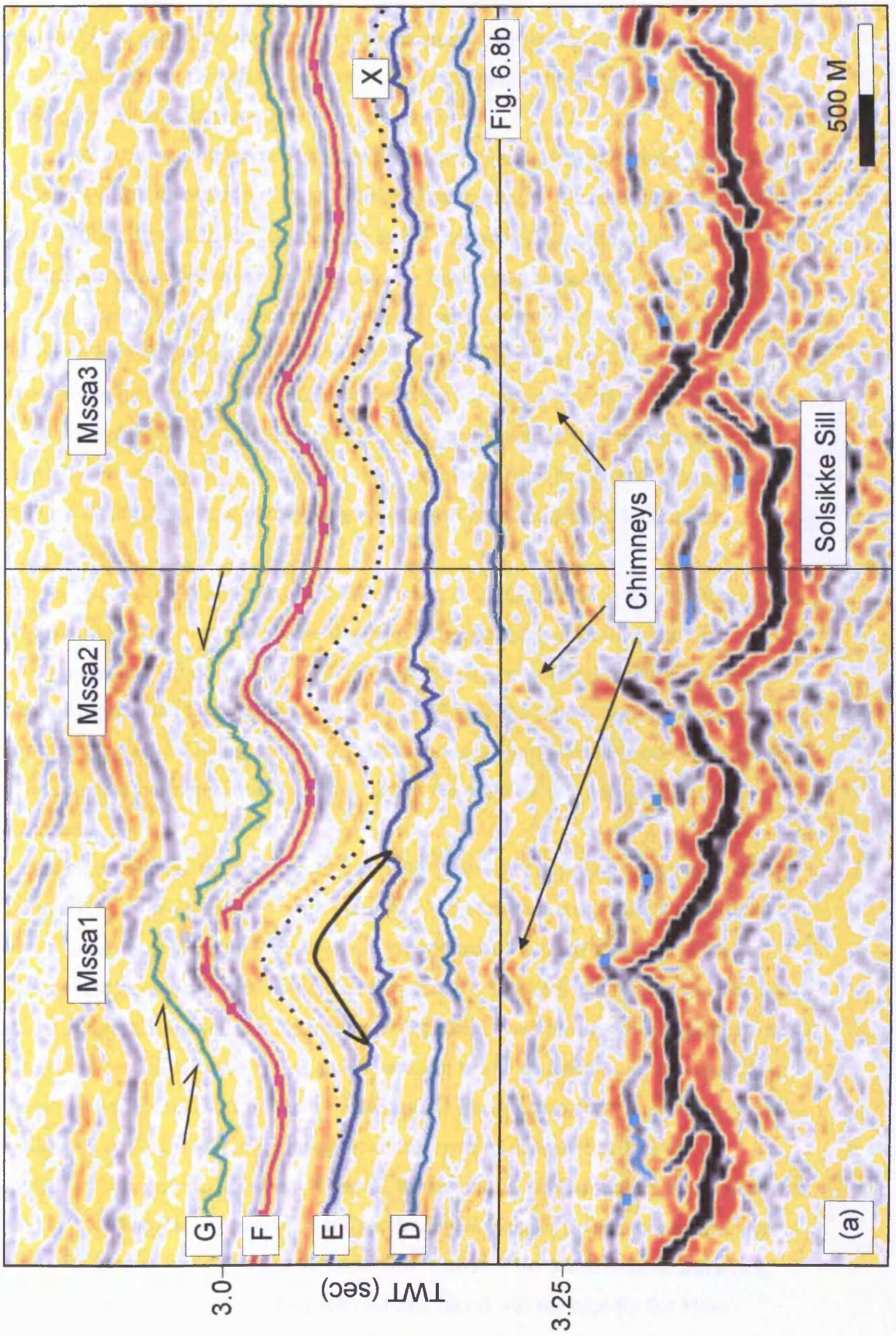

Fig. 6.8 (a) Seismic section showing the cross-sectional geometry of three Mssa mounds in the Solsikke survey area. See Fig. 6.7 for line location. Note indications of slice level of Fig. 6.8b.

horizon G has a uniform thickness of approximately 100 m and comprises a number of concordant reflections. Where horizon X is not present the reflections within this unit are concordant with horizon E.

The M*ss*a mounds range in diameter between 500 and 1300 m with the average mound having a diameter of 730 m. The average mound is 135 m high (E-X interval) and has flank dips of 13-23° decreasing to 2-3° towards the margin of the mound. The mounds are developed overlying crests in the underlying Solsikke Sill and are linked to these by poorly defined vertical zones of less continuous reflections (chimneys) including horizon D (Fig. 6.8a and 6.8b). The map shown in Fig. 6.8b shows a slice through a variance cube in the north-western part of the survey area. The slice is taken at 3200 ms and thus shows the variance in the interval underlying the mounds and above the underlying sills. The map (Fig. 6.8b) shows that the vertical chimneys seen in Fig. 6.8a are circular in planview and penetrate highly fractured sediments.

The second type of mound structure (M*ss*b; Fig. 6.9) interpreted in the Solsikke survey area is primarily seen in the northern part of the survey area and along the eastern survey boundary (Figs. 6.6 and 6.7). These mounds are lensoidal in shape and are downwards defined by horizon E onto which internal reflections within the mounds downlap (Fig. 6.9). The upper limit of the mounds is poorly constrained. The mounds influence both horizons F and G above which the relief on the mounds rapidly decreases.

The representative section shown in Fig. 6.9 shows three lensoidal mounds (M*ss*b1-3) located near the eastern survey boundary. Two of the mounds (M*ss*b1 and M*ss*b3) have a truncational base and are downwards defined by horizon E, which is seen to truncate underlying reflections including horizon D. M*ss*b2 is smaller than M*ss*b1 and M*ss*b3 and does not exhibit a clear truncational base. Underlying this mound horizons D and E are bent downwards, forming a depression below the centre of the mound. The uppermost reflections within the underlying C-D interval also show some sign of down-bending as well as possible thinning towards a zone of disturbed reflectivity immediately underlying the central part of the mound. A similar deformation pattern has been seen underlying more poorly defined lensoidal mounds in the more northern part of the survey area overlying the Solsikke Sill. Upwards the M*ss*b mounds influence both horizon F and G and the E-G interval can, like it was the case for the M*ss*a mounds, be divided into a downlapping lower unit and an overlying approximately

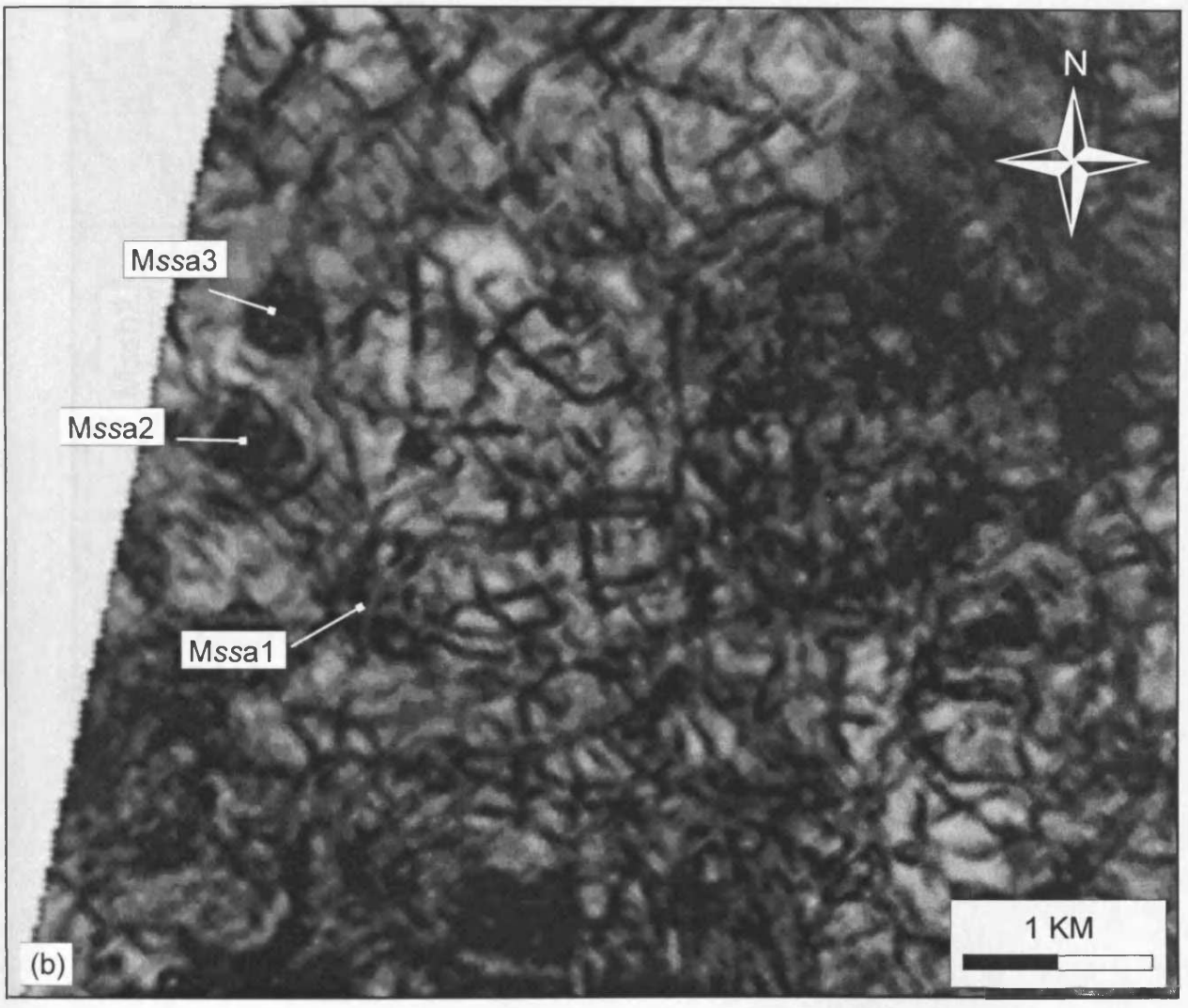

Fig. 6.8 (continued) (b) Variance slice (3200 ms) showing planview expression of circular pipe-like feeders penetrating highly fractured sediments underlying the *Mssa* structures. See Fig. 6.8 for slice level.

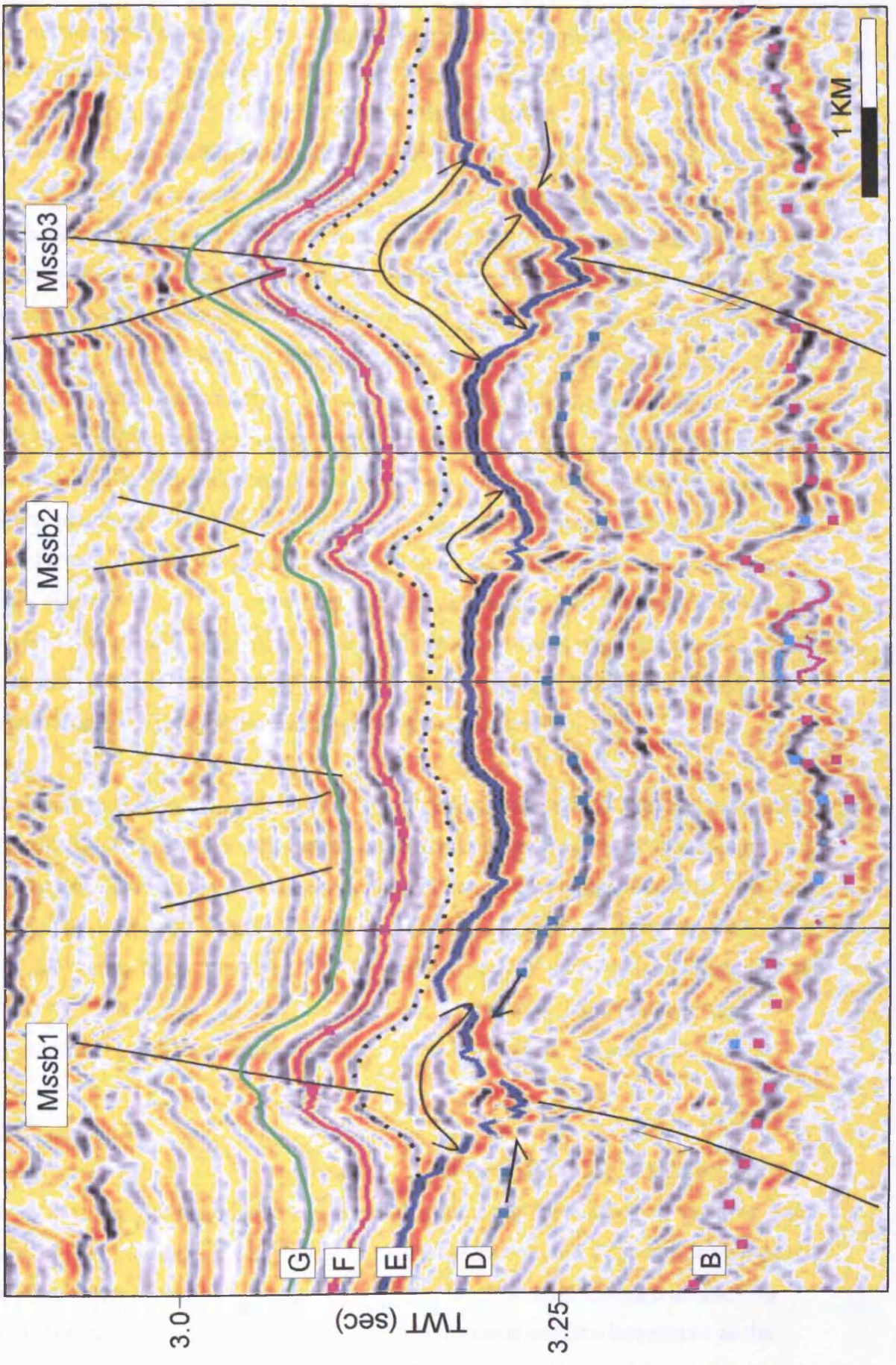

Fig. 6.9 Seismic section showing the cross-sectional geometry of three Mssb mounds in the Solsikke survey area. See Fig. 6.7 for line location.

100 m thick concordant upper unit, separated by the locally mapped horizon Y (moderate amplitude reflection). The M*ss*b mounds range in diameter between 500 to 1200 m and in height (E-Y interval) between 60 and 225 m.

The majority of the M*ss*b mounds are seen overlying the periphery of the Solsikke Sill, but four of the mounds (M*ss*b1-4; Figs. 6.6 and 6.7) are located between 3 and 13 km from the Solsikke Sill and show no apparent spatial relationship with this sill. Common for at least the three larger of these mounds (M*ss*b1, 3, and 4) is that they are located above the upper tips of faults that can be seen to offset the strata underlying horizon D (Figs. 6.9 and 6.10). The faults underlying M*ss*b1 and M*ss*b3 can be seen on the cross-section shown in Fig. 6.9 and as poorly defined continuations of E-W trending fault traces on the time-dip map of horizon E shown in Fig. 6.11. M*ss*b4 is a lensoidal mound structure with a slightly truncational base located approximately 3 km east of the eastern periphery of the Solsikke Sill (Fig. 6.10). It has a diameter of approximately 700 m and a vertical relief of approximately 120 m. From the time-dip maps of horizons E and F shown in Fig. 6.6 it can be seen that the mound is located above an intersection between a large south dipping, E-W striking fault and a large west dipping, N-S striking fault both of which clearly offset the underlying horizons A, B, and C and penetrate downwards to the level of the deeper parts of the sill complex.

As already mentioned constraining the top of the mounds in the Solsikke survey area is difficult. The E-X and E-Y units represent added volume of sediment that is only present locally where the mounds are found, whilst the overlying concordant X-G and Y-G units (equivalent to the E-G unit where the local horizons X and Y are not present) are found across the survey area. The detailed lithology of the lower and upper units are unknown, but it is suggested that the upper unit is a pelagic drape unit that was deposited following the extrusion (see section 6.4.4.1) of the mounds.

6.2.4 Tranche 38

Conical mound structures are seen at one stratigraphic level in the T38 3D seismic survey area. Only two mounds have been interpreted and these are shown in Figs. 5.10 and 6.12. The mounds are very large, circular in planview, and delimited downwards by the lower flows of flow unit B onto which some bi-directional downlap is seen (Fig. 6.12). The material within the mounds exhibits the same acoustic impedance as the surrounding sediment and the mounds are delimited upwards through interpretation of

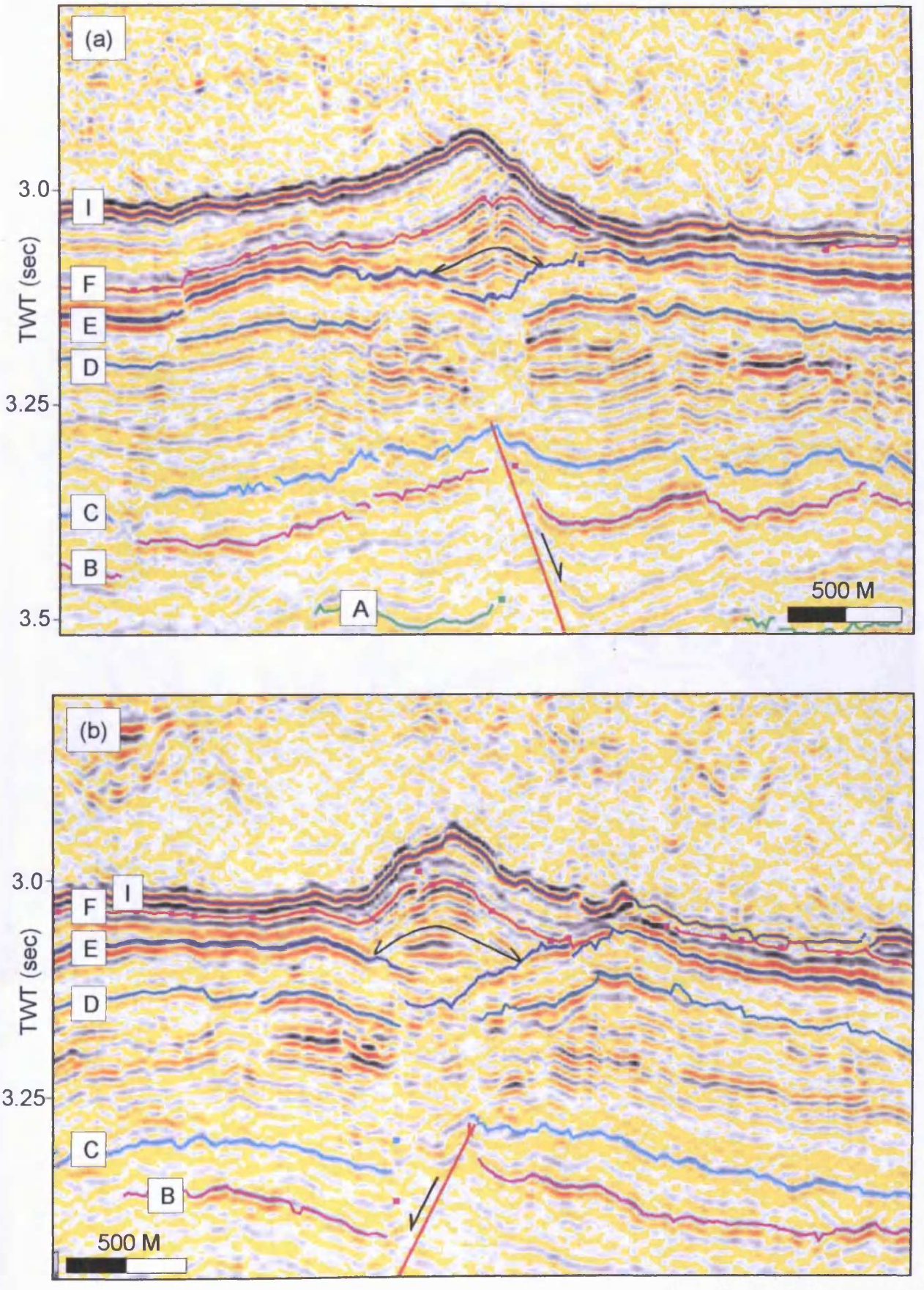

Fig. 6.10 Mound Mssb4 is lensoidal in shape and is located above a fault intersection. Note that the mound has not been removed by the overlying horizon I unconformity. See Fig. 6.7 for line locations.

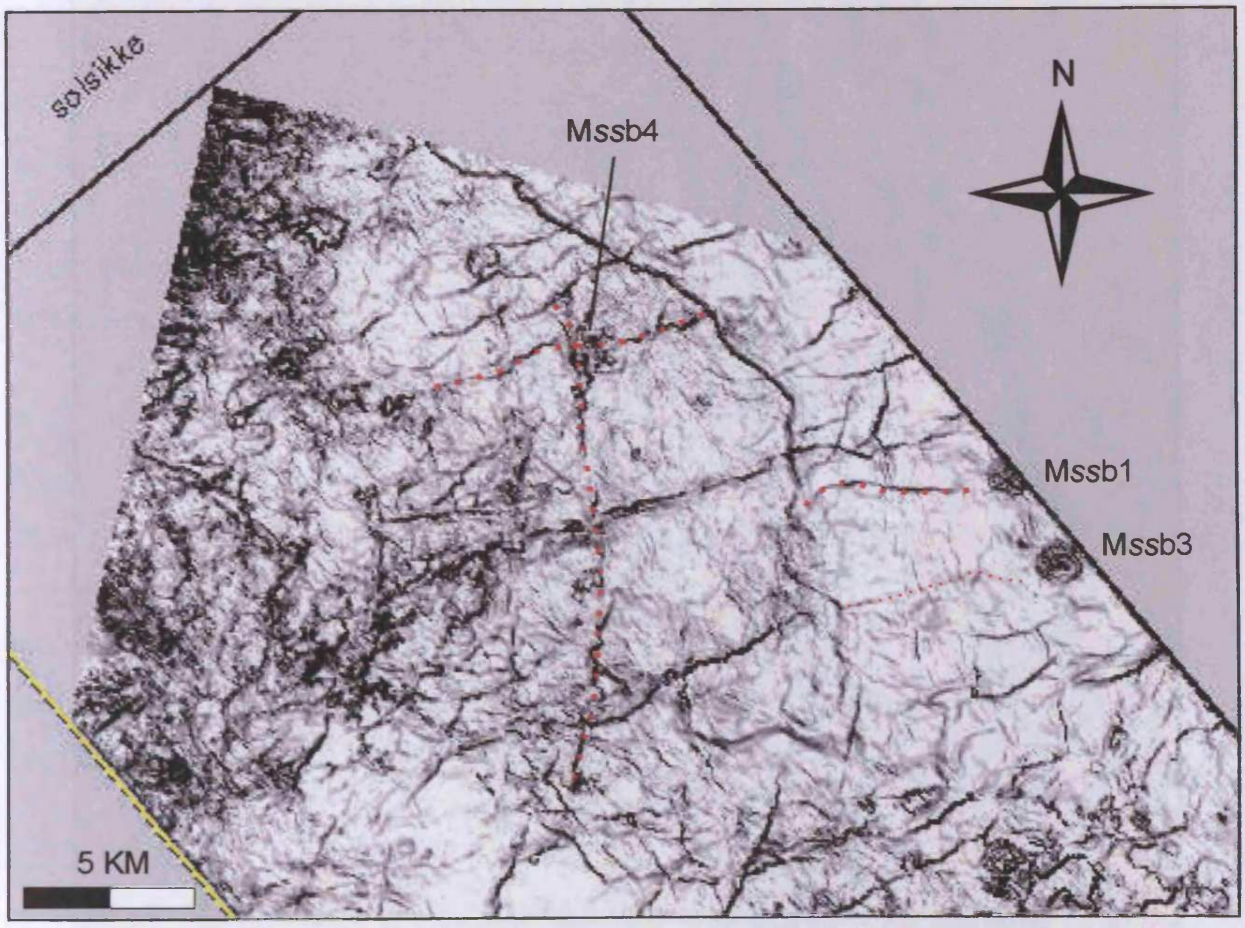

Fig. 6.11 Time-dip map of horizon E showing the structural context of mounds M*ss*b1, M*ss*b3, and M*ss*b4.

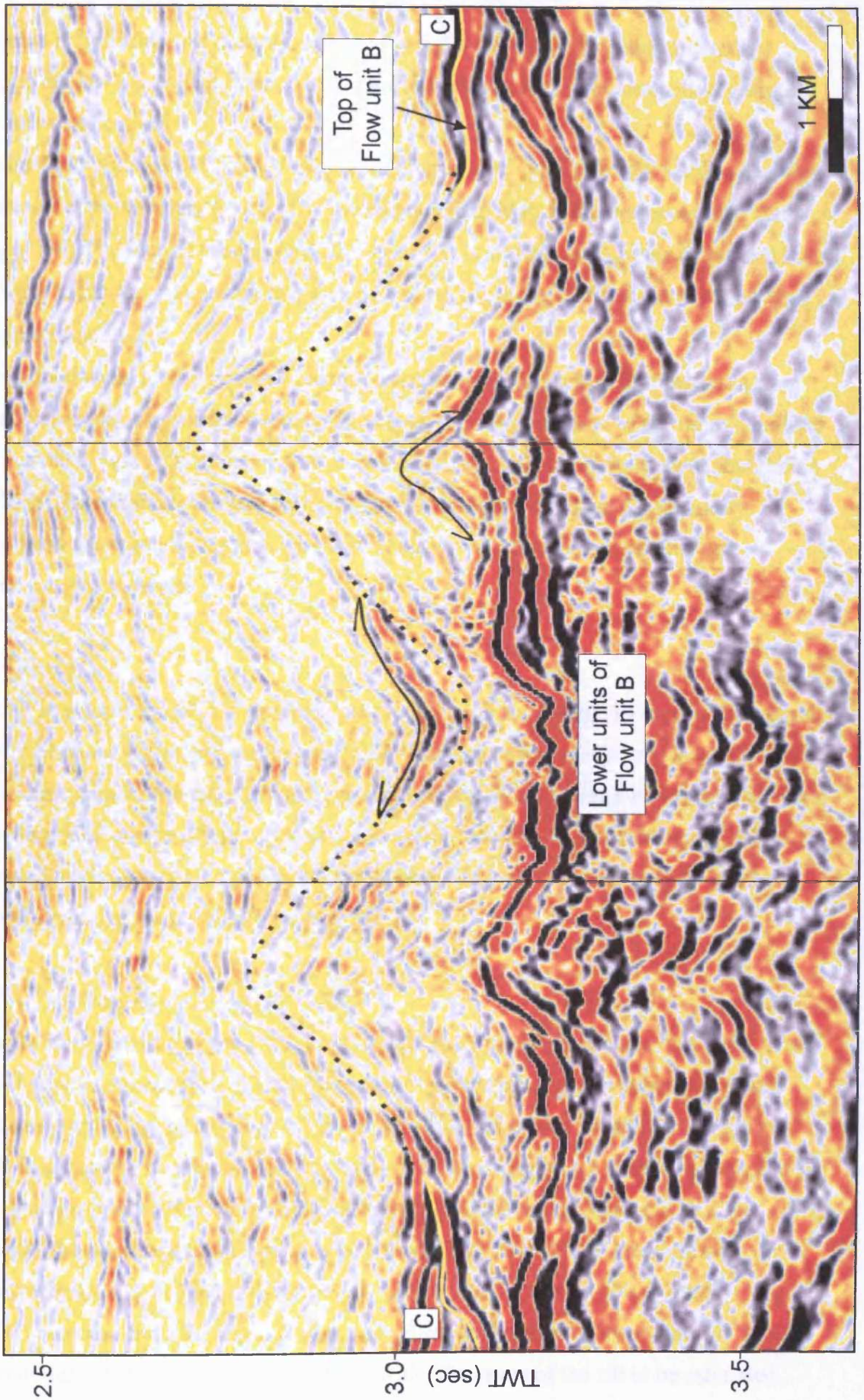

Fig. 6.12 M381 and M382 mapped in the T38 3D seismic survey area. The mounds rest on the lower units of Flow unit B. They are poorly defined upwards and exhibit acoustic properties very similar to the surrounding mud-dominated host-rock lithology.

an onlap relationship. As described in section 5.2.2 this upwards delimiting onlap surface may be equivalent to horizon C (Early Eocene), but could alternatively slightly pre-date this horizon.

The first mound (M*381*; Fig. 6.12) has a diameter of approximately 3 km and covers an area of approximately 6 km^2. The mound is 550 m high and has approximate flank dips of 20°. The second mound (M*382*; Fig. 6.12) is slightly bigger than M38a and has a diameter of 3.5 km and covers and area of 7.5 km^2. It is 640 m high and has flank dips of approximately 20°.

The mounds exhibit an overall chaotic internal reflection configuration, but a few reflections adopt a mounded geometry and downlap onto the base of the mound defined by high amplitude reflections of flow unit B. The high amplitude reflections that define the base of the mounds are largely continuous, but do shown local discontinuity underlying the mounds. There is no clear evidence of chimneys or velocity effects underlying the mounds.

6.2.5 Tranche 4

Mound structures are seen at one stratigraphic level in the T4 survey area of the central Faeroe-Shetland Basin and these are described in this section (Figs. 6.1 & 6.13). The T4 3D seismic dataset and the geological context of the T4 3D seismic survey area have not been described previously in this thesis and a brief introduction to these is, therefore, provided in sections 6.2.5.1 and 6.2.5.2, respectively, prior to the description of the mound structures themselves in section 6.2.5.3.

6.2.5.1 The Tranche 4 3D seismic survey

Detailed interpretation of the seismic response from the water-sediment interface in the T4 3D seismic dataset (Fig. 6.13b) shows that the data display this positive acoustic impedance boundary as a trough followed by a peak of similar magnitude (Fig. 6.14). From this it can be concluded that the data are close to minimum phase migrated and are displayed using normal polarity (SEG standards). At the depth where the sills are intruded, the dominant frequency is approximately 25 Hz and half the dominant wavelength around 111 m (assuming a sill velocity of 5.55 km/s; Skogly, 1998). The seismic response from the top and base of a sill or sill segment thinner than 111 m will thus interfere to an extent that will not allow the thickness of the sill to be estimated.

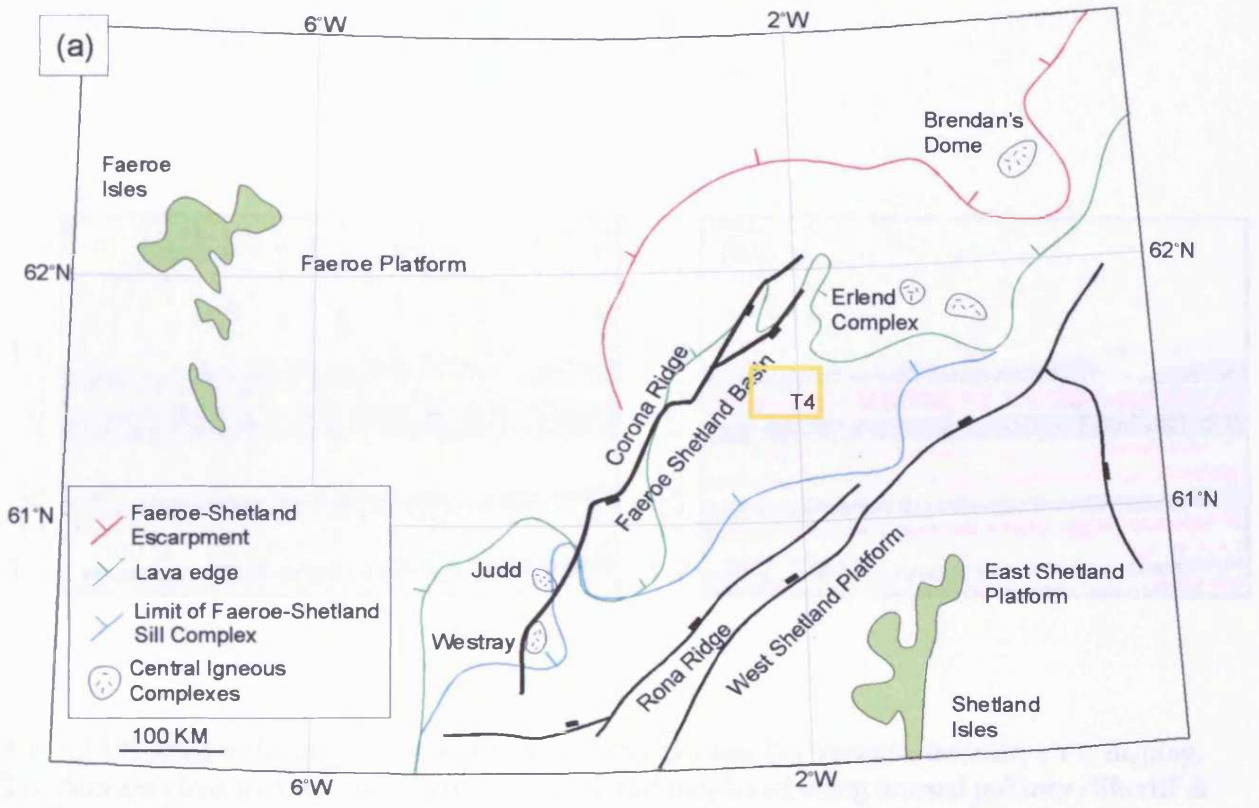

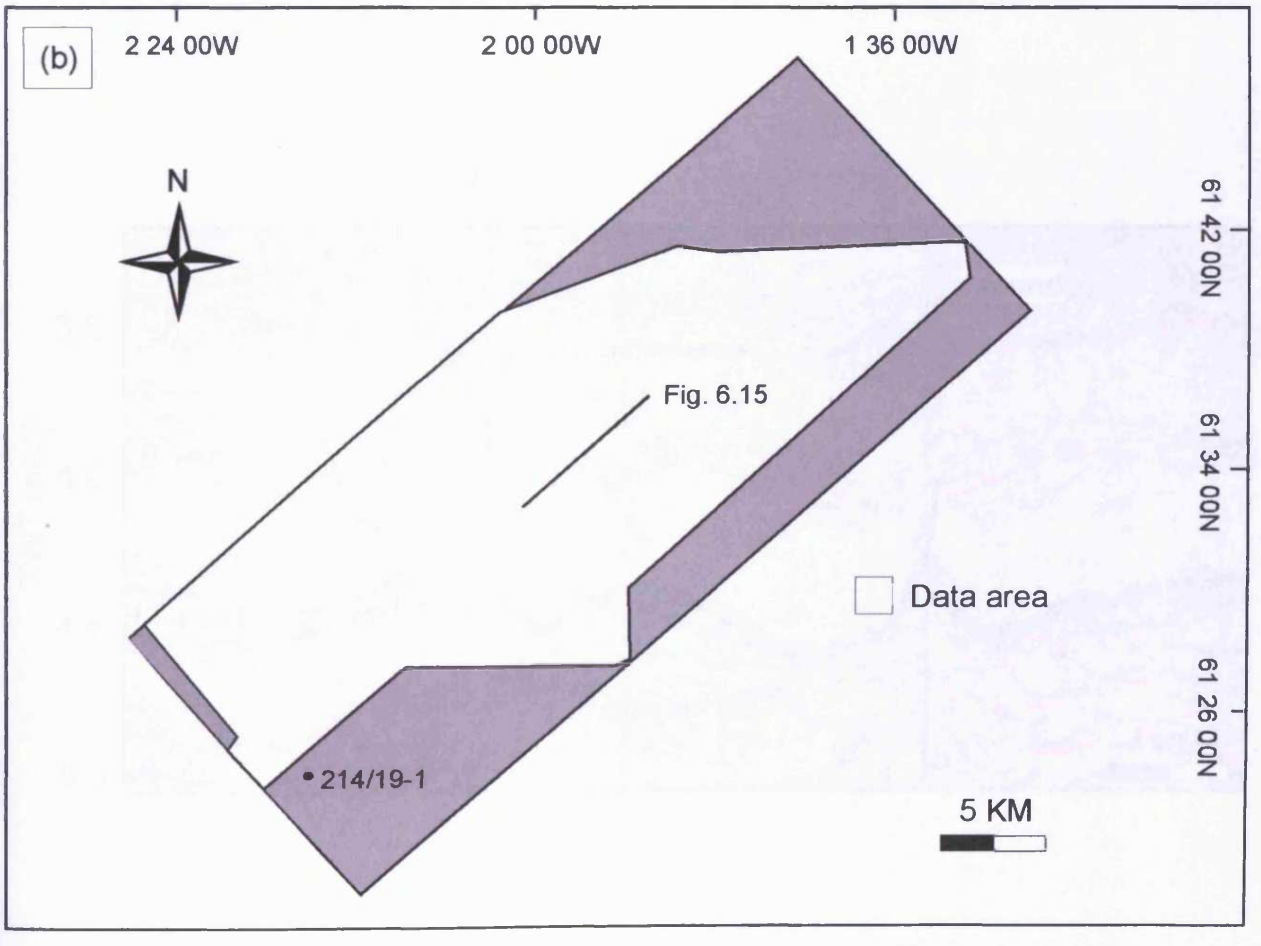

Fig. 6.13 (a) Location map showing the location of the T4 3D seismic survey area. After Naylor et al. (1999). (b) Map showing the outline of the T4 3D seismic survey area. Note line location for Fig. 6.15.

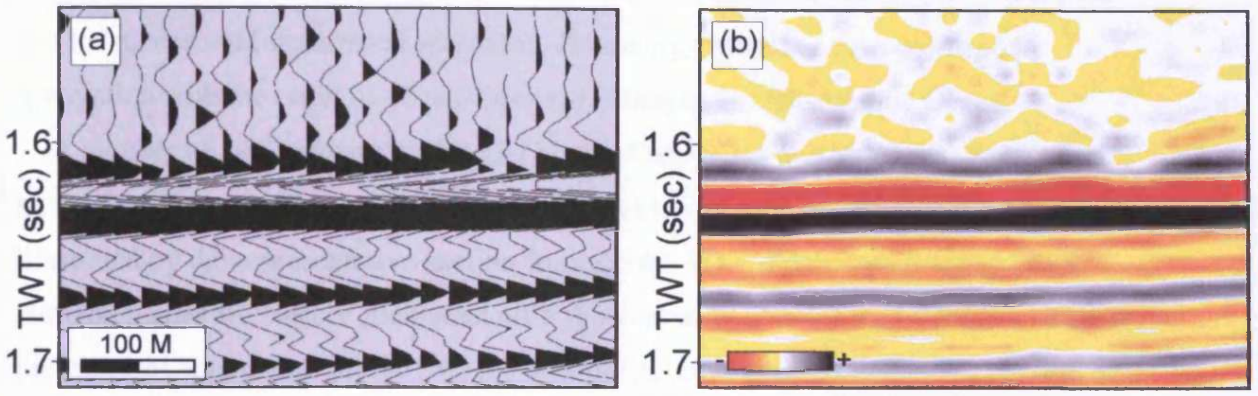

Fig. 6.14 Seabed reflection. (a) Variable area (VA) display. (b) Variable intensity (VI) display. The data are close to minimum phase migrated and displayed using normal polarity (Sheriff & Geldart, 1995).

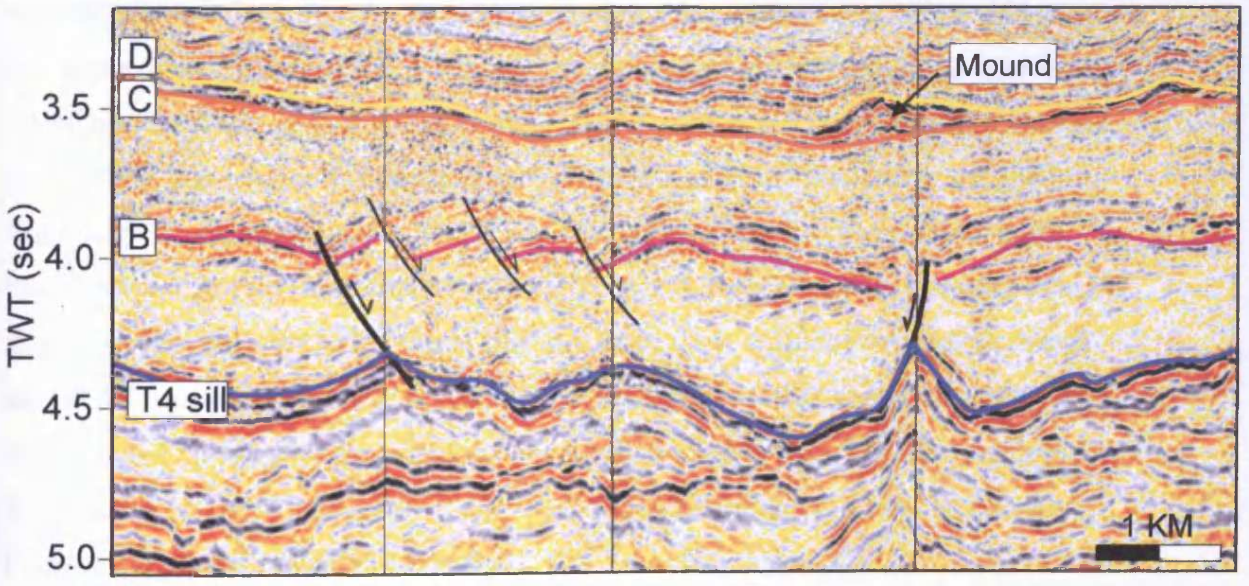

Fig. 6.15 representative seismic cross-section from the T4 3D seismic survey. Note the location of mound above crest in the T4 sill. See Fig. 6.13b for line location.

6.2.5.2 Geological context

Tranche 4 is located in a basin-floor setting in the central part of the Faeroe-Shetland Basin just south of the Corona Ridge (Fig. 6.13a). Like T67, located in the northern part of the Faeroe-Shetland Basin, igneous sills were here intruded into Upper Cretaceous and Paleocene mud-dominated sediments following Paleocene extension and in association with the onset of ocean-floor spreading in the NE Atlantic Ocean.

A number of key horizons within the Upper Cretaceous and Paleogene succession have been interpreted in the T4 3D seismic survey area. The interpreted horizons are illustrated by the representative section through the 3D volume shown in Fig. 6.15. Horizon names are largely consistent with those used by Davies et al. (2002) to describe the identical horizons in the T61/62 3D seismic surveys situated immediately north of the T4 survey area, however, their horizon A is here referred to as the T4 sill. Davies et al. (2002) tied their horizons to the near-by exploration well 214/19-1.

The lowermost part of the section is dominated by a series of high amplitude, sub-parallel reflections, which locally cross-cut stratal reflections. The uppermost of these is coincident with the boundary between Lower Paleocene clay-dominated sediments and a regional sill complex in the 214/19-1 exploration well and will here be referred to as the T4 sill. A time-structure map of the T4 sill (Fig. 6.16) reveals a highly irregular and complex geometry, which takes the form of a series of wide (2-8 km), cuspate depressions with flank dips of 20-40° separated by relatively narrow ridges. No accurate date is available for the T4 sill. Horizon B is a moderate to high amplitude reflection, which ties to the top of a sand unit in the 214/19-1 well and is dated as Late Paleocene (ca. 58 Ma). The horizon forms a number of upward convex structures bound by low-angle listric faults that tip out within the B-C interval. The timing of extension and deformation of horizon B is constrained to the Late Paleocene, by the presence of small growth wedges adjacent to the faults. Horizon C is a low amplitude reflection, which dips at 3-4 ° towards the NNW and forms the base to a series of mound structures that are delimited upwards by a continuous, moderate to high amplitude reflection, horizon D. Horizon C is latest Paleocene in age (54.9 Ma) and horizon D dates close to the Paleocene-Eocene boundary (54.6 Ma).

6.2.5.3 Mound structures

Numerous discrete mounds with circular to elongated planforms are seen on an isochore map of the interval between horizons C and D (54.9-54.6 Ma) of the T4 3D seismic

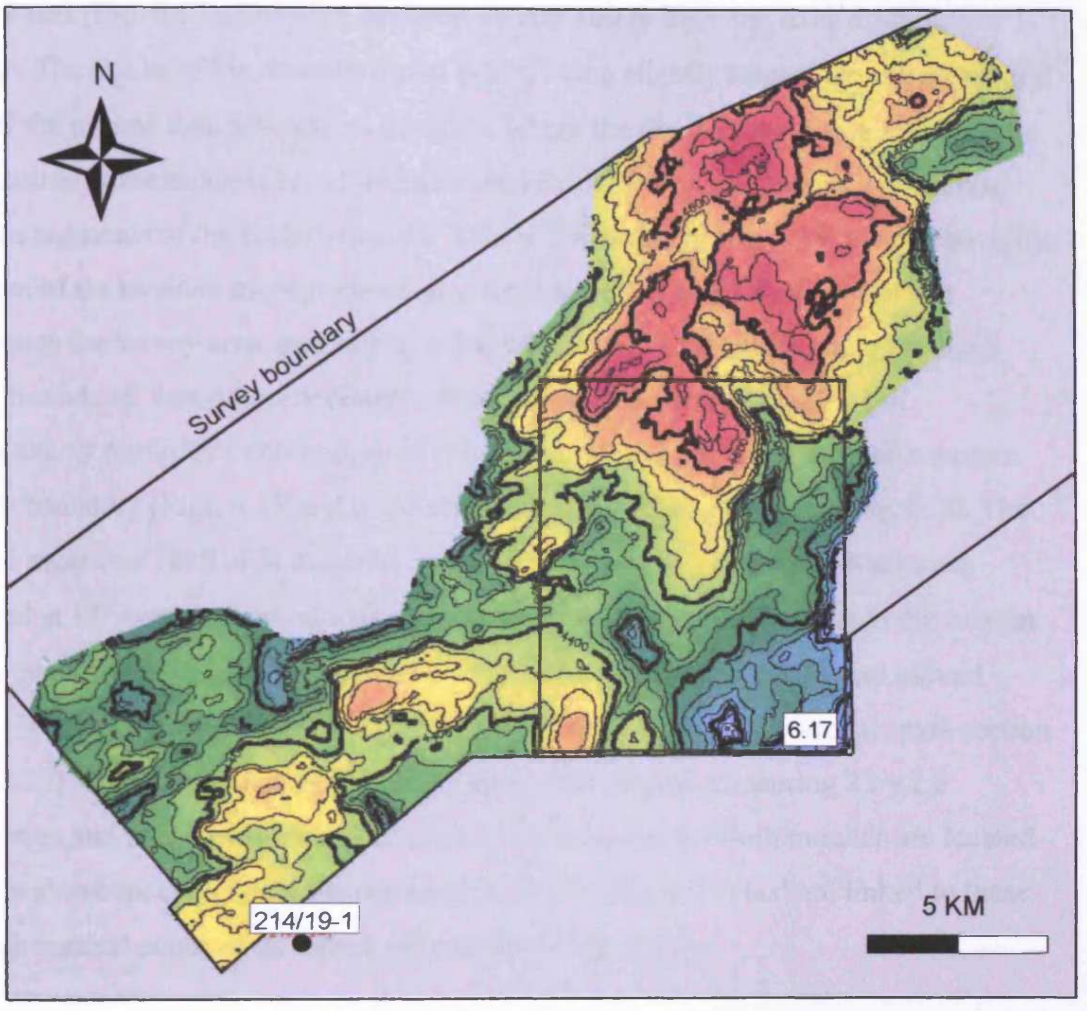

Fig. 6.16 Time-structure map of the T4 sill. Note location of Fig. 6.17.

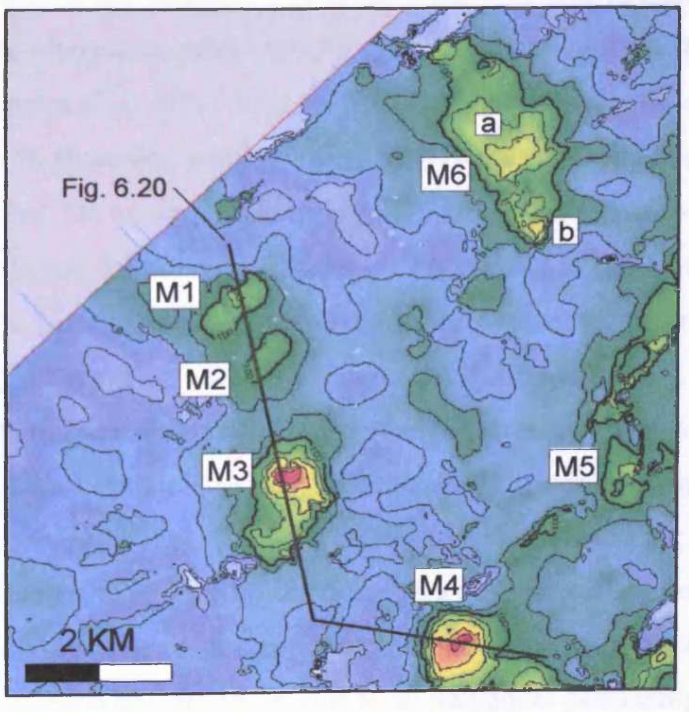

Fig. 6.17 Isochore map of the C-D interval showing a number of mound structures. See Fig. 6.18 for location. Note line location for Fig. 6.20.

survey area (Fig. 6.17). They are between 70 and 160 m high and have diameters of 1-2.7 km. The flanks of the mounds dip at 6-21°, being slightly steeper around the central axis of the mound than towards its margins, where the dip is reduced to a few degrees. The centres of the mounds are all located above ridges formed between intersecting cuspate segments of the underlying sill. This is illustrated in Fig. 6.18, which shows the location of six mounds superimposed on a time-structure map of the T4 sill that dominates the survey area, and in Fig. 6.19, which shows a vertical section through three mounds all located immediately above crests in the underlying T4 sill.

An almost perfectly circular mound (M44) structure is seen near the south-eastern survey boundary (Figs. 6.17 and 6.18) and is shown in cross-section in Fig. 6.20. The mound measures 1850 m in diameter and 276 m in height. The mound flanks are inclined at 17° near the central axis of the mound decreasing to 2° towards the margin of the mound. The mound is onlapped by the surrounding strata. A second mound (M43) is seen slightly further towards the north-west on the same vertical cross-section (Fig. 6.20). This mound has a NNE-SSW elongated shaped measuring 2 by 2.6 kilometres and it has a vertical relief of just less than 300 m. Both mounds are located directly above local highs on the underlying T4 sill (Fig. 6.18) and are linked to these through vertical zones of disturbed seismic data (Fig. 6.20).

6.2.5.4 The geometry of a polygonal fault system above mounds in the T4 survey area

Vertical seismic sections through the crest of the mound structures and attribute maps of horizon D reveal an interesting relationship with polygonal faults developed in the overlying Eocene strata (Fig. 6.21). The polygonal faults generally tip out downwards just above horizon D. However, some of these faults offset the top of the mounds several tens of metres. On an amplitude map of horizon D the planview relationship between the mounds and the polygonal faults is clearly imaged and these maps show that sets of opposite dipping polygonal fault traces intersect at the centres of the mounds to form a radiating pattern (Fig. 6.22). As mentioned in section 4.3.2.4, polygonal fault systems are thought to form under conditions of radial stress as a result of three-dimensional compaction, possibly through the process of syneresis (Cartwright & Dewhurst, 1998; Cartwright et al., 2003). The relationship between the location of mounds in the C-D interval and triple-junctions between intersecting polygonal faults on horizon D is unlikely to be coincidental. Numerous factors have been found to cause polygonal fault patterns to deviate from their ideal polygonal planview pattern (e.g

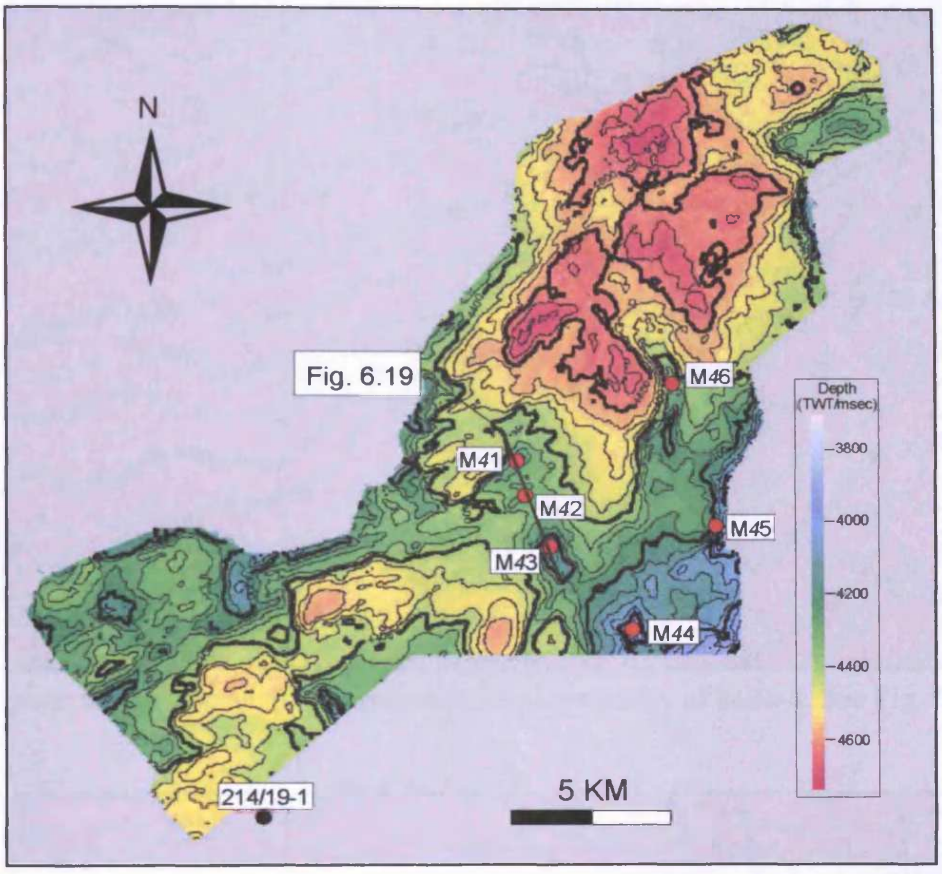

Fig. 6.18 Mound locations superimposed on a time-structure map of the T4 sill. Note line location for Fig. 6.19.

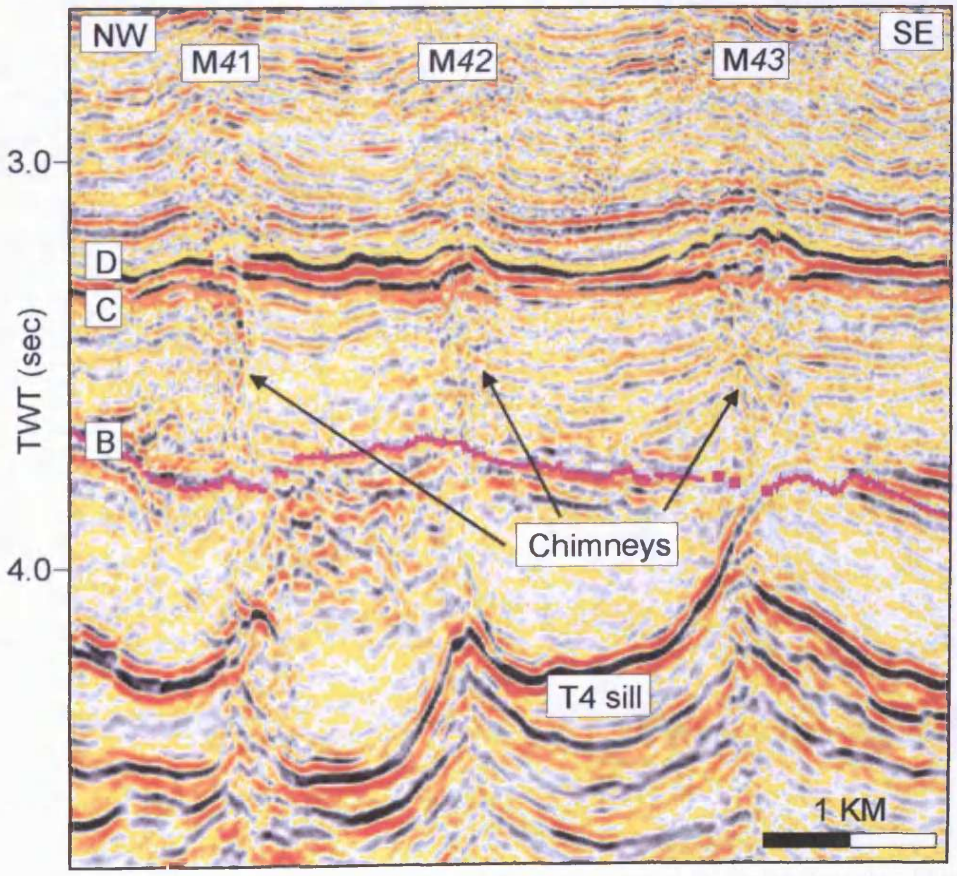

Fig. 6.19 Vertical seismic section showing the cross-sectional geometry of three mounds. The mounds are linked to crests in the T4 sill by seismic chimneys. See Fig. 6.18 for line location.

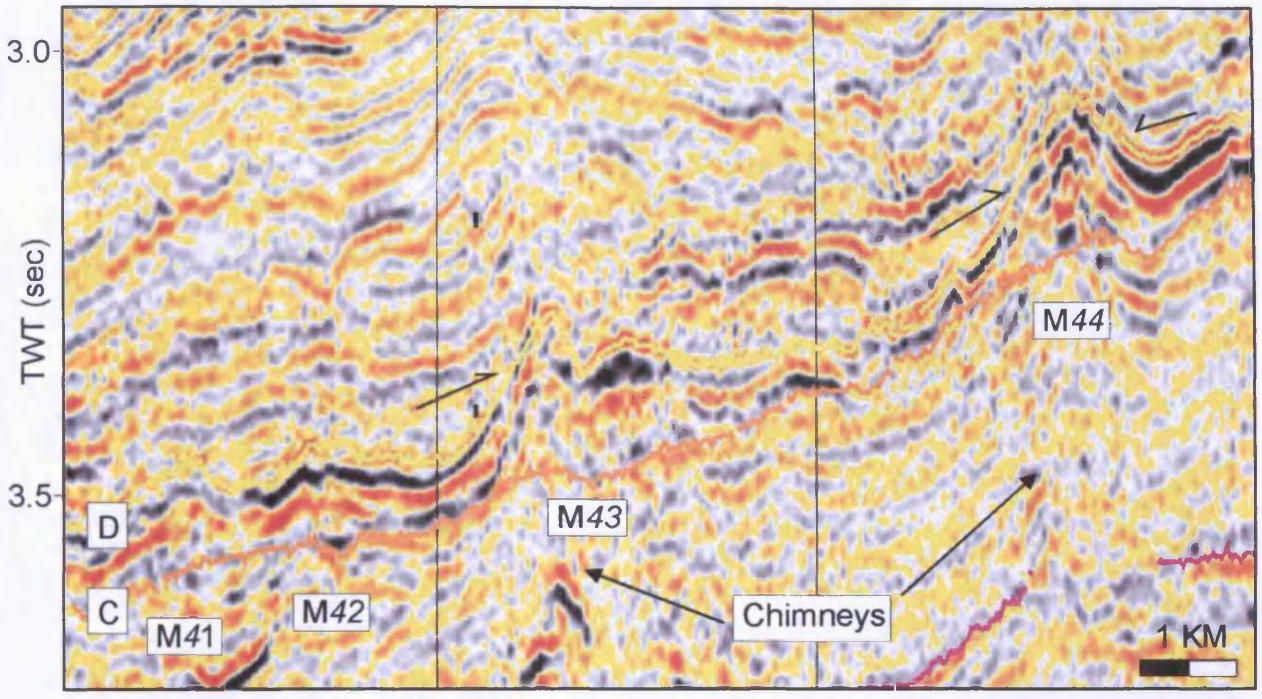

Fig. 6.20 Seismic section showing the cross-sectional geometry of M41-4. See Fig. 6.17 for line location.

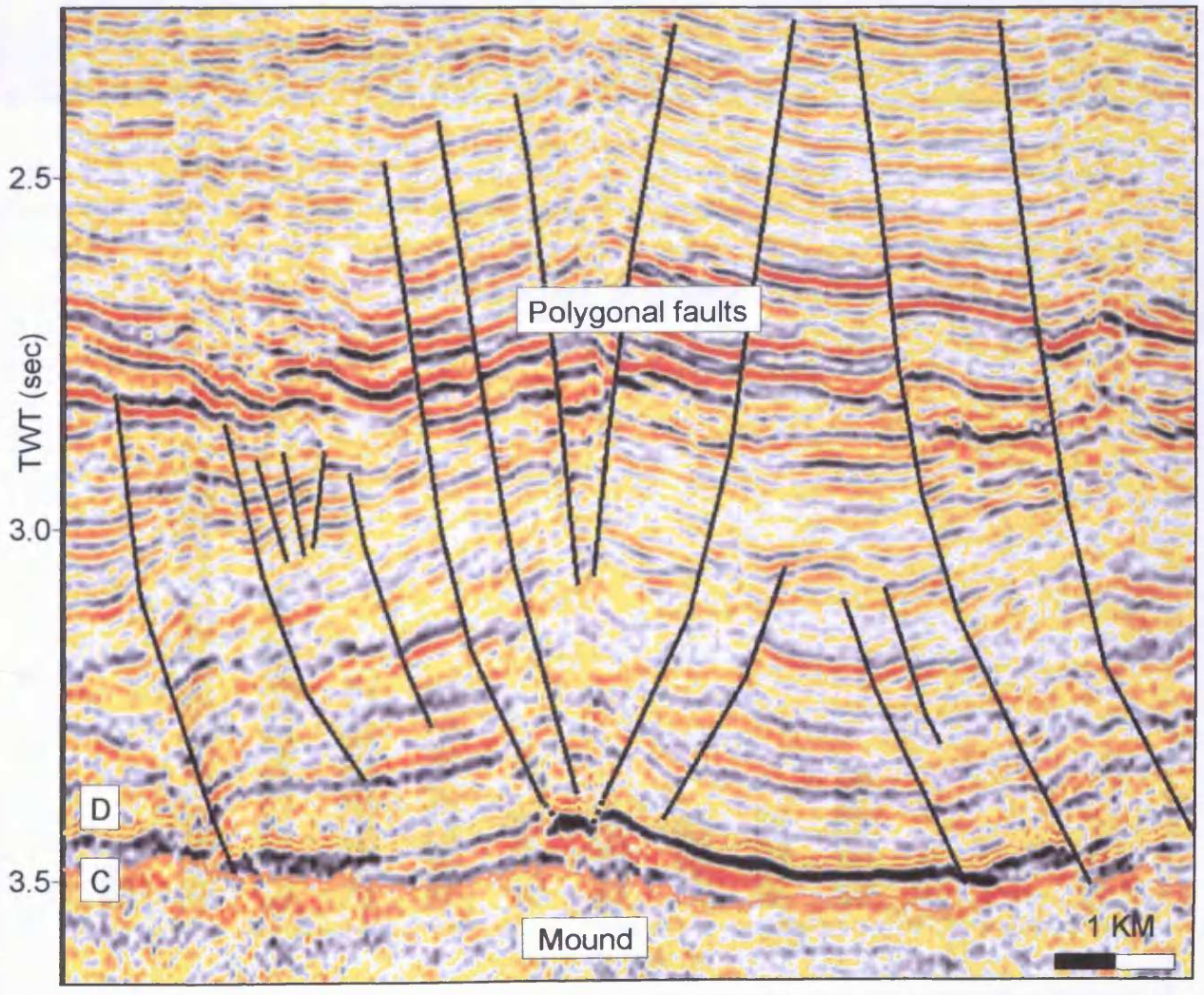

Fig. 6.21 Seismic section showing preferential dip of polygonal faults in the post-D successions towards a central mound structure. Some faults offset the top mound reflection. See Fig. 6.22 for line location.

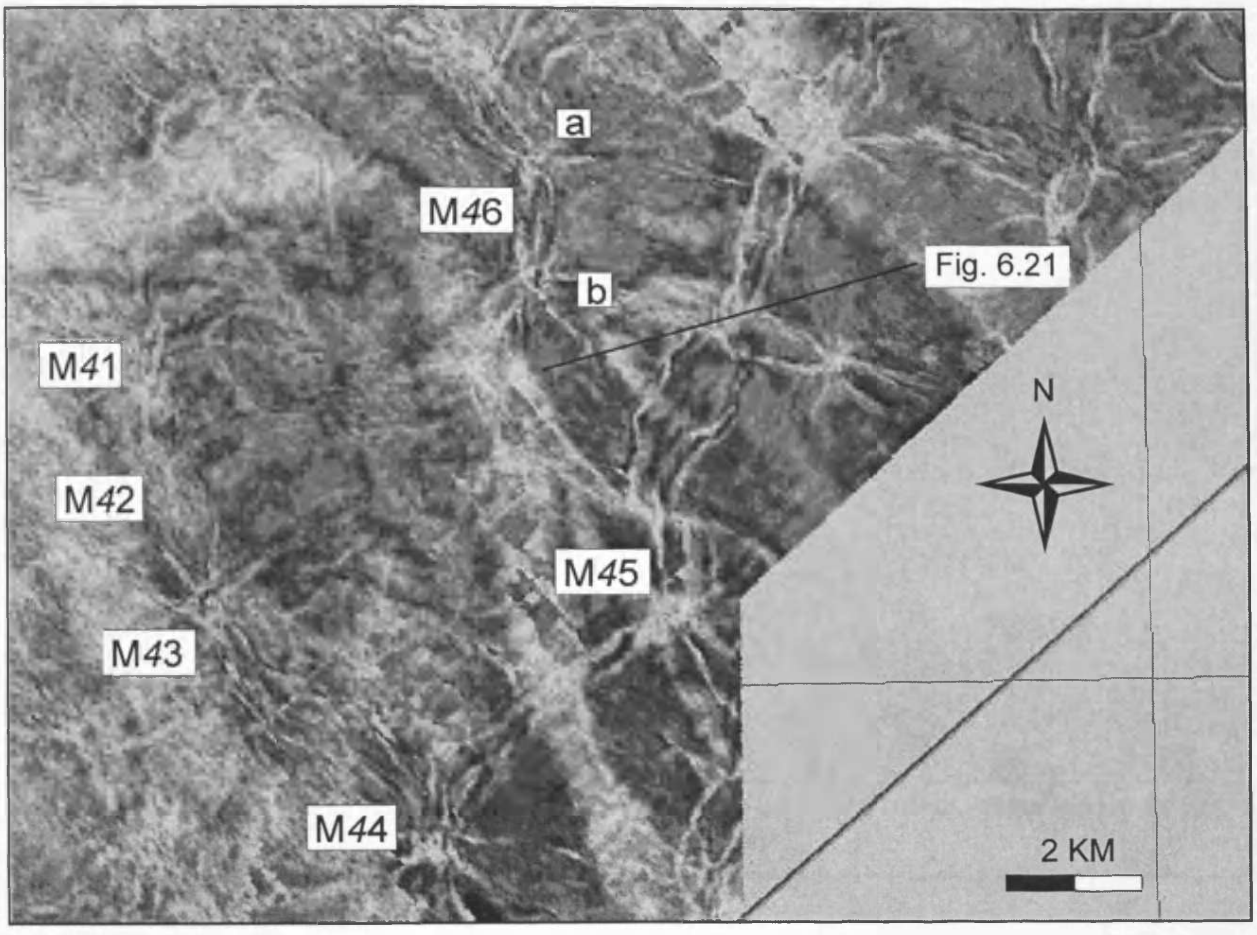

Fig. 6.22 Amplitude map of horizon D showing the polygonal fault pattern formed in the strata overlying the mound structures. The development of mound structures is interpreted to have influenced the geometry of the fault pattern. Note line location for Fig. 6.21.

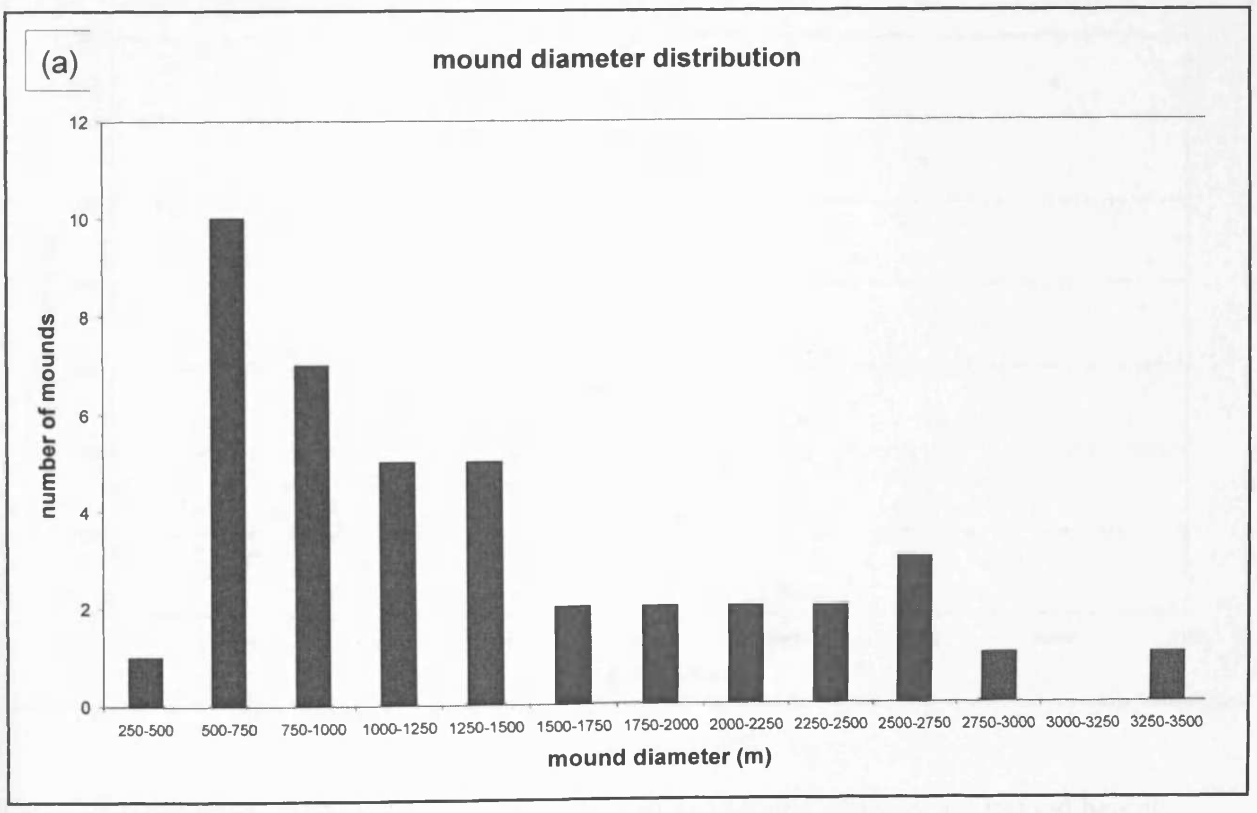

Fig. 6.23 (a) Mound diameter distribution. N=41.

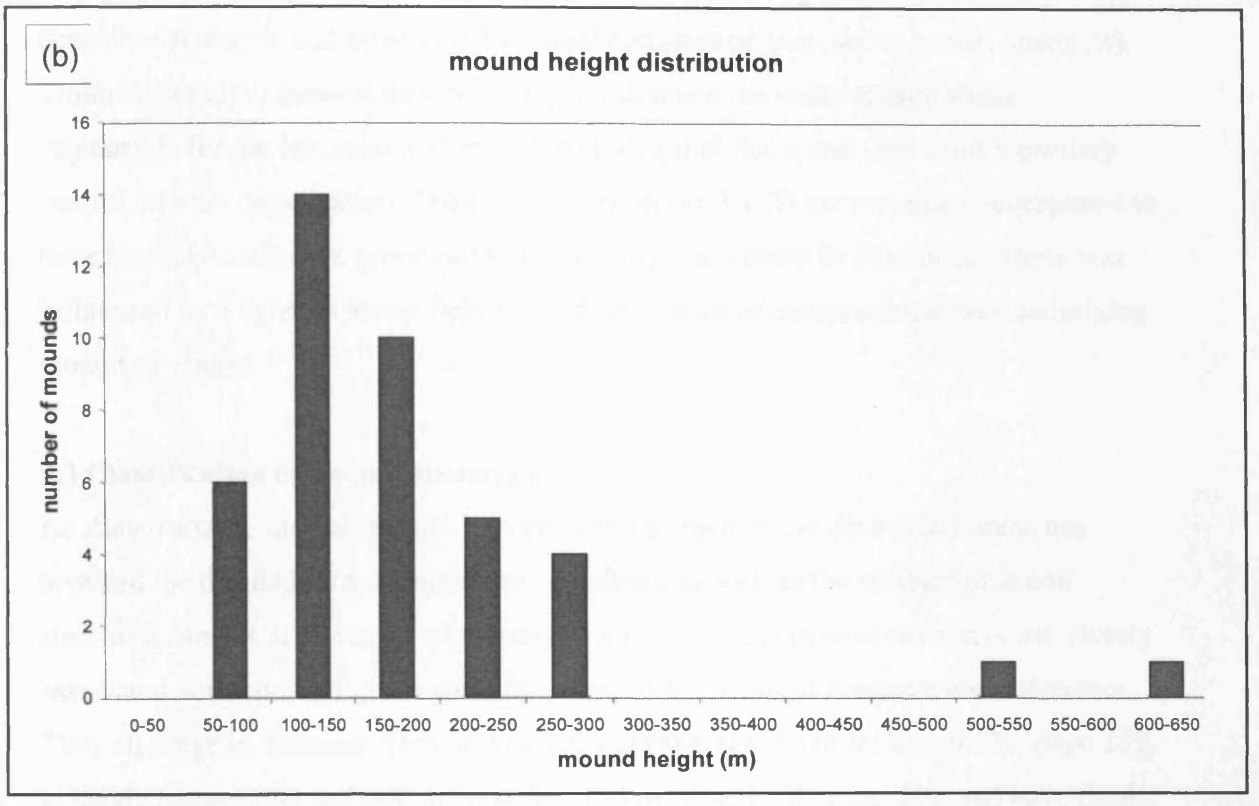

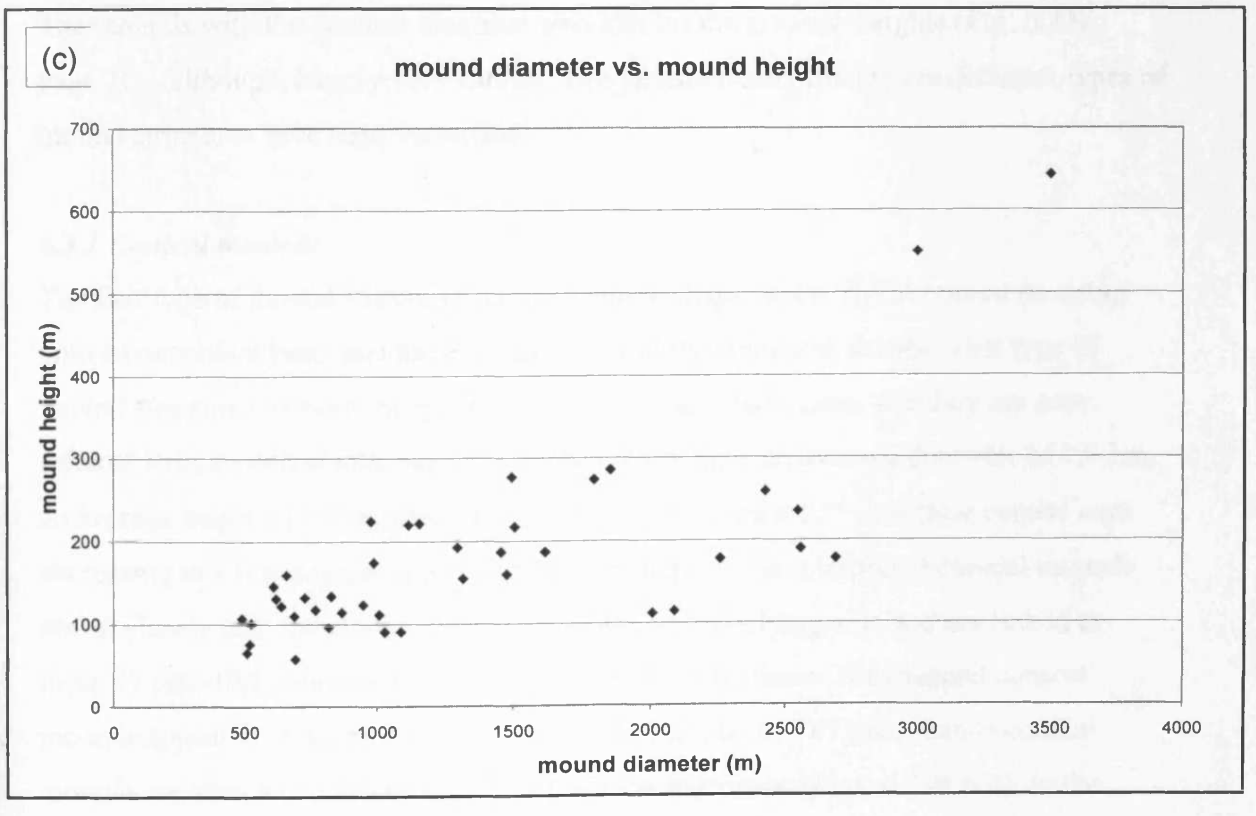

Fig. 6.23 (continued) (b) Mound height distribution. (c) Mound diameter vs. mound height. N=41.

Cartwright, 1994). These include growing shale and salt diapirs, active tectonic faults, depositional slopes, and areas of differential compaction (e.g. above buried channels). Common for all of these is that they locally influence the radial tensile stress responsible for the initiation and growth of polygonal faults and thus exert a primary control on their organisation. The pattern seen in the T4 3D survey area is interpreted to have formed because the propagation of the polygonal faults in the Eocene strata was influenced by a external stress field formed as a result of compaction above underlying mound structures.

6.3 Classification of mound structures

As shown above, careful seismic interpretation in each of the case-study areas has revealed the detailed three-dimensional geometry as well as the stratigraphic and structural context of a number of mound structures. These mound structures are closely associated with underlying sill complexes and share many of the same characteristics. They all range in diameter from 500 to 3500 m (average: 1348 m; Fig. 6.23a, page 25), in height between 60 and 640 m (average: 178 m; Fig. 6.23b, page 26), and have flank dips of 6-26° near the central axes, decreasing to a few degree towards their margins. The mounds with the greatest diameter also exhibit the greatest heights (Fig. 6.23c, page 26). Although, largely very similar, two geometrically distinctive different types of mound structures have been identified.

6.3.1 Conical mounds

The first type of mound structures have a conical shape, show bi-directional downlap onto a concordant base, and have circular to slightly elongated shapes. This type of mound structure has been interpreted in all four case-study areas and they are here referred to as a ***conical mounds*** (Fig. 6.24a). They have an average diameter of 1.5 km, an average height of 190 m, and have flank dips between 6-23° near their central axes decreasing to a few degrees towards their peripheries. The interpreted conical mounds are all closely associated with sill tips or crests on underlying sills and are linked to these by pipe-like zones of discontinuous seismic reflections. The mapped conical mounds appear at different discrete stratigraphic levels. In T67 the mounds conical mounds are seen a two discrete levels within the Paleocene (Figs. 6.3 & 6.4). In the Solsikke survey area conical mounds are also seen within the Paleocene (Fig. 6.8),

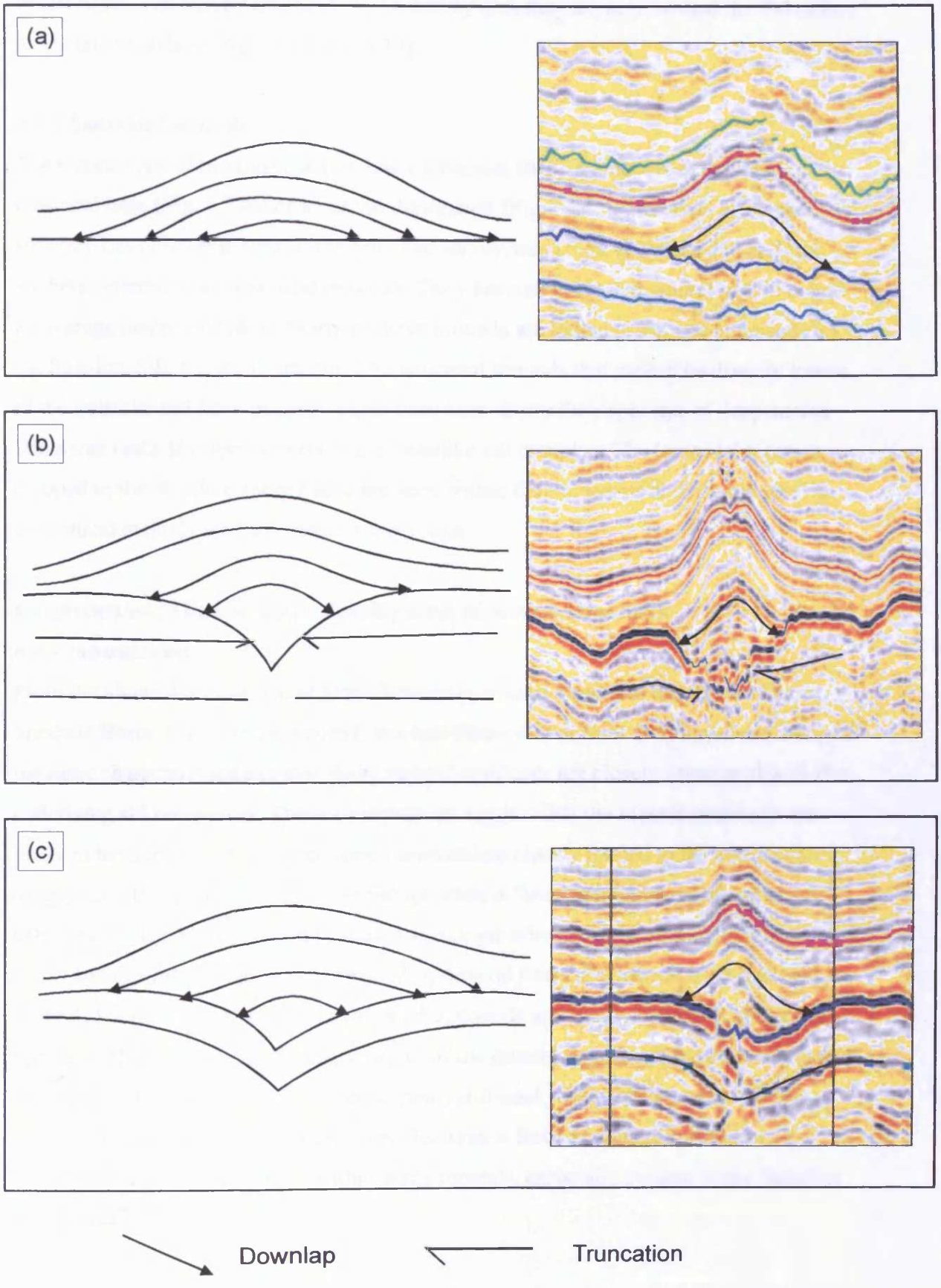

Fig. 6.24 Schematic and seismic examples of different classes of mound structures. (a) Conical mound. (b) Lensoidal mound above erosional base. (c) Lensoidal mound above central depression.

whilst in the T38 survey area and the T4 survey area they are seen around the Paleocene to Eocene boundary (Figs. 6.12 and 6.19).

6.3.2 Lensoidal mounds

The second type of mound structure has a lensoidal shape and downlap onto an erosional base (Fig. 6.24b) or a central depression (Fig. 6.24c). This type of mound structure has only been seen in the Solsikke survey area (Figs. 6.9 and 6.10) and they are here referred to as ***lensoidal mounds***. They have an average diameter of 980 m and an average height of 224 m. Many of these mounds are linked to sill tips and crests on the Solsikke Sill, but some are not. The lensoidal mounds that cannot be directly linked to the Solsikke Sill have in many cases been seen above the upper tips of deep-seated faults that reach the deeper parts of the Solsikke sill complex. The lensoidal mounds mapped in the Solsikke survey area are seen within the Paleocene at the same level as the conical mounds mapped in this survey area.

6.4 Discussion: The kinematic development of mound structures

6.4.1 Introduction

From the above description and classification of mound structures seen in the Faeroe-Shetland Basin, Møre Basin, and NE Rockall Basin it is evident that they share many of the same characteristics and that these mound structures are closely associated with the underlying sill complexes. These observations suggest that the mound structures are likely to have formed due to a common mechanism closely related to the emplacement of igneous sill complexes. One essential question is "are the mounds intrusive or extrusive ?". They have been interpreted as extrusive by previous authors (see section 6.4.2) and this interpretation is supported by several lines of evidence arising from this study: (1) Within individual survey areas the mounds are found at one or two discrete horizons. This supports an extrusive origin of the mounds because if they were intrusive they would most likely have intruded at many different stratigraphic levels. (2) The interpretation of the mounds as extrusive features is further supported by the clear downlap of internal reflections within some mounds, especially evident in the Solsikke survey area.

In the following sections the described mound structures are compared with previously described similar structures and their origin and implications are discussed. The

implications of mound structures in relation to the timing of intrusive events will be discussed in section 7.4.

6.4.2 Seismic and field analogues

Mound structures similar to those described in the previous section have previously been described from 2D and 3D seismic data from basins along the NE Atlantic margin (Joppen & White, 1990; Skogseid et al., 1992; Bell & Butcher, 2002; Davies et al., 2002; Svensen et al., 2004) and it has recently been proposed that field analogues exist in the Karoo, South Africa (S. Planke, pers. comm.; Svensen et al., 2004). These previously interpreted seismic and field analogues are described and compared with those interpreted in this study in the following. The geometrical characteristics, stratigraphic context, and proposed origins of these previously described mound structures, as well as those interpreted in this study are summarised in Table 6.1.

6.4.2.1 Seismic analogues

2D seismic based studies from the Rockall Trough (Joppen & White, 1990) and Vøring Basin (Skogseid et al., 1992; Fig. 6.25) describe features very similar to the lensoidal mound structures described in the Solsikke survey area. The geometries of these mound structures are not described in detail but the published seismic examples show that they are elliptical in cross-section and associated with underlying high amplitude reflections interpreted as igneous sills. The mounds described by Joppen & White (1990) and Skogseid et al. (1992) are linked to the tips of underlying sills by vertical zones of disturbed seismic reflections that have been interpreted as dykes. Skogseid et al. (1992), for example, interpreted these elliptical features as dyke fed volcanic vents or craters that probably contain an igneous component and formed at the seafloor.

Hodges et al. (1999) interpreted a number of mound structures on top of the lava plateau in the T65/66/67 3D seismic survey areas of the northern Faeroe-Shetland Basin that are very similar to the two M67b mounds interpreted in the T67 survey area (Fig. 6.26). They suggested that they were small volcanic feeder cones that fed lava flows.

Davies et al. (2002) examined nine conical mounds of unknown origin within the T61/62 3D seismic survey area of the central Faeroe-Shetland Basin, located approximately 20 km north of the T4 3D seismic survey area (Figs. 6.1 & 6.27). The mound structures that these authors describe are conical in shape, measure 1-2.7 km in diameter, are 70-160 m high, and have flank dips of 5-10° decreasing to 1-2° towards

Study	Data type	Location	Shape	Diameter	Height	Flank angles	Age	Fill	Origin
Joppen & White (1990)	2D seismic	Rockall Trough					L. Paleocene		Dyke fed
Skogseid et al. (1992)	2D seismic	Vøring Basin	Elliptical/ conical				W/in U. Paleocene seds.	Partly igneous (diff. compact.)	Dyke fed volcanic vents or craters formed at the seafloor
Hodges et al. (1999)	3D seismic	FSB (T65/66/67)	Conical				E. Eocene	Igneous	Volcanoes
Davies et al. (2002)	3D seismic	FSB (T61/62)	Conical	1-1.7 km	50-300 m	5-16° (1°)	54.9-54.6 Ma	Igneous	Dyke-fed submarine volcanoes
Bell & Butcher (2002)	3D seismic	FSB (T67)	Conical with circular or elliptical shapes	< 2 km	> 100 m	< 15° (4°)		Basaltic rock or heavily-cemented clastic materials	Submarine hyaloclastite-dominated vents
Svensen et al. (2004)	2D & 3D seismic	Møre and Vøring Basins	Eye-shaped Dome-shaped Craters				55.0-55.8 My Some Paleocene in the Møre Basin		Hydrothermal vents
T67	2D & 3D seismic	FSB (T67)	Conical (M67a)	800-1300 m	90-195 m	3-10°	Paleocene	Sedimentary	
			Conical (M67b)	1.5-1.8 km	~275 m	8°	L. Paleocene	Partly magmatic	
Solsikke	3D seismic	Møre Basin (T38)	Conical (Mssa)	500-1300 m	65-150 m	6-15° (2-3°)	Paleocene	Sedimentary	
			Lensoidal (Mssb)	500-1200 m	60-225 ms	8-15° (3-7°)	Paleocene	Sedimentary	
T38	3D seismic	NE Rockall Basin	Conical	3-3.5 km	550-640 m	10-11°	L. Paleocene-E. Eocene	Sedimentary	
T4	3D seismic	FSB (T4)	Conical	1-2.7 km	70-160 ms	5-10° (1-2°)	54.9-54.6 My	Partly magmatic	

Table 6.1 Summary of the geometrical characteristics, stratigraphic context, and proposed origins of previously described mound structures, as well as the ones interpreted in the case-study areas.

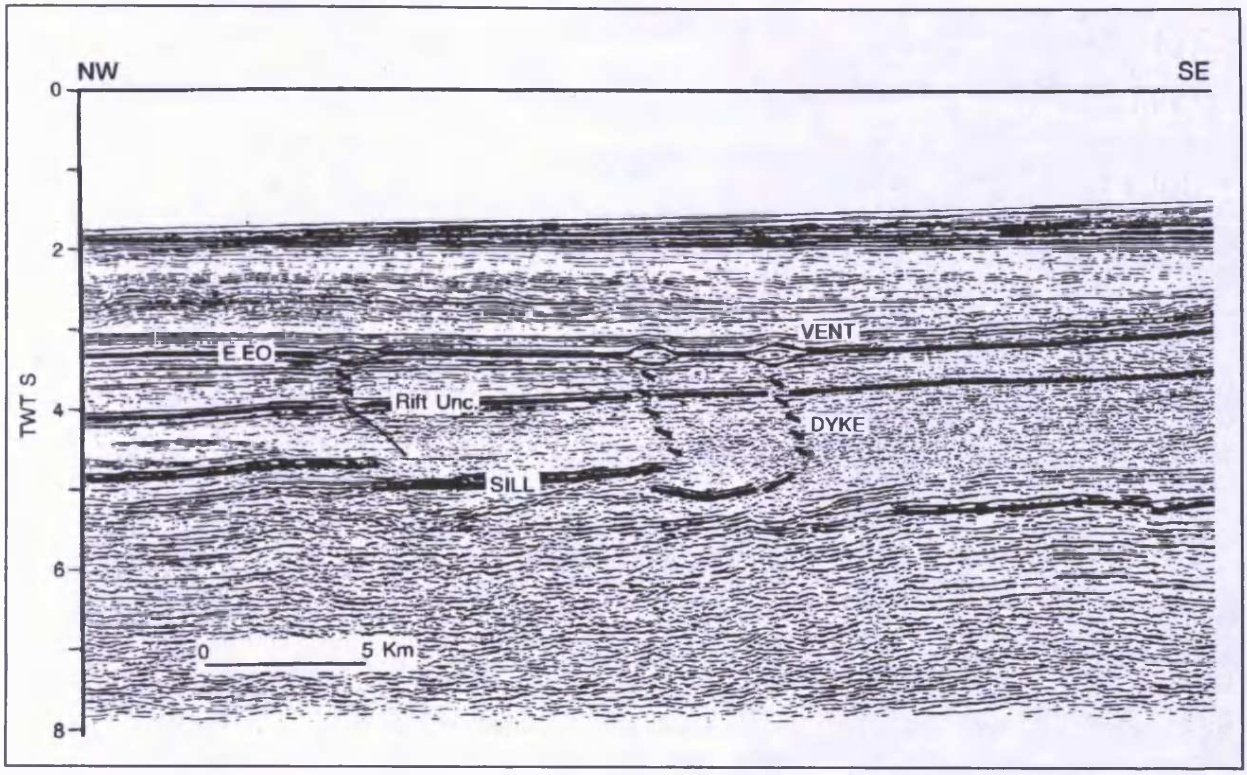

Fig. 6.25 Lensoidal mound structures ('eye-structures') interpreted above sills in the Voering Basin (Fig. 6.1) by Skogseid et al. (1992).

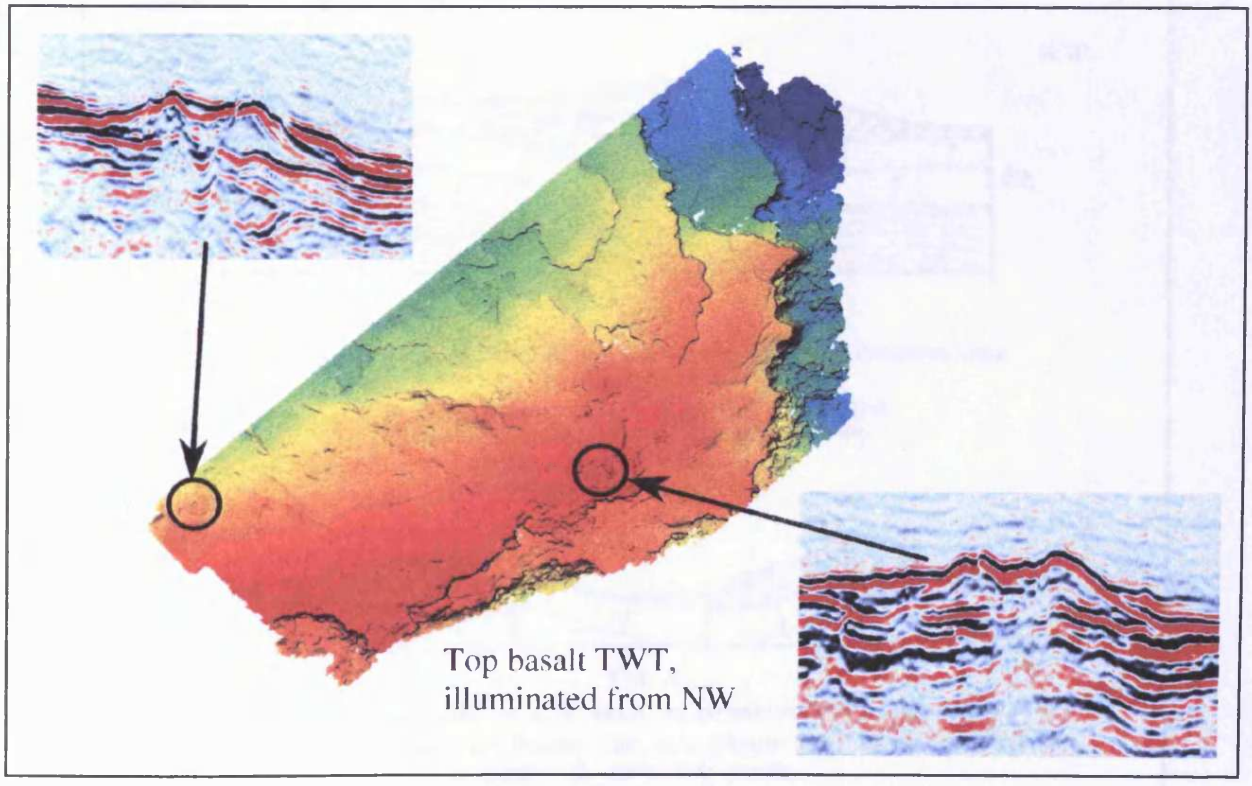

Fig. 6.26 Mound structures interpreted by Hodges et al (1999) on the top of the lava plateau in the T65/66/67 3D seismic survey area in the Brendan's Dome area (Fig. 6.1) in the northern part of the Faeroe-Shetland Basin.

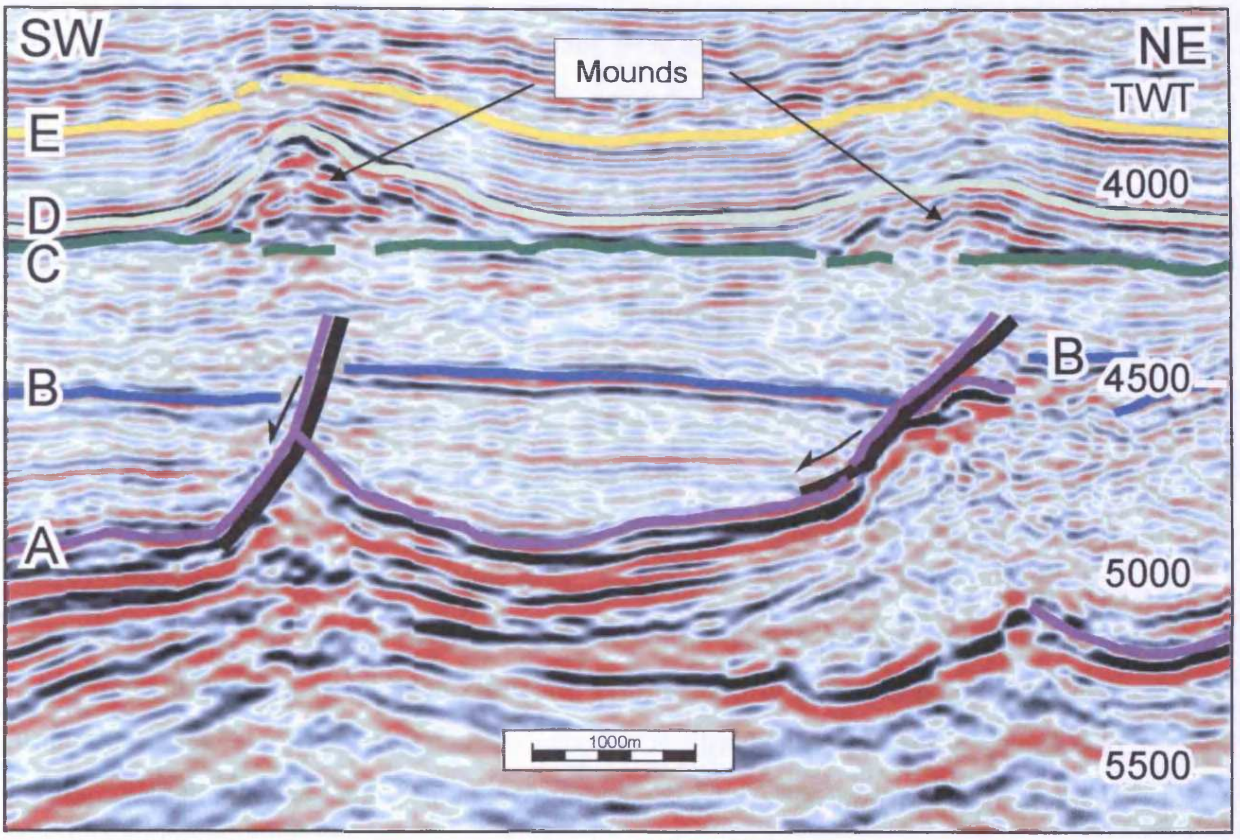

Fig. 6.27 Mound structures interpreted by Davies et al. (1999) in the T61/62 3D seismic survey area (Fig. 6.1), located immediately north of the T4 3D seismic survey area.

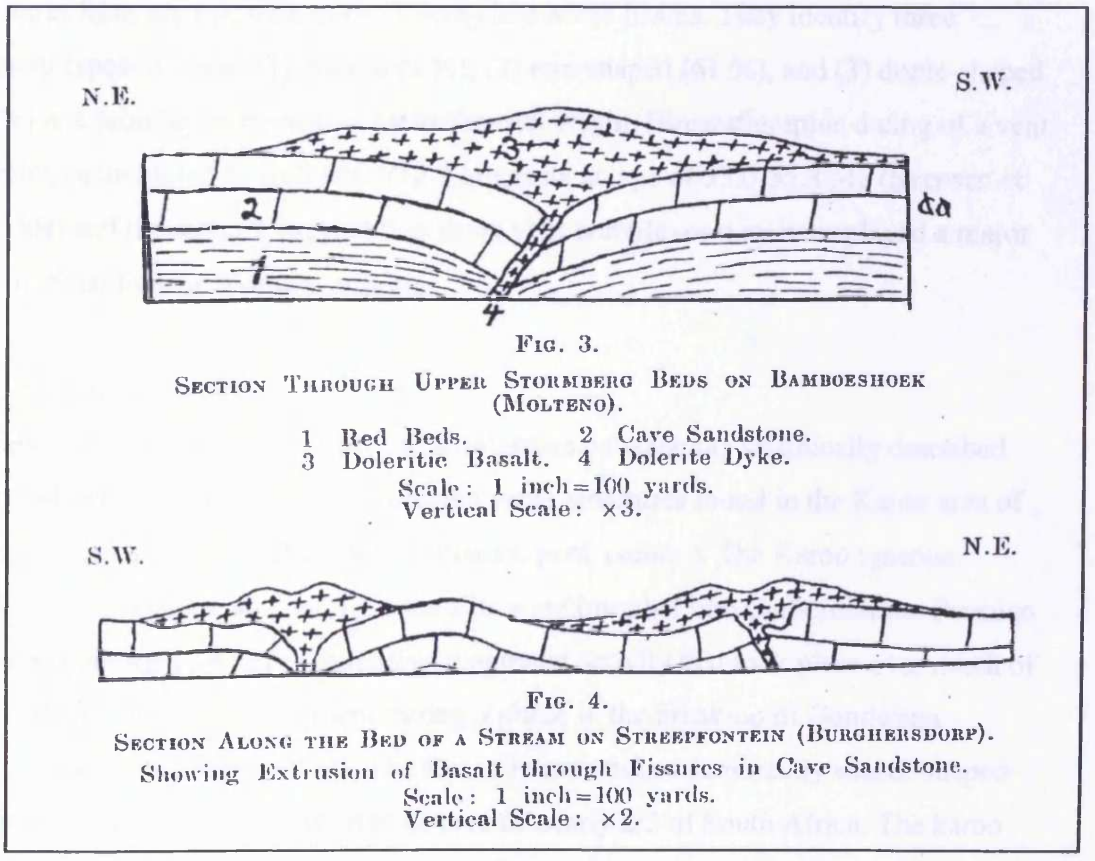

FIG. 3.

SECTION THROUGH UPPER STORMBERG BEDS ON BAMBOESHOEK (MOLTENO).

1 Red Beds. 2 Cave Sandstone.
3 Doleritic Basalt. 4 Dolerite Dyke.
Scale: 1 inch = 100 yards.
Vertical Scale: ×3.

FIG. 4.

SECTION ALONG THE BED OF A STREAM ON STREEPFONTEIN (BURGHERSDORP).
Showing Extrusion of Basalt through Fissures in Cave Sandstone.
Scale: 1 inch = 100 yards.
Vertical Scale: ×2.

Fig. 6.28 Schematic illustrations from Gevers (1928) showing the cross-sectional geometry of mound structures of the western Stormberg. These mounds structures are considered to be outcrop analogues of the mound structures interpreted on 3D seismic data.

their margins. They proposed that the mounds were accreted onto the seabed, directly above the tips of igneous dykes, between 54.9 and 54.6 Ma. They used the highly organised internal mound structure, consisting of bulbous layers arranged concentrically around a central vent, along with a clear vertical link between the mounds and the underlying sills and dykes, as well as modern seafloor analogues to argue that they represent pillowed basaltic lava and hyaloclastite mounds that were fed by dykes extruding onto the seafloor.

The mound structures interpreted in the T67 survey area in this study have previously been described by Bell & Butcher (2002). They found that the mounds were conical with circular or elliptical shapes, less than 2 km in diameter, and > 100 m high. These authors suggested that mounds formed at the contemporaneous seafloor as a result of sill emplacement. They suggested that 'seismic chimneys' seen between terminations of sills and the base of some of the mounds were formed as a result of vertical fluid migration. They interpreted the mounds linked to shallowly intruded sills as submarine hyaloclastite-dominated vents whilst the mounds linked to sills emplaced at greater depth were interpreted as sedimentary-hydrothermal mounds.

Very recently Svensen et al. (2004) have identified and characterised > 700 vent structures from seismic data in the Vøring and Møre basins. They identify three different types of vents: (1) craters (9 %), (2) eye-shaped (61 %), and (3) dome-shaped (30 %) and propose an explosive hydrothermal origin. Biostratigraphic dating of a vent complex encountered in well 6607/12-1 suggests an age of 55.0-55.8 Ma (Svensen et al., 2004) and the authors suggest that these vent complexes may have played a major part in initial Eocene global warming.

6.4.2.2 Field analogue

Recently, attention has been drawn to similarities between the seismically described mound structures and large-scale volcanic vents structures found in the Karoo area of South Africa (Svensen et al., 2004; S. Planke, pers. comm.). The Karoo igneous province is Jurassic in age and igneous sills were intruded into Carboniferous-Permian sediments during a period of extensive magmatic activity that took place over much of the southern African subcontinent during a phase in the break-up of Gondwana (Chevallier & Woodford, 1999). The Karoo intrusives are dominantly saucer-shaped dolerite sills and now crop out over an area of nearly 2/3 of South Africa. The karoo vent structures occur in the late Triassic to Early Jurassic (~195 Ma) fluvial Elliot Fm

and the Middle Jurassic (~180 Ma) eolian Clarens Fm and were first described in detail by Gevers (1928). Their geometry is not described in detail but schematic illustrations (Fig. 6.28) suggest that they adopt lensoidal shapes 150-300 m in diameter and up to 100 m in height. They are filled with indurated fine-grained sandstone, volcanic mud, and basaltic and doleritic lava, and thought to have formed in response to intrusion of igneous sills. They are erosionally resistant relative to the surrounding rocks and appear as elevated structures in the landscape (Fig. 6.29).

6.4.3 New insights from 3D seismic data

From the above it is clear that the mounds described in this study are geometrically and morphologically very similar to the seismic examples previously described at similar stratigraphic levels in basins along the NE Atlantic margin (Fig. 6.1 and Table 6.1). However, the detailed interpretation presented in this chapter of these mound structures in the T67, Solsikke, T38, and T4 3D seismic survey areas, has revealed a number of observations not previously recognised. These observations provide valuable insight into the origin of the mounds. They include:

- Two types of mounds (conical (Fig. 6.24a) and lensoidal (Fig. 6.24b and 6.24c)) have been recognised and described. These two informally defined classes of mound structures are distinctively different, but they may occur within the same stratigraphic interval within a few kilometres of each other.
- The mounds downlap onto discrete horizons and can in some cases be seen to be onlapped by overlying strata (e.g. Figs. 6.4).
- Mounds may be developed at more than one discrete stratigraphic level within a survey area (e.g. T67 survey area)
- Some mounds have strikingly different acoustic properties than the surrounding strata (Figs. 6.4 and 6.15), but the majority do not (Figs. 6.3, 6.8, 6.9, and 6.12).
- Most mounds are linked to underlying sills by vertical zones of discontinuous seismic reflections (Figs. 6.4, 6.8, 6.19, 6.20), but some mounds show no apparent link to underlying sills (Figs. 6.9 and 6.10).
- Some mounds are located directly above the upper tips of deep-seated faults and at fault intersections rather than above underlying sills (Figs. 6.9, 6.10, and 6.11).

Fig. 6.29 Photographs from the Karoo, South Africa, showing outcropping mound structures (Witkops) of the kind described by Gevers (1928). (a) Witkop I. (b) Witkop III.

- Lensoidal mounds have either truncational bases (Fig. 6.24b) or downlap onto a underlying central depression (Fig. 6.24c).
- Some mounds show an organised mounded internal geometry (e.g. Figs. 6.3, 6.9, 6.15), but many appear to have a chaotic internal geometry (Figs. 6.4, 6.12).
- The crests of the mounds may be offset 10s of metres by polygonal faults (Figs. 6.9 and 6.21).

Considering their abundance, clear association with igneous complexes, and high preservation potential it seems reasonable to expect that field analogues to the mound structures occur in large volcanic provinces such as the Karoo. The vents described by Gevers (1928) and subsequently by others (S. Planke, pers. comm.; Svensen et al., 2004) are erosional remnants of larger structures and it is, therefore, not possible to directly compare these with the seismically resolved structures. However, Bell & Butcher (2002) alluded to the possibility that some mounds are of hydrothermal and sedimentary origin rather than magmatic in composition, which corresponds well with the compositional range found within the Karoo vents and thus supports an interpretation of these as analogues.

Based on the above detailed interpretation of mounds within the T67, Solsikke, T38, and T4 survey areas and the new insights this has provided, as well as previous seismic studies, the possible origins of these mounds structures are discussed in the following sections.

6.4.4 The origin of mound structures

6.4.4.1 Introduction

The apparently most well resolved mound structures show clear bi-directional downlap of internal reflections onto discrete horizons (e.g. Figs. 6.6b, 6.11 & 6.12), have organised internal geometries (Fig. 6.22), and are onlapped by overlying strata (Fig. 6.7). As Davies et al. (2002) convincingly argued and as it was further argued in section 6.4.1 this is critical evidence for an interpretation of the mounds as constructional rather than erosional and as extrusive rather than intrusive bodies. The lack of internal reflections within some mounds could relate to lack of seismic resolution and it does not, therefore, exclude the possibility that the smaller or less well imaged mounds exhibit similar highly organised and downlapping internal reflection geometries. The

most fundamental properties of the mound structures thus seem to be that they are extrusive constructional bodies that show some degree of internal organisation and that are linked to the emplacement of igneous sill complexes. Because they are extrusive and linked to the intrusion of underlying sill complexes their stratigraphic relationship can be used to constrain the timing of intrusion with the age of the basal mound horizon marking the approximate age of sill intrusion. In the case of T67 use of mounds to constrain the timing allows the conclusion to be drawn that there are two episodes of sill intrusion. As already mentioned, the implications of mound structures for the timing of intrusion in the case-study areas will be discussed in detail in section 7.4.

The main remaining unknown associated with the mound structures described here is how best to constrain the composition of the mounds and the nature of their relationship with the underlying sill complexes.

Previous authors (Davies et al., 2002; Hodges et al., 1999; Joppen & White, 1990; Skogseid et al., 1992) have generally favoured a magmatic origin of the mound structures. Their interpretations have largely been based on an interpretation of the underlying seismic chimneys as feeder dykes due to their spatial relationship with underlying sills, slightly increased acoustic impedance, and vertical, cross-cutting nature. Davies et al. (2002) further argued that their observations; (1) that the acoustic impedance of the mounds was increased and (2) that the mounds exhibit an organised internal geometry suggests a magmatic rather than sedimentary composition. These authors also drew attention to the similarity with modern seafloor analogues that were originally interpreted as small dyke fed magmatic seamounts (Smith et al., 1995). However, the magmatic seamounts interpreted by Smith et al. (1995) were since re-interpreted as secondary features fed by lava tubes or channels (Smith & Cann, 1999) and thus form poor analogues for the extrusive mound structures they interpreted in the Faeroe-Shetland Basin.

The interpretation of mound structures in this chapter has revealed that not all mounds are linked to underlying sills by chimneys and not all chimneys display a significant increase in acoustic properties. It also shows that, most mounds, like the majority of those shown in Davies et al. (2002), do not display an increase in acoustic impedance. Further, an organised internal geometry does indeed point towards a constructional and extrusive origin of the mounds, but it does not exclude the possibility that they are sedimentary. Many examples, albeit on a smaller scale, of sandstone

volcanoes (e.g. Gill & Kuenen, 1958) show a clearly layered internal geometry that if formed on a larger scale would have the potential to be imaged by seismic data. The central depression seen underlying some lensoidal mounds (e.g. M*ss*b2) suggests collapse due to removal of existing material rather than intrusion of new material, which further discourages an interpretation of all mounds as igneous and thus purely comprised of added material. In addition, polygonal faults seen in the T4 survey area developed in the strata overlying the mounds occasionally offset the top of the mounds by several 10s of metres, which also seems incompatible with an entirely magmatic composition of the mounds as the development of polygonal faults is limited to fine-grained sedimentary succession (Cartwright & Dewhurst, 1998; Cartwright et al., 2003). These new observations encourage a re-interpretation or at least modification of the origin of both the chimneys and the mounds.

6.4.4.2 Origin of seismic chimneys

Where seen, the seismic chimneys are pipe-like (Fig. 6.8b) to slightly elongated (Fig. 3.58), and in some cases exhibit a slightly higher acoustic impedance than the surrounding strata (e.g. underlying M*4*1, Fig. 6.19). They appear between sill tips or crests on sills and the base of the mound structures, and do not extend upwards above the mounds or downwards below the sills. Because these chimneys are consistently located above sill tips and crests in the sills and link to the base of the mound structures it seems unlikely that they are seismic artefacts. The observation also implies that the chimneys were active at the time of intrusion and are now inactive. Possible interpretations of such vertical seismic chimneys are gas chimneys (Schroot & Schüttenhelm, 2003; Løseth et al., 2003), igneous dykes (Jenyon, 1987), and fluid conduits (Gay et al., 2003). Vertical features, such as these, are generally poorly imaged by seismic data and this makes it difficult to distinguish between them.

The chimneys resemble *gas chimneys* described elsewhere including places where gas seepage at the seafloor has lead to the development of carbonate mounds (Schroot & Schüttenhelm, 2003; Løseth et al., 2003). However, gas chimneys are transient features that disappear when gas migration terminates. The features imaged by the seismic data formed in the early Paleogene and it seems unlikely that any gas would still be left in the system if gas migration was indeed the cause of the features.

Igneous dykes are abundant in igneous provinces where they occur as laterally extensive features 10s of kilometres in length and several metres wide (Bell, 1984;

Chevallier & Woodford, 1999). The seismic chimneys are clearly linked to the igneous sills and some do display an increase in acoustic impedance as would be expected if magmatic in origin. The chimneys are only of limited lateral extent and if of magmatic origin would be better described as igneous pipes or diatremes. Based on their seismic properties and association with the igneous sills an interpretation of some of these as igneous pipes seems reasonable and this further suggests that some of the mounds are submarine volcanoes as previously proposed by most authors.

As mentioned earlier an igneous origin cannot apply to all the chimneys or mounds because these exhibit characteristics that do not concur with such an interpretation. A third interpretation of the seismic chimneys is that they represent *paleo fluid conduits*. Intrusion of igneous material into water-saturated sediments is known to promote large-scale hydrothermal systems (e.g. Einsele et al, 1980; Cathles et al., 1997). Large amounts of pore water may be mobilised surrounding igneous sills and subsequently expelled at the seafloor as a result (Einsele et al., 1980; Einsele, 1982). From drill sites in the Guaymas Basin, Gulf of California, for example, it has been estimated that a 30-40 m thick sill covering an area of just 1km^2 may lead to a total expulsion of 30-40 × 10^6 m^3 of pore water, capable of feeding a constant discharge of 10 L/s for a period of a 100 years (Einsele et al., 1980; Einsele, 1982). Heating of pore water by sill intrusion can significantly accelerate the dissolution of certain sediment components, and the mobilised hydrothermal fluid is thus likely to be enriched in elements such as calcite and zeolite, which will be partly precipitated and form a hydrothermal deposit at the seafloor upon contact with salt water (Einsele et al., 1980). The passage of these enriched hot hydrothermal fluids through sediments within fluid pathways could influence their later cementation (Bradley, 1965) and thus acoustic impedance. The forcible upward migration of the large amounts of fluids released in response to sill intrusion would most likely promote remobilisation of sediments in the vicinity of the sill and fluid conduit and subsequent extrusion and build-up of these sediments on the seafloor. The upward migration of fluids is focused at sill tips and Einsele (1982) suggested that shallower sills can act as barriers for fluids rising from deeper sills resulting in focused migration at the tips of the shallower sill.

The cooling time of an igneous sill and thus the time period over which a hydrothermal system can be sustained primarily depend upon the permeability of the intruded sediments and the thickness of the intrusion (Cathles et al., 1997). Cooling of sills intruded into wet sediments happens mainly through convection and will be

completed in at most a few tens of thousands of years, even if the intrusion is large (Cathles et al., 1997). Due to the limited time period in which the hydrothermal system will be active, extrusion of hydrothermal fluids and any remobilised sediments associated with the emplacement of a sill, through a single pulse, will be confined to a very limited stratigraphic interval. From the above it seems that an interpretation of the seismic chimneys as hydrothermal fluid conduits and of the mounds as remobilised sedimentary is compatible with their seismic appearance. This interpretation is in agreement with Bell & Butcher (2002) and Svensen et al. (2004).

6.4.4.3 Interpretation of case-study mound structures

Based on the above it is suggested that some of the mounds described in this chapter are sedimentary structures, formed as a result of sediment remobilisation by hydrothermal fluids and subsequent extrusion onto the paleo-seafloor, whilst others are believed to be entirely or at least dominantly igneous in origin as proposed by previous authors. The majority of the mounds do not exhibit significantly greater acoustic impedance than the surrounding strata, which would be expected if the mounds were comprised of magmatic material, and this suggests that most of the mound structures are remobilised sedimentary rather than igneous in origin.

The M*67*a, M*ss*a, M*ss*b, and M*38* mounds exhibit similar acoustic properties to the surrounding sediments and these are interpreted as sedimentary in origin. The M*67*b mounds and M*4* mounds appear to exhibit a slightly higher acoustic amplitude than the overlying Eocene mud-dominated strata and most likely contain some magmatic material possibly in the form of hyaloclastites. However, although the M*4* mounds are likely to comprise a magmatic component, the observation that the crests of many of these mounds have been offset by polygonal faults suggests that they comprise a significant amount of sedimentary material, as the strength of igneous material would most likely be able to resist the contractional forces responsible for the development of polygonal fault systems.

The suggestion here that the mounds range in composition from sedimentary to igneous is supported by field observations in the western Stormberg, South Africa, where large-scale vents thought to have formed in response to igneous activity expose a range of fills from fine-grained sandstone and volcanic mud to basaltic and doleritic lava (Gevers, 1928). Possible controls upon the composition of the mounds will not discussed in detail, but are likely to include magma viscosity and rate of supply, host

sediment lithology, pore-water volume in the host sediments, degree of sediment consolidation, and depth of intrusion.

6.4.4.4 Fault related mounds

The majority of the interpreted mounds are seen immediately overlying clearly imaged sills, however, there are examples in the Solsikke survey area where mound structures cannot be directly linked to the underlying sill complex, but rather overlie the upper tips of deep-seated faults (Figs. 6.9, 6.12 & 6.13). The above discussion suggested that the mounds are either volcanic or remobilised sedimentary fed either by dykes or hydrothermal conduits. The location of some mounds above fault tips suggests that the faults in these places have acted as conduits either for magma or hydrothermal fluids. As previously mentioned vertical igneous dykes are difficult to image with seismic data, but if magma is intruded along an inclined fault plane the fault plane should appear as a high amplitude event due to a difference in acoustic properties between the host rock and the intruding magma. The E-W and N-S trending fault sets in the Solsikke survey area both have average dips of approximately 30° (section 4.3.2). The fault planes associated with mounds do not exhibit a high acoustic impedance and it thus seems unlikely that magma was ever intruded along these. It is considered more likely that hydrothermal fluids from the deeper parts of the Solsikke sill complex locally utilised the fault planes as conduits and extruded material where the fault plane reached the seafloor. The location of M*ss*b4 (Fig. 6.13) immediately above a clear fault intersection suggests that such a location is particularly favourable for upwards migration of the hydrothermal fluid. This is in agreement with other studies of fluid flow through fractured and faulted sedimentary sequences (Mayo, 1958; Sibson, 1996; Gartrell et al., 2003).

6.4.4.5 Conical vs. lensoidal mounds

It remains to be addressed why some mounds are conical and others lensoidal and why some lensoidal mounds have erosional bases and others do not. Conical mounds are the most common and lensoidal mounds have only been observed in the Solsikke survey area in this study. However lensoidal mounds have previously been described from the Vøring and Møre Basins where they were interpreted to have adopted this form due to differential compaction of a relatively harder extrusive material (Skogseid et al., 2002) and most recently, by filling of an explosion crater (Svensen et al., 2004). Stratal

reflections surrounding many of the mounds show clear evidence of differential compaction in the form of thinning across the mound crests and this suggests that the mound material is less compactable than the surrounding host rock. This observation is supported by their high degree of preservation, occasional high acoustic impedance, and in the case of M*ss*b4 (Figs. 6.13 & 6.14) its resistance to the erosional process responsible for the development of the horizon I unconformity. Differential compaction thus seems like a possible explanation for the development of lensoidal mounds. However, the lensoidal mounds interpreted in the case-study area suggest that additional factors were involved in the development of these mounds. Locally (e.g. M*ss*b3; Fig. 6.12) it appears that the lensoidal shape has formed, at least partly, as a result of inflilling of a central depression formed due to collapse following extrusion of material (Fig. 6.24c), whilst in the case of M*ss*b1, 2, and 4 the mounds infill a crater-like depression (Fig. 6.24b), suggesting that these lensoidal structures developed by infill of an explosion crater as recently proposed by Svensen et al. (2004).

Most mounds, interpreted herein, are, however, conical not lensoidal and this could suggest that differential compaction and infilling of depressions is a local and relatively rarely occurring event. Lack of differential compaction can be explained in at least two ways; (1) the extruded mound material is very similar to the surrounding strata so these compact in a similar fashion or (2) the seafloor onto which the mound is extruded is resistant to compaction and compacts evenly underlying and surrounding the mound. The lack of a central depression, whether of the truncational (Fig. 6.24b) or non-truncational type (Fig. 6.24c), has different implications. Development of a truncational base (Fig. 6.24b) probably suggests that the initial stage in the development of these mounds was explosive. Lack of such a basal geometry is thus likely to suggest that the development of these mounds was non-explosive. The development of collapse-related depressions (Fig. 6.24c) underlying some lensoidal mounds most likely suggests that the extruded material was removed from the sedimentary unit immediately underlying the mound, whilst they may not be developed if the extruded material has been mobilsed from a more laterally extensive area.

6.5 Conclusions

- The development of the mound structures described in this chapter is linked to the intrusion of igneous complexes

- The mounds are interpreted to vary in composition from entirely remobilised sedimentary to dominantly magmatic
- The majority of mounds are linked to underlying sill complexes by seismic chimneys that are interpreted as paleo-hydrothermal fluid conduits and to a lesser extent igneous pipes
- The mounds are constructional bodies and extruded onto the contemporaneous seafloor during and immediately following the emplacement of underlying sills
- The mounds can be used to constrain the timing of sill emplacement independent of radiometric dating and the interpretation suggests that several discrete intrusive events took place
- There are two geometrically different types of mound structures: conical and lensoidal
  - Conical mounds may be either magmatic or sedimentary or a combination
  - Lensoidal mounds are entirely or pre-dominantly sedimentary and adopt their shape either due to (1) Differential compaction (2) Collapse of the sedimentary unit between the sill and the seafloor as a result of sediment re-mobilisation and expulsion (3) *In situ* remobilisation of sediments at the seafloor above the feeder pipe or (4) Development of a pockmark prior to sediment extrusion.
- Whether conical or ellipsoidal mounds form is likely to depend upon the lithology of the sill to seafloor interval, the hardness of the seafloor, the composition of the mound and differential compaction surrounding it
- Mound development influences subsequent deposition and compaction
- Controls upon the composition of the mound structures are likely to include magma viscosity and rate of supply, host sediment lithology, pore-water volume in the host sediments, degree of sediment consolidation, and depth of intrusion.
- The Karoo vents are likely to be direct analogues to the mound structures
- Fluids are mobilised along the length of the sill and transported towards the sill tips or highs on the sill
- Hydrothermal fluids are transported over great distances upwards and laterally along fault planes
- Shallower sills may act as barriers for fluids released from deeper sills
- Sedimentary mounds are likely to be indurated due to the close association with hydrothermal fluids

CHAPTER 7: SUMMARY AND DISCUSSION

7.1 Introduction

In this study industry 3D seismic datasets have been used to address the problem of magma transport in the upper crust based on datasets from volcanic basins along the NE Atlantic Margin. Four 3D seismic datasets from three NE Atlantic basins have been made available to this study from industry sponsors (Fig. 1.1); Tranche 67 (northern Faeroe-Shetland Basin; Chapters 3 and 6), the Solsikke survey (Møre Basin; Chapters 4 and 6), Tranche 38 (NE Rockall Basin; Chapters 5 and 6), and Tranche 4 (central Faeroe-Shetland Basin; Chapter 6). These datasets have provided a good coverage of the margin and have allowed for subsurface igneous complexes to be mapped in three-dimensions and at a much greater scale than possible in the field or from 2D seismic data. This has provided much new insight into the geometrical and mechanical properties of igneous complexes and has fulfilled the aims listed in Chapter 1.

Many of the issues addressed in this thesis have already been discussed in relation to the published literature in Chapters 3, 4, 5, and 6 and will not be discussed any further in this chapter. In this chapter the key findings of this study are summarised and compared with the results of previous published studies. Two key themes; (1) the development of saucer shaped sills and (2) the construction of igneous sill complexes are discussed in more detail based on observations made in the different case study areas and the published literature.

7.2 Igneous sill geometries

It is estimated that the NAIP comprises 5-10 million km^3 of intrusive igneous rock (White, 1988) of which at least 4.5-12.5*10^4 km^3 are comprised within igneous sill complexes (cf. Svensen et al., 2004). Based on an estimated average volume of sills in the Solsikke survey area of 2 km^3 this suggests that the NAIP comprises 20,000-65,000 sills. Considering their large distribution both laterally (> 40,000 km^2; Naylor et al., 1999) and vertically (up to 15 km; Larsen & Marcussen, 1992) and thus emplacement into host sediments of varying lithology and structural context and within different stress regime, it is expected that a wide range of geometrical styles of sills will develop. During this study approximately 150 sills have been mapped in three-dimensions and this has provided much insight into the basic geometrical characteristics of igneous sills. These observations are compiled in the following sections. Although only a very small

fraction of the total number of sills of the NAIP have been mapped the coverage provided by the case-study areas is considered to provide a good picture of the general styles of sills and their basic characteristics.

7.2.1 Terminology and sill classification

Detailed mapping of sills within each of the case study areas has clearly demonstrated that igneous sills vary in shape and size and that the majority of sills are partly discordant and thus do not fit the traditional conception that a sill is a tabular igneous intrusion with concordant surfaces of contact (Allaby & Allaby, 1999). This fundamental observation has encouraged a modification of the traditional definition of a sill, which considers the fully three-dimensional geometry of the sill (Figs. 3.32 and 3.33).

In this thesis the term ***sill*** has been used to describe any continuous igneous body spanning a limited (<1.5 km) stratigraphic interval. It may have one or more feeders. Saucers, sheets, and sill segments (see below) represent the simplest forms of sills and are most likely linked to a single feeder. They are generally recognised seismically as highly continuous, smooth, and very high amplitude reflections that may exhibit both concordant and discordant relationships with stratal reflections. More complex forms of sills with, locally, discontinuous cross-sectional geometries (however, continuous in three-dimensional space) and highly irregular peripheries also exist. These may form as a result of amalgamation of any number of more simple sills or as a result of emplacement into pre-intrusive deformed sedimentary units and are likely to have multiple feeders associated with them. Where a sill is easily sub-divided into a number of simpler sills the term ***compound sill*** may be used to further specify these.

A sill classification system (Fig. 3.32) was proposed in Chapter 3 based on sills of the T67 survey area and further interpretation of subsequent case studies has confirmed that these geometries are more general geometrical styles adopted by igneous sills along the NE Atlantic Margin. The classification scheme was erected to better constrain the range of geometrical styles recognised and to allow for any common controls to be identified. The classification system subdivides igneous sills into three different classes. (1) ***Saucers*** have overall concave cross-sectional geometries regardless of the orientation of the cut through the intrusion. They exhibit simple mapview geometries with smooth curved peripheries. The development of saucers will be further discussed in section 7.6. (2) ***Sheets*** have simple horizontal, curved, or transgressive cross-

sectional geometries depending on the orientation of the cut through the intrusion. They can have simple or complex mapview geometries. (3) ***Sill segment*** is used to refer to any intrusion that cannot be classified as a saucer or a sheet. They have irregular peripheries and complex cross-sectional geometries. These three main classes were further sub-divided into sub-classes based on their more detailed characteristics in order to further identify any differences.

Sill segments are the dominant type of sill class observed and a wide spectrum of geometrical styles of sill segments, ranging from saucer-shaped and sheet-like forms to much more complex folded and stepped forms, have been observed in all of the survey areas. Saucers were seen in all three survey areas, but were particularly well defined in T67 with the less complete saucer-shaped sill segments being more common in the Solsikke and T38 survey areas. Numerous discordant sheets were seen in the deeper section of the Solsikke survey area, whilst more concordant sheets were seen in the deep section of the T67 survey area. A number of sheet-like, concordant shallow sills were also seen at shallow depth in the T38 survey area.

The detailed interpretation has shown that igneous sills emplaced at shallow depths of a few 100 meters may behave partly as intrusive sills, developing slightly discordant and even saucer-like geometries and cause deformation of overburden, and partly as extrusive lava flows exhibiting flow ridge and lobate morphologies (Chapters 5 and 6). These geometries are interpreted to form due to the low resistance to magma flow and spread offered by the water-saturated low strength shallow marine sediments found at this depth level. These sediments are more likely to deform in a plastic manner than deeper sediments that deform more elastically.

The development of many of these different geometrical forms has been discussed in previous chapters. It has been shown that the stratigraphic and structural templates at the time of intrusion influence the local stress regime and as a result have important implications for the geometrical shape adopted by the sills and are in many cases responsible for deviations away from the simple saucer and sheet-like forms. It has also been shown that the depth of intrusion has some influence on the dimensions adopted by the sill and upon the nature of propagation. These controls are explored further in section 7.7.

7.2.2 Sill dimensions

Numerous sills have been mapped and described in detail from each of the case study areas. Observations related to sill dimensions made in this study will be summarised in this section and where possible compared with the previously published findings.

The mapped sills vary in size from a few km^2 to more than 100 km^2 with the largest mapped sill covering approximately 120 km^2. The majority of the sills have areas of a few 10's of km^2 with the Solsikke sills exhibiting slightly greater average sizes than those mapped in T67 and T38. The mapped sills almost all show some degree of discordance with stratal reflections and many of the sills display considerable vertical relief of several 100s of metres and in a few cases more than 1500 m. These basic sill characteristics obtained from sill complexes along the NE Atlantic margin are comparable to those of sills of other igneous provinces (Chapter 1). This agreement between the most basic characteristics of the sills mapped during this study and those previously mapped suggests that other findings of this study are likely to apply elsewhere.

7.2.2.1 Sill area, vertical relief, and emplacement depth

Compilation of statistical data within each of the case-study areas has identified a consistent relationship (moderate to high correlation values; $21\% < R^2 < 70\ \%$) between sill area and vertical sill relief, with large sills exhibiting greater vertical relief than smaller sills. The statistical data for individual case-study areas have also shown low to moderate correlation between sill area and maximum emplacement depth ($8\% < R^2 < 31\%$) and moderate correlation ($21\% < R^2 < 52\%$) between vertical relief and maximum emplacement depth (Figs. 3.21, 4.26, and 5.14).

The graphs shown in Fig. 7.1 are based on the statistical data compiled from all three case-study areas (n = 88). The graphs show moderate or high correlation and generally suggest that increasing the number of data points increases the correlation for all three relationships. The highest correlation ($R^2 = 69\%$) is seen between sill area and vertical relief (Fig. 7.1a), high correlation is also seen between maximum emplacement depth and vertical relief ($R^2 = 59\%$; Fig. 7.1b), whilst the graph for sill area vs. maximum emplacement depth shows a moderate correlation value of $R^2 = 41\%$ (Fig. 7.1c). The Solsikke sill, which was interpreted as a compound sill composed of a number of smaller sills with individual feeders (section 4.5.5), is shown on the graphs, but it has not been included in the calculation of correlation values. The relationship between sill

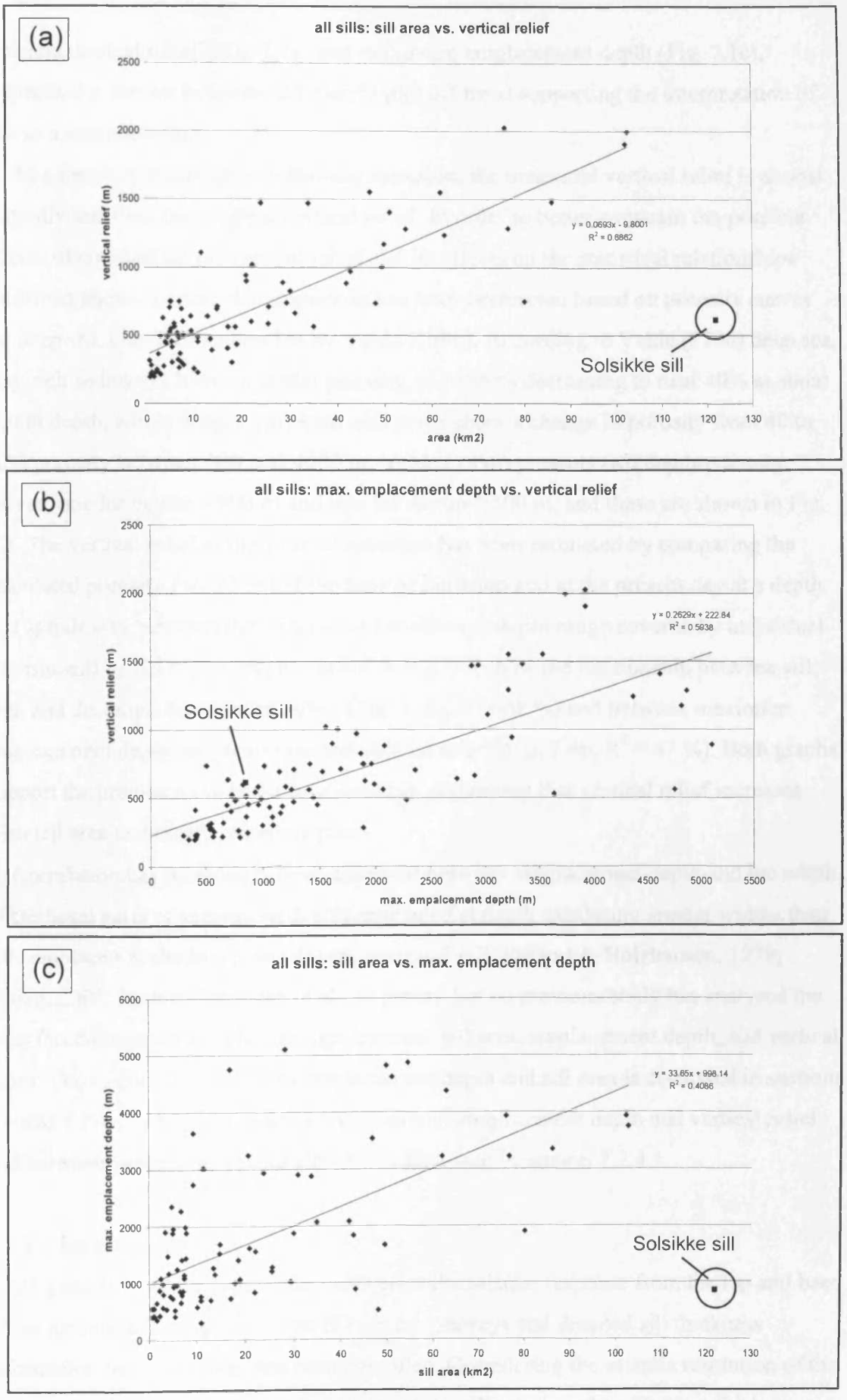

Fig. 7.1 Graphs showing statistical data based on data from the T67, Solsikke, and T38 case-study areas. (a) Sill area vs. vertical relief. (b) Maximum emplacement depth vs. vertical relief. (c) Sill area vs. maximum emplacement depth. Depth conversion done using Vsed = 3.0 km/s, see Chapter 2.

area and vertical relief (Fig. 7.1a) and maximum emplacement depth (Fig. 7.1c), respectively, for the Solsikke sill clearly plot off trend supporting the interpretation of this as a compound sill.

As a result of compaction following intrusion, the measured vertical relief is almost certainly less than the original vertical relief. In order to better constrain the possible effects of compaction on vertical relief and its effects on the statistical relationships described above, a crude decompaction has been performed based on porosity curves for deep sea, clay-rich sediments by Velde (1996). According to Velde (1996) deep sea, clay-rich sediments have an initial porosity of 75-90% decreasing to near 40% at about 500 m depth, whilst deeper clay-rich sediments show a change in porosity from 40 to 10% porosity between 500 and 4000 m. Velde (1996) presents two depth-porosity curves, one for depths <500 m and one for depths >500 m, and these are shown in Fig. 7.2. The vertical relief at the time of intrusion has been estimated by comparing the calculated porosity (+/- 25 %) at the time of intrusion and at the present day at a depth that is half way between the deepest and shallowest depth range covered by individual intrusions (Fig. 7.3). The graphs shown in Fig. 7.4 show the relationship between sill area and decompacted vertical relief (Fig. 7.4a; $R^2 = 68$ %) and between maximum emplacement depth and decompacted vertical relief (Fig. 7.4b; $R^2 = 47$ %). Both graphs support the previously derived relationships, suggesting that vertical relief increases with sill area and emplacement depth.

Correlation has previously been observed between emplacement depth and the width of the basal parts of saucers with sills emplaced at depth exhibiting greater widths than sills emplaced at shallower levels (see section 7.6.2; Pollard & Holzhausen, 1979; Fialko, 2001; Malthe-Sørensen et al., in press), but no previous study has analysed the fully three-dimensional relationships between sill area, emplacement depth, and vertical relief. The relationship between emplacement depth and sill area is discussed in sections 7.6 and 7.7.4.1, whilst the relationship between emplacement depth and vertical relief and between vertical relief and sill area is discussed in section 7.7.4.1.

7.2.2.2 Sill thickness

It has generally not been possible to separate the seismic response from the top and base of the igneous sills mapped in the 3D seismic surveys and detailed sill thickness information has, therefore, not been compiled. Considering the seismic resolution of the datasets the data suggest that the majority of the sills are less than 70-80 m thick.

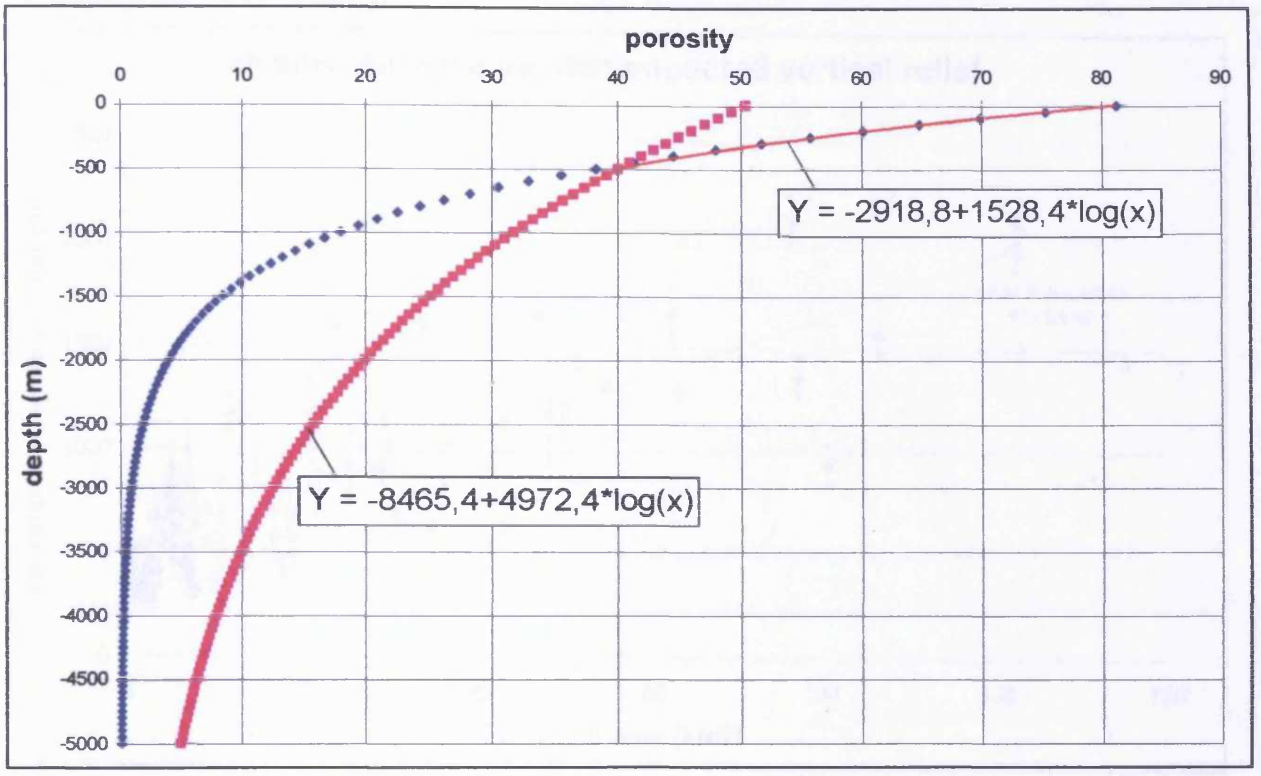

Fig. 7.2 Porosity vs. depth curves after Velde (1996). The blue curve has been used for depth < 500 m and the pink curve has been used for depths > 500 m.

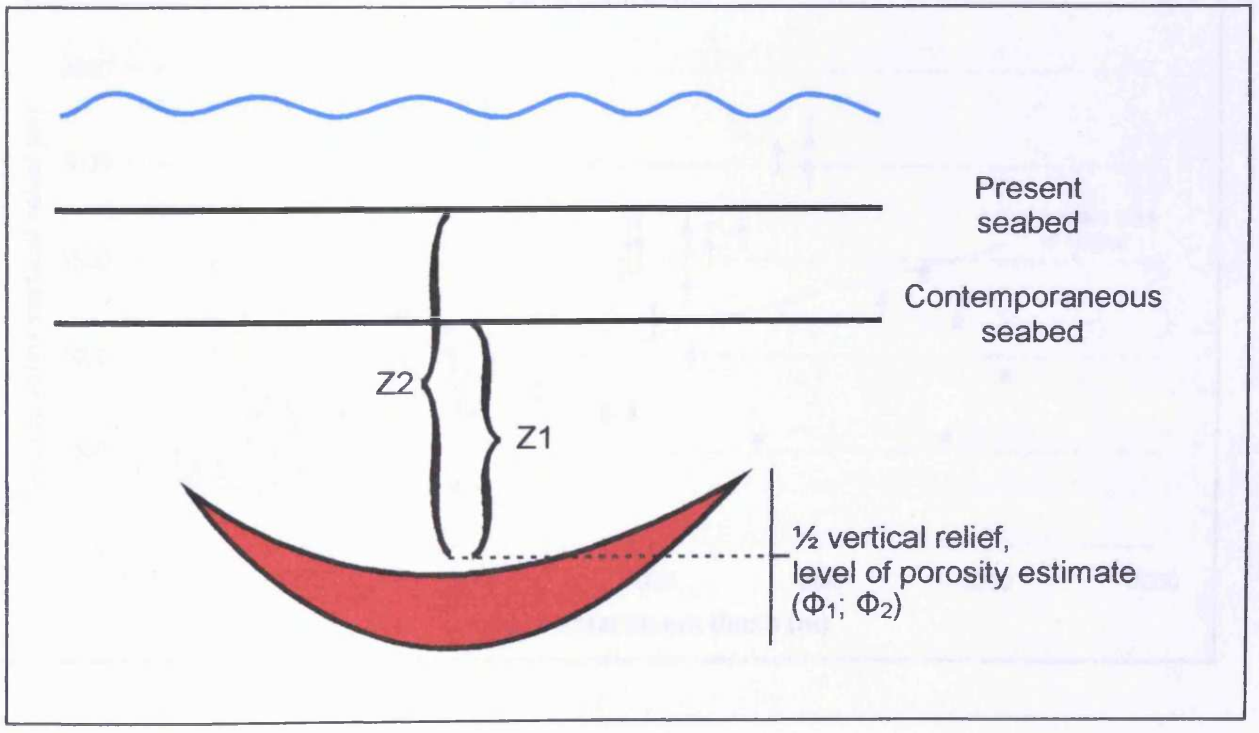

Fig. 7.3 Schematic illustration basic parameters used to decompact vertical relief on sills.

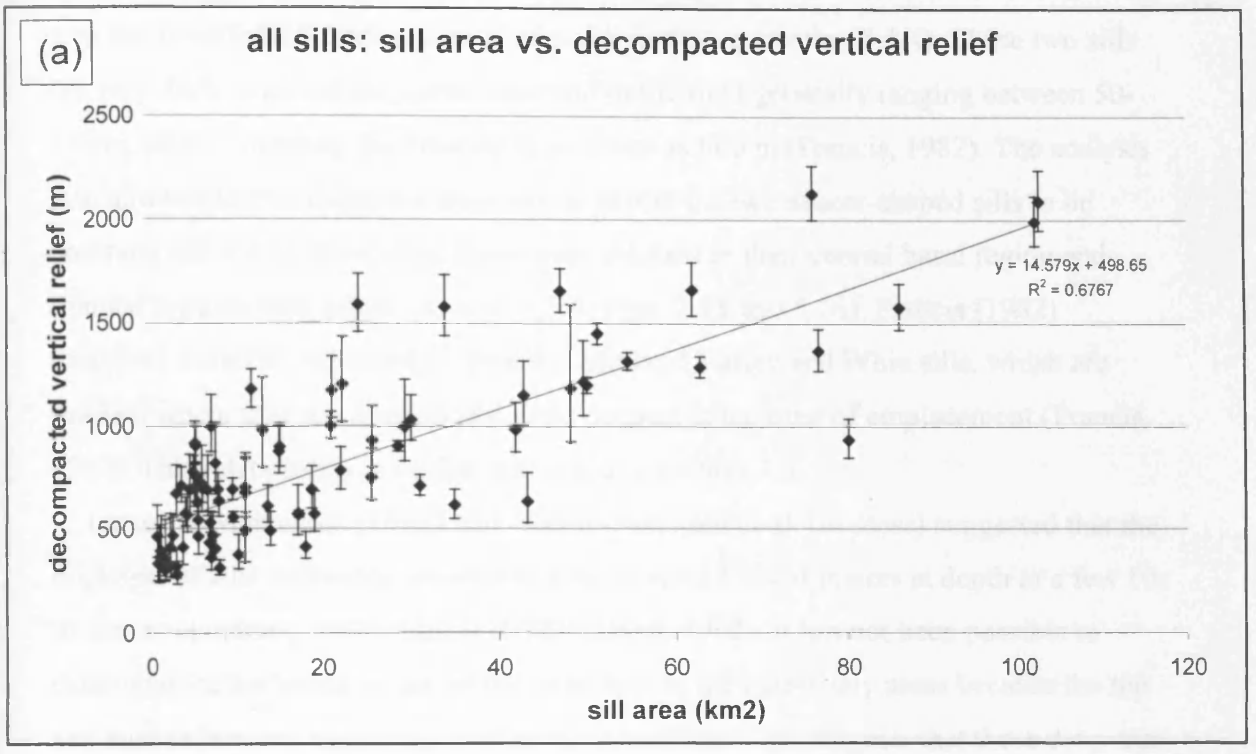

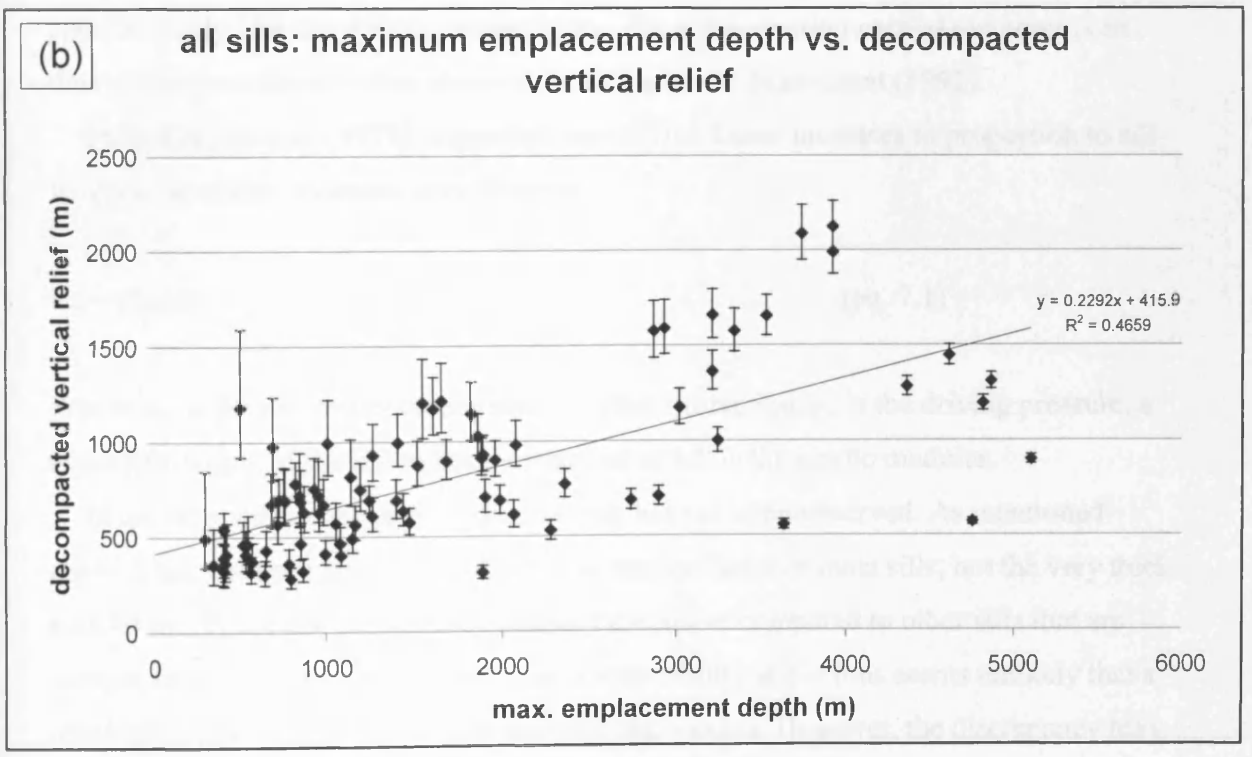

Fig. 7.4 Graphs showing (a) sill area vs. decompacted vertical relief (+/- 25%) and (b) maximum emplacement depth vs. decompacted vertical relief (+/- 25%) for sills mapped in the T67, Solsikke, and T38 case-study areas. Compare with Figs.7.1a and 7.1b. The Solsikke Sill has not been included.

However, mapping of two exceptionally well imaged and thick sills in the T38 3D data area has revealed sill thicknesses of as much as 400 m (section 5.3.4). These two sills are very thick, with sill thickness observed in the field generally ranging between 50-150 m, rarely obtaining thicknesses of as much as 600 m (Francis, 1982). The analysis also allowed for the thickness distribution across the two saucer-shaped sills to be analysed and it was shown that these were thickest in their central basal region and thinned towards their edges (section 5.3.4; Figs. 5.15 and 5.16). Francis (1982) described a similar relationship from the Midland Valley and Whin sills, which are thickest where they are deepest and were deepest at the time of emplacement (Francis, 1982). This relationship is further discussed in section 7.6.

Larsen & Marcussen (1992) and Malthe-Sørensen et al. (in press) suggested that the thickness of sills decreases up-section from several 100s of meters at depth to a few 10s of meters at outcrop level (Larsen & Marcussen, 1992). It has not been possible to determine the thickness of any of the deep sills in the case-study areas because the top and base reflections cannot be confidently identified. This suggests that these deep sills are probably no more than around 100 m thick, which is considerably less than the estimated thicknesses of the well imaged and shallowly emplaced sills 40 and 41 of approximately 350 and 400 m, respectively. The interpretation carried out herein can thus not support the previous observation of Larsen & Marcussen (1992).

Pollard & Johnson (1973) suggested that sill thickness increases in proportion to sill length in an elastic medium, according to:

$$w_m = (2p_d a)/ B \qquad \text{(eq. 7.1)}$$

Where w_m is the maximum displacement in the z direction, p_d is the driving pressure, a is the half-length of the sill in the x direction, and B is the elastic modulus.

In the case-study areas such a relationship has not been observed. As mentioned above it has not been possible to determine the thickness of most sills, but the very thick sills 40 and 41 are not particularly laterally extensive compared to other sills that are thought to be thinner than the thickness of separability and it thus seems unlikely that a relationship between sill thickness and sill length exists. However, the discrepancy may be ascribed to differences in emplacement depth and related ability of sills emplaced at different depths to deform the overburden. At shallow depth it is easier to deform the overburden because a lower driving pressure is required (Pollard & Johnson, 1973;

section 5.5.3, Fig. 5.51b). According to Pollard & Johnson (1973), once bending across a sill starts to influence the overburden equation 7.1 must be replaced by a model that considers the effective thickness of the overburden (T_e):

$$w_m = (p_d a^4)/ 2BT_e^3 \qquad \text{(eq. 7.2)}$$

Equating equations 7.1 and 7.2 shows the lateral extent of a sill (a) as function of effective thickness of overburden (T_e) required for a sill to deform the overburden:

$$a = T_e(4)^{1/3} \qquad \text{(eq. 7.3)}$$

This means that sills emplaced at shallow depth are likely to obtain a greater thickness to length ratio because these sills will have to spread laterally for a shorter distance (a) before inflating than a sill emplaced at greater depth. The thick sills 40 and 41 of the T38 survey area are both emplaced at shallow depth and should according to equation 7.3 exhibit a high thickness to length ratio relative to sills emplaced at greater depth and less laterally extensive sills emplaced at shallow depth. However, better constraints on sill thickness vs. sill length relationships in the case-study areas are required to fully test the model.

7.2.2.3 Sill volume

The poor constraints on sill thickness obtained through this study means that sill volumes are also poorly constrained. An attempt at compiling some volumetric information was made in Chapter 4 for sills of the Solsikke sill complex assuming a general sill thickness of 50 metres yielded sill volumes of a few km^3 with the Solsikke sill itself exhibiting the greatest volume of just over 6 km^3. In comparison it was estimated that the well-imaged sills 40 and 41 in the T38 survey area comprise magma volumes of approximately 1.5 km^3 and 1.3 km^3 (section 5.3.4), respectively. The Solsikke sill was interpreted to have multiple feeders (section 4.5.5.2), sills 40 and 41 of the T38 survey were interpreted to be connected to single feeders. It is interesting to note that the Solsikke lobe system, which was suggested to be fed by a single feeder (section 4.6.5.3) had an estimated volume of 1 km^3, i.e. similar to that of sills 40 and 41.

7.3 Soft-sediment deformation associated with sill emplacement

Two different types of seismic-scale soft-sediment deformation structures associated with sill emplacement have been identified in the case study areas; mound structures and 'jack-up' structures. The general characteristics of these two types of sill-related structures are summarised below. Their implications for constraining the timing of emplacement in each of the case-study areas will be discussed in section 7.4.

7.3.1 Mound structures

Mound structures interpreted to be associated with sill emplacement have been observed in each of the case study areas and their origin and implications were discussed in detail in Chapter 6. Based on observations made in this thesis and by previous authors (Gevers, 1928; Joppen & White, 1990; Skogseid et al., 1992; Davies et al., 2002) it is suggested that the majority of these mound structures are sedimentary structures, formed as a result of sediment remobilisation by hydrothermal fluids and subsequent extrusion onto the paleo-seafloor, whilst others are believed to be entirely or at least dominantly igneous in origin as proposed by Davies et al. (2002). The mound structures occur on one or two discrete horizons within each of the survey areas and these horizons are interpreted to represent times of sill intrusion.

The mound structures mapped in the different case-study areas share many of the same characteristics. They all range in diameter from 500 to 3500 m (average: 1348 m), and in height between 60 and 640 m (average: 178 m), and have flank dips of 6-26° near the central axes, decreasing to a few degree towards their margins (Table 6.1). The mounds with the greatest diameter also exhibit the greatest heights (Fig. 6.23c).

Two distinctively different geometrical classes have been informally defined; conical mounds and lensoidal mounds. *Conical mounds* are the most common and have a conical shape, show bi-directional downlap onto a concordant base, and have circular to slightly elongated shapes (Fig. 6.24a). Conical mounds may be either magmatic or sedimentary or a combination. *Lensoidal mounds* have a lensoidal shape and downlap onto an erosional base (Fig. 6.24b) or a depression underlying the centre of the structures (Fig.6.24c). Lensoidal mounds are entirely or pre-dominantly sedimentary and are interpreted to adopt their shape either due to (1) differential compaction, (2) collapse of the sedimentary unit between the sill and the seafloor as a result of sediment re-mobilisation and expulsion, (3) *in situ* remobilisation of sediments at the seafloor above the feeder pipe, or (4) development of a pockmark prior to sediment extrusion.

These structures are likely to be the seismic equivalent to outcropping 'Witkopps' found in the Karoo of South Africa (Figs. 6.28 and 6.29). These vents often comprise highly indurated sandstones and exhibit a number of interesting morphological features (i.e. sandstone dykes, flow structures, pipes, and crater-like depressions) that suggest that the vents were active for extended periods of time and possibly during multiple episodes of igneous activity.

7.3.2 'Jack-up' structures

Host-rock deformation in the form of upward vertical displacement of overburden above sills has been described from T38 and to a lesser extent T67. The deformation is interpreted to form in order to accommodate the added thickness associated with the forcible intrusion of igneous sills (section 5.5.3). The deformation affects the seafloor at the time of intrusion forming a positive relief structure, at least in the case of shallow intrusion, and subsequent onlap onto the structures can be used to constrain the timing of deformation and hence the timing of intrusion. The interpretation of jack-up structures has provided much new insight into the intrusion of sills and these findings are discussed in section 7.5.

7.4 Timing of intrusive and extrusive events along the NE Atlantic Margin

7.4.1 Introduction

This study has used seismic methods to constrain the timing of magmatic events in the four case-study areas. The mound structures described in section 7.3.1 were extruded onto the seafloor during or immediately following intrusion and the age of the base mound reflector thus represents the timing of intrusion. The jack-up deformation structures described in section 7.3.2 influence the water-sediment interface during intrusion and onlap onto such structures can, therefore, be used to constrain the timing of intrusion. In addition, the onset of extrusion of lava flows can be constrained seismically if the horizons onto which the flows were extruded can be dated.

Mound structures have been mapped in all four case study areas and the timing relationships within the T67 and T38 study areas are further constrained by the presence of jack-up structures. The interpretation has provided new information about the timing of sill emplacement both within individual surveys and between the different survey areas along the NE Atlantic Margin. The findings are summarised below in section 7.4.2 and in Table 7.1 and compared with previous work in section 7.4.3.

Case-study area	**Magmatic phase**	**Age**	**Evidence**
Tranche 67	Phase 1	Paleocene	Mounds: M*67*a Jack-up
	Phase 2	Late Paleocene	Mounds: M*67*b
Solsikke	Phase 1	Paleocene	Mounds: M*ss*a and M*ss*b
Tranche 4	Phase 1	54.9-54.6 Ma	Mounds: M*4*
Tranche 38	Phase 1	Late Paleocene-?Early Eocene	Mounds: M*38*
	Phase 2	Early Eocene	Jack-up

Table 7.1 Summary of timing of intrusive events in the case-study areas.

7.4.2 Timing of magmatic events in the case-study areas

Two different phases of intrusion have been identified in the ***T67 survey area***. The earliest phase has been constrained to the Paleocene based on the extrusion of mound structures (section 6.2.2; Fig. 6.3) and jack-up above sills 5, 11 and 12 (section 3.5; Figs. 3.59 and 3.60). This phase of intrusion was associated with the emplacement of the deeper and intermediate level sills. The later phase of intrusion has been dated as Late Paleocene based on the presence of mound structures (section 6.2.2; Figs. 6.4 and 6.5) and was associated with the emplacement of the shallowest sills in the survey area. Correlation suggests that the first phase of intrusion is approximately synchronous with the extrusion of the lava flow unit mapped in the survey area and the development of Escarpment 1, whilst the second phase of intrusion is synchronous with the development of Escarpment 2 (Fig. 3.19). This suggests that intrusion and extrusion occurred contemporaneously in the northern Faeroe-Shetland Basin.

In both the Solsikke and T4 3D seismic survey areas only one phase of sill intrusion has been identified and in both cases the timing is constrained by the presence of mound structures only. In the ***Solsikke survey area*** the ages of the mapped horizons are poorly constrained due to lack of well information available to this study. The mound structures in the survey area are well defined and clearly extruded onto Horizon E (section 6.2.3; Figs. 6.8 and 6.9). Horizon E is Tertiary in age and older than the Brygge Formation, which is Early Eocene-Early Miocene in age, constraining the age of the mounds and thus the timing of intrusion to the Paleocene. Previous work by Brekke (2002) suggested that sills in the Møre and Vøring Basins are probably Paleocene-earliest Eocene in age and Skogseid et al. (1992) interpreted 'eye-structures' (Fig. 6.25) similar to the lensoidal mounds mapped in the Solsikke survey area within Upper Paleocene sediments of the Vøring Basin, suggesting that sill intrusion occurred during the Late Paleocene. Based on the observations made in the Solsikke case study area and previous studies it is suggested that sills were intruded into the Upper Cretaceous and Lower Paleocene successions of the Solsikke survey area during the Late Paleocene.

In the ***T4 survey area*** numerous mound structures are seen within the latest Paleocene strata (section 6.2.5; Fig. 6.20) and have been dated at 54.9-54.6 My based on well tie to the near-by exploration well 214/19-1. Previous studies by Davies et al. (2002) and Trude et al. (2003) of sill complexes in the T61/ 62 area of the central Faeroe-Shetland Basin immediately north of the T4 survey area have yielded a similar

timing of intrusion based on interpretation of mound structures (Davies et al., 2002) and jack-up (Trude et al., 2003).

Two mound structures mapped in the ***T38 3D survey area*** downlap onto the lower units of Flow unit B and appear to be onlapped by the upper units of the flow (section 6.2.4; Figs. 5.10 and 6.12). Flow unit B has been extruded onto the Top Faeroe Group horizon that is of Late Paleocene age. This suggests that the extrusion of Flow unit B and the development of the mounds, and the intrusion event they are related to, are also Late Paleocene in age. This suggests that extrusion of Flow unit B and the first intrusive event in the T38 survey area occurred contemporaneously. Jack-up structures mapped in the T38 survey area suggest that there was a second, later phase of intrusion (section 5.5). The jack-up structures are delimited upwards by the Top Balder Formation horizon (horizon C; e.g. Figs. 5.41 and 5.43) of earliest Eocene age, suggesting that a second intrusive event occurred during the earliest Eocene.

7.4.3 Comparison with previous work

The above summary of timing of sill emplacement in the case-study areas suggests that intrusion took place within the Paleocene and the earliest Eocene, with the majority of the intrusive activity taking place in the Late Paleocene (Table 7.1). Extrusives in the T67 and T38 survey areas have been dated as Paleocene and Late Paleocene, respectively, and the interpretation in both areas suggests that intrusion and extrusion occurred contemporaneously. In the T38 survey area a late second phase of intrusion during the earliest Eocene post-dates the timing of extrusion in the survey area.

The timing of intrusive and extrusive events constrained in this study correlate well with those of previous studies (section 1.4.2) that generally suggest that the majority of the magmatic activity took place in the Late Paleocene approximately contemporaneous with the onset of seafloor spreading in the NE Atlantic Ocean. However, in the T67 survey area the interpretation presented herein differs from previous work by proposing that there are two Paleocene intrusive events in the T67 survey area in contrast to a single event of Early Eocene age proposed by Hodges et al. (1999). The igneous activity in this area has previously been linked to the development of Brendan's Dome that is of Paleocene age (Smythe et al., 1983; Hodges et al., 1999) and this hypothesis is not contradicted by this interpretation. Interpretation of the T38 3D seismic data has placed better constraints on the timing of magmatic events in the NE Rockall Basin than has previously been published. The interpretation, presented herein, suggests that there were

at least two intrusive events in the NE Rockall Basin as oppose to the single event suggested by Ritchie et al. (1999) and in agreement with the long period of magmatic activity suggested by Tate et al. (1999).

In the T67 survey area the two identified intrusive events appear to be contemporaneous with the development of two escarpments of the Ben Nevis Escarpment, which forms the northern continuation of the Faeroe-Shetland Escarpment. This supports previous suggestions (section 1.4.2) that the intrusion of sills was synchronous with the extrusion of the Middle and Upper lava series and the construction of the Faeroe-Shetland Escarpment, and post-dated the extrusion of the Lower lava series (Naylor et al., 1999; Ritchie et al., 1999).

7.5 Sill intrusion

7.5.1 Space for intrusion

Detailed depth conversion and decompaction of a pronounced jack-up structure (structure B; section 5.5.5, Fig. 5.55) in the T38 survey area has shown that the amount of vertical relief and volume of displaced sediment of the structure is comparable to the thickness and volume of the underlying sill 41. This suggests that space for the sill was created primarily by displacement of overburden and deformation of the water-sediment interface. Some previous authors have suggested that space for an intruding sill is created fully or at least primarily by expulsion of pore fluids from the sediments surrounding the sill (Einsele et al., 1980). This model cannot be supported by the detailed mapping in the T38 survey area.

The two different models for sill emplacement (overburden displacement vs. pore water expulsion) can be distinguished seismically (Fig. 5.56). If the overburden is deformed during intrusion to provide accommodation space for the sill it should be possible to identify onlaps onto the deformation structure, whereas if space for the intrusion is created through expulsion of pore fluids in the host-rock differential compaction, but no onlap would be seen in the sediments overlying the sill.

7.5.2 Growth of intrusions

The depth-conversion and decompaction of structure B has revealed the true shape of the forced fold (Fig. 5.55), which is considered to approximate the shape of the underlying sill. Although sill 41 is well imaged, the details of the edge of the sill are not revealed by the interpretation as the thickness drops below the limit of separability. The

shape of the fold shows a striking resemblance with crack opening displacement profiles for faults where inelastic tip deformation is considered (Fig. 7.5; Cowie & Scholz, 1992a). Considering that sills are in essence horizontal fractures this could suggest that the growth of sills is kinematically similar to the growth and accumulation of displacement on faults.

A fault growing by radial propagation gradually extends laterally as it accumulates displacement and exhibits a relationship between fault displacement and fault length, with the maximum displacement occurring approximately in the centre of the fault (Fig. 7.6; Walsh & Watterson, 1988; Cowie & Scholtz, 1992b; Cartwright et al., 1995). According to Cowie & Scholz (1992b) a fault grows laterally as a result of accumulation of displacement on the fault leading to an increase in the strain concentration and propagation at the fault tips. In section 7.2.2.2 work by Pollard & Johnson (1973) on the relationship between sill thickness vs. sill length was summarised. Their work suggested that sills initially spread laterally, whilst only accumulating limited thickness, and only after reaching a critical length relative to the depth of emplacement do they inflate (Fig. 7.7). In summary, faults are generally considered to accumulate displacement and subsequently grow laterally, whilst sills are considered to grow laterally and subsequently accumulate thickness. This suggests that the two types of structures achieve similar length vs. deformation (displacement and thickness) plots through two kinematically different growth models.

The standardised displacement vs. length profile for faults where inelastic tip deformation presented by Cowie & Scholz (1992a; Fig. 7.5) differs from displacement vs. length profiles for faults where inelastic tip deformation is not considered by tapering out gradually towards the fault tips rather than exhibiting an abrupt decrease in displacement right at the tip (Fig. 7.3). A similar gradual tapering towards the lateral tip of structure B is seen in Fig. 5.55, suggesting that inelastic deformation takes place at the sill tips during intrusion. This suggests that inelastic deformation at sill tips should be considered in numerical and analogue sill emplacement models.

7.6 Discussion: The development of saucer-shaped sills

7.6.1 Introduction

The interpretation of igneous sills carried out during this study suggests that igneous sills intruded into sedimentary basins commonly adopt circular or elongated saucer-shaped geometries either in the form of saucers with simple planform geometries or in

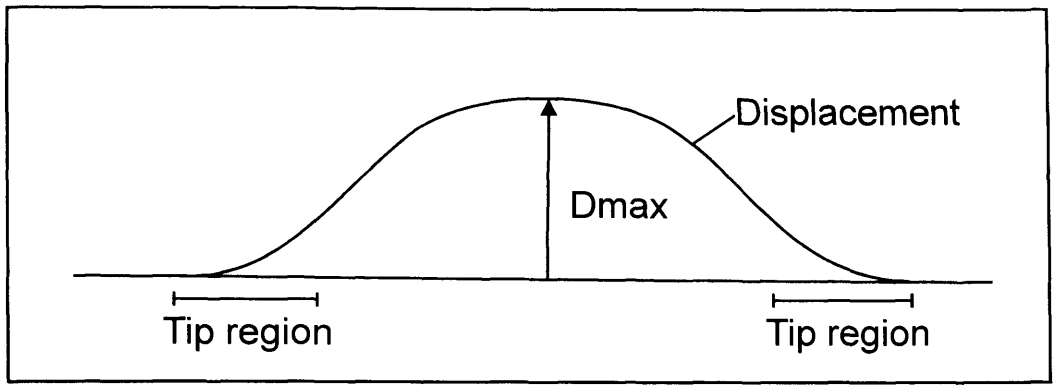

Fig. 7.5 Displacement vs. Length profile for fault with inelastic tip deformation. The profile tapers out gradually towards the sill tip. After Cowie & Scholtz (1992a).

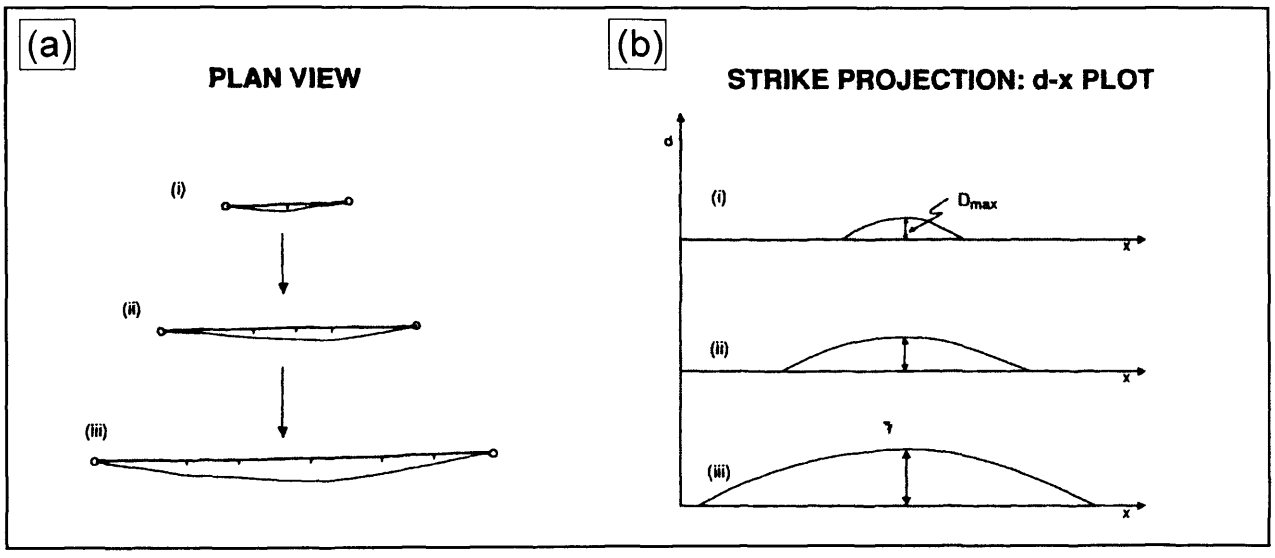

Fig. 7.6 Radial fault propagation. (a) Fault growth through time. The fault grows laterally as a result of accumulation of displacement on the fault leading to an increase in the strain concentration and propagation at the fault tips. (b) Length vs. Displacement plots for fault propagation through radial propagation. After Cartwright et al. (1995).

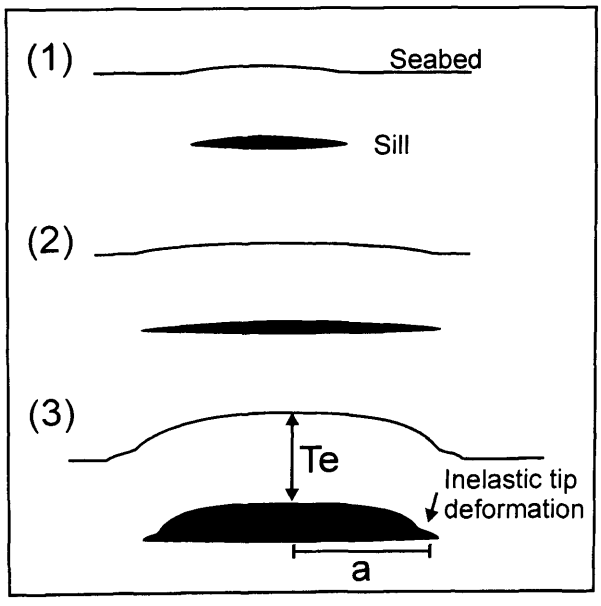

Fig. 7.7 Model for sill growth. (1) and (2) Intrusion and lateral spread with only limited deformation of the overburden. (3) sill inflation begins as the sill reaches a lateral half-length (a) equal to about three times the effective depth of emplacement (Te).

the less complete form of saucer-shaped sill segments. Saucers and saucer-shaped sill segments are here, collectively, referred to as saucer-shaped sills. This intriguing geometrical style has been the subject of several previous outcrop based studies, but only through the application of 3D seismic data has it been possible to reveal their fully three-dimensional geometry and context. This has provided new insights into the development of this particular geometrical style of sill and these observations are described and discussed in this section.

7.6.2 Saucer area, vertical relief, emplacement depth, and width

Statistical data illustrating the relationships between sill area, vertical relief, and emplacement depth were presented in section 7.2.2.1. Similar data have been compiled for near-circular, saucer-shaped sills separately, and these results will be presented in this section in order to constrain any significant relationships. Nine saucers and well-defined saucer-shaped sill segments (e.g. Figs. 3.25 and 3.29) and 13 less well-defined saucer-shaped sill segments (e.g. Fig. 5.35) were used in the analysis (i.e. total n = 22). The interpreted saucer-shaped sills included here were emplaced at depths of 350-1650 m below the contemporaneous seabed, cover areas of < 30 km^2, and exhibit decompacted vertical relief of 310-1490 m.

For each graph described in the following and shown in Fig. 7.8 the correlation value has been calculated for the full saucer-shaped sill dataset (n = 22) and for the saucers and well-defined saucer-shaped sills (n = 9) separately. The decompacted vertical relief calculated for each sill in section 7.2.2.1 has been used. The graph shown in Fig. 7.8a shows moderate correlation between sill area and decompacted vertical relief (R^2 = 45 %) when all saucer-shaped sills are included and high correlation (R^2 = 86 %) when only the most well-defined saucer-shaped sills are considered. The graph in Fig 7.8b shows poor correlation (R^2 = 35 %) between sill area and maximum emplacement depth when all saucer-shaped sills are considered, but exceptionally high correlation (R^2 = 94 %) when only the most well-defined saucer-shaped sills are considered. Finally, Fig. 7.8c reveals moderate correlation (R^2 = 58 %) between maximum emplacement depth and decompacted vertical relief for the full dataset and high correlation (R^2 = 76 %) when only the most well-defined saucer-shaped sills are considered. These values are generally comparable to those compiled for the full sill dataset (section 7.2.2.1; Figs. 7.1 and 7.4), however, with the small dataset of well-defined saucer-shaped sills generally showing better correlation than the larger saucer-shaped sill dataset.

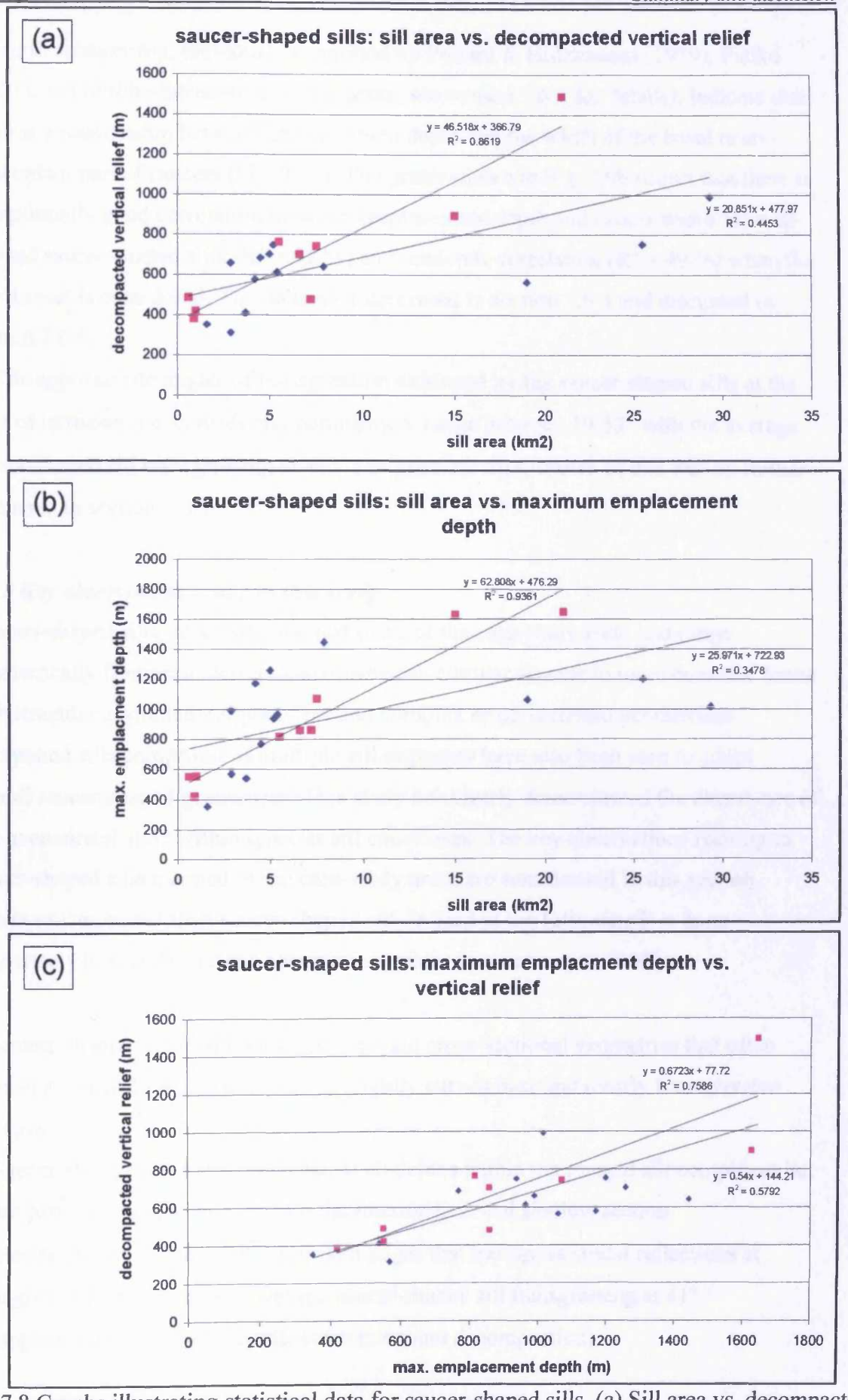

Fig. 7.8 Graphs illustrating statistical data for saucer-shaped sills. (a) Sill area vs. decompacted vertical relief. (b) Sill area vs. maximum emplacement depth. (c) Maximum emplacement depth vs. decompacted vertical relief. Blue points = full dataset, N=22. Pink points = saucers and well-defined saucer shaped sill segments, N=9.

A fourth relationship, previously suggested by Pollard & Holzhausen (1979), Fialko (2001), and Malthe-Sørensen et al. (in press; see section 7.6.4 for details), indicate that there is a relationship between emplacement depth and the width of the basal near-concordant part of saucers (Fig. 7.9a). The graph shown in Fig. 7.9b shows that there is exceptionally good correlation between emplacement depth and saucer width for well-defined saucer-shaped sills (R^2 = 92 %) and moderate correlation (R^2 = 49 %) when the full dataset is considered. This is further described in section 7.6.4 and discussed in section 7.6.5.

The approximate angles of transgression exhibited by the saucer-shaped sills at the time of intrusion, i.e. considering compaction, range between 19-52° with the average saucer-shaped sill transgressing at 41°. The possible significance of this will be further discussed in section 7.6.5.

7.6.3 Key observations made in this study

Saucers-shaped sills have been mapped in all of the case-study areas and range geometrically from near-perfectly symmetrical, circular saucers to more complex forms with irregular asymmetrical planview and complex cross-sectional geometrises. Compound sills comprised of multiple sill segments have also been seen to adopt overall saucer-shaped geometries. This study has clearly demonstrated the abundance of this geometrical style within igneous sill complexes. The key observations relating to saucer-shaped sills mapped in the case-study areas are summarised in this section. Where saucer, rather than saucer-shaped sill, is used in the following it is done deliberately to specify that the observation relates to saucers specifically.

- Saucer-shaped sills exhibit concave upward cross-sectional geometries that often have a relatively wide horizontal or slightly curved base and clearly transgressive edges
- Saucer-shaped sills have been seen at all depths within the imaged sill complexes but are particularly seen to dominate the intermediate and shallow section
- Saucer-shaped sills exhibit discordant edges that transgress stratal reflections at angles of 19-52°, with the average saucer-shaped sill transgressing at 41° (approximate angle after depth-conversion and decompaction)

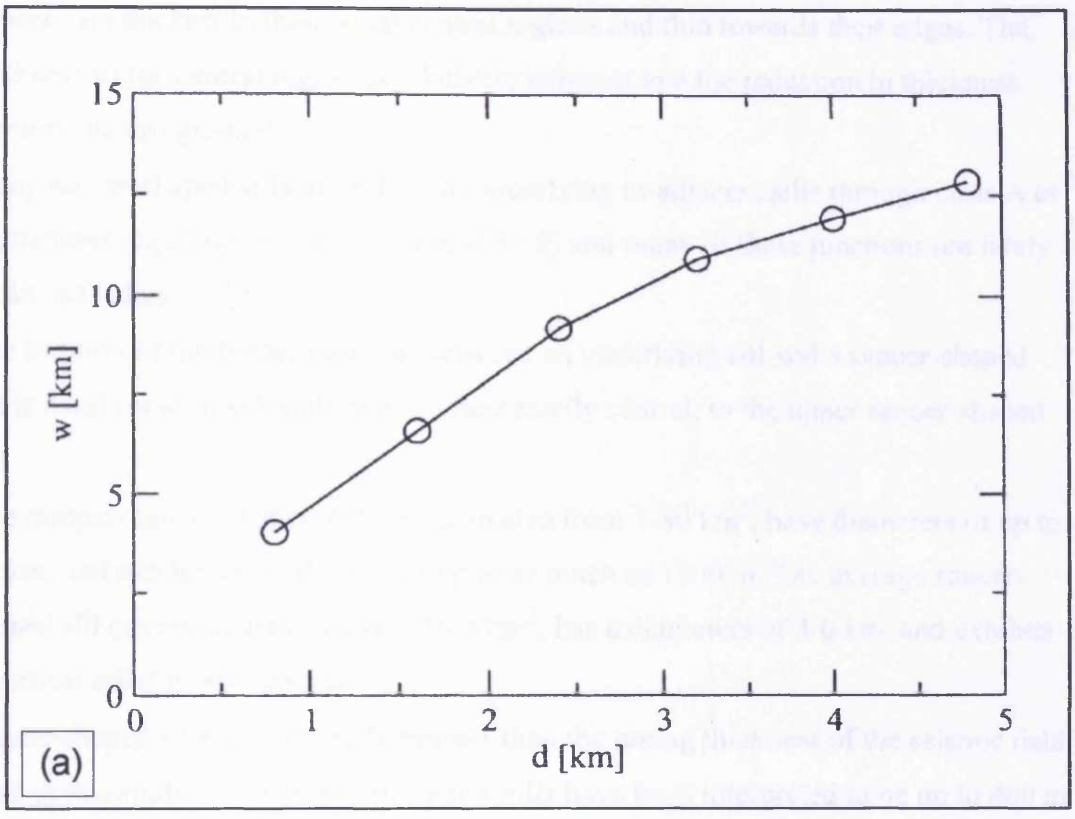

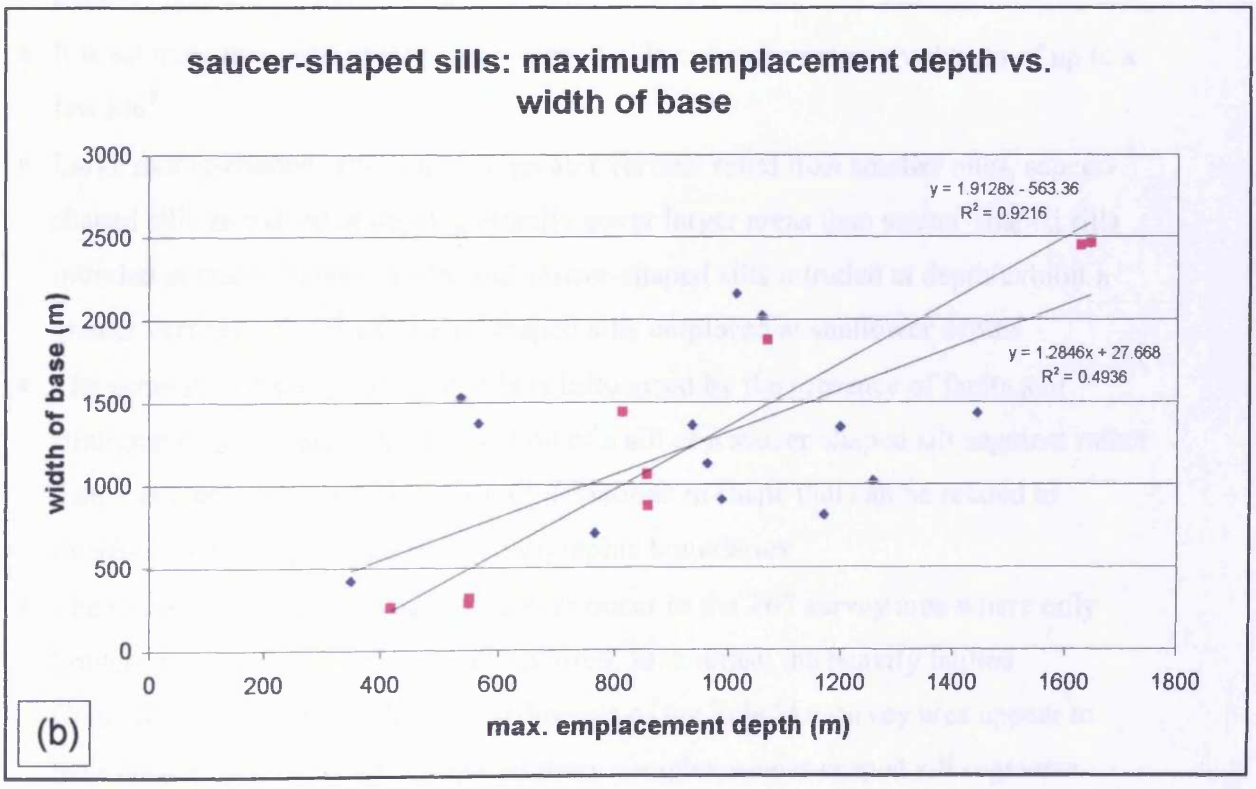

Fig. 7.9 (a) Graph showing modelled emplacement depth vs. saucer base width from Malthe-Soerensen et al. (in press). The graph shows that sills turn transgressive once they have propagated laterally for about 2-3 times the emplacement depth. (b) Graph showing correlation between emplacement depth vs. saucer width for saucer-shaped sills mapped in the T67, Solsikke, and T38 case-study areas. The graphs show that sills turns transgressive once they have propagated laterally for approximately 1.5 times the emplacement depth.

- Saucers are thickest in their basal central regions and thin towards their edges. The thickness of the central region is relatively constant and the reduction in thickness towards the tips gradual
- Many saucer-shaped sills are linked to underlying or adjacent sills through class A or B junctions (e.g. Figs. 3.11a, 3.37b, and 5.18) and many of these junctions are likely to act as feeders
- The location of the feeder junction between an underlying sill and a saucer-shaped sill is basal (or almost basal), but not necessarily central, to the upper saucer-shaped sill
- The mapped saucer-shaped sills range in size from 1-80 km^2, have diameters of up to 10 km, and exhibit vertical relief of up to as much as 1500 m. The average saucer-shaped sill covers an area of a few 10's km^2, has a diameters of 3-6 km, and exhibits a vertical relief of 400-650 m
- Saucer-shaped sills are generally thinner than the tuning thickness of the seismic data used in this study (< 70-80 m), but a few sills have been interpreted to be up to 400 m thick
- It is estimate that individual saucer-shaped sills comprise magma volumes of up to a few km^3
- Large saucer-shaped sills exhibit a greater vertical relief than smaller ones, saucer-shaped sills emplaced at depth generally cover larger areas than saucer-shaped sills intruded at more shallow depth, and saucer-shaped sills intruded at depth exhibit a greater vertical relief than saucer-shaped sills emplaced at shallower depths
- The geometry of saucer-shaped sills is influenced by the presence of faults and stratigraphic boundaries. Classification of a sill as a saucer-shaped sill segment rather than a saucer is often related to small deviations in shape that can be related to interference from fault planes or stratigraphic boundaries
- The vast majority of the mapped saucers occur in the T67 survey area where only limited structural deformation has occurred. In contrast, the heavily faulted Cretaceous and Lower Paleocene sediments of the Solsikke survey area appear to have encouraged the development of more complex saucer-shaped sill segments

7.6.4 Previous models for the development of saucer-shaped sills

Saucer-shaped sills were first described by du Toit (1920) who recognised the abundance of this non-concordant and ring-shaped geometrical style of sills in the Karoo Basin of South Africa (Figs. 1.7 and 1.8). Subsequently, igneous sills with simple circular saucer- or elongated trough-shaped geometries have often been described at outcrop (e.g. Bradley, 1965; Francis, 1972; Chevallier & Woodford, 1999) and have more recently been imaged by satellite imagery and 3D seismic data (Smallwood & Maresh, 2002; Hansen et al., 2004). They have been found to range between 2-15 km in diameter and cover areas of 10s or even 100s of km^2. They generally have thicknesses of 50-150 m (rarely reaching as much as 600 m). In cross-section they generally have concordant flat bases, but towards their edges become discordant and transgress stratigraphy (e.g. du Toit 1920; Francis 1982; Chevallier & Woodford 1999). These general geometrical characteristics are evidently very similar to the set of characteristics compiled from the case-study areas along the NE Atlantic Margin during this study (section 7.6.2).

Five main models have previously been proposed to explain the development of these extraordinary intrusions. These models are summarised in this section.

The first attempt at explaining the development of saucer-shaped sills was presented by *Lombard (1952)*, who studied the Karoo dolerites. Based on their geometrical similarity with cone-sheets (Anderson, 1936; Carey, 1958; Phillips, 1974) Lombard (1952) applied Anderson's (1936) explanation of cone-sheets to the development of saucer-shaped sills (Fig. 5.48). Lombard (1952) suggested that conical fractures develop around areas of maximum uplift above the sill and these are subsequently infilled by intruding magma.

A second model was proposed by *Bradley (1965)* again based on the Karoo dolerites. Bradley (1965) suggested that igneous sills follow a compensation surface, which is an ideal surface that, relative to a given body of rock and given static body of denser magma, joins all points having equal lithostatic and magmatic pressure (Fig. 7.10). The lithostatic pressure increases with depth and the magma pressure is assumed to be horizontal and to decrease away from the magma source at depth (i.e. upwards). Where the land surface overlying a sill is flat, horizontal sheet intrusions are expected to form at the level where the isopiestic surfaces for the lithostatic pressure and the magmatic pressure are equal. If, however, the land surface has an irregular topography the

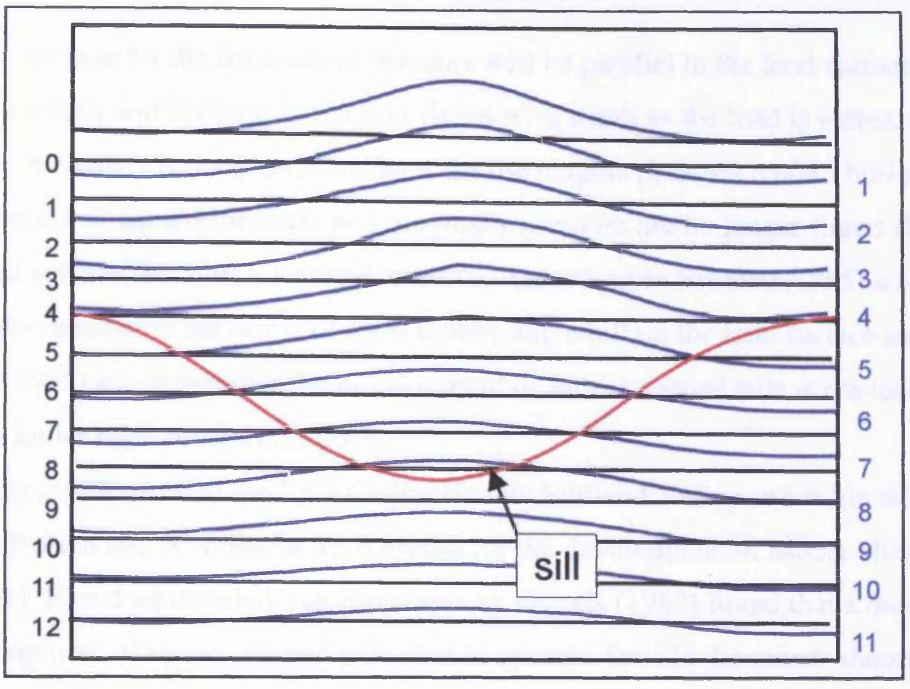

Fig. 7.10 Model for the development of saucer-shaped sills in which the level of intrusion (red) is governed by a compensation surface at which the curved isopiestic surfaces of lithostatic pressure (black) and isopiestic surfaces of magma pressure are equal. After Bradley (1965).

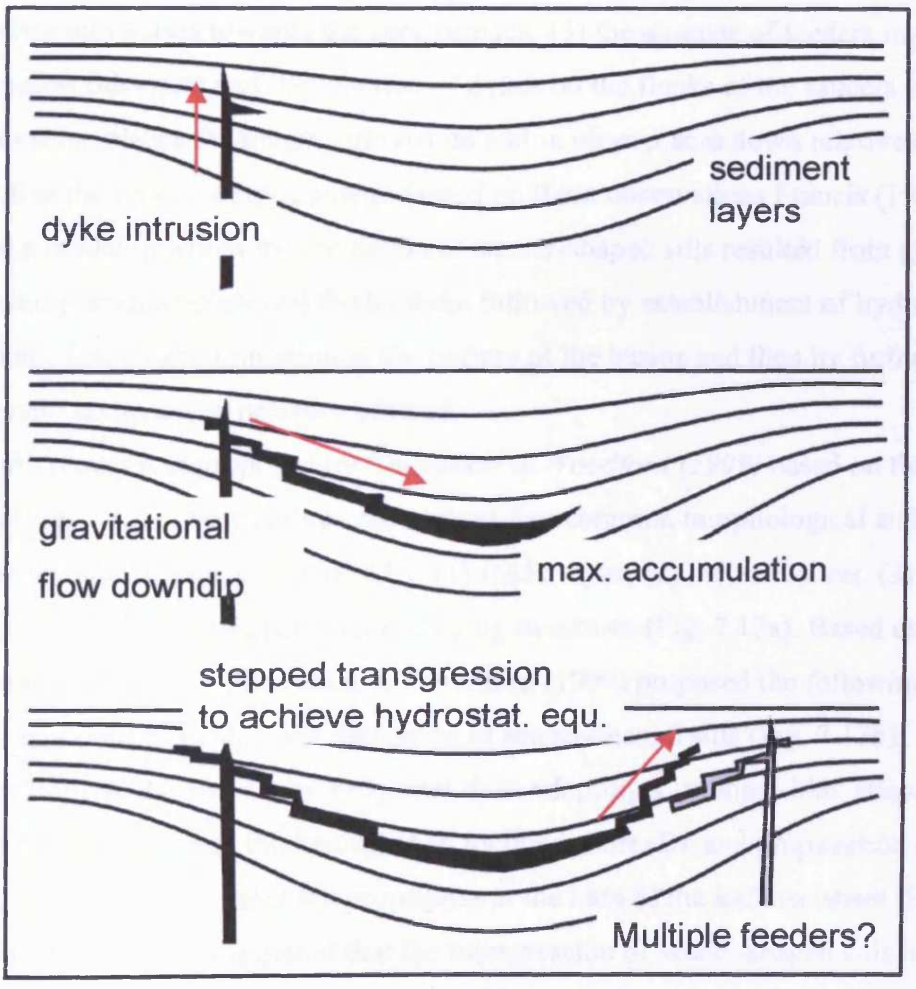

Fig. 7.11 Model for the development of saucer-shaped sills proposed by Francis (1982). The model is based on field observations made on the Whin sill and Midland Valley sill.

isopiestic surface for the lithostactic pressure will be parallel to the land surface in the shallow sections and become flatter and flatter with depth as the load is increasingly spread with depth. The isopiestic surfaces for the magma pressure remain horizontal. As a result points of equal lithostatic and magmatic pressure are no longer found along a horizontal surface, but along a curved surface. According to Bradley (1965) a concave upward compensation surface will form underlying a hill on the land surface and Bradley (1965) suggested that the development of saucer-shaped sills is related to intrusion under such stress conditions.

Francis (1982) studied the Late Carboniferous Midland Valley and Whin sills of northern Britain and proposed a third model for the development of saucer-shaped sills (Fig. 7.11). Based on detailed outcrop mapping Francis (1982) found that a model for the development of saucer-shaped sills should account for; (1) the saucer shape, (2) correspondence between the saucer-shape and bedding planes in earlier formed syn-sedimentary basins, (3) coincidence of maximum sill thickness with the bottoms of sedimentary basins, (4) the tendency of edges of saucers to be steeper than bedding and to dissociate into lenses towards the zero isopach, (5) the absence of feeders in the areas of the greatest thickness and the location of dykes on the flanks of the saucers or basins, and (6) in some places the magma moved up and in other places down relative to the horizontal at the time of emplacement. Based on these observations Francis (1982) proposed a model in which the formation of saucer-shaped sills resulted from gravity flow downdip from a peripheral feeder dyke followed by establishment of hydrostatic equilibrium; first by accumulation at the bottom of the basins and then by further advancement updip under pressure of head.

A fourth model was proposed by *Chevallier & Woodford (1999)* based on the Karoo dolerites (Fig. 7.12). These authors recognised five common morphological and structural features of saucer-shaped sills; (1) feeder dyke, (2) inclined sheet, (3) outer sill, (4) inner sill, and (5) minor secondary ring structures (Fig. 7.12a). Based on the recognition of the above, Chevallier & Woodford (1999) proposed the following sequence of events to explain the formation of saucer-shaped sills (Fig. 7.12b); curvature along strike and dip of a regional dyke adopting a 'trumpet-like' shape (A), followed by flattening and thickening of an inclined sheet (B), and propagation of an outer sill (C). Finally, an inner sill propagates at the base of the inclined sheet (D).

Several authors have suggested that the transgression of saucer-shaped sills is a result of interaction between the stress field surrounding the sill at depth and the free surface

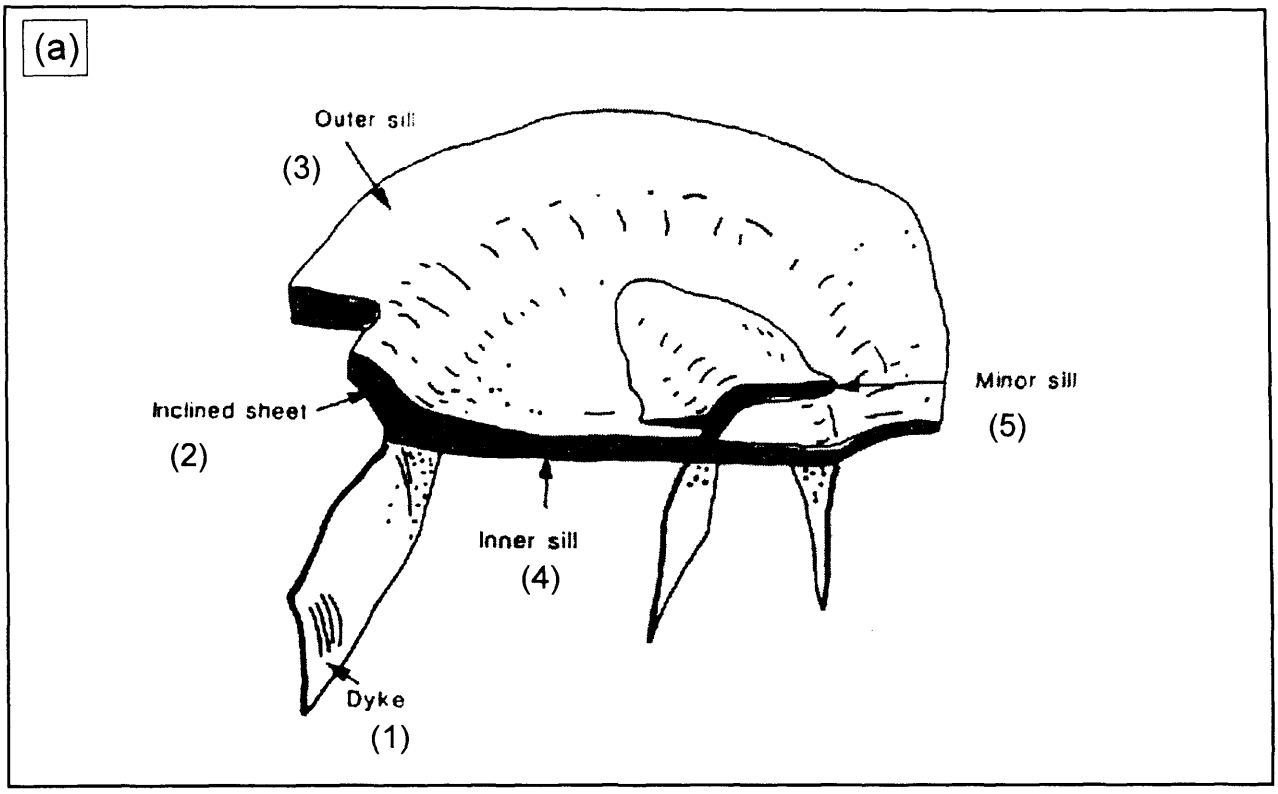

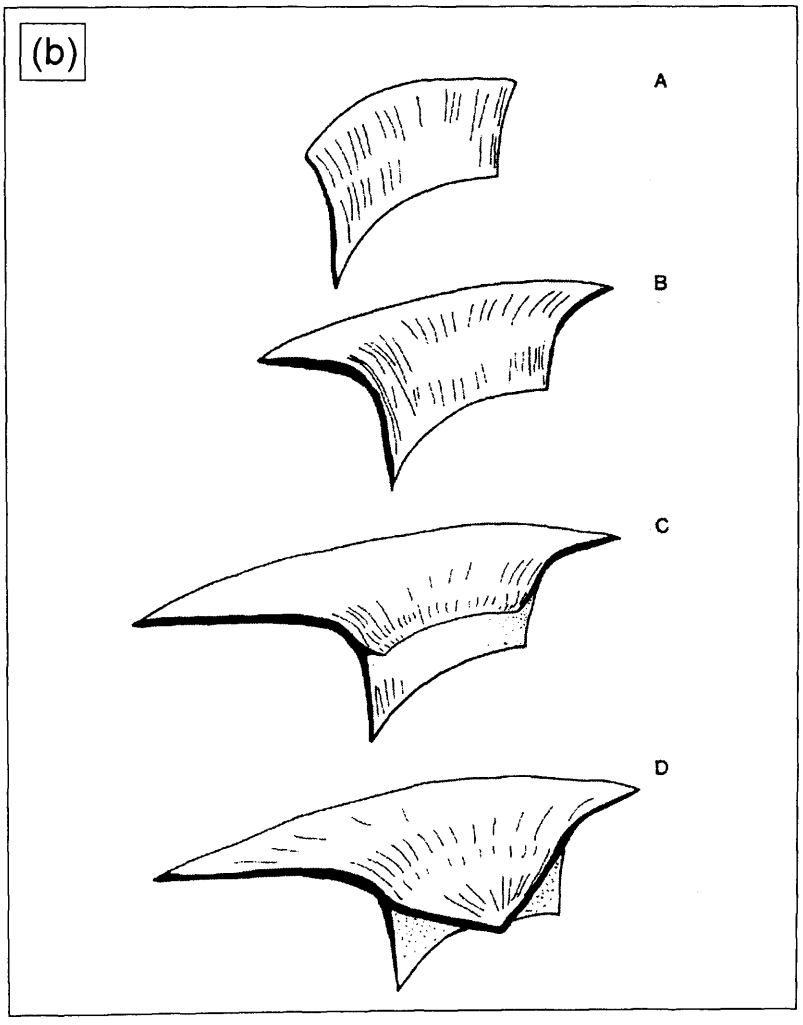

Fig. 7.12 Sketch showing morphological elements (a) and emplacement model (b) for saucer-shaped sills proposed by Chevallier & Woodford (1999).

(Pollard & Holzhausen, 1979; Fialko, 2001; Malthe-Sørensen et al., in press). Numerical modelling by *Pollard & Holzhausen (1979)* suggested that a sill turns transgressive once it has spread laterally over a distance of approximately four times the depth of intrusion. Once the intrusion has spread across this distance it will start to cause significant deformation of the overburden (Pollard & Johnson, 1973; section 7.2.2.2) and subsequently transgress towards the surface as a result of interaction between the stress distribution at the tip of the sill and the free surface (Pollard & Holzhausen, 1979). Mechanical modelling by *Pollard & Johnson (1973)* illustrates a similar idea (Fig. 5.49). In this case transgression occurs at the edge of a sill, forming a wing-like peripheral dyke as a result of infilling of fractures formed at the periphery of an intrusion in response to bending of the overburden due to intrusion. This model has recently been corroborated by computer modelling (*Fialko, 2001; Malthe-Sørensen et al., in press*). The computer modelling showed that once an intrusion reaches a certain length (approximately 2-3 times the depth of intrusion) an anisotropic stress field developed around the sill tips interacts with the free surface and causes the sill to turn transgressive giving the intrusion an overall concave upwards geometry. The exact ratio between saucer width and intrusion depth at which sills according to this model turn transgressive is poorly constrained (2-4), but the model suggests that deeper sills extend further laterally before turning transgressive than shallower sills.

The modelling performed by Malthe-Sørensen et al. (in press) further suggests that sill complexes dominated by saucer-shaped sills, such as the Karoo complex, are formed in the simplest basin configurations with homogeneous infill and initial isotropic stress conditions, whilst planar and segmented sheet intrusions are considered to be more common in structurally deformed basins (see section 7.7.4 for further discussion).

7.6.5 Discussion of previous models

The five models described above build upon a number of observations, many of which have been confirmed by similar observations made during this study. However, these previous models have been based on outcrop studies with their inherent scale and two-dimensional limitations as oppose to the large scale and three-dimensionality obtained during this study. The application of 3D seismic data to the problem of saucer-shaped sills has allowed for a number of more general observations to be made. In this section the previous models are discussed in the light of the insights obtained from seismic interpretation in the case-study areas.

Lombard (1952) compared saucer-shaped sills to cone-sheets. Cone-sheets differ geometrically from saucer-shaped sill in that they do not exhibit near-concordant basal sections, but rather have the shape of an inverted cone or a funnel in which the transgressive limbs originate from a central apex. However, it is possible that at least some of the smaller saucer-shaped sills (e.g. sill 38 of the T38 sill complex; Figs. 5.23 and 5.24) with limited basal concordant width (e.g. sill 38, width = 280 m) were intruded as cone-sheets and developed a more saucer-shaped geometry following flattening during burial. Although it is possible that some of the smaller saucer-shaped sills were originally intruded as cone-sheets, a cone-sheet model is considered insufficient to explain the basic saucer-shaped geometry.

In the case-study areas numerous saucer-shaped sills are seen at many different stratigraphic levels and they often overlap laterally. The model presented by *Bradley (1965)* is insufficient to explain these observations because it would require an exceptionally hilly land surface and multiple phases of intrusion, neither of which have been identified within the data.

Many of the observations made by *Francis (1982)* are in agreement with observations made on the 3D seismic data, e.g. overall shape and local concordance with stratigraphy, but differs in two important ways. (1) The saucer-shaped sills mapped in the case-study areas are linked to basal feeders from which they are interpreted to propagate outwards and upwards rather than to feeders located at the saucer flank from which the initial magma flow is downwards as proposed by Francis (1982). (2) The seismically interpreted saucers show some degree of concordance with stratal reflections, but the seismic data does not suggest that the saucer-shaped geometry in dependant upon a pre-existing saucer-shape basin configuration as proposed by Francis (1982).

Many of the morphological elements recognised by *Chevallier & Woodford (1999)* have also been observed during the seismic interpretation. However, essential to their model is the presence of a dyke, which forms the rim of the saucer. As Chevallier & Woodford (1999) point out themselves a major problem with this model is why a linear and vertical feeder dyke gently curves both along its strike and in depth to form a trumpet-like shape. Evidence of such feeder-dykes has not been seen on the seismic data from the case study areas. The seismic interpretation has revealed that sills are commonly fed by underlying sills and it may be that many of the apparent dykes

interpreted in the field are in fact transgressive sill tips. Such an interpretation could explain the observed curvature along strike, but does not readily explain the development of the inner sill.

The model proposed by *Pollard & Holzhausen (1979)*, *Fialko (2001)*, and *Malthe-Sørensen et al. (in press)* suggests that there is a relationship between emplacement depth and the width of the basal, near-concordant part of saucers. The graph shown in Fig. 7.9b shows emplacement depth plotted against the width of the basal near-concordant part of a number of saucer-shaped sills mapped in the case-study areas. As mentioned in section 7.6.2 the graph shows good correlation between the two parameters, especially when only the most well-defined saucer-shaped sills are considered (R^2 = 92 %). This supports the suggestion that there is a relationship between the emplacement depth and the width of the basal part of saucers. The relationship found based on the case-study areas is linear and suggests that the width of the basal section is approximately 1.5 times greater than the depth of emplacement. This values is less than that obtained through the modelling (2-4). This discrepancy could be due to the poor constraint on the sediment velocities in the survey area. An overall increase in the velocity with depth would cause a relative decrease in width with depth as seen on the graph presented by Malthe-Sørensen et al. (in press; Fig. 7.9a). It should also be taken into consideration that the ratio is dependant upon the material properties of the overburden and a direct comparison of the case-study data with modelled results would require good constraints on the host-rock properties (e.g. porosity, magma pressure, and Young's modulus). This model is further supported by correspondence between the measured angle of transgression (average of 41°; approximate value after depth conversion and decompaction) and the angle of the peripheral dykes and shear planes created at sill tips during propagation (~ 45°) in response to bending of the overburden (Bradley, 1965; Pollard & Johnson, 1973).

Modelling by Malthe-Sørensen et al. (in press) suggested that saucers are most likely to develop in simple basins with homogenous basin-fills and isotropic stress states. This observation is also supported by evidence from the case study areas. The seismic interpretation has shown that saucers are common in the structurally 'quiet' T67 survey area and abundant in the heavily faulted Solsikke survey area. This suggests that saucer-shaped sill segments are likely to be 'failed' saucers that, due to pre-existing heterogeneities (stratigraphic, lithological, or structural) or the nature of the actively

acting stress field at the time of intrusion, did not develop the ideal saucer shape, but some derivative thereof.

7.6.6 Models for the development of saucer-shaped sills

From the above discussion of previous models for the development of saucers and, more generally, saucer-shaped sills it is evident that these models account for many of the observations made during the seismic interpretation from the case study areas. However, none of the models comprises and fully explains all the observations and an alternative model for the development of saucers is, therefore, proposed in this section.

The observations that are here considered to be of greatest importance in relation to a genetic model for the development of saucers and that, therefore, must be explained by a general model for the development of saucers are:

- The feeder is basal to the saucer-shaped sill and is often linked to an underlying or adjacent sill
- Saucers are thickest in their basal central regions and thin towards their edges. The thickness of the central region is relatively constant and the reduction towards the tips is gradual
- Saucer-shaped sills have near-horizontal to slightly curved basal parts flanked by transgressive (19-52°; avg. ~41°) edges
- The width of the basal part of a saucer-shaped sill is related to the depth of emplacement. The width of the basal part is approximately 1.5 times greater than the (compacted) depth of intrusion
- Large saucer-shaped sills have greater vertical relief than smaller saucer-shaped sills
- Saucer-shaped sills emplaced at greater depth exhibit a greater vertical relief and are larger than saucer-shaped sills emplaced at shallower depth

Two models for the development of saucers are described below and illustrated in Fig. 7.13. The two models illustrate the development of saucers with (1) a basal central (Fig. 7.13a) and (2) a basal peripheral feeder (Fig. 7.13b), respectively. These models are idealised and intermediate forms almost certainly also occur. Both models have been subdivided into three main stages: (1) Initiation, (2) Inflation, and (3) Transgression.

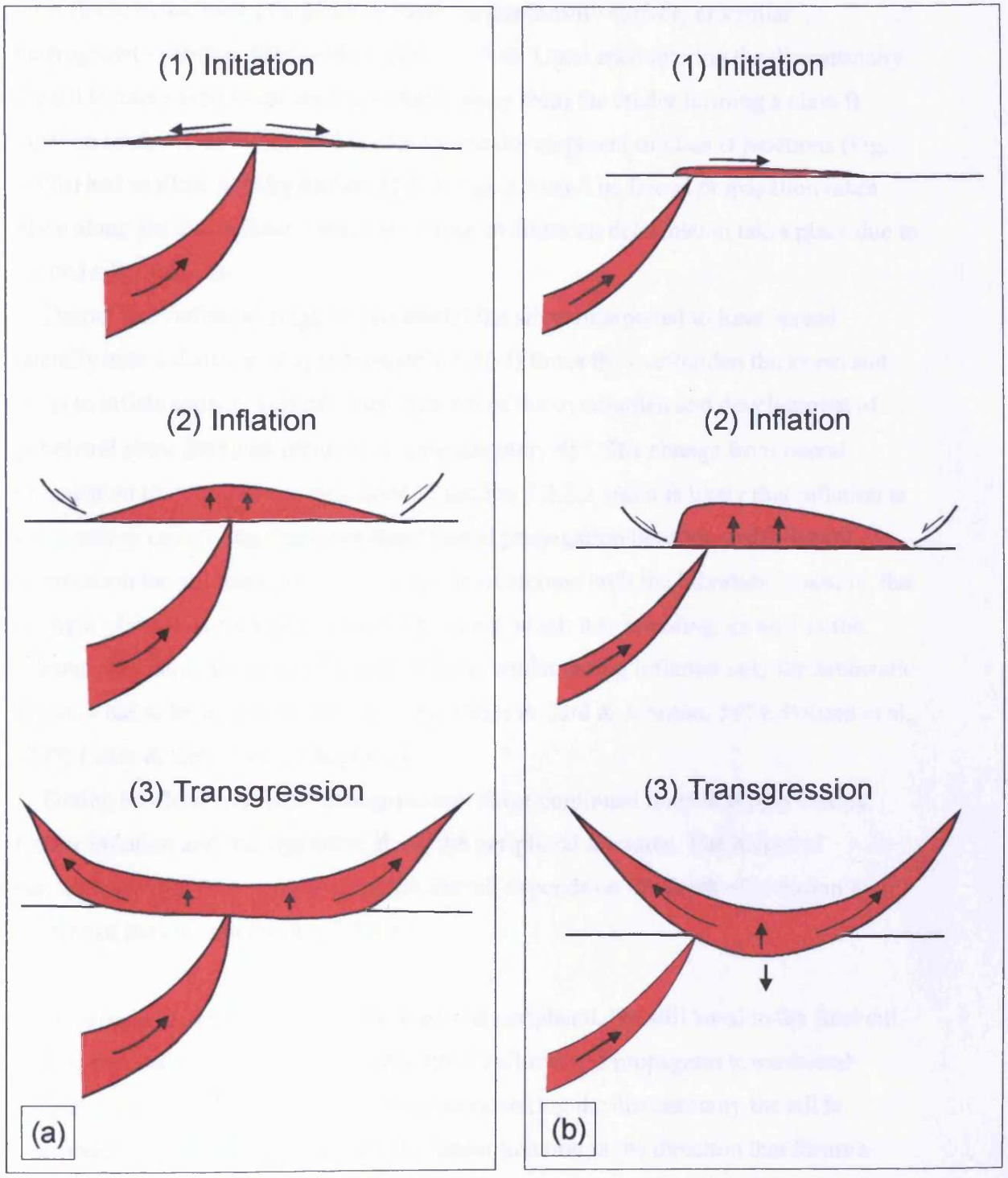

Fig. 7.13 Three-stage models for the growth of saucer-shaped sills. (a) Central near-vertical feeder. (b) Peripheral inclined feeder.

During the '*initiation*' stage of the ***first model*** (Fig. 7.13a) it is suggested that a near-vertical transgressive sill tip propagates towards and encounters a planar discontinuity, most likely in the form of a bedding plane, unconformity surface, or similar heterogeneity (further discussed in section 7.7.4). Upon encountering the discontinuity the sill is interpreted to spread out radially away from the feeder forming a class B junction as shown in the second model for the development of class B junctions (Fig. 3.52b) and as illustrated by Pollard (1973; Fig. 3.51a). The lateral propagation takes place along the discontinuity and only minor overburden deformation takes place due to limited sill thickness.

During the '*inflation*' stage of this model the sill is interpreted to have spread laterally over a distance of approximately 1.5(-4) times the overburden thickness and starts to inflate causing vertical displacement of the overburden and development of peripheral shear fractures inclined at approximately 45°. The change from lateral propagation to inflation was described in section 7.2.2.2 and it is likely that inflation is more energy conserving than continued lateral propagation because during lateral propagation the sill loses potential energy to overcome both the lithostatic pressure, the strength of the host-rock or discontinuity along which it is intruding, as well as the viscous drag along the sill-sediment contacts, whilst during inflation only the lithostatic pressure has to be overcome (cf. Bradley, 1965; Pollard & Johnson, 1973; Pollard et al., 1975; Lister & Kerr, 1991; Chapter 1).

During the third and final '*transgression*' stage continued magma supply causes further inflation and transgression along the peripheral fractures. The height of transgression and thus vertical relief on the sill depends on the depth of intrusion and the size of the sill (see section 7.7.4.1).

In the ***second model*** (Fig. 7.13b) the feeder is peripheral, but still basal to the final sill. During the '*initiation*' stage the feeder sill is inclined and propagates towards and encounters a planar discontinuity. Upon encountering the discontinuity the sill is interpreted to spread out away from the feeder junction in the direction that forms a continuum of the transgressive limb of the feeder sill (cf. Pollard, 1973; Fig. 3.51b). As a result a class A junction is formed between the feeder sill and the initial saucer-shaped sill it feeds as illustrated in the third model for the development of class A junctions (Fig. 3.50c) and described by Pollard (1973).

The '*inflation*' stage of this model is very similar to that of model 1. As the sill spreads laterally the class A junction that was initially formed between the feeder sill and the basal part of the initial sill it feeds changes into a class B junction.

The '*transgression*' stage of the second model is largely similar to the same stage of the first model. However, in this model it is suggested that the basal part of the developing saucer may sink (10s of metres) into the underlying sediments as a result of its higher density causing it to develop a slightly curved basal segment rather than the more horizontally concordant basal segment developed in model 1. This process is here informally termed 'basal settling'. The resultant curvature of the basal segment could be determined by factors such as (1) the density difference between the intruding magma and the host-rock and (2) the location of the feeder relative to the basal segment of the feeder. The more complex saucer-shaped sill geometries may arise as a result of gravity settling if soft sediment deformation, such as Rayleigh-Taylor instability between the intruding magma ($\rho \sim 2.7$ g/cm^3; Bardintzeff & McBirney, 2000) and the host-rock ($\rho \sim 2.4$ g/cm^3; Einsele, 1992) or lateral shale flow, occurs during intrusion. The flow in this final sill will be upwards away from the feeder along the edge that is nearest to the feeder location, but it will be slightly downwards towards the central basal part of the sill before rising along the edge that is opposite and away from the feeder location. This flow pattern is similar to that suggested by Francis (1982), however, it is not controlled by the pre-existing basin configuration, but by basal settling. The final sill exhibits a slightly curved base and is thickest across its basal part, possibly with the greatest thickness skewed towards the location of the feeder. The resolution of the seismic data has not allowed for this hypothesis to be tested, but if this type of deformation occurs it should be possible to find evidence through field studies.

In the discussion of kinematic models for the development of different sill junction geometries it was illustrated that modelling by Pollard (1973; Fig. 3.51) had shown that a class A junction is more likely to form when the feeder approaches a discontinuity at an angle than when it approaches the discontinuity perpendicularly. In the latter case a class B junction is most likely to form. Based on this it is suggested that whether the junction between a feeder sill and the saucer-shaped sill it feeds is central (model 1) or peripheral (model 2) may be controlled by the angle of incidence between the feeder sill and the discontinuity along which the sill spreads out during the initiation stage.

7.6.7 Width vs. thickness distribution during sill growth

The schematic illustration shown in Fig. 7.14 shows the possible width vs. thickness plots for the three kinematic stages of the models presented above. During the *'initiation'* stage of the models a thin concordant initial sill intrudes along the discontinuity. In the case of a near-vertical feeder the spread is radial away from the feeder junction (Fig. 7.14a), whilst in the case of a shallowly inclined feeder the spread is away from the feeder in the same direction as the transgression of the transgressive limb of the feeder sill (Fig. 7.14b). During this stage of propagation the thickness of the sill probably increases in proportion to the length of the sill (Pollard & Johnson, 1973). Due to the resolution of the data it has not been possibly to test this hypothesis. During the *'inflation'* stage the sill inflates and extends laterally in all directions regardless of the location of the feeder. The final width vs. thickness plots for the two models are identical and show a slight increase in thickness of the sill related to the increase in length of the sill. During the final *'transgression'* stages of the two models the sills transgress and further inflate and the width vs. thickness plots reflect the observed greatest thickness across the basal parts of the sill tapering off at similar gradients towards the (transgressive) sill tips. The final width vs. thickness plot for the peripheral feeder model (Fig. 7.14b) may be slightly skewed towards the location of the feeder.

7.7 Discussion: The development of igneous sill complexes

7.7.1 Introduction

This study has allowed for igneous sill complexes to be imaged in three-dimensions and this has allowed for the fully three-dimensional geometry of such complexes to be constrained. This has provided much new insight into the development of sill complexes and to the mechanics of magma transport in the upper crust in general. In this section the main findings of this study in relation to magma transport in the upper crust and the build-up of igneous complexes are summarised and discussed in relation to previous studies.

In this thesis the term ***sill complex*** has been used to refer to highly interconnected networks of sills that may develop through a succession of repeated intrusive events over discrete stratigraphic intervals to form vertically extensive systems of interlinked sills.

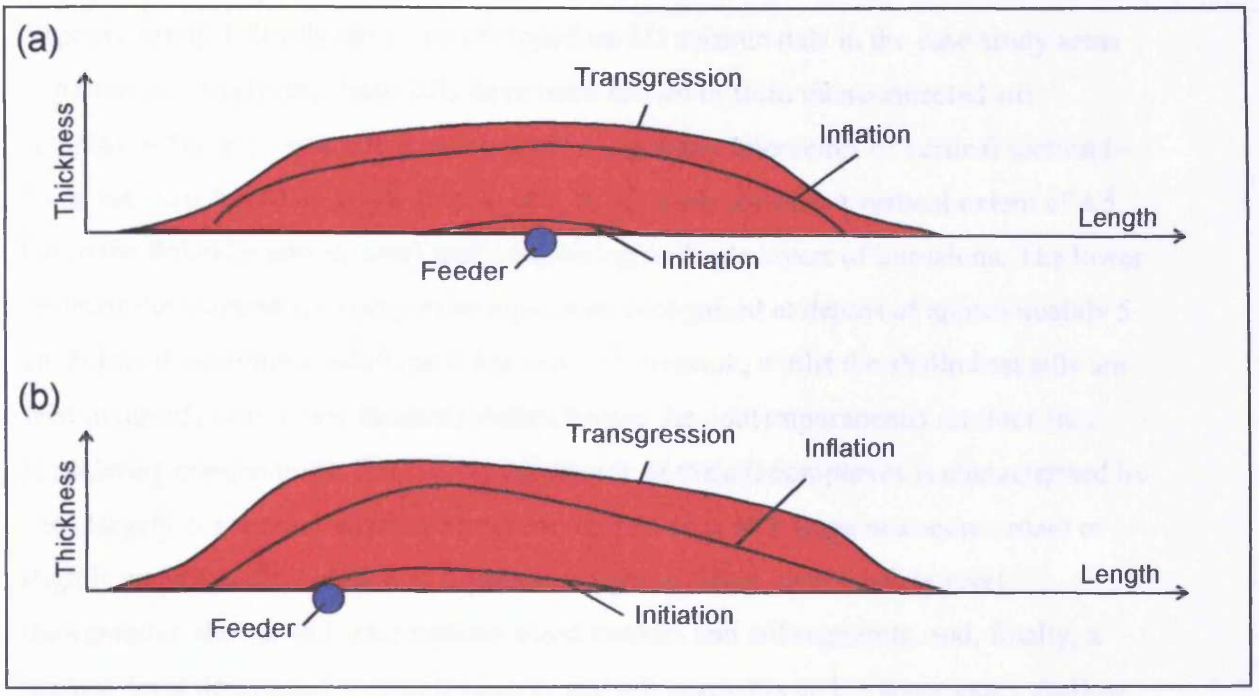

Fig. 7.14 Schematic illustrations of sill length vs. thickness during growth for (a) model 1: central near-vertical feeder and (b) model 2: peripheral inclined feeder.

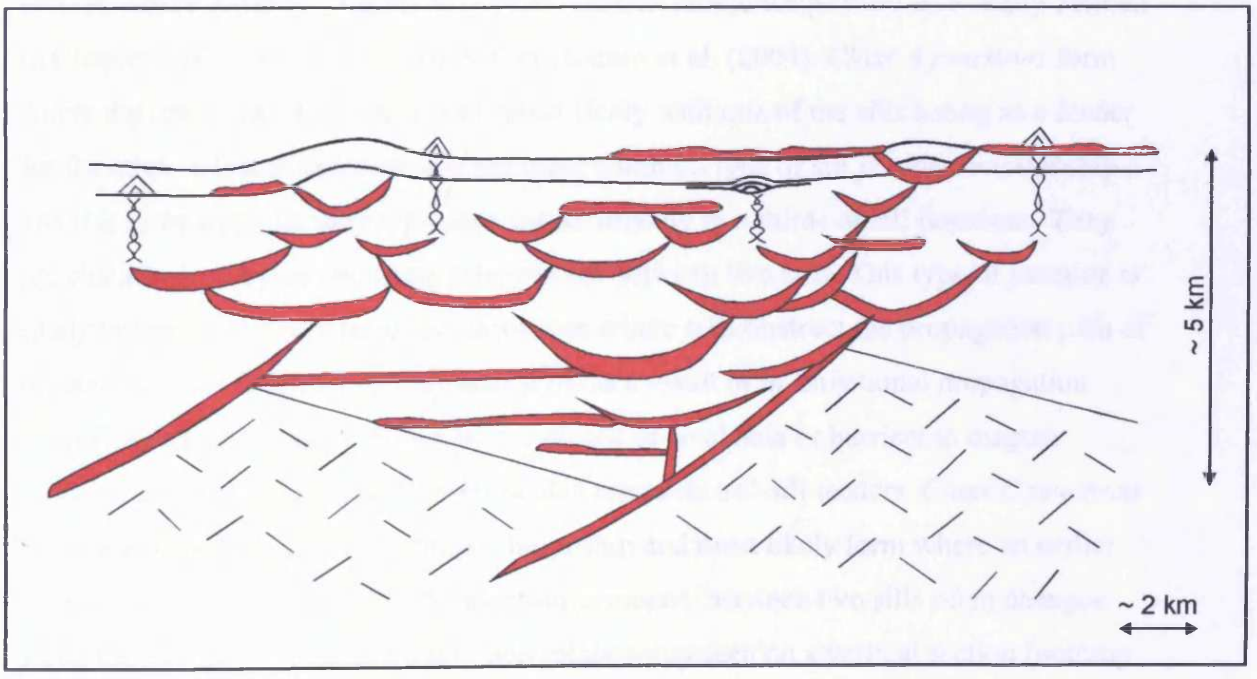

Fig. 7.15 Sill complex geometry. The overall geometry of a sill complex is characterised by deep largely concordant sheets and saucers with large concordant or slightly curved basal parts and impressive vertical relief, intermediate level transgressive sheets, and intermediate sized saucers and sill segments, and, a shallow level dominated by small saucers, sill segments, and concordant sills.

7.7.2 Sill complex geometry

Approximately 150 sills have been mapped on 3D seismic data in the case-study areas as part of this study and these sills have been shown to form interconnected sill complexes that are vertically extensive covering many kilometres of vertical section (~ 7 km, estimate based on crude decompaction of depth-converted vertical extent of 4.5 km in the Solsikke survey area) and comprising multiple layers of intrusions. The lower limits of the mapped sill complexes have been recognised at depths of approximately 5 km below the estimated seafloor at the time of intrusion, whilst the shallowest sills are seen to intrude only a few hundred meters below the contemporaneous seafloor (not considering compaction). The overall geometry of the sill complexes is characterised by deep largely concordant sheets and saucer-shaped sills with large near-concordant or slightly curved central parts and impressive vertical relief, intermediate level transgressive sheets, and intermediate sized saucers and sill segments, and, finally, a shallow level dominated by small saucers and sill segments and in some cases shallow concordant sills (Fig. 7.15).

Individual sills mapped within the sill complexes are linked through sill junctions and the intrusive networks can be followed continuously throughout the covered section. Three different classes of sill-sill junction relationships were informally defined in Chapter 3 (Fig. 3.47) and described in Hansen et al. (2004). *Class A junctions* form where the tips of two sills are linked, most likely with one of the sills acting as a feeder for the other. *Class B junctions* are the most common type of sill junction relationship and it is estimated that they represent approximately two thirds of sill junctions. They are characterised by an abutment relationship between two sills. This type of junction is likely to form in densely intruded sequences where sills obstruct the propagation path of other sills. Class B junctions may also form as a result of bi-directional propagation away from a transgressive sill tip where planes of weakness or barriers to magma transport are encountered and therefore also represent sill-sill feeders. *Class C junctions* are characterised by a cross-cutting relationship and most likely form where an earlier sill is cross-cut by a later sill. The junction geometry between two sills often changes along the line of junction and a junction relationship seen on a vertical section (outcrop or 2D seismic line) is unlikely to be representative of the entire junction.

7.7.3 Vertical development of sill complexes

7.7.3.1 Build-up or build-down?

The kinematic development of the above mentioned sill junction relationships has important implications for the development of sill complexes. Using a number of simple kinematic models for each of these three classes of sill junctions (section 3.4.6) it has been possible to reconstruct the development of compound sills and sill complexes. This has led to the major conclusion that sill complexes build up from deeper to shallower levels with the deeper sills acting as feeders for the more shallow and younger sills (Hansen et al., 2004). This conclusion is supported by the results of the analysis of timing relationships between deep and shallow sills in the T67 and T38 case-study areas where multiple intrusive events have been recognised (section 7.4.2).

The conclusion made here that sill complex build up from deeper to shallower levels is in agreement with suggestions by a number of previous studies (e.g. Bradley, 1965; Einsele, 1985), but contradicts du Toit's (1920) suggestion that the Karoo complex formed as a result of successive intrusion from the top downwards. Du Toit (1920) bases his argument that the Karoo complex formed from the top downwards on the observation that the deeper sills of the Karoo are intact and show hardly any evidence of cross-cutting relationship with later sills. From the 3D seismic analysis it is evident that such relationships do not have to exist for upwards build-up to occur because the shallower sills are fed by the deeper sills rather than by independent feeder systems. This suggests that du Toit's (1920) argument is insufficient to establish the succession of intrusion and it is suggested that the Karoo complex was constructed from deeper to shallower levels with the deeper sills acting as feeders for the shallower sills.

7.7.3.2 Feeder relationships

The detailed interpretation of sill complexes in the case-study areas suggests that sills act as feeders for other sills and thus questions the role of vertical dykes as feeders in sill complexes. No dykes have been observed in the case-study areas, but, as pointed out in Chapter 2, vertical dykes are impossible to image directly on reflection seismic data, which means that dykes may be present, but are undetectable with the seismic data. Outcrop studies suggest that igneous dykes are common features in heavily intruded areas and that they are responsible for transporting large amounts of magma (Harker, 1904; Walker, 1975; Bell, 1984). However, the interpretation presented here suggests that their role in feeding sills is likely to be secondary to that of sill-to-sill feeders.

Sills and lava flows have been found to form contemporaneously in both the T67 and T38 case-study areas (section 7.4.2). Nowhere have sills been seen to feed directly into the overlying lava flows and the latter have been linked to extrusion directly from the Brendan's Dome and Darwin igneous centres, respectively. It has previously been suggested that in the Karoo, sills along with dykes represent the roots and the feeders of the extrusive Drakensberg basalts, as they are identical in age and composition (S. Planke, pers. comm.). The suggestion that sills may feed flows cannot be directly supported by the mapping carried out as part of this study. However, in the case-study areas shallow sills that are fed by underlying sills have been mapped only a few 100 metres below the contemporaneous seabed, e.g. T38. Considering that the magma forming these sills has travelled through the underlying sill complex covering a vertical section of many kilometres it is considered likely that igneous sills may in some cases reach the seafloor and act as feeders for lava flows.

7.7.3.3 Duration of sill complex construction

Several episodes of intrusion, some which are synchronous with extrusion, have been identified in the T67 and T38 case-study areas (section 7.4.2). It is difficult to assess the duration of individual intrusive episodes based on seismic data alone. However, the downlap of internal reflections within the interpreted extrusive mound structure onto discrete reflections and the onlap of post-deformation strata onto well defined horizons interpreted to mark the top of jack-up structures, indicate that the duration of intrusion episodes was limited and fast relative to the rate of deposition. Discrete episodes of magma intrusion have been interpreted in the T67 and T38 case-study areas, with sills of the later episodes intruding stratigraphically above sills of the earlier episode. This suggests that there were intervals during which no intrusion occurred and that the later phases of intrusion reached a shallower level than the early phases. Intrusion rates and time between individual intrusion events are generally poorly constrained due to lack of direct observations, making it difficult to estimate the duration of sill complex construction.

Based on detailed studies of preserved stratigraphy of the Laki eruption in southern Iceland (1783-1785) and the Hekla eruption in March 1947, it has been estimated that initial effusion rates may be as high as 0.4-0.8 km^3/day decreasing to less than $4*10^{-4}$ km^3/day within a few months (Williams & McBirney, 1979; Thordarson & Self, 1993; Bardintzeff & McBirney, 2000). Based on the total volume of the Laki eruption

(~14.7±1 km^3) and the duration of extrusion (8 months; Bardintzeff & McBirney, 2000) it is estimated that the average effusion rate during the eruption was approximately 5.7-6.5*10^{-2} km^3/day. In Chapter 4 it was estimated that the sills mapped in the Solsikke 3D survey area comprise a total magma volume of approximately 60 km^3 with the Solsikke sill comprising approximately 6 km^3 of magma. Using the above calculated effusion rate for the Laki eruption as an estimate for the rate of intrusion, it is estimated the sills mapped in the Solsikke survey area were intruded within a 2½-3 year period with the Solsikke sill forming within just a few months.

Eldholm & Grue (1994) estimated an average emplacement rate in the NAIP of approximately 6.5*10^{-3} km^3/day based on the assumption that two thirds of the estimated flood basalt volume (1.8*10^6 km^3) was emplaced within 500,000 years. Applying the rate derived by Eldholm & Grue (1994) the mapped Solsikke sill complex could have been emplaced within less than 100 years, with the Solsikke sill intruding within a few days.

The finding that sill complexes build up from deeper to shallower levels and that deeper sills act as feeders for shallower sills suggests that the shallowest sills within a given sill complex must be emplaced before the deepest sills in the sill complex are fully solidified. Even if the sill complex is emplaced through a number of magma pulses, most likely involving the development of composite sills, the cooling time probably limits the duration of most sill complex construction to less than 10,000 years.

In the T67 and T38 survey areas where multiple episodes of sill emplacement have been interpreted (section 7.4.2), the shallow young sills of the second major phase of intrusion could have been fed in one of two different ways: (1) through the already existing plumbing system provided by sills intruded during the first phase of intrusion, most likely limiting the time between intrusive events to 10,000 years or less or (2) through a new set of feeders that, based on lack of extensive cross-cutting relationships, most likely took the form of dykes. Considering that the stratigraphic levels at which the mound structures and jack-up structures associated with the two intrusive events can be easily separated seismically, it is considered most likely that the two intrusive events were separated in time by more than 10,000 years and thus that the shallow sills of the latter event were fed through a secondary set of feeders.

The onset of Eocene global warming has been linked to a rapid (~10,000 years) input of isotopically depleted carbon and Svensen et al. (2004) proposed that this rapid event was related to the intrusion of sills close to the Paleocene/ Eocene boundary. These

authors suggested that intrusion of sills along the NE Atlantic Margin and an associated explosive release of methane, partly derived from the host-rock surrounding the sills and partly from melting of gas hydrates, was responsible for initial Eocene global warming. This very interesting idea requires that the sill complexes of the NAIP were intruded within a very short period of time (~10,000 years). The finding that several intrusive phases took place in the Faeroe-Shetland Basin and most likely the NE Rockall Basin presented herein and the occurrence of mound structures within the Paleocene as well as at the Paleocene/Eocene boundary of the Møre Basin (Svensen et al., 2004) does, however, suggest that sill emplacement took place over several tens of thousands of years and thus questions the direct link between sill intrusion in the NAIP and initial Eocene global warming.

From the above it is evident that establishing the timing of sill complex construction and duration has important implications and is bound to form the focus of future research. Better constraints on the different intrusive episodes, for example in the form of detailed well correlation of mound and jack-up horizons, is required to further elucidate these issues.

7.7.4 Controls upon the build-up of sill complexes

The geometry of igneous sill complexes, the thickness of the vertical section intruded, and the interconnectivity between individual sills all speak against a simple model for dyke-to-sill transition. The interpretation has shown that igneous sills form at different depth and that a sill may turn discordant, rise to a shallower stratigraphic level and then propagate laterally again, often forming a new sill. These observations are not compatible with a simple model in which dykes feed individual sills and the dyke to sill transition is governed solely by buoyancy forces or where the magma pressure is no longer sufficient to overcome the strength of the host-rock as proposed by several authors (e.g. Bradley, 1965; Lister & Kerr, 1991).

The detailed interpretation of igneous sills and their relationship with their host-rocks has confirmed previous suggestions that igneous sills exploit bedding planes and fault planes, and that the structural and stratigraphic templates at the time of intrusion significantly influence the geometry and emplacement of sills (e.g. Robertson & Haldane, 1937; Mudge, 1968; Gretener, 1969; Francis & Walker, 1987). This relationship is reflected in the geometry of the sill complexes they form. As it was pointed out in section 7.6, the T67 sill complex and the Karoo complex were both

intruded into largely undeformed sediments and are dominated by saucer-shaped sills, whilst the sill complex of the structurally deformed Solsikke survey area exhibits a much more complex geometry. These observations suggest that the process of sill complex build-up depends strongly on host-rock heterogeneity and local stress conditions. Another factor that has not previously been considered in this thesis is the possible effects of intrusion during a time of regional compression. In addition, a number of additional controls of a more local nature have been identified in the T38 3D seismic survey area. These controls are discussed in the following sections.

7.7.4.1 Stratigraphic and lithological controls

Gretener (1969) suggested that dyke to sill transition was controlled by stratigraphy with certain beds forming stress barriers at which the relationship between the three principal stresses are favourable for lateral intrusion ($\sigma_x > \sigma_y > \sigma_z$; section 1.5.4). The detailed lithological context of the stratal boundaries that have been seen to exert a control upon sill emplacement in the case-study areas is poorly constrained due to the limited well data available to the study. This means that it is not possible, from the seismic data, to determine the exact lithological controls that encourage sills to change from discordant to concordant and conversely from concordant to discordant within the case-study areas. However, the findings of this study that sills are seen at many different stratigraphic levels, often showing partial concordance with stratal reflections (e.g. Figs. 4.38 and 5.39), and that they are part of a continuous intrusive system (e.g. Fig. 4.28) rather than linked to individual feeders, more likely to exhibit different magma pressures, strongly support Gretener's (1969) model. Although sill reflections in the case-study areas often exhibit some concordance with stratal reflections they are very rarely seen to be fully concordant and usually turn discordant and transgress a given stratal stress barrier to form new sills at a shallower stratigraphic level (Fig. 4.31). This, can, according to Gretener's (1969) model, be attributed to variations in the mechanical properties of a bed or lateral variations in lithostatic pressure.

It seems that Gretener's (1969) model can account for many of the observations made in the case-study areas, however, the model does not consider the effect of varying magma pressure and its importance relative to that of the stress regime within the host-rock. Detailed mapping in the T38 3D seismic survey area has shown that space for an igneous sill is created mainly by vertical displacement of the overburden, which can only be achieved if the magma pressure is greater than the maximum vertical

effective stress due to overburden load at the level of intrusion (i.e. $P_m > \sigma_z$; Anderson, 1938; Mudge, 1968). If a sill intrudes at a level where $P_m \sim \sigma_z$ the sill would be in a state of pressure equilibrium with the host-rock and would most likely form a concordant intrusion. However, if a sill as a result of the presence of a stress barrier intrudes at a level where the stress condition $\sigma_x > \sigma_y > \sigma_z$ is fulfilled, but where $P_m >> \sigma_z$ the sill is 'over pressured' relative to the host-rock. This means that the sill has the potential to rise to a higher stratigraphic level.

Considering that the sills within a sill complex are interconnected and most likely linked to a common source at depth, deeper sills are more likely to be 'over pressured' than sills emplaced at shallower depth. This could explain the relationship found between emplacement depth and vertical relief on sills (section 7.2.2.1) because the deeper sills have the potential to transgress more than shallower sills before reaching equilibrium.

According to the findings of this study and in accordance with the ideas presented by Pollard & Holzhausen (1979), Fialko (2001), and Malthe-Sørensen et al. (in press) a sill will ideally start to transgress once it has spread laterally for a distance of about 1.5-4 times the depth of intrusion (section 7.6.5). However, if intruding along a stress barrier, a local change in the relationship between the principal stresses could locally change the orientation of the minimum principal stress from vertical to horizontal and favour dyke intrusion (or sill transgression) over sill intrusion. The high correlation value seen between the width of concordant basal sections of well-defined saucers and emplacement depth (Fig. 7.9) suggests that the model presented by Pollard & Holzhausen (1979), Fialko (2001), and Malthe-Sørensen (in press) is valid. However, the generally poor correlation between emplacement depth and sill (and saucer) area (Figs. 7.1c and 7.8b) may be attributed to changes in local stress regimes associated with stress barriers. It is possible that saucers represent an ideal shape that may only be achieved if there are no heterogeneities in the stress barrier and the transition from lateral to transgressive intrusion is controlled fully by interference between the isotropic stress field surrounding the sill and the free surface. The seismic data are insufficient to test this suggestion, however, it is noteworthy that in the modelled experiments (Pollard & Holzhausen, 1979; Failko, 2001; Malthe-Sørensen et al., in press) the level of initial emplacement is dictated and the overburden is homogeneous.

Regardless of which of the two above mechanisms for dominantly lateral to transgressive intrusion applies in a given case, a transgressive limb should have the

ability to rise to shallower stratigraphic levels for as long as the magma pressure is sufficient to overcome the lithostatic pressure and strength of the host-rock during transgression and great enough to overcome the lithostatic pressure during lateral intrusion. If, during transgression, the sill encounters another stress barrier where $\sigma_x > \sigma_y > \sigma_z$ the sill is likely to turn concordant again and propagate laterally until it reaches a lateral extent of 1.5-4 times the depth of emplacement or a local weakness in the stress barrier is encountered and the sill turns transgressive again. This model suggests that the sill complex will continue to build up from deeper to shallower levels through successive phases of lateral and transgressive intrusion governed by local stress barriers. The sill complex will continue to develop until the magma pressure is no longer sufficient to overcome the lithostatic pressure or the strength of the host-rock.

7.7.4.2 Structural controls

Sills have been found to exploit pre-existing and contemporaneously active fault planes during transgression in the case-study areas (e.g. Fig. 4.35 and 4.41), particularly in the heavily faulted Solsikke survey area. Pre-existing fault planes may constitute areas of weakness and low shear strength and thus be more favourable for intrusion than the surrounding undeformed host-rock (Robertson & Haldane, 1937; Antonellini & Cambray, 1992; Jolly & Sanderson, 1997). Jolley & Sanderson (1997) suggested that whether pre-existing faults can be re-opened during magma intrusion depends upon the magma pressure and the relationship between the minimum and maximum principal stresses acting on the fracture. Delaney et al. (1986) calculated a driving stress ratio (R) for magma to open pre-existing fractures based on magma pressure (P_m), mean stress (σ_m), and maximum shear stress (τ_{max}):

$$R = (P_m - \sigma_m)/ \tau_{max} > \cos 2\theta \qquad \text{(eq. 7.4)}$$

Using the Mohr circle Jolley & Sanderson (1997) concluded that when $P_m < \sigma_3$, no fracture can be open ($R < -1$), when $\sigma_3 < P_m < \sigma_1$, some fractures can be open ($-1 < R < 1$), and when $P_m > \sigma_1$, all fractures can be open ($R > 1$). If the maximum principal stress σ_1 is assumed to be the lithostatic load, $\sigma_1 = \sigma_z$, all fractures can be dilated where $P_m > \sigma_z$. Since the magma pressure much exceed the lithostatic pressure ($P_m > \sigma_z$) in order to intrude laterally, Jolley & Sanderson's (1997) conclusion suggests that faults of all directions may be dilated within the sedimentary section where sills are seen to occur,

whilst only some faults can be dilated in the uppermost part of a sill complex. However, if the sedimentary section is influenced by a regional tectonic extensional stress at the time of intrusion, faults oriented perpendicular to the tectonic stress are considered more likely to be utilised than other faults, and conversely, if influenced by a regional compressional stress at the time of intrusion, faults oriented perpendicular to the tectonic stress are less likely to be utilised than other faults.

In section 7.7.4.1 the transition from transgressive to lateral intrusion was suggested to be associated with the presence of stress barriers in the form of beds that caused the relationship between the principal stresses to change. Recently, it has been demonstrated that faults constitute local stress perturbations that have the ability to re-orient the principal stresses in their near vicinity (Bai et al., 2002; Maerten, et al., 2002). The presence of such stress perturbations has already been demonstrated in the Solsikke survey area (section 4.3.2) where orthogonal intersections are interpreted to form within a polygonal fault system between fault sets A and C due to local stress perturbation surrounding the dominant fault set A. Where such stress perturbations exist in a sedimentary section during magma intrusion it seems reasonable to suggest that they will influence the propagation of the intruding magma in a similar way to the lithological stress barriers described in section 7.7.4.1.

7.7.4.3 Compressional episodes

Evidence for Cenozoic compressional episodes in the form of domes, reverse faults, and broad basin inversion has been recognised from seismic data along the NE Atlantic Margin (Dore & Lundin, 1996; Boldrell & Andersen, 1999; Davies et al., 2004). Three main phases of compression have been recognised: (1) Late Paleocene-Early Eocene, (2) Oligocene, and (3) Middle to Late Miocene. These events have been linked to ocean spreading in the NE Atlantic and ridge-push associated with Alpine tectonics (Dore & Lundin, 1996; Boldrell & Andersen, 1999). The earliest phase of compression during the Late Paleocene-Early Eocene is generally poorly recognised and considered to have been concentrated in a relatively narrow zone including the Wyville-Thomson Ridge Complex and the Munkegrunnur Ridge (Boldrell & Andersen, 1999). However, interpretation in the Solsikke 3D seismic survey area suggests that the development of the Solsikke Dome, which is likely to be an inversion structure, was initiated during the Paleocene and thus that the Late Paleocene-Early Eocene compression may have been more widespread than previously suggested.

Compression is interpreted to have been occurring during the time of intrusion in the NAIP during the Paleocene and earliest Eocene (section 7.4). Compression in the Rockall region during the Late Paleocene-Early Eocene is considered to have been initiated prior to the termination of volcanic activity around the Paleocene-Eocene transition (Boldrell & Andersen, 1999). Similarly in the Solsikke survey area, compression is interpreted to have been initiated during the Early Paleocene (section 4.3.1) and to have been ongoing during the time of intrusion in the Late Paleocene (section 7.4.2).

Intrusion into sediments influenced by a regional compressive stress, as the above indicate may have been the case along much of the NE Atlantic Margin, is likely to encourage sill intrusion over dyke intrusion because it would increase the horizontal principal stress (σ_x) relative to the vertical principal stress (σ_z) and thus act towards fulfilling the basic condition for sill intrusion of $\sigma_x > \sigma_y > \sigma_z$. Compression at the time of intrusion is thus likely to have had a positive effect on the development of the NE Atlantic sill complex. However, the compressive stress regime has not hindered widespread sill transgression and there does not appear to be any evidence suggesting that sill transgression (fault related as well as non-fault related) is preferentially oriented perpendicular to the orientation of the compressive stress (Fig. 4.42), as it would be expected if the compressional stress regime exerted a major effect upon the host-rock sediments (section 7.7.4.2).

The Karoo igneous sill complex was intruded into Carboniferous-Permian Karoo sediments during the Jurassic (Chevallier & Woodford, 1999) following a transition from compression to extension in the Cape Fold Belt (Catuneanu et al., 1998). The Karoo intrusive system was thus intruded under condition of regional extension, further suggesting that although a compressional stress regime may encourage sill intrusion, such conditions are not a prerequisite for the development of extensive sill complexes.

7.7.4.4 Additional local controls

The above discussed controls are considered to be the most important and generally applicable controls upon the construction of sill complexes. However a number of controls of a local nature were identified during interpretation of the T38 case-study area and these are described in this section.

In the T38 case-study area it was suggested that the geometry of the shallow sill 44 was influenced by overburden deformation above underlying sills, with sill 44 being

confined to an elongated synform developed between vertically uplifted stratigraphy above the surrounding underlying sills (section 5.4.3; Fig. 5.38). A similar relationship has previously been described between jack-up structures affecting the seabed and the distribution of a lava flow (Trude et al., 2003) and has also been suggested to play a large role in the formation of the Rio Tinto supergiant massive sulfide deposit (Boulter, 1993).

During the interpretation of the T38 case-study it was noted that a number of sills were developed immediately beyond the eastern extent of Flow unit B (Fig. 5.24), whilst sills are generally not seen below the flow unit with the exception of a number of very small saucers that are emplaced not far below the general base-level of the flow unit. Although the apparent lack of intrusion below the flow unit could be attributed to an imaging problem (Chapter 2) it is interesting to consider this observation from a mechanical point of view in which the lack of intrusions is assumed to be genuine and attributed to the presence of the flow unit. Lava flow unit B was extruded during the early phases of the first intrusive episode in the case-study area. The addition of the flow unit would have led to an increase in the lithostatic pressure in the subsurface underlying the flow unit and most likely have increased the general magma pressure in the sill complex. Considering the difference in σ_z between the area underlying and that away from flow unit B and the condition for lateral intrusion that $P_m > \sigma_z$ it seems reasonable to suggest that it is more difficult for magma rising from a common source to intrude underlying flow unit B than away from it (Fig. 7.16). The concentration of sills immediately beyond the eastern extent of flow unit B suggests that the upward magma transport became focused in this area, possibly driven by the σ_z differential between the two areas.

7.8 Synthesis

This study has been one of the first to explore the application of 3D seismic to studies of subsurface igneous complexes in sedimentary basins. The volcanic rift basins along the NE Atlantic Margin that have been studied herein have been intruded by large volumes of igneous material, have very thick sedimentary fills, and are covered by extensive

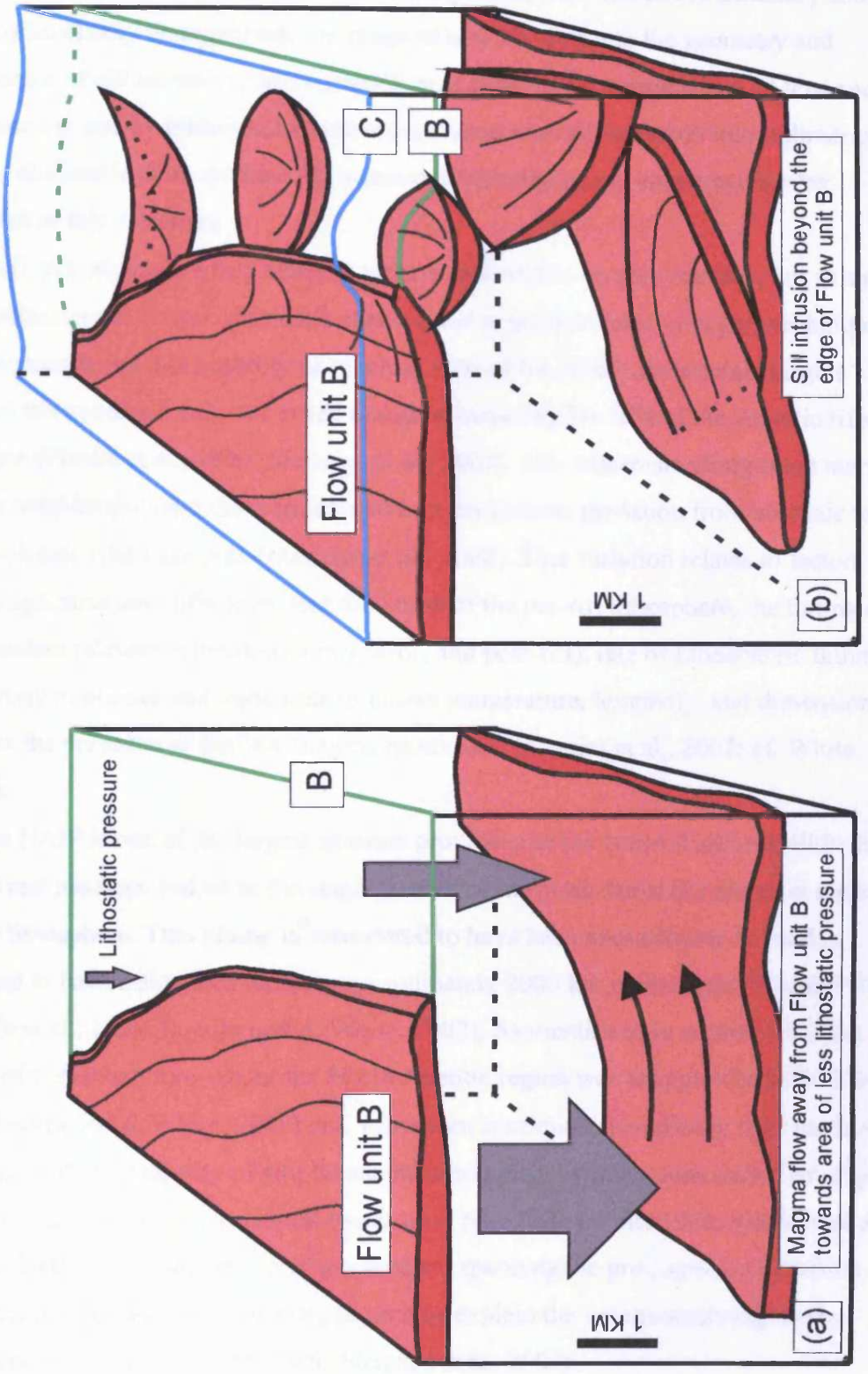

Fig. 7.16 Model illustrating intrusion of sills beyond the edge of flow unit B in the T38 case-study area. (a) Magma flow is driven away from the area underlying Flow unit B due to a difference in lithostatic pressure. (b) Sills intrude beyond the edge of Flow unit B.

seismic surveys and they have proven to be an ideal place to do a seismic study of the emplacement of igneous sills into sedimentary basin-fills. The above summary and discussion clearly demonstrates the range of new insights into the geometry and mechanics of sill intrusion, the construction of igneous sill complexes, and host-rock deformation and hydrothermal systems associated with sill intrusion into sedimentary basins obtainable from detailed 3D seismic interpretation and encourage further research in this direction.

Until recently most rifted margins were considered to be non-volcanic, but as a result of continuous collection of seismic surveys and improvements in imaging techniques it is now considered that possibly as much as 90% of the rifted continental margins around the world are volcanic rifted margins, including 70-75% of the Atlantic rifted margins (Planke et al., 1999; Menzies et al., 2002). The volcanism along these margins varies considerably and there appears to be a continuous gradation from volcanic to non-volcanic rifted margins (Menzies et al., 2002). This variation relates to factors such as the age, structure, lithology, and thickness of the pre-rift lithosphere, the timing of magmatism relative to break-up (pre-, syn-, and post-rift), rate of lithospheric thinning, proximity to plumes and variations in plume temperature, longevity, and dimensions, as well as the presence of shallow magma reservoirs (Menzies et al., 2002; cf. White, 1992).

The NAIP is one of the largest igneous provinces of the world (Coffin & Eldholm, 1992) and has been linked to the impingement of the proto-Icelandic plume at the base of the lithosphere. This plume is considered to have been anomalously hot and is inferred to have influenced an area approximately 2000 km in diameter (White, 1988; Ritchie et al., 1999; Smallwood & White, 2002). As mentioned in section 1.4.2 the onset of volcanism throughout the North Atlantic region was at approximately 62-61 Ma (Smallwood & White, 2002) and volcanism continued sporadically until the Early Eocene, with the majority of emplacement taking place within a time period of only 2-3 My around the time of continental break-up at 56-53 Ma (White 1988; Smallwood & White, 2002). This long period of magmatism spanning the pre-, syn-, and post-rift episodes and the anomalously hot plume may explain the voluminous magmatism observed in this area (White, 1988; Menzies et al., 2002).

The NE Atlantic Margin has undergone multiple extensional episodes and Cretaceous-Cenozoic Basins are superimposed over a complex array of Jurassic and older rift basins (section 1.4.1; Fig. 1.2; Dore et al., 1999). These structural trends are

likely to have been partly dilated by Paleocene extension (Fig. 1.3) at the time of initiation of seafloor spreading and magmatism, which would have aided the rise of igneous material from the mantle into and through the crust. The rift basins along the NE Atlantic Margin comprise very thick Cretaceous and Paleocene sedimentary packages that have allowed for the intruding igneous material to spread out, both laterally and vertically, leading to the construction of impressive igneous sill complexes the construction of which was, at least partially dictated by stratigraphic, lithological, and structural controls, and possibly further aided by compressional tectonic stresses during the Paleocene and earliest Eocene (section 7.7.4).

Important controls upon the volume and construction of igneous complexes along the NE Atlantic Margin, thus seem likely to include; the longevity of magmatism, plume properties, pre-existing structural context, the thickness of the Cretaceous and Paleocene sedimentary units, and compressional events during intrusion.

7.9 Implications for hydrocarbon exploration

Shallow level igneous intrusion in sedimentary basins can have significant impact on exploration and production strategies. This study is one of the first to provide a detailed seismic interpretation of a number of igneous sill complexes in hydrocarbon prone sedimentary basins along a volcanic rifted margin and it has provided much new insight that will aid in future recognition and prediction of igneous intrusions on seismic data.

The case-study datasets used in this study have been provided by oil company sponsors (Shell UK and Norsk Hydro) and the case-study areas have all been targeted during exploration for hydrocarbons along the NE Atlantic margin. Hydrocarbon exploration has been ongoing for the past 30 years and more than 160 exploration wells have been drilled (Davies et al., 2004). Hydrocarbons in the NE Atlantic have been sourced from Jurassic (Dore et al., 1997; Spencer et al., 1999) and possibly Cretaceous and Paleocene (Dore et al., 1997) source rocks and potential reservoirs occur within the Cretaceous and Paleocene interval in the form of gravity-driven sand incursions sealed by the mud-prone late Cretaceous and Cenozoic succession (Dore et al., 1997; Spencer et al., 1999). Hydrocarbon traps include tilted fault blocks and compression anticlines (Dore et al., 1997; Spencer et al., 1999).

In this section a number of implications for hydrocarbon exploration of sill emplacement in sedimentary basins are summarised. The general characteristics of igneous intrusions compiled from seismic examples in the case-study areas, as well as

the published outcrop-based literature, have already been summarised in section 7.2 and will not be further discussed in this section. However, it should be noted that this information is not standard petroleum geoscience curriculum and thus in itself provides a useful tool for interpretation geophysicist working in volcanic rifted margin settings.

7.9.1 Forced folds above sill: a new type of hydrocarbon trap

Forced folds above igneous sills represent a new type of trap in the form of a four way dip closure, the integrity of which has yet to be tested. Several examples of forced folds above sills have been interpreted in the T67 and T38 3D seismic survey areas (e.g. Figs. 3.59 and 5.43) and have previously been shown from 3D seismic data in Trude et al. (2004). They are interpreted to form by upward vertical displacement of sediments in order to accommodate the added thickness provided by the forcible intrusion of underlying sills. The structures form quickly (within weeks to months) and their timing can be constrained through onlap relationship (section 7.3.2).

If sandstone units are folded as part of the deformation process these structures have the potential to form hydrocarbon traps that may subsequently be charged. However, one of the big unknows about this type of trap is to what extent the folded sediments overlying the sill have been influenced by contact metamorphism and hydrothermal activity. As illustrated by Pollard & Johnson (1973; Fig. 5.49) bending of overburden above sills results in pervasive fracturing and thus increased permeability for transport of hydrothermal fluids, possibly leading to significant induration of the deformed stratigraphy, especially any natural aquifers such as a sandstone unit.

7.9.2 Hydrothermal mound structures: potential hydrocarbon reservoirs

The formation and composition of mound structures seen associated with sill intrusion was discussed in Chapter 6 and it was suggested that they are hydrothermal mounds that may range in composition from almost entirely magmatic to fully remobilised sedimentary (section 6.4.4). Field descriptions by Gevers (1928) and fieldwork carried out as part of this research and by others (S. Planke, pers. comm.) suggest that many mounds in the Karoo are comprised of indurated sandstone and conglomerates.

The crest of several of the interpreted mound structures are seen to be offset several 10s of metres by polygonal faults (Fig. 6.21), which suggests that induration must be limited since this type of fault system is considered to develop as a result of spontaneous three-dimensional compaction (Cartwright & Dewhurst, 1998; Cartwright

et al., 2003) and thus is unlikely to influence indurated units. This suggests that there is a possibility that some of these mounds may have reservoir potential. Even if indurated such sediment filled mound structures could potentially act as hydrocarbon reservoirs if fractured and, as it is the case in the case-study areas, overlain by low permeability mudstone sequences.

7.9.3 Hydrocarbon maturation and migration

Intrusion of hot magma and the initiation of hydrothermal systems introduce a major heat source into a sedimentary basin. This supplied heat may induce maturation of hydrocarbons (Raymond & Murchison, 1988; Didyk & Simoneit, 1992; Raymond & Murchison, 1991; Kennish et al., 1992; Svensen et al., 2004).

It has recently been estimated that in the Vøring and Møre basins alone, 0.3-3.0 * 10^{18} g of methane was produced in the metamorphic aureoles with the methane production in the entire NAIP possibly being five times greater (Svensen et al., 2004). The width of the hydrothermal aureole and thus the volume of heat-affected host-rock surrounding a sill from which hydrocarbons may be produced is approximately twice the thickness of the sill (Raymond & Murchison, 1991; Svensen et al., 2004). However, the thickness of the aureole and the hydrocarbon potential of the host-sediments depends on the lithology and degree of maturation of the host-sediments at the time of intrusion, the degree of consolidation of the sediments, and their volume of pore water when invaded by the magma (Raymond & Murchison, 1988; Raymond & Murchison, 1991). If intruded into highly water-logged unconsolidated sediments much of the heat will be used to vaporise the pore water rather than the host-sediments and combined with an increased cooling rate this will decrease the likelihood of hydrocarbon generation (cf. Raymond & Murchison, 1988; Raymond & Murchison, 1991).

CHAPTER 8: CONCLUSIONS

8.1 Introduction

The study has been one of the first to use 3D seismic data to study subsurface igneous complexes and from the preceding chapters it is evident that this novel approach has provided a vast amount of new insights into the geometry and mechanics of sill intrusion and sill complex construction, as well as a number of associated hydrothermal and deformational phenomena. Although igneous sills have been studied in the field for more than a century and many good models have been proposed to explain their geometrical variability and emplacement mechanics, these previous models generally lack three-dimensional and large-scale context. These limitations have been overcome through the use of 3D seismic data and the lessons learnt and presented in this thesis, clearly illustrate the potential of this method and strongly encourages further work in this direction.

In this chapter the most important conclusions drawn from this study are summarised and a number of recommendations for further work are made.

8.2 Conclusions

Sills and seismic

- 3D seismic interpretation offers an exceptional opportunity to re-evaluate previous field-based models related to shallow-level igneous complexes.
- Sills are generally recognised seismically as highly continuous, smooth, and very high amplitude reflections that may exhibit both concordant and discordant relationships with stratal reflections.

The geometry of igneous sills and sill complexes

- Sills adopt a wide range of geometrical styles, ranging from near-concordant sheet-like forms to complex discordant forms and the traditional definition of a sill as 'an intrusive igneous body with concordant surfaces of contact' has been found inadequate to describe the sills mapped in the case-study areas. The term ***sill*** is here used to describe any continuous igneous body spanning a limited (<1.5 km) stratigraphic interval. It may have one or more feeders.

- A new classification scheme for igneous sills has been proposed. Igneous sills mapped in the case-study areas can be ascribed to one of three informally defined sill classes: (1) saucers, (2) sheets, and (3) sill segments based on their three-dimensional geometry.
- Individual sills are linked through sill-sill junctions. Three different types of sill-sill junction geometries (class A-C junctions) have been identified. Sill junctions may act as sill feeders and their geometry may change through time and in space.
- The igneous sills mapped within sill complexes along the NE Atlantic Margin vary in area between 1-120 km^2 and exhibit decompacted vertical relief of up to 2 km, with the average sill covering an area of 22 km^2 and exhibiting a decompacted vertical relief of 670 m. It is estimated that the sills comprise magma volumes of a few km^3.
- Large sills exhibit greater vertical relief than small sills (R^2 = 69%), sills emplaced at depth exhibit a greater vertical relief than sills emplaced at more shallow levels (R^2 =59%), and there is some indication that sills emplaced at depth are larger than sills emplaced at more shallow levels (R^2 = 41%).
- Igneous sills emplaced at relatively shallow depth (*ca.* < 500 m) may behave partly as sills and partly as lava flows, developing lobate and flow ridge morphologies. This is suggested to relate to the low resistance to flow offered by the poorly consolidated host-rock at shallow intrusion depth.

Sill intrusion and the construction of sill complexes

- Space for an intrusion (at least shallow intrusions) is created primarily by upward vertical displacement (jack-up) of the overburden sediments. The amount and volume of displaced sediments is approximately equivalent to the thickness and volume of the underlying sill that causes the deformation.
- A model for the growth of intrusions has been proposed. Igneous sills are interpreted to intrude, spread laterally (probably maintaining a constant length to thickness ration), and subsequently inflate.
- A comparison of a length vs. vertical displacement plot of a jack-up structure and a length vs. displacement plot for a fault where inelastic tip deformation is considered show a striking resemblance, strongly suggesting that inelastic deformation at sill tips should be considered in numerical and analogue sill emplacement models.

- A new model for the construction of sill complexes has been proposed. In this model sills act as feeders for other sills and sill complexes build up vertically, as well as laterally, through a succession of sill-fed emplacement events from deeper to shallower stratigraphic levels and may cover extensive vertical sections of many kilometres (~8 km).
- Igneous sills often exploit fault planes and bedding surfaces. These planes of weakness act as local stress barriers and greatly influence the geometry of sills and the construction of sill complexes.
- Important controls upon the volume and construction of igneous complexes along the NE Atlantic Margin are likely to include; the longevity of magmatism, plume properties, pre-existing structural context, the thickness of the Cretaceous and Paleocene sedimentary units, and compressional events during intrusion.

Saucer-shaped sills

- The mapped saucer-shaped sills range in size from 1-80 km^2, have diameters of up to 10 km, and exhibit vertical relief of up to as much as 1500 m. The average saucer-shaped sill covers an area of a few 10s km^2, has a diameters of 3-6 km, and exhibits a vertical relief of 400-650 m
- Saucer-shaped sills are fed at the base, either centrally or peripherally, and subsequently propagated outwards and upwards. They are thickest in their basal central regions and thin towards their edges. The thickness of the central region is relatively constant and the reduction in thickness towards the tips gradual
- Saucer-shaped sills exhibit discordant edges that transgress stratal reflections at angles of 19-52°, with the average saucer-shaped sill transgressing at 41° (approximate depth-converted and decompacted angles).
- The basal width of the saucer-shaped sills mapped in the case-study areas correlates with the depth of intrusion, with the basal width being approximately 1.5 times greater than the (compacted) depth of intrusion.
- Two models (peripheral and central feeder) for the development of saucer-shaped sills has been proposed. It is suggested that saucer-shaped sills develop through three stages: (1) initiation, (2) inflation, and (3) transgression.
- A saucer-shaped sills may develop a curved, rather than a concordant base as a result of soft-sediment deformation following intrusion due to a density difference between

the intruding magma and the host-sediment. This process is here informally referred to as basal settling. It is suggested that a curved geometry is more likely to develop if the junction with the underlying feeder is inclined and peripheral than if the junction is at a high angle and central to the basal part of the saucer-shaped sill.

- The transgressive edges of sills are interpreted to exploit peripheral shear fractures formed as a result of forced folding above the sill.
- Large saucer-shaped sills exhibit a greater vertical relief than smaller ones, saucer-shaped sills emplaced at depth generally cover larger areas than saucer-shaped sills intruded at more shallow depth, and saucer-shaped sills intruded at depth exhibit a greater vertical relief than saucer-shaped sills emplaced at shallower depths

Mound structures

- Extrusive mound structures have been interpreted above sill tips and crests in sills in all four case-study areas. The mounds are interpreted as constructional bodies extruded onto the contemporaneous seafloor during and immediately following the emplacement of underlying sills.
- It is suggested that the majority of these mound structures are sedimentary structures, formed as a result of sediment remobilisation by hydrothermal fluids and subsequent extrusion onto the paleo-seafloor, whilst others are believed to be entirely or at least dominantly igneous in origin.
- The horizon onto which a mound is extruded is interpreted to mark the timing of intrusion of the underlying sill to which the mound can be linked.

Timing of sill intrusion

- The timing of sill intrusion can be constrained seismically and thus independent of radiometric dating through interpretation of mound structures and jack-up structures.
- Several phases of intrusion have been observed between and within individual case-study areas suggesting that sills were intruded during a number of discrete episodes during the Paleocene and earliest Eocene, rather than continuously throughout the period or during one single intrusive event.

Hydrocarbon exploration

- Forced folds (jack-up structures) formed above igneous sills during emplacement to accommodate the thickness of the intrusive body may form four way dip closures.
- Mound structures may form potential reservoirs if filled with remobilised sand or highly fractured rock. The mound structures mapped in the four case-study areas are draped by thick Eocene mud-dominated units that are likely to provide good seals.

8.3 Further work

As mentioned in section 8.1 this is one of the first studies to explore the application of 3D seismic data to the study of intrusive igneous rocks and the results strongly encourage further work in this direction.

The sill complexes interpreted here are all part of the same igneous province and of similar age, and intruded into similar mud-dominated sedimentary basin fills. The more general applicability of the conclusions drawn from this study has thus yet to be tested against sill complexes intruded into basins along other volcanic margins. Ideally this should be done by comparing the results of this study with results of 3D seismic-based studies of sill intrusion into volcanic rift basins elsewhere. Possible areas where seismic data are already available include the South Atlantic Margins and the Western Australia rifted margin. The knowledge gained from this study should also be tested in the field. The ideas proposed here from 3D seismic interpretation may allow for locations within classical field areas to be viewed in a new way and thus further the understanding of these.

Only very limited well data and 2D seismic data have been available to this study. Use of a greater well and 2D seismic database would allow for much better constraints to be placed on the lithological and stratigraphic context of the host-sediments and the regional context of the case-study areas. This would allow for the results of this study to be better linked to the structural evolution and magmatic history of the NAIP.

Constraining the age of individual horizons influenced by mound structures and jack-up would allow for the timing of intrusion to be better constrained and in the case of the T67 and T38 case-studies allow for the time between individual intrusive events to be constrained. As mentioned in section 7.7.3.3 constraining the timing of sill emplacement has significant implications in relation to determining the possible role of sill intrusion for initial Eocene global warming.

In this study models have been put forward to explain the mechanics of sill growth, the development of saucer-shaped sills, and the construction of sill complexes. A more detailed attempt at decompacting the host sedimentary units than that provided herein would allow for better constraints to be placed on intrusion depth, vertical relief on individual sills, and vertical extent of sill complexes. Combined with additional detailed interpretation of the amount of vertical displacement on large jack-up structures and thickness variation within sills the mechanical models proposed in this thesis could be further tested.

Seismic modelling of igneous sills intruded into sedimentary basins would further the understanding of their seismic expression and allow for constraints to be placed on the seismic resolvability of igneous sills (i.e. the presence of unresolved steps and thickness changes towards sill terminations)

Many of the recommendations for further work listed above could, ideally, be addressed by an IODP cruise. Issues that IODP drilling could most likely elucidate within the NAIP include: (1) The composition and age of mound structures within different areas of the NAIP and their role in initial Eocene global warming. (2) Compositional differences in sills at different stratigraphic levels within a given sill complex, between different areas of the NAIP, and across individual sills. This information would in combination with further seismic interpretation allow for the model for sill complex construction proposed here to be tested and would provide new insight into the general problem of magma transport in the upper crust. (3) The age and nature (e.g. diagenetic state) of jack-up structures and the relationship between the amount of vertical displacement and sill thickness. (4) The nature of stress barriers. (5) Hydrothermal alteration of host-rock surrounding sills and the development of thermal aureoles. In addition to these sill complex related issues IODP drilling in this region would also allow for better age constraints to be placed on the shallower section, which combined with the extensive seismic data base would be useful in relation to paleo-oceanography and paleo-climate studies.

REFERENCE LIST

A

Allaby, A. & Allaby, M. 1999. *Dictionary of earth sciences*. Oxford University Press.

Andersen, M. S. (1988) Late Cretaceous and early Tertiary extension and volcanism around the Faeroe Islands. *In*: Morton, A. C. & Parson, L. M. (eds.) *Early Tertiary volcanism and the opening of the NE Atlantic*. Geological Society, London, Special Publication, 39, 115-122.

Anderson, E. M. (1936) The dynamics of the formation of cone-sheets, ring-dykes, and caldron-subsidences. Proceeding of the Royal Society of Edinburgh, 56, 128-157.

Anderson, E. M. (1938) The dynamics of sheet intrusions. Proceedings Royal Society of Edinburgh, 58, 242-251.

Anderson, E. M. (1951) *The dynamics of faulting and dyke formation with applications to Great Britain*. Oliver and Boyd, London, 206p.

Antonellini, M. A. & Cambray, F. W. (1992) Relations between sill intrusions and bedding-parallel extensional shear zones in the Mid-continent Rift System of the Lake Superior region. Tectonophysics, 212, 331-349.

Athy, L. F. (1930) Density, porosity and compaction of sedimentary rocks. American Association of Petroleum geology Bulletin, 14, 1-24.

B

Badley, M. E. (1985) *Practical seismic interpretation*. International Human Resources Development Corporation, Boston, 266p.

Baer, G. & Beyth, M. (1990) A mechanism of dyke segmentation in fractures host rock. *In*: Parker, Rickwood & Tucker (eds.) *Mafic dykes and emplacement mechanisms*. p. 3-11. Balkema, Rotterdam.

Bardintzeff, J.-M. & McBirney, A. R. (2000) *Volcanology*. Jones and Bartlett Publisheres, Inc.

Barmin, A., Melnik, O. & Sparks, R. S. J. (2002) Periodic behaviour in lava dome eruptions. Earth and Planetary Science Letters, 199, 173-184.

Bauer, K., Trumbull, R. B. & Vietor, T. (2003) Geophysical images and a crustal model of intrusive structures beneath the Messum ring complex, Namibia. Earth and planetary Science Letters, 216, 65-80.

Bell, B. R. (1984) The geochemistry of Lower tertiary basic dykes in the Eastern Red Hill district, Isle of Skye, and their significance for the proposed magmatic evolution of the Skye Centre. Mineralogical Magazine, 48, 365-373.

Bell, B. R. & Pankhurst, R. J. (1993) Sr-isotope variations in a composite sill: crystal-liquid processes and the origin of the Skye granites. Journal of the Geological Society, London, 150, 121-124.

Bell, B. & Butcher, H. (2002) On the emplacement of sill complexes: evidence from the Faroe-Shetland Basin. *In*: Jolley, D. W. & Bell, B. R. (eds.) *The North Atlantic Igneous Province: Stratigraphy, tectonic, volcanic and magmatic processes*. Geological Society, London, Special Publications, 197,

Bell, B. R. & Williamson, I. T. (2002) Tertiary igneous activity. *In*: Trewin, N. H. (ed.) *The Geology of Scotland*. The Geological Society, London, 371-408.

Berndt, C. Planke, S. Alvestad, E. Tsikalas, F. & Rasmussen, T. (2001) Seismic volcanostratigraphy of the Norwegian Margin: constraints on tectonomagmatic break-up processes. Journal of the Geological Society, 158, 413-426.

Boldreel, L. O. & Andersen, M. S. (1993) Late Paleocene compression in the Faeroe-Rockall area. *In*: Parker, J. R. (ed.) *Petroleum Geology of Northwest Europe: Proceedings of the 4th Conference*, Geological Society, London, 1025-1034.

Boudier, F., Nicolas, A. & Ildefonse, B. (1996) Magma chambers in the Oman ophiolite: fed from the top and the bottom. Earth and Planetary Letters, 144, 239-250.

Boulter, C. A. (1993) Comparison of Rio Tinto, Spain, and Guaymas Basin, Gulf of California: An explanation of the supergiant massive sulfide deposit in an ancient sill-sediemtn complex. Geology, 21, 801-804.

Boulter, C. A. (1996) Extensional tectonics and magmatism as drivers of convection leading to Iberian Pyrite Belt massive sulphide deposits?. Journal of the Geological Society, London, 153, 181-184.

Bradley, J. (1965) Intruion of major dolerite sills. Transactions of the Royal Society of New Zealand, 3, 27-54.

Brekke, H. (2000) The tectonic evolution of the Norwegian Sea continental margin with emphasis on the Vøring and Møre basins on the Norwegian Sea continental margin. *In:* Nøttvedt, A. (ed.) *Dynamics of the Norwegian Margin.* Geological Society, London, Special Publication, 167, 327-378.

Brekke, H., Dahlgren, S, Nyland, B. & Magnus, C. (1999) The prospectivity of the Vøring and Møre basins on the Norwegian Sea continental margin. *In*: Fleet, A. J. & Boldy, S. A. R. (eds.) *Petroleum Geology of Northwest Europe: Proceedings of the 5th Conference*, Geological Society, London, 261-274.

Buist, D. S. (1959) The composite sill of Rudh' an Eireannaich, Skye. Geological Magazine, 96, 247-252.

Buist, D. S. (1961) The composite sill of Rudh' a' Chromain, Carsaig, Mull. Geological Magazine, 98, 67-76.

C

Carey, S. W. (1958) The isostrat, a new technique for the analysis of the structure of the Tasmanian dolerite. In: *Dolerite: A symposium.* Hobart University of Tasmania. 130-164.

Cartwright, J. A. 1994. Episodic basin-wide fluid expulsion from geopressured shale sequences in the North Sea Basin. Geology, 22, 447-450.

Cartwright, J. A., Trudgill, B. D. & Mansfield, C. S. (1995) Fault growth by segment linkage: an explanation for scatter in maximum displacement and trace length data from the Canyonlands Grabens of SE Utah. Journal of Structural Geology, 17, 1319-1326.

Cartwright, J. A. & Dewhurst, D. (1998) Layer-bound compaction faults in fine-grained sediments. Bulletin of the Geological Society of America, 110, 1242-1257.

Cartwright, J., James, D. & Bolton, A. (2003) The genesis of polygonal fault systems. *In*: Van Rensbergen, P., Hillis, R.R., Maltman, A. J. & Morley, C. K. (eds.) *Subsurface sediment remobilisation.* Geological Society, London, Special publications, 216, 223-244.

Cathles, L. M., Erendi, A. H. J. & Barrie, T. (1997) How long can a hydrothermal system be sustained by a single intrusive event ?. Economic Geology, 92, 766-771.

Catuneanu, O., Hancox, P. J. & Rubidge, B. S. (1998) Reciprocal flexural behaviour and contrasting stratigraphies: a new basin development model for the Karoo retroarc foreland system, South Africa. Basin Research, 10, 417-439.

Chambers, L. M. & Pringle, M. S. (2001) Age and duration of activity at the Isle of Mull Tertiary igneous centre, Scotland, and confirmation of the existence of subchrons during Anomaly 26r. Earth and Planetary Science Letters, 193, 333-345.

Chevallier, L. & Woodford, A. (1999) Morpho-tectonics and mechanism of emplacement of the dolerite ring and sills of the western Karoo, South Africa. South African Journal of Geology, 102, 43-52.

Childs, C., Watterson, J. & Walsh, J. J. (1995) Fault overlap zones within developing normal fault systems. Journal of Geological Society, London, 152, 535-549.

Coffin, M. F. & Eldholm, O. (1992) Volcanism and continental break-up: a global compilation of large igneous provinces. *In*: Storey, B. C., Alabaster, T. & Pankhurst, R. J. (eds.) *Magmatism and the Causes of Continental Break-up.* Geological Society, London, Special Publication, 68, 17-30.

Cowie, P. A. & Scholz, C. H. (1992a) Physical explanation for the displacement-length relationship of faults using a post-yield fracture mechanics model. Journal of Structural Geology, 14, 1133-1148.

Cowie, P. A. & Scholz, C. H. (1992b) Displacement-length scaling relationship for faults: data synthesis and discussion. Journal of Structural Geology, 14, 1149-1156.

D

Daly, R. A. (1933) *Igneous rocks and the depth of the earth.* McGraw-Hill, New York.

Davies, R, Bell, B. R, Cartwright, J. A. & Shoulders, S. 2002. Three-dimensional seismic imaging of Paleogene dike-fed submarine volcanoes from the northeast Atlantic margin. Geology, 30, 223-226.

Davies, R., Cloke, I., Cartwright, J., Robinson, A. & Ferrero, C. (2004) Post-breakup compression of a passive margin and its impact on hydrocarbon prospectivity: An example from the Tertiary of the Faeroe-Shetland Basin, United Kingdom. American Association of Petroleum Geologists Bulletin, 88, 1-20.

Delaney, P. T. & Pollard, D. D. (1981) Deformation of host rocks and flow of magma during growth of minette dikes and breccia-bearing intrusions near Ship Rock, New Mexico. U. S. geological Survey Professional Paper 1202, 61p.

Delaney, P. T., Pollard, D. D., Ziony, J. I. & McKee, E. H. (1986) Field relations between dikes and joints: Emplacement processes and paleostress analysis. Journal of Geophysical Research, 91, 4,920-4,938.

Didyk, B. M. & Simoneit, B. R. T. (1989) Hydrothermal oil of Guaymas Basin and implications for petroleum formation mechanisms. Nture, 342, 65-342.

Doré, A. G. & Lundin, E. R. (1996) Cenozoic compressional structures on the NE Atlantic margin: nature, origin and potential significance for hydrocarbon exploration. Petroleum Geoscience, 2, 299-311.

Doré, A. G., Lundin, E. R., Birkland, Ø., Eliassen, P. E. & Jensen, L. N. (1997) The NE Atlantic Margin: implications of late Mesozoic and Cenozoic events for hydrocarbon prospectivity. Petroleum Geoscience, 3, 117-131.

Doré, A. G., Lundin, E. R., Jensen, L. N., Birkeland, P. E. & Fichler, C. (1999) Principal tectonic events in the evolution of the northwest European Atlantic margin. *In*: Fleet, A. J. & Boldy, S. A. R. (eds.) *Petroleum Geology of Northwest Europe: Proceedings of the 5th Conference*, Geological Society, London, 41-61.

du Toit, A. I. (1920) The Karoo dolerites. Transactions Geological Society of South Africa, 33, 1-42.

E

Ebrom, D., Li, X. & McDonald, J. (1995) Bin spacing in land 3-D seismic surveys and horizontal resolution in time slices. The Leading Edge, 1, 37-40.

Egerton, P. D. (1998) Seismic characterization of Palaeogene depositional sequences: northeastern Rockall Trough. *In*: Stoker, M. S., Evans, D. & Cramp, A. (eds.) *geological processes on continental margins: Sedimentation, mass-wasting and stability.* Geological Society, London, Special Publication, 129, 217-228.

Einsele, G. (1982) Mechanism of sill intrusion into soft sediment and expulsion of pore water. Initial Reports of the DsDP, 64, 1169-1176.

Einsele, G. (1985) Basaltic sill-sediment complexes in young spreading centers: Genesis and significance. Geology, 13, 249-252.

Einsele, G. (1986) Interaction between sediments and basalt injections in young Gulf of California-type spreading centers. Geologische Rundschau, 75, 197-208.

Einsele, G. (1992) *Sedimentary basins*. Springer-Verlag, 628p.

Einsele, G., Gieskes, J. M., Curray, J., Moore, D. M, Aguayo, E., Aubry, M-P., Fornari, D., Guerrero, J., Kastner, M., Kelts, K., Lyle, M., Matoba, Yasumochi, Molina-Cruz, Adolfo, Niemitz, J., Rueda, J., Saunders, A., Schrader, H., Simoneit, B. & Vacquier, V. (1980) Intrusion of basaltic sills into highly porous sediments, and resulting hydrothermal activity. Nature, 283, 441-445.

Ellis, D., Brian, B. B., Jolley, D. W. & O'Callaghan, M. (2002) The stratigraphy, environment of eruption and age of the Faroes Lava Group, NE Atlantic Ocean. *In*: Jolley, D. W. & Bell, B. R. (eds.) *The North Atlantic Igneous Province: Stratigraphy, tectonic, volcanic and magmatic processes*. Geological Society, London, Special Publications, 197, 253-269.

F

Fialko, Y. (2001) On origin of near-axis volcanism and faulting at fast spreading mid-ocean ridges. Earth and Planetary Science Letters, 190, 31-39.

Fink, J. (1980) Surface folding and viscosity of rhyolite flows. Geology, 8, 250-254.

Francis, E. H. (1982) Magma and sediment-I: Emplacement mechanism of late Carboniferous tholeiite sills in northern Britain. Journal of the Geological Society, London, 139, 1-20.

Francis, E. H. & Walker, B. H. (1987) Emplacement of alkali-dolerite sills relative to extrusive volcanism and sedimentary basins in the Carboniferous of Fife, Scotland. Transactions of the Royal Society of Edinburgh: Earth Sciences, 77, 309-323.

G

Gartrell, A., Zhang, Y., Lisk, M. & Dewhurst, D. (2003) Enhanced leakage of fault intersections: an example from the Timor Sea, Northwest Shelf, Australia. Journal of Geochemical Exploration, 78-79, 361-365.

Gay, A., Lopez, M., Cochonat, P., Sultan, N., Cauquil, E. & Brigaud, F. (2003) Sinuous pockmark belt as indicator of a shallow buried turbiditic channel on the lower slope of the Congo basin, West African margin. *In*: Van Rensbergen, P., Hillis, R.R., Maltman, A. J. & Morley, C. K. (eds.) *Subsurface sediment remobilisation*. Geological Society, London, Special publications, 216, 173-190.

Gevers, T. W. (1928) The volcanic vents of the Western Stormberg. Transactions Geological Society of South Africa, 31, 43-62.

Gibb, F. G. F. & Kanaris-Sotiriou, R. (1988) The geochemistry and origin of the Faeroe-Shetland sill complex. *In*: Morton, A. C. & Parson, L. M. (eds.) *Early Tertiary volcanism and the opening of the NE Atlantic.* Geological Society, London, Special Publication, 39, 241-252.

Gieskes, J. M., Kastner, M., Einsele, G., Kelts, K & Niemitz, J. (1982) Hydrothermal activity in the Guaymas Basin, Gulf of California: A synthesis. Initial Reports of the DSDP, 64, 1159-1167.

Gill, W. D. & Kuenen, P. H. (1958) Sand volcanoes on slumps in the Carboniferous of County Clare, Ireland. Quaterly Journal of the Geological Society of London, 113, 441-460.

Gregg, T. K. P. & Fink, J. H. (1995) Quantification of submarine lava-flow morphology through analog experiments. Geology, 23, 73-76.

Gretener, P. E. (1969) On the mechanics of the intrusion of sills. Canadian Journal of Earth Sciences, 6, 1415-1419.

Gudmundsson, A. (1998) Magma chambers modelled as cavaties explain the formation of rift zone central volcanoes and their eruption and intrusion statistics. Journal of Geophysical Research, 103, 7401-7412.

Gudmundsson, A. (2002) Dynamics of volcanic systems in Iceland: Example of tectonism and volcanism at juxtaposed hot spot and mid-ocean ridge systems. Annual Review of Earth and Planetary Sciences, 28, 107-140.

H

Hansen, D. M., Cartwright, J. A. & Thomas, D. (2004) 3D seismic analysis of the geometry of igneous sills and sill junction relationships. *In*: Davies, R. J., Cartwright, J. A., Stewart, S. A., Lappin, M. & Underhill, J. R. (eds.) *3D Seismic Technology: Application to the Exploration of Sedimentary Basins.* Geological Society, London, Memoirs, 29, 199-208.

Hanson, R. E. & Wilson, T. J. (1993) Large-scale rhyolite peperites (Jurassic, southern Chile). Journal of Volcanology and Geothermal Research, 54, 247-264.

Harker, A. 1904. *The Tertiary igneous rocks of Skye.* J. Hedderwick & Sons, Glasgow.

Hodges, S., Line, C. & Evans, B. 1999. The other millennium dome. Presented at the 1999 SPE Offshore Europe Conference, Aberdeen, Scotland, 7-9 September 1999. Society of Exploration Engineers Inc.

Hon, K., Kauahikaua, J., Denlinger, R. & MacKay, K. (1994) Emplacement and inflation of pahoehoe sheet flows: Observations and measurements of active lava flows on Kilauea Volcano, Hawaii. Geological Society of America Bulletin, 106, 351-370.

Hotz, P. E. (1952) Form of diabase sheets in south eastern Pennsylvania. American Journal of Science, 250, 375-388.

Howard, K. A. (1991) Intrusion of horizontal dikes: Tectonic significance of Middle Proterozoic diabase sheets widespread in the upper crust of the southwestern United States. Journal of Geophysical Research, 96, 12,461-12,478.

I

J

Jenyon, M. K. (1987) Characteristics of some igneous extrusive and hypabyssal features in seismic data. Geology, 15, 237-240.

Johnson, A. M. & Pollard, D. D. (1973) Mechanics of growth of some laccolithic intrusions in the Henry Mountains, Utah. Tectonophysics, 18, 261-309.

Johnson, G. A. L. & Dunham, K. C. (2001) Emplacement of the Great Whin Dolerite Complex and the Little Whin Sill in relation to the structure of northern England. Proceedings of the Yorkshire Geological Society, 53, 177-186.

Jolley, D. W., Clarke, B. & Kelley, S. (2002) Paleogene time scale miscalibration: Evidence from the datingof the North Atlantic igneous province. Geology, 30, 7-10.

Jolley, R. J. H. & Sanderson, D. J. (1997) A Mohr circle construction for the opening of a pre-existing fracture. Journal of Structural Geology, 19, 887-892.

Joppen, M. & White, R. S. (1990) The structure and subsidence of Rockall Trough from two-ship seismic experiments. Journal of Geophysical Research, 95, 19,821-19,837.

K

Kennish, M. J., Lutz, R. A. & Simoneit, B. R. T. (1992) Hydrothermal activity and petroleum generation in the Guaymas Basin. Reviews in Aquatic Sciences, 6, 467-477.

Kerr, R. C. & Lister, J. R. (1995) The lateral intrusion of silicic magmas into unconsolidated sediments: the Tennant Creek porphyry revisited. Australian Journal of Earth Sciences, 42, 223-224.

Kiørboe, L. (1999) Stratigraphic relationships of the Lower Tertiary of the Faeroe Basalt Plateau and the Faeroe-Shetland Basin. *In*: Fleet, A. J. & Boldy, S. A. R. (eds.) *Petroleum Geology of Northwest Europe: Proceedings of the 5th Conference*, Geological Society, London, 559-572.

Knox, J. (1954) The economic geology of the Fife Coalfields, area III. Memoir of the Geological Survey of Great Britain. 134 p.

Knox, R. W. O'B. & Holloway, S. (1992) Paleogene of the Central and Northern North Sea. *In*: Knox, R. W. O'B. & Cordey, W. G. (eds.) *Lithostratigraphic nomenclature of the UK North Sea*. British Geological Survey, Nottingham.

Kokelaar, B. P. (1982) Fluidization of wet sediments during emplacement and cooling of various rocks. Journal of the Geological Society, London, 139, 21-33.

Krynauw, J. R., Behr, H.-J. & Van den Kerkhof, A. M. (1994) Sill emplacement in wet sediments: fluid inclusion and cathodoluminescence studies at Grunehogna, western Dronning Maud Land, Antarctica. Journal of the Geological Society, London, 151, 777-794.

L

Larsen, H. C. & Marcussen, C. (1992) Sill-intrusion, flood basalt emplacement and deep crustal structure of the Scoresby Sund region, East Greenland. *In*: Storey, B. C., Alabaster, T. & Pankhurst, R. J. (eds.) *Magmatism and the Causes of Continental Break-up*. Geological Society, London, Special Publication, 68, 365-386.

Leaman, D. E. (1975) Form, mechanism, and control of dolerite intrusion near Hobart, Tasmania. Journal of the Geological Society of Australia, 22, 175-186.

Lister, J. & Kerr, R. (1991) Fluid-mechanical models of crack propagation and their application to magma transport in dykes. Journal of Geophysical research, 96, 10,049-10,077.

Loewinson-Lessing, F. (1936) A contributions to the mechanics of intrusions. XVI International Geological Congress Report, 333-352.

Lombard, B. V. (1952) Karoo dolerites and lavas. Transactions Geological Society of South Africa, 55, 175-198.

Lonsdale, P. (1983) Laccoliths (?) and small volcanoes on the flank of the East Pacific Rise. Geology, 11, 706-709.

Lonsdale, P. & Lawver, L. A. (1980) immature plate boundary zones studied with a submersible in the Gulf of California. Geological Society of America Bulletin, 91, 555-569.

Løseth, H., Wensaas, L., Arntsen, B. & Hovland, M. (2003) Gas and fluid injection triggering shallow mud mobilization in the Hordaland Group, North Sea. *In*: Van Rensbergen, P., Hillis, R.R., Maltman, A. J. & Morley, C. K. (eds.) *Subsurface sediment remobilisation*. Geological Society, London, Special publications, 216, 139-158.

M

Maerten, L., Gillespie, P. & Pollard, D. D. (2002) Effects of local stress perturbation on secondary fault development. Journal of Structural Geology, 24, 145-153.

Malthe-Sørensen, A., Planke, S., Svensen, H. & Jamtveit, B. (in press) Formation of saucer-shaped sills. Geological Society, London, Special Publication, 7p.

Mayo, E. B. (1958) Lineament tectonics and some ore districts of the southwest. Mining Engineering, 10, 1169-1175.

McBirney, A. R. (1963) Factors governing the nature of submarine volcanism. Bulletin of Volcanology, 26, 455-469.

Menzies, M. A., Klemperer, S. L., Ebinger, C. J. & Baker, J. (2002) Characteristics of volcanic rifted margins. *In*: Menzies, M. A., Klemperer, S. L., Ebinger, C. J. & Baker, J. (eds.) *Volcanic rifted margins.* The Geological Society of America, Special Paper, 362, 1-14.

Morton, A. C., Dixon, J. E., Fitton, J. G., Macintyre, R. M., Smythe, D. K. & Taylor, P. N. (1988) *In*: Morton, A. C. & Parson, L. M. (eds.) *Early Tertiary volcanism and the opening of the NE Atlantic.* Geological Society, London, Special Publication, 39, 293-308.

Mudge, M. R. (1968) Depth control of some concordant intrusions. Geological Society of America Bulletin, 79, 315-332.

N

Naylor, P. H., Bell, B. R., Jolley, D. W., Durnall, P. & Fredsted, R. (1999) Palaeogene magmatism in the Faeroe-Shetland Basin: influences on uplift history and sedimentation. *In*: Fleet, A. J. & Boldy, S. A. R. (eds.) *Petroleum Geology of Northwest Europe: Proceedings of the 5th Conference*, Geological Society, London, 545-558.

O

P

Parsons, T., Sleep, N. & Thompson, G. (1992) Host rock rheology controls on the emplacement of tabular intrusions: implications for underplating of extending crust. Tectonics, 11, 1,348-1,356.

Peterson, D. W., Holcomb, R. T. Tilling, R. I. & Christiansen, R. L. (1994) Bulletin of Volcanology, 56, 343-360.

Pitcher, W. S. (1979) The nature, ascent and emplacement of granite magmas. Journal of the Geological Society of London, 136, 627-662.

Planke, S., Alvestad, E. & Eldholm, O. (1999) Seismic characteristics of basaltic extrusive and intrusive rocks. The Leading Edge, 18, 342-348.

Planke, S., Symonds, P., Alvestad, E. & Skogseid, J. (2000) Seismic volcanostratigraphy of large-volume basaltic extrusive complexes on rifted margins. Journal of Geophysical Research, 105, 19,335-19,351.

Pollard, D. D. (1973) Derivation and evaluation of a mechanical model for sheet intrusions. Tectonophysics, 19, 233-269.

Pollard, D. D. & Holzhausen, G. (1979) On the mechanical interaction between a fluid-filled fracture and the earth's surface. Tectonophysics, 53, 27-57.

Pollard, D. D. & Johnson, A. M. (1973) Mechanics of growth of some laccolithic intrusions in the Henry Mountains, Utah, II: Bending and failure of overburden layers and sill formation. Tectonophysics, 18, 311-354.

Pollard, D. D., Muller, O. H. & Dockstader, D. R. (1975) The form and growth of fingered sheet intrusions. Bulletin of the Geological Society of America, 86, 351-363.

Press, F. & Siever, R. (1994) *Understanding Earth.* W. H. Freeman and Company, New York.

Price, N. J. (1966) *Fault and joint development in brittle and semi-brittle rock.* Pergamon Press. 176p.

Q

R

Ramsay, J. G. & Huber, M. I. (1983) *The techniques of modern structural geology. Volume 1: Strain analysis*. Academic Press, 1-307.

Ramsay, J. G. & Lisle, R. J. (2000) *The techniques of modern structural geology. Volume 3: Applications of continuum mechanics in structural geology*. Academic Press, 701-1061.

Rasmussen, J. & Noe-Nygaard, A. (1970) Beskrivelse til geologiske kort over Færøerne i målestok 1:50.000. Danmarks Geologiske Undersøgelse, 11th Series, 24.

Rasmussen, J. & Noe-Nygaard, A. (1990) *The origin of the Faroe Islands*. Ministry of the Environment, Geological Survey of Denmark.

Raymond, A. C. & Murchison, D. G. (1988) Development of organic maturation in the thermal aureoles of sills and its relation to sediment compaction. Fuel, 67, 1,599-1,608.

Raymond, A. C. & Murchison, D. G. (1991) The relationship between organic maturation, the widths of thermal aureoles and the thickness of sills in the Midland Valley of Scotland and Northern England. Journal of the Geological Society, London, 148, 215-218.

Rickwood, P. C. (1990) The anatomy of a dyke and the determination of propagation and magma flow directions. *In*: Parker, Rickwood & Tucker (eds.) *Mafic dykes and emplacement mechanisms*. p. 81-100. Balkema, Rotterdam.

Ritchie, J. D. & Hitchen, K. (1996) Early Paleogenen offshore igneous activity to the northwest of the UK and its relationship to the North Atlantic igneous province. *In*: Knox, R. B. O' B., Corfield, R. M. & Dunay, R. E. (eds.) *Correlation of the Early Paleogenen in Northwest Europe*. Geological Society, London, Special Publication, 101, 63-78.

Ritchie, J. D., Gatliff, R. W. & Richards, P. C. 1999. Early Tertiary magmatism in the offshore NW UK margin and surrounds. In: Fleet, A. J. & Boldy, S. A. R. (eds.) *Petroleum Geology of Northwest Europe: Proceedings of the 5th Conference*, Geological Society, London, 573-584.

Roberts, D. G., Thompson, M., Mitchener, B., Hossack, J., Carmichael, S. & Bjørnseth, H.-M. (1999) Paleozoic to Tertiary rift and basin dynamics: mid-Norway to the Bay of Biscay – a new context for hydrocarbon prospectivity in the deep water frontier. *In*: Fleet, A. J. & Boldy, S. A. R. (eds.) *Petroleum Geology of Northwest Europe: Proceedings of the 5th Conference*, Geological Society, London, 7-40.

Robertson, T. & Haldane, D. (1937) The economic geology of the Central Coalfield: Area I, Kilsyth and Kirkintilloch. Memoir of the Geological Survey of Great Britain. 169p.

Rogers, N. W. & Gibson, I. L. (1977) The petrology and geochemistry of the Creag Dubh composite sill, Whiting Bay, Arran, Scotland. Geological Magazine, 114, 1-8.

S

Schirnick, C., Van den Bogaard, P. & Schmincke, H.-U. (1999) Cone sheet formation and intrusive growth of an oceanic island – The Miocene Tejeda complex on Gran Canaria (Canary Islands). Geology, 27, 207-210.

Schroot, B. M. & Schüttenhelm, R. T. E. (2003) Expressions of shallow gas in the Netherlands North Sea. Netherlands Journal of Geosciences, 82, 91-105.

Sclater, J. G. & Christie, P. A. F. (1980) Continental stretching: An explanation of the post-Mid-Cretaceous subsidence of the Central North Sea Basin. Journal of Geophysical Research, 85, 3,711-3,739.

Sheridan, R. E. (1981) Recent research on passive continental margins. Society of Economic Palaeontologists and Mineralogists Special Publication, 32, 39-55.

Sheriff, R. E. & Geldart, L. P. (1995) *Exploration seismology*. Cambridge University Press, 592 p.

Sibson, R. H. (1996) Structural permeability of fluid-driven fault-fracture meshes. Journal of Structural Geology, 18, 1031-1042.

Skogly, O. (1998) *Seismic characterization and emplacement of intrusives in the Vøring Basin.* University of Oslo, M.Sc. thesis, 140p.

Skogseid, J., Pedersen, T., Eldholm, O. & Larsen, B. T. (1992) Tectonism and magmatism during the NE Atlantic continental break-up: the Vøring Margin. *In*: Storey, B. C., Alabaster, T. & Pankhurst, R. J. (eds.) *Magmatism and the Causes of Continental Break-up.* Geological Society, London, Special Publication, 68, 305-320.

Smallwood, J. R. & Gill, C. E. (2002) The rise and fall of the Faroe-Shatland Basin: evidence from seismic mapping of the Balder Formation. Journal of the Geological Society, London, 159, 627-631.

Smallwood, J. R. & Maresh, J. (2002) The properties, morphology and distribution of igneous sills: modelling, borehole data and 3D seismic from the Faroe-Shetland area. *In*: Jolley, D. W. & Bell, B. R. (eds.) *The North Atlantic Igneous Province: Stratigraphy, tectonic, volcanic and magmatic processes.* Geological Society, London, Special Publication, 197, 271-306.

Smallwood, J. R. & White, R. S. (2002) Ridge-plume interaction in the North Atlantic and influence on continental breakup and seafloor spreading. *In*: Jolley, D. W. & Bell, B. R. (eds.) *The North Atlantic Igneous Province: Stratigraphy, tectonic, volcanic and magmatic processes*. Geological Society, London, Special Publication, 197, 15-37.

Smith, D. K. & Cann, J. R. (1999) Constructuing the upper crust of the Mid-Atlantic Ridge: A reinterpretation based on the Puna Ridge, Kilauea Volcano. Journal of Geophysical Resarch, 104, 25,379-25,399.

Smith, D. K., Cann, J. R., Dougherty, M. E., Lin, J., Spencer, S., MacLeod, C., Keeton, J., McAllister, E., Brooks, B., Pascoe, R. & Robertson, W. (1995) Journal of Volcanology and Geothermal Research, 67, 233-262.

Smythe, D., Chalmers, J., Skuce, A., Dobinson, A. & Mould, A. (1983) Early opening history of the North Atlantic – I. Structure and origin of the Faeroe-Shetland escarpment. Geophysical Journal of the Royal Astronomical Society, 72, 373-398.

Spencer, A. M., Birkland, Ø., Knag, G. Ø. & Fredsted, R. (1999) Petroleum systems of the Atlantic margin of northwest Europe. *In*: Fleet, A. J. & Boldy, S. A. R. (eds.) *Petroleum Geology of Northwest Europe: Proceedings of the 5th Conference*. Geological Society, London, 231-246.

Stuevold, L. M., Faerseth, R. B., Arnsen, L., Cartwright, J. & Möller, N. (2002) Polygonal faults in the Ormen Lange Field, Møre Basin, offshore Mid Norway. *In*: Van Rensbergen, P., Hillis, R. R. Maltman, A. J. & Morley, C. K. (eds.) *Subsurface sediment mobilization.* Geological Society, London, Special Publication, 216, 263-282.

Svensen, H., Planke, S., Malthe-Sørensen, A., Jamtveit, B., Myklebust, R., Eidem, T. R. & Rey, S. S. (2004) Release of methane from a volcanic basin as a mechanism for initial Eocene global warming. Nature, 429, 542-545.

T

Tate, M. P., Dodd, C. D. & Grant, N. T. (1999) The Northeast Rockall Basin and its significance in the evolution of the Rockall-Faeroes/ East Greenland rift system. *In*: Fleet, A. J. & Boldy, S. A. R. (eds.) *Petroleum Geology of Northwest Europe: Proceedings of the 5th Conference*. Geological Society, London, 391-406.

Tegner, C. Duncan, R. A., Bernstein, S. Brooks, C. K., Bird, D. K. & Storey, M. (1998) ^{40}Ar-^{39}Ar geochronology of tertiary mafic intrusions along the East Greenland rifted margin: Relation to flood basalts and the Iceland hotspot track. Earth and Planetary Science Letters, 156, 75-88.

Thompson, R. N. (1982) Magmatism of the British Tertiary Volcanic Province. Scottish Journal of Geology, 18, 49-107.

Thordarson, Th. & Self, S. (1993) The Laki (Skaftár Fires) and Grímsvötn eruptions in 1783-1785. Bulletin of Volcanology, 55, 233-263.

Trude, K. J. (2004) Kinematic indicators for shallow level igneous intrusion from 3D seismic data; evidence of flow direction and feeder location. *In*: Davies, R. J., Cartwright, J. A., Stewart, S. A., Lappin, M. & Underhill, J. R. (eds.) *3D Seismic Technology: Application to the Exploration of Sedimentary Basins*. Geological Society, London, Memoirs, 29, 209-217.

Trude, K. J., Cartwright, J. A., Davies, R. J. & Smallwood, J. R. (2003) A new technique for dating igneous sills. Geology, 31, 813-816.

Tweto, O. (1951) Form and structure of sills near Pando, Colorado. Geological Society of America Bulletin, 62, 507-532.

U

V

W

Waagstein, R. (1988) Structure, composition and age of the Faeroe basalt plateau. *In*: Morton, A. C. & Parson, L. M. (eds.) *Early Tertiary volcanism and the opening of the NE Atlantic.* Geological Society, London, Special Publication, 39, 225-238.

Waagestein, R., Hald, N., Jørgensen, O., Nielsen, P. H., Noe-Nygaard, A., Rasmussen, J. & Schönharting, G. (1984) Deep drilling on the Faroe Islands. Bulletin of the Geological Society of Denmark, 32, 133-138.

Waagestein, R., Guise, P. & Rex, D. (2002) K/Ar and $^{39}Ar/^{40}Ar$ whole-rock dating of zeolite facies metamorphosed flood basalts: the upper Paleocene basalts of the Faroe Islands, NE Atlantic. *In*: Jolley, D. W. & Bell, B. R. (eds.) *The North Atlantic Igneous Province: Stratigraphy, tectonic, volcanic and magmatic processes*. Geological Society, London, Special Publication, 197, 219-252.

Waddams, P. & Cordingley, T. (1999) The regional geology and exploration potential of the NE Rockall Basin. *In*: Fleet, A. J. & Boldy, S. A. R. (eds.) *Petroleum Geology of Northwest Europe: Proceedings of the 5th Conference*. Geological Society, London, 379-390.

Wadge, G., Walker, G. P. L. & Guest, J. E. (1975) The output of the Etna volcano. Nature, 255, 385-387.

Wadge, G. & Lopes, R. M. C. (1991) The lobes of lava flows on Earth and Olympus Mons, Mars. Bulletin of Volcanology, 54, 10-24.

Walker, G. P. L. (1975) A new concept of the evolution of the British Tertiary intrusive centres. Journal of the Geological Society of London, 131, 121-141.

Walker, G. P. L. (1989) Gravitational (density) controls on volcanism, magma chambers and intrusions. Australian Journal of Earth Sciences, 36, 149-165.

Walker, F. & Poldervaart, A. (1949) Karoo dolerites of the Union of South Africa. Geolgical Society of America Bulletin, 60, 591-706.

Walsh, J. J. & Watterson, J. (1988) Analysis of the relationship between displacement and dimensions of faults. Journal of Structural Geology, 10, 239-247.

Walsh, J. J., Nicol, A. & Childs, C. (2002) An alternative model for the growth of faults. Journal of Structural Geology, 24, 1669-1675.

Walsh, J. J., Bailey, W. R., Childs, C., Nicol, A. & Bonson, C. G. (2003) Formation of segmented normal faults: a 3-D perspective. Journal of Structural Geology, 25, 1251-1262.

White, R. S. (1988) A hot-spot model for early Tertiary volcanism in the NE Atlantic. *In*: Morton, A. C. & Parson, L. M. (eds.) *Early Tertiary volcansim and the opening of the NE Atlantic.* Geological Society, London, Special Publication, 39, 3-13.

White, R. S. (1992) Magmatism during and after continental break-up. *In*: Storey, B. C., Alabaster, T. & Pankhurst, R. J. (eds.) *Magmatism and the Causes of Continental Break-up.* Geological Society, London, Special Publication, 68, 1-16.

White, R. & McKenzie, D. (1989) Magmatism at rift zones: The generation of volcanic continental margins and flood basalts. Journal of Geophysical Research, 94, 7,685-7,729.

Williams, H. & McBirney, A. R. (1979) *Volcanology*. Freeman, Cooper & Co., San Francisco, 384p.

Wood, M. V., Hall, J. & Doody, J. J. (1988) Distribution of early Tertiary lavas in the NE Rockall Trough. *In*: Morton, A. C. & Parson, L. M. (eds.) *Early Tertiary volcanism and the opening of the NE Atlantic.* Geological Society, London, Special Publication, 39, 283-292.

X

Y

Yilmaz, Ö. (1987) *Seismic data processing*. Society of Exploration Geophysicists, Tulsa, 526p.

Z

Zenri, H. & Keer, L. M. (2001) Machanical analyses of the emplacement of laccoliths and lopoliths. Journal of Geophysical Research, 106, 13,781-13,792.